UNIVERSITÀ DI PARMA

UNIVERSITA' DEGLI STUDI DI PARMA

DOTTORATO DI RICERCA IN SCIENZE CHIMICHE

CICLO XXXVI

Synthesis and studies of small molecule- and calixarene-based ligands for interaction with biomacromolecules

Coordinatore:

Chiar.ma Prof.ssa Alessia Bacchi

Tutor:

Chiar.mo Prof. Francesco Sansone

Dottorando:

Davide Dell'Accantera

ANNI ACCADEMICI 2020/2021-2022/2023

ABSTRACT

Within the spectrum of biomolecules, proteins emerge as the primary agents orchestrating biological activities within organisms. Owing to their extensive variability in terms of structure, configuration, and constitution, proteins have been ingeniously utilized by nature to fulfill diverse roles, serving as enzymes, receptors, signaling molecules, and structural elements, and playing an important role in the immune system. Disruptions in the correct protein function or the protein-protein interaction between human cells and pathogens, are implicated in the pathogenesis of various human diseases. For this reason, proteins represent viable targets that can be leveraged to mitigate or potentially halt the progression of diseases. In protein targeting, small molecules have an affirmed role due to the development of many drugs based on several strategies such as inhibitors of enzymes. Supramolecular chemistry plays an important role in the disruption of protein-protein interactions thanks to the possibility of covering a surface area. From the standpoint of supramolecular interactions for protein targeting, recent findings highlight the promising approach centered on multi-target directed compounds (MTDCs). These compounds possess the capability to concurrently impact multiple targets, offering potential solutions for treating complex diseases. In the present thesis work, based on the established expertise of the research group, the current scientific interests, and ongoing collaborations, we developed both small molecule- and calixarene-based ligands for different types of proteins, all of biomedical interests.

The first chapter presents findings from a study focused on producing calix[4]arenes bearing amino acid units (peptidocalixarenes) able to interact with the SARS-CoV-2 virus. Our objective was to create ligands working as inhibitors of the interaction between the virus Spike protein and the ACE2 receptor of the mammalian cells. This part of the doctoral research, based on a previous molecular modeling analysis, is constituted by a significant synthetic effort aimed at the selective functionalization of the upper rim of the calix[4]arene with different pairs of amino acids. Unfortunately, the preliminary biological tests did not evidence an inhibitory activity of the produced peptidocalixarenes, but the work done provided new important knowledge about the possible selective functionalization of this macrocycle.

In the second chapter, we report the work on the synthesis and studies of compounds designed for the interaction with biomolecules involved in neurodegenerative diseases. In the first part, our attention is focused on ligands for α-synuclein, a protein involved in Parkinson's disease. The strategy behind this work is to exploit negatively charged calix[4]arenes blocked in a rigid cone geometry for the complexation of lysine residues. Complexation studies were performed to verify the ability of including this amino acid by using simple models. Moreover, through biological studies using an

engineered *Saccharomices cerevisiae* yeast model, the ability in disaggregating the toxic α-synuclein oligomers was successfully ascertained. In the second part, we deal with the synthesis of tolcapone analogs as stabilizers of the transthyretin tetramer, an amyloidogenic protein involved in neuropathies. Starting from a molecular docking investigation, two possible analogs were selected as potential stabilisers able to cross the blood brain barrier. After their synthesis, we tested their ability to stabilize the protein tetramer, their toxicity and lipophilicity. The crystal structure of their complexes with the transtyretin tetramer was determined by X-Ray diffraction showing the mode of binding of the two stabilisers.

The third chapter displays our work on the synthesis of two photosensitizers containing benzenesulfonamide-based inhibitors of human Carbonic Anhydrase (hCA) IX. The goal of this project is to exploit a possible synergistic effect between the inhibition of hCA IX, involved in the hypoxic tumor growth, and the photodynamic therapy, exploiting a photosensitizer. In this project, we worked on the synthesis of the two photosensitizers, the evaluation of the inhibition, and the production of singlet oxygen.

Finally, the fourth chapter describes the synthesis of saccharides and glycocalixarenes with the aim of developing immunostimulants against encapsulated bacteria. In the first part, we reported the synthesis of glycocalixarene functionalized at the upper rim with multiple copies of the capsular polysaccharide (CPS) repeating unit of *Streptococcus pneumoniae* serotype 19F. The second part is focused on the work performed at the Institut Pasteur, in Paris, for the synthesis of the CPS trisaccharide repeating unit of *Campylobacter Jejuni* serotypes HS 23/36. This trisaccharide, in the future, could be used both for the synthesis of oligomers and for the functionalization of calixarene scaffolds to develop synthetic saccharide-based immunogenic derivatives and vaccines against *C. jejuni* HS 23/36.

Chapter 1: Introduction

1. Protein Targeting

Proteins, the workhorses of cellular function, are pivotal in maintaining the intricate balance of biological processes within living organisms. The precise spatial and temporal regulation of protein localization is crucial for ensuring the proper functioning of cellular pathways and signalling networks[1–4]. Disruptions in the correct protein function are implicated in the pathogenesis of various human diseases, underscoring the importance of understanding the underlying molecular mechanisms governing protein localization and trafficking[5,6]. For this reason, proteins can be used as convenient targets for limiting or even stopping the incoming disease. In particular, in this chapter, we will introduce briefly on small molecules as inhibitors of enzymes and stabilizers of protein-protein interaction and calixarene-based ligands for peptide and proteins.

1.1 Small molecules ligands

Since the discovery of aspirin in 1889, small molecules have provoked great interest as potential drugs. Small compounds have consistently paved the way for significant advancements in medicine and have addressed medical challenges that were previously unmet, consequently preserving innumerable lives. Furthermore, these small compounds have played a critical role as chemical tools in biomedical exploration, contributing to the comprehension of disease mechanisms[7].

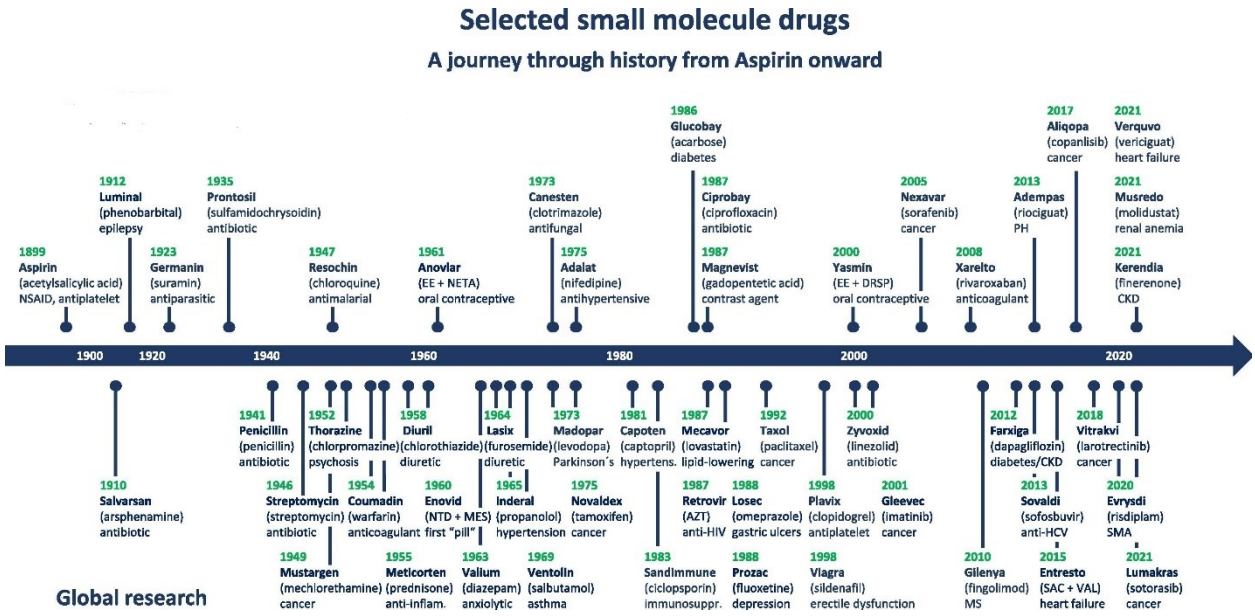

Figure 1: the time scale of the small compounds drugs. Image taken by reference[7].

Small molecules consistently diversify their modes of operation, conquering fresh target areas and expanding the conventional toolkit for drug exploration. Targeted covalent inhibitors, RNA-targeting small molecules or PROTACs activators are just a few examples of applications of small molecules.

1.1.1 Small molecule-based enzyme inhibitors

Roughly half of the orally administered drugs currently in clinical use exerts its pharmacological impact through the inhibition of enzymes, a function indeed carried out by small molecules[8].

In the realm of enzymatic reactions, compounds that exert influence on their activity rates go by the name of modulators, moderators, or modifiers[9]. The typical outcome is a reduction of the reaction rate, resulting in an inhibitory effect. Conversely, there are instances where the reaction rate is augmented, determining activation. Accordingly, these compounds are categorized as inhibitors or activators. Enzyme inhibitors serve diverse roles, finding applications as pharmaceutical agents in both human and veterinary medicine, as well as in herbicides and pesticides. Due to its considerable significance, the study of enzyme inhibition is extensively undertaken, contributing valuable insights into enzyme mechanisms[10] and playing a major role in pharmacological studies[11]. Enzymatic inhibitors can be classified into two main categories: reversible inhibitors, binding the enzyme through a non-covalent bond and producing an inhibitory action proportional to concentration, and irreversible inhibitors, with stoichiometric enzyme inhibition. For reversible inhibitors, it is possible to define a dissociation constant, K_i. A lower K_i indicates a stronger binding to the enzyme, with ideal values in the range of nM or pM to be considered an effective inhibitor. K_i represents the inhibitor concentration at which half of the enzyme sites are boundrequired to produce half maximum inhibition. In some cases, reversible inhibition occurs even when a labile covalent bond is involved, which can be broken, for example, by hydrolysis, at a rate similar to its formation. Irreversible inhibitors cause stoichiometric inhibition, with a ratio of one inhibitor per one enzyme, and they bind through a stable covalent bond[12]. Among the enzyme inhibitors, noteworthy for their impact on public health, we can cite the reversible inhibitors of angiotensin converting enzyme (ACE) and acetyl salicylic acid as irreversible inhibitor of cyclooxygenase. Angiotensin-converting enzyme inhibitors (ACE inhibitors or ACEIs) find extensive use in reducing blood pressure and minimizing cardiac oxygen consumption[13]. They are typically constituted by a functional group to interact with zinc ion (like sulfhydryl, phosphate or carboxylate group) blocking the zinc-based active site of ACE[14] (Fig. 2). Acetyl salicylic acid induces irreversible inhibition in cyclooxygenase by acetylating a serine at the active site, resulting in a stable modification that negatively impacts on the initial step in the prostaglandin biosynthesis from arachidonate. To restore the activity, new cyclooxygenase must be synthesized. Aspirin serves various purposes, functioning as an anti-inflammatory, antipyretic, and analgesic agent. Additionally, it is employed prophylactically to impede platelet aggregation and prevent coronary thrombosis (Fig. 2)[15].

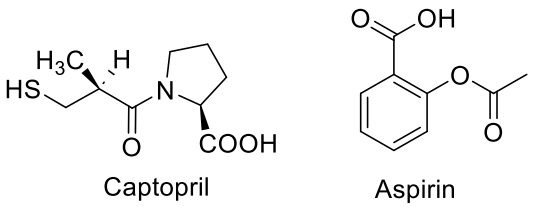

Figure 2: The molecular structure of Captopril, the first drug used as ACEI. The molecular structure of acetyl salicylic acid, inhibitor of cyclooxygenase.

1.1.2 Small molecules as protein stabilizers

Protein-protein interactions (PPIs) play a crucial role in the functioning of living organisms. Among the prominent strategies, the modulation of PPIs through small-molecule intervention is a key approach, achievable through two complementary methods: stabilization or inhibition. In this paragraph, we will focus on the stabilization of protein complexes.

Small-molecule stabilizers of PPIs exhibit two primary modes of action. Firstly, a stabilizer may attach to a single protein partner, enhancing the mutual binding affinity of the protein partners in an allosteric manner. Alternatively, the stabilizing molecule can bind to the interfacial surface of a protein complex, establishing contacts with both binding partners and thereby increasing their mutual binding affinity. Consequently, the distinct types will be referred to as allosteric (pertaining to one protein partner) or direct (involving at least two protein partners) PPI stabilizers[16].

An example of an allosteric PPI stabilizer is found in the case of microtubules (MTs). MTs consist of protein heterodimers comprising α- and β-tubulin. These αβ-heterodimers assemble into linear protofilaments, ultimately forming cylindrical polymers. MTs play crucial roles in both non-dividing and dividing cells[17]. Paclitaxel is one of the extensively investigated MT modulators. It demonstrates a high-affinity binding to a hydrophobic pocket located exclusively on the β -subunit of polymerized tubulin, thereby stabilizing the structures of polymerized MTs[18].

Amyotrophic lateral sclerosis (ALS), a motor neuron disease characterized by mutations in the gene encoding the dimeric enzyme superoxide dismutase 1 (SOD1), provides a second example[19]. Certain mutations in this gene lead to SOD1 monomerization and subsequent disordered protein aggregation[20]. In addressing this, some works that targeted the stabilization of the SOD1 dimer to hinder monomerization, employed small molecules as stabilizer to prevent aggregation[21].

1.2 Calixarene-based ligands

In the last decades, some researchers started to explore the possibility of exploiting larger molecules as potential drugs, resorting for example to molecules typically studied in the field of supramolecular chemistry such as the macrocycles. Apart the case of cyclodextrins, that however are used as carrier and in such role are at the basis of numerous formulations where the actual drug is a small molecule[22],

there is not yet any example of approved therapeutics constituted by similar systems. Nevertheless, some of the results reported are of interest and can assume relevance due to their ability to disrupt the PPIs. Indeed, these interactions occur through interaction of wide surface area (1000-4000 $Å^2$) resulting undruggable by small molecules for many years[23].In contrast, in the last two decades, several examples were reported in literature on the use of supramolecules in the PPI disruption, due to the possibility to cover a large surface area[24]. In the perspective of the supramolecules for protein targeting, results interesting the more recent approach based on the so-called multi-target directed compounds (MTDCs), able of simultaneously affecting more than a single target in the treatment of multifaceted diseases characterized by a complex pathoetiology[25–28].

In the framework of this thesis, it is interesting the use of calixarenes for interaction with proteins that in the last years produced noteworthy examples and data[29].

Through the condensation of p-tert-butylphenol and formaldehyde in a basic environment, different calix[n]arenes (Fig. 3, on the left) can be selectively obtained as cyclic oligomers of different sizes depending on the cation associated with the base (NaOH or KOH)[30]. The wide diffusion of calixarenes as scaffolds, in particular of calix[4]arene, is due to the high versatility in selective functionalization of the hydroxyl groups (called lower rim) or positions in para to them (called upper rim). The most common and most easily prepared calixarenes are those with 4, 6 and 8 phenolic units. The conformational mobility of the calixarene scaffold is influenced by the number of phenol units in the macrocycle. Calix[6]- and calix[8]arenes, due to their larger size allowing rotation of the aromatic rings around the methylene bridges, exhibit considerable flexibility. In contrast, calix[4]arene, can result blocked in the so-called cone geometry when the boundary conditions make possible a network of hydrogen bonding among the hydroxyl groups. Moreover, when functionalized at the lower rim with alkyl groups larger than ethyl, the calix[4]arene can adopt four distinct geometries (cone, partial cone, 1,3-alternate, and 1,2-alternate), that cannot interconvert one into the other and can be selectively produced and isolated by exploiting proper conditions for the lower rim functionalization (Fig. 3, right).

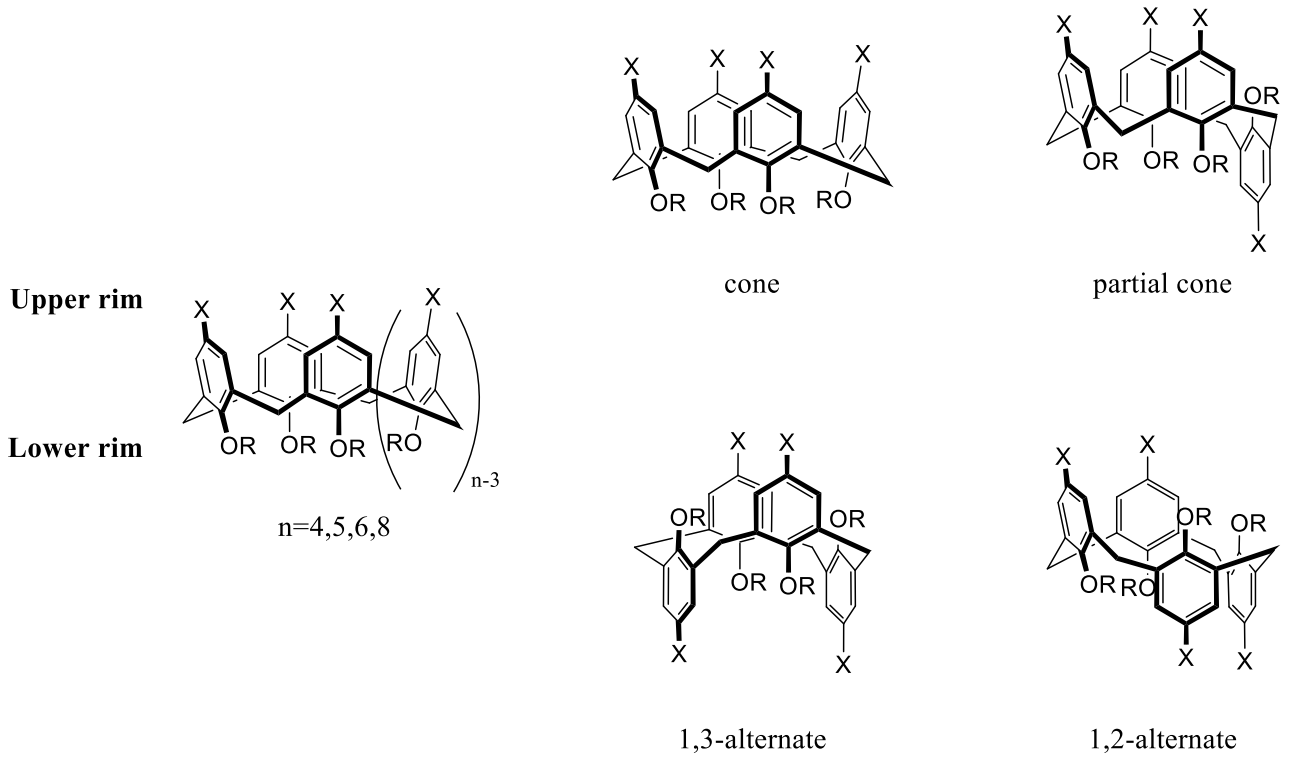

Figure 3: General structure of a calix[n]arene and possible conformations of calix[4]arene

The advantageous capability to selectively modulate the conformational mobility is evident when designing ligands and receptors based on the calixarene scaffold. Depending on the specific goal, they can be designed to be adaptable and mobile, conforming to the target shape (induced fit), or rigid and preorganized, to leverage entropic effects.. As mentioned above, calix[4]arenes unsubstituted at the lower rim adopt a rigid cone structure, promoted by a circular arrangement of robust hydrogen bonds between the OH groups (Fig. 4, left). Conversely, cone calix[4]arenes functionalized at the lower rim with four alkyl groups larger than ethyl undergo maintain a residual flexibility that allows a rapid interconversion in solution between two conformers (Fig. 4, right) termed flattened or pinched cone. In these structures, two distal phenol rings align parallel, while the remaining two tilt outward.

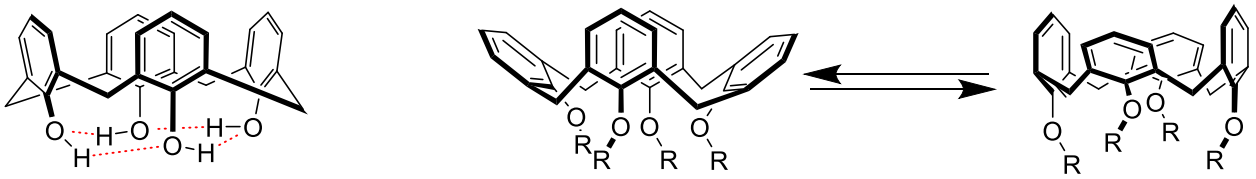

Figure 4: (left) rigid cone structure of a calix[4]arene with free OH groups at the lower rim; (right) interconversion between the two pinched or flattened cone conformations of calix[4]arenes functionalized at the lower rim with four alkyl groups larger than ethyl.

Calixarenes are versatile scaffolds and they found different applications for interaction with medically relevant biomolecules. Often, to this aim, calixarenes were functionalized with sugars or peptides leading to the new classes of calixarenes named peptido- and glycocalixarenes[31].

The conjugation of amino acids or small peptides to obtain peptidocalixarenes was performed through their terminal amino or carboxylic group, obtaining N-linked[32] and C-linked[33] peptidocalixarenes, respectively. These compounds found different applications: as crystal-growth modifiers[34], for recognition of protein surface[35], disruption of protein-protein interaction (PPI)[36], DNA delivery[37]. An example are the peptidocalix[4]arenes designed as mimics of vancomycin. The vancomycin group of antibiotics constitutes an intriguing class of biologically active molecules, exerting their effects through a relatively straightforward molecular recognition process. These antibiotics have the ability to bind to the terminal L-lysyl-D-alanyl-D-alanine (L-Lys-D-Ala-D-Ala) sequence of the cell wall mucopeptide precursors in Gram-positive bacteria, leading to the inhibition of cell wall growth and eventual cell lysis. To replicate the binding mode of vancomycin, a macrobicyclic calix[4]arene ligand, belonging to the class of upper rim N-linked peptidocalix[4]arenes, was developed (Fig. 5). This ligand has a pseudopeptide bridge at the 1,3 positions of the upper rim. The results reported for this compound showed a significant and selective antibacterial activity[38], ascribable to its ability of complexing the D-Ala-D-Ala residue[39].

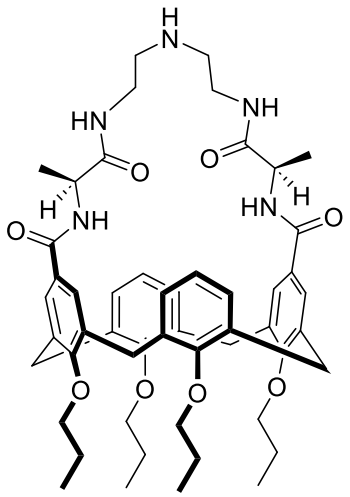

Figure 5: Molecular structure of peptidocalixarene as mimic of vancomycin.

Compared to the peptides, carbohydrates have a low affinity for their receptors. To contrast this problem, Nature frequently exploits the phenomenon called multivalency that entails the simultaneous interaction of more units of the same saccharide with multiple copies of carbohydrate binding sites to enhance the affinity for the receptor, the strength and selectivity of the interaction. To mimic the same mechanism, calixarenes have proved to be a good scaffold for multi presentation of sugar units[40]. Lectins are proteins with a high specificity for binding to carbohydrates that are integrated into glycoconjugates leading to the agglutination of specific cells or triggering cascade processes into cells. These proteins are involved in cellular and molecular recognition, playing various roles in biological recognition phenomena, both physiologic and pathologic, that encompass

cells, carbohydrates, and proteins[41]. Glycocalixarenes showed a good inhibition ability of bacterial[42], viral[43] and tumor[44] lectins. An example is that with cholera toxin (CT), an AB_5 multimeric protein where the five identical B binding units recognize the pentasaccharide of the GM1 ganglioside present on the cell surface. In this context, a calix[5]arene was specifically designed (Fig. 6), featuring five GM1 oligosaccharide units at the upper rim connected through an appropriate spacer. This arrangement facilitates and make in principle possible the simultaneous complexation of the five saccharide units of a single macrocycle by the five CT recognition sites, resulting in the formation of a 1:1 complex, however not yet demonstrated. The inhibitory activity of this macrocyclic ligand proved highly effective, showing a remarkable multivalent effect with a 20,000-fold increase per single GM1 ganglioside[45].

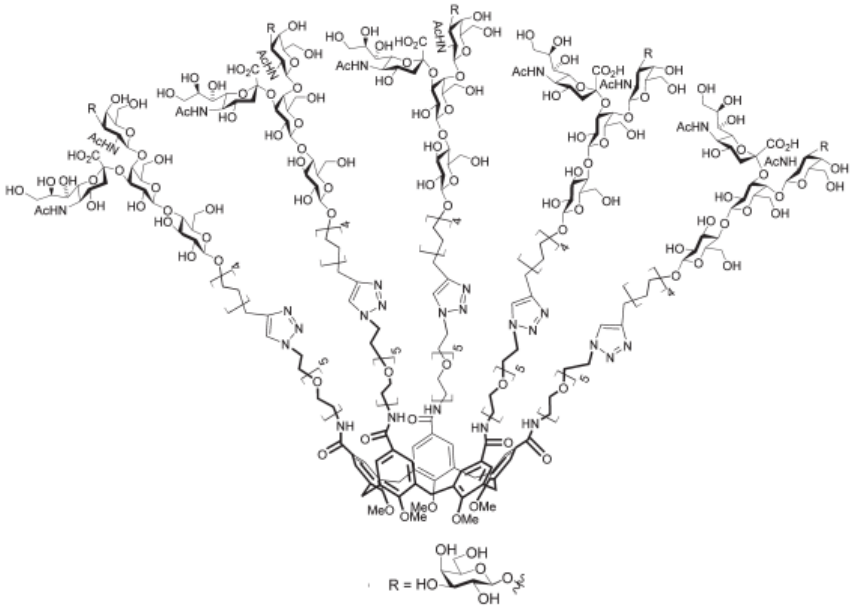

Figure 6: molecular structure of calixarene as inhbitor of GM1 ganglioside. Image adapted by reference[45].

The use of calixarene for interaction with protein is possible not only through functionalization with biomolecules. This is the case of the positively and negatively charged calixarenes that exploit the multi-presentation of charged functional groups, like guanidinium or sulfonate, to interact with protein. An example was reported by De Mendoza demonstrating that a positively charged tetra(guanidinomethyl)calixarene (Fig.7) can restore the structural integrity of a damaged protein-protein interaction (PPI) in a mutated form of p53, a protein implicated in various human cancers. The wild-type p53 functions as a tetramer, regulating DNA repair or apoptosis in response to DNA damage. However, in mutated p53, the tetrameric assembly is destabilized due to the absence of a critical ion pair interaction. Guanidino-calixarene reinstates the wild-type tetrameric structure by interacting, like a harpoon, simultaneously with four Glu carboxylates of the protein through its four guanidinium groups[46].

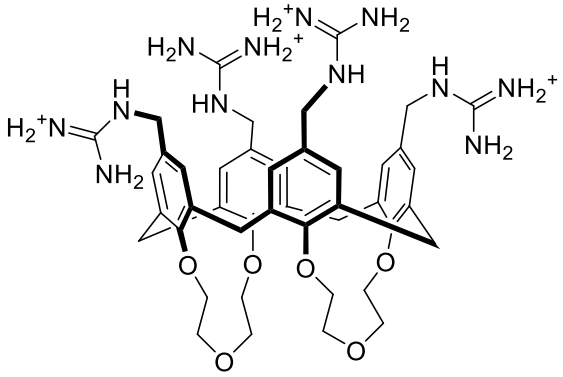

Figure 7: Molecular structure of guanidinio-calixarene.

2. Thesis outlook

In this introduction, we have presented various examples aimed at discussing the concepts expounded in the following chapters of this thesis. Within the broad realm of small molecules serving as protein ligands, enzyme inhibitors play a pivotal role in scientific research and drug development. On the other hand, the stabilization of proteins has proven to be a significant facet of Protein-Protein Interactions (PPIs). Furthermore, calixarenes have demonstrated their versatility as scaffolds for designing ligands targeting proteins and biomolecules. In this doctoral work, both small molecules and calixarenes were employed to craft optimal ligands by adapting the molecular design to the project's requirements and the pertinent literature.

Building upon these concepts, the first chapter elucidates the design and synthesis of peptidocalix[4]arenes tailored to inhibit the SARS-CoV-2 virus. Our objective was to create molecules capable of interacting with the viral Spike protein, a pivotal factor in the infection process, with the ultimate goal of impeding its biological activity and preventing cellular infection.

The second chapter focuses on the development of various ligands for interacting with amyloidogenic proteins implicated in neurodegenerative diseases. This includes calixarene-based ligands designed for interaction with α-synuclein, a protein associated with Parkinson's disease, and two small molecule-based ligands for stabilizing transthyretin, an amyloidogenic protein linked to transthyretin amyloidosis. The use of these two distinct approaches stems from the diverse strategies employed to prevent amyloid fibril formation.

In the third chapter, the inhibition of carbonic anhydrases IX is addressed using a small molecule-based approach. This decision is informed by previous research from our group, aiming to exploit the inhibition of carbonic anhydrases IX, implicated in hypoxic tumor growth, combined with the photodynamic therapy to possibly achieve a synergistic effect.

The final chapter details the use of glycocalixarenes as potential immunostimulant against bacterial infections. As explained above, calixarene serves as an excellent scaffold for the multi-presentation of carbohydrate units. Consequently, we designed and developed two calix[4]- and calix[6]arenes exposing the repetitive unit of *Streptococcus pneumoniae* 19F capsular polysaccharide. Additionally, during a six-month period in Paris, at the Institut Pasteur, we were engaged in the synthesis of the trisaccharide repeating unit of the *Campylobacter jejuni* capsular polysaccharide.

3. Bibliography

(1) McEver, R. P. Selectins: Lectins That Initiate Cell Adhesion under Flow. *Current Opinion in Cell Biology* **2002**, *14* (5), 581–586. https://doi.org/10.1016/S0955-0674(02)00367-8.

(2) Leckband, D.; Sivasankar, S. Mechanism of Homophilic Cadherin Adhesion. *Current Opinion in Cell Biology* **2000**, *12* (5), 587–592. https://doi.org/10.1016/S0955-0674(00)00136-8.

(3) Lutz, R. J. Role of the BH3 (Bcl-2 Homology 3) Domain in the Regulation of Apoptosis and Bcl-2-Related Proteins. *Biochemical Society Transactions* **2000**, *28* (2), 51–56. https://doi.org/10.1042/bst0280051.

(4) Supuran, C. T. Structure and Function of Carbonic Anhydrases. *Biochemical Journal* **2016**, *473* (14), 2023–2032. https://doi.org/10.1042/BCJ20160115.

(5) Waheed, A.; Sly, W. S. Carbonic Anhydrase XII Functions in Health and Disease. *Gene* **2017**, *623*, 33–40. https://doi.org/10.1016/j.gene.2017.04.027.

(6) Pinu, F. R.; Villas-Boas, S. G.; Aggio, R. Analysis of Intracellular Metabolites from Microorganisms: Quenching and Extraction Protocols. *Metabolites* **2017**, *7* (4), 53. https://doi.org/10.3390/metabo7040053.

(7) Beck, H.; Härter, M.; Haß, B.; Schmeck, C.; Baerfacker, L. Small Molecules and Their Impact in Drug Discovery: A Perspective on the Occasion of the 125th Anniversary of the Bayer Chemical Research Laboratory. *Drug Discovery Today* **2022**, *27* (6), 1560–1574. https://doi.org/10.1016/j.drudis.2022.02.015.

(8) Hopkins, A. L.; Groom, C. R. The Druggable Genome. *Nature Reviews Drug Discovery* **2002**, *1* (9), 727–730. https://doi.org/10.1038/nrd892.

(9) *Enzymes and Their Inhibitors: Drug Development*; Simons, H. J. S., Claire, Ed.; CRC Press: Boca Raton, 2004. https://doi.org/10.1201/9780203414583.

(10) Cleland, W. W. 3 Steady-State Kinetics. In *The Enzymes*; Sigman, D. S., Boyer, P. D., Eds.; Academic Press, 1990; Vol. 19, pp 99–158. https://doi.org/10.1016/S1874-6047(08)60196-1.

(11) *Design of Enzyme Inhibitors as Drugs, Volume 2*; Sandler, M., Smith, H. J., Sandler, M., Smith, H. J., Eds.; Oxford University Press: Oxford, New York, 1994.

(12) Saboury, A. A. Enzyme Inhibition and Activation: A General Theory. *Journal of the Iranian Chemical Society* **2009**, *6* (2), 219–229. https://doi.org/10.1007/BF03245829.

(13) Herman, L. L.; Padala, S. A.; Ahmed, I.; Bashir, K. Angiotensin-Converting Enzyme Inhibitors (ACEI). In *StatPearls*; StatPearls Publishing: Treasure Island (FL), 2023.

(14) Zheng, W.; Tian, E.; Liu, Z.; Zhou, C.; Yang, P.; Tian, K.; Liao, W.; Li, J.; Ren, C. Small Molecule Angiotensin Converting Enzyme Inhibitors: A Medicinal Chemistry Perspective. *Frontiers in Pharmacology* **2022**, *13*.

(15) Roskoski, R. Modulation of Enzyme Activity. In *xPharm: The Comprehensive Pharmacology Reference*; Enna, S. J., Bylund, D. B., Eds.; Elsevier: New York, 2007; pp 1–11. https://doi.org/10.1016/B978-008055232-3.60042-X.

(16) Thiel, P.; Kaiser, M.; Ottmann, C. Small-Molecule Stabilization of Protein–Protein Interactions: An Underestimated Concept in Drug Discovery? *Angewandte Chemie International Edition* **2012**, *51* (9), 2012–2018. https://doi.org/10.1002/anie.201107616.

(17) Inoué, S.; Sato, H. Cell Motility by Labile Association of Molecules : The Nature of Mitotic Spindle Fibers and Their Role in Chromosome Movement. *Journal of General Physiology* **1967**, *50* (6), 259–292. https://doi.org/10.1085/jgp.50.6.259.

(18) Nogales, E.; Grayer Wolf, S.; Khan, I. A.; Ludueña, R. F.; Downing, K. H. Structure of Tubulin at 6.5 Å and Location of the Taxol-Binding Site. *Nature* **1995**, *375* (6530), 424–427. https://doi.org/10.1038/375424a0.

(19) Andersen, P. M.; Nilsson, P.; Keränen, M. L.; Forsgren, L.; Hägglund, J.; Karlsborg, M.; Ronnevi, L. O.; Gredal, O.; Marklund, S. L. Phenotypic Heterogeneity in Motor Neuron Disease Patients with CuZn-Superoxide Dismutase Mutations in Scandinavia. *Brain* **1997**, *120* (10), 1723–1737. https://doi.org/10.1093/brain/120.10.1723.

(20) Hough, M. A.; Grossmann, J. G.; Antonyuk, S. V.; Strange, R. W.; Doucette, P. A.; Rodriguez, J. A.; Whitson, L. J.; Hart, P. J.; Hayward, L. J.; Valentine, J. S.; Hasnain, S. S. Dimer Destabilization in Superoxide Dismutase May Result in Disease-Causing Properties: Structures of Motor Neuron Disease Mutants. *Proceedings of the National Academy of Sciences* **2004**, *101* (16), 5976–5981. https://doi.org/10.1073/pnas.0305143101.

(21) Ray, S. S.; Nowak, R. J.; Brown, R. H.; Lansbury, P. T. Small-Molecule-Mediated Stabilization of Familial Amyotrophic Lateral Sclerosis-Linked Superoxide Dismutase Mutants against Unfolding and Aggregation. *Proceedings of the National Academy of Sciences* **2005**, *102* (10), 3639–3644. https://doi.org/10.1073/pnas.0408277102.

(22) Wankar, J.; Kotla, N. G.; Gera, S.; Rasala, S.; Pandit, A.; Rochev, Y. A. Recent Advances in Host–Guest Self-Assembled Cyclodextrin Carriers: Implications for Responsive Drug Delivery and Biomedical Engineering. *Advanced Functional Materials* **2020**, *30* (44), 1909049. https://doi.org/10.1002/adfm.201909049.

(23) Sable, R.; Jois, S. Surfing the Protein-Protein Interaction Surface Using Docking Methods: Application to the Design of PPI Inhibitors. *Molecules* **2015**, *20* (6), 11569–11603. https://doi.org/10.3390/molecules200611569.

(24) van Dun, S.; Ottmann, C.; Milroy, L.-G.; Brunsveld, L. Supramolecular Chemistry Targeting Proteins. *Journal of the American Chemical Society.* **2017**, *139* (40), 13960–13968. https://doi.org/10.1021/jacs.7b01979.

(25) L. Bolognesi, M. Polypharmacology in a Single Drug: Multitarget Drugs. *Current Medicinal Chemistry* **2013**, *20* (13), 1639–1645.

(26) Bolognesi, M. L.; Cavalli, A. Multitarget Drug Discovery and Polypharmacology. *ChemMedChem* **2016**, *11* (12), 1190–1192. https://doi.org/10.1002/cmdc.201600161.

(27) Ramsay, R. R.; Popovic-Nikolic, M. R.; Nikolic, K.; Uliassi, E.; Bolognesi, M. L. A Perspective on Multi-Target Drug Discovery and Design for Complex Diseases. *Clinical and Translational Medicine* **2018**, *7* (1), 3. https://doi.org/10.1186/s40169-017-0181-2.

(28) Viayna, E.; Sola, I.; Di Pietro, O.; Munoz-Torrero, D. Human Disease and Drug Pharmacology, Complex as Real Life. *Current Medicinal Chemistry* **2013**, *20* (13), 1623–1634.

(29) Baldini, L.; Casnati, A.; Sansone, F. Multivalent and Multifunctional Calixarenes in Bionanotechnology. *European Journal of Organic Chemistry* **2020**, *2020* (32), 5056–5069. https://doi.org/10.1002/ejoc.202000255.

(30) Arduini, A.; Casnati, A. Calixarenes. In *Macrocycle Synthesis: A Practical Approach*; Parker, D., Ed.; Oxford University Press, 1996; p 0. https://doi.org/10.1093/oso/9780198558415.003.0007.

(31) Casnati, A.; Sansone, F.; Ungaro, R. Peptido- and Glycocalixarenes: Playing with Hydrogen Bonds around Hydrophobic Cavities. *Accounts of Chemical Research* **2003**, *36* (4), 246–254. https://doi.org/10.1021/ar0200798.

(32) Sansone, F.; Barboso, S.; Casnati, A.; Fabbi, M.; Pochini, A.; Ugozzoli, F.; Ungaro, R. Synthesis and Structure of Chiral Cone Calix[4]Arenes Functionalized at the Upper Rim with L-Alanine Units. *European Journal of Organic Chemistry* **1998**, *1998* (5), 897–905. https://doi.org/10.1002/(SICI)1099-0690(199805)1998:5<897::AID-EJOC897>3.0.CO;2-K.

(33) Lazzarotto, M.; Sansone, F.; Baldini, L.; Casnati, A.; Cozzini, P.; Ungaro, R. Synthesis and Properties of *Upper Rim C* -Linked Peptidocalix[4]Arenes. *European Journal of Organic Chemistry* **2001**, *2001* (3), 595–602. https://doi.org/10.1002/1099-0690(200102)2001:3<595::AID-EJOC595>3.0.CO;2-#.

(34) Goh, C. Y.; Baldini, L.; Casnati, A.; Jones, F.; Mocerino, M.; Ogden, M. I.; Sansone, F.; Ungaro, R. Upper-Rim Acidic Peptidocalixarenes as Crystal Growth Modifiers. *Supramolecular Chemistry* **2014**, *26* (7–8), 488–499. https://doi.org/10.1080/10610278.2014.891738.

(35) Francese, S.; Cozzolino, A.; Caputo, I.; Esposito, C.; Martino, M.; Gaeta, C.; Troisi, F.; Neri, P. Transglutaminase Surface Recognition by Peptidocalix[4]Arene Diversomers. *Tetrahedron Letters* **2005**, *46* (10), 1611–1615. https://doi.org/10.1016/j.tetlet.2005.01.078.

(36) Wei, Y.; McLendon, G. L.; Case, M. A.; Purring, C. B.; Yu, T.; Hamilton, A. D.; Lin, Q.; Park, H. S.; Lee, C.-S. Disruption of Protein–Protein Interactions: Design of a Synthetic Receptor That Blocks the Binding of Cytochrome c to Cytochrome c Peroxidase. *Chemical Communications.* **2001**, No. 17, 1580–1581. https://doi.org/10.1039/b104142h.

(37) Bagnacani, V.; Franceschi, V.; Bassi, M.; Lomazzi, M.; Donofrio, G.; Sansone, F.; Casnati, A.; Ungaro, R. Arginine Clustering on Calix[4]Arene Macrocycles for Improved Cell Penetration and DNA Delivery. *Nature Communications* **2013**, *4* (1), 1721. https://doi.org/10.1038/ncomms2721.

(38) Casnati, A.; Fabbi, M.; Pelizzi, N.; Pochini, A.; Sansone, F.; Unguro, R.; Di Modugno, E.; Tarzia, G. Synthesis, Antimicrobial Activity and Binding Properties of Calix[4]Arene Based

Vancomycin Mimics. *Bioorganic & Medicinal Chemistry Letters* **1996**, *6* (22), 2699–2704. https://doi.org/10.1016/S0960-894X(96)00493-3.

(39) Frish, L.; Sansone, F.; Casnati, A.; Ungaro, R.; Cohen, Y. Complexation of a Peptidocalix[4]Arene, a Vancomycin Mimic, with Alanine-Containing Guests by NMR Diffusion Measurements. *Journal of Organic Chemistry* **2000**, *65* (16), 5026–5030. https://doi.org/10.1021/jo0001784.

(40) Sansone, F.; Casnati, A. Multivalent Glycocalixarenes for Recognition of Biological Macromolecules: Glycocalyx Mimics Capable of Multitasking. *Chemical Society Reviews* **2013**, *42* (11), 4623–4639. https://doi.org/10.1039/C2CS35437C.

(41) Rutishauser, U.; Sachs, L. Cell-to-Cell Binding Induced by Different Lectins. *Journal of Cell Biology* **1975**, *65* (2), 247–257. https://doi.org/10.1083/jcb.65.2.247.

(42) Cecioni, S.; Lalor, R.; Blanchard, B.; Praly, J.-P.; Imberty, A.; Matthews, S. E.; Vidal, S. Achieving High Affinity towards a Bacterial Lectin through Multivalent Topological Isomers of Calix[4]Arene Glycoconjugates. *Chemistry – A European Journal* **2009**, *15* (47), 13232–13240. https://doi.org/10.1002/chem.200901799.

(43) Chakroun, K.; Taouai, M.; Porkolab, V.; Luczkowiak, J.; Sommer, R.; Cheneau, C.; Mathiron, D.; Ben Maaouia, M. A.; Pilard, S.; Abidi, R.; Mullié, C.; Fieschi, F.; Cragg, P. J.; Halary, F.; Delgado, R.; Benazza, M. Low-Valent Calix[4]Arene Glycoconjugates Based on Hydroxamic Acid Bearing Linkers as Potent Inhibitors in a Model of Ebola Virus Cis-Infection and HCMV-gB-Recombinant Glycoprotein Interaction with MDDC Cells by Blocking DC-SIGN. *Journal of Medicinal Chemistry* **2021**, *64* (19), 14332–14343. https://doi.org/10.1021/acs.jmedchem.1c00818.

(44) André, S.; Sansone, F.; Kaltner, H.; Casnati, A.; Kopitz, J.; Gabius, H.-J.; Ungaro, R. Calix[n]Arene-Based Glycoclusters: Bioactivity of Thiourea-Linked Galactose/Lactose Moieties as Inhibitors of Binding of Medically Relevant Lectins to a Glycoprotein and Cell-Surface Glycoconjugates and Selectivity among Human Adhesion/Growth-Regulatory Galectins. *ChemBioChem* **2008**, *9* (10), 1649–1661. https://doi.org/10.1002/cbic.200800035.

(45) Garcia-Hartjes, J.; Bernardi, S.; Weijers, C. A. G. M.; Wennekes, T.; Gilbert, M.; Sansone, F.; Casnati, A.; Zuilhof, H. Picomolar Inhibition of Cholera Toxin by a Pentavalent Ganglioside GM1os-Calix[5]Arene. *Organic and Biomolecular Chemistry* **2013**, *11* (26), 4340–4349. https://doi.org/10.1039/C3OB40515J.

(46) Gordo, S.; Martos, V.; Santos, E.; Menéndez, M.; Bo, C.; Giralt, E.; de Mendoza, J. Stability and Structural Recovery of the Tetramerization Domain of P53-R337H Mutant Induced by a Designed Templating Ligand. *Proceedings of the National Academy of Sciences* **2008**, *105* (43), 16426–16431. https://doi.org/10.1073/pnas.0805658105.

Chapter 2: Synthesis of peptidocalix[4]arenes as ligands of SARS-CoV-2 Spike protein

1. Introduction

Coronavirus Disease 2019 (COVID-19) is a Severe Acute Respiratory Syndrome caused by a virus named Coronavirus 2 (SARS-CoV-2). The first cases of infection were reported in the city of Wuhan (China) in December 2019[1], and due to its rapid spread worldwide, the World Health Organization (WHO) declared a state of emergency on March 11, 2020[2]. To frontage the spreading of the virus, since the first weeks scientific research produced a huge effort to find an efficient treatment or a vaccine, leading the WHO to declare the end of the emergency state on 5 May 2023[3].

1.1 Structure of SARS-CoV-2 and mechanism action

SARS-CoV-2 belongs to the coronavirus family, specifically the β-coronaviruses. The name is derived from the characteristic circular shape of the virion, adorned with distinctive protrusions known as Spike glycoproteins. These viruses can infect humans and animals and are associated with developing various diseases, ranging from common colds to more severe conditions such as Middle East Respiratory Syndrome (MERS) and Severe Acute Respiratory Syndrome (SARS), which can lead to fatal outcomes. Specifically, SARS-CoV-2 primarily affects the upper and lower respiratory tracts but can also cause damage to other organs and systems. The infection is asymptomatic in most cases, while about a third of cases exhibit flu-like symptoms, and a smaller minority experience moderate to severe effects[4,5].

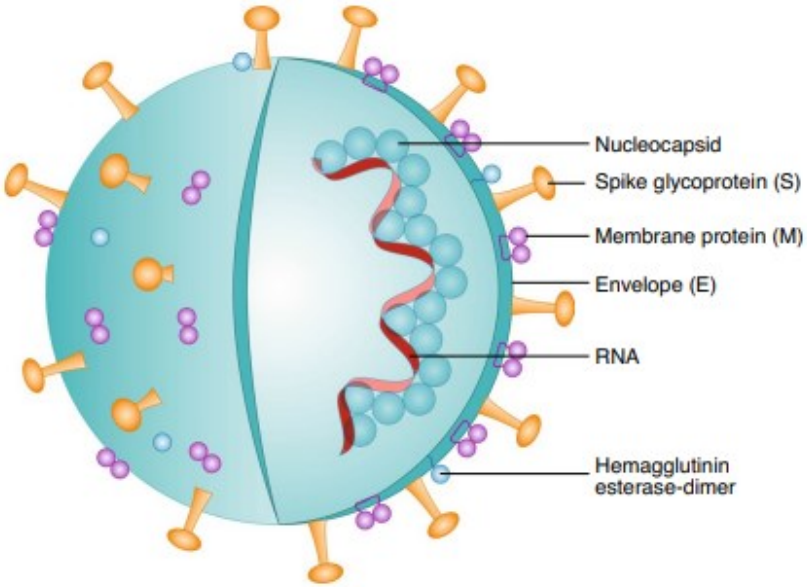

Figure 1: Structure of SARS-CoV-2. Imagine adopted by reference[6].

SARS-CoV-2 is an RNA virus, with its genome consisting of a single positive-strand RNA enclosed within a nucleocapsid. The genome encodes for several non-structural proteins (NSPn), three of

which are essential for viral replication: Papain-like protease (PLpro), Main protease (3CLpro), and RNA-dependent RNA polymerase (RdRp). Once inside the target cells, the virus's genome is released and translated through protein synthesis. Both proteases are responsible for cleaving the expressed proteins into functional units, while the polymerase facilitates viral genome replication by synthesizing a negative-strand RNA as a template[7]. Given their importance, these non-structural proteins have sparked significant interest in the scientific community as potential targets for pharmacological therapies[8–11].

The main role in the initial phase of the infection process is played by the Spike (S) glycoprotein. The S protein enables the virus to anchor to the cell membrane and facilitates its subsequent entry into the host cell. The interaction between the Spike protein and the host organism's Angiotensin Converting Enzyme 2 (ACE2) cellular receptor is at the core of this process. The S protein consists of 1273 amino acids, divided into two regions: the S1 and S2 subunits. The S1 subunit of the SARS-CoV-2 Spike protein is a highly flexible region and includes the Receptor Binding Domain (RBD), through which the virus can recognize and bind to the ACE2 receptor, specifically in the region of the aminopeptidase N. In this subunit, we also find the N-terminal domain (NTD) and the C-terminal domain (CTD). The S2 subunit, responsible for viral entry and fusion, includes the Fusion Peptide (FP), heptapeptide repeat sequence 1 (HR1), heptapeptide repeat sequence 2 (HR2), transmembrane domain (TM), and cytoplasmic domain (CT). The repetitive HR1 and HR2 heptapeptides interact to form a six-helix structure called 6-HB, which allows the virus to approach the plasma membrane. FP, through hydrophobic residues, can disrupt and connect the lipid bilayers of the cell membrane, thus promoting virus internalization[12,13] (Figure 2).

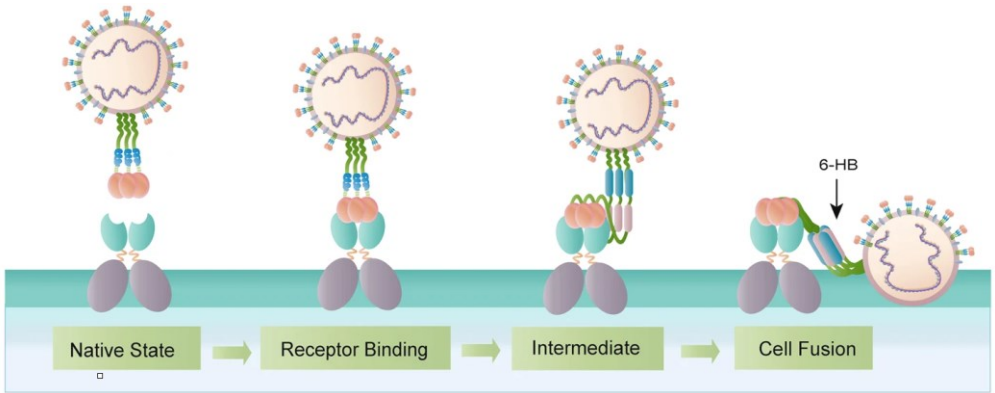

Figure 2: Representation of viral fusion process. Imagine taken by reference[13]

Given the essential role of the Spike protein in the development of viral infection, it is crucial to define its structural characteristics. The determination of the ACE2-Spike protein complex through X-ray diffraction has allowed the identification of the nature of the different interactions between the

RBD and the Protease Domain (PD) of the ACE2 receptor. From the resolved structure, shown in Figure 3, it is evident that a large region of the RBD is exposed in correspondence to the alpha helix α1 of the ACE2-PD. It is precisely in this region of the ACE2-Spike protein interface that we find the key interactions for the formation of the complex, divided into three different clusters known as receptor binding motifs (RBMs). In zone A, there are hydrogen bonds between the residues Tyr41, Gln42, Lys353, and Arg357 of ACE2, and Gln498, Thr500, and Asn501 of the RBD. Zone B presents a hydrogen bond between the RBD's Tyr453 and ACE2's His34, as well as an ionic pair between Lys417 and Asp30. In zone C, there is a hydrogen bond between Gln474 and Gln24 and a weak interaction between Phe486 and Met82 of the RBD and ACE2, respectively[14] (Figure 3).

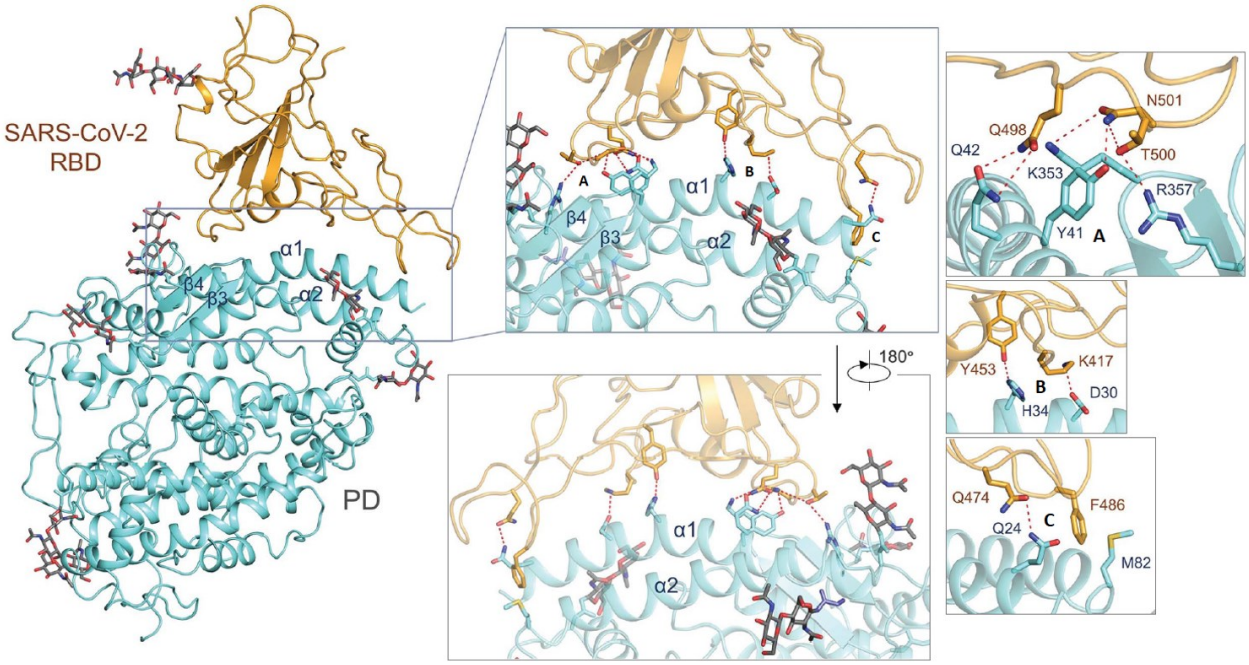

Figure 3: Complex between ACE2 and the RBD of SARS-CoV-2. Division into three regions (A-B-C) of the interactions responsible for the complex formation. Image taken from reference[14].

Blocking the SARS-CoV-2 S-protein function would render the virus harmless. Several studies and related research aim to inhibit the interaction between the S protein and the ACE2 receptor, thus preventing the formation of the complex and blocking the infection process at its onset. In a study by Chaoyong Yang and colleagues[15] (Figure 4), a bivalent circular aptamer is proposed to bind to the RBD of the Spike protein, as confirmed by molecular docking studies. The high affinity and, above all, the inhibitory efficacy are validated through in vitro tests. In addition to these results, the proposed aptamers possess several properties that distinguish them from traditional antibodies. These properties include reduced size, minimal immunogenic risk, stability, and programmability. The latter allows them to be easily assembled for the development of highly specific and efficient molecular recognition devices.

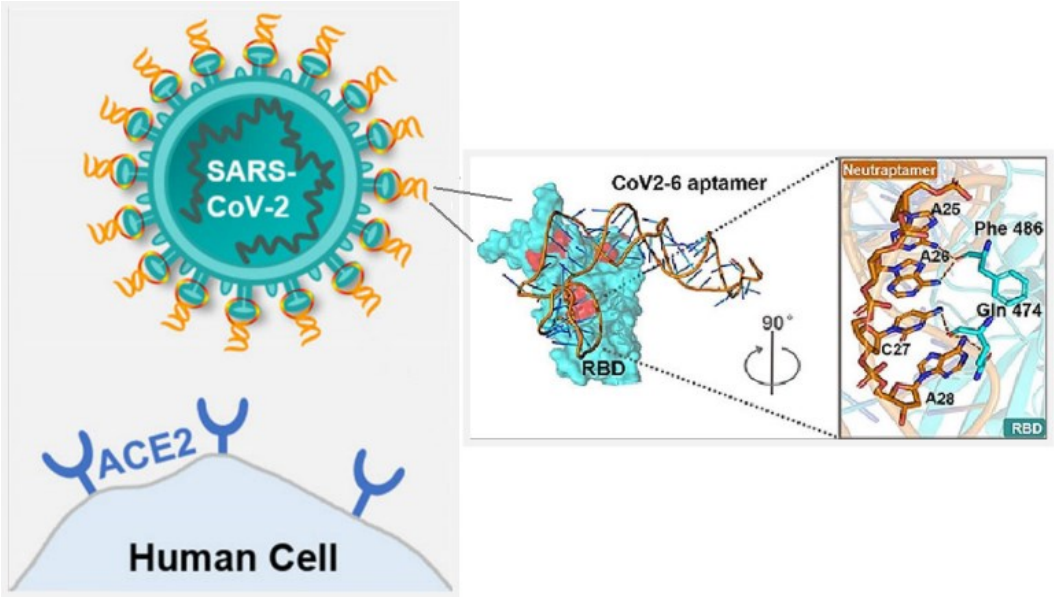

Figure 4: Inhibition of complex ACE2-S protein exploiting the aptamer strategy. Image taken from reference[15].

Another research group, utilizing the trimeric structure of SARS-CoV-2 S-protein in the pre-fusion conformation[16], conducted a virtual screening with the aim of exploring the DrugBank database for small molecules as potential inhibitors of the S-protein[17]. Special attention is directed towards the internal cavity of the S glycoprotein (Figure 5A), which imparts the S2 subunit with the necessary conformational flexibility for the formation of the 6-HB and, therefore, the predisposition for cell fusion. The occupation of this cavity would prevent the internalization of the virus and, therefore, the progression of the infection.

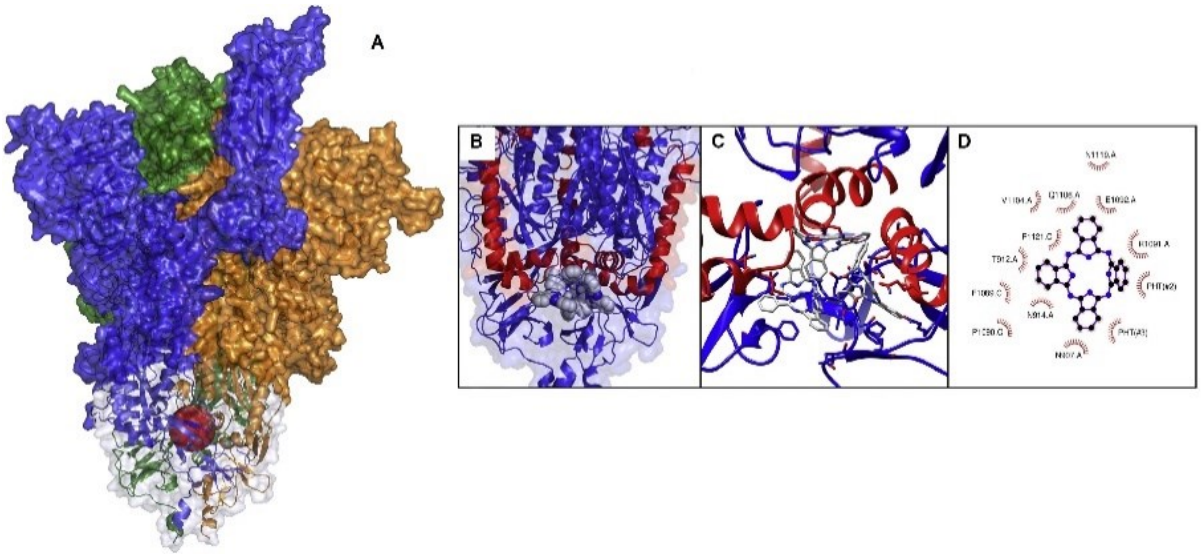

Figure 5:(A) Inner cavity of the Spike glycoprotein in the pre-fusion conformation. (B-D) Complex of three phthalocyanines with the S protein, and visualization of contacts. Reprinted from Virus Research, 286, 198068, Romeo, A.; Iacovelli, F.; Falconi, M., Targeting the SARS-CoV-2 spike glycoprotein prefusion conformation: virtual screening and molecular dynamics simulations applied to the identification of potential fusion inhibitors, 2, © (2020), with permission from Elsevier[17]

The results of this research reveal how phthalocyanine is a potential inhibitor as it can form several hydrophobic interactions with the residues exposed inside the cavity (Figure 5D).

Another example in the literature is the study by Galia Blum and colleagues[18], where the inhibitory effect on the formation of the ACE2-Spike protein complex by a compound found in nature, kobophenol A, is evaluated. Molecular docking studies identify two binding sites of the inhibitor: one at the interface between ACE2 and RBD (Figure 6), and the other located in an internal pocket of the ACE2 receptor. The results demonstrate and confirm the dual inhibitory action of kobophenol A.

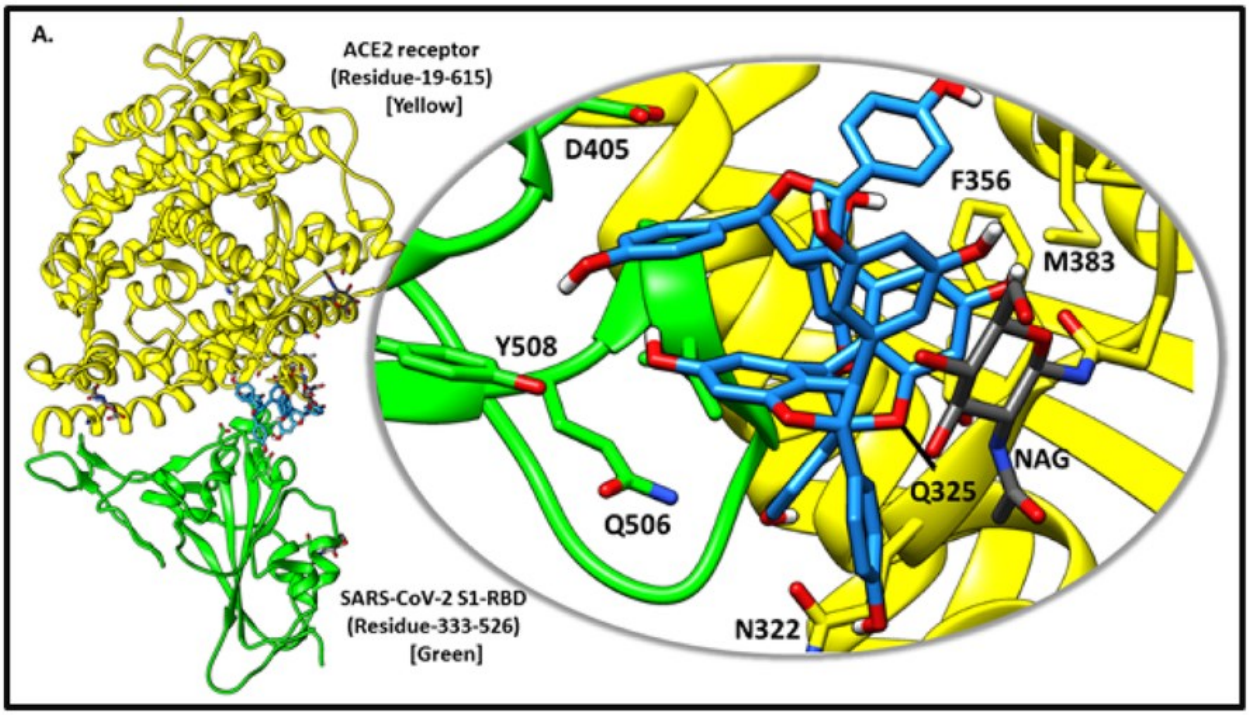

Figure 6: Illustration of the SARS-CoV-2 spike S1 receptor-binding domain (green) bound with the ACE2 receptor (yellow) and Kobophenol A (blue). Image taken by reference[18]

There are various strategies that can inhibit the function of the Spike glycoprotein. In a study by Irene Yarovsky and colleagues[19], the focus is on the structure of the ACE2 receptor, particularly on the importance of conformational flexibility in the process of binding to the RBD site. Molecular modelling studies and binding enthalpy calculations determine the effect of the inhibitor MLN-4760 (Figure 7C) on the binding affinity between the Spike protein and the ACE2 receptor. When the inhibitor is bound to the ACE2 receptor, a conformational rearrangement occurs (Figure 7B), leading to reduced accessibility of the active site for the formation of the ACE2-Spike protein complex.

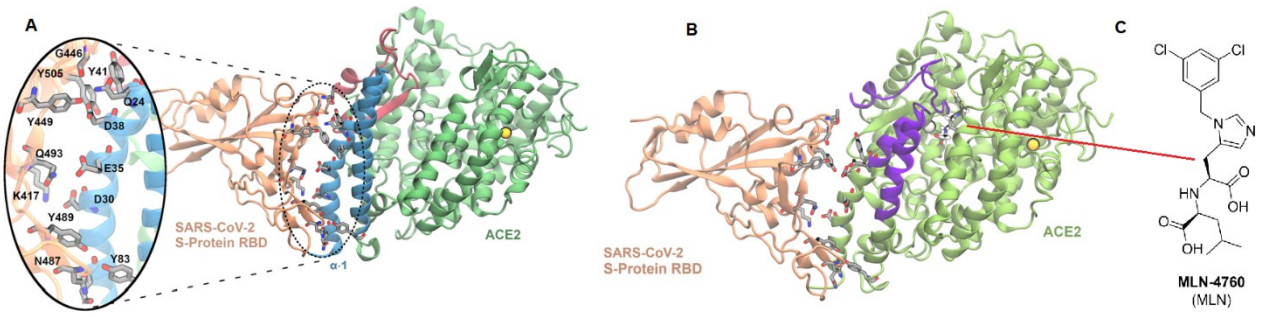

Figure 7:(A) ACE2-RBD complex, (B) Structural rearrangement of the exposed surface of ACE2 receptor induced by the presence of MLN-4760, (C) Molecular structure of the inhibitor MLN-4760. Image take by reference[19].

The previously demonstrated and well-known property of calixarenes to bind the surface of proteins[20–22] led us to design calix[4]arenes functionalized with amino acids at the upper rim, exploiting the experience of our research group[23,24], as potential inhibitors of the binding between S-protein and ACE2. The selection of the scaffold is due to the observation of the similar size that exists between calix[4]arene and zone A of the S protein. The functionalization of calix[4]arene with amino acids displayed by ACE2 would have to bring to compounds able to interact with zone A of S-protein and thus prevent its complexation with the cell membrane receptor.

2. Results and discussions

2.1 Design of ligands

In the initial phase of this project, our focus revolved around refining the ligand design. To ascertain the optimal amino acids for facilitating the most effective interactions, our starting point was the molecular docking analyses documented in Carlo Alberto Vezzoni's doctoral dissertation[25]. These molecular docking simulations started from the X-ray structure of the complex formed between the spike protein's RBD and ACE2, as elucidated by Qiang Zhou and his research collaborators (PDB 6M17)[14]. Within this structure, the RBD featured three distinct RBMs, as describe in the introduction and, among them, RBM A stood out due to its paramount interactions, outlined in the provided illustration (Figure 8). Among the results obtained in the previous doctoral thesis, there was the evidence that a calix[4]arene with four amino acid units at the upper rim, Arg and Asn in that case, has dimensions sufficient to cover the area of RBM A (Figure 8). This kind of macrocycle, if the exposed amino acids could establish effective interactions with those of RBM A, thus could be able to inhibit the binding of this S-protein region with ACE2.

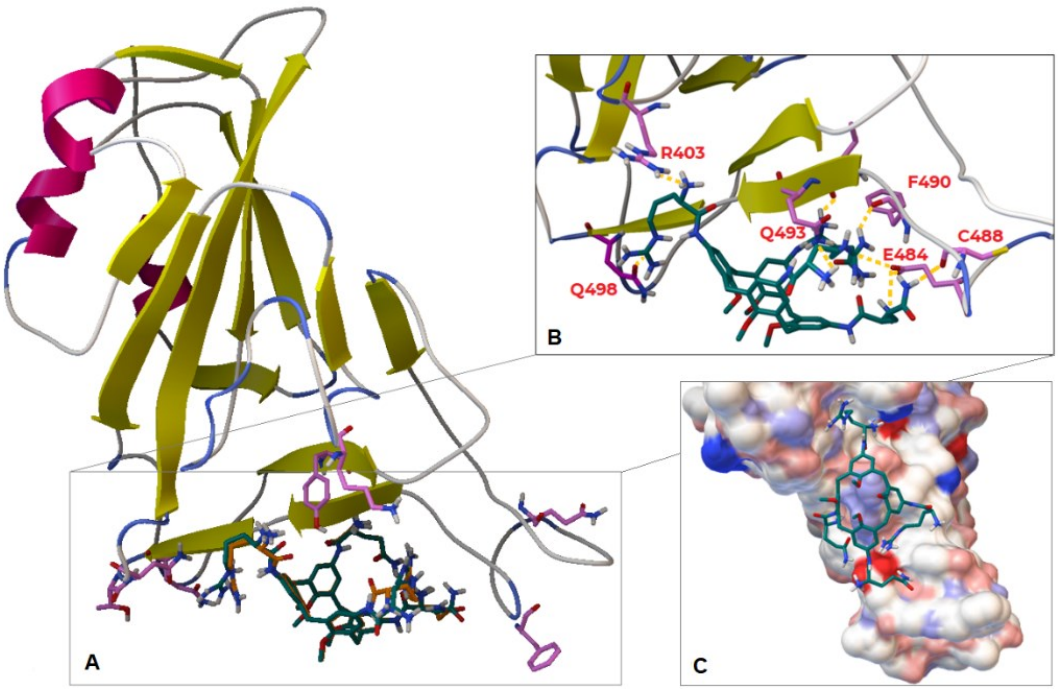

Figure 8: (A) SI4-RBM Complex; (B) Specific interactions between SI4 and RBM; (C) SI4-RBM complex with receptor electron density visualization. Image taken by reference[25]

For synthetic reasons, we considered only calix[4]arenes functionalized with two pairs of amino acids at the upper rim, in both possible arrangements, distal (1,3-2,4) and vicinal (1,2-3,4) as reported in Figure 9.

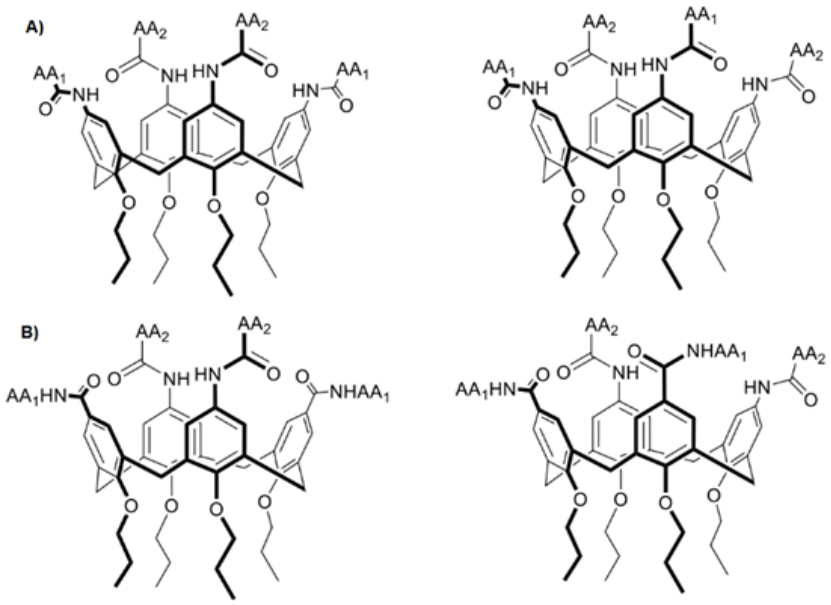

Figure 9: representative structures of ligands. A) distal and vicinal representation of C-linked peptidocalixarenes; B) distal and vicinal representation of C,N-linked peptidocalixarenes.

The experience of our research group in synthetizing peptidocalixarenes led us to design calixarenes functionalized at the upper rim with amino acids exploiting the formation of the amide bond through two possible approaches[23,26], that generate C-linked and C,N-linked derivatives (Figure 9). These two

options allow to selectively conjugate the two different amino acids in the desired positions of the macrocyclic upper rim, exploiting some already established procedures, which will be described below, set up to distinguish the phenol rings and differentiate their functionalization. Arg as the main interacting amino acid. Glutamic acid (Glu) and Glutamine (Gln) also appear to contribute significantly to the interaction, given their consistent presence in the ligands that showed higher efficiency. Although absent in the ligands with the highest affinity, Lys holds a significant position at the interface between RBD and ACE2. Considering these findings, we deemed it appropriate to use these aforementioned amino acid residues for calix[4]arene functionalization.

2.2 Synthesis of the ligands

The synthesis of the different peptidocalixarenes was carried out in parallel, focusing firstly on the synthesis of the two calixarene scaffolds necessary for the C- and C,N-linkage. As the side chains of the amino acids are involved in the interaction between S-protein and ACE2, the type of connection with the calixarene platform was substantially considered relevant depending on the chance it would have given us of selectively introducing the amino acid units on the macrocycle. Based on established procedures[25–27] allowing the functionalization of the calix[4]arene upper rim with carboxylic and nitro groups as well as the protection of amino groups, the C- and C,N-linkage seemed to ensure the achievement of this goal.

Said that, the two amino acid units of each desired pair can be situated in the peptidocalixarene either in distal position (1,3 or 2,4) or in vicinal position (1,2 or 3,4). A further evaluation regarding the impact of the different polarity and/or amphiphilicity of the peptidocalixarene on the inhibition process also prompted us to synthesize compounds functionalized on the phenolic unit at the lower rim with ethoxyethyl or propyl groups. Both groups ensure the cone geometry, when linked in proper experimental conditions, but ethoxyethyl groups provide higher solubility in polar environment, hopefully aqueous, and prevent self-association processes in solution.

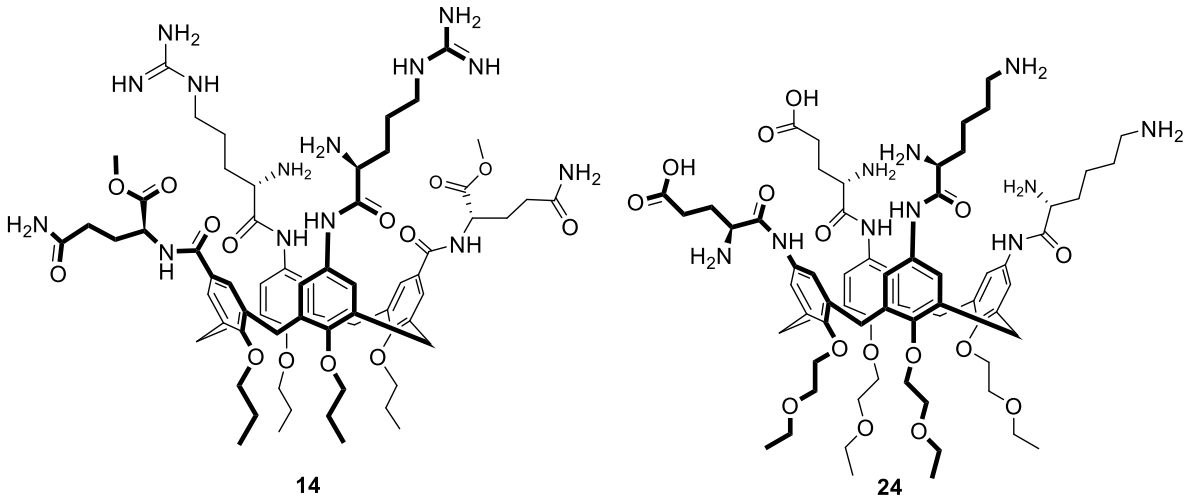

Figure 10: structure of the two target ligands

In Figure 10, compounds **14** and **24** are depicted, which, accounting for all these variables, have been identified as the synthetic targets of this work. Compound **14** is functionalized with Gln and Arg in a distal disposition (1,3-2,4) on the upper rim, and with propyl groups on the lower rim. Compound **24** is functionalized with Glu and Lys in a vicinal disposition (1,2-3,4) on the upper rim, and with ethoxyethyl groups on the lower rim. The selection of amino acids is based on the results of molecular docking and the reagent availability in our laboratory.

The design of the calixarenes scaffold was imposed to optimize the synthetic strategy obtaining a selective functionalization at the upper rim with the higher possible yield. Therefore, we synthesized the C,N-linked ligand to obtain a distal disposition and the C-linked ligand for the vicinal disposition.

2.2.1 C,N-linked ligand

Considering the experience of our research group, we started with the C,N-linked ligand synthesis. The synthesis of the desired compound is divided into two steps: the synthesis of the scaffold and its functionalization with amino acids.

2.2.1.1 Synthesis of the calixarene platform

Considering the synthetic strategies reported in the literature[25], we started with the idea to replicate the preparation of the 5,17-dicarboxylic acid-11,23-dinitro-25,26,27,28-tetrapropoxycalix[4]arene **4** as reported in the scheme 1, which describes the pathway already exploited by our research group. However, in this procedure, the nitration of the upper rim from **1** to **2** is performed on the basis of a statistical approach. This reaction, is carried out in a mixture of glacial acetic and 65% nitric acid with continuous monitoring by TLC and obtaining all possible products: mono-, di-(1,2 and 1,3), tri- e tetranitro.

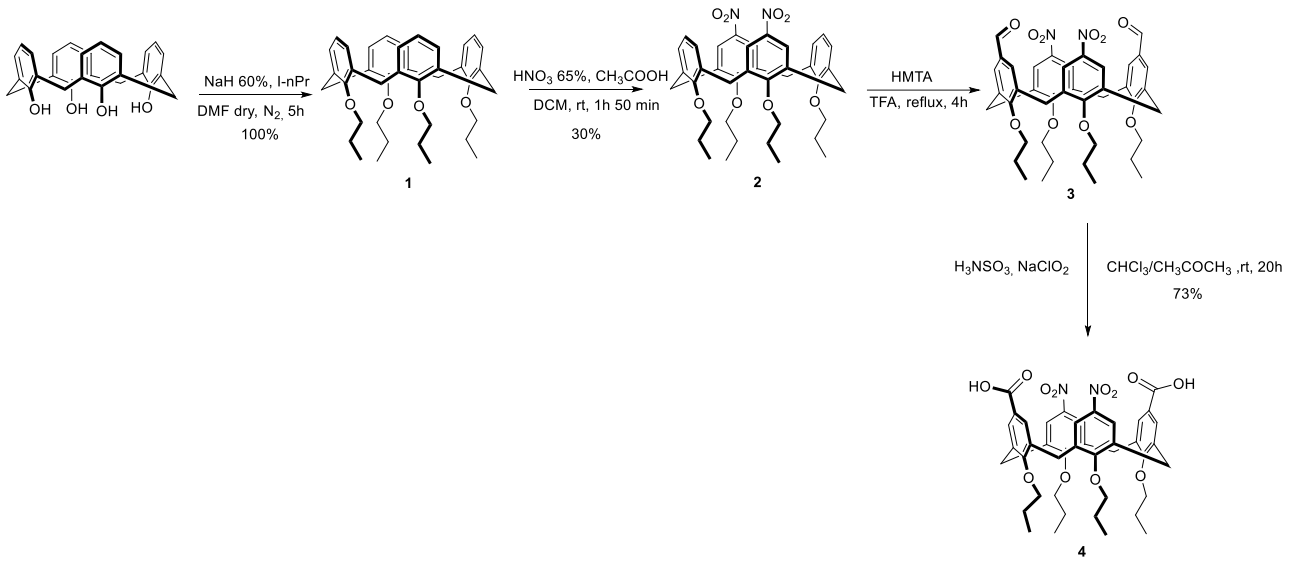

Scheme 1: Synthesis of 5,17-dicarboxylic acid-11,23-dinitro-25,26,27,28-tetrapropoxycalix[4]arene. The yield reported was taken by reference[25].

Moreover, the isolation of the distal functionalized dinitro-calixarene often requires purification through column chromatography instead of the precipitation from DCM/MeOH, as reported in the literature. For all these reasons, the nitration step usually results with rather low yield. Therefore, we decided to use an alternative approach as reported in scheme 2. This synthetic strategy is based on the use of the nosyl group at the lower rim (compound **6**) to carry out a regioselective reaction at the upper one to obtain the 1,3-dinitro functionalization (compound **7**). The electron-withdrawing effect of nosyl group linked to the phenol oxygen, in fact, strongly reduces the reactivity at the *para* position of the aromatic ring leading to a selective reaction, as reported by Lhoták and colleagues[28]. With the aim of having two different types of functional units at the upper rim reciprocally located in distal position, this strategy present also the advantage that the two nitro groups are on the two already alkylated phenolic rings. In fact, it had already been established that attempting to alkylate the hydroxyl groups of a calix[4]arene in para position at the nitro function did not yield the expected outcome, likely due to the strong electron-withdrawing effect of NO_2.

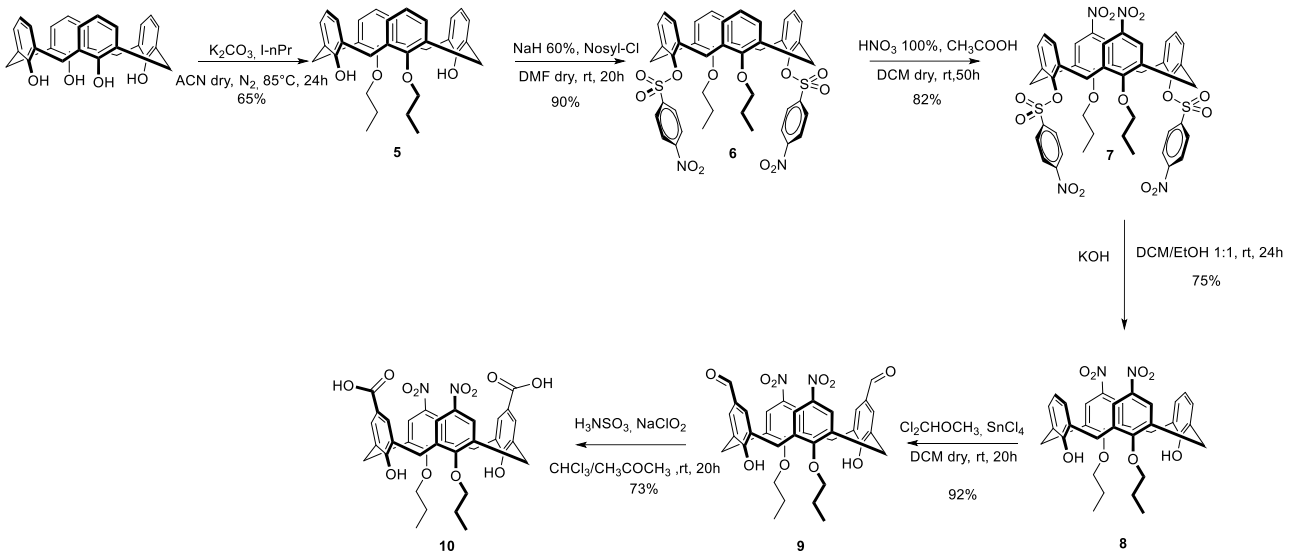

Scheme 2: Synthesis of calixarene platform.

The initial step consisted in the well-known dialkylation reaction at the lower rim of the tetrahydroxycalix[4]arene to give **5**. K_2CO_3 was employed as a base for the deprotonation of two distal hydroxyl groups. The alkylating agent utilized was 1-iodopropane. Subsequently, to achieve regioselective control over the functionalization of the upper rim, a nosyl protection was carried out on the two free phenolic hydroxyl groups. The protection reaction was carried out employing NaH as a base to allow the deprotonation of the OH groups. As evidence of successful protection and achievement of **6**, the absence in the ^{1}H NMR spectrum in $CDCl_3$ of signal related to the hydroxyl protons and the appearance of signals corresponding to the aromatic protons of the nosyl groups were observed, along with upfield shifts of signals of the propyl groups due to the shielding effect of the introduced aromatic units. Then, was nitrated with 100% HNO_3 and CH_3COOH to yield compound **7** whit high yields having only the distal configuration of the nitro derivative. The subsequent step involved deprotection from the nosyl group under basic conditions, utilizing KOH to hydrolyze the sulfonic ester bond. The resulting product **8** was purified through simple recrystallization in methanol, with a 75% yield. ^{1}H-NMR and mass analyses confirmed the desired product's identity. As previously documented in literature, a comparison with the ^{1}H-NMR spectrum of the analogous calix[4]arene bearing the two nitro groups in para positions to the hydroxyls ensured that the functionalization in compound **8** was indeed as expected and represented in the scheme.

In a prior thesis work[25], an attempt to alkylate the free hydroxyls in compound **8** had been made, but unexpectedly, rotation of one of the two rings carrying the nitro group occurred, resulting in the derivative blocked in partial cone geometry. For this reason, the decision was taken to proceed with the formylation of compound **8** and postpone the exhaustive alkylation of the lower rim. The Gross formylation was performed using dichloromethyl methyl ether as the formyl group source and $SnCl_4$

as a catalyst, yielding compound **9**. Following purification through reprecipitation in DCM/MeOH, product **9** was characterized. Subsequently, the formyl groups were oxidized using $NaClO_2$ in the presence of sulfamic acid, which acted as a proton donor to generate $HClO_2$ (oxidizing agent) *in situ* and as a scavenger for HClO to prevent undesired reactions. The resulting product **10** was purified through chromatographic separation and obtained with a yield of 73%. Considering no literature references were available, compound **10** was thoroughly characterized.

Ultimately, an attempt was made to alkylate the remaining free hydroxyl functionalities with propyl chains. Initially, a well-established procedure was followed, utilizing 60% NaH as a base, 1-iodopropane as an alkylating agent (Scheme 3), and DMF as the solvent. Not only does NaH allow the deprotonation of the hydroxyl groups, but the presence of Na^+ ion and the use of DMF were expected to ensure the maintenance of the cone geometry. Nevertheless, despite these conditions, the ^{1}H-NMR spectrum (Figure 11b) of the reaction product evidenced the presence of a mixture of different types of geometries for the calixarenes in solution.

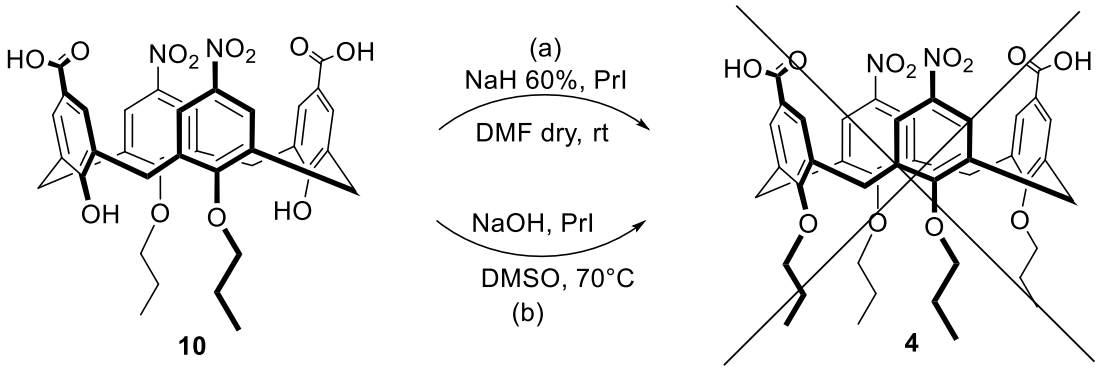

Scheme 3: Attempts to synthesize compound 4

Given the obtained result, another already-known alkylation procedure was carried out, involving NaOH as the base and DMSO as the solvent[29]. The ^{1}H-NMR spectrum (Figure 11c) of the isolated product from this reaction disclosed the formation of the propyl ester of the two carboxy groups but lacking alkylation at the two phenolic OH. This identification was based on the appearance of signals relative to the propyl group (δ = 4.47 and 2.31 ppm) that were more deshielded with respect those of the alkyl chains at the lower rim (δ = 4.15 and 1.88 ppm), along with the presence of the hydroxyl group signal at δ = 8.48 ppm.

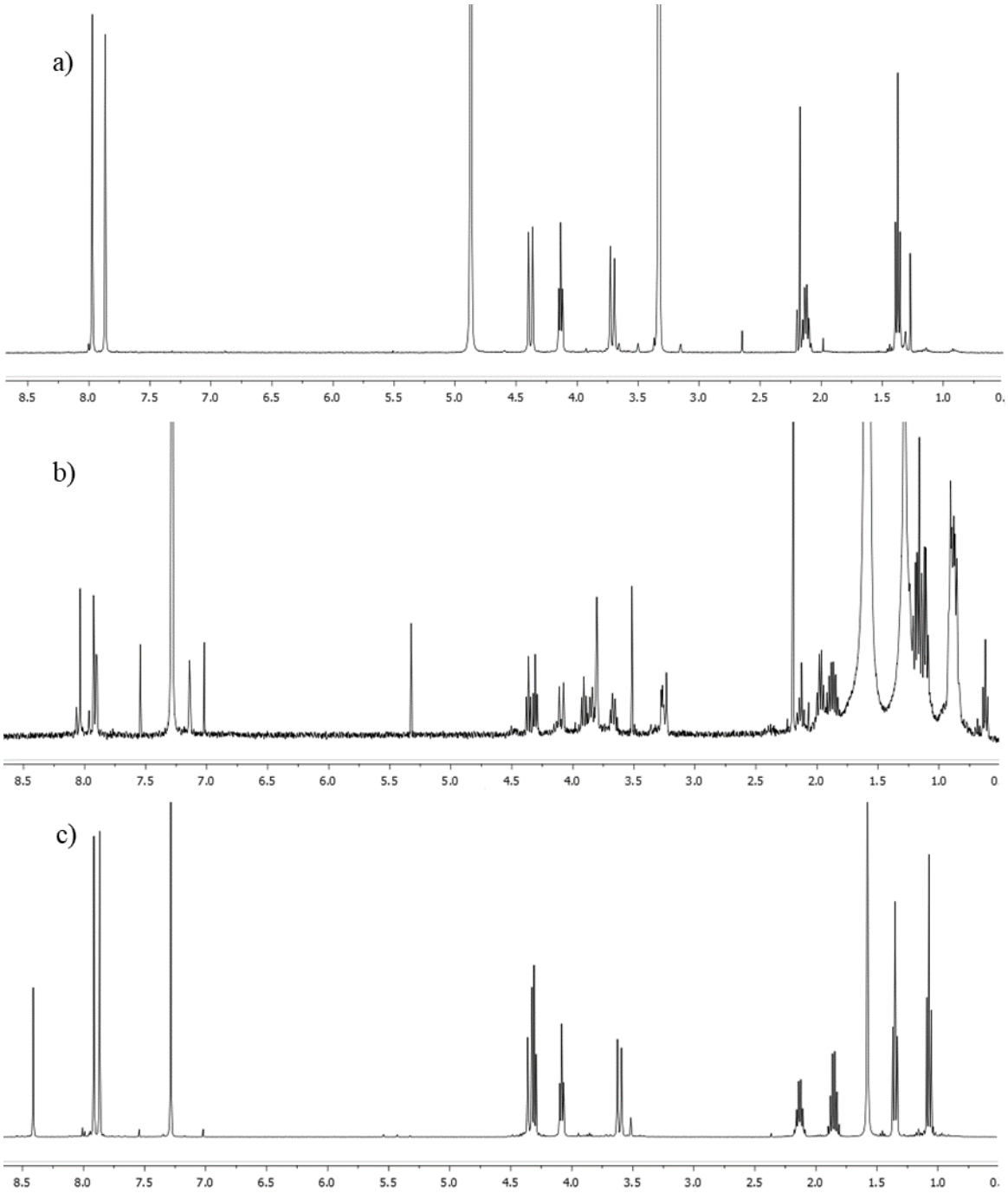

*Figure 11: ^{1}H NMR spectra (400MHz, 298 K): (a) of product **10** in MeOD, (b) of the mixture of tetrapropoxy derivatives with cone and partial cone conformations in $CDCl_3$, (c) of the dinitro-dipropyl ester derivative in $CDCl_3$*

Based on these experimental findings, the decision was made to abandon the objective of fully alkylating the lower rim of compound **10** and to go ahead with the remaining free OH groups The functionalization with amino acids at the upper rim of this compound was thus pursued. The presence of the two hydroxyl groups at the lower rim, in fact, still ensures that the final product adopts a cone geometry, even if they could constitute a weakness point in case of oxidizing conditions that could act on them transforming the rings in quinone-like species. Notably, the absence of two propyl chains

compared to the initially conceived objective might contribute to an increased solubility in aqueous environments.

2.2.1.2 Functionalization with amino acids

To introduce amino acid units starting from the 1,3-dinitro-2,4-dicarboxylic compound **10**, the synthetic sequence outlined in Scheme 4 was followed. Specifically, the reduction of the nitro groups was carried out only after the initial functionalization of the two carboxylic groups. This approach avoided protection and deprotection steps that would have been required if the nitro groups had been reduced to amines since the outset. The two nitro groups were thus employed as a sort of protective groups for the two amines.

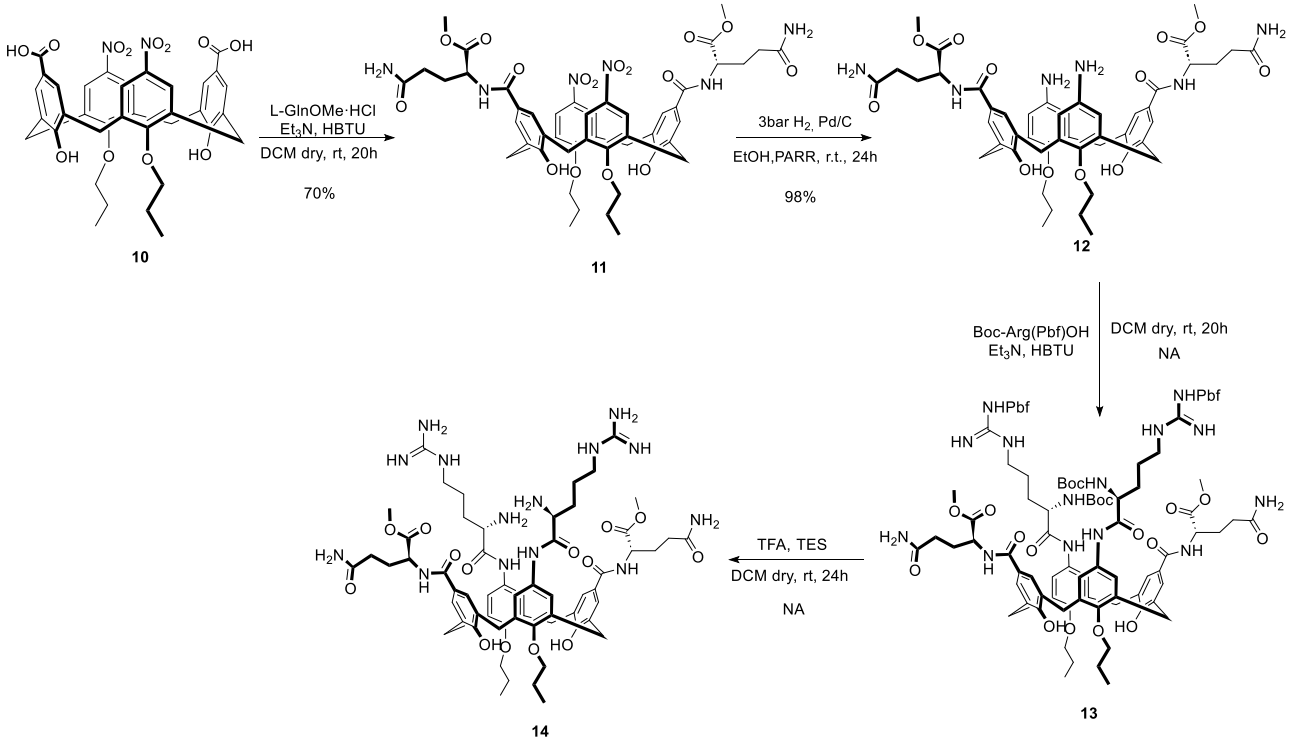

*Scheme 4: synthetic strategy for the functionalization of calixarene **10** with amino acids*

The functionalization of compound **10** with L-GlnOCH$_3$·HCl, using HBTU as a coupling reagent, was executed (Scheme 4). The purified product **11** was obtained through chromatographic separation and characterized. Both the ^{1}H-NMR spectrum (Figure 12a) and mass analysis confirmed the successful outcome of the coupling reaction. Subsequently, it became necessary to reduce the nitro groups. In this case, a significant upfield shift (δ = 6.45 ppm) of the aromatic proton signals adjacent to the NH_2 group (^{1}H-NMR spectrum, Figure 12b) with respect to the resonance value for the same protons in ortho position to NO_2 (δ = 7.84 ppm) served as a indication of the successful reaction.

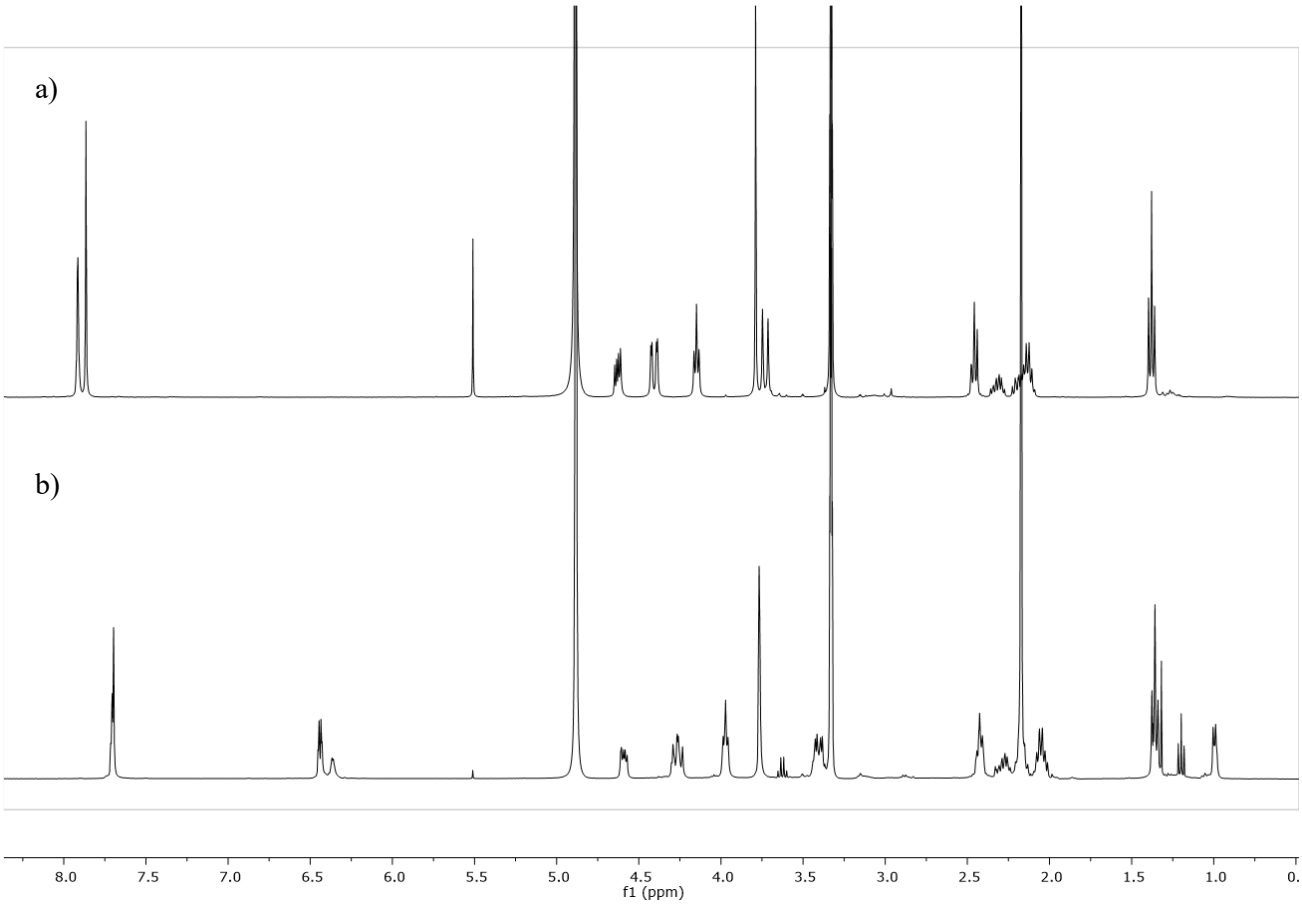

*Figure 12: ^{1}H-NMR spectra (CD_3OD, 400MHz, 298 K) of (a) product **11** and (b) product **12**.*

However, these signals exhibited an unusual pattern instead of the expected singlet or, in alternative, two doublets with J_{meta} if the two protons convey the effects of the Gln chirality. A possible explanation for this pattern could be attributed to possible partial protonation of the amino groups. This hypothesis is supported by the pattern of the methylene bridge (δ = 4.26 and δ=3.40 ppm), reported in Figure 13, where the lack of the doublet as multiplicity could confirm the loss of symmetry showed by **11**. Our hypothesis was validated thanks to the presence of the molecular ion and adduct with sodium signals to the ESI-MS, even though other unattributed signals are indeed present as reported below in the discussions.

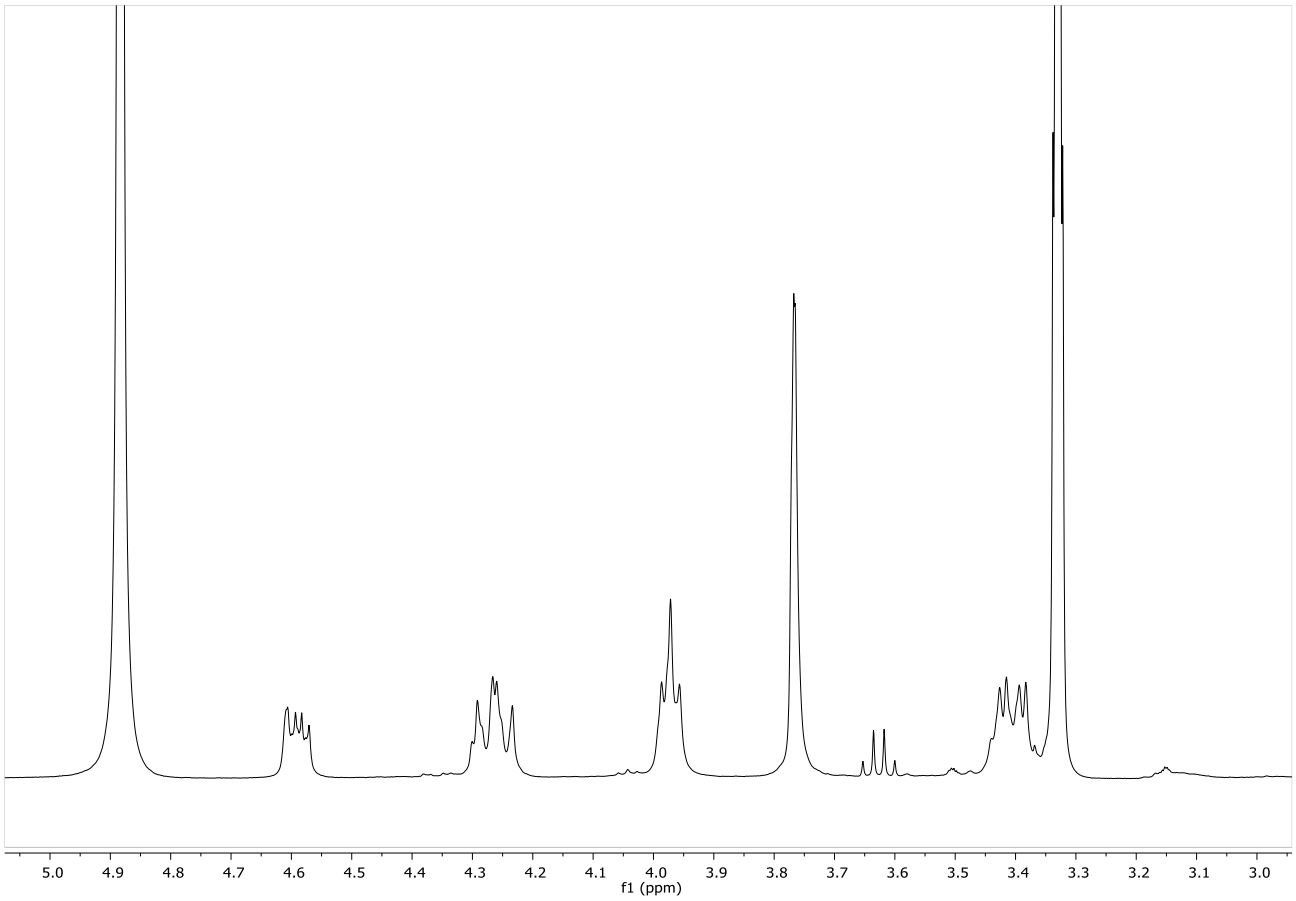

*Figure 13: Zoom of ^{1}H-NMR spectrum (CD_3OD, 400MHz, 298 K) of product **12** from 5.00 ppm to 3.00 ppm.*

Then, was carried out the reaction between compound **12** and Boc-Arg(Pbf)OH to complete the upper rim functionalization, introducing the second pair of amino acids. To prevent or at least minimize potential intramolecular cyclization of Arg, the amino acid was added last to the reaction environment containing HBTU and a concentrated solution of product **12**. This approach limited the cyclization process by promoting rapid contact between the activated amino acid and the calixarene. Despite purification efforts, the spectrum of the isolated compound was notably complex (Figure 14), characterized by unexpected and unexplainable signals not justifiable if considering present only the desired product **13**. In particular, the splitting in two of the Gln methyl ester group signal and the diversification of the aromatic proton signals made the interpretation difficult and debatable. The complexity might arise from the presence of multiple species in solution or a specific perturbation in the macrocycle's symmetry. Intramolecular interactions and/or partial protonation of the amino acid residues could disrupt the symmetry, leading to the differentiation of the two methyl ester groups. In an attempt to rule out this possibility, the ^{1}H-NMR spectrum was recorded in DMSO; however, no improvements were observed in this regard.

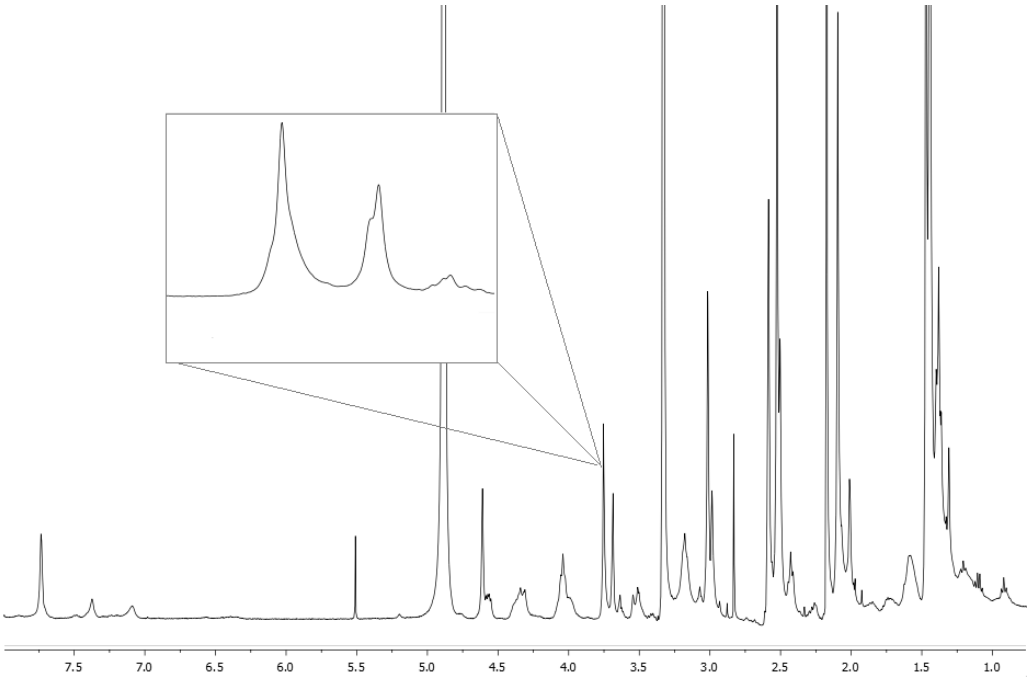

*Figure 14: ^{1}H-NMR spectrum (400MHz, CD_3OD, 298 K) of the isolated product from the reaction to obtain compound **13**. Methyl ester signals in the inset.*

The mass analysis confirmed the presence of product **13** thanks to the molecular ion signal $[M]^+$ (m/z=1928.19, 1.48%) but gave us also the indication of the byproduct with the signal m/z=1462.87. Initially, the hypothesis was that signal is attributable to the partially functionalized byproduct, but the m/z found not correspond to any adduct of this possible byproduct (MW=1419.66).

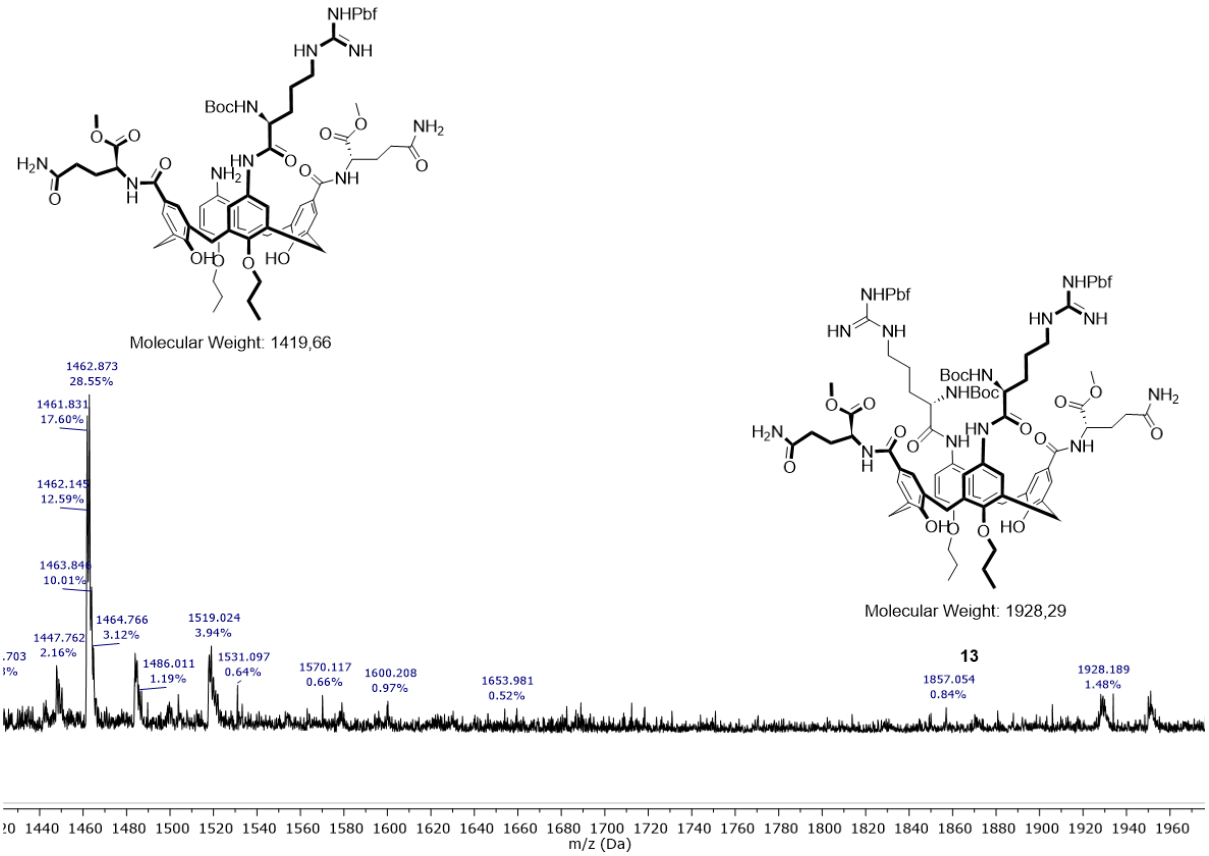

*Figure 15: 1420-1960 m/z region of the mass spectrum of presumed compound **13***

As a result, a review of the preceding synthetic steps and the data collected on the isolated products, specifically the spectra of the various intermediates obtained, was undertaken to pinpoint the source of the problem. Attention focused on compound **12** and the reduction reaction due to the presence of certain signals in the ^{1}H-NMR spectrum that were not attributable to the compound under examination. Particularly, the doublet at 0.99 ppm, previously not considered with sufficient attention, caught our attention. Trituration with ethyl ether was carried out to remove possible impurities; however, the signal persisted in the spectrum recorded after these operations (Figure 16). The frequency and multiplicity of this signal resembled the doublet of an isopropyl methyl group. With this observation, the formation of an imine on the amino functionalities due to traces of acetone in the reaction environment for the reduction of nitro was considered. The formation of the imine and its subsequent reduction would indeed explain the presence of isopropylamine groups at positions 5 and/or 17, accounting for the appearance and persistence of this doublet.

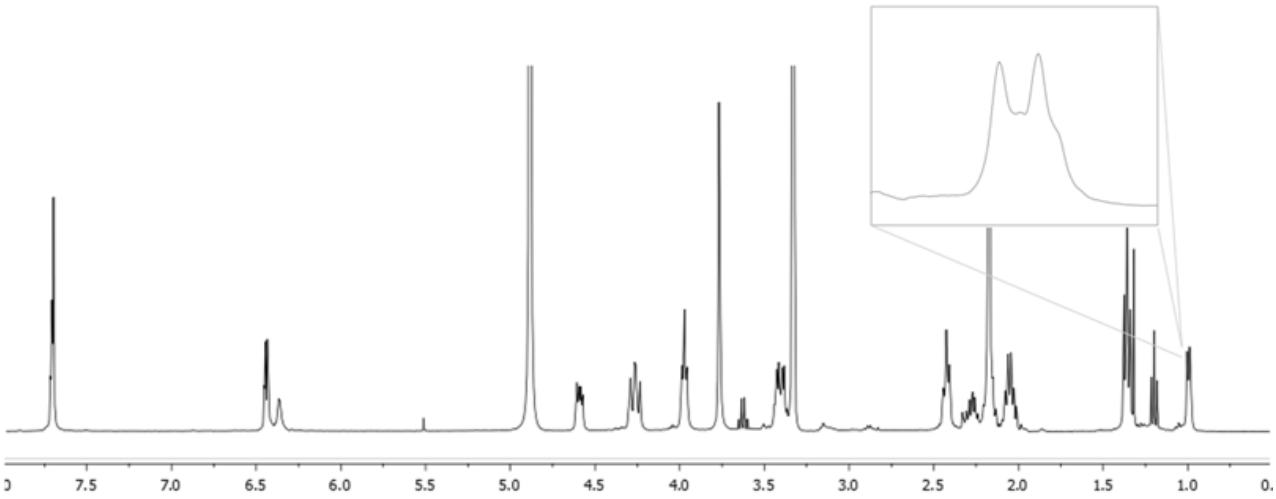

*Figure 16: ^{1}H-NMR spectrum (400MHz, CD_3OD, 298 K) of the presumed compound **12**. The signal at 0.99 ppm in the inset.*

With this hypothesis in mind, we went back also to the mass spectra that were further examined to confirm the formation of the unintended product resulting from the reaction between the aniline function and acetone, followed by imine reduction to an amine. A more aware analysis of the mass spectrum of the presumed product **12** (Figure 17) supported this hypothesis. Indeed, in addition to the protonated molecular ion signal of **12** $[M+H]^+$ (m/z = 911.49, 48%) and the sodium adduct $[M+Na]^+$ (m/z = 933.38, 13.2%), signals attributable to the mono-isopropylamine derivative and the di-isopropylamine derivative were present at m/z = 953.53 (100%, $[M+H]^+$) and m/z = 995.56 (20%, $[M+H]^+$), respectively. Corresponding adducts with sodium were observed at m/z = 975.25 (11%, $[M+Na]^+$) and m/z = 1017.09 (7%, $[M+Na]^+$). Similarly, in the mass spectrum of the presumed compound **13**, alongside the desired product signal, finds explanation the signal with m/z=1462.87 that results to be the molecular ion of partially functionalized mono-isopropylamine derivative ($[M+H]^+$, 28.55%). Based on these findings, a reconsideration of the two ^{1}H NMR signals corresponding to the aromatic protons adjacent to the amino group was undertaken, revealing that they were indicative of different calixarene species, rather than simply being due to protonation or chirality as previously hypothesized.

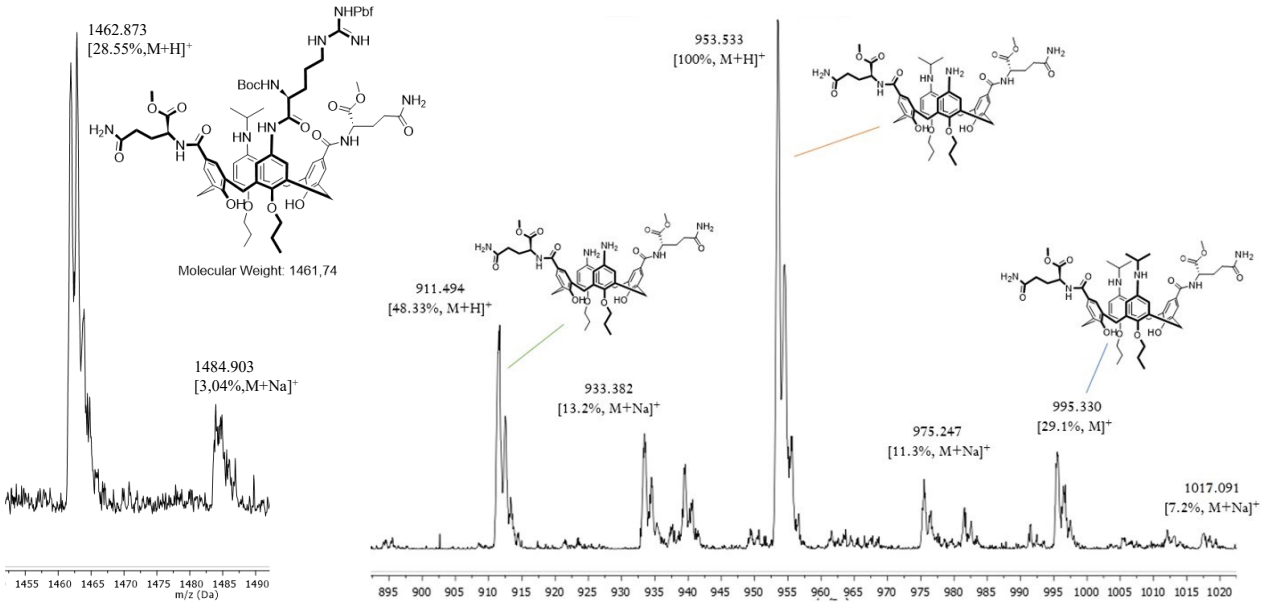

*Figure 17: On the left: 1455-1490 m/z region of the mass spectrum of presumed compound **13**; on the right: 890-1025 m/z region of the mass spectrum of presumed compound **12***

Even in the mass spectrum of the product resulting from the removal of Pbf and Boc groups under acidic conditions with TFA in the presence of TES on a portion of the presumed derivative, signals corresponding to the unintended mono-isopropylamine-mono arginine derivative (m/z 1110.73 [69.84%, M+H]$^+$) were evident, alongside the product **14** signal (m/z 1224.57 [7.80% M+H]$^+$, m/z 612.96 [100%, M+H]$^{2+}$).

Having access to another batch of compound **11**, the reduction reaction was repeated. Unfortunately, in this second attempt, both the ^{1}H-NMR and mass spectra (Figure 18) exclusively indicated the presence of the di-isopropylamino derivative. This outcome was again attributed to residual traces of acetone in the reaction environment within the Parr hydrogenator, even after repeated washing, prior to proceeding with the reaction. Consequently, efforts were made to purify product **12**, which had indeed been obtained, through chromatographic separation. Despite various attempts, the intended goal was not achieved.

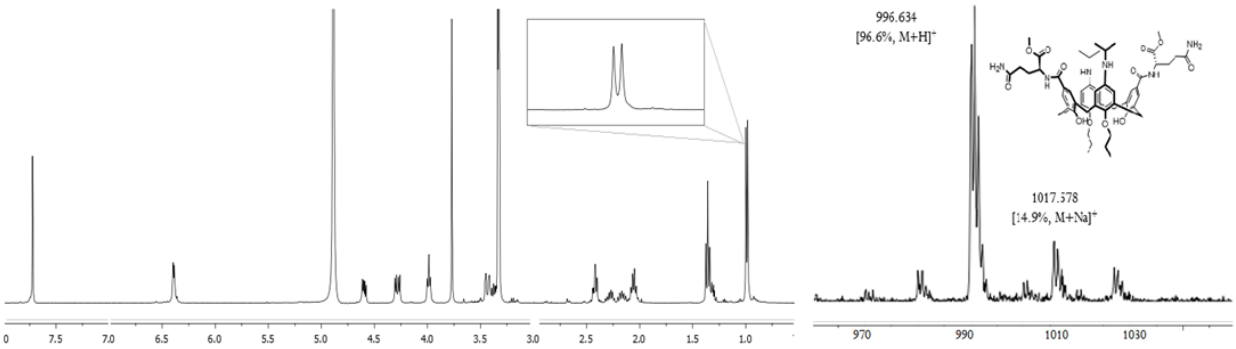

Figure 18: ^{1}H NMR spectrum (400MHz, CD_3OD, 298 K) (left) and ESI mass spectrum (right) of the undesired product 5,17-di(isopropylamino)-11,23-di[(methoxy-L-Gln)carbonyl]-25,27-dihydroxy-26,28-dipropoxycalix[4]arene.

Therefore, a decision was made to synthesize compound **12** anew. However, since acetone seemed surprisingly impossible to be eliminated, a small amount of water was added to the reaction to prevent imine formation by shifting the equilibrium toward the amine, as reported in the scheme 5.

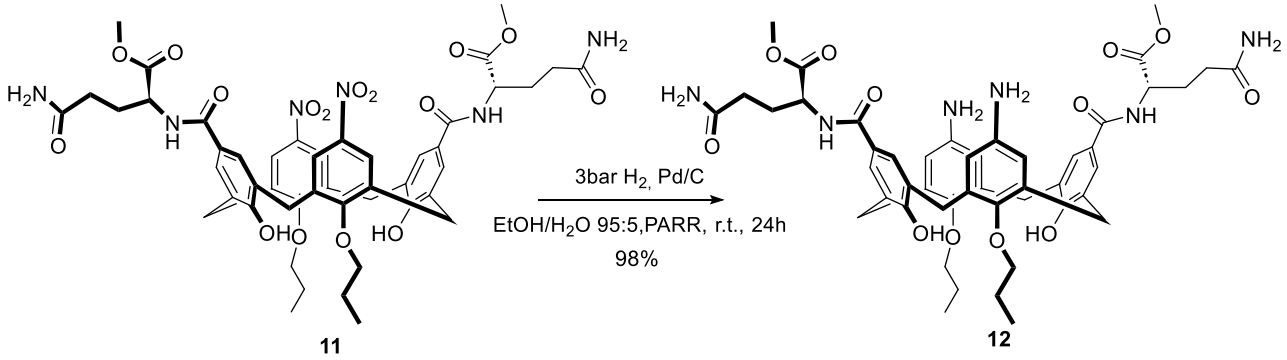

*Scheme 5: synthesis of compound **12***

The observation of imine formation was probably due to the presence of free OH groups at the lower rim, which render the reaction environment sufficiently acidic, catalyzing imine formation with acetone. As such, compound **12** was obtained cleanly, and no longer displayed the signal splitting observed in the following figure, which compares the two ^{1}H-NMR spectra (Figure 19).

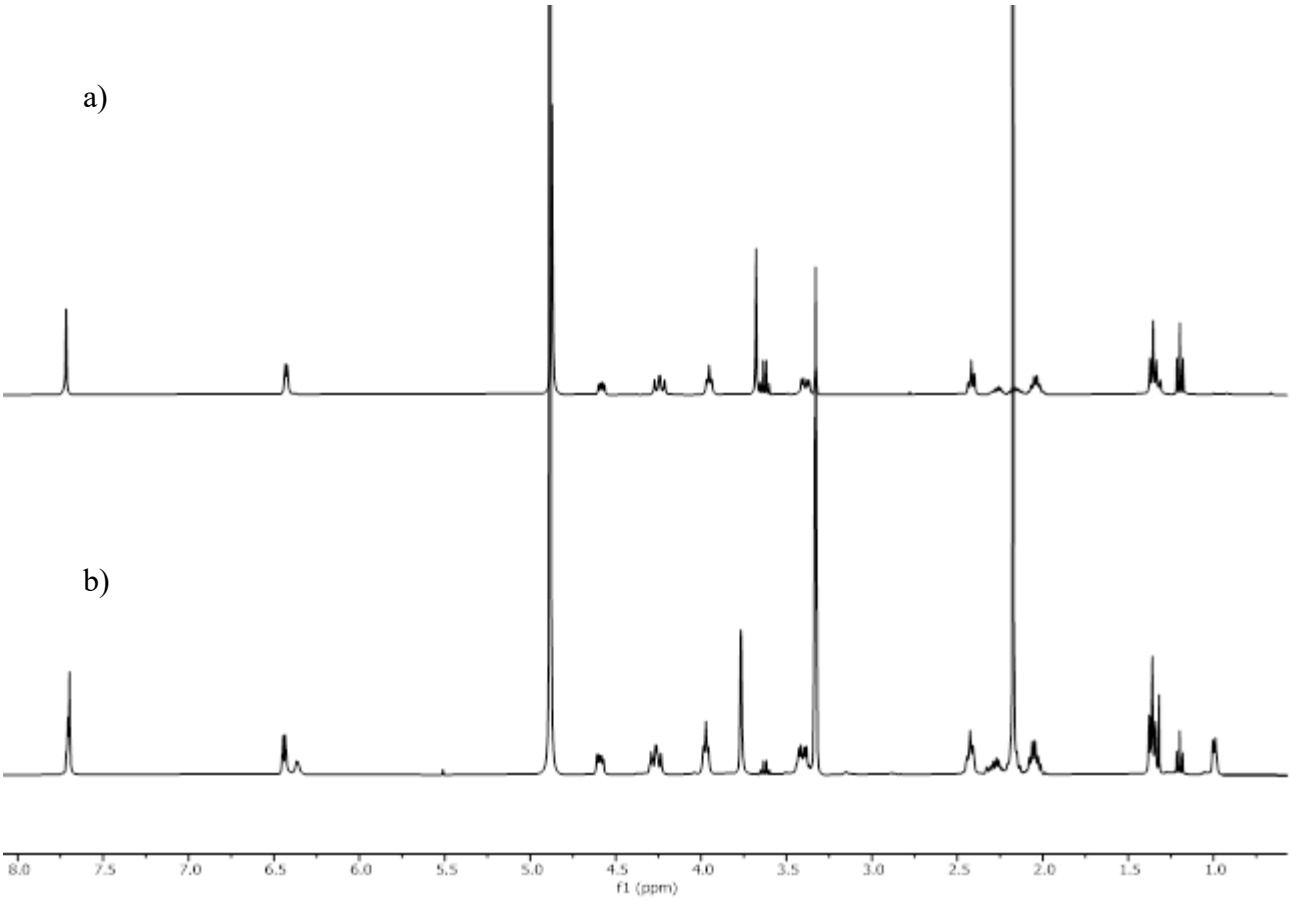

*Figure 19: ^{1}H NMR spectra (400MHz, CD_3OD, 298 K) of (a) pure compound **12** and (b) when contaminated by the isopropylamine containing analogue.*

Subsequently, with the pure **12** an attempt was made to obtain compound **13**, using the same conditions as for the previous couplings. However, a complex mixture of products was obtained, difficult to purify, and ESI-MS analysis (Figure 20) indicated the presence of the desired product, as $[M]^+$ (m/z =1928.07) but also of one byproduct, as $[M+H]^+$ (m/z =1518.67). Notably, the base peak in the spectrum seemed to correspond to a byproduct resulting from the reaction between the coupling agent and one of the two amines, as depicted in Figure 20, which in turn can not react. This secondary reaction is well-documented in the literature[30], but we never observed it in condensation reaction between aminocalixarenes and amino acids. The formation of the byproduct is probably due to the limited reactivity of the second amine, perhaps due to steric hindrance from the presence of three other amino acids with their corresponding protecting groups. Unfortunately, the desired product resulted not isolable from the reaction mixture.

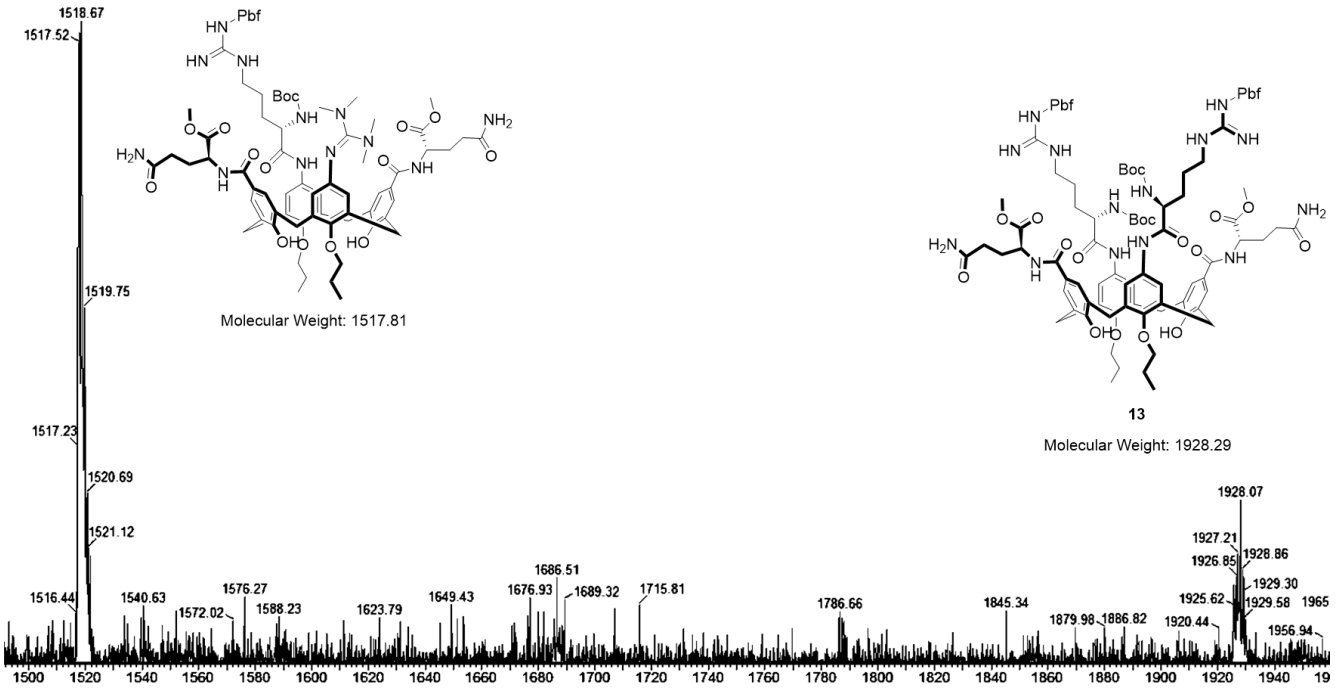

*Figure 20: mass spectrum of attempt of reaction to obtain **13***

Therefore, trying to solve the several met problems, considering the cyclization of arginine when its carboxylic acid is activated and the observed outcome of the coupling reaction, a new synthetic approach was planned. With this new strategy, the aim was to modify the order of functionalization of the calixarene scaffold, coupling arginine as an N-linked and glutamine as a C-linked amino acid. Reaction between calixarene **6** and L-Arg(Pbf)OMe·HCl produced compound **15** with a 45% yield (scheme 6). The rather low yield could be due to the limited reactivity of arginine in this context.

Due to time constraints, it was not possible to proceed with and complete the new synthetic route.

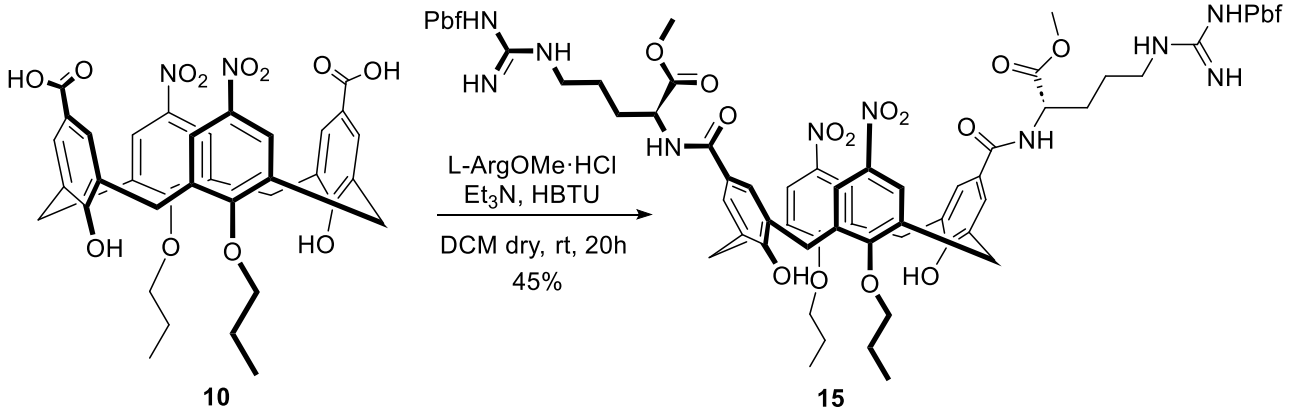

*Scheme 6: Synthesis of compound **15***

2.2.2 Synthesis of the C-linked ligand

The synthesis of this ligand was based on the possible selective protection of amine groups at the upper rim of the tetraamino-calix[4]arene, as demonstrated by Bohmer and colleagues[27]. Compared

to what done for the C,N-linked peptidocalixarene, this compound was alkylated at the lower rim with four chains. To avoid low solubility in water, we decided to alkylate it using the ethoxyethyl group that determines improved solubility in water as reported in the literature[31].

2.2.2.1 Synthesis of calixarene platform

In Scheme 7, the synthetic steps that were followed to obtain the 5,11,17,23-tetramino-25,26,27,28-tetraethoxyethoxycalix[4]arene as a platform for constructing compound **24** are depicted.

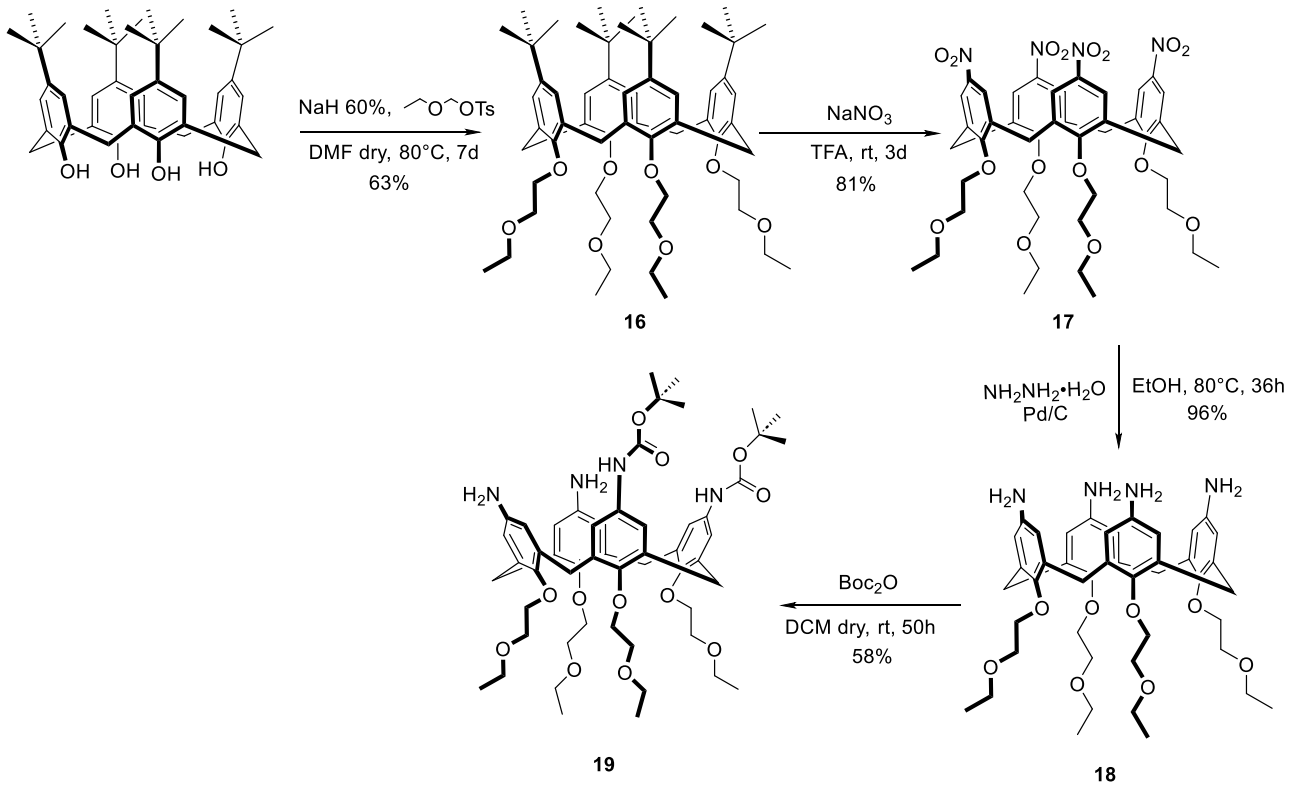

Scheme 7: Synthesis of calixarene platform

The initial reaction involved the tetraalkylation of the lower rim. NaH was employed as the base for deprotonation of the phenolic groups. Ethoxyethyl tosylate, previously synthesized, served as the alkylating agent. Using ethoxyethyl tosylate as the alkylating agent demonstrated significant enhancement of the reaction, particularly in terms of speed and conversion, compared to prior reactions conducted with bromoethoxyethyl. Subsequently, tert-butyl groups were substituted by ipso-nitration using $NaNO_3$ in TFA. ^1H NMR and mass analyses confirmed the identity of product **17**. Product **18** was obtained by reducing the nitro groups of **17** using hydrazine and Pd/C as the catalyst. The tetraamine product was reacted with two equivalents of bis-Boc anhydride in the absence of base. As reported by Bohmer and Vogt[27], under these conditions such reaction favored pronounced protection of two out of the four amino groups at the upper rim of the calixarene derivative in vicinal position. If reproducible in our hands, this selectivity would enable a two steps functionalization with two different types of amino acids, crucial for obtaining our target peptidocalixarene. This selection

of vicinal amines was explained by the authors with the possible interaction between the Boc-anhydride and the Boc-protecting group after the first protection. Actually, the ^{1}H NMR spectrum of the compound obtained from this reaction confirmed the expected favorable outcome. The appearance of three doublets for both the axial and equatorial methylene protons and the splitting of signals corresponding to the ethoxyethyl chains (Figure 21) highlighted the breaking of C_{4v} symmetry in the macrocycle induced by the presence of two Boc groups at positions 1,2.

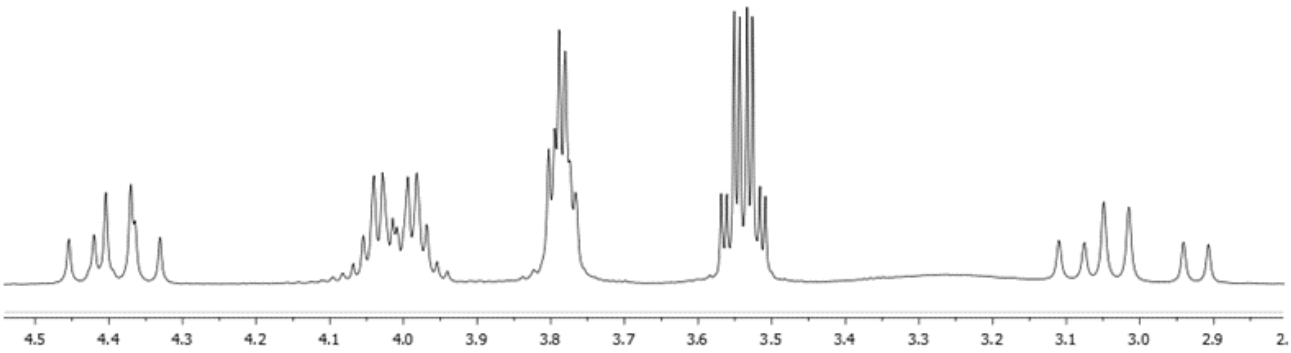

*Figure 21: ^{1}H NMR Spectrum (400MHz, $CDCl_3$, 298 K) of product **19** in the range 4.5-2.8 ppm.*

2.2.2.2 Functionalization with amino acids

Scheme 5 outlines the synthetic steps exploited for functionalizing macrocycle **19**. As amino acids we selected Glu and Lys, on the basis of the modelling studies previously reported and mentioned at the beginning of the results and discussion section. Specifically, the initial functionalization reaction was performed with Fmoc-Glu(OAll)OH, properly protected in view of the subsequent removal of the Boc group from the calixarene upper rim. The product was obtained and purified through chromatographic separation. NMR and mass analyses confirmed the identity of product **20**, completing its characterization.

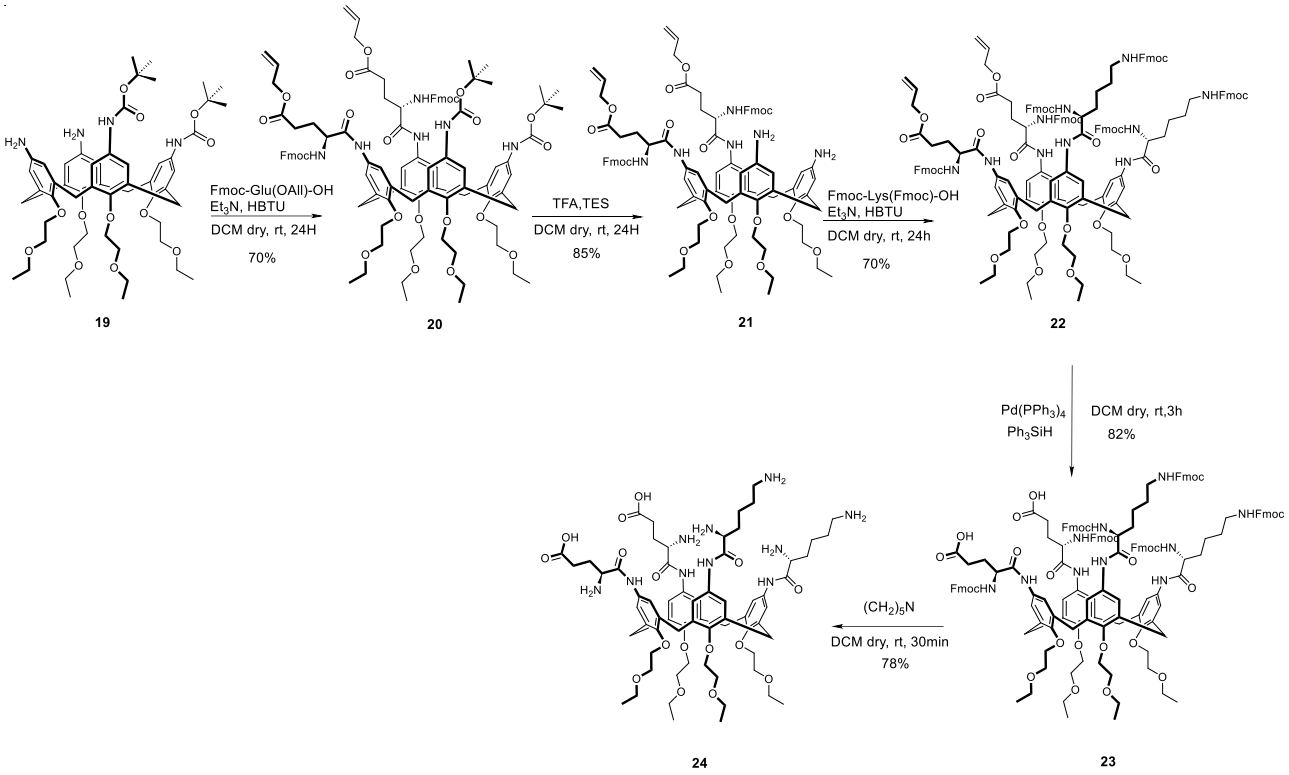

*Scheme 8: functionalization of calixarene **19** with amino acids*

The Boc groups protecting the amino groups of product **20** were removed using a standard TFA procedure in the presence of TES[27]. Product **21** was characterized and subsequently functionalized with the second type of amino acid, the Fmoc-Lys(Fmoc)OH. Product **22** was purified through chromatographic separation and characterized (Figure 23a). Considering the complexity of the ^{1}H NMR spectrum, the ESI-MS spectrum (Figure 22) become essential to verify the successful outcome of the reaction. The product was confirmed thanks to the presence of multicharged signals (m/z 1351.68 $[M+2H]^{2+}$, m/z 1362.75 $[M+H+Na]^{2+}$, m/z 1373.50 $[M+2Na]^{2+}$).

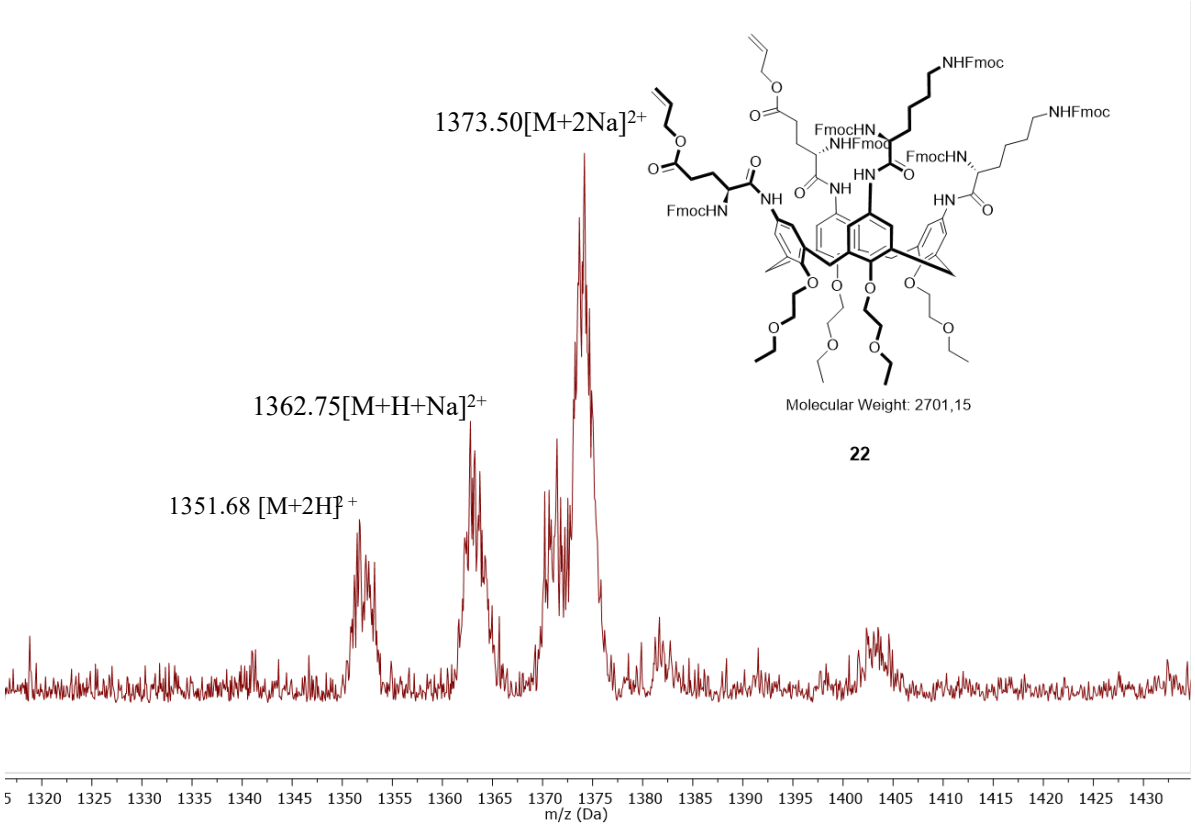

*Figure 22: 1320-1430 m/z region of the mass spectrum of compound **22***

The final removal of the Fmoc and allyl protecting groups required two distinct steps. To simplify purification, the deprotection of the allylic groups was carried out first. A literature-known procedure involving Ph_3SiH as a hydride donor and $Pd(Ph_3)_4$ for total allyl group removal was adopted[32]. The product was obtained through chromatographic purification. Confirmation of successful deprotection was the disappearance of signals related to the allylic group (Figure 23b). After obtaining product **23**, the final cleavage of the Fmoc group was performed. The deprotection reaction necessitated basic conditions, specifically obtained with piperidine. Successful removal of the protecting group was indicated by low-field signals in the ^1H NMR spectrum, corresponding to dibenzofulvene in solution (narrow signals alongside the broad signals of calixarene). The remaining piperidine was removed through repeated washes and centrifugations in isopropanol, which facilitated the separation of **24** without significant loss.

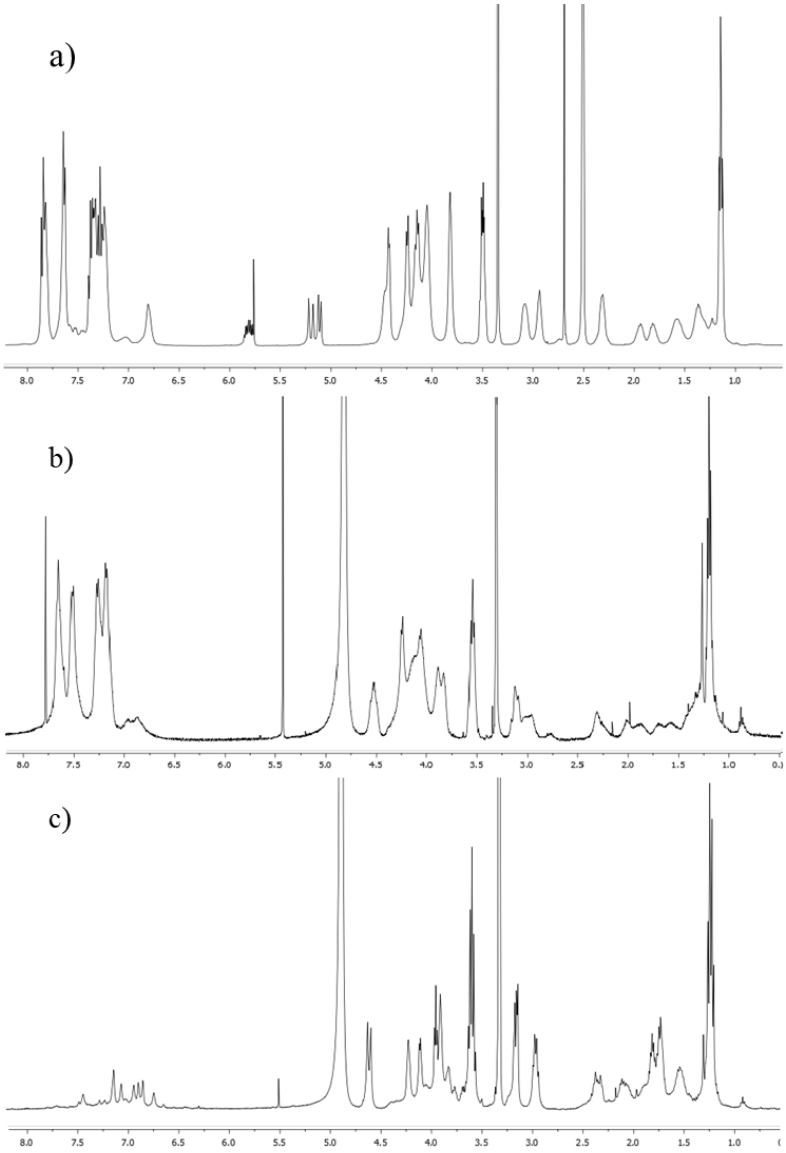

*Figure 23: ^{1}H NMR Spectra (400MHz,298 K) of (a) product **22** in DMSO-d_6, (b) product **23** in $CD_3OD/CDCl_3$ 3.5/1.5, (c) product **24** in CD_3OD.*

The absence of allyl group (δ=5.75 ppm) confirms the successful outcome of the ally removal (Figure 22b) and the reduction of integral for aromatic signal indicates the Fmoc groups removal (Figure 22c). With these considerations, pure ligand **24** was successfully obtained as also confirmed by ESI-MS spectrum with the presence of molecular ion signal (m/z 1287.475 $[M]^+$) and the multicharged signal (m/z 644.368 $[M+H]^{2+}$) as reported in Figure 24.

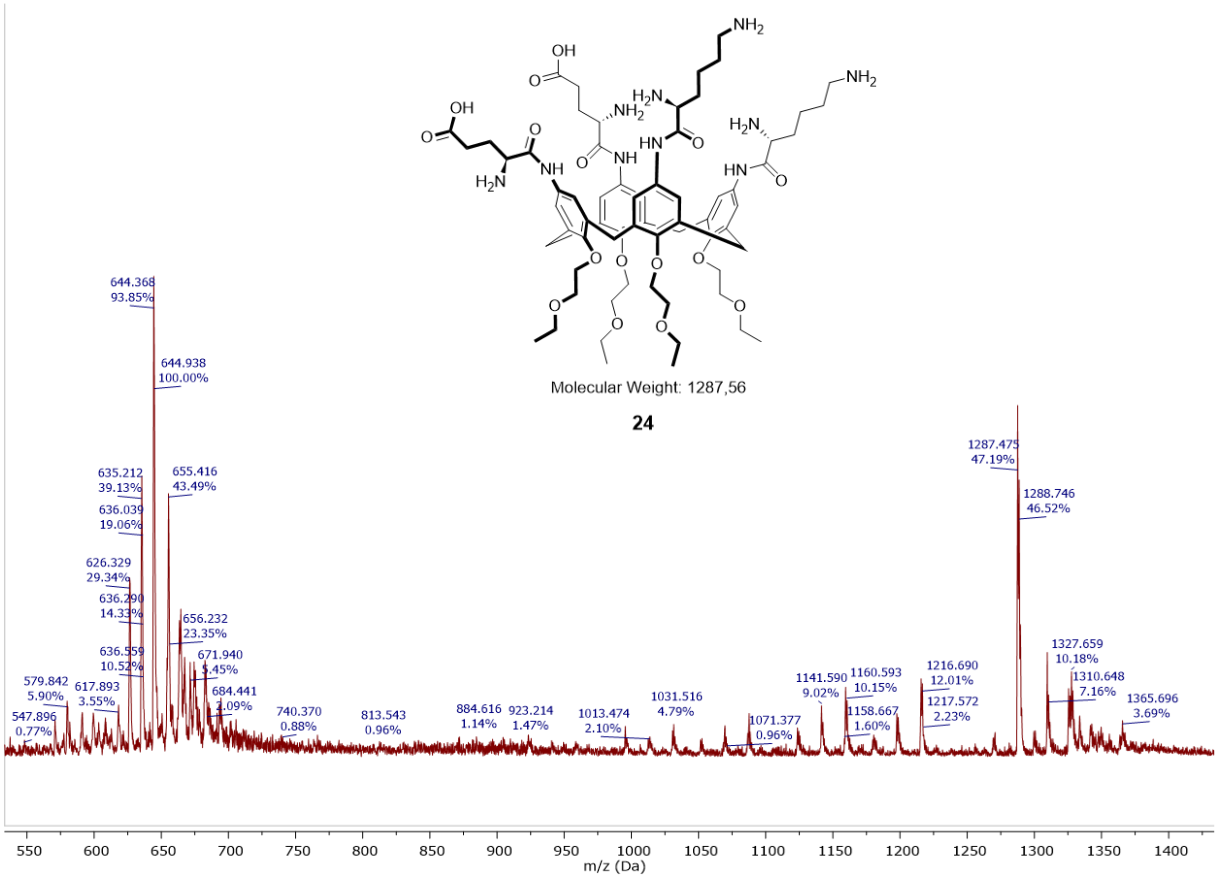

*Figure 24: 550-1287 m/z region of the mass spectrum of compound **24***

2.3 Inhibition test

Professor Gaetano Donofrio from the Department of Medical Veterinary Sciences at the University of Parma conducted experiments involving the synthesized compound **24**. To study the behavior of SARS-CoV-2 without the risks associated with direct handling of the infectious virus, he devised a pseudovirus system. This system allowed him to investigate the coronavirus's behavior by engineering a lentivirus that displayed the SARS-CoV-2 Spike protein on its surface. Additionally, he modified the pseudovirus to include genetic material encoding the green fluorescent protein (GFP)[33].

Furthermore, Professor Donofrio established a cultured cell line derived from modified HEK293T cells. He engineered these cells to express the ACE2 receptor on their surface by electroporating them with a suitable plasmid containing the receptor's genetic code. Having both the pseudovirus and the ACE2-expressing cell line prepared, he proceeded to examine the effectiveness of the peptidocalixarene ligand.

In an initial step, a population of the modified cells was exposed to the pseudovirus. Normally, the pseudovirus would infect these cells, causing them to produce GFP, which could be quantified through fluorimetry to gauge cell transduction. Professor Donofrio had previously demonstrated that pre-incubating the pseudovirus with sera from SARS-CoV-2 infected patients and then using it to infect the same cell line resulted in no observable fluorescence. This indicated that antibodies in the serum hindered the Spike protein-ACE2 receptor interaction, preventing cell infection[33].

Subsequently, he replicated the experiment by using instead of the human sera a water-based solution containing our ligand at a concentration of 200 μM. Regrettably, despite testing compound **24**, the cells still emitted green light. Consequently, it was concluded that our compounds were ineffective in obstructing the interaction between the Spike protein and the ACE2 receptor. As a result, they were unable to inhibit the pseudovirus, which proceeded to infect the cells.

3. Conclusions

Throughout our project duration, we successfully produced a novel peptidocalix[4]arene **24**. With respect to our initial plans, this represents a rather limited result. In fact, if the synthesis of the two calixarene-based platforms properly equipped for the amino acid conjugation was much more straightforward and effective we could generate even a small battery of potential ligands simply varying the pairs of amino acids to link. This would have given also much more relevance and significance to the biological studies and their results to understand the potential of this approach and design for the inhibition of the S-protein/ACE2 interaction. However, the various challenges encountered during the synthesis process notably enhanced our proficiency in the synthesis and modification of calixarenes.

Although our compound did not demonstrate inhibitory activity against a pseudovirus presenting the SARS-CoV-2 Spike protein, it remains worthwhile to consider conducting inhibition tests using the authentic SARS-CoV-2 virus. This step could provide valuable insights into the potential efficacy of our compounds against the genuine virus, thereby contributing to the advancement of our research.

4. Experimental Part

General information

Commercially available reagents and solvents were used without carrying out any prior purification or treatment except as indicated. All moisture- and air-sensitive reactions were conducted under nitrogen atmosphere. Dry solvents were prepared according to standard procedures and stored in the presence of molecular sieves. Monitoring of synthetic processes was performed by direct-phase thin-layer chromatography (TLC) using 60 F254 silica gel plates. For the detection of reagents and

products with amine groups, the TLCs were sprayed with a 5% solution of ninhydrin in ethanol; for those with phenolic groups, a solution of $FeCl_3$ in water was used; for those with aldehydic groups, a solution of acidic 2,4-dinitrophenylhydrazine in ethanol was used; and for easily oxidized compounds, a 0.05% solution of $KMnO_4$ in water was used. Flash chromatography columns on silica gel 60 (230-400 mesh), under nitrogen pressure, and commercial preparative TLC 20×20 cm, silica gel F_{254}, 0.5 mm were used for products purification.

Products characterization was performed by ^1H and ^{13}C NMR spectroscopy and mass spectrometry using ESI technique. NMR spectra were recorded with Bruker AVANCE 400 spectrometer (^1H at 400 MHz, ^{13}C at 100 MHz); chemical shift values are reported in ppm using the resonance frequency of the partially deuterated solvent as a reference. Mass spectra were recorded with a single quadrupole SQ detector spectrometer, Waters. Melting points were determined with Gallenkamp apparatus in closed capillaries.

25,27-dihydroxy-26,28-dipropoxycalix[4]arene (5)

In a two-necked flask, under a nitrogen flow, tetrahydroxycalix[4]arene (3.0 g, 7.05 mmol) was dissolved in 100 mL of dry ACN is added. Then, K_2CO_3 (3.9 g, 28.3 mmol) was added, and the mixture was stirred for 30 minutes. Next, 1-iodopropane (2.75 mL, 28.23 mmol) was added. The reaction was kept stirring under reflux while periodically monitoring the progress using TLC (eluent: hexane/EtOAc 6:4). After approximately 24 hours, the reaction was quenched by adding 1M HCl (50 mL). A yellow precipitate was formed, which is filtered using a Büchner funnel and washed with water, then dried under vacuum. The solid was further purified through precipitation in DCM/Hex, resulting in a white solid.

Yield= 65% (2.27g)

^1H NMR (400 MHz, $CDCl_3$) δ (ppm): 8.34 (s, 2H, -OH), 7.07 (d, J = 7.5 Hz, 4H, Ar*H* meta), 6.95 (d, J = 7.6 Hz, 4H, Ar*H* meta), 6.77 (t, J = 7.5 Hz, 2H, Ar*H* para), 6.66 (t, J = 7.5 Hz, 2H, Ar*H* para), 4.35 (d, J = 12.9 Hz, 4H, axial ArCH_2Ar), 4.00 (t, J = 6.3 Hz, 4H, OC$H_2CH_2CH_3$), 3.40 (d, J = 13.0 Hz, 4H, equatorial ArCH_2Ar), 2.10 (h, J = 7.4 Hz, 4H, $OCH_2CH_2CH_3$), 1.34 (t, J = 7.4 Hz, 6H, $OCH_2CH_2CH_3$).

The spectroscopic data found are in agreement with those reported in literature[34].

25,27-di(p-nitrobenzensulfonyloxy)-26,28-dipropoxycalix[4]arene (6)

In a two-necked flask, under a nitrogen flow, compound **1** (1.86 g, 3.66 mmol) was dissolved in 70 mL of dry DMF. Next, 60% NaH (0.60 g, 14.99 mmol) was added, and the mixture was kept stirring

for 30 minutes at 0°C. P-nitrobenzenesulfonyl chloride (3.25 g, 14.63 mmol) was then added, and the solution was kept stirring at room temperature. The reaction is monitored by TLC (eluent: Hex/EtOAc 7:3, visualized with $FeCl_3$). After 20 hours, the reaction is complete, and was quenched by adding 100 mL of 1M HCl. A yellow precipitate was filtered and then reprecipitated in DCM/MeOH obtaining the product as yellow solid.

Yield= 90% (2.902 g)

^{1}H NMR (400 MHz, $CDCl_3$) δ (ppm): 8.42 (d, J = 8.8 Hz, 4H, NosAr*H*), 8.06 (d, J = 8.8 Hz, 4H NosAr*H*), 7.07 (d, J = 7.4 Hz, 4H, Ar*H* meta), 6.93 (t, J = 7.5 Hz, 2H, Ar*H* para), 6.43 (t, J = 7.6 Hz, 2H, Ar*H* para), 6.21 (d, J = 7.7 Hz, 4H, Ar*H* meta), 4.01 (d, J = 13.8 Hz, 4H, axial ArCH_2Ar), 3.85 – 3.81 (m, 4H, O$CH_2CH_2CH_3$), 2.86 (d, J = 13.9 Hz, 4H, equatorial ArCH_2Ar), 1.88 (h, J = 7.6 Hz, 4H, $OCH_2CH_2CH_3$), 0.89 (t, J = 7.4 Hz, 6H, O $OCH_2CH_2CH_3$).

The spectroscopic data found are in agreement with those reported in literature[34].

5,17-dinitro-25,27-di(p-nitrobenzensulfonyloxy)-26,28-dipropoxycalix[4]arene (7)

In a two-necked flask, calixarene **2** (2.612 g, 2.97 mmol) was dissolved in 200 mL of dry DCM. Glacial CH_3COOH (35.7 mL, 624.036 mmol) was added, and 100 % HNO_3 (10.6 mL, 252.586 mmol) was very slowly dripped in. The reaction was kept stirring at room temperature while monitoring its progress using TLC (eluent: Hex/EtOAc 7:3). After 50 hours, the reaction was completed and quenched with 350 mL of water. The aqueous phase was extracted with DCM (3x100 mL). The organic phases were collected, washed with water, and a saturated solution of $NaHCO_3$. The organic phase was dried with Na_2SO_4 and then evaporated under reduced pressure. The product was purified through recrystallization in hot MeOH, yielding an orange solid.

Yield= 82% (2.132g)

^{1}H NMR (400 MHz, DMSO-d_6) δ (ppm): 8.52 (d, J = 8.8 Hz, 4H, NosAr*H*), 8.25 (s, 4H, Ar*H*-NO_2 *orto*), 8.14 (d, J = 8.9 Hz, 4H, NosAr*H*), 6.57 (t, J = 7.6 Hz, 2H, Ar*H* para), 6.35 (d, J = 7.7 Hz, 4H, Ar*H* meta), 3.92 (d, J = 13.8 Hz, 4H, axial ArCH_2Ar), 3.83 (t, J=7.4Hz, 4H, O$CH_2CH_2CH_3$), 3.29 (d, J = 14.0 Hz, 4H, equatorial Ar*CH2*Ar), 1.73 (h, J = 7.5 Hz, 4H, $OCH_2CH_2CH_3$), 0.76 (t, J = 7.4 Hz, 6H, $OCH_2CH_2CH_3$).

The spectroscopic data found are in agreement with those reported in literature[28].

Synthesis of 5,17-dinitro-25,27-dihydroxy-26,28-dipropoxycalix[4]arene (8)

In a flask, compound **3** (1.61 g, 1.66 mmol) was dissolved in 400 mL of a DCM/EtOH 1:1 mixture, and powdered KOH (4.7 g, 83.08 mmol) was added with 1.5 mL of H_2O. The reaction was kept stirring at room temperature, monitoring the progress with TLC (eluent: Hex/AcOEt 7:3, revealed with $FeCl_3$). After 24 hours, the reaction was finished and quenched with 80 mL of 1M HCl. The organic phase was extracted with DCM (3x100 mL), washed with water and brine, dried with Na_2SO_4, and then dried under reduced pressure. Purification was performed through recrystallization in hot CH_3OH, resulting in a dark orange solid.

Yield = 75% (0.75 g)

^{1}H NMR (400 MHz, $CDCl_3$) δ (ppm): 7.96 (s, 2H, -OH), 7.87 (s, 4H, Ar*H*-NO_2 ortho), 7.17 (d, J = 7.5 Hz, 4H, Ar*H* meta), 6.77 (t, J = 7.5 Hz, 2H, Ar*H* para), 4.38 (d, J = 13.1 Hz, 4H, axial ArC*H*$_2$Ar), 4.06 (t, J = 6.2 Hz, 4H, OC*H*$_2$$CH_2CH_3$), 3.52 (d, J = 13.1 Hz, 4H, equatorial ArC*H*$_2$Ar), 2.14 (h, J = 6.9 Hz, 4H, OCH_2C*H*$_2$$CH_3$), 1.36 (t, J = 7.4 Hz, 6H, OCH_2C*H*$_2$$CH_3$).

The spectroscopic data found are in agreement with those reported in literature[28].

Synthesis of 5,17-dinitro-11,23-carbaldehyde-25,27-dihydroxy-26,28-dipropoxy-calix[4]arene (9)

In a two-necked flask, under a nitrogen flow, compound **4** (0.63 g, 1.05 mmol) was dissolved in 250 mL of dry DCM. The solution was cooled to -10°C for 10 minutes, and then Cl_2CHOCH_3 (0.26 mL, 2.84 mmol) and $SnCl_4$ (1.25 mL, 10.52 mmol) were added. The mixture was kept stirring at room temperature. The reaction progress was monitored by TLC (eluent: Hex/EtOAc 7:3, detected with 2,4-dinitrophenylhydrazine). After 20 hours, the reaction was quenched by adding 100 mL of HCl. The aqueous phase was extracted with DCM (3x100 mL), and the organic phase was washed with water, dried with Na_2SO_4, and then evaporated under reduced pressure. The product was purified by reprecipitation in DCM/ MeOH, resulting in a white solid.

Yield = 92% (0.63 g)

^{1}H NMR (400 MHz, $CDCl_3$) δ (ppm): 9.90 (s, 2H, -C*H*O), 8.70 (s, 2H, -OH), 7.88 (s, 4H, Ar*H*-NO_2 ortho), 7.77 (s, 4H, Ar*H*-CHO ortho), 4.37 (d, J = 13.9 Hz, 4H, axial ArC*H*$_2$Ar), 4.10 (t, J = 7.4 Hz,

4H, OC*H*$_2$CH$_2$CH$_3$), 3.65 (d, J = 14.0 Hz, 4H, equatorial ArC*H*$_2$Ar), 2.18 – 2.10 (m, 4H, OCH$_2$C*H*$_2$CH$_3$), 1.36 (t, J = 7.4 Hz, 6H, OCH$_2$CH$_2$C*H*$_3$).

^{13}C NMR (101 MHz, CD3Cl3) δ (ppm): 190.4 (-*C*HO), 158.9 (*Ar*-O ipso), 156.9 (*Ar*-OH ipso), 145.1 (*Ar*-NO$_2$ ipso), 134.0 (*Ar*-CHO ipso), 131.3 (*Ar*-CHO ortho), 124.9 (*Ar*-NO$_2$ ortho), 79.4 (O*C*H$_2$CH$_2$CH$_3$), 31.4 (Ar*C*H$_2$Ar), 23.4 (OCH$_2$*C*H$_2$CH$_3$), 10.8 (OCH$_2$CH$_2$*C*H$_3$).

ESI-MS: m/z calc 654.67 found: 677.3 $[M + Na]^+$, 693.37 $[M + K]^+$, 1309.49 $[2M + H]^+$, 1331.4 $[2M + Na]^+$, 1347.48 [M + K]+.

p.f. > 300 °C (decomposition).

Synthesis of 5,17-dinitro-11,23-dicarboxylic acid-25,27-dihydroxy-26,28-dipropoxycalix[4]arene (10)

In a flask, compound **5** (0.253 g, 0.386 mmol) was dissolved in 50 mL of a CHCl$_3$/(CH$_3$)$_2$CO mixture. Subsequently, H$_3$NSO$_3$ (0.17 g, 1.55 mmol) and NaClO$_2$ (0.123 g, 1.35 mmol) previously dissolved in the minimum amount of H$_2$O were added. The reaction was kept stirring at room temperature. The progress of the reaction was monitored using TLC (eluent: hexane/AcOEt 3:7). After 20 hours, the reaction was quenched by evaporation under reduced pressure. It was washed with 1M HCl and extracted with DCM. Purification was performed through recrystallization in MeOH, resulting in a pale yellow solid.

Yield= 73% (0.218g)

^{1}H NMR (400 MHz, CD$_3$OD) δ (ppm): 7.95 (s, 4H, Ar*H*-COOH ortho), 7.85 (s, 4H, Ar*H*-NO$_2$ ortho), 4.36 (d, J = 13.3 Hz, 4H, H$_{ax}$ di ArC*H*$_2$Ar), 4.11 (t, J = 6.1 Hz, 4H, O*CH*$_2$CH$_2$CH$_3$), 3.70 (d, J = 13.3 Hz, 4H, H$_{eq}$ di ArC*H*$_2$Ar), 2.11- (h, J = 7.5 Hz ,4H, OCH$_2$*CH*$_2$CH$_3$), 1.37 (t, J = 7.4 Hz, 6H, OCH$_2$CH$_2$*CH*$_3$).

^{13}C NMR (101 MHz, CD$_3$OD) δ (ppm): 156.9 (*Ar*-OH ipso), 144.7 (*Ar*-NO$_2$ ipso) 134.9 (*Ar*-COOH *ipso*), 130.9 (*Ar*-COOH ortho), 126.52 (*Ar*-CH$_2$), 124.1 (*Ar*-NO$_2$ ortho), 78.5 (O*C*H$_2$CH$_2$CH$_3$), 30.6 (ArC*H*$_2$Ar), 23.0 (OCH$_2$*C*H$_2$CH$_3$), 9.7 (OCH$_2$CH$_2$*C*H$_3$).

ESI-MS: m/z calc 686.21 found: 709.183 $[M + Na]^+$, 725.154 $[M + K]^+$, 1395.334 $[2M]^+$.

m.p. > 250 °C (decomposition).

Synthesis of 5,17-dinitro-11,23-di[(methoxy-L-glutamine)carbonyl]-25,27-dihydroxy-26,28-dipropoxycalix[4]arene (11)

In a two-necked flask under nitrogen flow, compound **6** (0.134 g, 0.19 mmol) was dissolved in 25 mL of dry DCM. To the flask, Et_3N (0.2 mL, 1.34 mmol), L-GlnOMe (0.12 g, 0.57 mmol), and HBTU (0.29 g, 0.768 mmol) were added. The reaction is kept stirring at room temperature, and the progress was monitored using TLC (eluent: DCM/MeOH 9.8:0.2). After 20 hours, the reaction was finished and was quenched with 20 mL of H_2O. The organic phase was washed with 0.1 M HCl (2x10 mL) and then with water, followed by evaporation under reduced pressure. The product was isolated through column chromatography (DCM/ MeOH 96:4). A yellow solid was obtained**.**

Yield = 70% (0.13 g)

^{1}H NMR (400 MHz, CD_3OD) δ (ppm): 7.90 (s, 4H, Ar*H*-CONH ortho), 7.84 (s, 4H, Ar*H*-NO_2 ortho), 4.62-4.59 (m, 4H, 2H, -C*H*-), 4.41-4.36 (2d, J = 13.44 4H, axial ArC*H*$_2$Ar), 4.13 (t, J = 6.1 Hz, 4H, OC*H*$_2$$CH_2CH_3$), 3.77 (s, 6H -OC*H*$_3$), 3.71 (d, J = 13.3 Hz, 4H, equatorial ArC*H*$_2$Ar), 2.43 (t, J=7.08Hz, 4H, -C*H*$_2$$CH_2$CH-), 2.33- 2.14 (m, 4H, -*CH*$_2$CHNH-), 2.13-2.07 (m, 4H, OCH_2C*H*$_2$$CH_3$), 1.35 (t, J = 7.4 Hz, 6H, OCH_2CH_2C*H*$_3$).

^{13}C NMR (101 MHz, CD_3OD) δ (ppm): 128.6 (*Ar*-NO_2 ortho), 124.2 (*Ar*-CONH- ortho), 78.8 (-OC*H*$_2$$CH_2CH_3$), 52.8 (-CH-), 51.4 (-$OCH_3$), 31.3 (-*C*$H_2CH_2$CH-), 30.6 (ArC$H_2$Ar), 26.5(-$CH_2CH_2$CH-), 23.1 ($OCH_2CH_2CH_3$), 9.9 ($OCH_2CH_2CH_3$).

ESI-MS: m/z calc 970.36 found: 993.206 $[M + Na]^+$.

m.p. > 250 °C (decomposition).

Synthesis of 5,11-diamino-11,23-di[(methoxy-L-glutamine)carbonyl]-25,27-dihydroxy-26,28-dipropoxycalix[4]arene (12)

In a PARR glass reactor, compound **7** (0.13 g, 0.134 mmol) was dissolved in 5 mL of ethanol and 0.5 of water, and a catalytic amount of Pd/C (10%) was added. The reaction was kept to stir under a hydrogen pressure of 3 bar. The progress of the reaction was monitored using TLC (eluent: DCM/MeOH 9:1, revealed with ninhydrin). After 24 hours, the reaction was finished, and the catalyst was removed by double filtration. Upon drying, a dirty white solid was obtained.

Yield= 98% (0.12 g)

^{1}H NMR (400 MHz, CD_3OD) δ (ppm): 7.67 (s, 4H, Ar*H*-CONH ortho), 6.45 (s, 4H, Ar*H*-NH_2 ortho), 4.61-4.57 (m, 2H, -CH-) 4.29-4.23 (dd, J = 12.8 Hz , 4H, axial ArCH_2Ar), 3.97 (t, J = 6.1 Hz, 4H, OC$H_2$$CH_2CH_3$), 3.43 (d, J = 13 Hz, 4H, equatorial ArCH_2Ar), 2.45-2.40 (m, 4H, -C$H_2$$CH_2$CH), 2.33-2.13 (m, 4H, -CH_2CH-), 2.17- 2.09 (m, 4H, OCH_2C$H_2$$CH_3$), 1.37 (t, J = 7.4 Hz, 6H, OCH_2CH_2CH_3).

^{13}C NMR (101 MHz, CD_3OD) δ (ppm): 115.2 (*Ar*-NH_2 ortho), 123.4 (*Ar*-CONH- ortho), 78.1 (-O*C*$H_2CH_2CH_3$), 52.8 (*C*H), 51.4 (-O*C*H_3), 31.4 (-*C*H_2CH_2CH-), 30.9 (Ar*C*H_2Ar), 26.5 (-CH_2*C*H_2CH), 20.9 (OCH_2*C*H_2CH_3), 10.16 (OCH_2CH_2*C*H_3).

ESI-MS: m/z calc 910.41 found: 911.5 [M + H]933.5 [M+Na+H]$^+$, 949.3 [M+K+H]$^+$.

m.p. > 250 °C (decomposition).

Synthesis of 5,11-dinitro-11,23-di[(methoxy-L-Arg(Pbf))carbonyl]-25,27-dihydroxy-26,28-dipropoxycalix[4]arene (15)

In a two-necked flask under nitrogen flow, compound **7** (0.150 g, 0.22 mmol) was dissolved in 5 mL of dry DCM. To the flask, Et_3N (0.15 mL, 0.77 mmol), L-Arg(Pbf)OMe·HCl (0.22 g, 0.46 mmol), and HBTU (0.16 g, 0.43 mmol) were added. The reaction was kept stirring at room temperature, and the progress was monitored using TLC (eluent: DCM/ MeOH 9:1). After 20 hours, the reaction was complete and quenched with 20 mL of H_2O. The aqueous phase was extracted with DCM (3x5 mL), the organic phases were combined, washed with HCl 1M (1x 20 ml), dried with Na_2SO_4, and then the solvent was removed under reduced pressure. The crude was purified through column chromatography (DCM/MeOH 96:4) obtaining the product as white solid.

Yield: 45% (0.15 g)

^{1}H NMR (400 MHz, CD_3OD) δ (ppm): 7.90 (s, 4H, Ar*H*-CONH ortho), 7.84 (s, 4H, Ar*H*-NO_2 ortho), 4.61 (dd, *J* = 9.3, 5.2 Hz, 2H, C*H*), 4.40 (dd, *J* = 13.3, 3.8 Hz, 4H, axial ArCH_2Ar), 4.15 (t, *J* = 6.0 Hz, 4H, OC$H_2$$CH_2CH_3$), 3.78 – 3.69 (m, 9H, OCH_3, equatorial ArCH_2Ar), 3.30 – 3.19 (m, 4H, CH_2guanidine), 2.96 (s, 4H, ArCH_2C$(CH_3)_2$O), 2.83 (s, 6H, ArCH_3), 2.58 (s, 6H, ArCH_3), 2.51 (s, 6H, ArCH_3), 2.13 (quint, J = 6.9 Hz, 3H, OCH_2CH_2CH_3), 2.00 – 1.60 (m, 6H, CH(CH_2)$_2$$CH_2$), 1.42 – 1.34 (m, 18H, C(CH_3)$_2$O, OCH_2CH_2CH_3).

13C NMR (101 MHz, CD_3OD) δ(ppm): 172.9 (*C*OOMe), 168.5 (*C*ONH), 158.5 (*Ar*OCH_2), 157.1 (*Ar*OC$(CH_3)_2$), 156.8 (C guanidine), 156.5 (*Ar*OH), 144.8 (*Ar*NO_2), 137.9 (*Ar*SO_2), 134.8 (*Ar*CONH), 133.0 (*Ar*CH_2*Ar*), 132.1(*Ar*CH_2*Ar*), 128.8 (*Ar* ortho CONH), 126.8 (*Ar*CH_3), 124.9

(*Ar*CH_3), 124.6 (*Ar*CH_3), 124.3 (*Ar* ortho NO_2), 117.0 (*C*$(CH_3)_2$), 78.8 (O*C*$H_2CH_2CH_3$), 52.8 (*C*H), 51.4 (OMe), 42.5 (Ar*C*$H_2C(CH_3)_2O$), 40.1 (*C*H_2guanidine), 37.5 (Ar*C*H_3) 30.7 (Ar*C*H_2Ar), 28.3 (CH(*C*$H_2)_2CH_2$), 27.2 (C(*C*$H_3)_2O$), 25.9 (CH(*C*$H_2)_2CH_2$), 23.1 (OCH_2*C*H_2CH_3), 18.1 (Ar*C*H_3), 16.9 (Ar*C*H_3), 9.8 (OCH_2CH_2*C*H_3)

ESI-MS: calc: 1531.76 found: 1531.75 $[M]^+$

m.p >200 (decomposition)

Synthesis of 5,11,17,23-tetra-tert-butyl-25,26,27,28-tetra-(2-ethoxyethoxy)calix[4]arene (16)

In a two-necked flask under nitrogen flow, tetra-tert-butyl-tetraethoxycalix[4]arene (5 g, 7.7 mmol) was dissolved in 100 mL of dry DCM. NaH 60% (1.11 g, 46.2 mmol) was added, and the solution is heated to 80°C for 20 minutes. Then, the solution was allowed to cool, and 2-ethoxyethyl-4-methylbenzenesulfonate (15 g, 61.6 mmol) was added slowly. The reaction was carried out under stirring and reflux at 80°C, monitoring the progress with TLC (eluent: hexane/AcOEt 7:3, detected with $FeCl_3$). After 7 days, the reaction was quenched with HCl. The precipitate was filtered and purified by reprecipitation in DCM/MeOH. A white solid was obtained.

Yield=63% (4.54 g).

^{1}H NMR (400 MHz, $CDCl_3$) δ (ppm): 6.77 (s, 8H, Ar*H*), 4.44 (d, 4H, J = 12.9Hz, axial ArC*H*$_2$Ar), 4.10 (t, 8H, J = 6.3Hz, -OC*H*$_2$CH$_2$O-), 3.93 (t, 8H, J = 6.3Hz, -OCH$_2$C*H*$_2$O-), 3.59 (q, 8H, J = 6.3Hz, -OCH$_2$C*H*$_3$), 3.11 (d, 4H, J = 12.7Hz, equatorial ArC*H*$_2$Ar), 1.23 (t, 12H, J = 7.1Hz, -OCH$_2$C*H*$_3$), 1.07 (s, 36H, -C(C*H*$_3$)$_3$).

The spectroscopic data found are in agreement with those reported in literature[35].

Synthesis of 5,11,17,23-tetranitro-25,26,27,28-tetra-(2-ethoxyethoxy)calix[4]arene (17)

In a 100 mL flask, product **11** (1 g, 1.07 mmol), $NaNO_3$ (3.63 g, 42.67 mmol), and TFA (6 mL) wereadded. The reaction was carried out under stirring, and the progress was monitored using TLC (eluent: hexane/AcOEt 6:4). The reaction was quenched by adding H2O, and the precipitate was filtered and extracted with DCM (3x20 mL). Purification was performed through recrystallization in MeOH. A yellow solid was obtained.

Yield= 81% (1.53 g).

^{1}H NMR (400 MHz, $CDCl_3$) δ (ppm): 7.59 (s, 8H, Ar*H*), 4.68 (d, 4H, J = 12.8Hz, axial ArC*H*$_2$Ar), 4.23 (t, 8H, J = 6.1Hz, -OC*H*$_2$CH$_2$O-), 3.77 (t, 8H, J = 6.1Hz, -OCH$_2$C*H*$_2$O-), 3.49 (q, 8H, J = 6.1Hz, -OC*H*$_2$CH$_3$), 3.37 (d, 4H, J = 12.6Hz, equatorial ArC*H*$_2$Ar), 1.16 (t, 12H, J = 7.0Hz, -OCH$_2$C*H*$_3$).

The spectroscopic data found are in agreement with those reported in literature[31].

Synthesis of 5,11,17,23-tetraamino-25,26,27,28-tetra-(2-ethoxyethoxy)calix[4]arene (18)

In a two-necked flask under nitrogen flow, was dissolved product **12** (1.4 g, 1.34 mmol) in 50 mL of ethanol, and hydrazine (1.31 mL, 27 mmol) and a Pd/C (catalytic amount) were added. The reaction was kept stirring under reflux. The progress of the reaction was monitored using TLC (eluent: DCM/ MeOH 8:2, detected with ninhydrin). The reaction was complete after 36 hours, then was filtered and the solvent was evaporated under reduced pressure. A yellow solid was obtained.

Yield = 96% (1.15 g).

^{1}H NMR (400 MHz, CD_3OD) δ (ppm): 6.07(s, 8H, Ar*H*-NH$_2$), 4.33 (d, 4H, J = 13.3 axial ArC*H*$_2$Ar), 3.98 (t, 8H, J = 5.9, -OC*H*$_2$CH$_2$O-), 3.79 (t, 8H, J = 5.9, -OCH$_2$C*H*$_2$O-), 3.53 (q, 8H, J = 6.5, -OC*H*$_2$CH$_3$), 2.91 (d, 4H, equatorial ArC*H*$_2$Ar), 1.19 (t, 12H, J = 7.1, -OCH$_2$C*H*$_3$).

The spectroscopic data found are in agreement with those reported in literature[31].

Synthesis of 5,11-di(Boc-amino)-17,23-tetramino-25,26,27,28-tetra-(2-ethoxyethoxy)calix[4]arene (19)

In a two-necked flask under nitrogen flow, was dissolved the product **13** (1.1 g, 1.42 mmol) in 10 mL of dry DCM. Subsequently, was added dropwise di-tert-butyl decarbonate (0.62 g, 2.84 mmol), previously dissolved in 3 mL of dry DCM. The reaction was kept to stir, monitoring the progress with TLC (eluent: DCM/MeOH 95:5). After 50 hours, the reaction is complete. The solvent is removed under reduced pressure. The product was purified by column chromatography (AcOEt/hexane = 7/3). A yellow resin was obtained.

Yield: 58% (0.803 g).

^{1}H NMR (400 MHz, $CDCl_3$) δ (ppm): 6.95 (s, 2H, -N*H*CO-), 6.64 (s, 2H, Ar*H*- NHCO ortho), 6.42 (s, 2H, Ar*H*- NHCO ortho), 6.03 (s, 4H, Ar*H*-NH_2 ortho), 4.43-4.31 (m, 4H, axial ArCH_2Ar), 4.04-3.91 (m, 8H, -OC$H_2$$CH_2$O-), 3.78-3.74 (m, 8H, -$OCH_2CH_2$O-), 3.57-3.51 (m, 8H, -OC$H_2$$CH_3$), 3.09-2.88 (m, 4H, equatorial ArCH_2Ar), 1.48 (s, 18H, -C(CH_3)$_3$), 1.20-1.16 (m, 12H, -OCH_2CH_3).

^{13}C NMR (101 MHz, $CDCl_3$) δ (ppm): 122.1 (*Ar*H-NHCO), 115.16 (*Ar*H-NH_2), 73.1, 73.0 (-OC$H_2$$CH_2$O-), 69.6 (-$OCH_2CH_2$O-), 66.4 (-OC$H_2$$CH_3$), 30.9 (ArC$H_2$Ar), 28.4 (-C(C$H_3$)$_3$), 15.3 (-$OCH_2CH_3$).

p.f. > 250 °C (decomposizione).

ESI-MS: m/z calc: 972.55, found: 773.40 $[M+H-2Boc]^+$, 873.50 $[M+H-Boc]^+$

Synthesis of 5,11-di(Boc-ammino)-17,23-di[(N-Fmoc-glutamic acid (OAll))-ammino]- 25,26,27,28-tetra-(2-Etossietossi)calix[4]arene (20)

In a two-necked flask, under a nitrogen flow, compound 14 (0.361 g, 0.37 mmol) was dissolved in 50 mL of dry DCM. To the flask, Et_3N (0.1 mL, 0.74 mmol), Fmoc-Glu(OAll)OH (0.56 g, 1.11 mmol), and HBTU (0.562 g, 1.48 mmol) were added. The reaction was kept to stir at room temperature and was monitored using TLC (eluent: DCM/AcOEt/Hex 5:5:1). After 24 hours, the reaction was complete and quenched with 20 mL of water. The aqueous phase was extracted with DCM (3x5 mL), and the organic phases were combined and washed with water. The mixture was then dried over Na_2SO_4 and subjected to reduced pressure to remove the solvent. The product was isolated through chromatographic separation (DCM/AcOEt/Hex 5:5:2), yielding a dark yellow solid.

Yield: 70% (0.45g)

^{1}H NMR (400 MHz, CD_3OD) δ (ppm): 7.80-7.17 (m, 16*H*, Fmoc), 7.07-6.69 (m, 8H, Ar*H*), 5.96-5.81 (m, 2H, CH_2=C*H*CH_2-) 5.30-5.13 (m, 4H, CH_2=CHCH_2-), 4.60-4.48 (m, 8H, CH_2=CHCH_2O-, axial ArCH_2Ar), 4.37-4.31 (m, 4H, -CH_2-(Fmoc)), 4.22-4.05 (m, 12H, -OC$H_2$$CH_2$O-, -C*H*- (Fmoc), -C*H*-)), 3.92-3.87 (m, 8H, -OCH_2CH_2OEt), 3.61-3.56 (m, 8H, -OC$H_2$$CH_3$), 3.16- 3.07 (m, 4H, equatorial ArCH_2Ar), 2.46-2.33 (m, 4H, -C$H_2$$CH_2$CH-), 2.16-1.86 (m, 4H, -CH_2CH_2CH-), 1.39-1.36 (m, 18H, -CH_3), 1.24-1.20 (m, 12H, -OCH_2CH_3)

^{13}C NMR (101 MHz, CD_3OD) δ (ppm): 132.1 (CH_2=*C*HCH_2-),127.4 (Fmoc), 126.6 (Fmoc), 124.7(Fmoc), 120.9 (-*Ar*H), 119.5 (-*Ar*H), 116.9 (*C*H_2=CHCH_2-), 73.1 (-O*C*$H_2$$CH_2$OEt), 69.6 (-

OCH_2CH_2OEt), 66.5 (-CH_2-(Fmoc)), 65.9 (-OCH_2CH_3), 64.9 (CH_2=$CHCH_2O$-), 54.9 (-CH-),47.0 (-CH-(Fmoc)),30.6 (ArCH_2Ar), 29.9 (-CH_2CH_2CH-), 27.4 (CH_3), 26.9 (-CH_2CH_2CH-) 14.2 (-OCH_2CH_3).

ESI-MS: m/z calc: 1754.83 found: 1656 $[M-Boc+2H]^+$, 1773.6 $[M+Na]^+$.

m.p. > 200 °C (decomposition).

Synthesis of 5,11-diamino-17,23-bis[(N-Fmoc-glutamic acid(OAll))-amino]-25,26,27,28-tetra-(2-ethoxyethoxy)calix[4]arene (21)

In a flask, compound 15 (0.378g, 0.215 mmol) was dissolved in 1 mL of DCM, then TFA (1 mL) and TES (0.1 mL, 0.43 mmol) were added. The reaction was kept stirring at room temperature and monitored using TLC (AcOEt/DCM 1:1, visualized with ninhydrin). The reaction was complete after 24 hours, and it was terminated by drying under reduced pressure obtaining the product as a dark yellow solid.

Yield: 85% (0.33g)

^{1}H NMR (400 MHz, CD_3OD) δ (ppm): 7.80-7.23 (m, 16*H*, Fmoc), 7.06-6.67 (m, 8H, Ar*H*), 5.96-5.84 (m, 2H, CH_2=C*H*CH_2-) 5.30-5.16 (m, 4H, CH_2=$CHCH_2$-), 4.60-4.48 (m, 8H, CH_2=$CHCH_2O$, axial ArCH_2Ar), 4.40-4.26 (m, 4H, -CH_2-(Fmoc)), 4.21-4.07 (m, 12H, -OCH_2CH_2O-, -C*H*- (Fmoc), -C*H*-)), 3.86 (t, J=6.5 Hz, 8H, -OCH_2CH_2OEt), 3.59-3.53 (m, 8H, -OCH_2CH_3), 3.13- 2.98 (m, 4H, equatorial ArCH_2Ar), 2.48-2.40 (m, 4H, -CH_2CH_2CH-), 2.15-1.88 (m, 4H, -CH_2CH_2CH-), 1.22 (t, J= 8Hz, 12H, -OCH_2CH_3).

^{13}C NMR (101 MHz, CD_3OD) δ (ppm): 132.2 (CH_2=$CHCH_2$-), 127.4 (Fmoc), 126.7(Fmoc), 124.7 (Fmoc), 121.5 (-*Ar*H), 119.5 (Fmoc), 117.7 (-*Ar*H), 116.9 (CH_2=$CHCH_2$-), 73.3 (-OCH_2CH_2OEt), 69.7 (-OCH_2CH_2OEt), 66.5 (-CH_2-(Fmoc)) 65.8 (-OCH_2CH_3), 64.9 (CH_2=$CHCH_2O$-), 54.8 (-CH-), 47.0 (-CH- (Fmoc)), 30.6 (ArCH_2Ar), 29.7 (-CH_2CH_2CH-), 26.9 (-CH_2CH_2CH), 14.3 (-OCH_2CH_3).

ESI-MS: m/z calc 1554.73 found: 1556.843 $[M + 2H]^+$, 1578.807 $[M+Na]^+$.

m.p. > 250 °C (decomposition)

Synthesis of 5,11-bis[(N-Fmoc-L-lysine(Fmoc))amino]-17,23-bis[(N-Fmoc-glutamic acid(OAll))-amino]-25,26,27,28-tetra-(2-ethoxyethoxy)calix[4]arene (22)

In a two-necked flask, under a nitrogen flow, compound 16 (0.15 g, 0.096 mmol) was dissolved in 50 mL of dry DCM. To the flask, Et_3N (0.03 mL, 0.193 mmol), Fmoc-Lys(Fmoc)OH (0.17 g, 0.29 mmol), and HBTU (0.146 g, 0.386 mmol) were added. The reaction was kept stirring at room temperature and was monitored using TLC (eluent: DCM/AcOEt 2:8, visualized with ninhydrin). After 24 hours, the reaction was complete and quenched with 20 mL of water. The aqueous phase was extracted with DCM (3x5 mL), and the organic phases were combined, washed with water, dried over Na_2SO_4, and subjected to reduced pressure for drying. The product was isolated through chromatographic separation (DCM/AcOEt 2:8). A pale-yellow solid was obtained.

Yield: 70% (0.14 g)

^{1}H NMR (400 MHz, DMSO-d_6) δ (ppm): 7.85-7.23 (m, 48H, Fmoc), 7.09-6.76 (m, 8H, Ar*H*), 5.85-5.75 (m, 2H, CH_2=C*H*CH_2-), 5.21-5.09 (m, 4H, C*H*$_2$=CHCH_2-), 4.49-4.39 (m, 4H, CH_2=CHC*H*$_2$O-, axial ArC*H*$_2$Ar), 4.24-4.02 (m, 30H, -C*H*$_2$-(Fmoc), -C*H*- (Fmoc), -OC*H*$_2$$CH_2$O-, -$CH_2CH_2CH_2CH_2$C*H*- , -$CH_2CH_2$C*H*-), 3.83-3.79 (bs, 8H, -OCH_2C*H*$_2$O-), 3.52-3.46 (m, 8H, -OC*H*$_2$$CH_3$), 3.10-3.04 (m, 4H, equatorial ArC*H*$_2$Ar), 2.93 (bs, 4H, -C*H*$_2$C$(CH_2)_3$CH-), 2.33-2.28 (m, 4H, -C*H*$_2$$CH_2$CH-), 1.98-1.76 (m, 4H, -CH_2C*H*$_2$CH-), 1.62-1.20 (m, 12H, -CH_2C*H*$_2$*CH*$_2$*CH*$_2$CH-), 1.16-1.12 (2t, 12H, -OCH_2C*H*$_3$).

^{13}C NMR (101 MHz, DMSO-d_6) δ (ppm):133.0 (CH_2=*C*HCH_2-), 128.1 (Fmoc), 127.4 (*Ar*H), 125.5 (Fmoc), 120.4 (Fmoc), 119.7 (*Ar*H), 118.1 (*C*H_2=CHCH_2-), 73.7 (-O*C*$H_2$$CH_2$O-), 69.5 (-$OCH_2$*C*$H_2$O-), 65.9 (-O*C*$H_2$$CH_3$), 65.7(-*C*$H_2$-(Fmoc), 64.8 ($CH_2$=CH*C*$H_2$O-), 55.0 (-$CH_2CH_2$*C*H-), 47.1 ((-*C*H-(Fmoc)), 32.2-29.5-23.3(-CH_2(*C*H_2)$_3$CH-), 31.3 (Ar*C*H_2Ar), 30.7 (-*C*$H_2$$CH_2$CH-), 27.8 (-$CH_2$*C*$H_2$CH-), 15.6 (-$OCH_2$*C*$H_3$).

ESI-MS: m/z calc 2699.19 found: 1351.62 $[M + 2H]^{2+}$, 1373.56 $[M+Na+H]^{2+}$.

m.p. > 200 °C (decomposition)

Synthesis of 5,11-di[(N-Fmoc-L-lysine(Fmoc))-amino]-17,23-di[(Fmoc-glutamic acid)-amino]-25,26,27,28-tetra-(2-ethoxyethoxy)calix[4]arene (23)

In a two-necked flask, under a nitrogen flow, compound 17 (0.05g, 0.0185 mmol) was dissolved in 2 mL of dry DCM. $Pd(PPh_3)_4$ (0.001g, 0.0075 mmol) and $PhSiH_3$ (0.008g, 0.075 mmol) were added. The mixture was kept stirring at room temperature. The reaction progress was monitored using TLC (eluent DCM/EtOAc 2:8). After 3 hours, the reaction was completed, and then it was quenched by adding 2 mL of water. The aqueous phase was extracted with DCM (3x5 mL). The organic phases were combined, dried with Na_2SO_4, and evaporated under reduced pressure. The purification was carried out using chromatographic separation (eluent: DCM/MeOH 98:2). A white solid was obtained.

Yield: 82% (0.04g)

^{1}H NMR (400 MHz, $CD_3OD/CDCl_3$ 3.5/1.5) δ (ppm): 7.67-7.17 (m, 48H, Fmoc), 7.02-6.80 (m, 8H, Ar*H*), 4.55-4.50 (m, 4H, axial $ArCH_2Ar$), 4.27-3.83 (m, 38H, $-CH_2CH_2CH_2CH_2CH-$, $-CH_2CH_2CH-$, $-CH_2$-(Fmoc), -C*H*- (Fmoc), $-OCH_2CH_2O-$, $-OCH_2CH_2O-$), 3.55 (m, 8H, $-OCH_2CH_3$), 3.16-3.09 (m, 4H, equatorial $ArCH_2Ar$), 3.05-2.90 (m, 4H, $-CH_2(CH_2)_3CH-$), 2.34-2.23 (m, 4H, $-CH_2CH_2CH-$), 2.06-1.82 (m, 4H, $-CH_2CH_2CH-$), 1.76-1.25 (m, 12H, $-CH_2(CH_2)_3CH-$), 1.23-1.16 (m, 12H, $-OCH_2CH_3$).

^{13}C NMR (101 MHz, $CD_3OD/CDCl_3$ 3.5/1.5) δ (ppm): 127.4-126.8-124.8-119.6 (Fmoc), 73.3 ($-OCH_2CH_2O-$), 69.6 ($-OCH_2CH_2O-$), 66.4 ($-CH_2$-(Fmoc), 66.1 ($-OCH_2CH_3$), 30.8 ($ArCH_2Ar$), 28.9-22.3 ($-CH_2(CH_2)_3CH-$), 14.6 ($-OCH_2CH_3$).

ESI-MS: m/z calc 2619.12 found: 1333.04 $[M + Na + H]^{2+}$.

m.p. > 200 °C (decomposition)

Synthesis of 5,11-di[(L-lysine)-amino]-17,23-di[(glutamic acid)-amino]-25,26,27,28-tetra-(2-ethoxyethoxy)calix[4]arene (24)

In a flask, compound 18 (0.04g, 0.015 mmol) was dissolved in 2 mL of DCM. 0.4 mL of piperidine was added. The mixture was kept stirring at room temperature. The reaction progress was monitored using TLC (eluent: DCM/MeOH 9:1). After 30 minutes, the reaction was completed, and then the solution was evaporated under reduced pressure. Purification was carried out by triturating in isopropanol. A slightly off-white solid was obtained.

Yield: 78% (0.015 mmol).

^{1}H NMR (400 MHz, CD_3OD) δ (ppm): 7.47-6.28 (m, 8H, Ar*H*), 4.60 (s, J = 12.6 Hz, 4H, axial ArC*H*$_2$Ar), 4.21-4.08 (m, 8H, -O*C*H$_2$CH$_2$O-), 3.98-3.65 (m, 4H, -*C*H-), 3.95-3.88 (m, 8H, -OCH$_2$*C*H$_2$O-), 3.61-3.54 (m, 8H, -O*C*H$_2$CH$_3$), 3.16-3.13 (m, 4H, equatorial ArC*H*$_2$Ar), 2.99-2.92 (m, 4H -C*H*$_2$CH$_2$CH$_2$CH-), 2.39-2.29 (m, 4H, -C*H*$_2$CH$_2$CH-), 2.16-1.84 (m, 4H, -CH$_2$C*H*$_2$CH-), 1.82-1.67 (m, 4H, -CH$_2$CH$_2$C*H*$_2$CH-), 1.75-1.67 (m, 4H, - CH$_2$C*H*$_2$CH$_2$CH-),1.58-1.67(m, 4H, CH$_2$C*H*$_2$CH$_2$CH-), 1.27-1.19(m, 12H, -OCH$_2$C*H*$_3$).

^{13}C NMR (101 MHz, CD_3OD) δ (ppm): 120.9-120.0 (ArH), 73.7-73.3(-O*C*H$_2$CH$_2$O-), 69.7-69.6(-OCH$_2$CH$_2$O-), 66.0 (-O*C*H$_2$CH$_3$), 53.8-53.4 (-*C*H-), 38.9 (-*C*H$_2$CH$_2$CH$_2$CH-), 32.9 (-*C*H$_2$CH$_2$CH-), 30.6 (Ar*C*H$_2$Ar), 28.75 (-CH$_2$*C*H$_2$CH-), 26.7 (-CH$_2$CH$_2$*C*H$_2$CH-), 22.4-21.8 (-CH$_2$(*C*H$_2$)$_2$CH-), 14.3 (-OCH$_2$*C*H$_3$).

ESI-MS: m/z calc 1286.48 found: 644.61 $[M+H]^{2+}$, 1287.68 $[M+H]^{+}$.

m.p. > 200 °C (decomposition).

5. Bibliography

(1) Zhu, N.; Zhang, D.; Wang, W.; Li, X.; Yang, B.; Song, J.; Zhao, X.; Huang, B.; Shi, W.; Lu, R.; Niu, P.; Zhan, F.; Ma, X.; Wang, D.; Xu, W.; Wu, G.; Gao, G. F.; Tan, W. A Novel Coronavirus from Patients with Pneumonia in China, 2019. *New England Journal of Medicine* **2020**, *382* (8), 727–733. https://doi.org/10.1056/NEJMoa2001017.

(2) *WHO Director-General's opening remarks at the media briefing on COVID-19 - 11 March 2020*. https://www.who.int/director-general/speeches/detail/who-director-general-s-opening-remarks-at-the-media-briefing-on-covid-19---11-march-2020 (accessed 2023-08-20).

(3) *Statement on the fifteenth meeting of the IHR (2005) Emergency Committee on the COVID-19 pandemic*. https://www.who.int/news/item/05-05-2023-statement-on-the-fifteenth-meeting-of-the-international-health-regulations-(2005)-emergency-committee-regarding-the-coronavirus-disease-(covid-19)-pandemic (accessed 2023-08-20).

(4) Prasad, S.; Potdar, V.; Cherian, S.; Abraham, P.; Basu, A.; Team, I. C. Transmission Electron Microscopy Imaging of SARS-CoV-2. *Indian Journal of Medical Research* **2020**, *151* (2–3), 241. https://doi.org/10.4103/ijmr.IJMR_577_20.

(5) Malik, Y. A. Properties of Coronavirus and SARS-CoV-2. The *Malaysian Journal of Pathology* **2020**, *42* (1), 3–11.

(6) Florindo, H. F.; Kleiner, R.; Vaskovich-Koubi, D.; Acúrcio, R. C.; Carreira, B.; Yeini, E.; Tiram, G.; Liubomirski, Y.; Satchi-Fainaro, R. Immune-Mediated Approaches against COVID-19. *Nature Nanotechnology* **2020**, *15* (8), 630–645. https://doi.org/10.1038/s41565-020-0732-3.

(7) Safiabadi Tali, S. H.; LeBlanc, J. J.; Sadiq, Z.; Oyewunmi, O. D.; Camargo, C.; Nikpour, B.; Armanfard, N.; Sagan, S. M.; Jahanshahi-Anbuhi, S. Tools and Techniques for Severe Acute Respiratory Syndrome Coronavirus 2 (SARS-CoV-2)/COVID-19 Detection. *Clinical Microbiology Review* **2021**, *34* (3), e00228-20. https://doi.org/10.1128/CMR.00228-20.

(8) Martin, W. R.; Cheng, F. Repurposing of FDA-Approved Toremifene to Treat COVID-19 by Blocking the Spike Glycoprotein and NSP14 of SARS-CoV-2. *J Proteome Research* **2020**, *19* (11), 4670–4677. https://doi.org/10.1021/acs.jproteome.0c00397.

(9) Zhang, C.-H.; Stone, E. A.; Deshmukh, M.; Ippolito, J. A.; Ghahremanpour, M. M.; Tirado-Rives, J.; Spasov, K. A.; Zhang, S.; Takeo, Y.; Kudalkar, S. N.; Liang, Z.; Isaacs, F.; Lindenbach, B.; Miller, S. J.; Anderson, K. S.; Jorgensen, W. L. Potent Noncovalent Inhibitors of the Main Protease of SARS-CoV-2 from Molecular Sculpting of the Drug Perampanel Guided by Free Energy Perturbation Calculations. *ACS Central Science* **2021**, *7* (3), 467–475. https://doi.org/10.1021/acscentsci.1c00039.

(10) Hatada, R.; Okuwaki, K.; Mochizuki, Y.; Handa, Y.; Fukuzawa, K.; Komeiji, Y.; Okiyama, Y.; Tanaka, S. Fragment Molecular Orbital Based Interaction Analyses on COVID-19 Main Protease − Inhibitor N3 Complex (PDB ID: 6LU7). *Journal of Chemical Information and Modeling* **2020**, *60* (7), 3593–3602. https://doi.org/10.1021/acs.jcim.0c00283.

(11) Ghahremanpour, M. M.; Tirado-Rives, J.; Deshmukh, M.; Ippolito, J. A.; Zhang, C.-H.; de Vaca, I. C.; Liosi, M.-E.; Anderson, K. S.; Jorgensen, W. L. Identification of 14 Known Drugs as Inhibitors of the Main Protease of SARS-CoV-2. *bioRxiv* **2020**, 2020.08.28.271957. https://doi.org/10.1101/2020.08.28.271957.

(12) Murgolo, N.; Therien, A. G.; Howell, B.; Klein, D.; Koeplinger, K.; Lieberman, L. A.; Adam, G. C.; Flynn, J.; McKenna, P.; Swaminathan, G.; Hazuda, D. J.; Olsen, D. B. SARS-CoV-2 Tropism, Entry, Replication, and Propagation: Considerations for Drug Discovery and Development. *PLOS Pathogens* **2021**, *17* (2), e1009225. https://doi.org/10.1371/journal.ppat.1009225.

(13) Huang, Y.; Yang, C.; Xu, X.; Xu, W.; Liu, S. Structural and Functional Properties of SARS-CoV-2 Spike Protein: Potential Antivirus Drug Development for COVID-19. *Acta Pharmacologica Sinica* **2020**, *41* (9), 1141–1149. https://doi.org/10.1038/s41401-020-0485-4.

(14) Yan, R.; Zhang, Y.; Li, Y.; Xia, L.; Guo, Y.; Zhou, Q. Structural Basis for the Recognition of SARS-CoV-2 by Full-Length Human ACE2. *Science* **2020**, *367* (6485), 1444–1448. https://doi.org/10.1126/science.abb2762.

(15) Sun, M.; Liu, S.; Wei, X.; Wan, S.; Huang, M.; Song, T.; Lu, Y.; Weng, X.; Lin, Z.; Chen, H.; Song, Y.; Yang, C. Aptamer Blocking Strategy Inhibits SARS-CoV-2 Virus Infection. *Angewandte Chemie International Edition* **2021**, *60* (18), 10266–10272. https://doi.org/10.1002/anie.202100225.

(16) Wrapp, D.; Wang, N.; Corbett, K. S.; Goldsmith, J. A.; Hsieh, C.-L.; Abiona, O.; Graham, B. S.; McLellan, J. S. Cryo-EM Structure of the 2019-nCoV Spike in the Prefusion Conformation. *Science* **2020**, *367* (6483), 1260–1263. https://doi.org/10.1126/science.abb2507.

(17) Romeo, A.; Iacovelli, F.; Falconi, M. Targeting the SARS-CoV-2 Spike Glycoprotein Prefusion Conformation: Virtual Screening and Molecular Dynamics Simulations Applied to the Identification of Potential Fusion Inhibitors. *Virus Research* **2020**, *286*, 198068. https://doi.org/10.1016/j.virusres.2020.198068.

(18) Gangadevi, S.; Badavath, V. N.; Thakur, A.; Yin, N.; De Jonghe, S.; Acevedo, O.; Jochmans, D.; Leyssen, P.; Wang, K.; Neyts, J.; Yujie, T.; Blum, G. Kobophenol A Inhibits Binding of Host ACE2 Receptor with Spike RBD Domain of SARS-CoV-2, a Lead Compound for Blocking COVID-19. *The Journal of Physical Chemistry Letters* **2021**, *12* (7), 1793–1802. https://doi.org/10.1021/acs.jpclett.0c03119.

(19) Williams-Noonan, B. J.; Todorova, N.; Kulkarni, K.; Aguilar, M.-I.; Yarovsky, I. An Active Site Inhibitor Induces Conformational Penalties for ACE2 Recognition by the Spike Protein of SARS-CoV-2. *Journal of Physical Chemistry B* **2021**, *125* (10), 2533–2550. https://doi.org/10.1021/acs.jpcb.0c11321.

(20) Wei, Y.; McLendon, G. L.; Case, M. A.; Purring, C. B.; Yu, T.; Hamilton, A. D.; Lin, Q.; Park, H. S.; Lee, C.-S. Disruption of Protein–Protein Interactions: Design of a Synthetic Receptor That Blocks the Binding of Cytochrome c to Cytochrome c Peroxidase. *Chemical Communications* **2001**, No. 17, 1580–1581. https://doi.org/10.1039/b104142h.

(21) Lin, Q.; Hamilton, A. D. Design and Synthesis of Multiple-Loop Receptors Based on a Calix〚4〛arene Scaffold for Protein Surface Recognition. *Comptes Rendus Chimie* **2002**, *5* (5), 441–450. https://doi.org/10.1016/S1631-0748(02)01408-X.

(22) Sebti, S. M.; Hamilton, A. D. Design of Growth Factor Antagonists with Antiangiogenic and Antitumor Properties. *Oncogene* **2000**, *19* (56), 6566–6573. https://doi.org/10.1038/sj.onc.1204121.

(23) Lazzarotto, M.; Sansone, F.; Baldini, L.; Casnati, A.; Cozzini, P.; Ungaro, R. Synthesis and Properties of *Upper Rim C* -Linked Peptidocalix[4]Arenes. *European Journal of Organic Chemistry* **2001**, *2001* (3), 595–602. https://doi.org/10.1002/1099-0690(200102)2001:3<595::AID-EJOC595>3.0.CO;2-#.

(24) Sansone, F.; Baldini, L.; Casnati, A.; Lazzarotto, M.; Ugozzoli, F.; Ungaro, R. Biomimetic Macrocyclic Receptors for Carboxylate Anion Recognition Based on *C* -Linked Peptidocalix[4]Arenes. *Proceedings of the National Academy of SciencesU.S.A.* **2002**, *99* (8), 4842–4847. https://doi.org/10.1073/pnas.062625499.

(25) Vezzoni C.A. Multivalent peptido- and glycocalixarenes as ligands for microorganisms. PhD thesis, University of Parma.

(26) Baldini, L.; Sansone, F.; Scaravelli, F.; Casnati, A.; Ungaro, R. *Proximal* and *Distal N* , *C* -Linked Tetra-Peptidocalix[4]Arenes as Bifunctional Receptors: Synthesis, Conformation and Preliminary Binding Studies. *Supramolecular Chemistry* **2010**, *22* (11–12), 776–788. https://doi.org/10.1080/10610278.2010.506548.

(27) Saadioui, M.; Shivanyuk, A.; Böhmer, V.; Vogt, W. Selective N-Protection of a Tetraamino Calix[4]Arene Tetraether. *Journal of Organic Chemistry* **1999**, *64* (10), 3774–3777. https://doi.org/10.1021/jo982524b.

(28) Hudecek, O.; Curinova, P.; Budka, J.; Lhoták, P. Regioselective Upper Rim Substitution of Calix[4]Arenes. *Tetrahedron* **2011**, *67* (29), 5213–5218. https://doi.org/10.1016/j.tet.2011.05.049.

(29) Boyko, V. I.; Podoprigorina, A. A.; Yakovenko, A. V.; Pirozhenko, V. V.; Kalchenko, V. I. Alkylation of Narrow Rim Calix[4]Arenes in a DMSO-NaOH Medium. *Journal of Inclusion Phenomena and Macrocyclic Chemistry* **2005**, *50* (3), 193–197. https://doi.org/10.1007/s10847-005-5240-4.

(30) Rehman, M. M.-U.-; Jabeen, A.; Mariya, M. Side Reactions in Peptide Synthesis: An Overview. *International Journal of Pharmacy Research & Technology (IJPRT)* **2018**, *8* (1), 1–11. https://doi.org/10.31838/ijprt/08.01.01.

(31) Baldini, L.; Cacciapaglia, R.; Casnati, A.; Mandolini, L.; Salvio, R.; Sansone, F.; Ungaro, R. Upper Rim Guanidinocalix[4]Arenes as Artificial Phosphodiesterases. *Journal of Organic Chemistry* **2012**, *77* (7), 3381–3389. https://doi.org/10.1021/jo300193y.

(32) Guibé, F. Allylic Protecting Groups and Their Use in a Complex Environment Part II: Allylic Protecting Groups and Their Removal through Catalytic Palladium π-Allyl Methodology. *Tetrahedron* **1998**, *54* (13), 2967–3042. https://doi.org/10.1016/S0040-4020(97)10383-0.

(33) Donofrio, G.; Franceschi, V.; Macchi, F.; Russo, L.; Rocci, A.; Marchica, V.; Costa, F.; Giuliani, N.; Ferrari, C.; Missale, G. A Simplified SARS-CoV-2 Pseudovirus Neutralization Assay. *Vaccines* **2021**, *9* (4), 389. https://doi.org/10.3390/vaccines9040389.

(34) Casnati, A.; Pochini, A.; Ungaro, R.; Ugozzoli, F.; Arnaud, F.; Fanni, S.; Schwing, M.-J.; Egberink, R. J. M.; De Jong, F.; Reinhoudt, D. N. Synthesis, Complexation, and Membrane Transport Studies of 1,3-Alternate Calix[4]Arene-Crown-6 Conformers: A New Class of Cesium Selective Ionophores. *Journal of the American Chemical Society* **1995**, *117* (10), 2767–2777. https://doi.org/10.1021/ja00115a012.

(35) van Loon, J.-D.; Heida, J. F.; Verboom, W.; Reinhoudt, D. N. Calix[4]Arenes as Building Blocks for Molecular Receptors. *Recueil des Travaux Chimiques des Pays-Bas* **1992**, *111* (7–8), 353–359. https://doi.org/10.1002/recl.19921110704.

Chapter 3: Synthesis and studies of ligands for amyloidogenic protein involved in neurodegenerative diseases

1. Introduction

Neurodegenerative diseases refer to a group of neurological disorders in which a range of conditions lead to the damage of neurons in the human brain, spinal cord, and peripheral nervous system. They pose a threat to human health and the percentage of these disorders, mainly but not only linked to age, is continuously rising with the increase in the elderly population. When synapses are impaired, cerebral functionality is compromised. A significant phenomenon that characterizes various stages of the evolution of these diseases is the formation of protein aggregates that accumulate within the brain. These protein aggregates, known as amyloids[1], vary based on the chemical composition of the precursor protein, which differs according to the pathology (Figure 1). The formation of these aggregates results from certain protein modifications that disrupt the natural structure and physiological function, leading to the formation of oligomers. These then evolve into aggregates of soluble proteins of varying sizes, eventually taking on the form of insoluble fibrils[2]. These latter are highly organized, defined by a cross-β structure, where the β filaments develop perpendicular to the axis of the fibrils[3]. Over 30 neurodegenerative diseases are caused by these issues, and for many of them, there is no available treatment. At best, the available therapy manages the symptoms but not the root cause of the disease. The development of new drugs capable of interacting with amyloidogenic proteins, preventing and/or disrupting their assembly in toxic fibrils, would offer a direct approach to treating these neuropathies.

protein	length (aa)	Lys	% Lys	Arg	% Arg	associated disease
Aβ40, Aβ42	40, 42	2	5.0, 4.8	1	2.5, 2.4	AD
Tau (embryonic)	352	37	10.5	14	4.0	AD, tauopathies
α-Synuclein	140	15	10.7	0	0.0	PD, synucleinopathies
IAPP	37	1	2.7	1	2.7	Type-2 diabetes
CT	32	1	3.1	0	0.0	Medullary Carcinoma of the Thyroid
Insulin	51	2	3.9	1	2.0	Injection-related nodular amyloidosis
β_2m	99	8	8.1	5	5.1	Dialysis-related amyloidosis
TTR	147	8	5.4	5	3.4	Senile systemic amyloidosis, Familial amyloid polyneuropathy
Lysozyme	130	5	3.8	13	10.0	Familial visceral amyloidosis
PrP(106–126)	21	2	9.5	0	0.0	

Figure 1: the most important amyloidogenic diseases. Image taken by reference[4].

In this chapter, we have focused on the synthesis of organic molecules capable of interacting with two of the main proteins responsible for the onset of these pathologies: α-synuclein (AS) and Transthyretin (TTR). The former, synthesized by neurons, is associated with Parkinson's disease (PD), a chronic neurodegenerative disorder that affects the central nervous system with a slow and progressive course, resulting from the selective and progressive degeneration of dopamine-producing

neurons in the substantia nigra[5–7]. The latter is present in the bloodstream and in the brain and is responsible for the emergence of a severe condition known as Transthyretin amyloidosis (ATTR).

1.1 α-Synuclein

Alpha-Synuclein (AS) is a small 14 kDa protein abundant in the human brain, primarily expressed in nerve terminals at the presynaptic level[8]. In its native state, it is a soluble protein without a defined morphology. Its physiological function has not been fully understood yet, but there is information about its role in both regulating synaptic vesicle release in presynaptic terminals and dopamine (DA) neurotransmission. Structurally, AS consists of 140 amino acid residues organized into three distinct domains[9] (Figure 2, left): N-terminal (residues 1-60), Central NAC (residues 61-94) and C-terminal (residues 95-140). The N-terminal region is a lysine-rich region that features a substantially conserved motif (KTKEGV), typical of apolipoproteins[10], and plays a significant role in modulating the protein's interaction with membranes[11]. The C terminal domain is an acidic and proline-rich terminus characterized by an intrinsically disordered (ID) region[12]. In general, the principal characteristic of ID proteins is that in the absence of an external partner (such as a ligand or cation) lack of a well-defined 3D structure. This aspect is also detectable in AS that adopts a random coil conformation in aqueous media but, in the presence of a lipid membrane, their interaction leads to change conformation into defined α-helical structure for NAC and N-terminus regions[13].

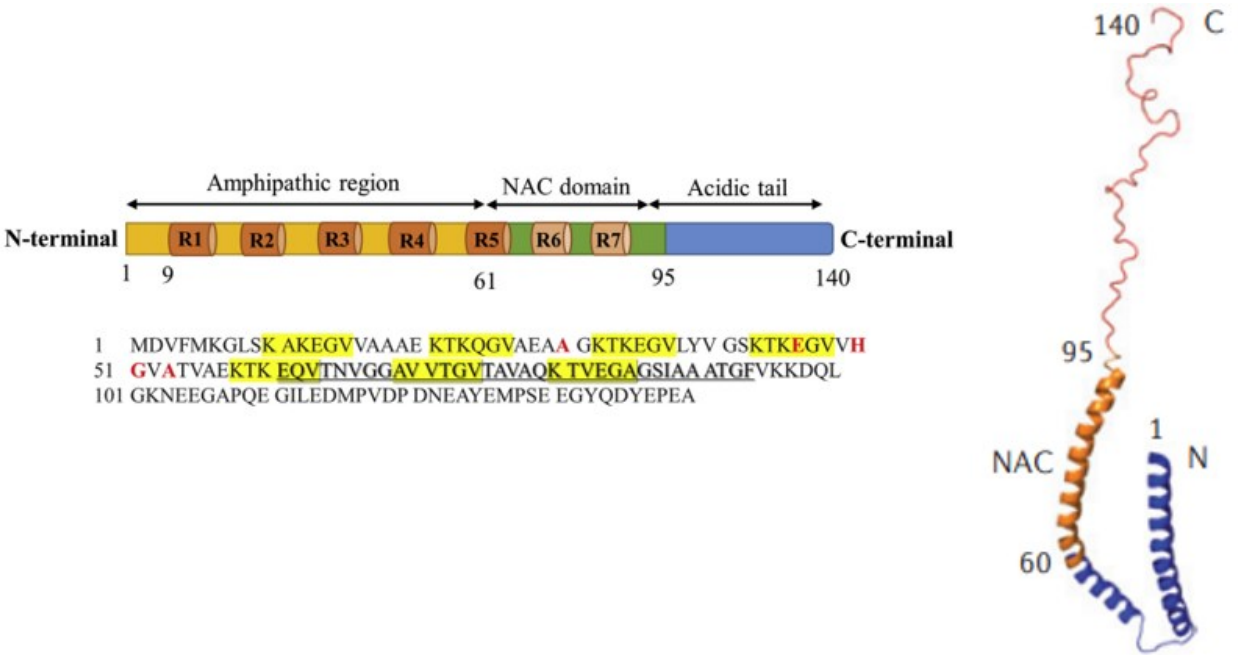

Figure 2:. The amino acid sequence of α- syn with clinical mutations (A30P, E46K, H50Q, G51D, A53T, and A53E) shown in red. The conserved motif is highlighted in yellow (left). The NAC domain is underlined. Right: quaternary structure of α- syn and distinction of the 3 domains. Imagine adapted from references[14,15].

AS can normally exist in different dynamic equilibria leading to a dimer, trimer, and tetramer of extended-α-helical form. The homotetramer seems to be more resistant to aggregation. This peculiar

interaction is due to the existence of long-range interaction between the N-terminal and C-terminal regions[16].

1.1.2 Mutation of α-synuclein and mechanism of aggregation

The central NAC domain is the portion of the protein that plays a crucial role in its aggregation process, as it is characterized by a hydrophobic amino acid sequence. This domain is also known as the non-amyloid-β component NAC because it is the second major component in amyloid plaques. The gene encoding for AS is SNCA[17]. Six possible mutations of this gene (A30P, E46K, H50Q, G51D, A53T, and A53E) have been identified, all located in the N-terminal domain, indicating the significant role of this region in AS aggregate formation[14]. These mutations are rare but indicate a clear connection between AS and PD. Point mutations in this gene, such as the A53T mutation[18] (where the 53rd residue changes from the native alanine to threonine), A30P[19], and E46K[20], are linked to familial forms of parkinsonism. The A30P mutation causes clinical symptoms like those observed in sporadic PD, while other known mutations lead to an early onset of PD with rapid progression. Several studies have shown that due to mutations or variations in external conditions, the protein structure tends to lose its natural conformation, triggering incorrect folding that is responsible for aggregation[14]. In some cases of genetically originated PD, duplications or triplications of the SNCA gene have been observed, indicating that the overexpression of wild-type AS leads to the formation of toxic aggregates[21]. The aggregation of this protein is the cause of a series of neurodegenerative pathologies known as α-synucleinopathies. This class of pathologies includes, strictly related to PD, Lewy body dementia; the term "Lewy bodies" refers to the protein aggregates responsible for dementia[22,23]. The aggregation process of AS can be divided into three phases: a latency phase where monomers groups form aggregation nuclei, an elongation phase where fibrils grow exponentially, and a stationary phase where fibril growth decreases[24]. The protein's aggregation evolves from initially being in the form of an oligomer, then a protofibril, and finally into fibrils (Figure 3). Recent studies suggest that soluble AS oligomers, characterized by heterogeneity, instability, and structural/morphological variability, are the real toxic forms related to PD[25]. Biological evidence supports the idea that fibrils could represent an extreme effort by neurons to reduce this toxicity, as fibrils are more stable and less dynamic structures[26]. During aggregation, AS oligomers undergo a sequence of conformational changes from an α-helical structure to a β-sheet structure, allowing assembly into fibrils or cell internal aggregation. This aggregation phase sees a drastic increase in the β-sheet portion[6]. These aggregates can accumulate in the cytoplasm and on the surface of the endoplasmic reticulum.

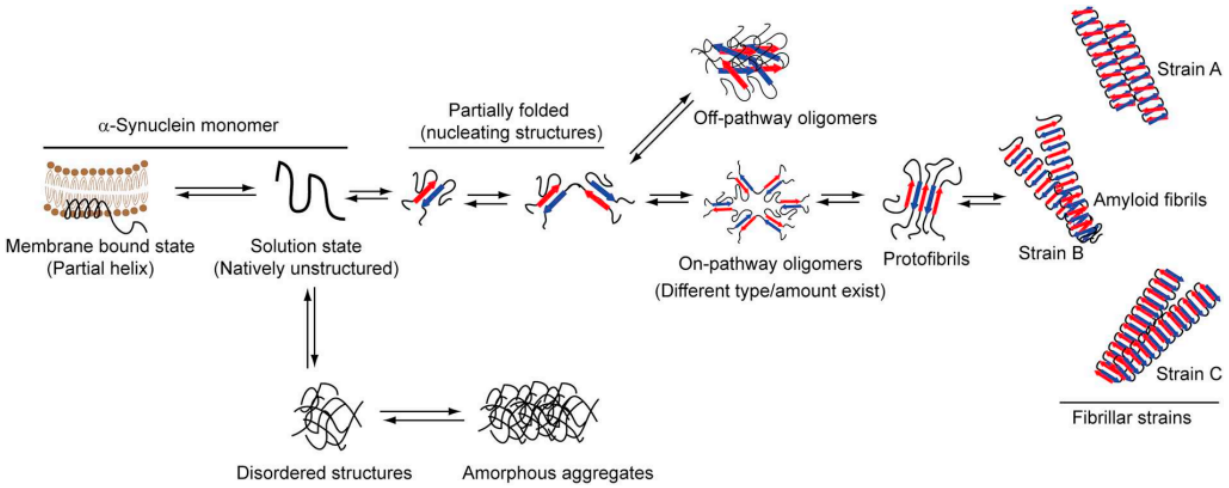

Figure 3: Aggregation stages of AS from monomer to fibril. Image taken by reference[6].

Computational studies have revealed that the conserved motif KTKEGV of the N-terminal domain significantly stabilizes the fibril structure. Furthermore, the charged residues within each repetition prefer to be solvent-exposed to further stabilize the structure, and the organization of the KTKEGV repeat (residues 58-63) significantly influences the stability of the NAC domain[26].

Since the discovery of Lewis bodies and their correlation with PD, scientific research has focused on the modulation and inhibition of this phenomenon. In this context, different approaches brought different strategies based on small-molecule inhibitors[27], dendrimers[28], peptide-[29], nucleic acid-[30], and supramolecular[31]-based inhibitors.

The small molecules seem to be the most studied as inhibitors for AS aggregation[27]. The (poly)phenolic scaffold is a rather common, repetitive motif in this class of inhibitors. The presence of the exposed hydroxylic groups destabilizes the aggregates and the aromatic core interact with β-sheet[32]. Some example of these molecules are curcumin[33], baicalein[34], and gallic acid[35] (Figure 4).

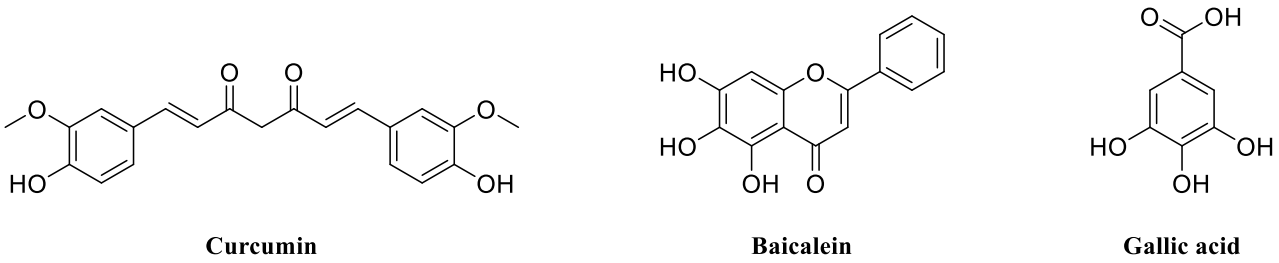

Figure 4: structure of curcumin, baicalein and gallic acid

There are several example about the use of supramolecular host-guest interaction for the inhibition of amyloid protein aggregation[36]. Schrader and colleagues reported a selective supramolecular host-guest interaction between lysine and molecular "tweezer"[37]. Lys is one of the most important and

abundant amino acids in the AS. The molecular tweezer are molecules able to bind selectively to the lysine side chain exploiting specific interactions. In this complex we can individuate different interactions: the ion-ion interaction between ammonium on lysine and phosphate on molecular tweezer, the CH-π interaction between CH_2 of the lysine chain and aromatic ring, and the hydrogen bond between the amide and the phosphate (Figure 5).

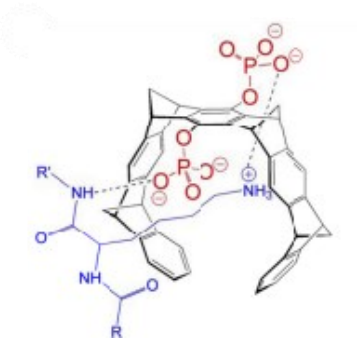

Figure 5: interaction between peptide containing lysine and molecular tweezer. Image adapted by reference[31].

Encouraged by the results reported in the literature and starting from the experience of our research group in this field, we decided to explore the known properties of calix[4]arene to complex amino acids.

1.1.3 Calix[4]arene as potential ligands of α-synuclein aggregation

It is known that calix[4]arenes functionalized at the upper rim with negatively charged groups can interact with the side chain of lysine. They establish electrostatic interactions and hydrogen bonding between their anionic groups and the ammonium moiety of lysine. Furthermore, the presence of the lipophilic cavity created by the aromatic rings allows for the establishment of CH-π interactions between the four CH_2 constituting the amino acid side chain and the calixarene. A pronounced hydrophobic effect contributes to further stabilize the lysine-calixarene complex. In the literature[38–40], several studies demonstrate the ability of calix[4]arenes functionalized at the upper rim with phosphonate or sulfonate groups to include the side chains of lysine and arginine. The cone geometry, in which all polar groups converge in a single direction in space and there is no residual conformational freedom, leading to locked aromatic rings and a pre-organized, effectively accessible lipophilic cavity, proves to be the most efficient. For instance, the p-sulfonated calix[4]arene forms highly stable 1:1 complexes with lysine and arginine, as well as di- and tri-peptides of these amino acids. This complexation process is driven by electrostatic forces, hydrogen bonding, and hydrophobic interactions [41]. Studies conducted using microcalorimetry on calix[4]arenes of three different sizes (n = 4, 6, 8) functionalized with sulfonate groups at the upper rim showed that the measured association constant decreases as the size of the calixarene ring increases[42] (Figure 6). This outcome demonstrates that the structural rigidity of the ring plays a fundamental role in the formation

of a stable inclusion complex. The needed preorganisation of the macrocyclic cavity found in the calix[4]arene is due to the OH groups at the lower rim that form a stable array of hydrogen bonding. The deprotonated form of one of them, regularly present at neutral pH, reinforces this arrangement. The hydrogen bond network prevents the interchange between the two flattened (or pinched) cone conformations that otherwise make the cavity less available and the guest complexation less efficient or even impossible.

		K'
pH 8	I_4–Arg	1520 ± 90
	I_4–Lys	735 ± 10
pH 1	I_4–Arg	2830 ± 110
	I_4–Lys	1400 ± 100
pH 8	I_6–Arg	186 ± 7
	I_6–Lys	94 ± 4
pH 1	I_6–Arg	45 ± 1
	I_6–Lys	18 ± 1
pH 8	I_8–Arg[b]	350 ± 50
	I_8–$(Arg)_2$[c]	41 ± 1
	I_8–Lys[b]	400 ± 140
	I_8–$(Lys)_2$[c]	23 ± 1
pH 1	I_8–Arg[b]	73 ± 16
	I_8–$(Arg)_2$[c]	49 ± 1
	I_8–Lys[b]	143 ± 27
	I_8–$(Lys)_2$[c]	27 ± 1

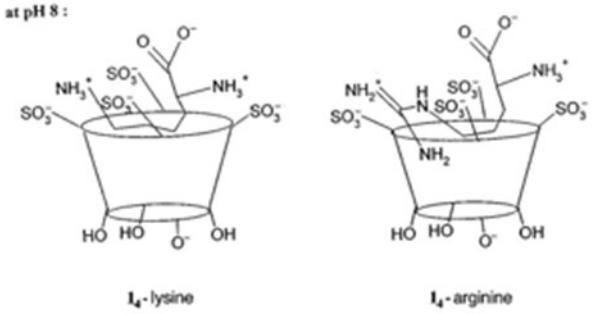

Figure 6: Complexation studies of p-sulfonato calix[n]arenes with n=4,6,8 at different pH values of 1 and 8. Image taken by reference.[42]

Another way to preorganise the calix[4]arene cavity is the functionalisation at the lower rim with short bridges connecting vicinal 1,2 and 3,4 phenols. In the past, our group verified that an anionic biscrown-peptidocalixarene was able to include in the macrocyclic cavity the aromatic moiety of α-amino acids and ammonium salts with a significantly higher efficiency than the corresponding tetrapropoxy analog hindered by the aforementioned residual conformational mobility with exchange between the two C_{2v} cone conformers[43]. On the other hand, another study, in this case conducted on tetraphosphonated calix[4]arenes, comparing the effects of various substituents at the lower rim, demonstrated that calix[4]arenes substituted, at the lower rim,with a butyl chain exhibit a notable ability to complex amino acids whose side chain can readily engage in π-π interactions, as is the case with arginine and tryptophan[40]. This capability stems from the mobility of these calixarenes which, through movement, can maximize π-π interactions with the guest.

In addition to the numerous studies documented in literature that attest to the calix[4]arene capability to complex free lysine or lysine within small peptides, several studies also demonstrate the capacity of these compounds to selectively complex lysines even when they are part of complex protein structures, such as cytochrome-c[39,44] and lysozyme[45]. Both of these proteins feature lysines exposed on their surface, with which calixarenes can interact. NMR and crystallographic analyses have facilitated the determination of the selectivity of calix[4]arene derivatives in the complexation of lysines. To this end, images of two calix[4]arenes are presented (Figure 7), one bearing sulfonate groups (right) and the other methylphosphonate groups (left), both binding to the side chain of Lys86 of cytochrome-c, as confirmed through X-ray diffraction-based solid-state structure resolution of the complexes[38].

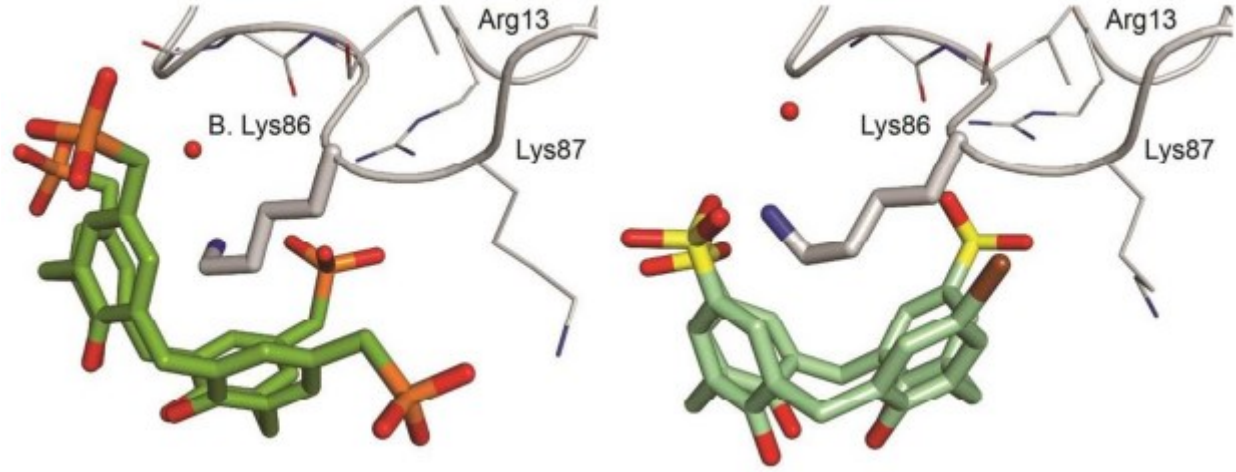

Figure 7: Inclusion of the side chain of Lys86 of cytochrome-c by two calix[4]arenes: on the left, p-methyl-phosphonate calix[4]arene. On the right, p-bromo-trisulfonate calix[4]arene. The proteins are oriented identically to highlight differences in calixarene-protein contacts. Image taken by reference [38]

Therefore, based on the reported studies, calix[4]arenes undeniably serve as an excellent starting point for the selective complexation of specific amino acids even when incorporated within a protein sequence. The upper rim functionalization with anionic groups such as phosphonate and sulfonate, alongside the macrocyclic ring rigidity, meets the essential requirements for complexing the side chain of lysine units present in α-synuclein.

In part of this chapter is reported the design, synthesis, and studies of negatively-charged calix[4]arenes studied to this aim. Different approaches for the lysine complexation are tried by design of different functionalized-calix[4]arene in order to find the best inhibitor/modulator of aggregation.

1.2 Transthyretin

Transthyretin (TTR) is primarily synthesized within the hepatic tissue, and to a lesser extent in the choroid plexi of the cerebral ventricles. Subsequently, it is secreted into the bloodstream and cerebrospinal fluid. Its quaternary structure is composed of a 55 kDa homotetramer, derived from four identical monomeric units, each with an apparent mass of 14 kDa. The individual monomeric unit is comprised of approximately 127 amino acids, featuring a singular α-helix containing 9 residues, as well as eight β-strands, designated A through H, as illustrated in Figure 8. These elements are connected by unstructured loops, collectively forming a cylindrical conformation termed a "β-barrel"[46]. The β-strands within the monomeric unit are organized into an internal and external β-sheet, oriented relatively orthogonal to one another. This arrangement is stabilized through antiparallel interactions. Notably, only ten N-terminal and five C-terminal residues appear to remain uninvolved in the folding process, effectively existing as mere "head" and "tail" segments. In dimeric form, two monomeric units aggregate, yielding a stable 37 kDa molecular weight entity (Figure 8A). The interface between the monomeric units is notably small, wherein structural cohesion is maintained via an intricate network of hydrogen bonds, predominantly engaging the H and F strands from each monomer. This intricate arrangement culminates in the establishment of a resilient dimeric structure[47].

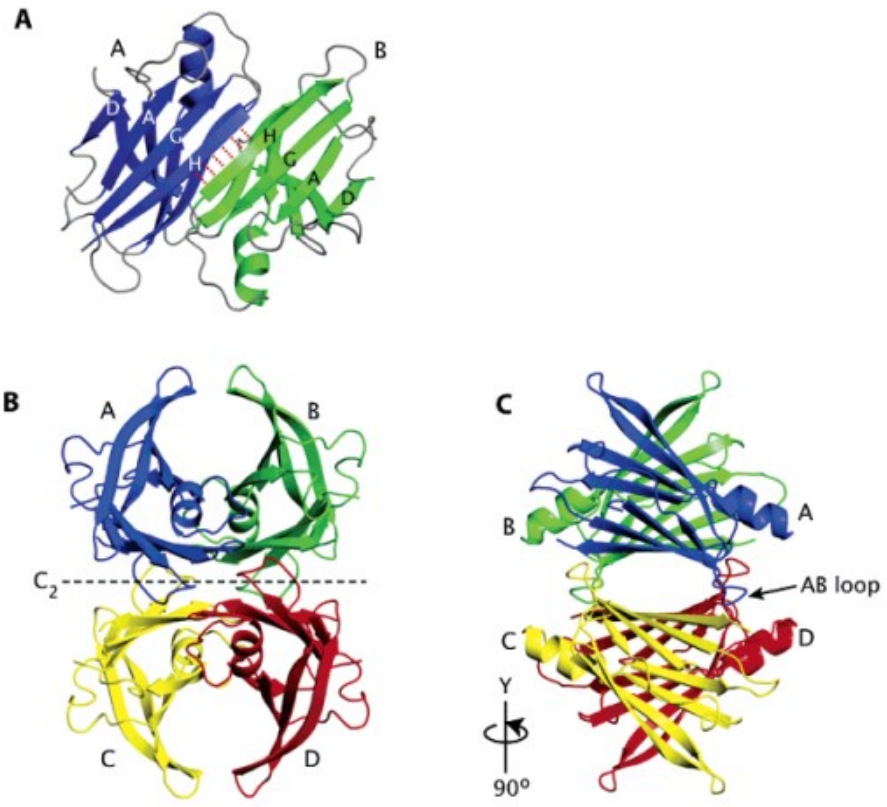

Figure 8: Structure of Transthyretin. A) Association of the dimer from the two monomers A and B, through hydrogen bonds (in red). B) Two symmetrical dimers associate to form the tetramer. C) 90° rotation of the protein structure. Image taken from reference[47].

Subsequently, two dimers associate to form the ultimate tetrameric structure (Figure 8B), wherein at the dimer-dimer interface, the formation of a funnel-shaped central cavity occurs[48] (Figure 8C). TTR functions as a carrier for the thyroid hormone L-thyroxine (T4) and retinol (vitamin A) via retinol-binding protein (RBP) in both blood circulation and cerebrospinal fluid[49,50]. Thyroid hormones are essential for a proper organism development and the regulation of all metabolic processes. In cerebrospinal fluid, where neither albumin nor thyroxine-binding globulin (TBG) are present in appreciable quantities, TTR stands as the sole protein capable of transporting thyroid hormones. The transported thyroxine T4 molecules are accommodated within two binding sites located at the interface between the two dimers, where the cylindrical "β-barrel" conformation extends (Figure 9). The site spans 50 Å in length, has a diameter of 8 Å, and entirely envelops the two hormone molecules. The iodine atoms of the thyroxine molecule are lodged within the binding site, which is lined with two sets of three hydrophobic pockets binding the halogens[50].

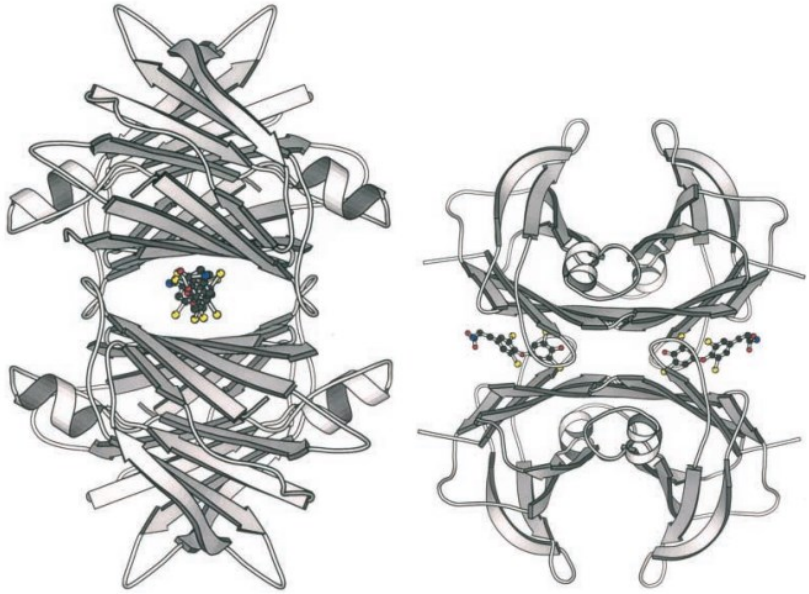

Figure 9: Binding sites of the thyroid hormone L-thyroxine (T4) in Transthyretin. Image taken by reference [46].

As initially described, the protein is implicated in the formation of amyloid fibrils and the pathogenesis of amyloidoses. Amyloidosis due to Transthyretin accumulation (ATTR) is a pathological condition caused by the aggregation of TTR monomers. Following the dissociation of the tetramer and subsequent abnormal folding, these monomers accumulate to form large amyloid fibrils within tissues (Figure 10). It has been observed that Transthyretin accumulation (ATTR) originates from both wild-type Transthyretin (wt-TTR) as well as from mutated, more aggressive and hazardous versions. wt-TTR amyloidosis, also known as Senile Systematic Amyloidosis, is the most frequently identified condition. It manifests in the elderly and is primarily characterized by cardiomyopathy[51,52]. Currently, 120 variants of mutated TTR responsible for hereditary (or familial)

ATTR have been recognized. Many of these are the result of point mutations in the amino acid sequence. These genetic variants associated with the TTR gene result in cardiac dysfunctions, cardiomyopathy, and peripheral neuropathy[53,54].

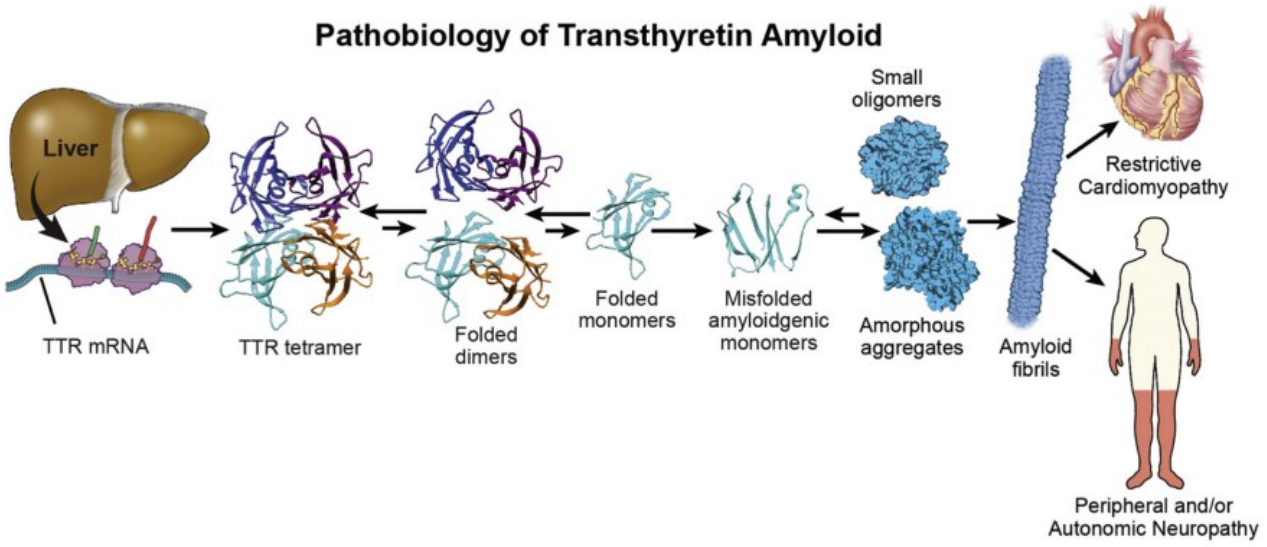

Figure 10: Mechanism of Transthyretin (TTR) protein dissociation, misfolding, and re-aggregation, leading to target organ dysfunction. Reprinted from Journal of the American College of Cardiology, 73, Ruberg, F. L.; Grogan, M.; Hanna, M.; Kelly, J. W.; Maurer, M. S., Transthyretin Amyloid Cardiomyopathy: JACC State-of-the-Art Review, 2872, © (2019), with permission from Elsevier[52].

The main therapeutic strategies employed for the treatment of TTR amyloidosis are aimed at either reducing gene expression or focusing on tetramer stabilization. Historically, liver transplantation has proven to be one of the most effective approaches for ATTR treatment[55]. Replacing a liver carrying the mutant gene with a healthy liver can drastically reduce mutant TTR levels (by up to 5% of pre-transplant levels). Unfortunately, when the central nervous system is affected by TTR amyloidosis, liver transplantation becomes entirely ineffective. To address this variant, the development of new drugs, sufficiently lipophilic to effectively traverse the blood-brain barrier, has become imperative.

Numerous natural compounds have been documented as inhibitors of transthyretin amyloidosis, serving as potential neuroprotective agents[56]. However, the pool of TTR ligands approved or currently under investigation for pharmacological therapy against ATTR remains limited (Figure 11).

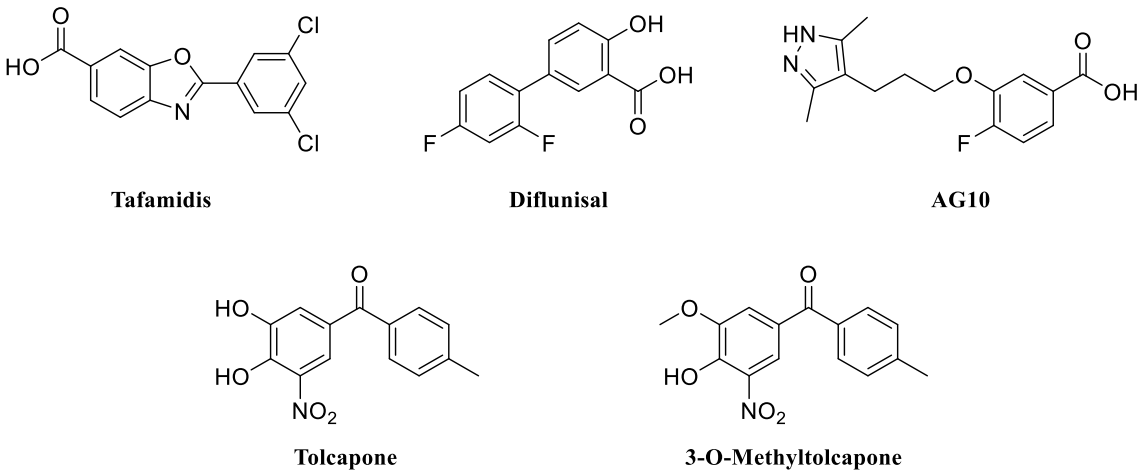

Figure 11: Chemical structures of present TTR amyloidosis inhibitors and of 3-O-methyltolcapone (3-OMT)

Among these, Tafamidis stands as an approved medication capable of slowing disease progression in individuals within the early stages of ATTR polyneuropathy[57,58] and cardiomyopathy[59]. Another noteworthy candidate is Diflunisal, a nonsteroidal anti-inflammatory drug that has shown efficacy in arresting the progression of ATTR amyloidosis by stabilizing the tetrameric structure of TTR. The application of these two medications has led to enhancements in both polyneuropathy and cardiac failure[60]. However, the deficiencies observed in approved therapies involving tafamidis, inotersen, patisiran, and diflunisal[61] underline the necessity for supplementary approaches to address ATTR. AG10, developed specifically for treating TTR amyloidosis cardiomyopathy (ATTR-CM), is currently studied through clinical trials. AG10 operates by stabilizing both wt-TTR and the V122I-TTR mutant, which are implicated in the development of familial amyloid cardiomyopathy[62]. Demonstrably, AG10 emulates the protective effects exhibited by the non-pathogenic TTR variants T119M and R104H[63]. By stabilizing the heterotetramers of these variants, wt-TTR, and TTR amyloidogenic mutants, AG10 effectively thwarts in vitro amyloidogenesis.

Furthermore, Tolcapone, an FDA-approved medication for PD, has been repurposed as a robust and selective TTR stabilizer[64]. In fact, Tolcapone demonstrated ex vivo anti-amyloidogenic activity surpassing that of tafamidis and suggesting its potential effectiveness in treating TTR amyloidosis. Having the capability to traverse the blood-brain barrier[65], tolcapone obstructs the aggregation of the V30M TTR variant, which is accountable for CNS amyloidosis[66]. Nevertheless, while the V30M TTR variant instigates an earlier onset of CNS amyloidosis, its amyloid accumulations are primarily composed of full-length wt-TTR[67]. These findings harmonize with the concept that the heightened amyloidogenic potential of human pathogenic TTR variants, especially those situated in β-strands, stems from the destabilization of their intrinsic structures. Conversely, wt-TTR itself possesses a substantial intrinsic propensity for β-aggregation, unaltered by amyloidogenic mutations[68].

Consequently, while the stabilization of TTR variants might postpone the commencement of amyloid aggregation, stabilizing wt-TTR serves to retard its progression toward amyloidogenesis[69].

In this context, it is noteworthy that tolcapone exhibits hepatotoxicity[70] and boasts a short half-life within the plasma (approximately 3 hours), attributed to rapid glucuronidation of its free 3-hydroxy group, and subsequent swift elimination via the urinary tract. The glucuronidation process targets solely the 3-hydroxy group of tolcapone, as evidenced by the absence of glucuronidation products for the free 4-hydroxy group[71]. The hepatotoxicity associated with tolcapone has also been linked to the glucuronidation activity of the enzyme UDP-glucuronosyl transferase. On the contrary, 3-O-methyltolcapone (3-OMT), a metabolite of tolcapone, exhibits significantly more favorable pharmacokinetics in humans compared to tolcapone.

In 2020, our team documented the synthesis of 3-OMT and 3-deoxytolcapone as potential TTR stabilizers, establishing insightful structure-activity relationships for both compounds. Notably, the absence of a free 3-hydroxy group was found to impede glucuronidation[72]. Employing a Western Blot analysis, when exposed to plasma proteins, 3-OMT exhibited superior effectiveness and selectivity when compared to 3-deoxytolcapone in stabilizing the tetrameric native structure of human plasma TTR. The outcomes were notably comparable to those of tolcapone, aligning well with their closely resembling chemical structures and the minor distinctions in their interactions with TTR (Figure 12).

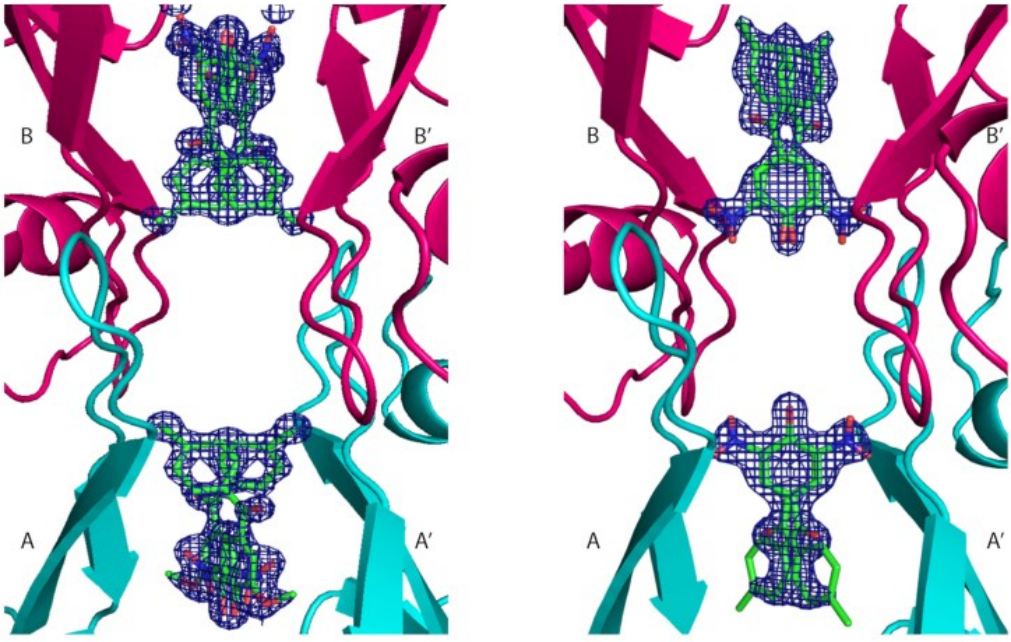

Figure 12: Electron density map of the crystal structure of TTR3-O-methyltolcapone and TTR3-deoxytolcapone complexes. On the left: Representation of 3-O-methyltolcapone in the 2 binding sites of L-thyroxine. On the right: Representation of 3-deoxytolcapone. Reprinted from Bioorganic chemistry, 103,Loconte, V.; Cianci, M.; Menozzi, I.; Sbravati, D.; Sansone, F.; Casnati, A.; Berni, R., Interactions of Tolcapone Analogues as Stabilizers of the Amyloidogenic Protein Transthyretin, 104144, © (2020), with permission from Elsevier.[72]

The methylation of the free 3-hydroxy group in tolcapone is also anticipated to confer heightened lipophilicity in contrast to tolcapone, thus potentially enhancing brain permeability for the pharmacological treatment of CNS TTR amyloidosis (including leptomeningeal and oculo-leptomeningeal amyloidosis).

Starting from previously reported works, we designed 5 different 3-OMT-like candidates and, exploiting molecular docking studies, two of these compounds were selected to be synthesized and studied, as reported in section 2.2 of this chapter.

2. Results and discussions

2.1 Negatively-charged calix[4]arenes as AS ligands

Based on the information provided in the introduction, calix[4]arenes possess specific characteristics that enable them to interact with proteins, particularly with the lysine side chain residue. These characteristics include the presence of negatively charged groups and a rigid, accessible cavity. Given these attributes, derivatives **1**-**6** were identified as useful for our purposes. (Figure 13).

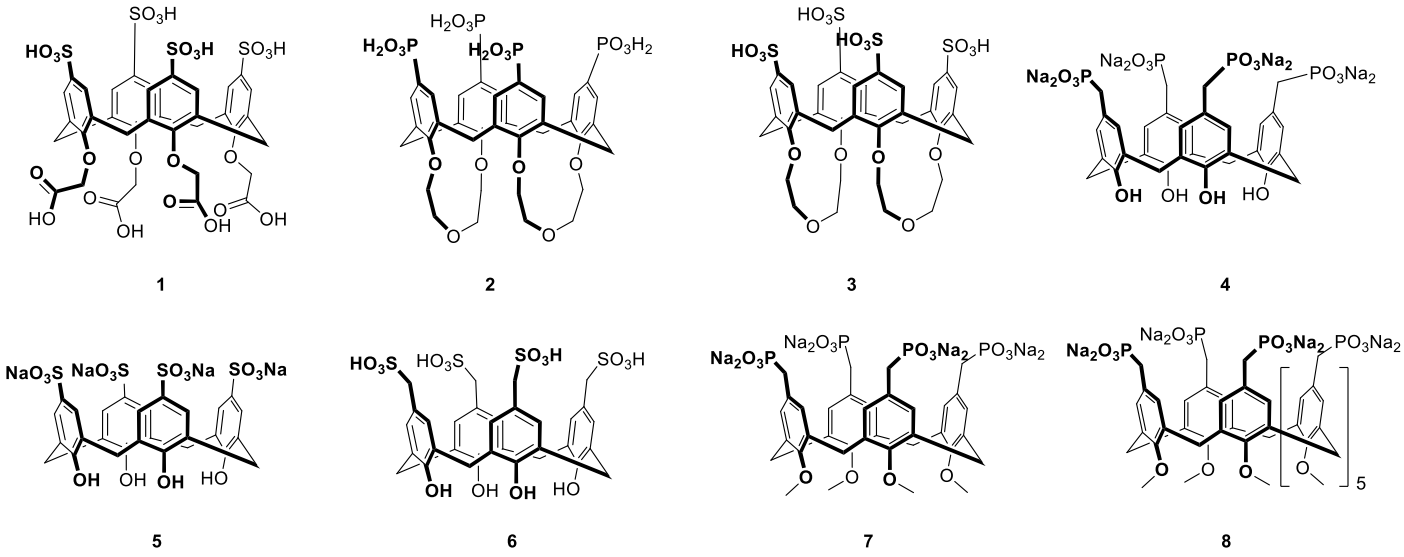

Figure 13: calixarene derivates as possible ligands for AS.

. In the case of compound **1**, the rigidity of the cavity is provided by the complexation of Na^+ by the four carboxylate chelating units (O-CH_2-COO-) at the lower rim. It has been experimentally proven that this complexation of small metal ions enhances the structural rigidity and enables the cavity to accommodate the lysine side chain. Notably, studies have demonstrated that, under these conditions, compound **1** effectively binds to the lysine side chain found in the structure of cytochrome-c53[73] (figure 14).

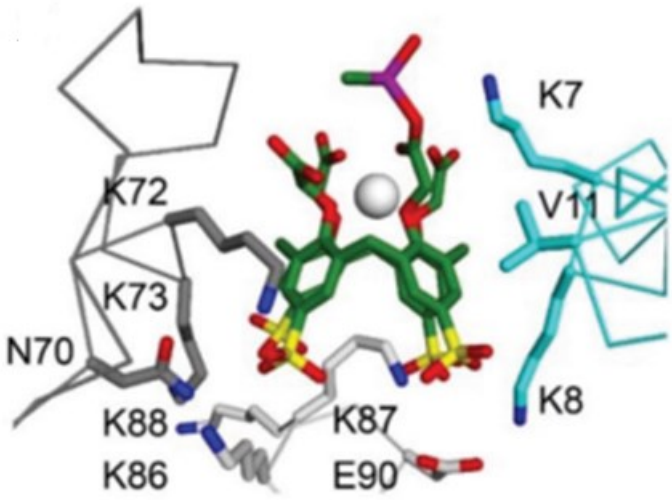

Figure 14: Complexation of calix[4]arene 4 and the lysine side chain of cytochrome-c. In the image, it is possible to observe the presence of the sodium cation (white sphere) complexed in the lower rim of the calix[4]arene, while in the upper rim with the amino acid. Image taken by reference[73].

For compounds **2** and **3** the rigid conical structure is ensured to the calixarene by the two short di(ethylene glycol) chains, each attached to adjacent oxygen atoms on the rings (positions 1,2 and 3,4). These bis-crown calixarenes have similarly proven effective in maintaining the cavity's accessibility and interacting with lysine side chains[40]. The idea of exploiting compounds **1**, **2**, and **3** as potential ligands for α-synuclein arises from the possibility of utilizing the functional groups and attached chains at the lower rim to incorporate one or more antioxidant groups into the structure. In this way, in fact, this can be achieved without compromising the macrocycle's rigidity, and thus, the actual availability of the cavity. In contrast, functionalizing even a single phenolic hydroxyl group in the other calixarene derivatives, namely **4**, **5**, and **6**, could introduce detrimental flexibility. An additional factor that underscores the danger of α-synuclein misfolding is the formation of reactive oxygen species (ROS), which can lead to oxidative stress and neuronal damage. The inclusion of an antioxidant unit serves the purpose of reducing or, ideally, inhibiting this detrimental effect. Consequently, the compound would have a dual function: preventing the formation of toxic oligomeric aggregates or disassembling existing ones, while also reducing oxidative stress. In this context, it is plausible that the phenolic units in derivatives **4**, **5**, and **6** may also participate in redox processes that are beneficial for reducing ROS levels.

Compounds **7** and **8** were also chosen for our studies. Both compounds contain phosphonate groups and exhibit conformational flexibility. The former is a calix[4]arene with relatively small methyl groups on the lower rim, allowing the aromatic rings to rotate freely through the macrocycle's annulus. The latter, being a calix[8]arene, is larger and known for its conformational flexibility. By introducing these two compounds into our research, we aimed to determine whether the presence of a rigid cavity plays a pivotal role in their interaction with α-synuclein. It is worth noting that the related derivative

in its rigid form, **4**, had previously demonstrated favourable results in complexing lysine side chains within cytochrome-c.

2.1.1 Synthesis of negatively-charged calix[4]arene for selective host-guest interaction with AS

2.1.1.1 Synthesis of compound 1

Compound **4** was synthesized following a known literature procedure, as illustrated in Scheme 1.

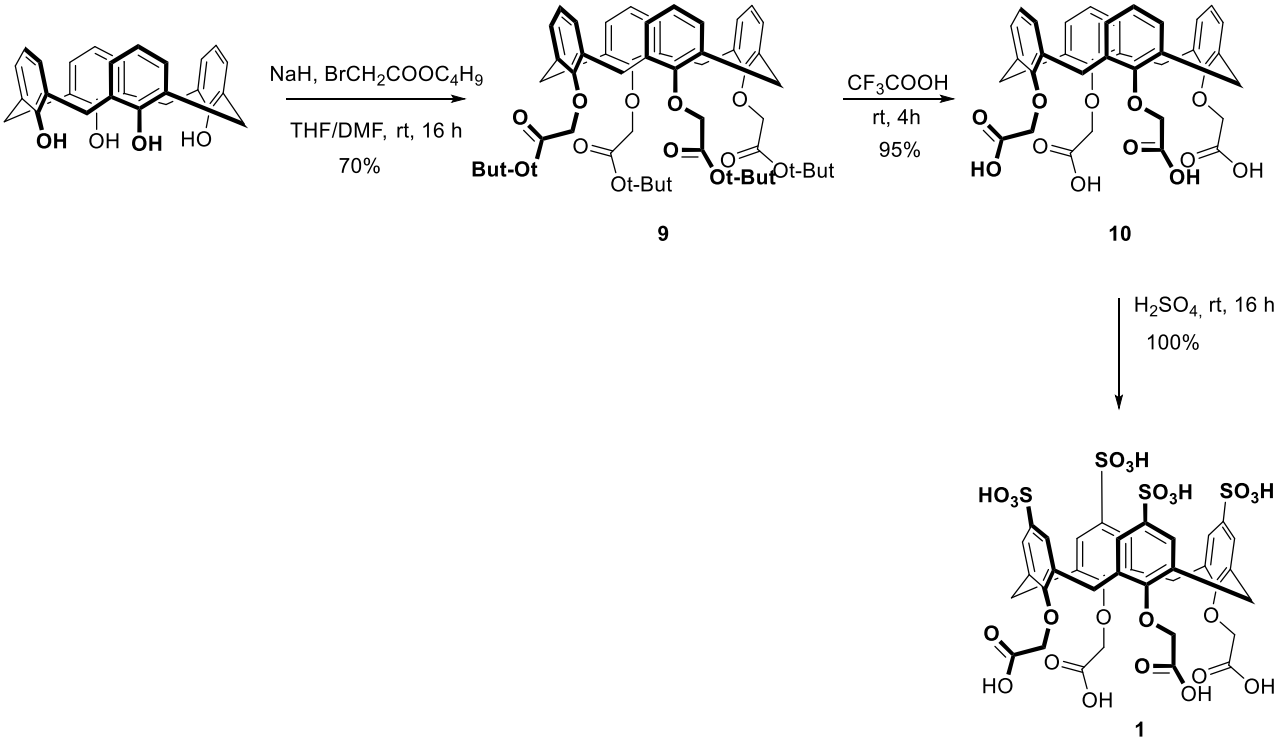

*Scheme 1: Synthesis scheme of compound **1**.*

The initial step involved the functionalization of the lower rim through a nucleophilic substitution reaction to generate compound **9**. NaH was employed to fully deprotonate all four hydroxy groups of the aromatic rings, promoting tetra-functionalization. Tert-butyl bromoacetate served as the alkylating agent. Confirmation of successful functionalization was obtained through the presence of specific signals in the ^{1}H NMR spectrum notably the singlet at 4.63 ppm corresponding to the eight protons of the -OCH_2CO- methylene groups and the singlet at 1.46 ppm attributed to tert-butyl ester methyl groups. Additionally, the presence of well-resolved doublets at 4.5 ppm and 3.5 ppm indicates that the macrocycle adopts a cone geometry. The ester groups were subsequently hydrolyzed to yield tetraacid derivative **10**. The use of tert-butyl esters was advantageous for hydrolysis with trifluoroacetic acid, as by simply evaporating, byproducts could be eliminated. Finally, sulfonation was performed using concentrated sulfuric acid, an electrophilic aromatic substitution reaction at the para position of the aromatic rings. The recovery and purification of compound **1** involved different steps compared to those reported in the literature. This procedure entailed acidification and

basification steps to neutralize the acid and remove the inorganic salts formed. In literature, a quick and practical method for removing the sulfuric acid employed washing with diethyl ether. The presence of only one signal in the aromatic region at 7.51 ppm, integrating for 8 protons corresponding to the aromatic protons of the calix[4]arene, was observed in the ^{1}H NMR spectrum in a 5% w/w NaOD in D_2O solution (Figure 15). This signal, along with the singlet for the methylene groups on the lower rim and the two doublets corresponding to the bridge methylene, unequivocally confirmed successful sulfonation on all four aromatic rings.

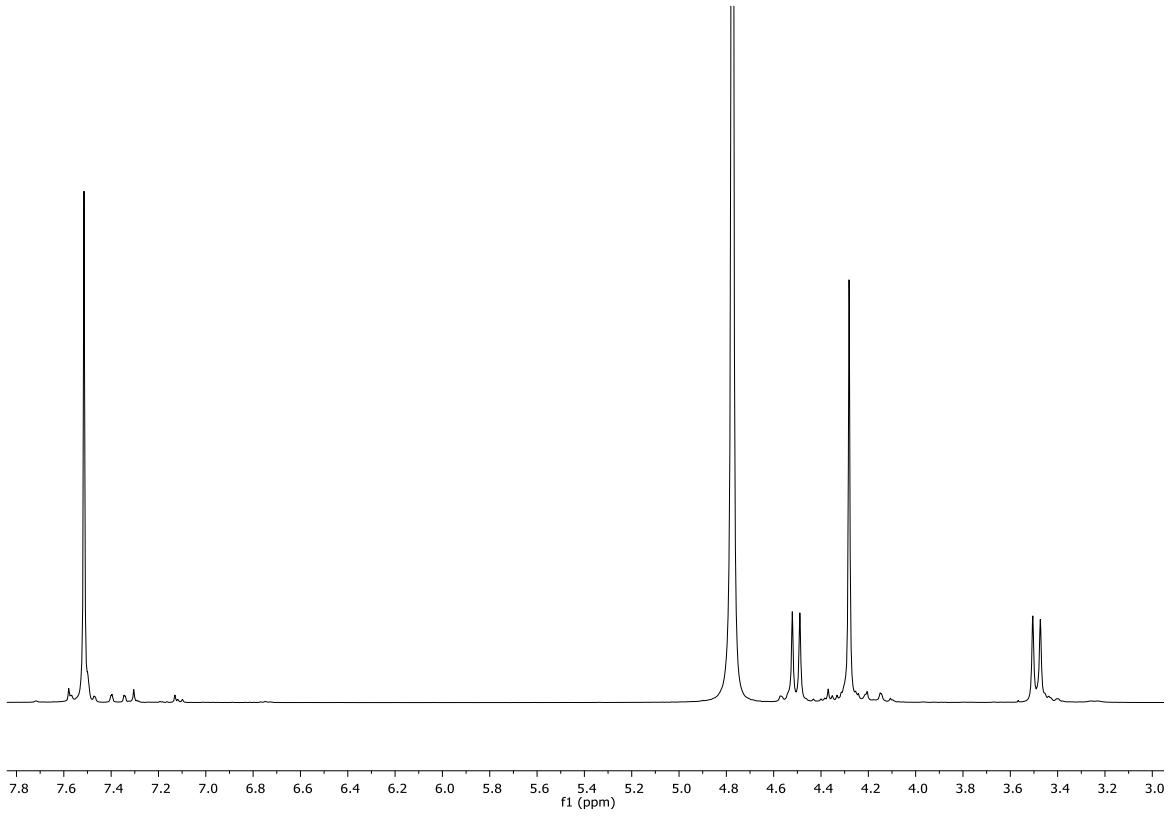

*Figure 15: ^{1}H NMR spectrum (400 MHz, D_2O+NaOD 5%, 298 K) of compound **1***

2.1.1.2 Synthesis of compound 2

Starting from the compound 25,26-27,28-biscrown-3-calix[4]arene, already present in the laboratory, compound **2** was prepared as reported in the scheme 2.

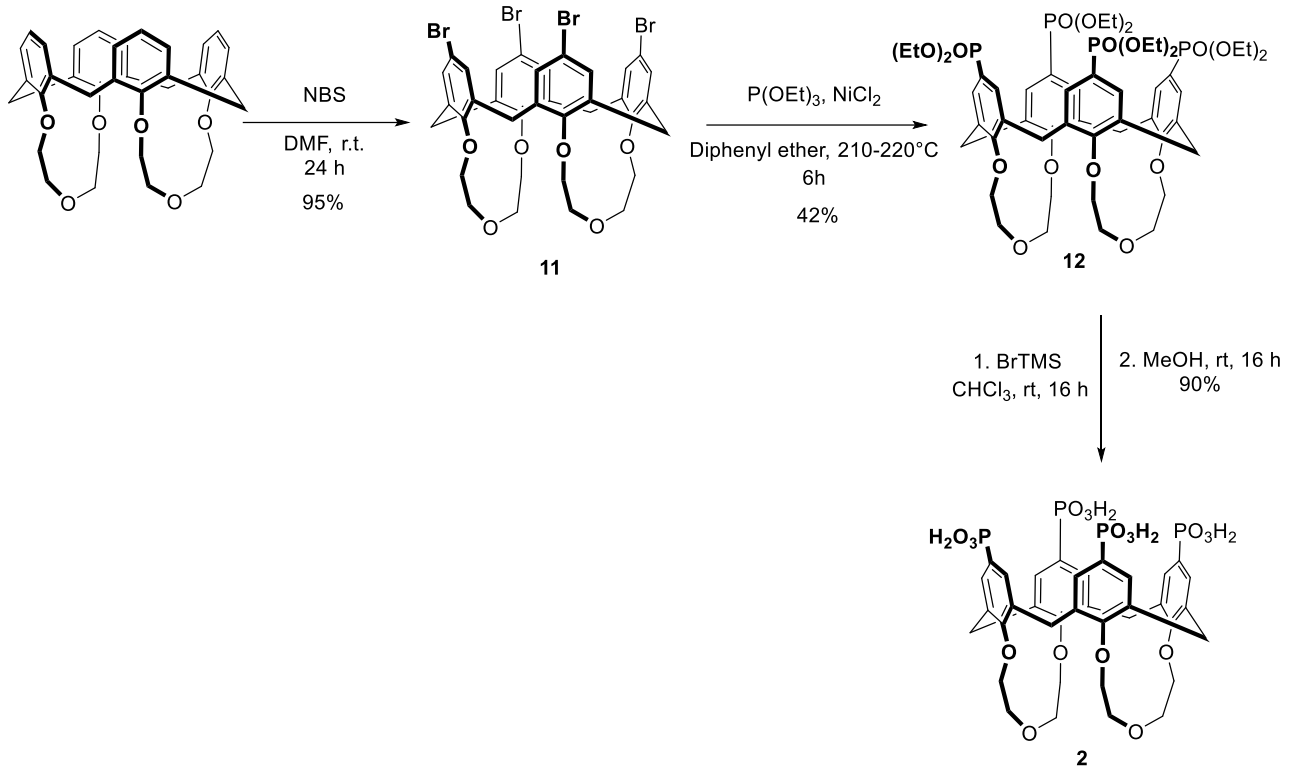

*Scheme 2: Synthesis strategy of intermediate **11***

The reaction was conducted using N-bromosuccinimide, and tetra-bromo calixarene **11** was isolated with nearly quantitative yield. The formation of the desired product **11** was confirmed by ^{1}H NMR, in particular thanks to the two doublets at 7.15 and 7.12 ppm, respectively, each integrating for four of the eight aromatic protons. The presence of the crown bound to two adjacent rings results in different chemical shifts for the two hydrogens on each ring, leading to two distinct signals with meta-coupling.

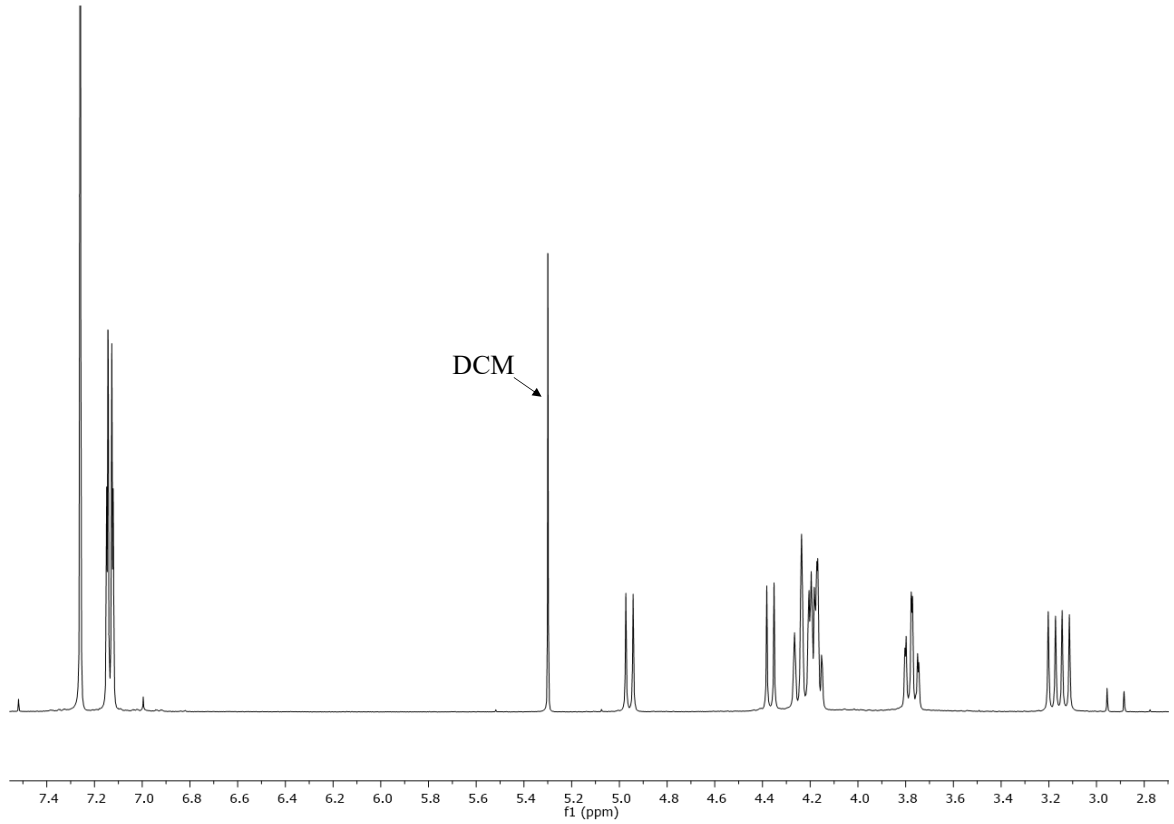

*Figure 16: ^{1}H NMR spectrum (400 MHz, 298 K, $CDCl_3$) of compound **11**.*

Subsequently, compound **11** was converted into **12** via a phosphorylation reaction, utilizing triethyl phosphite and $NiCl_2$ in diphenyl ether. The Michaelis-Arbuzov reaction is limited to the preparation of alkyl phosphonates from alkyl halides. In this case, starting from an aryl halide, a variant, the nickel(II)-catalysed Arbuzov reaction, was necessary. Differently from the literature procedure, triethyl phosphite was used instead of trimethyl phosphite due to its availability in the laboratory. The obtained compound was purified using column chromatography to separate the product from the formed nickel species. Finally, compound **11** was reacted with trimethylsilyl bromide for the hydrolysis of the phosphonic esters. Compound **12** was identified through ^{1}H NMR in D_2O in the presence of NaOD (5% w/w). In the spectrum, two doublets at 7.05 and 7.02 ppm, each integrating for four of the eight aromatic protons, were present, along with doublets at 4.37 ppm and 4.01 ppm associated with the axial methylene protons of the bridge -CH_2- between the calixarene rings, and at 2.99 ppm and 2.95 ppm for the corresponding equatorial protons.

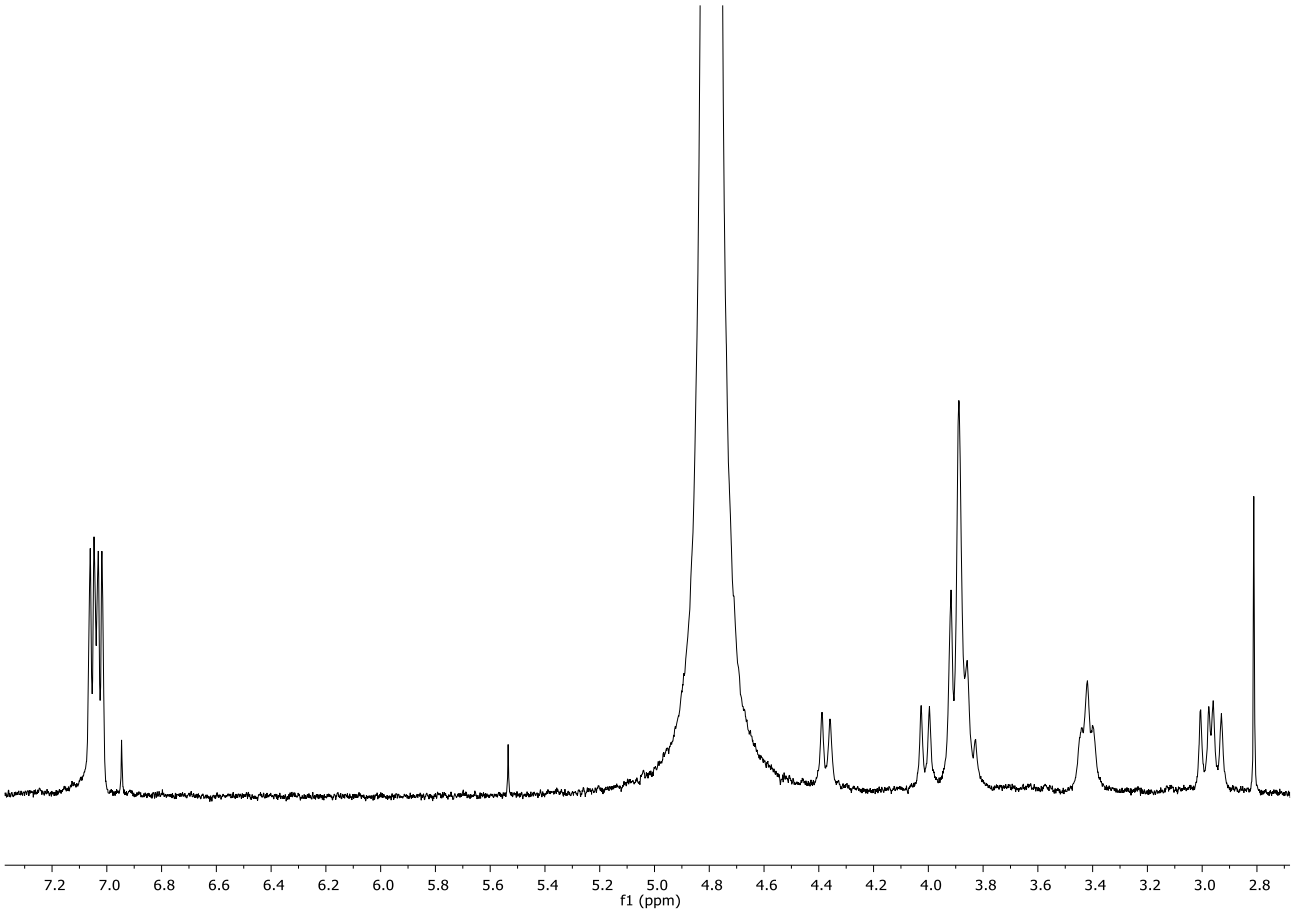

*Figure 17: ^{1}H NMR spectrum (400 MHz, D_2O+NaOD 5%, 298 K) of compound **2**.*

2.1.1.3 Synthesis of compound 3

Starting once again from the 25,26-27,28-biscrown-3-calix[4]arene, compound **3** was subsequently prepared following a procedure found in the literature[74]. The reaction was conducted using chlorosulfonic acid in dry dichloromethane at -15 °C, employing an acetone and ice bath.

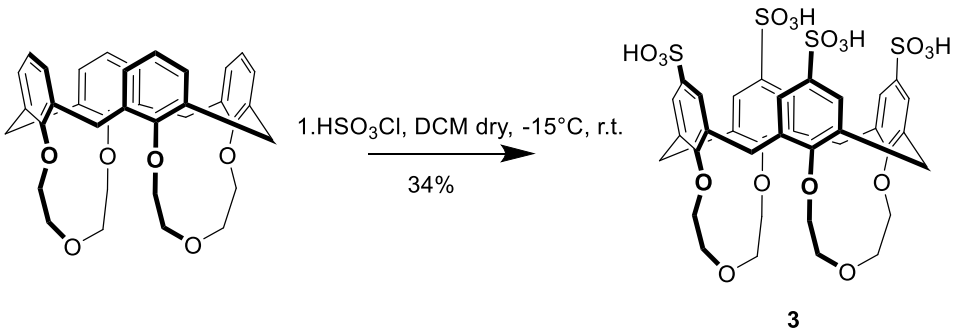

*Scheme 3: Synthesis strategy of compound **3**.*

Contrary to what was reported in the literature, instead of obtaining the chlorosulfonated calix[4]arene derivative at the end of the reaction, the desired product **3** was obtained directly, eliminating an additional reaction step. It is hypothesized that, after the addition of ice to quench the reaction, the chlorosulfonated derivative, with highly reactive chlorosulfonic acid groups, reacted directly to form

the final product **3**. The formation of the compound was confirmed through ^{1}H NMR in DMSO-d_6 and ESI-MS(-) (Figure 18) where no peaks relative to the chlorosulfonated derivative or intermediates due to partial hydrolysis were present and the peaks for **3** as $[M-H]^-$ at m/z=883.189 was found.

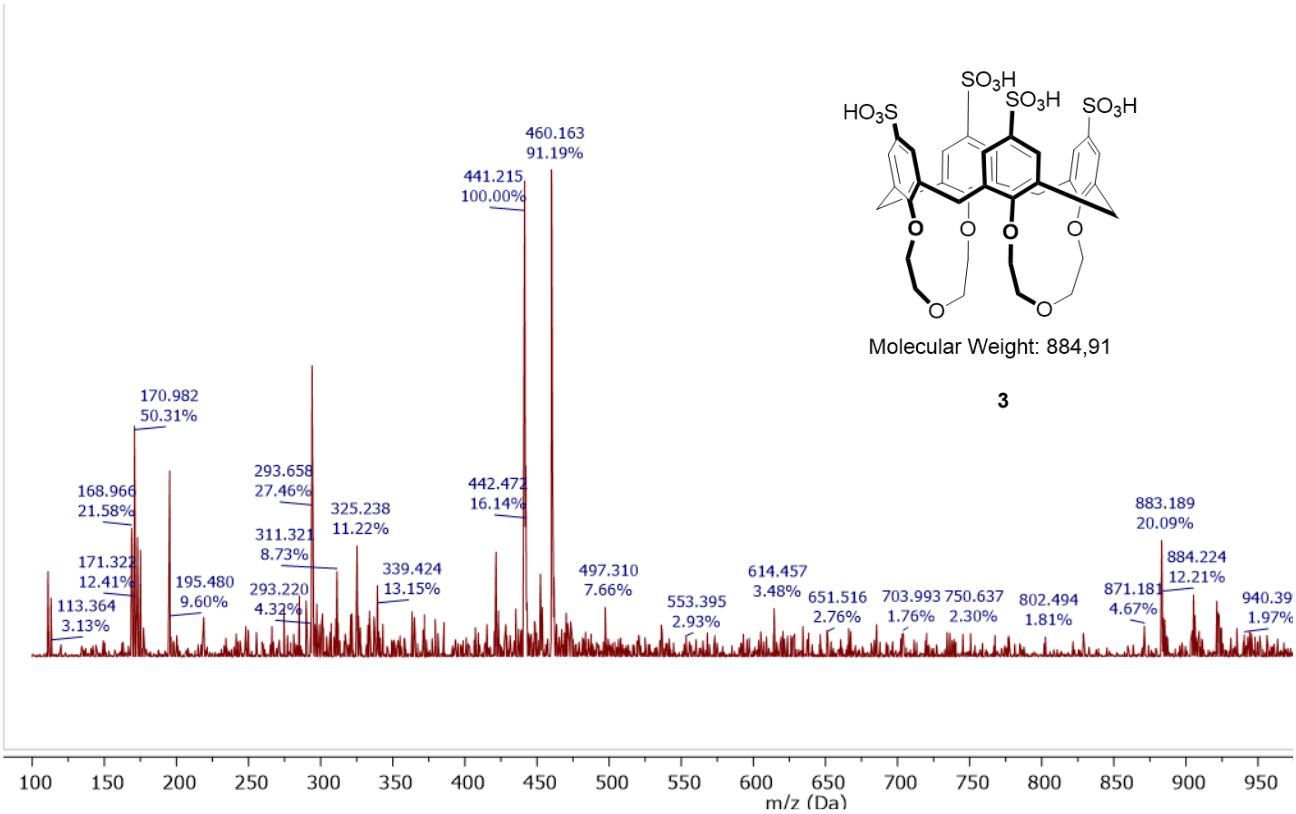

*Figure 18: zoom in the range 100/950 of ESI-MS(-) spectrum of compound **3**.*

2.1.1.4 Synthesis of compound 4

Starting from calix[4]arene, already present in lab, functionalized at the upper rim with -CH_2Br groups, target **4** was synthetized carrying out a Lewis's acid catalysed Michaelis-Arbuzov reaction using triethyl phosphite and zinc bromide (II) (scheme 4).

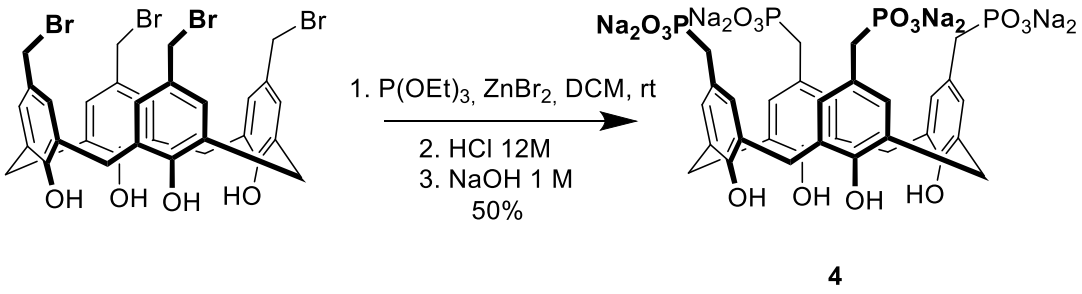

*Scheme 4: Synthesis of compound **4***

After extraction with water, for zinc bromide (II) removal, the solvent was evaporated and directly, without other purification, the compound was treated with a 12 M solution of HCl. An additional treatment with 1 M NaOH solution allowed us to obtain compound **4**. The identity and purity of

compound **4** was confirmed by comparison of its ^{1}H NMR spectrum (figure 19) with that reported in literature[73]. The two very broad signal between 3.25 and 4.25 ppm for the equatorial and axial protons of the methylene bridges are typical for this kind of calixarene in cone geometry but having free hydroxyl groups at the lower rim.

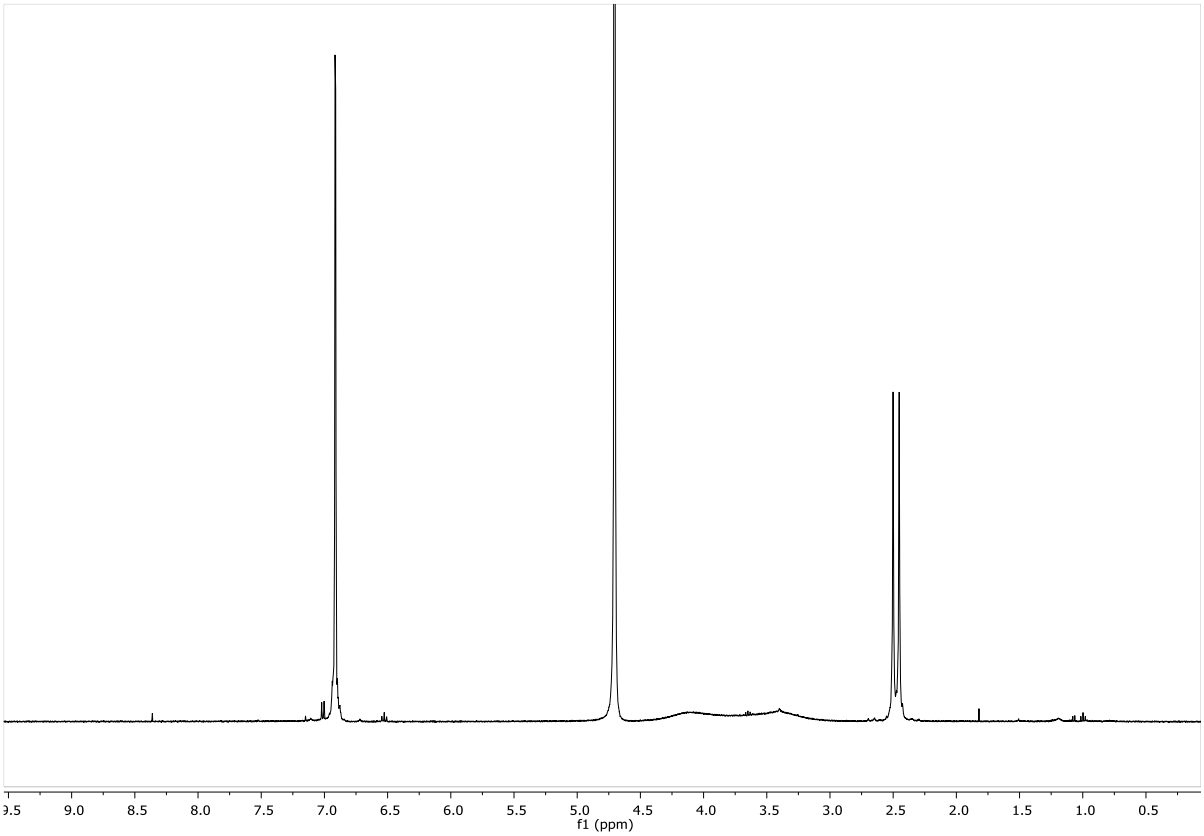

*Figure 19: ^{1}H NMR spectrum (400 MHz, 298 K) in D_2O of compound **4***

2.1.1.5 Synthesis of compound 7

The synthetic strategy employed for preparing compound **7** utilized the 25,26,27,28-tetramethoxycalix[4]arene already present in the laboratory as the starting compound. This was modified through a chloromethylation reaction (Scheme 5), resulting in the introduction of a -CH_2Cl group at the para position of the aromatic ring, following a procedure found in the literature[75].

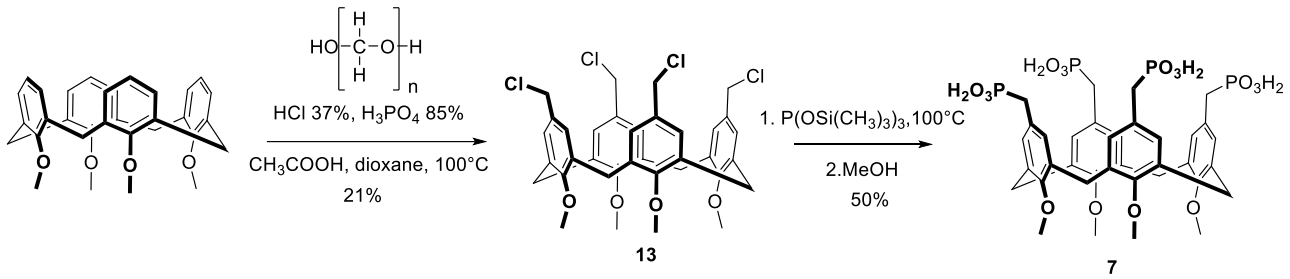

Scheme 5: Synthesis strategy of intermediate 5.

Following the procedure, compound **13** was obtained as a white solid, although with a yield of only 40% in agree with the literature[75]. The formation of compound **13** was confirmed by comparing it to literature data. The subsequent steps involved a Michaelis-Arbuzov reaction, introducing the diesterphosphonic group through a reaction with $P(OSi(CH_3)_3)_3$, followed by treatment with MeOH promoting hydrolysis. In Figure 20, the ^1H NMR spectrum in D_2O+NaOD of compound **7** is presented. Due to the presence of multiple conformers of the calixarene slowly interconverting on the NMR timescale, all the signals are broad or, as in the case of the aromatic protons, splitted. No signals attributable to the ethyl groups of the phosphonic ester are present confirming the complete hydrolysis.

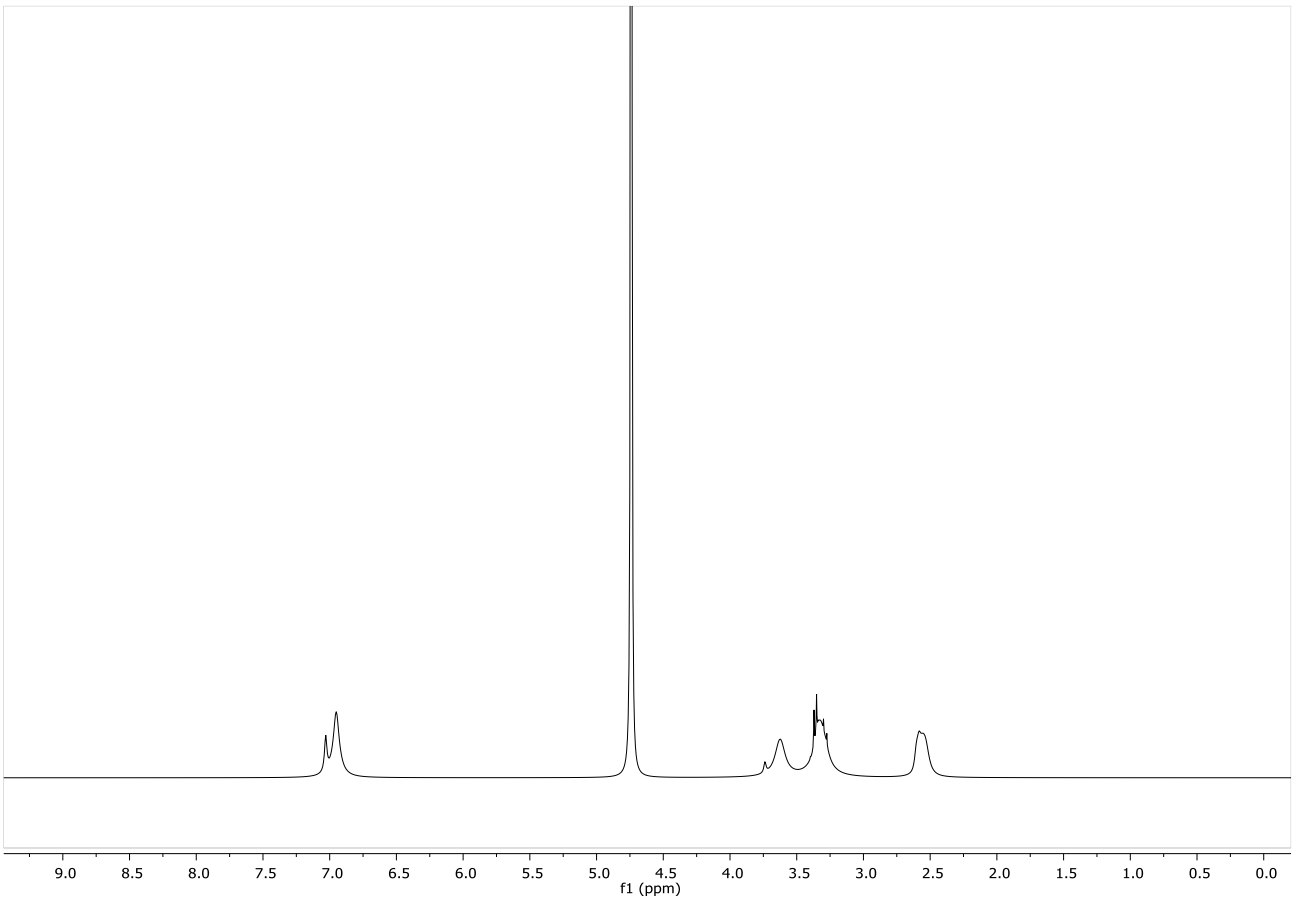

*Figure 20: ^1H NMR spectrum (400 MHz, D_2O+NaOD 1%, 298 K) of compound **7**.*

Compounds **5**, **6**, and **8** were already available in the laboratory.

2.1.1.6 Synthesis of N-Acetyl-L-Lysyl-Glycine Methyl Ester

To have an extremely simplified model for very preliminary titration studies, we synthesised the N-acetyl-L-lysyl-glycine methyl ester dipeptide. This dipeptide was chosen based on the hypothesis that the inhibition of toxic AS oligomer formation by the prepared derivatives may occur through the inclusion of the lysine side chain. In this dipeptide, lysine forms an amide bond with the acetate group and a peptide bond with glycine, which is in turn esterified. This arrangement places lysine, in terms

of functional groups, as if it is part of a peptide sequence. Notably, there are no free amino groups (α-amino and carboxyl) in solution, which could introduce disturbances during the complexation process, differing from the lysine's terminal position in α-syn. Glycine was chosen as it is the only α-amino acid without functional groups on the side chain, requiring no additional adjustments during synthesis steps and is unlikely to hinder complexation between calixarenes and lysine. The methyl ester on glycine was incorporated to prevent repulsion effects between negatively charged groups between the two structures during complexation. The dipeptide was synthesized following the synthetic strategy outlined in Scheme 6.

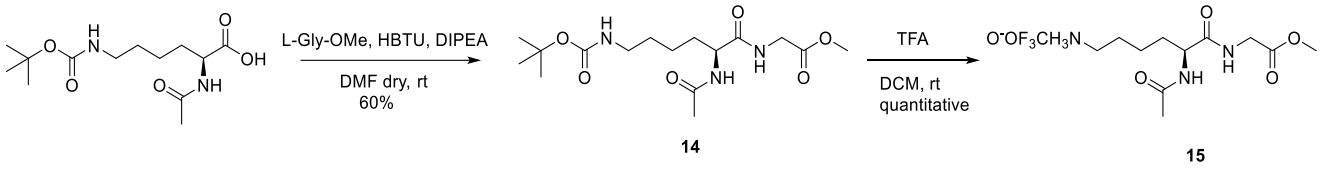

Scheme 6: Synthesis strategy of compound 15.

Starting from (S)-2-acetamido-6-((tertbutoxycarbonyl)aminohexanoic acid, compound **14** was obtained through a coupling reaction with methyl ester of glycine. HBTU was used as the carboxylic acid activator. To prepare the final product **15**, the Boc group was removed by treatment with trifluoroacetic acid (TFA). The desired product was obtained with a quantitative yield.

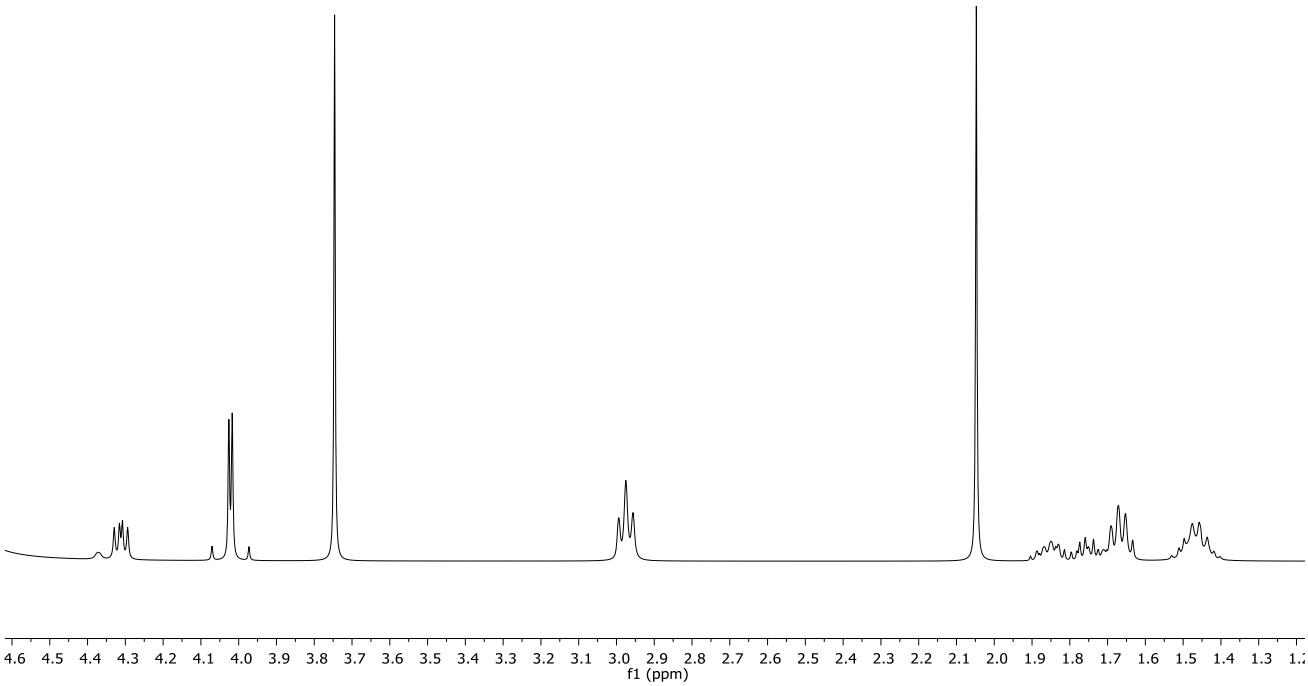

*Figure 21: ^{1}H NMR spectrum (400 MHz, D_2O, 298 K) of compound **14**.*

2.1.2 Biological studies

The Saccharomyces cerevisiae yeast, commonly known as brewer's yeast, is a unicellular organism belonging to the fungal kingdom[76]. This yeast is employed in significant research endeavors as a potent system for studying the molecular mechanisms of synucleinopathies, particularly those implicated in the onset of PD. The overexpression of human α-synuclein (α-syn) in yeast cells indeed induces a series of hallmark PD-like phenomena, such as dose-dependent toxicity and global cellular dysfunction. The overexpression of AS affects various cell functions, from vesicular trafficking to proteasomal activity, leading to disruptions in lipid metabolism or mitochondrial dysfunction, ultimately culminating in cell death[77].

Through a collaboration with Professor Roberta Ruotolo, who works in the Department of Chemical Sciences of Life and Environmental Sustainability at the University of Parma and is an expert in using this yeast as a validated PD model[78], experiments were conducted to determine the potential of each synthesized calix[4]arene to inhibit fibril formation and/or promote their disaggregation. In this model, a strain that produce AS (HiTox) with slightly higher toxicity was used, causing abnormal mitochondrial morphology and oxidative stress in yeast. The HiTox strain, carrying two copies of the -syn gene integrated, was used as PD model mimicking the overexpression of the protein as the cause

of the disease. Furthermore, the overexpression of AS disrupts vesicle trafficking in yeast and inhibits cell growth due to the formation of "clusters" of vesicles containing oligomeric α-syn. An additional useful aspect is that in the engineered yeast the toxic oligomeric species of AS do not evolve in larger aggregates and fibrils that, as previously underlined, are not the harmful species. Analyses were performed using fluorescence microscopy, as the AS expressed is linked to the Green Fluorescent Protein (GFP) thanks to the proper integration of the AS- and the GFP-encoding genes into the yeast genome. This enables the identification of points where the protein accumulates and forms aggregates. The start of the ASover-expression is controlled, being triggered when yeast is exposed to a galactose-rich substrate, leading to the subsequent growth of the toxic oligomers within the cells.

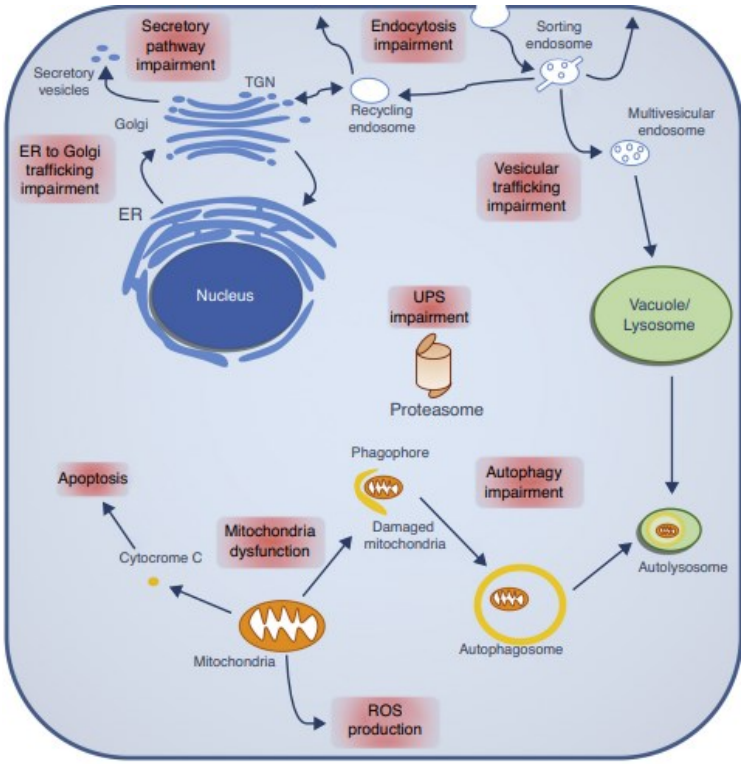

Figure 22: The image depicts several pathways that are impaired within yeast during and following AS aggregation, including vesicular trafficking, protein quality control, mitochondrial dysfunction, and oxidative stress (highlighted in red). Reprinted from Current Opinion in Genetics & Development, 44, Tenreiro, S.; Franssens, V.; Winderickx, J.; Outeiro, T. F, Yeast Models of Parkinson's Disease-Associated Molecular Pathologies, 74, © (2017), with permission from Elsevier[76].

To assess whether calixarenes can mitigate α-syn-induced toxicity, the engineered yeast cells expressing AS were preliminarily cultured and treated following a previously reported procedure[77]. Subsequently, they were exposed to various concentrations of the different calixarenes, which were preferably dissolved in water or alternatively in DMSO or water/DMSO mixtures due to their limited solubility. In any case, the % of DMSO present in the culture could not exceed 1% to prevent problems to cells. After 48 hours of growth under conditions inducing AS production, the cells were observed using both an optical and a fluorescence microscope. By comparing the results obtained

from untreated yeast with those of the samples treated with calixarenes, it was possible to determine the effect of the synthesized ligands on the aggregates.

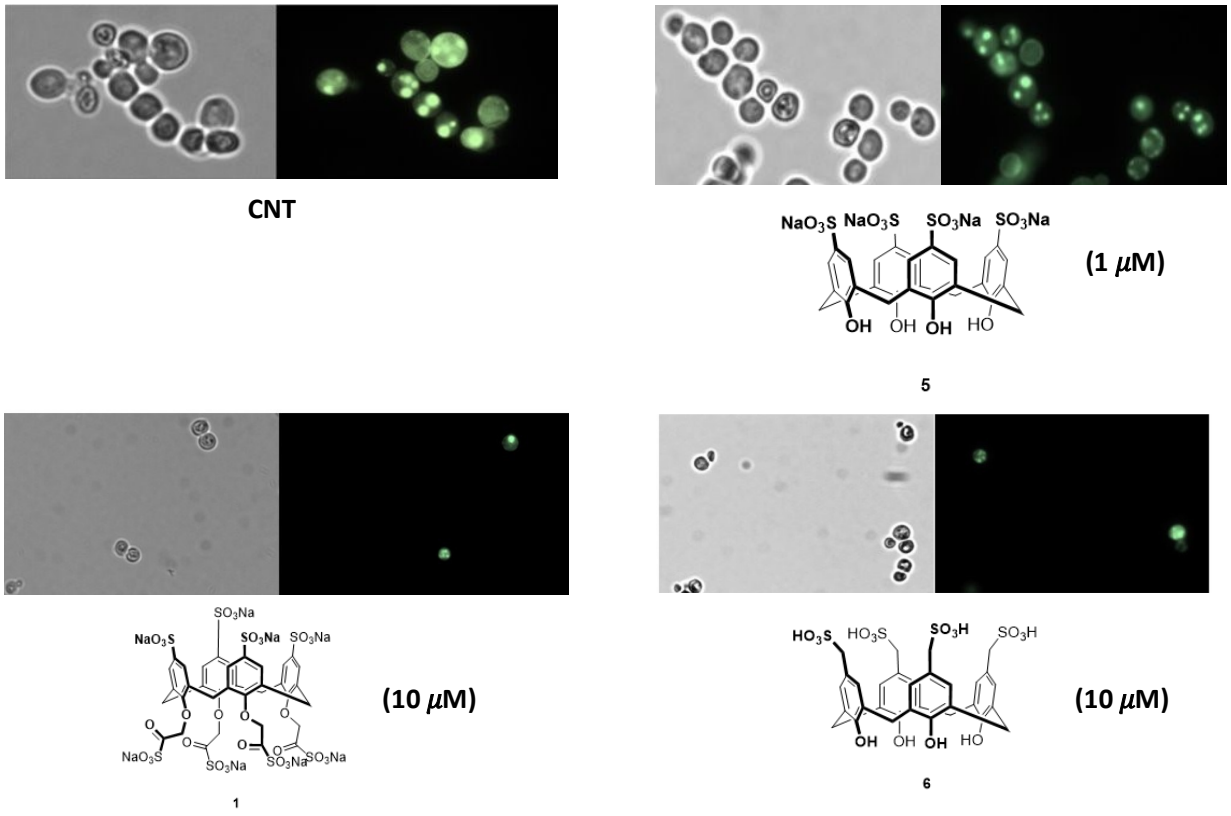

Figure 23: Cells expressing α-syn-GFP treated with sulfonate-calix[4]arene after 48 hours of incubation at 28°C. For each sample, images by a phase-contrast (on the left) and fluorescence (on the right) microscope are provided.

For the untreated yeast (CNT, in Figure 23), in which the overexpression of AS leads to the formation of aggregates inside the cells, well defined and delimited fluorescent spots are clearly visible corresponding to the toxic oligomers. Moreover, a characteristic that evidences the suffering conditions of the is the presence of larger mother cells and smaller daughter cells. In addition, all of them show a round shape that distinguishes sick cells from healthy ones that, on the contrary, have a typical oval shape. When yeast was treated with compound **5**, calix[4]arene p-sulfonate, at a concentration of 1 µM, both small and large aggregates were observed inside the cells (Figure 23). Among the living cells, some maintained their oval shape, indicating a healthy condition. However, like CNT, rounded and aberrant forms were observed in others, indicating significant alteration and distress. Unfortunately, increasing the concentration in the attempt to enhance the effect proved to be toxic to yeast. Compared to CNT, many more yeast cells died, and those that survived exhibited much more pronounced distress, characterized by very low fluorescence indicating minimal activity and

highly distorted cell sizes, much smaller and extremely aberrant. This aspect of toxicity appeared to align with previous studies that had shown fungicidal activity for this specific derivative[79]. In the case of compound **6**, calix[4]arene p-methyl-sulfonate, initially dissolved in its protonated form, very few cells were still alive after 48 hours, and these cells exhibited the presence of AS aggregates and altered morphology. An entirely analogous result was obtained with compound **1**, dissolved in its fully deprotonated form as a sodium salt, complexed with sodium ions at the lower rim. This deprotonated form was obtained by dissolving the starting solid **1** in 1M NaOH and reprecipitating it by subsequent addition of MeOH. It was not possible to use compound **3**, tetrasulfonate biscrown-3, in these experiments due to solubilization issues in both its neutral and salified forms. Using water, DMSO, or mixtures of the two solvents, it was not possible to achieve complete solubility for either form.

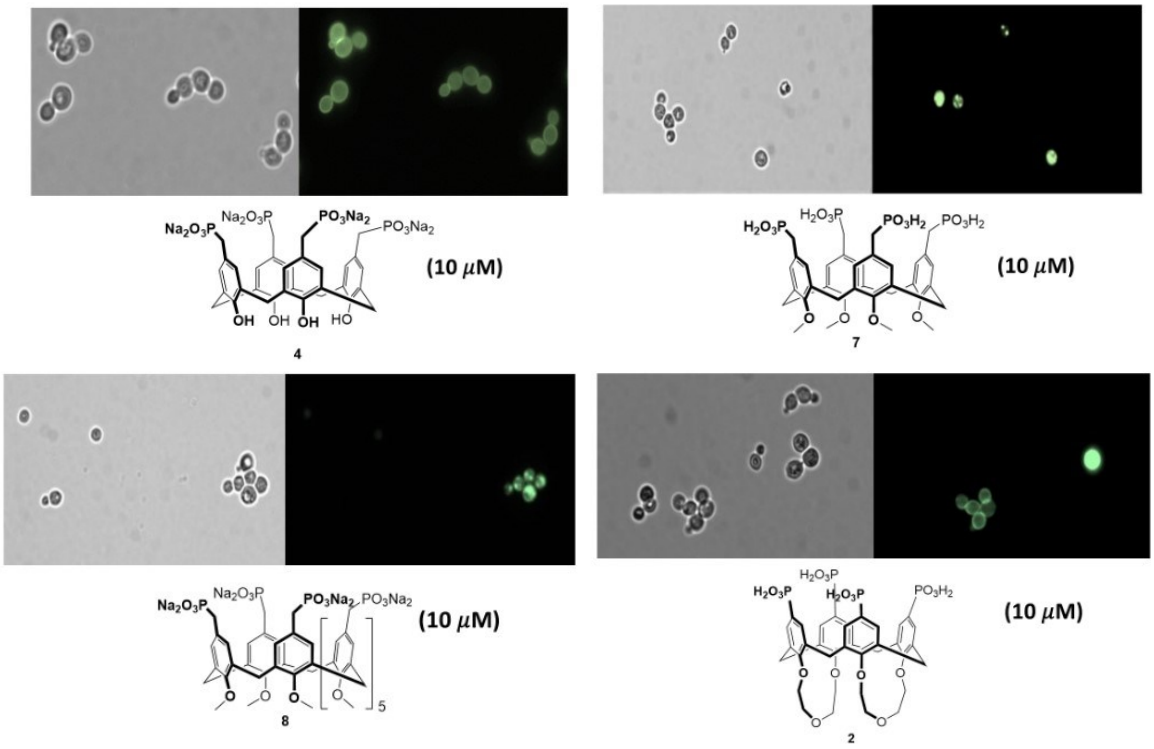

*Figure 24: Cells expressing α-syn-GFP treated with calix[4]arenes **8**, **2**, **7** and **4** after 48 hours of incubation at 28°C. For each sample, images by a phase-contrast (on the left) and fluorescence (on the right) microscope are provided.*

The use of calixarene **4**, the tetramethylphosphonate derivative with free OH groups at the lower rim, led to interesting and decidedly positive results. Specifically, following treatment with this compound at a concentration of 10 µM, most yeast cells remained alive, and did not exhibit the presence of aggregates within them. A diffuse fluorescence in the membrane indicated the localization of AS in that region of the cells in a form evidently non-toxic to the cell, and thus not as toxic oligomeric aggregates. The natural oval shape of the cells confirmed their good health. Biological activity was concentration-dependent, decreasing when the calixarene was tested at 1 µM. Using the same

calix[4]arene in its protonated form **4'**, a decrease in activity was observed, with a slightly lower phenotypic effect and a smaller number of surviving cells. The presence of a high number of acidic hydrogens on calix[4]arene **4'** could generated a lower pH compared to the starting conditions in which the yeast is placed. This pH reduction might make it difficult for complete deprotonation of the calixarene, which would then have less efficiency in complexing lysine fragments as it would not have all deprotonated oxygens available. This could explain the lower activity of **4'** and, at the same time, support the hypothesis set forth in this study, that these calixarenes may act by complexing the lysine side chain present in α-syn, and that their investigated biological activity is related to this. Another relevant point could be the different propensity/ability between calixarene **4** and its acidic form **4'** to cross the cell membrane. How the uptake of the calixarene occurs was not clarified in our study, but it certainly affects the activity of our derivatives inside the yeast cells.

The experiments were conducted also with the tetramethylphosphonate derivative **7**, tested only in its fully protonated form since in its salified one it was found to be insoluble in both water and DMSO, as well as in mixtures of the two, and the corresponding octamer **8**. Compounds **7** and **8**, both with methoxy groups at the lower rim and conformationally mobile, showed a complete lack of activity. This, as we hypothesized and aimed to demonstrate, seems to indicate that the presence of the preorganized cavity is a necessary structural element for interaction with α-syn. However, these tests will need to be repeated and confirmed to consider the results definitive, not excluding how other factors, such as a different uptake efficiency by the yeast cells towards the different calixarene derivatives, could be involved in determining a different activity extent. Finally, regarding compound **2**, the tetramethylphosphonate biscrown-3 used in its protonated form, results obtained at a concentration of 1 μM of calix[4]arene indicated a substantial lack of activity. However, at higher concentrations of 10 μM, some cells remained alive, were oval, and exhibited no aggregates inside them. Also these preliminary results will need to be further investigated, particularly by testing the salified equivalent. Based on what was observed for **4** and **4'**, compound **2** in its anionic form might have greater efficacy in acting against AS aggregates. Currently, it has not been possible to proceed in this direction because homogeneous solutions could not be obtained with the salified compound to treat yeast cells. Achieving this would be important because, if **2** in its anionic form should show significant activity, it would provide us with a derivative modifiable at the lower rim with other functions, such as an antioxidant unit, without altering the rigidity of the lipophilic cavity.

After the evaluation of the good activity of compound **4**, several further biological experiments were carried out to understand how it intervenes in the dysregulation of aggregate formation and to evaluate more in general the benefits provided to the cells.

The observation of the cell status 48 hours after the stimulation of AS overexpression and the simultaneous treatment with the calixarene derivatives, due to the experiment timing, did not allow us to conclude whether the action of **4** and, for a lower extent, of **4'** entails the inhibition of oligomeric aggregate formation or their disaggregation. Therefore, to understand what kind of action calixarene **4** exerts towards the α-syn aggregates, the experiments were performed monitoring the yeast health after a shorter time interval from the AS expression induction. The images reported in figure 25 shows the cells untreated (on the left) and treated (on the right), after 24 hours. The presence of aggregates after 24 hours and the different dimensions of them in the two conditions (untreated and treated with calixarene), together with the absence of aggregates in the treated cells after 48 h as previously detected, suggests that compound **4** does not inhibit the formation of the oligomers but, on the contrary, it disrupts them after their formation.

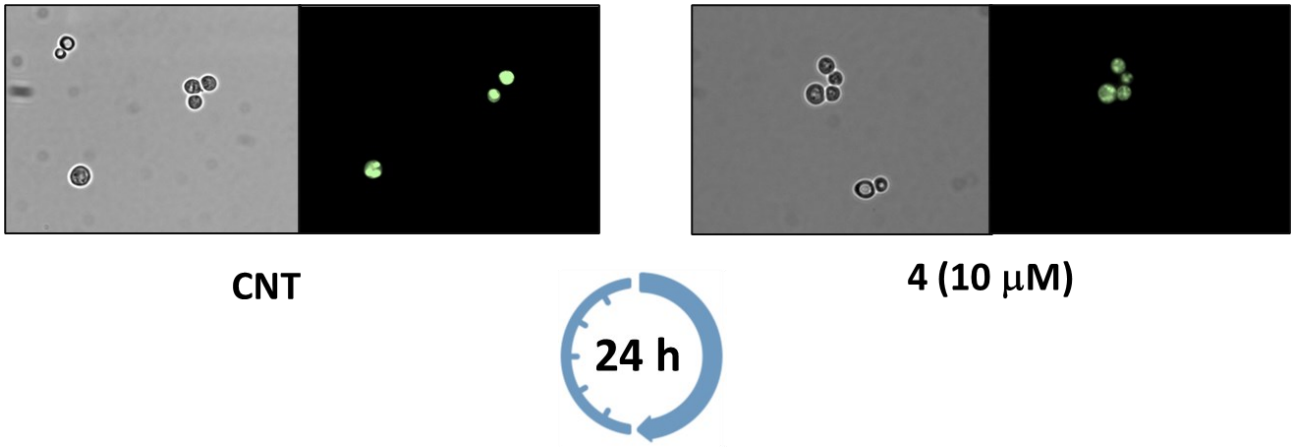

Figure 25: Images collected under a phase-contrast microscope (on the left) and fluorescence (on the right) of cells expressing AS-GFP untreated (CNT) and treated with calix[4]arene

The same experiments were performed using different concentrations of compound **4**, in order to confirm the dose dependency of its biological activity within 24 h. In the Figure 26 are reported two histograms on the data collected performing the same experiments at different concentration of calixarene **4**. The first histogram, on the left, allowed us to visualize an apparently curious trend: increasing the concentration of calixarene **4**, the number of cells with aggregates increases until 5 μM and then decrease at 10 μM. This behavior is due to the efficiency of compound **4** at different concentration. In fact, starting from 0.5 μM, we have more fluorescent cell compared to the control sample meaning that there are more alive cells compared to the control sample (where the almost all cells are died for the AS aggregation). Increasing the concentration to 1 and 5 μM, the situation is the same: the percentage of fluorescent cell is increased but it is also increased the number of alive cells meaning that the ratio between fluorescent cell and cell alive is decreased. At 10 μM, we have the maximum effect of the compound **4** where the percentage of fluorescent cells is decreased but it is

also increased the number of cells in the sample, showing a good health state of the yeast. This trend is confirmed by the second histogram on the right. At a calixarene concentration of 0.5 μM, we found the highest number of cells with big aggregates and the lowest number of cells with small aggregates apart the CNT, and, vice versa, using the concentration of 10 μM we found the lowest number of cells with big aggregates and the lowest number of cells with small aggregates. Administering the compound **4** using different concentrations (0.5, 1, 5 and 10 μM), we demonstrated that the number of cells with big and small aggregates is dependent to the concentration and time.

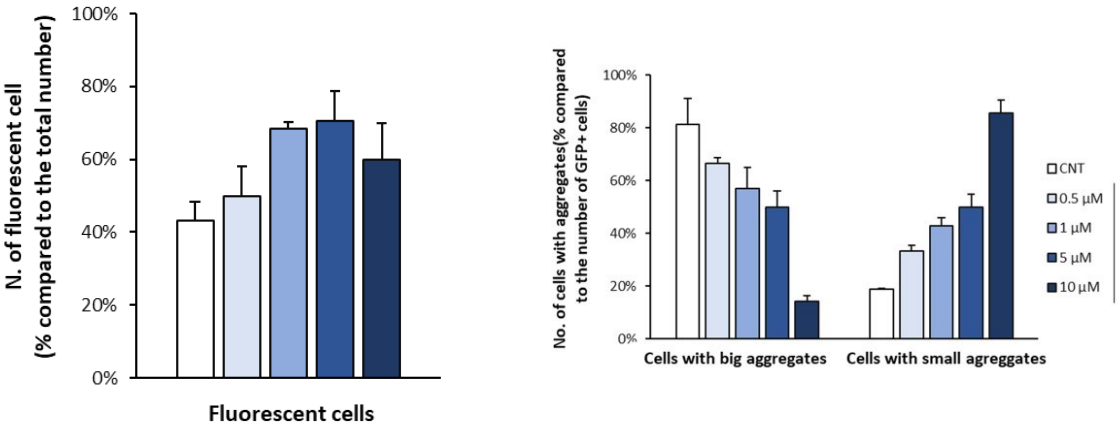

*Figure 26: The results of the experiment to evaluate the activity of compound **4** using different concentrations (0.5, 1, 5 and 10 μM). On the left: the histogram reports the number of fluorescent cells at different concentration; on the right: the histogram reports the number of small and big aggregates at different concentration.*

To evaluate more in depth the activity of compound **4**, we studied its possible effect on the oxidative stress in the cells. The formation of AS aggregates generates the increase of radical oxygen species (ROS) caused by the suppression of mithocondrial complex I by AS aggregates[77]. We used the CellROX^{TM} Orange assay to evidence the presence of ROS. While in its reduced state, this dye, capable of permeating cells, does not emit fluorescence, but when exposed to reactive oxygen species (ROS), it undergoes oxidation, demonstrating a vivid orange fluorescence with absorption/emission maxima at approximately 545/565 nm[80]. The assay was carried out after few hours from the administration of galactose to the cells (galactose activates the expression of AS as explained above). As reported in Figure 27, the level of cells containing ROS was three folds decreased in the samples treated with **4** compared to the CNT untreated sample.

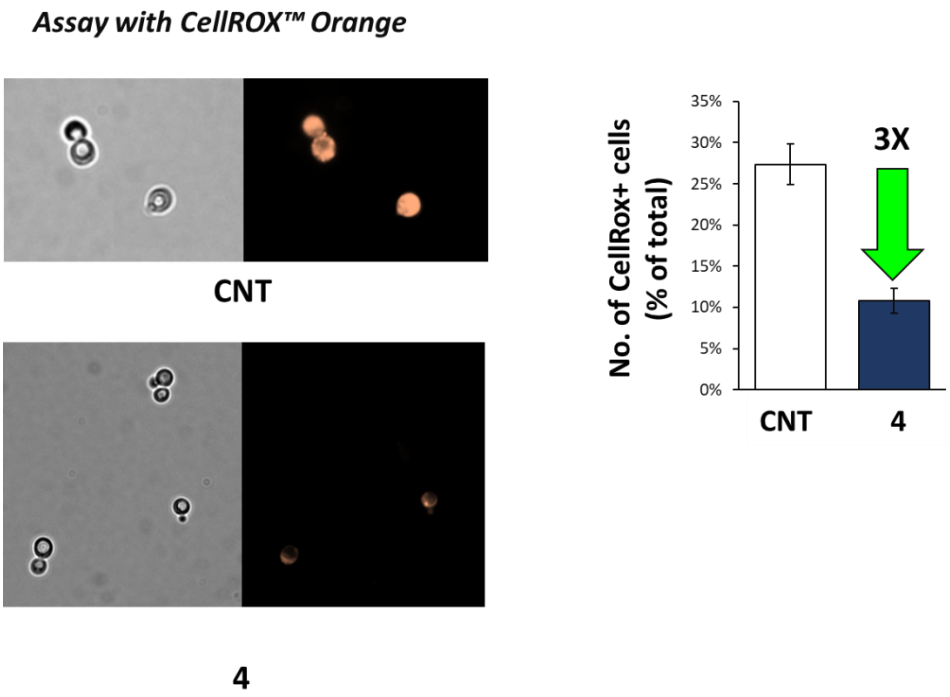

*Figure 27: CellROX™ Orange assy. On the left: Images collected under a phase-contrast microscope (on the left) and fluorescence (on the right) of cells expressing AS-GFP untreated (CNT) and treated with calix[4]arene **4** after administration of dye; on the right: The histogram reported the number of cell percentage dyed.*

Another study performed on yeast cells to evaluate the benefits of treatment with compound **4** was a test for the accumulation of lipid droplets (LDs). The LDs are involved in to the aggregation of AS[81]. Through the Nile Red assay, we were able to estimate the decrease of LDs in cells treated with **4**. Nile red (Figure 28), a phenoxazone dye, exhibits strong and diverse fluorescence in organic solvents and hydrophobic lipids. Nonetheless, this fluorescence is completely suppressed in water. As a result, the dye serves as an effective fluorescent hydrophobic probe. Leveraging this unique characteristic of nile red, it is exploited a sensitive fluorescent histochemical stain for LDs[82]. In the Figure 28 is reported the comparison between the sample treated with calixarene **4** and the untreated one showing the visible decrease of the presence of LDs as consequence of the presence of the macrocyclic compound.

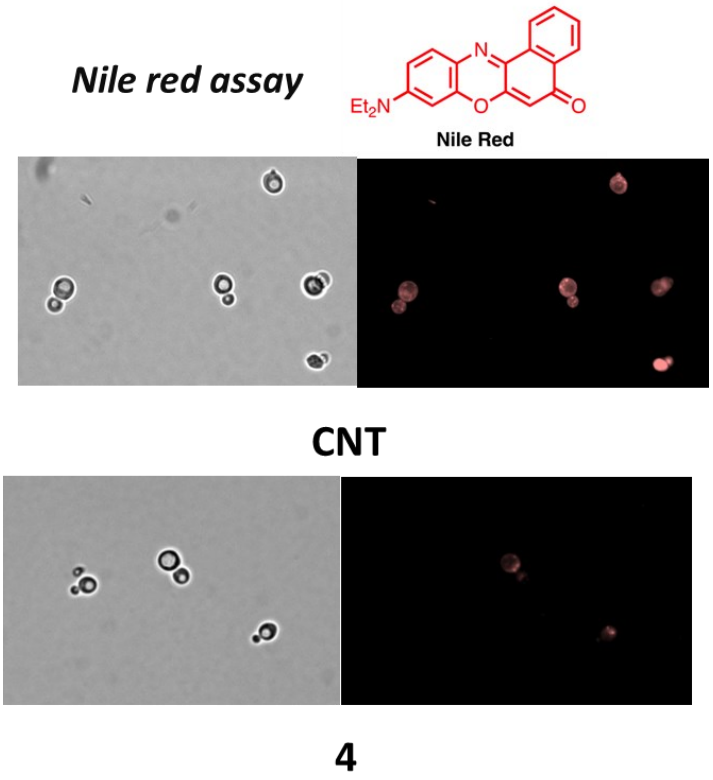

*Figure 28: Nile red assay performed to evaluate the accumulation of lipid droplets (LDs). Images are collected under a phase-contrast microscope (on the left) and fluorescence (on the right) of cells expressing AS-GFP untreated (CNT) and treated with calix[4]arene **4** after administration of dye.*

The last biological study performed was the genic expression analysis. This analysis was carried out to evaluate the effect of the treatment with compound **4** on several pathways that typically are altered by the AS aggregates. In Figure 29 is reported a histogram in which the fold change of several genes is reported for the untreated (white) and treated with **4** (blue) sample.

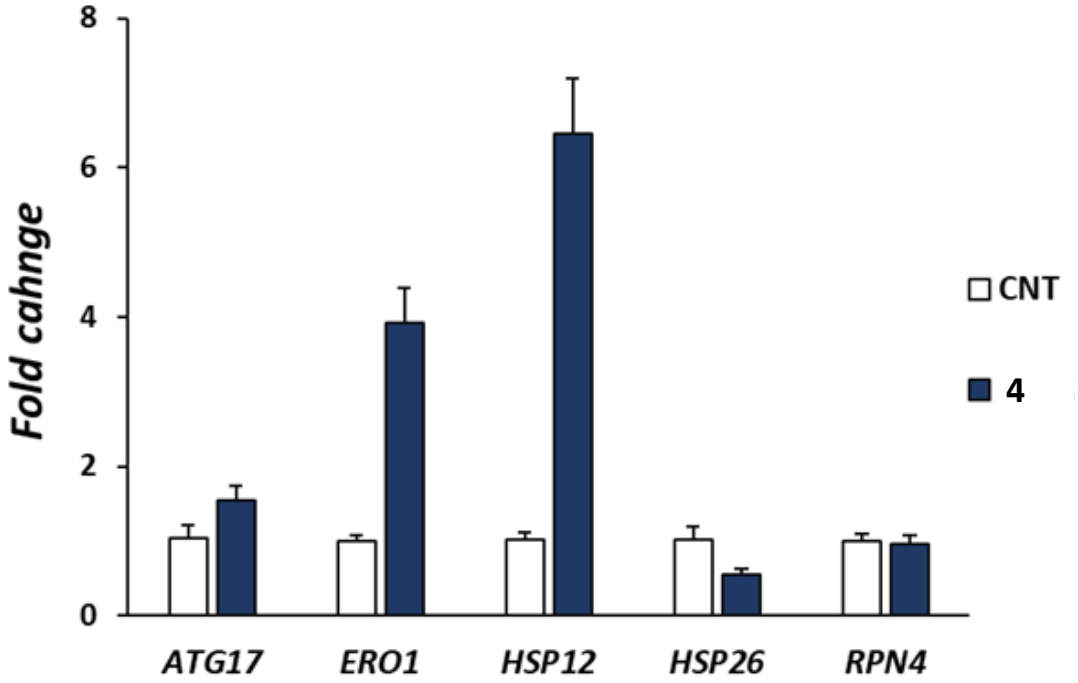

Figure 29: Histogram of the genic expression analysis. One-way ANOVA, followed by Dunnett's multiple comparison test

Among the five genes investigated, the restoration of three of them resulted more significant. ERO1 is a gene encoding a protein essential for maintaining redox balance within the endoplasmic reticulum (ER) and necessary for counteracting the stress generated by the accumulation of misfolded proteins in the ER. The HSP12 gene encodes a small heat shock protein that safeguards membranes against stress caused by high temperatures, and possibly even stress induced by the expression of AS which binds to biological membranes. ATG17 is a gene encoding a regulator of the autophagic process, the inefficiency of which is known to be associated with the onset of PD. The activation of these three genes is a proof of the benefit induced by the treatment with calixarene **4**.

2.1.3 Host-guest complexation studies

Following the information obtained from the yeast analyses and particularly the promising results regarding compound **4**, the affinity of this macrocycle for the dipeptide Nα-acetyl-L-lysyl-glycine-OMe was evaluated using ^{1}H NMR titrations. In the analysis, the dipeptide (Figure 30) was used, which has trifluoroacetate as the counterion, having removed the Boc group with trifluoroacetic acid at the end of the synthesis.

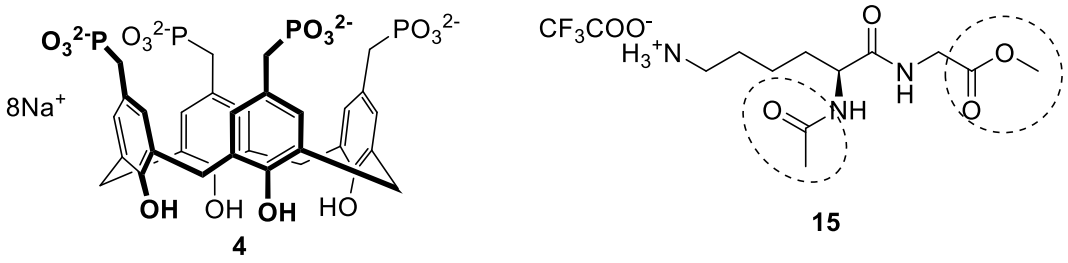

*Figure 30: calixarene **4** as host and dipeptide as guest*

The ^{1}H NMR titrations were conducted in deuterated water and in the presence of 100 mM phosphate buffer (PBS, pD = 7.4), starting from a guest concentration of 1.5 mM and adding increasing aliquots of the host from a mother solution prepared at a concentration of 10 mM. Figure 31 shows the spectra related to one of the ^{1}H NMR titration experiments in deuterated water conducted at room temperature. From preliminary analysis, it is possible to observe that as the host is added, some dipeptide signals shift. This result indicates two effects: first, there is an interaction between the host and guest, and second, this interaction is occurring in a fast exchange regime on the ^{1}H NMR timescale.

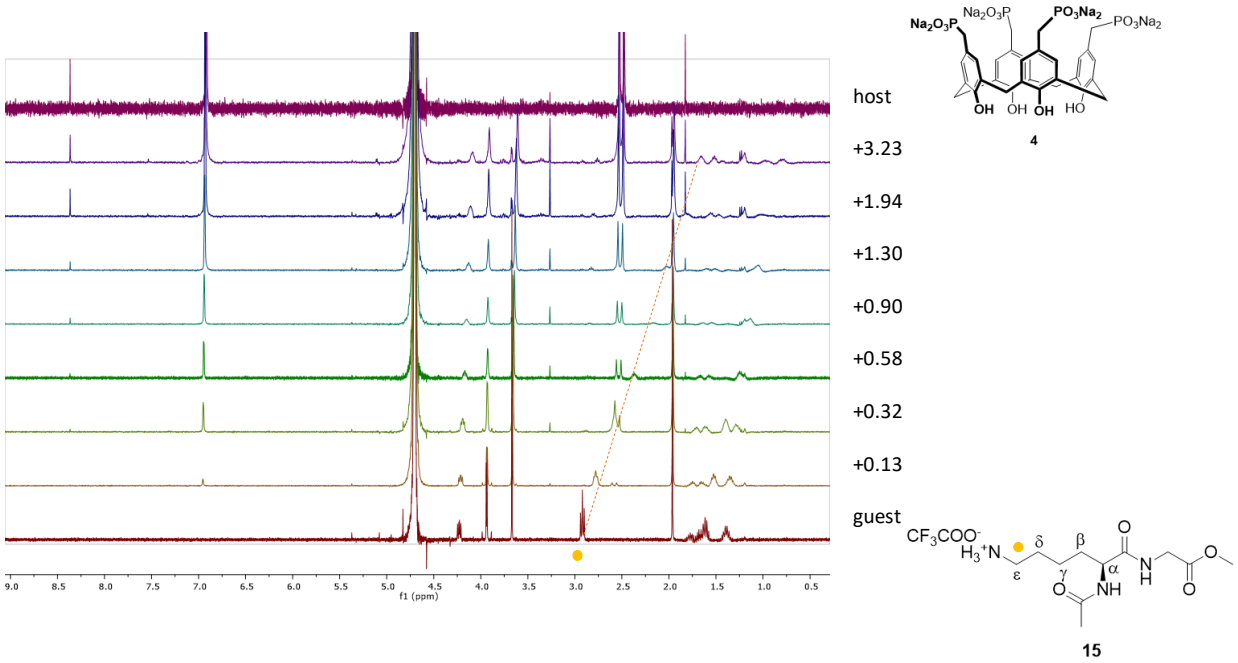

Figure 31: Spectra related to the 1H NMR titration in D2O (400 MHz, 298 K) of dipeptide 15 with calix[4]arene methylphosphonate 4.

The complexation effect is most pronounced on the signals of the lysine side chain. The signals corresponding to the CH_2 of the side chain are the multiplets in the low ppm range from 1.2 to 1.8 ppm and as the triplet at 2.9 ppm. With increasing host concentration, these signals shift to lower ppm values and lose definition, changing from multiplets or triplets (traces 1-5) to broadened and singlet-

like signals (from trace 6 onwards). Considering the signal at 2.9 ppm corresponding to the CH_2 near the ammonium group (trace 1), there is a clear shift of the signal to lower resonance frequencies, from 2.91 ppm to 1.64 ppm. The chemical shift variation of the signal correlates well with the results of lysine complexations reported in the literature and can be attributed to the inclusion of the side chain within the macrocycle cavity, which accompanies the interaction between the ammonium group of the side chain and one or more phosphonate groups of the calixarene.

Using the software sopramolecular.org, it was possible to determine the association constant of the complex. The program performs a nonlinear optimization on the provided data using the Nelder-Mead method and provides a function (solid line in Figure 32) corresponding to the binding isotherm. Below is the graph with the chemical shift data collected from the titration as a function of the $[G_0]/[H_0]$ ratio. Considering the chemical shifts corresponding to the methylene directly bonded to the terminal ammonium group of the lysine ($CH_2NH_3^+$), an association constant K_a was calculated to be 1517 (± 6) M^{-1}.

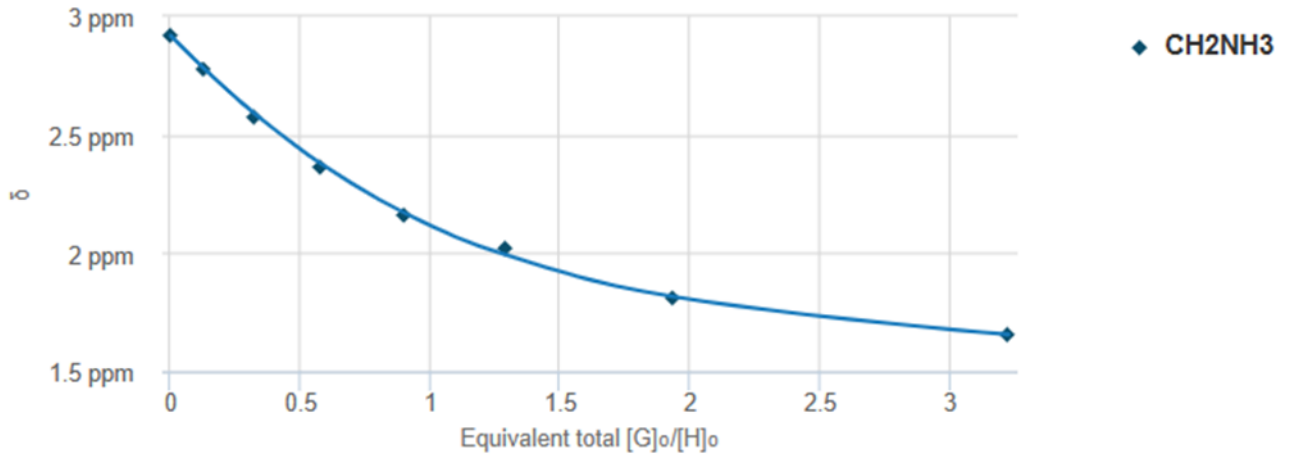

Figure 32: Experimental points and binding isotherm related to the shift of $CH_2NH_3^+$ during the titration of dipeptide 15 with calix[4]arene 4 in D_2O.

A peptide dilution experiment, over the range of concentrations reached during the titration, was conducted to ensure that the chemical shift variations observed during the titration were not caused even in part by changes in guest concentration. The shifts observed with calixarene **4** were not observed in this case.

To eliminate any effects due to deprotonation that could overlap with the host-guest interaction process and, instead, consider the increased ionic strength that might better simulate the situation in which the macrocycle finds itself during biological experiments with yeast, titration in deuterated phosphate buffer (100 mM, pD = 7.4) was also carried out (Figure 33).

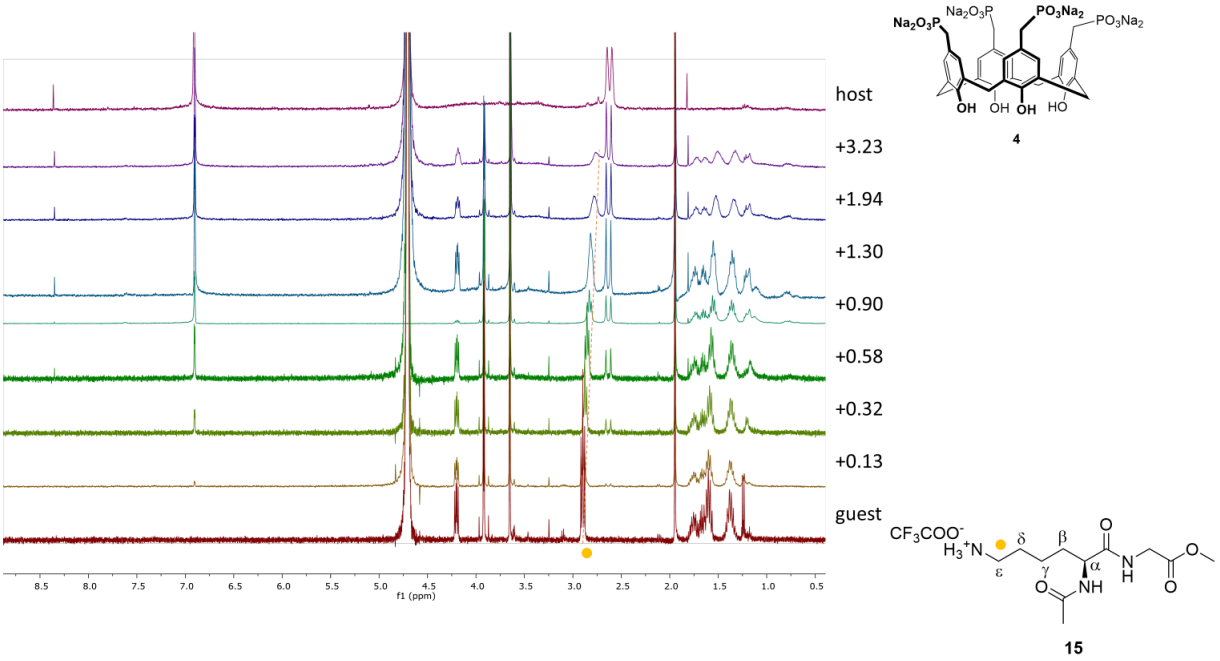

Figure 33: Spectra relating to ^1H NMR titration in D_2O with 100 mM phosphate buffer (400 MHz,298 K) of dipeptide 15 with calix[4]arene methylphosphonate 4

Comparing the observable variations in the spectra during the two titrations, a significant reduction in the chemical shift variation of the $CH_2NH_3^+$ lysine signal was observed. By calculating the association constant under these experimental conditions, still using the frequency shift of the $CH_2NH_3^+$ signal, a value of 189 (± 14) M^{-1} was obtained. It is conceivable that phosphate anions present in solution interact with the lysine ammonium, significantly interfering with the complexation process by **4**.

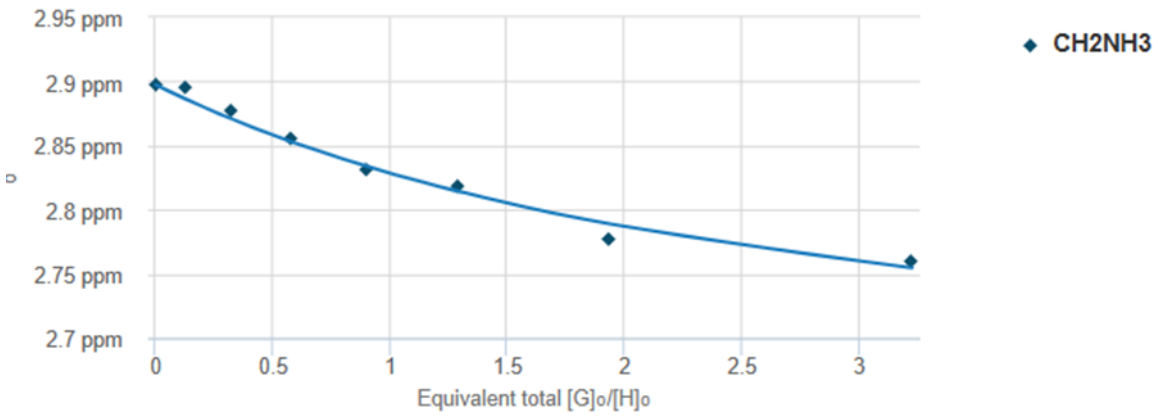

Figure 34: Experimental points and complexation isotherm relating to the displacement of $CH_2NH_3^+$ during titration of dipeptide 15 with calix[4]arene 4 in D_2O with deuterated phosphate buffer (pD 7.4)

After the demonstration of the lysine complexation in the calixarene cavity, we studied through isothermal titration calorimetry (ITC) the association constant and the thermodynamics values. ITC

is a powerful analytical technique used in biochemistry, biophysics, and chemistry to study interactions between molecules. It provides insights into the thermodynamic parameters associated with binding reactions, such as the binding affinity (K_a), enthalpy change (ΔH), entropy change (ΔS), and stoichiometry of binding. The experiments were carried out by titration of **4** with dipeptide **15** using 19 injections (Figure 34A). As shown in figure 34C, the host-guest interaction resulted to be endothermic. However, the free energy variation (ΔG) is negative thanks to the big contribute of entropy change. In this phenomenon, the driving force seems to be the entropic effect due to the hydrophobic effect given by interaction of the lipophilic cavity and the hydrophobic part of the lysine residue chain. The ITC shows a n value close to 0.5 (Figure 34 B) where n is the ratio between host and guest and this would mean that there is a second dipeptide unit interacting with the calixarene.

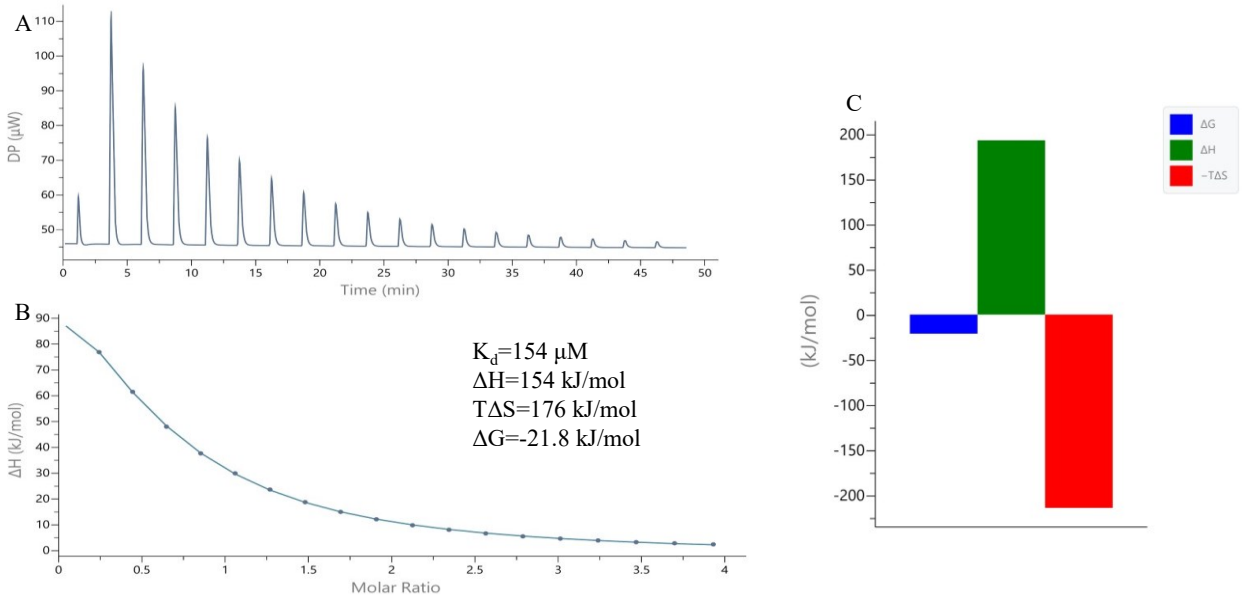

Figure 34: A) raw data binding of ITC; B) Isothermal binding of titration and the thermodynamic values of titration; C) graphical representation of thermodynamical parameters.

Further, to visualize this complexation process between the dipeptide and calixarene, some computational calculations were performed using the SPARTAN software (Spartan '14, version 1.1.4. Wavefunction, Inc. Irvine, CA). Molecular mechanics (MMFF) methods were used for calculation. Operationally, a crystal structure published in the literature (PDB:5NCV)[38] was used as a starting point, representing a complex of cytochrome-c in which the side chain of a lysine is enclosed by calix[4]arene methylphosphonate **4**. From this structure, lysine and calixarene were extracted. The lysine was then modified using SPARTAN's "build" function by adding an acetyl group on N_α and glycine methyl ester linked to the carbonyl to obtain dipeptide **15**. Geometric optimization in vacuum was then performed. As expected, lysine appears located inside the macrocyclic cavity, which is

effectively made available by the hydrogen bonds between the hydroxyl groups of the phenols (Figure 35).

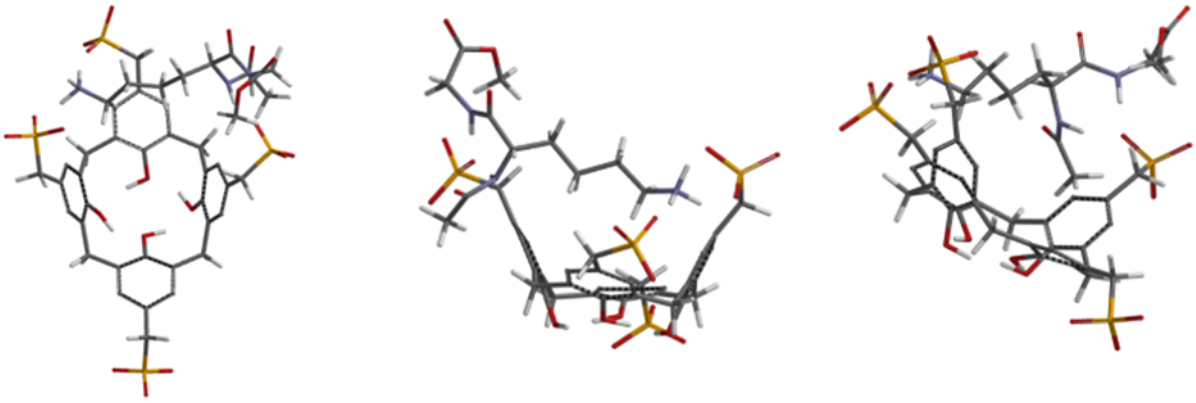

Figure 35: Left: Structure of the complex seen from above. Center: Ammonium-phosphate interaction. Right: Peptide bond-phosphonate interaction.

2.2 Stabilizers for transthyretin

This part of the thesis is the outcome of a multidisciplinary collaboration that involved our group in a joint work together with researchers at Free University of Bolzano, University of California, University of Rome "La Sapienza", Catholic University of Sacred Heart, TES Pharma S.r.l. and University of Marche. The collected data were recently published in a paper entitled "3-O-Methyltolcapone and Its Lipophilic Analogues Are Potent Inhibitors of Transthyretin Amyloidogenesis with High Permeability and Low Toxicity"[83].

2.2.1 Design of possible stabilizers

The known stabilizers for transthyretin work interacting with the protein hormone binding-sites. These sites are generated by the folding of the two dimers. In these cavities, we can individuate some regions where take place the interaction with iodine, a typical atom that characterizes the thyroid-produced hormones T3 and T4. These regions are called halogen-binding pockets (HBPs)[50]. The three HBPs present in the binding sites can be further categorized into an external binding subsite (HBP1 and HBP1', with 1 and 1' indicating the two constituent dimers), an internal binding subsite (HBP3 and HBP3'), and an intermediate interface (HBP2 and HBP2'). HBP1 is constituted by the amino acid residues Lys15, Leu17, Thr106, and Val121 and, from the compositions, we can understand that is the more hydrophilic site. In contrast, HBP2 is predominantly hydrophobic, comprised of Leu17, Ala108, Ala109, Leu110, along with the side chain of Lys15. HBP3 is formed by the side chains of Ser117, Leu110, Thr119, and Ala108[50].

The stabilizers are defined to bind the site in a forward or reverse binding mode[84]. When the hydrophilic part interact with the outermost region of the site is defined forward binding mode. The examples of this mode are tolcapone and 3-OMT. Contrarily, if the polar moiety is in the innermost part, it is called reverse binding mode as for 3-deoxytolcapone. Particularly, the polar moiety of 3-OMT interacts with HBP1 and HBP1' generating a hydrogen bond with Lys15. In turn, this interaction increases the stability of the ionic couple between Lys15 and Glu54. Meanwhile, the hydrophobic moiety is deeply seated within the TTR hydrophobic HBP2/HBP2' and HBP3/HBP3' pairs, nestled between Leu110 and Thr119 residues. Considering the efficient binding of 3-OMT, we designed five compounds (Figure 36) keeping the same polar moiety but increasing the number of methyl groups in the hydrophobic moiety. This design aimed to enhance the compounds' lipophilicity, permeability through the blood-brain barrier, binding selectivity, and structural stability.

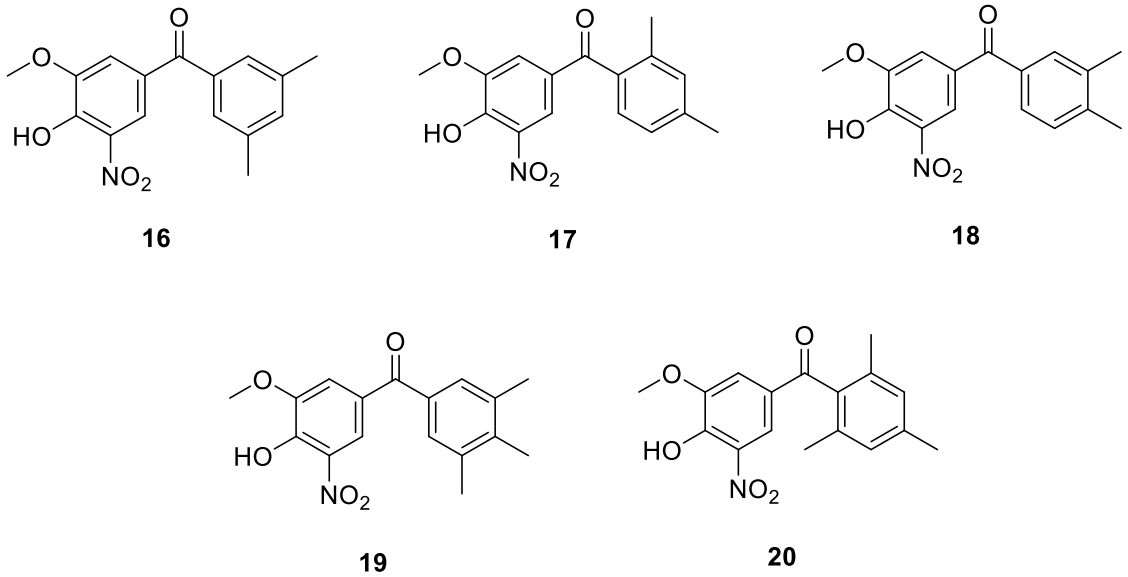

Figure 36: Selected molecules as potential stabilizers.

2.2.2 In silico Docking of 3-OMT Lipophilic Analogues

We initially carried out analyses on the interaction between the TTR protein structure and the designed analogues, thanks to the collaboration with Dr. Valentina Loconte at the Department of Anatomy, University of California San Francisco and Lawrence Berkeley National Laboratory, Molecular Biophysics and Integrated Bioimaging Division, Berkeley (USA). Starting from the well-known 3D structure of TTR tetramer and the knowledge of the binding pocket and the amino acids involved in the interactions with 3-OMT, she employed in silico docking methods to predict how the new ligands might bind. This approach offers a computationally less intensive alternative to Molecular Dynamics, which was employed more recently[85] to assess ligand poses within this protein. Firstly, using 3-OMT as a benchmark, we confirmed that the simulation effectively replicated the

original ligand binding. The most promising binding configurations for the five compounds were determined through a focused search within the known protein halogen binding pockets. These top-ranking binding molecules were identified based on criteria involving lower ΔGbinding and FullFitness (FF) values. Although all the compounds exhibited greater hydrophobicity compared to tolcapone and **3-OMT**, analogues **16** and **17** demonstrated the most favorable interactions with the HBPs displaying a higher affinity for the HBPs. Their binding site is situated at the base of HBP3 and HBP2 and involves interactions with Ser117, Leu110, Thr119, and Leu17, which interact with the hydrophobic ring of the compounds. Simultaneously, the hydrophilic ring is stabilized by Lys15. The positioning of the binding pocket and the nature of interactions crucial for compound stabilization align with those observed with tolcapone, **3-OMT**, flurbiprofen, and tafamidis. The docking analysis identified the most favourable binding mode as the "forward one," consistent with previous findings regarding lipophilic analogues of tolcapone.

In contrast, analogues **18** and **19** exhibited a lower affinity for the HBPs in terms of binding energy and FF, while analogue **20** displayed no affinity for the HBPs. We hypothesize that analogues **16** and **17** have more favourable binding energy due to reduced steric clashes compared to the other compounds. Conversely, the binding og analogues **19** and **20** is disfavoured due to increased steric hindrance.

2.2.3 Synthesis of analogues 16 and 17

To synthesize the two identified compounds **16** and **17**, a synthetic strategy published in the Journal of Medicinal Chemistry[86], used to prepare molecules similar to ours starting from vanillin, was particularly interesting.

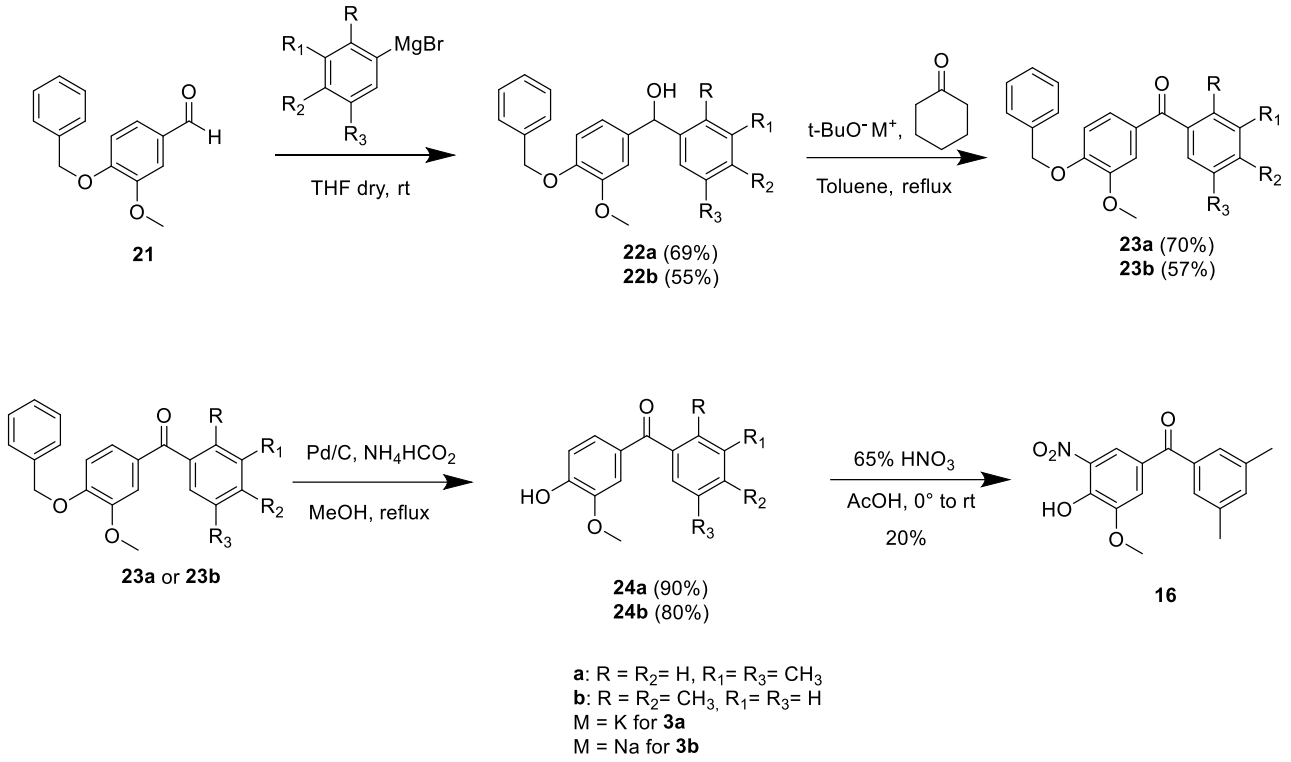

*Scheme 7: First synthetic route of compounds **16** and **17***

The first step involved reaction between the aldehyde group of the O-benzyl protected vanillin with the appropriate Grignard reagent to form compounds **22a** and **22b** (Scheme 7). The Grignard reagent was prepared under anhydrous conditions by reacting magnesium turnings with 1-bromo-3,5-dimethylbenzene for the synthesis of compound **22a** and with 1-bromo-2,4-dimetilbenzene for the synthesis of compound **22b** in THF. After preparing the Grignard reagent, the slow addition of aldehyde **21** was carried out.

In an initial attempt to synthesize **22a**, the reaction was quenched using 2M HCl. However, a rather complicated crude product was obtained, from which only one derivative was isolated, albeit in very small quantitiesThe ^{1}H-NMR analysis (Figure 37) revealed the presence of some signals that cast doubt on whether it was indeed the desired compound. In particular, there were two singlets at 3.87 and 3.85 ppm related to the OCH_3 group, as well as two singlets at 2.30 and 2.33 ppm attributable to the CH_3 groups attached to the aromatic ring. While the presence of two signals for the CH_3 groups could potentially be explained by restricted rotation around the bond between C=O and Ar, there was no reason for two OCH_3 signals in the expected molecule.

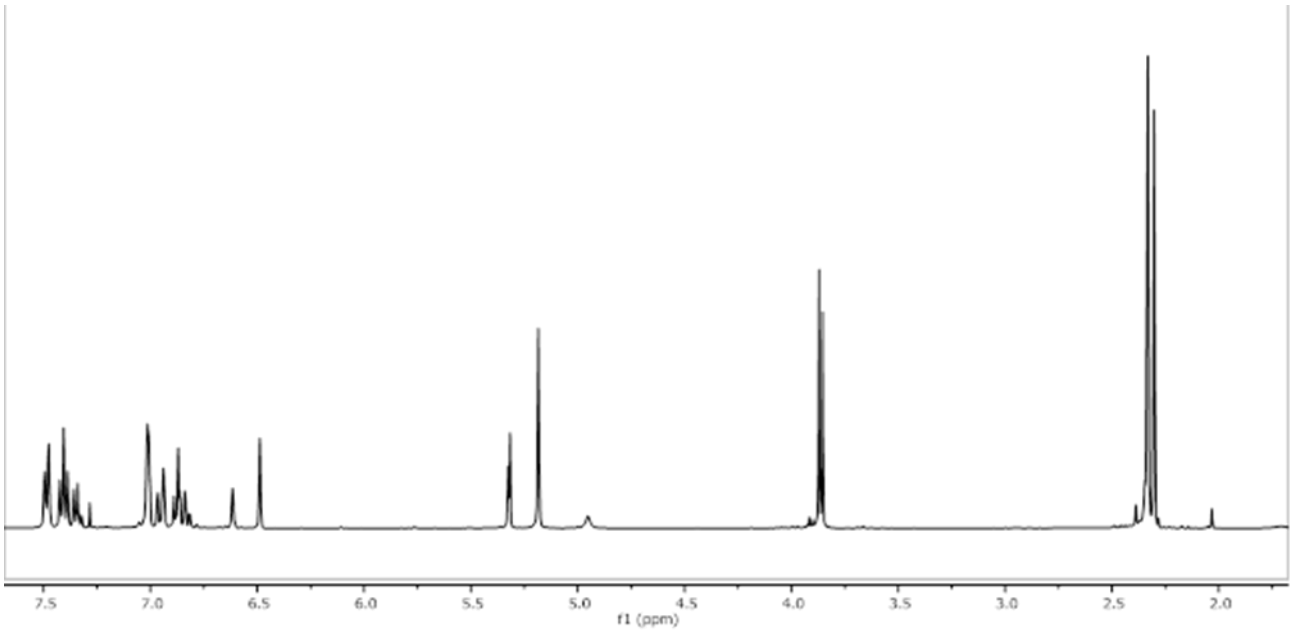

Figure 37. ^{1}H NMR spectrum (400 MHz, 298 K) in $CDCl_3$ of product for first attempt of alcohol formation.

Simultaneous mass spectrometry analysis identified an ion with m/z = 701, equivalent to a sodium-containing species which was presumed to be the molecule described in Figure 38, outlining the proposed mechanism that would have led to its formation. According to this mechanism, treatment with strong acid to quench the reaction in the desired product **22a** led to the formation of a secondary and doubly benzylic carbocation, which then perfomed electrophilic attack on an aromatic ring of a second molecule of **22a**. Figure 38 illustrates one of the possible carbocation attacks on the aromatic ring, considering the position characterized by the best compromise between activation and steric hindrance. This reaction could further proceed with the extraction of the OH group from the resulting compound, potentially leading to an oligomerization process that could explain the complexity of the crude product.

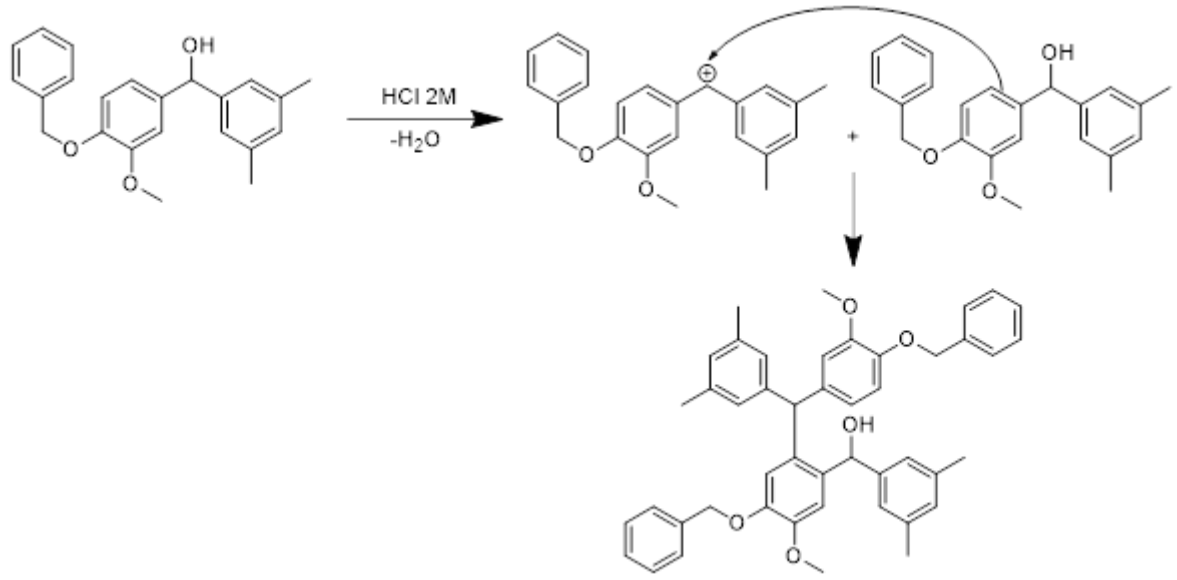

Figure 38: Possible mechanism of product degradation

The identification of this undesired byproduct was, therefore, very useful when, repeating the reaction between the aldehyde and Grignard reagent, we proceeded with quenching using NH_4Cl. Following this precaution, compound **22a** was obtained and isolated with a yield close to 70%. Similarly, for the reaction between **21** and the Grignard of 1-bromo-2,4-dimethylbenzene, compound **22b** was obtained with a yield of approximately 55%.

Subsequent reactions involved the oxidation of alcohols **22a** and **22b** to the corresponding ketones **23a** and **23b** using the Oppenauer-Woodward oxidation. The reaction was conducted in toluene with t-BuONa as the base for deprotonation of alcohols **22a** and **22b**, and cyclohexanone as the hydride acceptor, refluxed overnight. Compounds **23a** and **23b** were obtained as white crystals with a yield of around 70% and 57%, respectively.

The next step involved the deprotection of compounds **23a** and **23b** from the benzyl group through benzyl ether hydrogenolysis. The reaction was carried out under reflux in MeOH using 10% Pd/C as a catalyst and ammonium formate for the in-situ production of H_2. Compounds **24a** and **24b** were obtained, after recrystallization, with a yield slightly above 80% and 90%, respectively. In this case as well, the two products were identified through NMR analysis and mass spectrometry.

The final step for the synthesis of the end product **16** involved a nitration reaction of compound **24a**, conducted at room temperature, using glacial acetic acid and 65% HNO_3. Compound **16** was obtained, after recrystallization, in the form of yellow needle-like crystals with a yield around 20%. The low yield might be partly attributed to the premature quenching of the reaction when there was still some of the reagent **24a** present to prevent poly-nitration events. The right identity of the product was confirmed by the analysis of the ^{1}H-NMR spectrum in DMSO-d_6, as shown below (Figure 39), where

we can observe two doublets at 7.75 and 7.57 ppm corresponding to the hydrogens on the aromatic ring bearing the nitro group, a signal at 7.35 ppm related to the two equivalent hydrogens in the ortho position to the C=O on the other aromatic ring, and a signal at 7.32 ppm related to the hydrogen in para-position on the same aromatic ring.

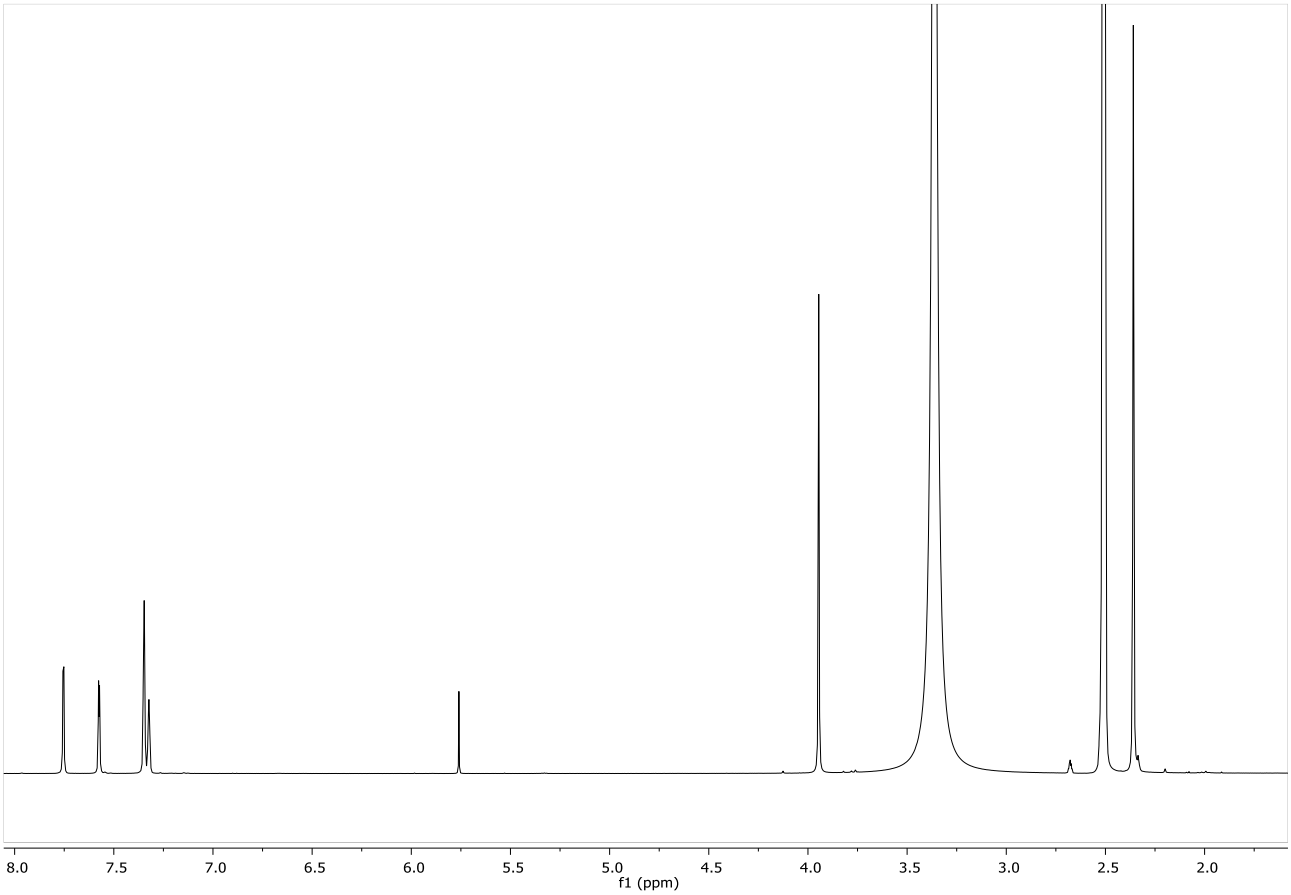

*Figure 39: ^{1}H NMR spectrum (400 MHz, 298 K) in DMSO-d_6 of compound **16***

For the nitration of compound **24b**, the same experimental procedure applied for the synthesis of **16** was followed. From recrystallization with EtOH, yellow needle-like crystals were obtained, albeit in small quantities. However, from the ^{1}H-NMR analysis, they did not appear to be the desired compound **17**.

In the ^{1}H-NMR spectrum recorded (Figure 40), there were two doublets with a J value of 2.6 Hz at 7.98 and 8.72 ppm as the only signals related to aromatic hydrogens, which, from the integrations, appeared to be only two. There was also a signal at 11.23 ppm related to the OH group and a signal at 4.08 ppm related to the OCH_3 group. Additionally, the ^{13}C-NMR spectrum indicated the presence of only 7 carbons in the molecule, and the ESI-MS analysis showed a peak with m/z = 237, $[M+Na]^+$.

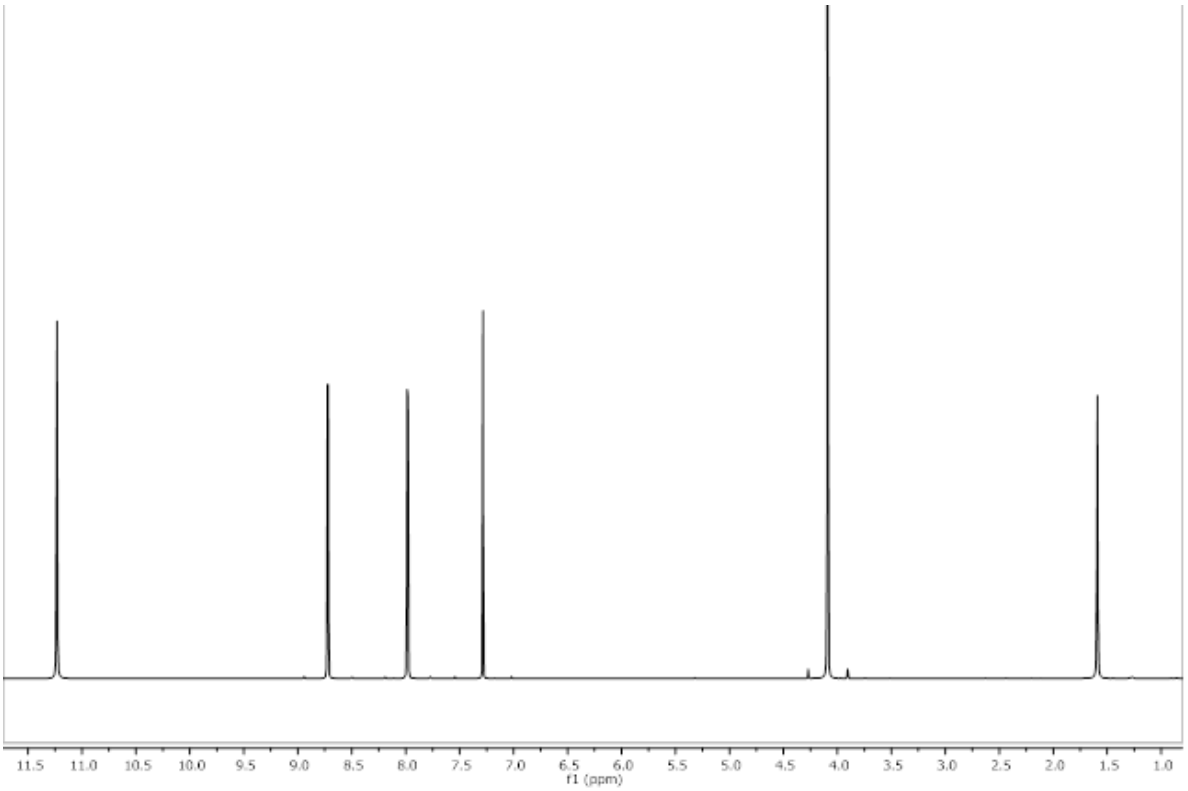

Figure 40: ^{1}H NMR spectrum (400 MHz, 298 K) in $CDCl_3$ of side-product of nitration

This last observation, unless considering fragmentation caused by the analysis technique, which was not verified in the case of compound **16**, would correspond to the molecular ion of the examined molecule. Therefore, it was hypothesized to be the one represented in Figure 40. This led us to the conclusion that during the nitration reaction, unlike **24a**, compound **24b** degraded with the cleavage of bonds between the two aromatic rings.

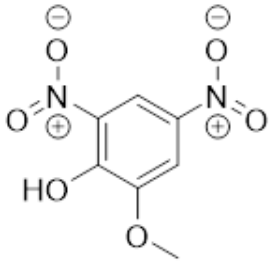

Figure 41: product of degradation

The material obtained from the reaction was then re-examined in an attempt to identify the presence of the desired product **17**. For this purpose, a separation was carried out using column chromatography on the mother liquors remaining from the previous recrystallization. The ^{1}H-NMR spectra of the various separated fractions were recorded to see if any of them might contain product **17**. However, it was not found in any of them.

A second attempt to nitrate compound **24b** was then made, essentially following the same procedure, but conducting the reaction in an ice bath and under a nitrogen flow. In this case as well, after column chromatography and analysis of the fractions via ^{1}H-NMR and ESI-MS, it was concluded that the reaction had not correctly occurred.

In a third attempt, the reaction was carried out using H_2SO_4 as the solvent and $NaNO_3$ as the nitrating agent, mixing the reagents and allowing them to proceed for 40 minutes at -10 °C and then for 3 hours at room temperature. Again, the reaction proved to be entirely unsuccessful.

We attributed this negative outcome of the reaction to the different position of the methyl groups in **24b** with respect to **24a** that seems to allow an ipso-nitration with the release of the stabilised 2,4-dimethyl-benzoyl cation.

An alternative strategy was then performed to obtain compound **17**, starting from 5-nitrovanillic acid **25**[87] (Scheme 8). This was transformed in the corresponding acyl chloride that was reacted, without preliminary isolation, with m-xylene in a Friedel-Craft reaction producing the target derivative **17**.

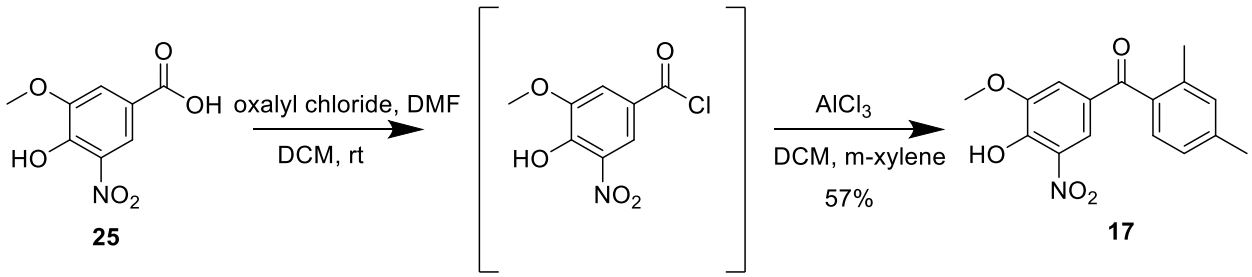

*Scheme 8: Synthetic route of compound **17***

The ^{1}H-NMR confirmed the successful result of the reaction showing a significant shift in the down-field region, compared to the precursor **25**, for the doublet corresponding to the aromatic hydrogen in ortho to the nitro group (figure 42).

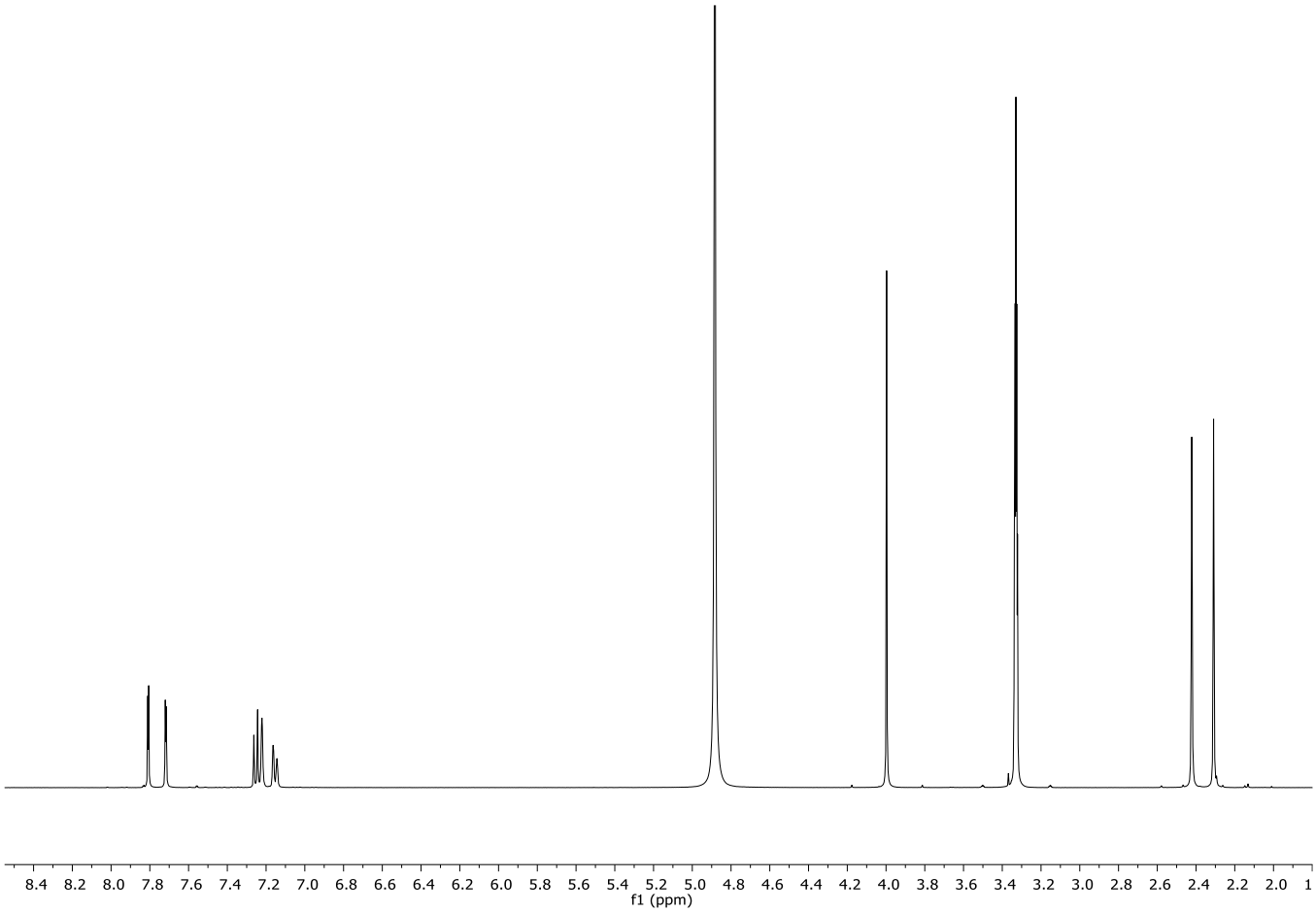

*Figure 42: ^{1}H NMR spectrum (400 MHz, 298 K) in DMSO-d_6 of compound **17***

2.2.4 X-Ray crystal structures of hTTR/16 and hTTR/17 complexes

The X-Ray crystal structure of the complexes obtained at the solid state between human TTR and the two synthesised ligands **16** and **17** was determined at the PETRA III storage ring (DESY, Hamburg, Germany) and analysed by Dr T. Poonsili and Prof. Benini at the Free University of Bolzano and Prof. Cianci at Università Politecnica delle Marche.

2.2.4.1 hTTR/16 complex

The crystallographic analysis of the TTR/**16** complex, resolved at resolution of 1.19 Å, unveils the "forward binding mode" (Figure 43). Both binding cavities were refined to be equally occupied (0.50/0.50), with electron densities for both ligands clearly defining the positions of the 3-methoxy-4-hydroxy-5-nitrophenyl ring and the innermost apolar 3,5-dimethyl-phenyl ring. The 3,5-dimethyl-phenyl ring of compound **16** is deeply embedded within the inner hydrophobic binding sites HBP3. It is situated between Leu110 and the γ-methyl group of Thr119' side chain on one side, and Leu110' and the γ-methyl group of Thr119 side chain on the other side (as shown in Figure 43). The 3,5-dimethyl groups are oriented towards Ser117/Ser117'. Furthermore, the central carbonyl group of

compound **16** is directed towards the γ-hydroxyl group of Thr119' in the HBP2'. Similar to the TTR-tolcapone complex[64], the 3-methoxy-4-hydroxy-5-nitrophenyl ring remains situated in HBP1, held in place through hydrophilic interactions with Lys15/Lys15' and Thr119. The 3-methoxy group is at a distance of 3.17 Å from the γ-amino group of Lys15 and 2.90 Å from the γ-amino group of Lys15'. The 4-hydroxy moiety is at a distance of 2.75 Å from the γ-amino group of Lys15'. The 5-nitrophenyl group is anchored by the γ-hydroxyl group of Thr119. The positive charges of Lys15/Lys15' are balanced by carboxylic groups of Glu54/Glu54' at a distance of 3.01 Å.

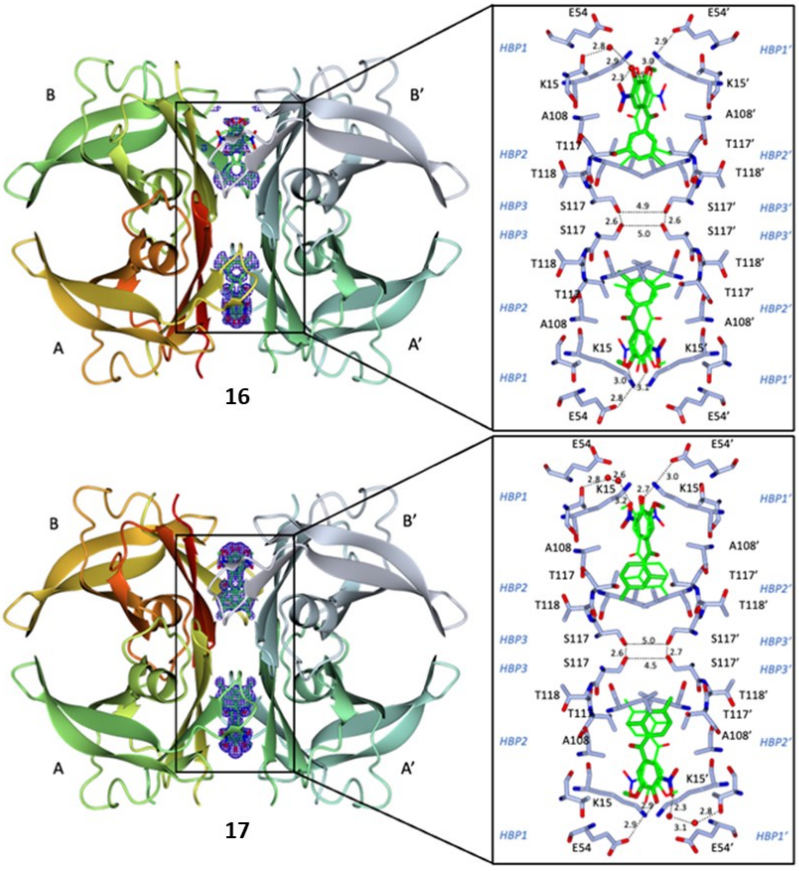

Figure 43: TTR-ligand interactions are observed in the crystal structures of the two TTR complexes, namely 1 (PDB ID: 8C85) and 2 (PDB ID: 8C86). On the left, the OMIT (Fo-Fc) Fourier difference electron density maps (depicted in blue and contoured at 3 σ) reveal the presence of tolcapone analogues (1 on top and 2 at the bottom) bound within the two cavities of the TTR tetramer. On the right, detailed views illustrate the two symmetry-related binding modes of each ligand (shown in green) within the T4 binding cavity. These interactions occur through residues present in HBP1/ HBP1' (Lys15, Glu54, and Thr106), HBP2/ HBP2' (Leu110, Leu17, Lys15), and HBP3/ HBP3' (Ser117, Leu110, Ala108, and Thr119). Both the interacting residues and ligands are depicted as sticks, with the symmetry-related image of the ligands represented as fine bonds. Carbon, nitrogen, and oxygen are shown in light blue (green for the ligands), blue, and red, respectively. Additionally, water molecules are represented as red spheres, while hydrogen bonds are illustrated as dotted lines, with distances indicated in Å.

2.2.4.2 hTTR/17 complex

The crystallographic analysis of the TTR/**17** complex, resolved at 1.10 Å resolution, unequivocally validates also in this case the "forward binding mode" (Figure 44). The presence of a 2-fold axis traversing the binding pocket results in two symmetrical binding modes for the ligand, rotated by 180 degrees relative to each other. The Fo-Fc electron density map, at a confidence level of 3 σ, distinctly delineates both the 3-methoxy-4-hydroxy-5-nitrophenyl ring and the innermost apolar 2,4-dimethyl-phenyl ring. These two binding cavities are evenly occupied (0.50/0.50). The 2,4-dimethyl-phenyl ring of compound **17** is positioned deeply within the inner hydrophobic binding sites HBP3. It is nestled between Leu110 and the γ-methyl group of the Thr119' side chain on one side, and Leu110' and the γ-methyl group of the Thr119 side chain on the other side (as depicted in Figure 44). The 4-methyl group of the 2,4-dimethyl groups is directed towards Ser117/Ser117', while the 2-methyl group of the 2,4-dimethyl groups points towards Ala108'-Ala109'. Additionally, the central carbonyl group of compound 2 is oriented towards the γ-methyl group of Thr119' and the γ-methyl group of Ala108' within the HBP2'. The 3-methoxy-4-hydroxy-5-nitrophenyl ring remains situated in HBP1, anchored by hydrophilic interactions involving Lys15/Lys15'. The oxygen atom of the 3-methoxy group is 3.17 Å away from the γ-amino group of Lys15, with the methyl group pointing towards the γ-methyl group of Ala121' and the γ-methyl group of Ala106'. The 4-hydroxy moiety is at a distance of 2.77 Å from the γ-amino group of Lys15' and 2.9 Å from the γ-amino group of Lys15. The 5-nitrophenyl group is tethered by the γ-amino group of Lys15' at a distance of 3.0 Å. The positive charges stemming from Lys15/Lys15' are balanced by carboxylic groups from Glu54/Glu54' at a distance of 2.87 Å.

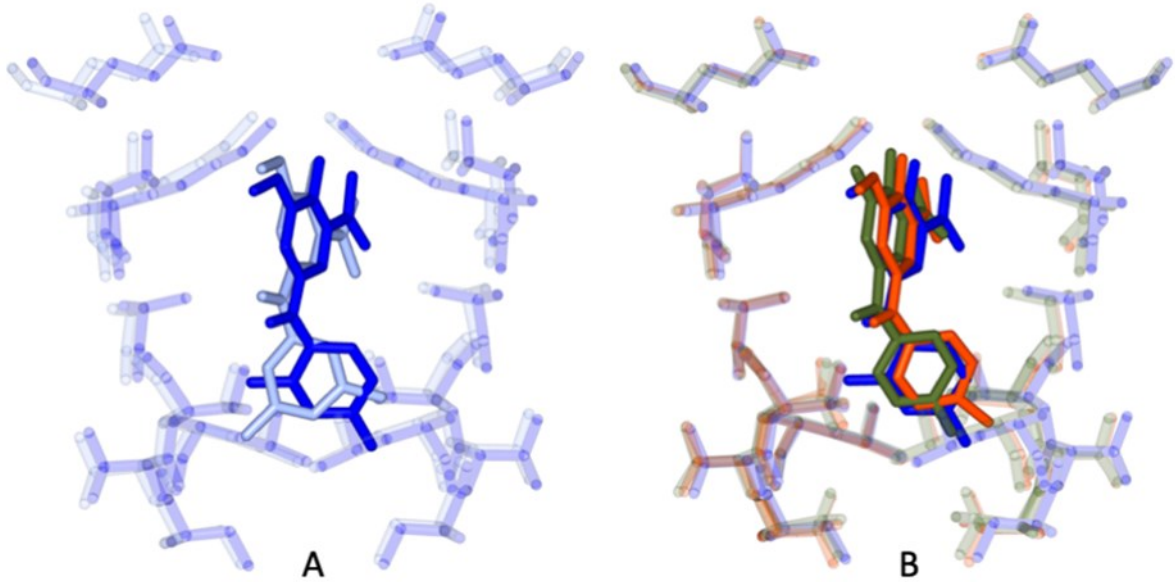

*Figure 44: Superposition of the pose within the binding site of TTR of compound **16**(colored in blue) with: A) compound **17** (light blue); B) **3-OMT** (green) and tolcapone (red).*

2.2.5 Isothermal titration calorimetry studies

ITC, as explained some paragraphs above, is an important technique to evaluate the affinity between a host and guest calculating the dissociation constant (K_d) by measuring the heat exchange between the solution and the external environment. These experiments were performed by prof. Rinaldo's research group at University of Rome "La Sapienza". These experiments were carried out for tolcapone, tafamidis, **16** and **17**. The set of experiments consisted of a 5 μM protein solution that was titrated with 100 μM of each compound and the titration profile is depicted in Figure 45 (A-E). Fitting the values of recorded heat *vs* the molar ratio, we could calculate the dissociation constant (K_d), the enthalpy, and the stoichiometry of binding as reported in Table 1.

Ligand	**n**	**K_d (nM)**	**ΔH (kcal mol^{-1})**	**ΔS (kcal mol^{-1} T^{-1})**
tafamidis	2.4±0.1	128±63	-3.2±0.3	20.9±2.1
tolcapone	2.0±0.1	26±4	-11.8±0.5	-4.8±1.9
3-OMT	1.9±0.2	33±9	-8.9±0.3	4.6±0.5
16	1.8±0.1	71±26	-11.5±1.3	-2.9±0.9
17	2.1±0.3	25±5	-10.5±0.2	-0.4±0.1

Table 1: thermodynamic values of ITC studies

The encouraging data are the better affinities for **16** and **17** compared to **3-OMT** showing that the addition of methyl groups also has a positive effect for the binding. The comparison between **16** and **17** allows us to understand the effect of the different configuration of the two compounds showing a higher affinity for **17** compared to **16**. **3-OMT**, **16** and **17** have towards TTR a better affinity than tafamidis.

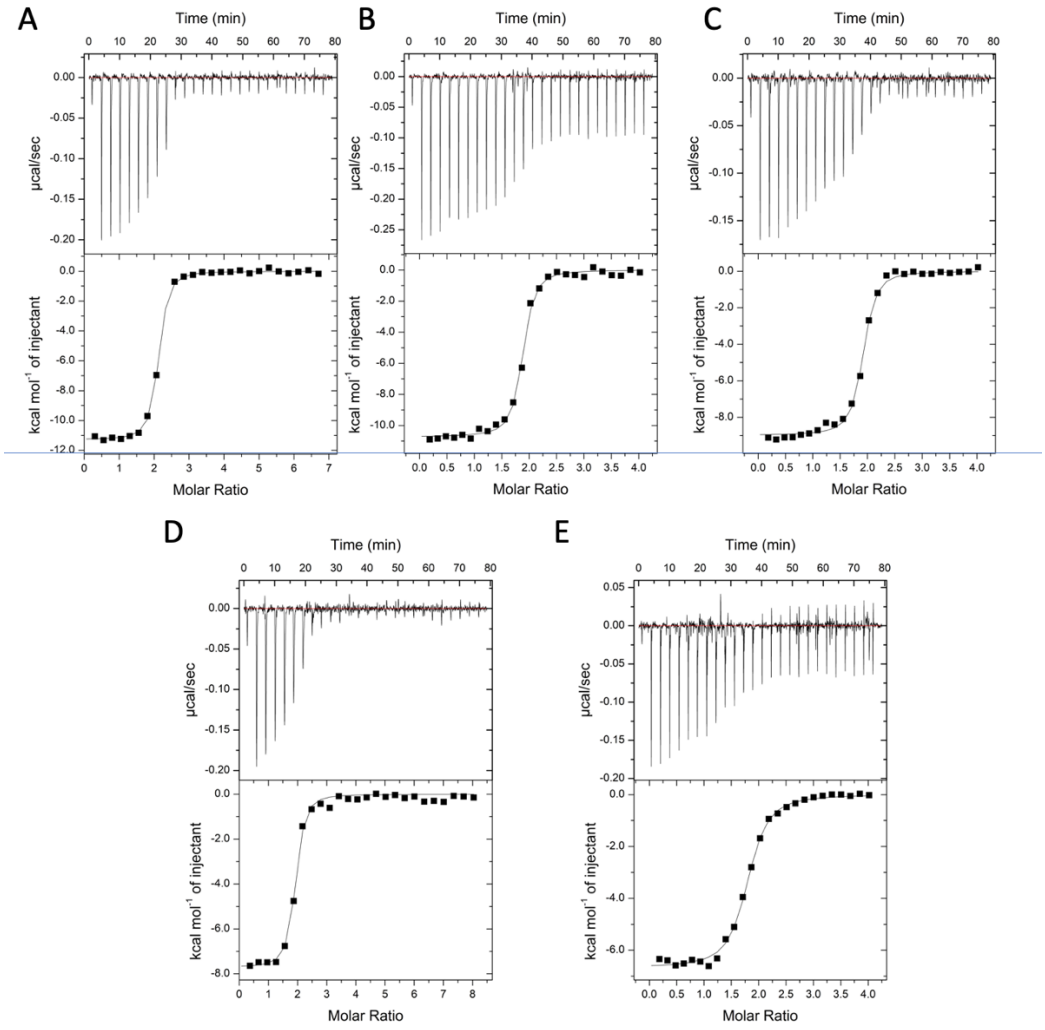

*Figure 45: Raw data for ITC data binding of selected inhibitors to TTR. Analysis by ITC measurements was performed by titrating 3 or 5 µM http protein solution with 100 µM (A) tolcapone, (B) **17**, (C) **3-OMT**, (D) **16**, or (E) tafamidis, in 1× buffer A (25 mM Hepes pH 7,4, 100 mM KCl, 1 mM EDTA) and 5% DMSO.*

2.2.6 Biological studies

2.2.6.1 Western-Blotting studies

Western blotting is a versatile and widely used technique in molecular biology and biochemistry for studying proteins, identifying post-translational modifications, quantifying protein concentrations, and more. Also known as immunoblotting, is a laboratory technique used to detect specific proteins in a biological sample. This technique relies on separating proteins based on their size through polyacrylamide gel electrophoresis and then identifying them using specific antibodies. Here iss how Western blotting works:

1. Protein Extraction: First, proteins need to be extracted from the biological sample of interest. This can be done by homogenizing cells or tissues in a protein extraction buffer that disrupts cell membranes and releases the proteins within.

2. Gel Electrophoresis: The extracted proteins are then separated based on their size through electrophoresis on a polyacrylamide gel. Smaller proteins migrate more quickly through the gel compared to larger ones. This process separates proteins according to their molecular sizes.

3. Membrane Transfer: After electrophoresis, the separated proteins on the gel need to be transferred onto a membrane, typically a nitrocellulose or PVDF (polyvinylidene difluoride) membrane. This step is called "blotting." The transfer is achieved by applying a constant electric current through the gel, causing the proteins to move from the gel matrix to the membrane while maintaining the same size-based arrangement.

4. Blocking: After transfer, the membrane is treated with a blocking solution that prevents nonspecific antibody binding and minimizes background noise.

5. Incubation with Primary Antibodies: The membrane is then incubated with a primary antibody specific to the target protein of interest. This primary antibody specifically binds to the target protein.

6. Washing: After incubation with the primary antibody, the membrane is washed to remove any unbound antibodies.

7. Incubation with Secondary Antibodies: The membrane is subsequently incubated with a secondary antibody conjugated with a marker, such as an enzyme or a fluorescent substance. This secondary antibody binds to the primary antibody, allowing for the detection of the presence of the protein of interest.

8. Detection: The membrane is treated with a substrate specific to the enzyme or fluorophore conjugated to the secondary antibody. This triggers a chemical reaction that produces a detectable signal, such as luminescence or fluorescence. The signal is proportional to the amount of protein present.

9. Image Acquisition and Analysis: Finally, the membrane image is captured using specialized equipment, such as a chemiluminescent imaging system or a fluorescence scanner. The results are then analyzed to determine the quantity and size of proteins present in the sample.

The research group of Prof. Claudia Folli, at University of Parma, performed these experiments. To evaluate the selectivity of the binding of the ligands towards TTR, the experiments were carried out using human plasma. This environment, compared *in vitro* assays using a purified TTR, is more complicated for the presence of the other plasma proteins (i.e., albumins, globulins, etc.); therefore give an idea of the ability of the ligand to stabilise the TTR tetramer in a context where other proteins can interfere with this process and/or sequester the small organic molecule. Different concentrations

of the two target compounds **16** and **17**, **3-OMT**, tolcapone and tafamidis, this latter used as a reference, were tested. The evaluation of the efficiency of the stabilization was performed estimating the percentage of TTR monomer in plasma after incubation of the stabilizer with TTR in slightly denaturing conditions (Figure 46).

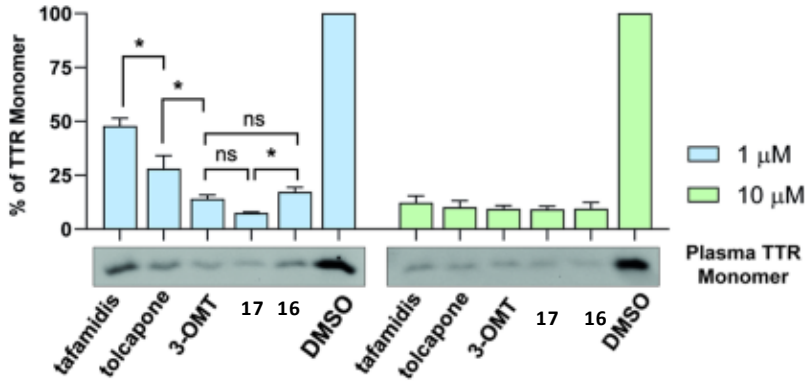

Figure 46: Binding selectivity and structural stabilisation of human TTR in diluted plasma samples, by tolcapone analogues. Histograms represent the relative abundance of TTR monomer after supplementation of tolcapone analogues at two different concentrations (1 μM, left and 10 μM, right), in comparison to the negative control (DMSO). Data are expressed as mean (SD) of three independent experiments, and a representative western blot result is shown below each graph. Data were analysed by one-way ANOVA and symbols indicate statistical difference between treatments: P>0.05 (ns), P≤0.05 (*).

Dimethyl sulfoxide (DMSO) was used as reference negative control totally unable to stabilise the protein tetramer. At 10 μM concentration, every stabilizer showed a very similar good efficiency. Using a lower concentration (1 μM), we could observe difference among the stabilizers. Tafamidis proved to be the less efficient compound (47% of TTR monomer). Target compound **17** shows a very good ability of stabilization recording the lowest value among the tested stabilizers (7% of TTR monomer). On the other hand, for target **16** was determined an effect comparable to that of **3-OMT** (17% TTR monomer). From these tests, compound **17** seems to be the best stabilizer for TTR.

2.2.6.2 *In-vitro* Intestinal and Blood-Brain Barrier Permeability, Solubility and Chromatography Hydrophobicity Index (CHI)

The cellular-based Caco-2 assay is a test that was performed by Nicola Giacchè and colleagues from TES Pharma to evaluate the human intestinal permeability and drug efflux of the TTR stabilisers. The assays were set to determine the rate of the molecules transported across the Caco-2 cell in two directions, apical to basolateral (A→B) and basolateral to apical (B→A), expressed as apparent permeability P_{app} (Table 2). Stabilizers **16**, **17**, **3-OMT** and tolcapone showed good permeability and no efflux active transport.Among them, tolcapone displayed the lowest permeability with (A→B) and (B→A) P_{app} value of 101 and 206 nm/s, respectively. **3-OMT** showed better permeability with a (A→B) Papp value of 160 nm/s, but in particular the two compounds **16** and **17** prepared in this work showed a 2.5-fold increase of the (A→B) P_{app} value compared to tolcapone, with a P_{app} value (A→B)

of 240 nm/s and 250 nm/s, respectively. Although lower, they showed an increase also of the (B→A) P_{app}.

Compound	Direction/ ±inhibitor	P_{app} (nm/s) [expected value]	Recovery %	Efflux ratio (reduction %)
tolcapone	A→B	101±12	53±1	2
	B→A	206±58	70±4	
3-OMT	A→B	160±29	66±4	1.5
	B→A	243±30	83±8	
16	A→B	240±21	64±4	1
	B→A	231±23	77±2	
17	A→B	250±3	69±8	1
	B→A	268±25	80±9	

Table 2: Caco-2 Intestinal Permeability. † reference compounds.

The Chromatographic hydrophobicity index (CHI) is a value very useful for quantifying the hydrophobicity of a compound. This index is calculated for every molecule using a reverse silica phase and estimating the retention time using as eluent a mixture of acetonitrile and a buffer solution. The buffer solution depends on the pH used in every experiment. This index is evaluated at different pH (2, 7.4, and 10.5) to have a complete profile of the hydrophobicity. As we expected, working at acidic pH the four tested molecules displayed a good hydrophobicity index because the molecules are in the neutral form. Among these molecules, **16** and **17** have the highest values as reported in the table. At pH 7.4, it was impossible to estimate the index for tolcapone caused by a large time interval over the peak extended. Considering the values in the different pH, **16** and **17** displayed higher hydrophobicity compared to tolcapone (Table 3).

	CHI (pH 2.0)	CHI (pH 7.4)	CHI (pH 10.5)
tolcapone	78.2	n.d.	49.3
3-OMT	89.2	50.2	46.0
16	97.8	55.5	51.7
17	96.1	53.8	50.2

Table 3: CHI values of the four tested compounds.

To evaluate the permeability through the Brain-Blood Barrier (BBB) an experiment was carried out exploiting a parallel artificial membrane permeability assay (PAMPA) using porcine brain lipid extracts to simulate BBB permeation (PAMPA-BBB). This assay can simulate the transcellular passive diffusion that is the most significant mechanism for the exogenous brain uptake of small molecules. Verapamil, caffeine and theophylline were used as reference compound to verify the reliability of the assay in our hands and the results obtained for them in term of BBB permeability (BBB-Pe) confirmed this. The BBB-Pe value indicates the rate at which a molecule overcomes the barrier and is expressed in cm/s. Comparing the results reported in Table 4, **3-OMT** and the two target compounds **16** and **17** have a 2.5-fold higher permeability BBB-Pe with respect to tolcapone. For these three compounds it is close to the highest value obtainable with this in vitro model (~20×10^{-6} cm/s).

Another important aspect is the solubility of the compound. **3-OMT** and tolcapone are very soluble in phosphate buffer solution (PBS) at physiological pH (Table 4). The presence of a second methyl group to **3-OMT** doesn't influence the solubility of compounds that remains >500 µM.

The collected data allow us to affirm that the target molecules can overcome the BBB classifying them as CNS+.

Compound	BBB-Pe (10^{-6} cm/s) [expected values]	1-Rm	CNS Class [expected values]	Solubility (µM)
verapamil	12.0 (±2.4) [>10]	0.8	+ [+]	>500
caffeine	1.9 (±0.1) [1.3]	0.9	- [-]	>500
theophylline	0.2 (±0.1) [0.12]	1.0	- [-]	>500
tolcapone	5.6 (±1.2)	0.9	+	>500
3-OMT	14.4 (±0.2)	0.9	+	>500
16	15.3 (±2.0)	0.9	+	>500
17	13.5 (±3.9)	1.0	+	>500

*Table 4: Determined solubility (Kinetic) and Blood-Brain Barrier Permeability (PAMPA-BBB) values for control molecules (verapamil, caffeine and theophylline) and tested compounds (tolcapone, **3-OMT**, **16** and **17**). Expected values are reported in brackets. Rm is the membrane retention factor. 1 − Rm between 1.2 and 0.8 is considered fully acceptable for the reliability of the results.*

2.2.6.3 Neuronal- and hepato- toxicity studies

One of the most relevant limitations of tolcapone as a drug is its toxicity. Evaluation of the toxicity of the target compounds was then crucial to understanding the possible benefits of these 3-OMT-based derivatives. Toxicity studies were carried out by Nicola Giacchè and colleagues from TES

Pharma measuring the ATP level after 48 hours of the compound administration. The level of ATP is directly correlated with the cell viability (Figure 47). This assay was conducted on neuroblastoma human cell line SH-SY5Y for neuronal toxicity evaluation and on hepatocarcinoma HepG2 for hepatoxicity evaluation.

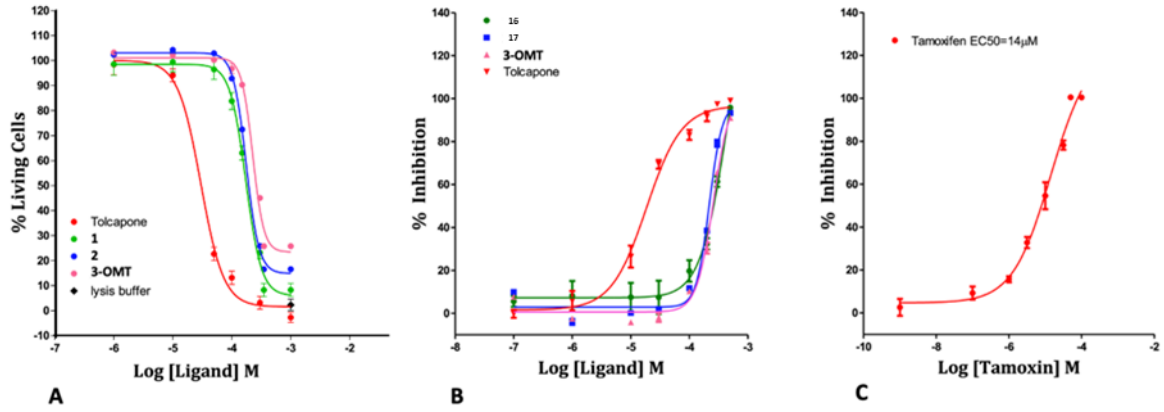

Figure 47: A) Cytotoxicity in Neuroblastoma SH-SY5Y cell line (ATP Viability Assay). B) Cytotoxicity in Hepatocarcinoma HepG2 cell line (ATP Viability Assay). C) Positive control (Tamoxifen) of the HepG2 assay. The full dose response curves at the tested concentrations are shown as the average and standard error for each concentration. Percentage of living cells were calculated, and four-parameter nonlinear regression curve was generated using Prism; GraphPad Software Inc., to calculate EC50 values.

Table 5 reports the results of these studies as EC_{50} where this value indicates the concentration to obtain the death of 50% of the cells meaning that the higher values are associated with a lower toxicity. The values found for the two target compounds **16** and **17** are 6-fold higher compared to tolcapone in neuronal cells and more than 10-fold times higher in liver cells demonstrating that the methylation of OH in position 3 reduces significantly the toxicity of the compounds especially in the liver.

Compound	**SH-SY5Y EC_{50} (μM)**	**HepG2 EC_{50} (μM)**
tolcapone	29.8 ±1.1	17.5 ±2.4
3-OMT	226.3 ±1.3	262.3 ±20.7
16	172.1 ±5	410 ±33
17	174.4 ±3.7	215.6 ±2.2

*Table 5: EC_{50} results reported for reference compounds (**3-OMT** an tolcapone) and target compound (**16** and **17**).*

3. Conclusion

As widely discussed in the introduction of this chapter, the neurodegenerative diseases cases are increasing in parallel to the average age of the human people. For this, it became strongly necessary

to find solutions. In the studies reported in this chapter, we focalized our attention on two different pathologies: Parkinson's disease (PD) and Amyloidosis due to Transthyretin Accumulation (ATTR).

Starting from the common key event, amyloidogenic aggregates, we worked to avoid their formation starting from the proteins involved: α-synuclein (AS) for PD and transthyretin (TTR) for ATTR. Considering the structure of the protein involved in the two diseases and the mechanism of the aggregation at the origin of the toxicity, we decided to use two different approaches: inhibition/disaggregation of the aggregates for PD and stabilization of the physiological TTR tetrameric species for ATTR. AS is a protein characterized by a not well-defined structure but is rich in lysine, especially in the NAC domains. Otherwise, TTR is a protein with a quaternary structure defined by the interaction of four identical subunit generating two sites for several physiological molecules.

Therefore, for AS aggregates we decided to exploit negatively-charged calix[4]arene for the interaction with the numerous lysine units and thus interfering with the aggregation phenomenon. Starting from the knowledge of the research group on calix[4]arene, we synthetized several compounds. They were studied by Prof. Ruotolo of the University of Parma exploiting a yeast model that can produce AS fused with green fluorescence protein (GFP). This fluorescent probe allows to visualize the cells through fluorescent microscopy. The results reported in the chapter show the efficiency of the compound **4**, a tetramethylphosphonate calix[4]arene blocked in rigid cone geometry, to avoid the death of cells by disruption of the AS aggregates. Several biological studies (evaluation of ROS and LDs formation, genic expression analysis) were carried out to evaluate the benefits of the administration to the cells of calixarene **4**. The Host-Guest complex studies with ITC and NMR titration on compound **4** allowed us to hypothesize that the dysregulation of AS aggregation would be possible thanks to the interaction between the calixarene anionic units and the ammonium of lysine, together with the inclusion into the macrocyclic cavity of the carbon side chain of the amino acid.

Compounds **16** and **17**, two different derivatives of 3-O-methyltolcapone, were evaluated as stabilizers of TTR by different studies. Thanks to ITC titration and Western Blotting experiments we were able to estimate, respectively, the ability of interaction and stabilization of the two derivatives. The co-crystallization of the target compounds with TTR allowed us to understand how the two compounds form complexes with the tetramer, stabilizing it. One of the main reasons that prompted the design and synthesis of these two derivatives was the need of finding molecules with improved ability of cross the BBB compared to tolcapone for which the scarce availability in the CNS represents a relevant limitation. The performed studies showed indeed that both of them have a good BBB

permeability, significantly increased with respect to tolcapone. They also showed an improved profile in term of neuronal- and hepato- toxicity being these other weak points of tolcapone.

In this chapter is reported the synthesis and the studies of different compounds that resulted to be good ligands for AS and TTR, respectively disrupting aggregates or avoiding their formation.

4. Experimental Part

General information

Commercially available reagents and solvents were used without carrying out any prior purification or treatment except as indicated. All moisture- and air-sensitive reactions were conducted under nitrogen atmosphere. Dry solvents were prepared according to standard procedures and stored in the presence of molecular sieves. Monitoring of synthetic processes was performed by direct-phase thin-layer chromatography (TLC) using 60 F254 silica gel plates. For the detection of reagents and products with amine groups, the TLCs were sprayed with a 5% solution of ninhydrin in ethanol; for those with phenolic groups, a solution of $FeCl_3$ in water was used; for those with carboxylic acid groups, a solution of acidic bromocresol green in ethanol was used; and for easily oxidized compounds, a 0.05% solution of $KMnO_4$ in water was used. Flash chromatography columns on silica gel 60 (230-400 mesh), under nitrogen pressure, and commercial preparative TLC 20×20 cm, silica gel F_{254}, 0.5 mm were used for products purification. Products characterization was performed by ^{1}H and ^{13}C NMR spectroscopy and mass spectrometry using ESI technique. NMR spectra were recorded with Bruker AVANCE 400 spectrometer (^{1}H at 400 MHz, ^{13}C at 100 MHz); chemical shift values are reported in ppm using the resonance frequency of the partially deuterated solvent as a reference. Isothermal titration calorimetry was performed by ITC Isothermal Titration Calorimeter MicroCal PEAQ. Mass spectra were recorded with a single quadrupole SQ detector spectrometer, Waters. The purity degree of compounds **16** and **17** was determined with an Agilent 1260 HPLC, using a SUPELCO C18 column (3 μm, 150 mm × 4.6 mm) at 40 °C. Mobile phase A: 0.1% TFA in water; mobile phase B: 0.1% TFA in acetonitrile. Gradient conditions: 0−5 min, phase A 100%; 5−15 min, phase A 60%, phase B 40%; 15−25 min, phase A 20%, phase B 80%; 25-30, phase B 100%; 30-35 min, phase A 100%. Flow rate: 1.5 mL/min. The peaks were detected at 270 nm.

4.1 Negatively-charged calix[4]arenes as inhibitors of AS aggregation

25,26,27,28-tetra(tert-butoxycarbonylmethoxy)calix[4]arene (9)

In a two-necked flask under a nitrogen flow, 25,26,27,28-tetrahydroxycalix[4]arene (2,12 g, 4.99 mmol) was added to a mixture of THF (120 mL) and DMF (30 mL). Then, NaH (1.20 g, 24.97 mmol) was added, and the mixture was stirred for about 5 minutes. Subsequently, tert-butyl bromoacetate

(4.2 mL, 49.94 mmol) was added, and the mixture was brought to reflux by heating at 66°C for 16 hours. The reaction progress was monitored by TLC (eluent: Hex/EtOAc 7:3, visualized with $FeCl_3$). Upon the disappearance of the starting material, the THF was evaporated under reduced pressure using a rotary evaporator. Then, 1 M HCl was added, and the resulting white precipitate was filtered through a Buchner funnel, washed with 1 M HCl, and then with water. The compound was purified through recrystallization from dichloromethane/methanol and finally washed with cold methanol. The resulting compound was dried using a mechanical pump. The obtained compound appeared as a white powder.

Yield= 70% (3.03 g,)

^{1}H NMR (400 MHz, $CDCl_3$) δ (ppm): 6.66 – 6.50 (m, 12H, Ar*H*), 4.89 (d, *J* = 13.7 Hz, 4H, axial ArC*H*$_2$Ar), 4.63 (s, 8H, OC*H*$_2$CO), 3.22 (d, *J* = 13.7 Hz, 4H, equatorial ArC*H*$_2$Ar), 1.46 (s, 36H, C*H*$_3$).

The spectroscopic data found are in agreement with those reported in literature[88].

25,26,27,28-tetra(hydroxycarbonylmethoxy)calix[4]arene (10)

In a round-bottom flask, **9** (2.0 g, 2.27 mmol) and CF_3COOH (7.81 mL, 102.10 mmol) were introduced, and the solution was kept stirring for 5 hours at room temperature. The reaction was monitored by TLC (eluent: Hex/EtOAc 3:7, bromocresol green). Once the reaction was completed, the solvent was evaporated under reduced pressure using a rotary evaporator. Then, water was added, and the resulting mixture was stirred for 15 minutes to promote the precipitation of the desired product. The obtained white solid was filtered through a Buchner funnel and left to dry using a mechanical pump. The product appeared as a white powder.

Yield= 95% (1.42 g)

^{1}H NMR (400 MHz, DMSO-d_6) δ (ppm): 12.37 (br s, COOH), 6.92 (d, *J* = 7.6 Hz, 8H, Ar*Hmeta*), 6.68 (t, *J* = 7.5 Hz, 4H Ar*Hpara*), 4.89 (d, *J* = 13.0 Hz, 4H, axial ArC*H*$_2$Ar), 4.67 (s, 8H, OCH_2CO), 3.29 (d, *J* = 13.0 Hz, 4H, equatorial ArC*H*$_2$Ar).

The spectroscopic data found are in agreement with those reported in literature[88].

5,11,17,23-tetrasulfonate-25,26,27,28-tetrakis(hydroxycarbonylmethoxy)calix[4]arene (1)

In a round-bottom flask, **10** (700 mg, 1.07 mmol) and H_2SO_4 (3 mL, 56.28 mmol) were introduced. The reaction was kept stirring at room temperature. The progress of the reaction was monitored using

mass spectrometry. After 16 hours, when the starting material was no longer observed, diethyl ether (20 mL) was added and the mixture was stirred for 1 hour. The oily precipitate was separated from diethyl ether by centrifugation. Further washes with diethyl ether were performed, yielding a dense red oil that was dried using a mechanical pump for 1 day. The product was obtained as an amaranth powder.

Yield: quantitative (1.07 g)

^{1}H NMR (400 MHz, D_2O+NaOD 5% wt) δ (ppm): 7.53 (s, 8H, Ar*H*), 4.52 (d, *J* = 12.7 Hz, 4H, axial ArC*H*$_2$Ar), 4.30 (s, 8H, OCH_2CO), 3.50 (d, *J* = 12.7 Hz, 4H, equatorial ArC*H*$_2$Ar).
The spectroscopic data found are in agreement with those reported in literature[88].

5,11,17,23-tetrabromo-25,26,27,28-bis-crown-3-calix[4]arene (11)

In a round-bottom flask, a solution of 25,26-27,28-biscrown-3-calix[4]arene (100 mg, 0.18 mmol) in DMF (3 mL) and NBS (264 mg, 1.48 mmol) was added. The reaction mixture was stirred at room temperature for 24 hours. The reaction progress was monitored using TLC (eluent: Hex:EtOAc 6:4). After 24 hours, no more reagent was present. Then, water was added to the reaction mixture, and the resulting precipitate was filtered through a Buchner funnel and recrystallized with MeOH. The product was obtained as a straw-yellow solid.

Yield=95% (0.15 g)

^{1}H NMR (400 MHz, $CDCl_3$) δ(ppm): 7.15 (d, *J* = 2.5 Hz, 4H, ArH), 7.12 (d, *J* = 2.5 Hz, 4H, ArH), 4.96 (d, *J* = 12.2 Hz, 2H, axial ArC*H*$_2$Ar), 4.37 (d, *J* = 12.2 Hz, 2H, axial ArC*H*$_2$Ar), 4.28 – 4.13 (m, 12H, OCH_2CH_2O), 3.77 (dt, *J* = 10.7, 2.2 Hz, 4H, ArOCH*H*CH_2*O*), 3.19 (d, *J* = 12.2 Hz, 2H, equatorial ArC*H*$_2$Ar), 3.13 (d, *J* = 12.2 Hz, 2H, equatorial ArC*H*$_2$Ar).
The spectroscopic data found are in agreement with those reported in literature[89].

5,11,17,23-tetrakis(diethylphosphono)-25,26,27,28-bis-crown-3-calix[4]arene (12)

In a two-neck flask equipped with a condenser, a suspension of **11** and anhydrous $NiCl_2$ (34 mg, 0.19 mmol) in diphenyl ether (10 mL) was introduced. The reaction mixture was heated to 210-220 °C, and $P(OEt)_3$ (166 mg, 5.64 mmol) was added dropwise over 15 minutes. The reaction mixture was maintained at 210-220 °C for 2 hours. The reaction was followed by TLC (eluent: Hex/EtOAc 6:4). The solvent was co-evaporated with diethylene glycol. The resulting solid was purified using silica gel column chromatography ($CHCl_3$/MeOH). A white solid was obtained.

Yield= 42% (0.22 g)

^{1}H NMR (400 MHz, $CDCl_3$) δ(ppm): 7.43 (dd, *J* = 9.3, 1.9 Hz, 4H, ArH), δ 7.40 (dd, *J* = 9.3, 1.9 Hz, 4H, ArH) 5.14 (d, *J* = 12.4 Hz, 2H, axial ArC*H*$_2$Ar), 4.50 (d, *J* = 12.5 Hz, 2H, axial ArC*H*$_2$Ar), 4.32 (d, *J* = 11.1 Hz, 4H, ArOCH*H*CH_2O), 4.28 – 4.13 (m, 8H, $POCH_2$), 4.00 – 3.81 (m, 20H, POC*H*$_2$, OC*H*$_2$C*H*$_2$O), 3.34 (d, *J* = 12.5 Hz, 2H, equatorial ArC*H*$_2$Ar), 3.29 (d, *J* = 12.4 Hz, 2H, equatorial ArC*H*$_2$Ar), 1.10 (dt, *J* = 7.1, 4.3 Hz, 24H, C*H*$_3$).
The spectroscopic data found are in agreement with those reported in literature[40].

5,11,17,23-tetrakis(dihydroxyphosphono)-25,26,27,28-bis-crown-3-calix[4]arene (2)

In a two-necked round-bottom flask, nitrogen flow was established, and then **12** (100 mg, 0.09 mmol) previously dissolved in dry $CHCl_3$ (0.36 mL) was added. The reaction mixture was stirred until complete dissolution of the reagent, and then TMSBr (0.48 mL, 2.73 mmol) was added. The reaction, carried out at room temperature, was monitored using mass spectrometry. After 16 hours, the solvent was evaporated under reduced pressure first with a rotary evaporator and then with a mechanical pump. To the resulting residue, methanol (10 mL) was added and stirred for 16 hours. An orange-yellow solution with orange precipitate formed, which was centrifuged. The product was separated as a straw-yellow solid.

Yield=90% (0.071 g)

^{1}H NMR (400 MHz, D_2O+NaOD 5% wt) δ(ppm): 7.05 (d, *J* = 5.5 Hz, 4H, ArH), 7.02 (d, *J* = 5.2 Hz, 4H, ArH), 4.37 (d, *J* = 12.0 Hz, 2H, axial ArC*H*$_2$Ar), 4.01 (d, *J* = 12.2 Hz, 2H, axial ArC*H*$_2$Ar), 3.96 – 3.78 (m, 12H, OCH_2CH_2O), 3.42 (t, *J* = 8.3 Hz, 4H, ArOC*H*HCH_2O), 2.99 (d, *J* = 12.2 Hz, 2H, equatorial ArC*H*$_2$Ar), 2.95 (d, *J* = 12.0 Hz, 2H, equatorial ArC*H*$_2$Ar)
The spectroscopic data found are in agreement with those reported in literature[40].

5,11,17,23-tetrasulfonate-25,26,27,28-bis-crown-3-calix[4]arene (3)

Under a nitrogen atmosphere, HSO_3Cl (0.5 mL) was cooled in a flask using an ice bath. 25,26,27,28-bis-crown-3-calix[4]arene (100 mg, 0.27 mmol) was dissolved in dry dichloromethane (2.5 mL) and added dropwise to HSO_3Cl over the course of an hour. The reaction mixture was brought to room temperature and stirred for 6 hours and monitored by ESI-MS, after which the reaction was quenched by adding ice (as needed). A viscous brown solid precipitated. The solid was separated by filtration from the liquid phase, dried, triturated with MeOH/DCM 1:1, filtered, and dried again, yielding the desired compound as an opaque white solid.

Yield=34% (0.081 g)

^{1}H NMR (400 MHz, DMSO-d_6) δ(ppm): 7.60 – 7.26 (m, 8H, ArH), 4.98 (d, J = 11.9 Hz, 2H, axial ArCH_2Ar), 4.44 (d, J = 12.0 Hz, 2H, axial ArCH_2Ar), 4.34 – 4.15 (m, 12H, OCH_2CH_2O), 3.66 (dt, J = 11.6, 6.1 Hz, 4H, ArOCHHCH_2O), 3.41 (d, J = 12.2 Hz, 2H, equatorial ArCH_2Ar), 3.34 (d, J = 11.9 Hz, 2H, equatorial ArCH_2Ar).

The spectroscopic data found are in agreement with those reported in literature[74].

5,11,17,23-Tetrakis(Dihydroxyphosphonoyl)methyl-25,26,27,28-tetrahydroxycalix[4]arene (4)

In a round-bottom flask, calix[4]arene (1.0 g, 1.62 mmol) dissolved in dry DCM (10 mL) and zinc bromide (0.413 g, 1.62 mmol) were introduced. Then, triethyl phosphite (1.4 mL, 8.10 mmol) was added. The mixture was kept stirring at room temperature for 2 hours and minotired by ESI-MS. The organic solvent was evaporated under reduced pressure. The resulting residue was dissolved in 12 M HCl (5 mL), and the reaction was kept stirring for 16 hours at reflux. The progress of reaction was monitored by ESI-MS. After the end of the reaction, the solution was cooled at rt and was added carefully a solution of 1 M NaOH until pH=14. The product was obtained by precipitation with MeOH as pink powder.

Yield= 50% (0.648 g)

^{1}H NMR (400 MHz, D_2O) δ(ppm): 6.80 (br s, 8H, ArH), 3.60 (br s, 8H, $ArCH_2Ar$), 2.64 (br s, 8H, CH_2P).

The spectroscopic data found are in agreement with those reported in literature[90].

5,11,17,23-tetrakis(chloromethyl)-25,26,27,28-tetramethoxycalix[4]arene (13)

In a round-bottom flask, 5,11,17,23-tetramethoxycalix[4]arene (500 mg, 1.04 mmol) dissolved in dioxane (40 mL) and paraformaldehyde (650 mg, 20.8 mmol) were introduced. Then, acetic acid (3.3 mL), 37% hydrochloric acid (6.8 mL), and 85% phosphoric acid (6.25 mL) were added. The mixture was heated to 100 °C for 8 hours and then cooled in an ice bath. The organic solvent was evaporated under reduced pressure. The resulting residue was dissolved in dichloromethane and washed with water until pH=7. The organic phase was evaporated under reduced pressure, and the obtained residue was purified using column chromatography (eluent: Hex/EtOAc 1:7) to yield the organic compound as a white solid.

Yield= 21% (0.147 g)

^{1}H NMR (400 MHz, $CDCl_3$) cone conformation: δ(ppm): 6.72 (s, 2H, ArH), 4.37 – 4.28 (m, 3H, CH_2Cl, axial ArCH_2Ar), 3.80 (s, 3H, OCH_3), 3.18 (d, J = 13.4 Hz, 1H, equatorial ArCH_2Ar); partial

cone conformer: δ (ppm): 7.27 (s, 2H, Ar*H*), 7.11 (s, 2H, Ar*H*), 6.94 (s, 2H, Ar*H*), 6.37 (s, 2H, Ar*H*), 4.61 (s, 4H, ArCH_2Cl), 4.25 (s, 4H, ArCH_2Cl), 4.03 (d, J = 13.8 Hz, 2H, syn axial ArCH_2Ar), 3.73 – 3.57 (m, 13H, 3 OCH_3, anti ArCH_2Ar), 3.10 (d, J = 14.2 Hz, 2H, syn equatorial ArCH_2Ar), 3.02 (s, 3H, OCH_3).

The spectroscopic data found are in agreement with those reported in literature[75].

5,11,17,23-tetrakis(dihydroxyphosphonoylmethyl)-25,26,27,28-tetramethoxycalix[4]arene (7)

In a schlenk, nitrogen flow was established by heating with a heat gun to create a dry environment. Then, **13** (200 mg, 0.033 mmol) was dissolved in $P(OSi(CH_3)_3)_3$ (3 mL) The reaction mixture was kept stirring at 100 °C for 16 hours. The reaction progress was monitored using mass spectrometry. At the end of the reaction, once the starting calixarene was consumed, the phosphite was removed by distillation under reduced pressure. Methanol (10 mL) was added to the obtained residue, and the mixture was stirred at room temperature for 16 hours. The solvent was removed by evaporation under reduced pressure. The compound was obtained as a pink powder.

Yield = 50% (0.097 g)

^{1}H NMR (400 MHz, D_2O+1% NaOD) δ(ppm): 6.99 (br s, 8H, ArH), 3.68 (br s, 8H, $ArCH_2Ar$), 3.43 – 3.23 (br s, 12H, OCH_3), 2.57 (br s, 8H, CH_2P).

^{31}P (162 MHz, D_2O) δ(ppm): 18.7.

^{13}C NMR (101 MHz, D_2O) δ(ppm): 154.4, 134.4, 133.5, 130.5, 59.2, 57.0, 48.7, 37.1, 35.8, 23.7.

MS-ESI: m/z cal: 856.3 found: 855.3 $[M-H]^-$

Methyl N^{α}-acetyl-N^{ε}-(tert-butoxycarbonyl)-L-lysylglycinate (15)

To a two-necked round-bottom flask under nitrogen, was dissolved glycine methyl ester hydrochloride (0.085 g, 0.68 mmol), (S)-2-acetamido-6-((tert-butoxycarbonyl)aminohexanoic acid (0.2 g, 0.69 mmol) and HBTU (0.261 g, 0.69 mmol) in DMF (5 mL) at 0 °C. Then DIPEA was (0.23 mL, 1.36 mmol) was added. The mixture was kept on ice bath for 30 min, and subsequently stirred overnight at room temperature. The reaction was monitored by TLC (eluent: DCM/MeOH 95:5). The mixture was diluted with EtOAc, transferred to a separatory funnel and washed with 0.5 M K_2CO_3

and brine. The aqueous phase was extracted with EtOAc and the organic layer were collected. The combined organic phases were washed with 0.1 M HCl and then dried over Na_2SO_4. Evaporation of solvent gave a crude product which was recrystallized from a mixture of 30 mL ethyl acetate and 20 mL n-heptane to provide the title compound as a white solid.

Yield=61% (0.150 g)

^{1}H NMR (400 MHz, $CDCl_3$) δ (ppm): 6.77 (s, 8H, Ar*H*), 4.44 (d, 4H, J = 12.9Hz, axial ArC*H*$_2$Ar), 4.10 (t, 8H, J = 6.3Hz, -OC*H*$_2$CH$_2$O-), 3.93 (t, 8H, J = 6.3Hz, -OCH$_2$C*H*$_2$O-), 3.59 (q, 8H, J = 6.3Hz, -OCH$_2$C*H*$_3$), 3.11 (d, 4H, J = 12.7Hz, equatorial ArC*H*$_2$Ar), 1.23 (t, 12H, J = 7.1Hz, -OCH$_2$C*H*$_3$), 1.07 (s, 36H, -C(C*H*$_3$)$_3$).

The spectroscopic data found are in agreement with those reported in literature[91].

Methyl N$^{\alpha}$-acetyl-L-lysylglycinate

To a two-necked round-bottom flask under nitrogen, Methyl N$^{\alpha}$-acetyl-N$^{\varepsilon}$-(tert-butoxycarbonyl)-L-lysylglycinate (0.035 g, 0.097 mmol) was dissolved in DCM (2 mL) and TFA was added (1 mL). The reaction was monitored by TLC (eluent: DCM/MeOH 8:2). At the end of the reaction the volatile part was removed under reduced pressure. The product was obtained as white solid.

Yield=quantitative (0.036 g)

^{1}H NMR (400 MHz, $CDCl_3$) δ (ppm): 6.77 (s, 8H, Ar*H*), 4.44 (d, 4H, J = 12.9Hz, axial ArC*H*$_2$Ar), 4.10 (t, 8H, J = 6.3Hz, -OC*H*$_2$CH$_2$O-), 3.93 (t, 8H, J = 6.3Hz, -OCH$_2$C*H*$_2$O-), 3.59 (q, 8H, J = 6.3Hz, -OCH$_2$C*H*$_3$), 3.11 (d, 4H, J = 12.7Hz, equatorial ArC*H*$_2$Ar), 1.23 (t, 12H, J = 7.1Hz, -OCH$_2$C*H*$_3$), 1.07 (s, 36H, -C(C*H*$_3$)$_3$).

^{13}C NMR (101 MHz, CD_3OD) δ 173.3 (C=O), 172.3 (C=O), 170.3 (C=O), 53.2 (CH$_2$*C*H), 51.3 (OCH$_3$), 40.4(*C*H$_2$CO), 39.1 (CH$_2$NH$_3$), 31.0(*C*H$_2$CH), 26.7(*C*H$_2$CH$_2$NH$_3$), 22.2 (*C*H$_2$CH$_2$CH), 21.1 (CH$_3$)

ESI-MS: m/z calc: 373.3 found: 396.3 $[M+Na]^+$, 260.2 $[M\text{-}CF_3COO^-]^+$

^{1}H NMR in D_2O and in PBS (100 mM) (pD = 7,4) titrations

Starting concentration of the two solutions:

[Peptide] mM	[calix] mM
1.58	10

	V added (µl)	V tot. added (µl)	V tot. (µl)	$[Calix]_0$ (mM)	$[Peptide]_0$ (mM)	$[Calix]_0/[Peptide]_0$
1	0	0	500	0.00	1.58	0.00
2	10	10	510	0.20	1.55	0.13
3	15	25	525	0.48	1.50	0.32
4	20	45	545	0.83	1.45	0.57
5	25	70	570	1.23	1.39	0.89
6	30	100	600	1.67	1.32	1.27
7	50	150	650	2.31	1.22	1.90
8	100	250	750	3.33	1.05	3.16

ITC experiments

For direct titrations, all experiments were conducted in a water maintained at atmospheric pressure and 25° C. A fixed volume of 2.00 micro Liters per injection of the guest solution ranging from 2.00 to 5.00 millimolar was injected into the reaction cell with a 280 micro Liter capacity. The reaction cell was charged with either 100 or 200 microMolar of the **4** solution, and each injection was completed within 4 seconds under stirring at 750 rpm. A total of nineteen consecutive injections were made for each titration. The heat of dilution was gauged by introducing the guest (dipeptide) solution in water. The actual reaction heat was determined by deducting the dilution heat from the apparent reaction heat. The resulting net reaction heat was then processed through computer simulation employing the "One Set of Sites" model using the MicroCal PEAQ-ITC Analysis Software. The binding stoichiometry was held constant at 1. The association constants were determined from the reciprocal of the dissociation constants provided by the software.

4.2 Synthesis of TTR stabilizers

(4-(benzyloxy)-3-methoxyphenyl)-1-(3,5-dimethylphenyl)methanol (22a)

In a flame-dried three-necked round-bottomed flask, magnesium turnings (0.30 g, 12.52 mmol) were suspended in dry THF (3 mL) under Ar atmosphere. Using a dropping funnel, a solution of 1-bromo-3,5-dimethylbenzene (2.31g, 12.52 mmol) in dry THF (2.3 mL) was slowly added in 1 hour. Then, a solution of **1** (2 g, 8.26 mmol) in dry THF (1.7 mL) was slowly added dropwise in 30 min into the under stirring reaction mixture. The reaction proceeding was monitored by TLC (eluent: hexane/ethyl acetate 7/3). After 1 hour the reaction was quenched by addition of saturated NH_4Cl aqueous solution

(5 mL) and extracted with Et_2O (3x10 mL). The organic phase was washed with NaCl saturated solution (3x10 mL), dried with anhydrous Na_2SO_4 and evaporated at reduced pressure. The residue was crystallized from Et_2O/petroleum ether to afford the product as white solid.

Yield= 69% (1.97 g)

^{1}H NMR (DMSO-d_6, 400MHz): δ 7.48 – 7.26 (m, 5H, ArH); 7.01 – 6.89 (m, 4H, ArH); 6.87 – 6.72 (m, 2H, ArH); 5.68 (d, *J* = 3.9 Hz, 1H, OH); 5.53 (d, *J* = 3.9 Hz, 1H, CH); 5.03 (s, 1H, CH_2); 3.74 (s, 3H, OCH_3); 2.23 (s, 6H, CH_3).
^{13}C NMR (DMSO-d_6, 100MHz): δ 149.3 (Ar), 147.0 (Ar), 146.2 (Ar), 139.4 (Ar), 137.8 (Ar), 137.3 (Ar), 128.8 (Ar), 128.4 (Ar), 128.2 (Ar), 128.2 (Ar), 124.4 (Ar), 118.8 (Ar), 113.8 (Ar), 110.9 (Ar), 74.49 (CH), 70.4 (CH_2), 56.0 (OCH_3), 21.5 (CH_3).

MS-ESI: m/z calc: 348.13, found: 371.14 $[M + Na]^+$.

m.p. 94-95 °C

(4-(benzyloxy)-3-methoxyphenyl)-1-(2,4-dimethylphenyl)methanol (22b).

In a flame-dried three-necked round-bottomed flask, magnesium turnings (0.30 g, 12.52 mmol) were suspende in dry THF (3 mL) under Ar atmosphere. Using a dropping funnel, a solution in dry THF (2.3 mL) of 1-bromo-2,4-dimethylbenzene (2.31 g, 12.52 mmol) was slowly added in 1 hour. Then, a solution of **1** (2 g, 8.26 mmol) in dry THF (1.7 mL) was slowly dripped in 30 min into the stirred reaction mixture. The reaction proceeding was monitored by TLC (eluent: hexane/ethyl acetate 4/1). After 1 hour, the reaction was quenched by addition of saturated NH_4Cl solution (5 mL), extracted with Et_2O (3x10 mL) and then the organic phase was washed with brine (3x10 mL). The organic phase was dried over anhydrous Na_2SO_4, evaporated under reduced pressure and the residue was crystallized from Et_2O/petroleum ether to afford the product as white solid.

Yield=56% (1.6 g)

^{1}H NMR (DMSO-d_6,400 MHz) δ 7.45 – 7.27 (m, 6H, ArH); 6.98 (brd, 1H, ArH); 6.96 – 6.88 (m, 3H, ArH); 6.67 (dd, *J* = 8.3, 2.0 Hz, 1H, ArH); 5.73 (d, *J* = 4.3 Hz, 1H, OH); 5.58 (d, *J* = 4.4 Hz, 1H, CH); 5.03 (s, 2H, CH_2); 3.72 (s, 3H, OCH_3); 2.24 (s, 3H, CH_3); 2.17 (s, 3H, CH_3).

^{13}C NMR (DMSO-d_6,100 MHz) δ 149.2 (Ar), 147.0 (Ar), 140.8 (Ar), 138.2 (Ar), 137.7 (Ar), 135.9 (Ar), 135.0 (Ar), 131.1 (Ar), 128.8 (Ar), 128.2 (Ar), 128.2 (Ar), 126.9 (Ar), 126.6 (Ar), 119.4 (Ar), 113.7 (Ar), 111.7 (Ar), 71.5 (CH), 70.4 (CH_2), 56.0 (OCH_3), 21.0 (CH_3), 19.5 (CH_3).

MS-ESI: m/z calc: 348.13, found: 371.13 $[M + Na]^+$.

m.p.: 59-60 °C

(4-(benzyloxy)-3-methoxyphenyl)-1-(3,5-dimethylphenyl)methanone (23a)

t-BuONa (0.451 g, 3.61 mmol) and cyclohexanone (1.47 mL, 14.35 mmol) were added to a solution of **22a** (1 g, 2.87 mmol) in toluene (4 mL). The mixture was stirred at reflux for 16 h. The reaction proceeding was monitored by TLC (eluent: hexane/ethyl acetate 7/3). The solution was cooled at 50 °C and then water (4 mL) was added. The organic phase was separated and the aqueous one was extracted with ethyl acetate (3x5 mL). The combined organic phases were washed with water (20 mL) and brine (20 mL) and, then, evaporated at reduced pressure obtaining an oily residue, which was crystallized with ethanol 96% to afford **3** as white powder.

Yield=75% (0.74 g)

^{1}H NMR (DMSO-d_6, 400 MHz): δ 7.53 – 7.31 (m, 6H, ArH); 7.32 – 7.24 (m, 4H, ArH); 7.20 (d, *J* = 8.3 Hz, 1H, BnOCCH); 5.20 (s, 2H, CH_2); 3.83 (s, 3H, OCH_3); 2.35 (s, 6H, CH_3).

^{13}C NMR DMSO-d_6, 100 MHz): δ 195.2 (C=O), 152.3 (Ar), 149.3 (Ar), 138.4 (Ar), 138.1 (Ar), 136.9 (Ar), 133.9 (Ar), 130.2 (Ar), 129.0 (Ar), 128.6 (Ar), 128.5 (Ar), 127.4 (Ar), 125.2 (Ar), 112.5 (Ar), 112.5 (BnOC*C*H), 70.4 (CH_2), 56.0 (OCH_3), 21.3 (CH_3).

MS-ESI: m/z cal: 346.11, found: 347.12 ($[M+H]^+$), 369.10 ($[M + Na]^+$).

m.p. 110-111 °C

(4-(benzyloxy)-3-methoxyphenyl)-1-(2,4-dimethylphenyl)methanone (23b)

t-BuONa (0.22 g, 2.32 mmol) and cyclohexanone (0.94 mL, 9.09 mmol) were added to a solution of **22b** (0.49 g, 1.40 mmol) in toluene (2 mL). The reaction proceeding was monitored by TLC (eluent: hexane/ethyl acetate 7/3). The solution was stirred at reflux for 16 h. The solution was cooled at 50 °C and then water (2 mL) was added. The organic phase was separated from water and the aqueous

phase was extracted with ethyl acetate (3x3 mL). The combined organic phases were collected and washed with water (10 mL) and brine (10 mL). Subsequently, the solvent was evaporated under reduced pressure obtaining an oily residue that was crystallized with ethanol 96% to afford **3** as white powder.

Yield=57% (0.27 g)

^{1}H NMR ($CDCl_3$,400 MHz): δ 7.58 (d, *J* = 2.0 Hz, 1H, ArH); 7.47 – 7.31 (m, 5H, ArH); 7.24 – 7.17 (m, 2H, ArH); 7.11 (brs, 1H, ArH); 7.05 (d, 1H, ArH); 6.86 (d, *J* = 8.4 Hz, 1H, ArH); 5.25 (s, 2H, CH_2); 3.97 (s, 3H, OCH_3); 2.39 (s, 3H, CH_3); 2.31 (s, 3H, CH_3).

^{13}C NMR ($CDCl_3$, 100 MHz) δ 197.3 (C=O), 158.3 (Ar), 152.5 (Ar), 149.5 (Ar), 140.1 (Ar), 136.6 (Ar), 136.3 (Ar), 136.0 (Ar), 131.7 (Ar), 131.2 (Ar), 128.5 (Ar), 128.1 (Ar), 127.2 (Ar), 125.7 (Ar), 125.7 (Ar), 111.9 (Ar), 111.7 (Ar), 70.8 (CH_2), 56.1 (OCH_3), 21.4 (CH_3), 19.9 (CH_3).

MS-ESI: m/z calc: 343.10, found: 369.11 $[M + Na]^+$.

m.p. 100-101 °C

(4-hydroxy-3-methoxyphenyl)-1-(3,5-dimethylphenyl)methanone (24a)

To a solution in methanol (4.3 mL) of **23a** (0.5 g, 1.44 mmol) and ammonium formate (0.36 g, 5.77 mmol), Pd/C 10% (catalytic amount) suspended in methanol (1.7 mL) was added. The reaction proceeding was monitored by TLC (eluent: hexane/ethyl acetate 7/3). The resulting mixture was stirred at reflux for 1 hour. Subsequently, it was cooled in an ice/water bath and water (2 mL) and HCl 2M (0.4 mL) were slowly added up to slightly acidic pH. After addition of DCM (6 mL), the mixture was filtered through a celite pad. The organic phase was separated and the aqueous one was extracted with DCM (3x6 mL). The combined organic phases were washed with water (20 mL) and brine (20 mL) and dried with anhydrous Na_2SO_4. Solvent was evaporated under reduced pressure and product was obtained by crystallization from DCM/petroleum ether as yellow crystals.

Yield= 81% (0.30 g)

^{1}H NMR ($CDCl_3$,400 MHz): δ 7.53 (d, *J* = 1.9 Hz, 1H, H_a); 7.39 – 7.33 (m, 3H, H_d, H_c); 7.22 (br s, 1H, H_e); 6.97 (d, *J* = 8.2 Hz, 1H, H_b); 6.08 (s, 1H, OH); 3.99 (s, 3H, OCH_3); 2.40 (s, 6H, CH_3).

^{13}C NMR ($CDCl_3$,100 MHz): δ 196.0 (C=O), 150.0 (Ar), 146.6 (Ar), 138.4 (Ar), 137.8 (Ar), 133.5 (C-He), 130.2 (Ar), 127.5 (Ar), 126.2 (C-H_c), 113.4 (C-H_b), 111.7 (C-H_a), 56.2 (OCH_3), 21.3 (CH_3)

MS-ESI: m/z calc: 256.10 found: 257.10 ($[M+H]^+$), 279.07 ($[M+Na]^+$)

m.p. 130-131°C

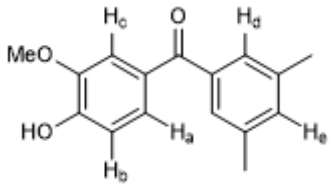

(4-hydroxy-3-methoxyphenyl)-1-(2,4-dimethylphenyl)methanone (24b)

To a solution in methanol (2.4 mL) of **9** (0.27 g, 0.79 mmol) and ammonium formate (0.20 g, 3.16 mmol), Pd/C 10% (catalytic amount) suspended in methanol (1.0 mL) was added. The resulting mixture was stirred at reflux for 1 hour. The reaction proceeding was monitored by TLC (eluent: hexane/ethyl acetate 7/3). Subsequently, it was cooled in an ice/water bath and water (1 mL) and HCl 2M (0.2 mL) were slowly added up to slightly acidic pH. After addition of DCM (3mL), the mixture was filtered through a celite pad. The organic phase was separated and the aqueous one was extracted with DCM (3x 3mL). The combined organic phases were washed with water (10 mL) and brine (10 mL) and dried with anhydrous Na_2SO_4. The solvent was evaporated under reduced pressure and the product was obtained by crystallization from DCM/petroleum ether as yellow crystals.

Yield= 94% (0.19 g)

^{1}H NMR (400 MHz, $CDCl_3$): 7.58 (d, J = 1.9 Hz, 1H, H_a); 7.24 – 7.20 (m, 2H, H_c, H_d); 7.12 (brs, 1H, H_f); 7.06 (brd, 1H, H_e); 6.91 (d, J = 8.2 Hz, 1H, H_b); 6.09 (s, 1H, OH); 3.99 (s, 3H, OCH_3); 2.40 (s, 3H, CH_3); 2.31 (s, 3H, CH_3).

^{13}C NMR (100 MHz, $CDCl_3$): δ(ppm) = 197.4 (C=O), 150.4 (Ar), 146.6 (Ar), 140.0 (Ar), 136.5 (Ar), 136.1 (Ar), 131.7 (C-H_f), 130.7 (Ar), 128.4 (Ar), 126.7 (Ar), 125.7 (C-H_e), 113.6 (C-H_b), 110.9 (C-H_a), 56.1 (OCH_3), 21.4 (CH_3), 19.8 (CH_3).

MS-ESI: m/z calc: 234.09, found: 257.10 $[M + Na]^+$.

m.p. 116-117 °C

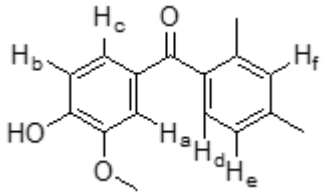

(4-hydroxy-3-methoxy-5-nitrophenyl)-1-(3,5-dimethylphenyl)methanone (16)

A mixture of glacial acetic acid (0.195 mL) and 65% nitric acid (0.140 mL) was slowly added to a suspension of **24a** (0.25 g, 0.97 mmol) in glacial acetic acid (1.95 mL). The reaction was stirred at room temperature. The reaction proceeding was monitored by TLC (eluent: hexane/ethyl acetate 3/2). After 30 minutes, an ice/water mixture was added. The precipitate was filtered and crystallized by EtOH 96% to obtain yellow needle-shape crystal (0.087 g, 30%).

^{1}H NMR (DMSO-d_6, 400 MHz): δ 7.75 (d, *J* = 2.0 Hz, 1H, H_a); 7.57 (d, *J* = 2.0 Hz, 1H, H_b); 7.35 (brs, 2H, H_c); 7.32 (brs, 1H, H_d); 3.95 (s, 3H, OCH_3); 2.36 (s, 6H, CH_3).

^{13}C NMR (DMSO-d_6, 100MHz): δ (ppm)= 193.8 (C=O), 150.1 (Ar), 147.3 (Ar), 138.4 (Ar), 137.4 (Ar), 136.7 (Ar), 134.4 (Ar), 127.5 (Ar), 127.1 (Ar), 120.1 (Ar), 115.5 (Ar), 57.2 (OCH_3), 21.2 (CH_3).

ESI-MS: m/z calc: 301.05, found: 324.08 $[M+Na]^+$) 346.05 ($[M-H+2Na]^+$).

HPLC (λ_{270}) purity 98.07%, t_R 18.084.

m.p. 144-145 °C

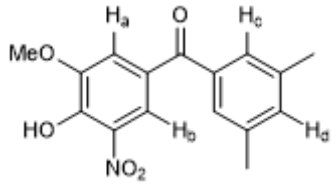

(4-hydroxy-3-methoxy-5-nitrophenyl)-1-(2,4-dimethylphenyl)methanone (17)

To a solution of 5-nitrovanillic acid (0.20 g, 0.93 mmol) in DCM (3 mL) prepared in a flame-dried two-necked round bottom flask, oxalyl chloride (0.16 mL, 1.86 mmol) was added followed by a few drops of DMF. The reaction proceeding was monitored by TLC (eluent: hexane/ethyl acetate 1/1). After 1 hours the solvent was evaporated under reduced pressure and all traces of oxalyl chloride

were removed under vacuum. The residue was dissolved in dry DCM (4 mL) and m-xylene (4 mL). The reaction mixture was cooled in an ice/water bath and $AlCl_3$ (0.16 g, 1.20 mmol) was added. The resulting suspension was kept stirred for 16 hours at rt. The reaction proceeding was monitored by TLC (eluent: hexane/ethyl acetate 1/1). The reaction was quenched by evaporation at reduced pressure of the volatiles. The residue was dissolved in DCM (5 mL), washed with HCl 1M (3x5 mL) and water (2x5 mL) and basified with 30% ammonia solution (pH 9). The precipitate was filtered and suspended in HCl 1 M (10 mL). DCM (10 mL) was added to dissolve the solid and the organic phase was separated, dried over anhydrous Na_2SO_4 and evaporated under reduced pressure to obtain the product as yellow powder.

Yield=57% (0.20 g)

^{1}H NMR (CD_3OD) δ 7.81 (d, *J* = 1.9 Hz, 1H, H_a), 7.72 (d, *J* = 1.9 Hz, 1H, H_b), 7.25 (d, *J* = 7.8 Hz, 1H, H_c), 7.21 (br s, 1H, H_e), 7.15 (d, *J* = 7.3, 1H, H_d), 4.00 (s, 3H, OCH_3), 2.42 (s, 3H, CH_3), 2.31 (s, 3H, CH_3).

^{13}C NMR (CD_3OD) δ 196.0 (C=O), 150.2 (Ar), 141.1 (Ar), 136.8 (Ar), 135.2 (Ar), 134.7 (Ar), 131.6 (Ar), 128.4 (Ar), 128.1 (Ar), 125.7 (Ar), 120.1 (Ar), 114.5 (Ar), 57.0(OCH_3), 21.8 (CH_3), 19.1 (CH_3).

ESI-MS: m/z calc: 301.09, found: 324.08 ($[M+Na]^+$) 346.06 ($[M-H+2Na]^+$).

HPLC (λ_{270}) purity 95.58%, t_R 17.685

m.p. 126-127 °C

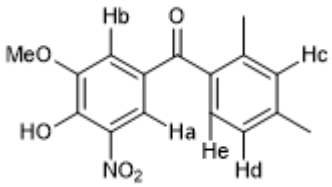

5. Bibliography

(1) Sipe, J. D.; Benson, M. D.; Buxbaum, J. N.; Ikeda, S.; Merlini, G.; Saraiva, M. J. M.; Westermark, P. Amyloid Fibril Protein Nomenclature: 2012 Recommendations from the Nomenclature Committee of the International Society of Amyloidosis. *Amyloid* **2012**, *19* (4), 167–170. https://doi.org/10.3109/13506129.2012.734345.

(2) Wells, C.; Brennan, S.; Keon, M.; Ooi, L. The Role of Amyloid Oligomers in Neurodegenerative Pathologies. *International Journal of Biological Macromolecules* **2021**, *181*, 582–604. https://doi.org/10.1016/j.ijbiomac.2021.03.113.

(3) Wolfe, K. J.; Cyr, D. M. Amyloid in Neurodegenerative Diseases: Friend or Foe? *Seminars in Cell & Developmental Biology* **2011**, *22* (5), 476–481. https://doi.org/10.1016/j.semcdb.2011.03.011.

(4) Sinha, S.; Lopes, D. H. J.; Du, Z.; Pang, E. S.; Shanmugam, A.; Lomakin, A.; Talbiersky, P.; Tennstaedt, A.; McDaniel, K.; Bakshi, R.; Kuo, P.-Y.; Ehrmann, M.; Benedek, G. B.; Loo, J. A.; Klärner, F.-G.; Schrader, T.; Wang, C.; Bitan, G. Lysine-Specific Molecular Tweezers Are Broad-Spectrum Inhibitors of Assembly and Toxicity of Amyloid Proteins. *Journal of the American Chemical Society* **2011**, *133* (42), 16958–16969. https://doi.org/10.1021/ja206279b.

(5) Wakabayashi, K.; Tanji, K.; Mori, F.; Takahashi, H. The Lewy Body in Parkinson's Disease: Molecules Implicated in the Formation and Degradation of α-Synuclein Aggregates. *Neuropathology* **2007**, *27* (5), 494–506. https://doi.org/10.1111/j.1440-1789.2007.00803.x.

(6) Mehra, S.; Sahay, S.; Maji, S. K. α-Synuclein Misfolding and Aggregation: Implications in Parkinson's Disease Pathogenesis. *Biochimica et Biophysica Acta (BBA) - Proteins and Proteomics* **2019**, *1867* (10), 890–908. https://doi.org/10.1016/j.bbapap.2019.03.001.

(7) Latif, S.; Jahangeer, M.; Maknoon Razia, D.; Ashiq, M.; Ghaffar, A.; Akram, M.; El Allam, A.; Bouyahya, A.; Garipova, L.; Ali Shariati, M.; Thiruvengadam, M.; Azam Ansari, M. Dopamine in Parkinson's Disease. *Clinica Chimica Acta* **2021**, *522*, 114–126. https://doi.org/10.1016/j.cca.2021.08.009.

(8) *Protein Folding and Misfolding: Neurodegenerative Diseases*; Ovádi, J., Orosz, F., Eds.; Focus on Structural Biology; Springer Netherlands: Dordrecht, 2009; Vol. 7. https://doi.org/10.1007/978-1-4020-9434-7.

(9) Stefanis, L. α-Synuclein in Parkinson's Disease. *Cold Spring Harb Perspect Med* **2012**, *2* (2), a009399. https://doi.org/10.1101/cshperspect.a009399.

(10) Emamzadeh, F. N. Role of Apolipoproteins and α-Synuclein in Parkinson's Disease. *J Mol Neurosci* **2017**, *62* (3–4), 344–355. https://doi.org/10.1007/s12031-017-0942-9.

(11) Villar-Piqué, A.; Lopes da Fonseca, T.; Outeiro, T. F. Structure, Function and Toxicity of Alpha-Synuclein: The Bermuda Triangle in Synucleinopathies. *Journal of Neurochemistry* **2016**, *139* (S1), 240–255. https://doi.org/10.1111/jnc.13249.

(12) Kim, T. D.; Paik, S. R.; Yang, C.-H. Structural and Functional Implications of C-Terminal Regions of α-Synuclein. *Biochemistry* **2002**, *41* (46), 13782–13790. https://doi.org/10.1021/bi026284c.

(13) Nuber, S.; Rajsombath, M.; Minakaki, G.; Winkler, J.; Müller, C. P.; Ericsson, M.; Caldarone, B.; Dettmer, U.; Selkoe, D. J. Abrogating Native α-Synuclein Tetramers in Mice Causes a L-DOPA-Responsive Motor Syndrome Closely Resembling Parkinson's Disease. *Neuron* **2018**, *100* (1), 75-90.e5. https://doi.org/10.1016/j.neuron.2018.09.014.

(14) Oliveri, V. Toward the Discovery and Development of Effective Modulators of α-Synuclein Amyloid Aggregation. *European Journal of Medicinal Chemistry* **2019**, *167*, 10–36. https://doi.org/10.1016/j.ejmech.2019.01.045.

(15) Lashuel, H. A.; Overk, C. R.; Oueslati, A.; Masliah, E. The Many Faces of α-Synuclein: From Structure and Toxicity to Therapeutic Target. *Nature Review Neuroscience* **2013**, *14* (1), 38–48. https://doi.org/10.1038/nrn3406.

(16) Bartels, T.; Choi, J. G.; Selkoe, D. J. α-Synuclein Occurs Physiologically as a Helically Folded Tetramer That Resists Aggregation. *Nature* **2011**, *477* (7362), 107–110. https://doi.org/10.1038/nature10324.

(17) Polymeropoulos, M. H.; Lavedan, C.; Leroy, E.; Ide, S. E.; Dehejia, A.; Dutra, A.; Pike, B.; Root, H.; Rubenstein, J.; Boyer, R.; Stenroos, E. S.; Chandrasekharappa, S.; Athanassiadou, A.; Papapetropoulos, T.; Johnson, W. G.; Lazzarini, A. M.; Duvoisin, R. C.; Di Iorio, G.; Golbe, L. I.; Nussbaum, R. L. Mutation in the α-Synuclein Gene Identified in Families with Parkinson's Disease. *Science* **1997**, *276* (5321), 2045–2047. https://doi.org/10.1126/science.276.5321.2045.

(18) Teravskis, P. J.; Covelo, A.; Miller, E. C.; Singh, B.; Martell-Martínez, H. A.; Benneyworth, M. A.; Gallardo, C.; Oxnard, B. R.; Araque, A.; Lee, M. K.; Liao, D. A53T Mutant Alpha-Synuclein Induces Tau-Dependent Postsynaptic Impairment Independently of Neurodegenerative Changes. *The Journal of Neuroscience* **2018**, *38* (45), 9754–9767. https://doi.org/10.1523/JNEUROSCI.0344-18.2018.

(19) Krüger, R.; Kuhn, W.; Müller, T.; Woitalla, D.; Graeber, M.; Kösel, S.; Przuntek, H.; Epplen, J. T.; Schols, L.; Riess, O. AlaSOPro Mutation in the Gene Encoding α-Synuclein in Parkinson's Disease. *Nature Genetics* **1998**, *18* (2), 106–108. https://doi.org/10.1038/ng0298-106.

(20) Zhao, K.; Li, Y.; Liu, Z.; Long, H.; Zhao, C.; Luo, F.; Sun, Y.; Tao, Y.; Su, X.; Li, D.; Li, X.; Liu, C. Parkinson's Disease Associated Mutation E46K of α-Synuclein Triggers the Formation

of a Distinct Fibril Structure. *Nature Communications* **2020**, *11* (1), 2643. https://doi.org/10.1038/s41467-020-16386-3.

(21) Rodríguez-Losada, N.; de la Rosa, J.; Larriva, M.; Wendelbo, R.; Aguirre, J. A.; Castresana, J. S.; Ballaz, S. J. Overexpression of Alpha-Synuclein Promotes Both Cell Proliferation and Cell Toxicity in Human SH-SY5Y Neuroblastoma Cells. *Journal of Advanced Research* **2020**, *23*, 37–45. https://doi.org/10.1016/j.jare.2020.01.009.

(22) Spillantini, M. G.; Schmidt, M. L.; Lee, V. M.-Y.; Trojanowski, J. Q.; Jakes, R.; Goedert, M. α-Synuclein in Lewy Bodies. *Nature* **1997**, *388* (6645), 839–840. https://doi.org/10.1038/42166.

(23) Schulz-Schaeffer, W. J. The Synaptic Pathology of α-Synuclein Aggregation in Dementia with Lewy Bodies, Parkinson's Disease and Parkinson's Disease Dementia. *Acta Neuropathology* **2010**, *120* (2), 131–143. https://doi.org/10.1007/s00401-010-0711-0.

(24) Wood, S. J.; Wypych, J.; Steavenson, S.; Louis, J.-C.; Citron, M.; Biere, A. L. α-Synuclein Fibrillogenesis Is Nucleation-Dependent: IMPLICATIONS FOR THE PATHOGENESIS OF PARKINSON′S DISEASE. *Journal of Biological Chemistry* **1999**, *274* (28), 19509–19512. https://doi.org/10.1074/jbc.274.28.19509.

(25) Emin, D.; Zhang, Y. P.; Lobanova, E.; Miller, A.; Li, X.; Xia, Z.; Dakin, H.; Sideris, D. I.; Lam, J. Y. L.; Ranasinghe, R. T.; Kouli, A.; Zhao, Y.; De, S.; Knowles, T. P. J.; Vendruscolo, M.; Ruggeri, F. S.; Aigbirhio, F. I.; Williams-Gray, C. H.; Klenerman, D. Small Soluble α-Synuclein Aggregates Are the Toxic Species in Parkinson's Disease. *Nature Communications* **2022**, *13* (1), 5512. https://doi.org/10.1038/s41467-022-33252-6.

(26) Winner, B.; Jappelli, R.; Maji, S. K.; Desplats, P. A.; Boyer, L.; Aigner, S.; Hetzer, C.; Loher, T.; Vilar, M.; Campioni, S.; Tzitzilonis, C.; Soragni, A.; Jessberger, S.; Mira, H.; Consiglio, A.; Pham, E.; Masliah, E.; Gage, F. H.; Riek, R. In Vivo Demonstration That α-Synuclein Oligomers Are Toxic. *Proceedings of the National Academy of Sciences* **2011**, *108* (10), 4194–4199. https://doi.org/10.1073/pnas.1100976108.

(27) Peña-Díaz, S.; García-Pardo, J.; Ventura, S. Development of Small Molecules Targeting α-Synuclein Aggregation: A Promising Strategy to Treat Parkinson's Disease. *Pharmaceutics* **2023**, *15* (3), 839. https://doi.org/10.3390/pharmaceutics15030839.

(28) Milowska, K.; Malachowska, M.; Gabryelak, T. PAMAM G4 Dendrimers Affect the Aggregation of α-Synuclein. *International Journal of Biological Macromolecules* **2011**, *48* (5), 742–746. https://doi.org/10.1016/j.ijbiomac.2011.02.021.

(29) Choi, M. Y.; Kim, Y. S.; Lim, D.; Kang, S. J.; Kim, Y.-H.; Lee, K.; Im, H. The Hexapeptide PGVTAV Suppresses Neurotoxicity of Human α-Synuclein Aggregates. *Biochemical and Biophysical Research Communications* **2011**, *408* (2), 334–338. https://doi.org/10.1016/j.bbrc.2011.04.034.

(30) Zheng, Y.; Qu, J.; Xue, F.; Zheng, Y.; Yang, B.; Chang, Y.; Yang, H.; Zhang, J. Novel DNA Aptamers for Parkinson's Disease Treatment Inhibit α-Synuclein Aggregation and Facilitate Its Degradation. *Molecular Therapy - Nucleic Acids* **2018**, *11*, 228–242. https://doi.org/10.1016/j.omtn.2018.02.011.

(31) Acharya, S.; Safaie, B. M.; Wongkongkathep, P.; Ivanova, M. I.; Attar, A.; Klärner, F.-G.; Schrader, T.; Loo, J. A.; Bitan, G.; Lapidus, L. J. Molecular Basis for Preventing α-Synuclein Aggregation by a Molecular Tweezer. *Journal of Biological Chemistry* **2014**, *289* (15), 10727–10737. https://doi.org/10.1074/jbc.M113.524520.

(32) Vidović, M.; Rikalovic, M. G. Alpha-Synuclein Aggregation Pathway in Parkinson's Disease: Current Status and Novel Therapeutic Approaches. *Cells* **2022**, *11* (11), 1732. https://doi.org/10.3390/cells11111732.

(33) Ahsan, N.; Mishra, S.; Jain, M. K.; Surolia, A.; Gupta, S. Curcumin Pyrazole and Its Derivative (N-(3-Nitrophenylpyrazole) Curcumin Inhibit Aggregation, Disrupt Fibrils and Modulate Toxicity of Wild Type and Mutant α-Synuclein. *Scientific Reports* **2015**, *5* (1), 9862. https://doi.org/10.1038/srep09862.

(34) Zhu, M.; Rajamani, S.; Kaylor, J.; Han, S.; Zhou, F.; Fink, A. L. The Flavonoid Baicalein Inhibits Fibrillation of α-Synuclein and Disaggregates Existing Fibrils. *Journal of Biological Chemistry* **2004**, *279* (26), 26846–26857. https://doi.org/10.1074/jbc.M403129200.

(35) Liu, Y.; Carver, J. A.; Calabrese, A. N.; Pukala, T. L. Gallic Acid Interacts with α-Synuclein to Prevent the Structural Collapse Necessary for Its Aggregation. *Biochimica et Biophysica Acta (BBA) - Proteins and Proteomics* **2014**, *1844* (9), 1481–1485. https://doi.org/10.1016/j.bbapap.2014.04.013.

(36) Maity, D. Recent Advances in the Modulation of Amyloid Protein Aggregation Using the Supramolecular Host-Guest Approaches. *Biophysical Chemistry* **2023**, *297*, 107022. https://doi.org/10.1016/j.bpc.2023.107022.

(37) Prabhudesai, S.; Sinha, S.; Attar, A.; Kotagiri, A.; Fitzmaurice, A. G.; Lakshmanan, R.; Ivanova, M. I.; Loo, J. A.; Klärner, F.-G.; Schrader, T.; Stahl, M.; Bitan, G.; Bronstein, J. M. A

Novel “Molecular Tweezer” Inhibitor of α-Synuclein Neurotoxicity in Vitro and in Vivo. *Neurotherapeutics* **2012**, *9* (2), 464–476. https://doi.org/10.1007/s13311-012-0105-1.

(38) Alex, J. M.; Rennie, M. L.; Volpi, S.; Sansone, F.; Casnati, A.; Crowley, P. B. Phosphonated Calixarene as a “Molecular Glue” for Protein Crystallization. *Crystal Growth & Design* **2018**, *18* (4), 2467–2473. https://doi.org/10.1021/acs.cgd.8b00092.

(39) McGovern, R. E.; Fernandes, H.; Khan, A. R.; Power, N. P.; Crowley, P. B. Protein Camouflage in Cytochrome c–Calixarene Complexes. *Nature Chemistry* **2012**, *4* (7), 527–533. https://doi.org/10.1038/nchem.1342.

(40) Dziemidowicz, J.; Witt, D.; Rachoń, J. Complexation of Amino Acids Derivatives in Water by Calix[4]Arene Phosphonic Acids. *Journal of Inclusion Phenomena and Macrocyclic Chemistry* **2008**, *61* (3), 381–391. https://doi.org/10.1007/s10847-008-9434-4.

(41) Douteau-Guével, N.; Perret, F.; Coleman, A. W.; Morel, J.-P.; Morel-Desrosiers, N. 33. *Jorunal of Chemical Society, Perkin Transcrition 2* **2002**, No. 3, 524–532. https://doi.org/10.1039/b109553f.

(42) Douteau-Guével, N.; Coleman, A. W.; Morel, J.-P.; Morel-Desrosiers, N. Complexation of the Basic Amino Acids Lysine and Arginine by Three Sulfonatocalix[n]Arenes (n = 4, 6 and 8) in Water: Microcalorimetric Determination of the Gibbs Energies, Enthalpies and Entropies of Complexation. *Jorunal of Chemical Society, Perkin Transcrition 2* **1999**, No. 3, 629–634. https://doi.org/10.1039/A806855K.

(43) Sansone, F.; Barboso, S.; Casnati, A.; Sciotto, D.; Ungaro, R. A New Chiral Rigid Cone Water Soluble Peptidocalix[4]Arene and Its Inclusion Complexes with α-Amino Acids and Aromatic Ammonium Cations. *Tetrahedron Letters* **1999**, *40* (25), 4741–4744. https://doi.org/10.1016/S0040-4039(99)00838-2.

(44) Perret, F.; Coleman, A. W. Biochemistry of Anionic Calix[n]Arenes. *Chemical Communications* **2011**, *47* (26), 7303–7319. https://doi.org/10.1039/C1CC11541C.

(45) McGovern, R. E.; Snarr, B. D.; Lyons, J. A.; McFarlane, J.; Whiting, A. L.; Paci, I.; Hof, F.; Crowley, P. B. Structural Study of a Small Molecule Receptor Bound to Dimethyllysine in Lysozyme. *Chem. Sci.* **2014**, *6* (1), 442–449. https://doi.org/10.1039/C4SC02383H.

(46) Hamilton, J. A.; Benson, M. D. Transthyretin: A Review from a Structural Perspective. *CMLS, Cellular and Molecular Life Science* **2001**, *58* (10), 1491–1521. https://doi.org/10.1007/PL00000791.

(47) Foss, T. R.; Wiseman, R. L.; Kelly, J. W. The Pathway by Which the Tetrameric Protein Transthyretin Dissociates. *Biochemistry* **2005**, *44* (47), 15525–15533. https://doi.org/10.1021/bi051608t.

(48) Hörnberg, A.; Eneqvist, T.; Olofsson, A.; Lundgren, E.; Sauer-Eriksson, A. E. A Comparative Analysis of 23 Structures of the Amyloidogenic Protein transthyretin11Edited by F. Cohen. *Journal of Molecular Biology* **2000**, *302* (3), 649–669. https://doi.org/10.1006/jmbi.2000.4078.

(49) Zanotti, G.; Berni, R. Plasma Retinol-Binding Protein: Structure and Interactions with Retinol, Retinoids, and Transthyretin. In *Vitamins & Hormones*; Academic Press, 2004; Vol. 69, pp 271–295. https://doi.org/10.1016/S0083-6729(04)69010-8.

(50) Wojtczak, A.; Cody, V.; Luft, J. R.; Pangborn, W. Structures of Human Transthyretin Complexed with Thyroxine at 2.0 Å Resolution and 3',5'-Dinitro- *N* -Acetyl- L -Thyronine at 2.2 Å Resolution. *Acta Crystallographica Section D* **1996**, *52* (4), 758–765. https://doi.org/10.1107/S0907444996003046.

(51) Galant, N. J.; Westermark, P.; Higaki, J. N.; Chakrabartty, A. Transthyretin Amyloidosis: An under-Recognized Neuropathy and Cardiomyopathy. *Clinical Science* **2017**, *131* (5), 395–409. https://doi.org/10.1042/CS20160413.

(52) Ruberg, F. L.; Grogan, M.; Hanna, M.; Kelly, J. W.; Maurer, M. S. Transthyretin Amyloid Cardiomyopathy: JACC State-of-the-Art Review. *Journal of the American College of Cardiology* **2019**, *73* (22), 2872–2891. https://doi.org/10.1016/j.jacc.2019.04.003.

(53) Gertz, M. A.; Mauermann, M. L.; Grogan, M.; Coelho, T. Advances in the Treatment of Hereditary Transthyretin Amyloidosis: A Review. *Brain and Behavior* **2019**, *9* (9), e01371. https://doi.org/10.1002/brb3.1371.

(54) Kristen, A. V.; Ajroud-Driss, S.; Conceição, I.; Gorevic, P.; Kyriakides, T.; Obici, L. Patisiran, an RNAi Therapeutic for the Treatment of Hereditary Transthyretin-Mediated Amyloidosis. *Neurodegenerative Disease Management* **2019**, *9* (1), 5–23. https://doi.org/10.2217/nmt-2018-0033.

(55) Holmgren, G.; Steen, L.; Suhr, O.; Ericzon, B.-G.; Groth, C.-G.; Andersen, O.; Wallin, B. G.; Seymour, A.; Richardson, S.; Hawkins, P. N.; Pepys, M. B. Clinical Improvement and Amyloid Regression after Liver Transplantation in Hereditary Transthyretin Amyloidosis. *The Lancet* **1993**, *341* (8853), 1113–1116. https://doi.org/10.1016/0140-6736(93)93127-M.

(56) Waddington Cruz, M.; Amass, L.; Keohane, D.; Schwartz, J.; Li, H.; Gundapaneni, B. Early Intervention with Tafamidis Provides Long-Term (5.5-Year) Delay of Neurologic Progression in Transthyretin Hereditary Amyloid Polyneuropathy. *Amyloid* **2016**, *23* (3), 178–183. https://doi.org/10.1080/13506129.2016.1207163.

(57) Keohane, D.; Schwartz, J.; Gundapaneni, B.; Stewart, M.; Amass, L. Tafamidis Delays Disease Progression in Patients with Early Stage Transthyretin Familial Amyloid Polyneuropathy: Additional Supportive Analyses from the Pivotal Trial. *Amyloid* **2017**, *24* (1), 30–36. https://doi.org/10.1080/13506129.2017.1301419.

(58) Lamb, Y. N.; Deeks, E. D. Tafamidis: A Review in Transthyretin Amyloidosis with Polyneuropathy. *Drugs* **2019**, *79* (8), 863–874. https://doi.org/10.1007/s40265-019-01129-6.

(59) Sultan, M. B.; Gundapaneni, B.; Schumacher, J.; Schwartz, J. H. Treatment With Tafamidis Slows Disease Progression in Early-Stage Transthyretin Cardiomyopathy. *Clinical Medicine Insights Cardiology* **2017**, *11*, 1179546817730322. https://doi.org/10.1177/1179546817730322.

(60) Berk, J. L.; Suhr, O. B.; Obici, L.; Sekijima, Y.; Zeldenrust, S. R.; Yamashita, T.; Heneghan, M. A.; Gorevic, P. D.; Litchy, W. J.; Wiesman, J. F.; Nordh, E.; Corato, M.; Lozza, A.; Cortese, A.; Robinson-Papp, J.; Colton, T.; Rybin, D. V.; Bisbee, A. B.; Ando, Y.; Ikeda, S.; Seldin, D. C.; Merlini, G.; Skinner, M.; Kelly, J. W.; Dyck, P. J.; for the Diflunisal Trial Consortium. Repurposing Diflunisal for Familial Amyloid Polyneuropathy: A Randomized Clinical Trial. *Journal of the American Medical Association* **2013**, *310* (24), 2658–2667. https://doi.org/10.1001/jama.2013.283815.

(61) Hammarström, P.; Jiang, X.; Hurshman, A. R.; Powers, E. T.; Kelly, J. W. Sequence-Dependent Denaturation Energetics: A Major Determinant in Amyloid Disease Diversity. *Proceedings of the National Academy of Sciences* **2002**, *99* (suppl_4), 16427–16432. https://doi.org/10.1073/pnas.202495199.

(62) Penchala, S. C.; Connelly, S.; Wang, Y.; Park, M. S.; Zhao, L.; Baranczak, A.; Rappley, I.; Vogel, H.; Liedtke, M.; Witteles, R. M.; Powers, E. T.; Reixach, N.; Chan, W. K.; Wilson, I. A.; Kelly, J. W.; Graef, I. A.; Alhamadsheh, M. M. AG10 Inhibits Amyloidogenesis and Cellular Toxicity of the Familial Amyloid Cardiomyopathy-Associated V122I Transthyretin. *Proceedings of the National Academy of Sciences* **2013**, *110* (24), 9992–9997. https://doi.org/10.1073/pnas.1300761110.

(63) Sekijima, Y.; Dendle, M. T.; Wiseman, R. L.; White, J. T.; D'haeze, W.; Kelly, J. W. R104H May Suppress Transthyretin Amyloidogenesis by Thermodynamic Stabilization, but Not by the Kinetic Mechanism Characterizing T119 Interallelic Trans-Suppression. *Amyloid* **2006**, *13* (2), 57–66. https://doi.org/10.1080/13506120600722449.

(64) Sant'Anna, R.; Gallego, P.; Robinson, L. Z.; Pereira-Henriques, A.; Ferreira, N.; Pinheiro, F.; Esperante, S.; Pallares, I.; Huertas, O.; Rosário Almeida, M.; Reixach, N.; Insa, R.; Velazquez-Campoy, A.; Reverter, D.; Reig, N.; Ventura, S. Repositioning Tolcapone as a Potent Inhibitor of Transthyretin Amyloidogenesis and Associated Cellular Toxicity. *Nature Communications* **2016**, *7* (1), 10787. https://doi.org/10.1038/ncomms10787.

(65) Olanow, C. W.; and the Tasmar Advisory Panel. Tolcapone and Hepatotoxic Effects. *Archives of Neurology* **2000**, *57* (2), 263–267. https://doi.org/10.1001/archneur.57.2.263.

(66) Spahr, L.; Rubbia-Brandt, L.; Burkhard, P. R.; Assal, F.; Hadengue, A. CASE REPORT: Tolcapone-Related Fulminant Hepatitis. *Digestive Disease and Sciences* **2000**, *45* (9), 1881–1884. https://doi.org/10.1023/A:1005549304404.

(67) Russ, H.; Müller, T.; Woitalla, D.; Rahbar, A.; Hahn, J.; Kuhn, W. Detection of Tolcapone in the Cerebrospinal Fluid of Parkinsonian Subjects. *Naunyn-Schmiedeberg's Archives of Pharmacology* **1999**, *360* (6), 719–720. https://doi.org/10.1007/s002109900168.

(68) Cendron, L.; Trovato, A.; Seno, F.; Folli, C.; Alfieri, B.; Zanotti, G.; Berni, R. Amyloidogenic Potential of Transthyretin Variants: INSIGHTS FROM STRUCTURAL AND COMPUTATIONAL ANALYSES. *Journal of Biological Chemistry* **2009**, *284* (38), 25832–25841. https://doi.org/10.1074/jbc.M109.017657.

(69) Pinheiro, F.; Varejão, N.; Esperante, S.; Santos, J.; Velázquez-Campoy, A.; Reverter, D.; Pallarès, I.; Ventura, S. Tolcapone, a Potent Aggregation Inhibitor for the Treatment of Familial Leptomeningeal Amyloidosis. *The FEBS Journal* **2021**, *288* (1), 310–324. https://doi.org/10.1111/febs.15339.

(70) Oshima, T.; Kawahara, S.; Ueda, M.; Kawakami, Y.; Tanaka, R.; Okazaki, T.; Misumi, Y.; Obayashi, K.; Yamashita, T.; Ohya, Y.; Ihse, E.; Shinriki, S.; Tasaki, M.; Jono, H.; Asonuma, K.; Inomata, Y.; Westermark, P.; Ando, Y. Changes in Pathological and Biochemical Findings of Systemic Tissue Sites in Familial Amyloid Polyneuropathy More than 10 Years after Liver Transplantation. *Journal of Neurology, Neurosurgery and Psychiatry* **2014**, *85* (7), 740–746. https://doi.org/10.1136/jnnp-2013-305973.

(71) Adams, D.; Koike, H.; Slama, M.; Coelho, T. Hereditary Transthyretin Amyloidosis: A Model of Medical Progress for a Fatal Disease. *Nature Review Neurology* **2019**, *15* (7), 387–404. https://doi.org/10.1038/s41582-019-0210-4.

(72) Loconte, V.; Cianci, M.; Menozzi, I.; Sbravati, D.; Sansone, F.; Casnati, A.; Berni, R. Interactions of Tolcapone Analogues as Stabilizers of the Amyloidogenic Protein Transthyretin. *Bioorganic Chemistry* **2020**, *103*, 104144. https://doi.org/10.1016/j.bioorg.2020.104144.

(73) Alex, J. M.; Brancatelli, G.; Volpi, S.; Bonaccorso, C.; Casnati, A.; Geremia, S.; Crowley, P. B. 31. *Org. Biomol. Chem.* **2020**, *18* (2), 211–214. https://doi.org/10.1039/C9OB02275A.

(74) Daze, K. D.; Pinter, T.; Beshara, C. S.; Ibraheem, A.; Minaker, S. A.; Ma, M. C. F.; Courtemanche, R. J. M.; Campbell, R. E.; Hof, F. Supramolecular Hosts That Recognize Methyllysines and Disrupt the Interaction between a Modified Histone Tail and Its Epigenetic Reader Protein. *Chemical Science* **2012**, *3* (9), 2695–2699. https://doi.org/10.1039/C2SC20583A.

(75) Nagasaki, T.; Sisido, K.; Arimura, T.; Shinkai, S. Novel Conformational Isomerism of Water-Soluble Calix[4]Arenes. *Tetrahedron* **1992**, *48* (5), 797–804. https://doi.org/10.1016/S0040-4020(01)88184-9.

(76) Tenreiro, S.; Franssens, V.; Winderickx, J.; Outeiro, T. F. Yeast Models of Parkinson's Disease-Associated Molecular Pathologies. *Current Opinion in Genetics & Development* **2017**, *44*, 74–83. https://doi.org/10.1016/j.gde.2017.01.013.

(77) Parihar, M. S.; Parihar, A.; Fujita, M.; Hashimoto, M.; Ghafourifar, P. Mitochondrial Association of Alpha-Synuclein Causes Oxidative Stress. *Cellular and Molecular Life Science* **2008**, *65* (7), 1272–1284. https://doi.org/10.1007/s00018-008-7589-1.

(78) Ruotolo, R.; De Giorgio, G.; Minato, I.; Bianchi, M. G.; Bussolati, O.; Marmiroli, N. Cerium Oxide Nanoparticles Rescue α-Synuclein-Induced Toxicity in a Yeast Model of Parkinson's Disease. *Nanomaterials (Basel)* **2020**, *10* (2), 235. https://doi.org/10.3390/nano10020235.

(79) Mourer, M.; Regnouf-de-Vains, J.-B.; Duval, R. E. Functionalized Calixarenes as Promising Antibacterial Drugs to Face Antimicrobial Resistance. *Molecules* **2023**, *28* (19), 6954. https://doi.org/10.3390/molecules28196954.

(80) Celeghini, E. C. C.; Alves, M. B. R.; de Arruda, R. P.; de Rezende, G. M.; Florez-Rodriguez, S. A.; de Sá Filho, M. F. Efficiency of CellROX Deep Red® and CellROX Orange® Fluorescent Probes in Identifying Reactive Oxygen Species in Sperm Samples from High and Low

Fertility Bulls. *Animal Biotechnology* **2021**, *32* (1), 77–83. https://doi.org/10.1080/10495398.2019.1654485.

(81) Cole, N. B.; Murphy, D. D.; Grider, T.; Rueter, S.; Brasaemle, D.; Nussbaum, R. L. Lipid Droplet Binding and Oligomerization Properties of the Parkinson's Disease Protein α-Synuclein. *Journal of Biological Chemistry* **2002**, *277* (8), 6344–6352. https://doi.org/10.1074/jbc.M108414200.

(82) Fowler, S. D.; Greenspan, P. Application of Nile Red, a Fluorescent Hydrophobic Probe, for the Detection of Neutral Lipid Deposits in Tissue Sections: Comparison with Oil Red O. *Journal of Histochemistry and Cytochemistry.* **1985**, *33* (8), 833–836. https://doi.org/10.1177/33.8.4020099.

(83) Poonsiri, T.; Dell'Accantera, D.; Loconte, V.; Casnati, A.; Cervoni, L.; Arcovito, A.; Benini, S.; Ferrari, A.; Cipolloni, M.; Cacioni, E.; De Franco, F.; Giacchè, N.; Rinaldo, S.; Folli, C.; Sansone, F.; Berni, R.; Cianci, M. 3-O-Methyltolcapone and Its Lipophilic Analogues Are Potent Inhibitors of Transthyretin Amyloidogenesis with High Permeability and Low Toxicity. *International Journal of Molecular Sciences* **2024**, *25* (1), 479. https://doi.org/10.3390/ijms25010479.

(84) Adamski-Werner, S. L.; Palaninathan, S. K.; Sacchettini, J. C.; Kelly, J. W. Diflunisal Analogues Stabilize the Native State of Transthyretin. Potent Inhibition of Amyloidogenesis. *Journal of Medicinal Chemistry* **2004**, *47* (2), 355–374. https://doi.org/10.1021/jm030347n.

(85) Pinheiro, F.; Pallarès, I.; Peccati, F.; Sánchez-Morales, A.; Varejão, N.; Bezerra, F.; Ortega-Alarcon, D.; Gonzalez, D.; Osorio, M.; Navarro, S.; Velázquez-Campoy, A.; Almeida, M. R.; Reverter, D.; Busqué, F.; Alibés, R.; Sodupe, M.; Ventura, S. Development of a Highly Potent Transthyretin Amyloidogenesis Inhibitor: Design, Synthesis, and Evaluation. *Journal of Medicinal Chemistry* **2022**, *65* (21), 14673–14691. https://doi.org/10.1021/acs.jmedchem.2c01195.

(86) Learmonth, D. A.; Vieira-Coelho, M. A.; Benes, J.; Alves, P. C.; Borges, N.; Freitas, A. P.; Soares-da-Silva, P. Synthesis of 1-(3,4-Dihydroxy-5-Nitrophenyl)-2-Phenyl-Ethanone and Derivatives as Potent and Long-Acting Peripheral Inhibitors of Catechol- *O* -Methyltransferase. *Journal of Medicinal Chemistry* **2002**, *45* (3), 685–695. https://doi.org/10.1021/jm0109964.

(87) Kiss, L. E.; Ferreira, H. S.; Torrão, L.; Bonifácio, M. J.; Palma, P. N.; Soares-da-Silva, P.; Learmonth, D. A. Discovery of a Long-Acting, Peripherally Selective Inhibitor of Catechol-O-Methyltransferase. *Journal of Medicinal Chemistry* **2010**, *53* (8), 3396–3411. https://doi.org/10.1021/jm1001524.

(88) Casnati, A.; Ting, Y.; Berti, D.; Fabbi, M.; Pochini, A.; Ungaro, R.; Sciotto, D.; Lombardo, G. G. Synthesis of Water Soluble Molecular Receptors from Calix[4]Arenes Fixed in the Cone Conformation. *Tetrahedron* **1993**, *49* (43), 9815–9822. https://doi.org/10.1016/S0040-4020(01)80183-6.

(89) Zhong, Z.; Ikeda, A.; Ayabe, M.; Shinkai, S.; Sakamoto, S.; Yamaguchi, K. Metal-Mediated Self-Assembly of Pyridylcalixarenes: Prevention of Intramolecular Metal Chelation Is Essential in Constructing Molecular Capsules. *Journal of Organic Chemistry* **2001**, *66* (3), 1002–1008. https://doi.org/10.1021/jo0011686.

(90) Almi, M.; Arduini, A.; Casnati, A.; Pochini, A.; Ungaro, R. Chloromethylation of Calixarenes and Synthesis of New Water Soluble Macrocyclic Hosts. *Tetrahedron* **1989**, *45* (7), 2177–2182. https://doi.org/10.1016/S0040-4020(01)80077-6.

(91) Kildahl-Andersen, G.; Schnaars, C.; Prandina, A.; Radix, S.; Borgne, M. L.; Jordheim, L. P.; Gjøen, T.; Andresen, A. M. S.; Lauksund, S.; Fröhlich, C.; Samuelsen, Ø.; Rongved, P.; Åstrand, O. A. H. Synthesis and Biological Evaluation of Zinc Chelating Compounds as Metallo-β-Lactamase Inhibitors. *Medicinal Chemistry Communications* **2019**, *10* (4), 528–537. https://doi.org/10.1039/C8MD00578H.

Chapter 4: Synthesis and studies of photosensitizers containing benzenesulfonamide-based inhibitor of human Carbonic Anhydrase IX

1. Introduction

1.1 Carbonic Anhydrases

Carbonic anhydrases (CAs) are a large family of zinc metalloenzymes that catalyse the reversible hydration of carbon dioxide[1]. They play a role in bone resorption[2], transport of CO_2 and bicarbonate[3], electrolyte secretion[4], calcification[5], acid-base balance[6], and various biological processes such as respiration[7]. CAs exhibit significant diversity in subcellular localization and tissue distribution and are categorized into different types, but we can distinguish 4 main types: α, present in vertebrates, bacteria, algae, and cytoplasm of green plants; β, in bacteria, algae, and chloroplasts of monocotyledons and dicotyledons; γ, mainly in archaea and some bacteria; δ, in marine diatoms[8]. Among these, α-CAs are the most extensively studied as they represent the most abundant group in nature. Human carbonic anhydrases (hCAs) consist of 15 sub-classes or isoforms within the α-CA family. These exhibit variations in catalytic activity, tissue and subcellular distribution, expression levels, oligomeric arrangement, and response to different inhibitors. They are commonly classified based on their subcellular distribution, as cytosolic hCAs (CA I, II, III, VII, XIII), membrane hCAs (CA IV, IX, XII, XIV, XV), mitochondrial hCAs (CA VA, VB), and saliva- and milk-secreted hCAVI[9].

All isoforms of α-CAs are characterized by the presence of zinc ion in the active site coordinated by three histidines (His94, His96, and His119; Figure 1) and a molecule of water. This last molecule is essential for the hydrolyzation of carbon dioxide[10].

Thanks to the hydrogen-bond with the hydroxyl moiety of Thr199, the zinc-bound water is bridged to the carboxylate moiety of Glu106. These interactions play a crucial role in enhancing the nucleophilicity of the zinc-bound water molecule and favorably positioning the substrate (CO_2) for a nucleophilic attack (Figure 1, right). The enzyme's active form is its basic form, wherein hydroxide is bound to Zn^{2+} (a). This potent nucleophile then attacks the CO_2 molecule, held within a hydrophobic pocket nearby (b), resulting in the creation of bicarbonate coordinated to Zn^{2+} (c). Subsequently, a water molecule displaces the bicarbonate ion, releasing it into the solution, and leading to the enzyme's acid form, with water coordinated to Zn^{2+} (d), rendering it catalytically inactive (Figure 1). The basic form is regenerated thanks to other residues of the active site or by buffer in the medium[11].

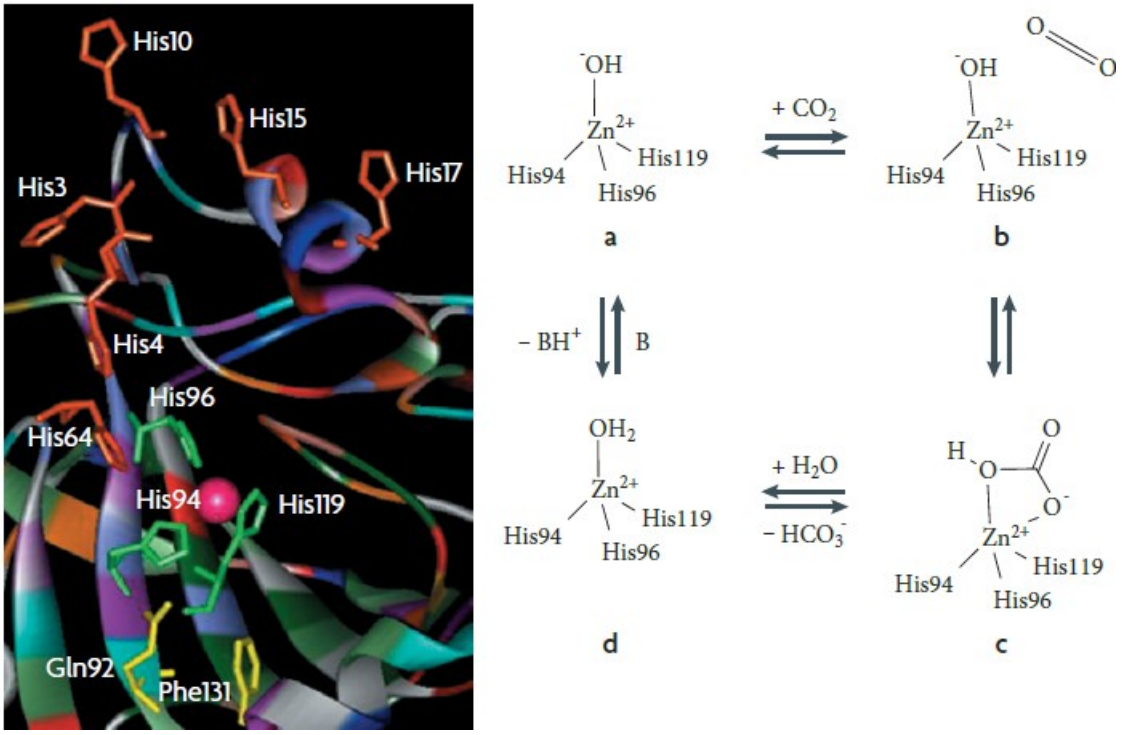

Figure 1: X-ray structure of the hCA active site (on the left) and representative scheme of the carbon dioxide hydration on the right. Image taken by reference[8].

Cytosolic hCAs are the most significant due to their excellent catalytic activity properties. The structure of human hCAs varies depending on their classification. Cytosolic and saliva- and milk-secreted hCAs have a globular structure similar to CARPs (Carbonic Anhydrase Related Proteins)[12], with the latter having additional internal disulfide bonds and oligosaccharides to enhance their stability and secretion. In contrast, plasma membrane hCA IV has a phosphatidylinositol glycan chain for linking itself to the cell surface[13], while hCAs IX, XII, and XIV are the most complex, consisting of four different domains[14]. Membrane-bound hCAs are associated with cell communication and tumor progression and are therefore studied in greater detail. hCA VIII, IX and XII are three isoforms that are frequently overexpressed in various types of tumors, particularly in solid tumors such as kidney, colorectal, skin, breast, renal, and others. A main feature that differentiates hCA IX from hCA VIII and hCA XII is the position relative to the tumor cell, being hCA IX exposed on the cell membrane toward the extracellular matrix, while hCA VIII and hCA XII are inside the cell. For this and for its overexpression caused by hypoxia, hCAIX is considered and studied as a bio-target for therapy against tumors [15].

1.2 Carbonic Anhydrases IX and Inhibitors

Embedded in the cell membrane through a transmembrane domain, CA IX, a complex protein, showcases diverse components essential for its functioning. Appearing as a compact globular domain, the CA IX catalytic domain displays an oval shape measuring approximately 47×35×42 $Å^3$. Its

structure exhibits a characteristic fold akin to other α-CAs, with a 10-stranded antiparallel β-sheet forming the core. Notably, the four molecules in the asymmetric unit of the CA IX catalytic domain crystals, denoted as A, B, C, and D, displays minor differences. Additionally, two glycans of a pentasaccharide core were observed to be N-linked to Asn-213. Similar to the configuration in other α-CA isozymes, the CA IX active site is situated within a sizable conical cavity, spanning from the surface to the protein's center, with the zinc ion positioned at the cavity's base. The active site is defined by two distinct regions consisting of hydrophobic and hydrophilic amino acids. Alongside the catalytic domain, CA IX houses a crucial cytoplasmic tail responsible for facilitating signal transduction processes. This tail comprises three phosphorylatable residues, enabling CA IX to effectively react to distinct signals and control various cellular mechanisms[16].

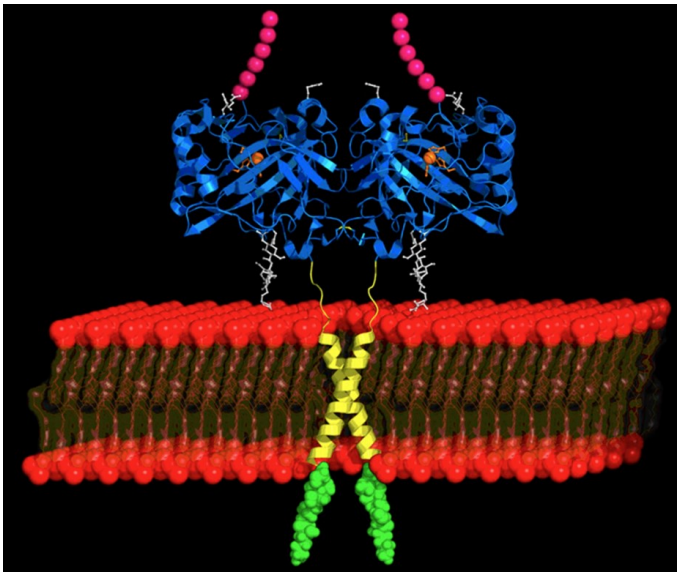

Figure 2: Adapted from reference 40, the proposed model displays the structural configuration of the CA IX dimer on the cellular membrane. The X-ray structure of the dimeric catalytic domain is denoted in cyan, featuring Arg-58, Arg-60, and Arg-130 highlighted in green, while the glycan moieties are represented in white. Schematically illustrated in the depiction are the hypothetical layouts of the glycans domains, the transmembrane helices, and the cytoplasmic segments, indicated in magenta, yellow, and green, respectively. Image taken by reference [16].

This enzyme plays a vital role in tumor growth activated by hypoxia. Tumor hypoxia, a key characteristic of many tumors, is strongly associated with tumor propagation, malignant progression, and resistance to chemotherapy and radiotherapy[10]. The hypoxia-inducible factor 1 (HIF1) cascade regulates the expression of various genes, including that of hCA IX, under hypoxic conditions[17]. Under the influence of hypoxia, the expression of hCA IX is significantly upregulated and is inversely regulated by the wild-type von Hippel-Lindau tumor suppressor protein (pVHL) (Figure 3)[18]. Under normoxia conditions, the HIFα, a subunit of HIF1, undergoes hydroxylation by prolyl-4-hydroxylase (PHD)[19] . This modification on HIFα allows the interaction with VHL leading to the degradation of HIFα. In the absence of oxygen, HIFα can enter the nucleus, where it can interact with HIFβ to

generate HIF1[20]. This factor can stimulate the transcription of some factors exploiting the interaction with the hypoxia response element (HRE). Among the factors expressed, there are the vascular endothelial growth factor (VEGF), which triggers neoangiogenesis, and the enzyme CAIX[21]. In certain cancer cells, a mutation in the VHL gene leads to the robust upregulation of CA IX (up to 150-fold) due to constant HIF activation.

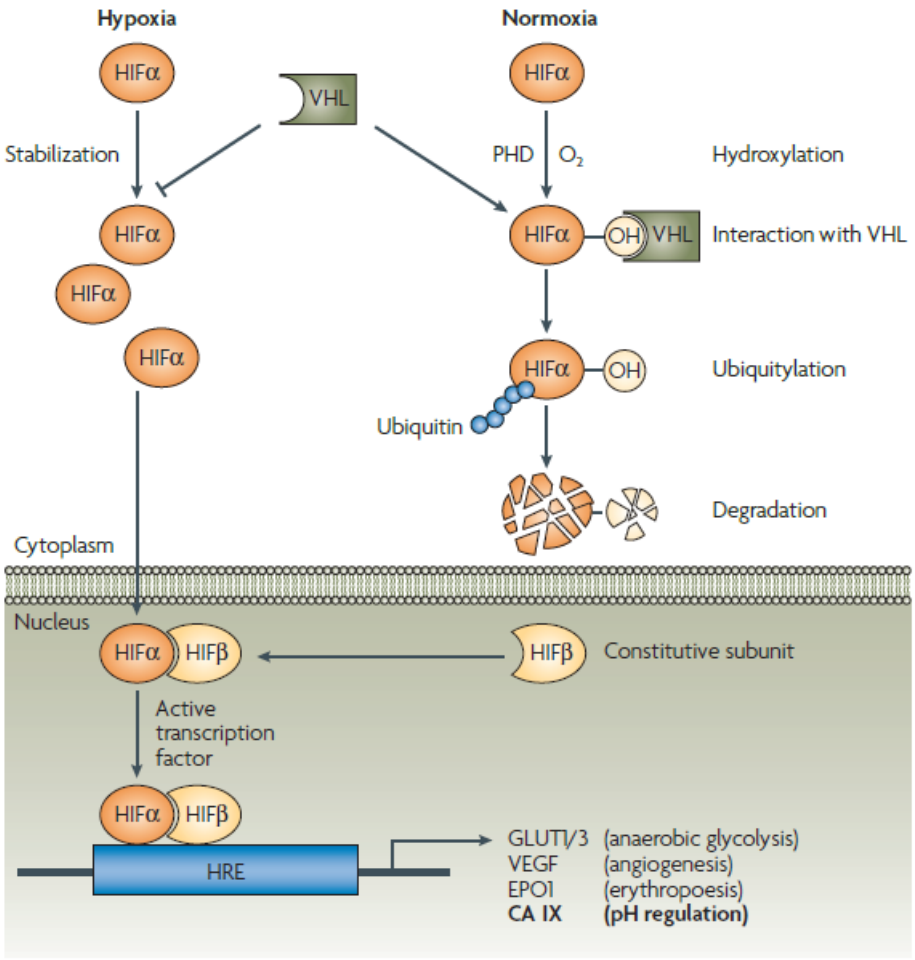

Figure 3: Hypoxia-induced gene expression mechanism. Image taken by reference[8].

By maintaining intracellular pH homeostasis through the reversible CO_2 hydration reaction, CA IX and XII help tumor cells and promote their survival and growth. Furthermore, they have been associated with increased tumor aggressiveness, invasiveness, and metastatic potential.

Considering the different phases of tumor growth, we can individuate the role of CA IX in every step:

- Proliferation: *In situ* ductal carcinoma induces CA IX expression through local hypoxia and pH regulation, facilitating adaptation to metabolic processes that produce an excess of acidic byproducts, enabling cancer cell survival and proliferation.

- In the growing tumor: CA IX additionally shields cancer cells from hypoxia and intracellular acidification. Furthermore, by exacerbating extracellular acidosis, CA IX appears to contribute to angiogenesis, extracellular matrix degradation, epithelial-mesenchymal transition, invasiveness, tumor-stroma crosstalk, and tumor-to-niche signaling.
- Metastasis formation: CA IX has the potential to mediate cancer cell adhesion to vessels and, through localized acidosis generation, facilitates transmigration to the lumen. While in circulation, CA IX purportedly protects cells from apoptosis and aids in their extravasation to the site of secondary residence.
- Metastasis adhesion: CA IX-assisted formation of focal adhesion contacts and cell spreading facilitate the metastatic lesion. The initial growth of metastasis benefits from CA IX-mediated pH regulation.
- Metastatic proliferation: metastatic expansion recapitulates the scenario in primary tumors, with a potential role of CA IX in shielding cells from hypoxia and acidosis.

Considering the several roles and the importance of CA IX in tumor growth, its overexpression in tumor cells, and its nature of transmembrane enzyme, carbonic anhydrase inhibitors (CAIs) became an important object study for cancer treatment[22], in particular for hypoxic tumors.

In the literature are reported several examples for the exploitation of the hCAIX targeting finalised to the selective interaction with tumor cells to fight cancer with different strategies[23–26]. One of these strategies is the photodynamic therapy[25,26].

1.3 Photodynamic therapy

Photodynamic therapy (PDT) is a treatment modality that uses a photosensitizer (PS), light, and principally molecular oxygen to generate reactive oxygen species (ROS) that can preferentially destroy cancer cells[27](Figure 4). When exposed to light of a specific wavelength, the photosensitizer absorbs the light energy and transfers it to oxygen molecules, resulting in the production of ROS, mainly singlet oxygen, that can damage cellular structures and induce cell death[28]. The photosensitizer is usually administered intravenously, topically, or orally, and it preferentially accumulates in tumor cells due to their higher metabolic activity and blood supply. One of the advantages of PDT is its ability to preferentially target cancer cells while mostly sparing healthy tissue, which reduces side effects and improves the patient's quality of life. PDT is currently approved by regulatory agencies for the treatment of a variety of cancers, including skin, lung, esophageal, and bladder cancers, among others.

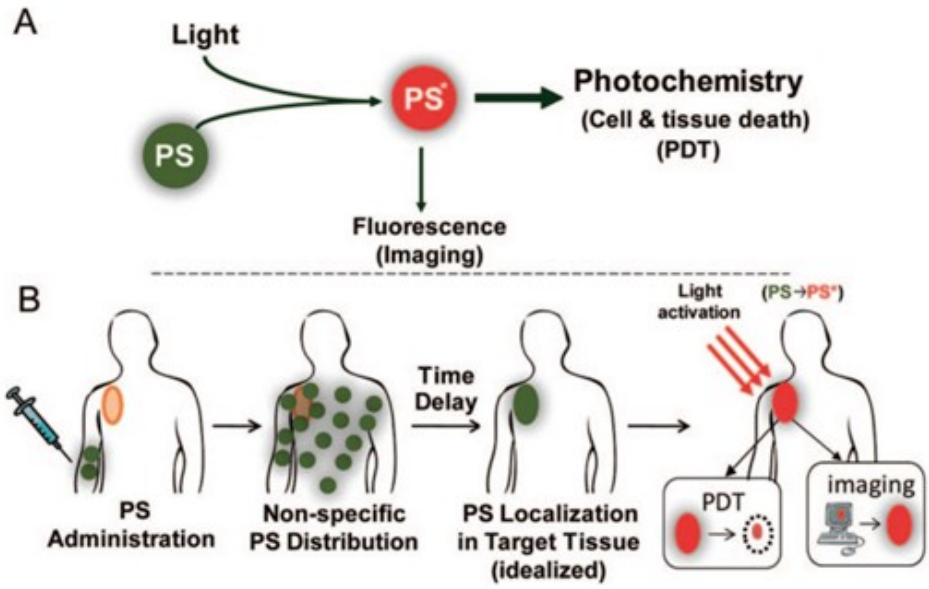

Figure 4: (A) Schematic representation of PDT where a PS, upon light activation can serve as both an imaging agent and a therapeutic agent. (B) Schematic representation of the sequence of administration, localization, and light activation of the PS for PDT or fluorescence imaging. Image taken by reference[29].

The mechanisms through which PDT elicits cellular demise can be broadly classified into two categories: type I and type II[30](Figure 5). Type I entails the transference of an electron from the excited photosensitizer (PS) to an adjacent molecule, culminating in the generation of radical species like superoxide ($O_2^{\bullet-}$) and hydroxyl radicals ($OH^{\bullet}$). These radicals engage with cellular components such as proteins, nucleic acids, and lipids, engendering impairment and eventual cellular decay. Conversely, type II involves the production of singlet oxygen ($^1O_2$) from the activated PS. Singlet oxygen interacts with cellular constituents including lipids, proteins, and DNA, inducing oxidative harm and cellular demise. Generally, type II mechanisms exhibit greater prevalence and efficiency in generating cytotoxic species compared to type I mechanisms[31]. The dominant mechanism in PDT is contingent upon several factors, including the specific PS utilized, the wavelength of the illuminating light, and the oxygen concentration within the target tissue. A comprehension of these mechanisms is imperative for the optimization of treatment protocols and the development of novel PSs and light sources to augment therapeutic outcomes. In certain cases, both type I and type II mechanisms simultaneously contribute to cellular death induced by PDT. Certain PSs can in fact generate singlet oxygen and free radicals when exposed to light, leading to a combination of type I and type II pathways. Additionally, the cellular context can influence the relative impact of type I and type II mechanisms[32]. Cells equipped with elevated levels of antioxidants may demonstrate heightened resistance to type I-mediated detriment, whereas those characterized by heightened unsaturated lipid content may be more susceptible to type II-mediated injury. It is noteworthy that the implementation of PDT results in a hypoxic state within cells due to the utilization of oxygen for the generation of reactive oxygen species (ROS) or singlet oxygen.

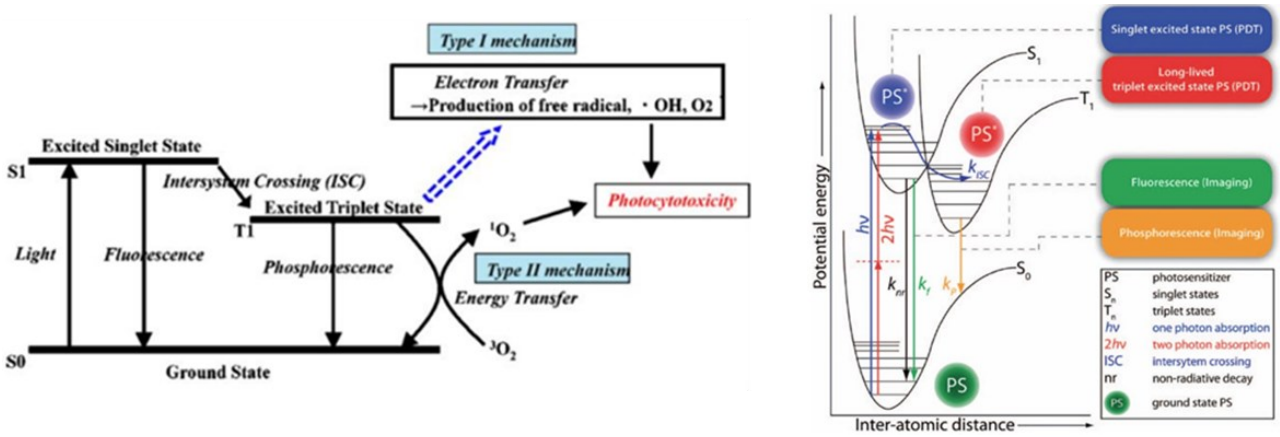

Figure 5: Perrin-Jablonski energy diagram for a photosensitizer (PS) molecule. Image taken by reference[29].

The biological transparency window is a spectral range within the electromagnetic spectrum where biological tissues are relatively transparent to light. It refers to the near-infrared (NIR) region of the spectrum, typically between 650 and 1300 nanometers, where light can penetrate deeper into biological tissues due to lower levels of absorption and scattering[33]. This window is important in photodynamic therapy (PDT) because it allows for deeper penetration, thus increasing the treatment depth[34] and widening its application scope. Various factors, including the wavelength of the light, the absorption and scattering properties of the tissue, and the concentration and distribution of the PS, can affect it[35].

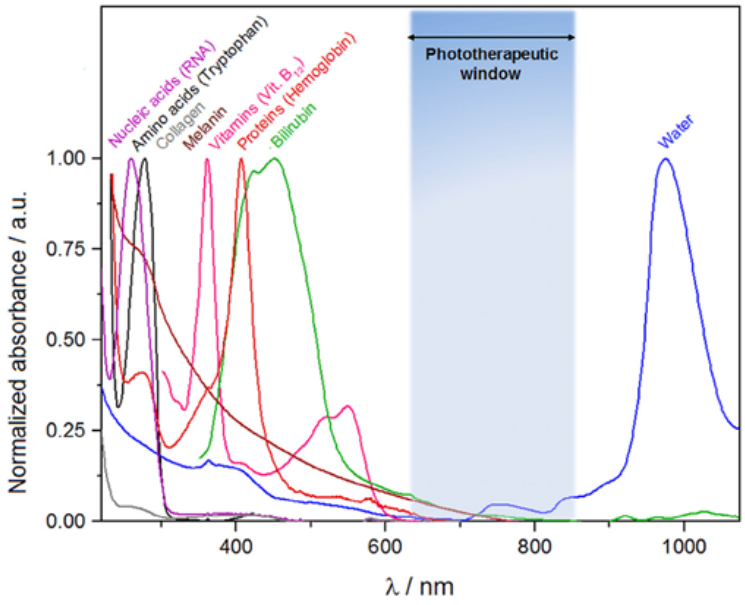

Figure 6:Phototherapeutic window: the spectral range of visible and NIR light (650–850 nm). In this range tissues are also the most transparent.

However, even within the biological transparency window, the depth of light penetration is still limited, particularly in thicker tissues or larger tumors. To address this limitation, various strategies have been developed to improve the delivery of light to deeper tissues, such as using fiber optic

probes, intratumoral injection of PS, or modifying the PS to improve tissue penetration[36]. In addition to the depth of light penetration, another critical factor in the efficacy of PDT is the distribution of the PS within the target tissue.

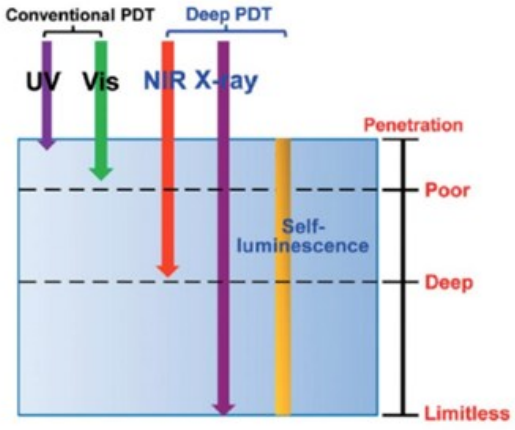

Figure 7:Comparison of tissue penetration of different excitation sources. Image taken by reference[36].

The PS must be able to accumulate preferentially in the target tissue, while avoiding uptake by normal tissues, to achieve selective cytotoxicity. Ongoing research is focused on developing new PS molecules, delivery strategies, and targeting mechanisms to improve the selectivity and efficacy of this promising therapeutic approach.

Tumor elimination through PDT can arise through both programmed (apoptotic) and non-programmed (necrotic) pathways. Typically, when high-intensity light is utilized, tumor cells undergo rapid destruction via necrosis. Necrosis is generally defined as a swift and expansive process of cell demise, characterized by cytoplasmic vacuolization and breakdown of the cell membrane. This, in turn, triggers a localized inflammatory response due to the discharge of cytoplasmic content and pro-inflammatory agents into the extracellular environment. Conversely, apoptotic death can be induced by PDT particularly with the use of low-light doses. Apoptosis is recognized as a genetically programmed and energy-dependent process of cell death. Morphologically, it is marked by chromatin condensation, fragmentation of chromosomal DNA into internucleosomal fragments, cell contraction, membrane corrugation, and the formation of apoptotic bodies without plasma membrane rupture. As no toxic substances are released, no significant immune response or effects are anticipated. The absence of a significant immune response induced by PDT is the reason why this therapy is typically administered with immune checkpoint blockade (ICB)[37]. These medications inhibit receptors and ligands that play a role in pathways that weaken T cell activation. This aspect combined with the limit of PDT in hypoxic tumor, led to the exploration of a new strategy to overcome these limitations[28,38].

Recently, Su and colleagues[26] published an article on which, exploiting PS for PDT, they are able to induce the death cell through pyroptosis (Figure 8).

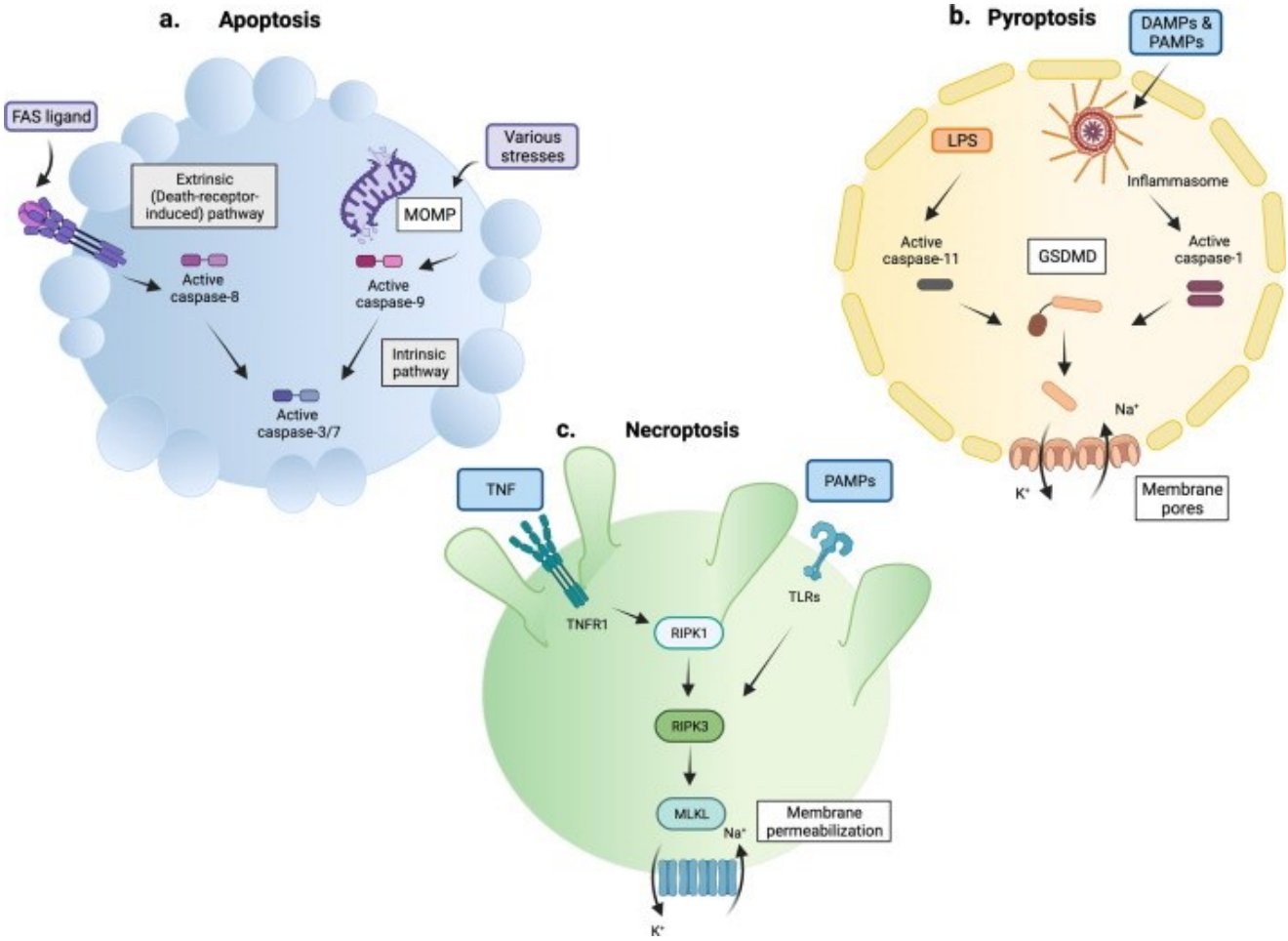

Figure 8: The difference type of cell death induced by PDT. Reprinted from Journal of Molecular Biology, 434, Ketelut-Carneiro, N.; Fitzgerald, K. A., Apoptosis, Pyroptosis, and Necroptosis—Oh My! The Many Ways a Cell Can Die, 167378, © (2022), with permission from Elsevier.[39]

Pyroptosis represents a distinctive form of programmed cell demise that is inherently inflammatory and vital for immune responses[40]. The enzymatic cleavage of gasdermin D (GSDMD) by inflammatory caspases serves as a pivotal event in facilitating pyroptosis, leading to the liberation of its N-terminal domain (GSDMD-N) that binds to membrane phospholipids and instigates the formation of pores on cell membranes[41]. Consequently, the disruption of the osmotic potential of the membrane triggers cellular swelling, membrane rupture, and the rapid discharge of inflammatory cytokines, such as IL-1b and IL-18[42]. Intriguingly, even inducing pyroptosis in less than 15% of tumor cells has proven sufficient for the eradication of an entire breast tumor graft[43]. Pyroptosis-induced PDT is possible only by exploiting the ROS in this case generated by a Re-based photosensitizer[26,44].

1.4 Photosensitizers

As described in the previous paragraph, photosensitizers are molecules able to absorb light and transfer it generating ROS. Starting from the PDT discovery, many photosensitizers were synthesized and studied to overcome the limits of this therapy and improve its efficacy and feasibility. We can distinguish two big families of PS: metal complexes PS and organic fluorophore[45]. Among the organic dyes, we select two scaffolds for PS: BODIPYs and phenothiazine derivatives.

1.4.1 BODIPYs

BODIPYs, or boron-dipyrromethene compounds, constitute a significant class of organic molecules viable for incorporation as photosensitizers within the realm of PDT[46].

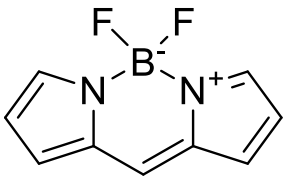

Figure 9: the core structure of BODIPYs.

BODIPYs offer several advantageous characteristics that render them particularly suitable for PDT application. Notably, they exhibit robust photostability and robust light absorption within the visible spectrum (500-600 nm) and demonstrated minimal toxicity[47]. By harnessing BODIPY derivatives, researchers can affix them to targeting molecules, thereby bolstering their preferential attraction to cancerous cells and subsequently enhancing the efficacy of PDT. Ongoing research on the utilization of BODIPYs as PS in PDT has yielded promising outcomes, especially concerning the management of diverse malignancies such as melanoma, breast cancer, and colon cancer, among others. Under specific light exposure, BODIPYs have demonstrated the capacity to generate reactive oxygen species (ROS) and singlet oxygen, both of which can elicit cellular harm, ultimately leading to cell mortality. Furthermore, the relatively brief duration of the triplet state in BODIPYs diminishes the likelihood of oxygen depletion during PDT, thereby facilitating the execution of multiple irradiation cycles. However, it is worth noting that the majority of BODIPY dyes are predominantly excited into higher-level singlet states and subsequently emit light from those states, rather than transitioning to triplets. Since the prevailing consensus is that photo-damage in PDT largely arises through triplet excited states, BODIPY dyes commonly employed in PDT underwent modifications intended to amplify intersystem crossing (ISC). Among the prevailing techniques to stimulate ISC, the introduction of heavy atoms, such as halogens, stands as the most widely utilized approach. The addition of heavy atoms serves to foster spin-orbit coupling without resulting in energy loss from excited states. Generally, heavy atoms are incorporated into positions on the BODIPY core that preserve planarity,

as any deviation from planarity would impede conjugation[48]. A distinctive advantage associated with the integration of BODIPYs as photosensitizers lies in their adaptability. BODIPY derivatives can be synthesized with a diverse array of functional groups, thus enabling alterations geared towards augmenting their solubility, stability, and targeting attributes. Moreover, BODIPYs have demonstrated efficacy in both type I and type II photochemical reactions, positioning them as highly promising candidates for integration into PDT protocols.

1.4.2 Phenothiazine derivatives

PSs constructed from phenothiazine derivatives commonly include methylene blue (MB) derivatives and Nile blue analogs (NBAs).

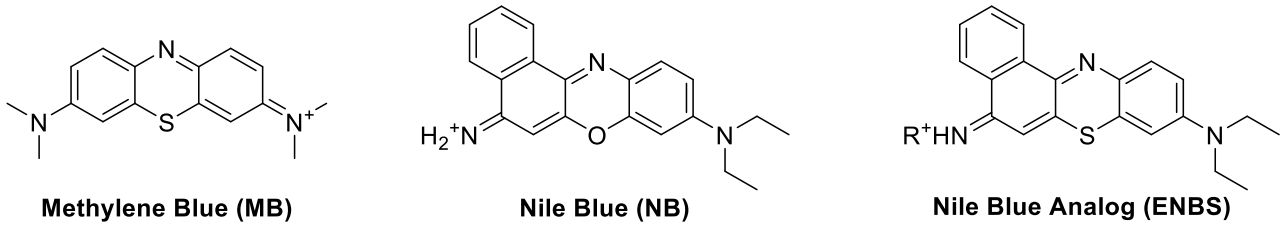

Figure 10: Phenothiazine-based structures

These derivatives are cationic dyes that dissolve readily in water and exhibit clear absorption within the therapeutic wavelength range. Initially employed as a stain for histological examinations targeting lysosomes and lipids in controlled environments, NB has demonstrated superior fluorescence and heightened stability compared to MB due to its compact aromatic structure. Although the original NB dye is not well-suited for PDT, the introduction of sulfur or selenium in place of the oxygen within its oxazine group has been found to significantly enhance its ability to produce ROSs[49]. Recognizing this potential, Peng et al.[50] modified the oxazine of NB with sulfur, resulting in the synthesis of ENBS (Figure 10) a NB analog. Their investigations revealed that this analog could effectively target the biotin receptor and function as a potent $O_2^{-\bullet}$ generator. Of significant note, their research discovered that a portion of the $O_2^{-\bullet}$ produced by ENBS could be transformed into $OH^{\bullet}$ via a cascade of reactions mediated by superoxide dismutase (SOD).

1.5 The Scope of the Study

Like other α-CAs, CA IX is effectively inhibited by diverse categories of inhibitors. These include inorganic anions, sulfonamides along with their bioisosteres (sulfamates, sulfamides, etc.), phenols, and coumarins. In the enzyme cavity, anions and sulfonamides/sulfamates/sulfamides interact with the metal ion, resulting in inhibition at millimolar–micromolar levels (for anions) or at micro–nanomolar levels (for sulfonamides and their counterparts)[51]. Zinc-coordinated water molecules are bound by phenols that function as CA IX inhibitors at generally low micromolar concentrations[52].

Coumarins were discovered to act as mechanism-based suicide inhibitors, undergoing hydrolysis by the enzyme's esterase activity to 2-hydroxy-cinnamic acids. These acids then bind to the enzyme through a non-zinc mediated mechanism, anchoring themselves at the entrance of the active site cavity. Recent studies have highlighted several isoform-selective CA IX inhibitors based on the coumarin/thiocoumarin ring, demonstrating inhibitory activity in the low nanomolar range[53]. Despite these findings, sulfonamides remain the most extensively researched class of inhibitors, with various low nanomolar CA IX inhibitors identified. These include heterocyclic/aromatic sulfonamides as well as aliphatic sulfonamides/sulfamates/sulfamides, exhibiting low nanomolar inhibitory activity against CA IX[54]. Many heterocyclic sulfonamides are in clinical use as anti-diuretics or anti-glaucoma drugs, e.g. acetazolamide (AAZ).

Starting from this knowledge, in our lab, several sulfonamide-based compounds as inhibitors for hCAs were recently synthesized linking one or more benzenesulfonamide units to a calixarene scaffold[55]. The inhibition studies against different CA isoforms, did not evidence the searched multivalent effect, but for some derivatives the stimulating perspective took place of having CA inhibitors based on a macrocyclic scaffold that could represent the platform for the design of multifunctional and multitargeting compounds for multifactorial diseases.

Moreover, in the same work, two simple, monovalent derivatives (**1** and **2** in Figure 11, actually prepared as reference compounds, rather surprisingly resulted very promising [55]. The two compounds were tested by Supuran's research group at the University of Florence using a stopped-flow technique. The inhibition constant (K_i) observed towards the tested CA isoforms were very interesting. In particular, compound **1** showed a better K_i against the investigated hCAs and, among these, against CAIX compared to the reference compound AAZ.

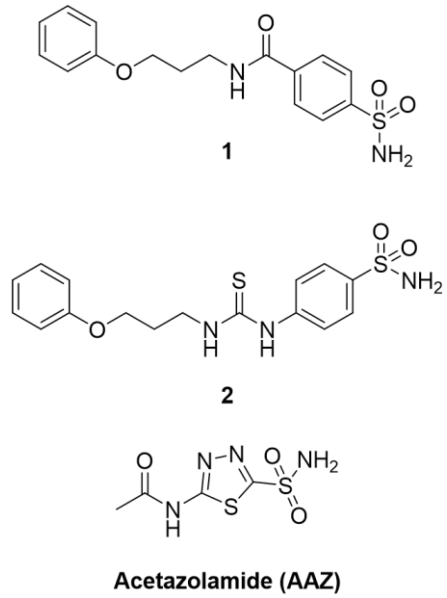

Compound	Inhibition Constant K_i [μM]		
	hCAI	hCAII	hCAIX
1	0.008±0.0007	0.004±0.0002	0.022±0.009
2	0.008±0.0008	0.008±0.0003	0.029±0.002
AAZ	0.25±0.01	0.012±0.0007	0.025±0.001

Figure 11: On the left: Most promising compounds; On the right: the inhibition constant. AAZ inhibition constants are reported as references.

This investigation centers on exploring Carbonic Anhydrase IX as a potential target for the specific treatment of tumors, owing to its overexpression on the surface of malignant cells. Consequently, our aim was to devise a ligand capable of binding to and inhibition of CA IX, at the same time conjugated to a PS unit, to yield a new generation of conjugates suitable for improved PDT. As mentioned before, PDT induces a hypoxic environment around the tumor, which triggers the tumor cells, as part of their defense mechanisms and apparatus, to further activate CA IX expression. Consequently, this phenomenon can render PDT ineffective over time, allowing the tumor to regain its strength. Utilizing a CA IX-specific ligand, which also inhibits the enzyme activity, can potentially enhance PDT effectiveness, reducing the tumor's capacity to shield itself from the treatment. To achieve binding with the CA IX active site, we thus opted to design a ligand comprising the previously reported sulfonamide-based inhibitor **2**. For the PS, we chose BODIPYs and ENBS derivatives. These options are characterized by low toxicity and a high rate of singlet oxygen generation, for BODIPY-based PS, and ROS generation, for ENBS, upon irradiation. Exploiting two different photosensitizers, it would be possible compare the type I and II mechanism for the PDT. Accordingly, we designed a molecule that, with the appropriate spacers and frameworks, featured a photosensitizer (BODIPY or ENBS) at one end and the benzensulfonamide group at the other.

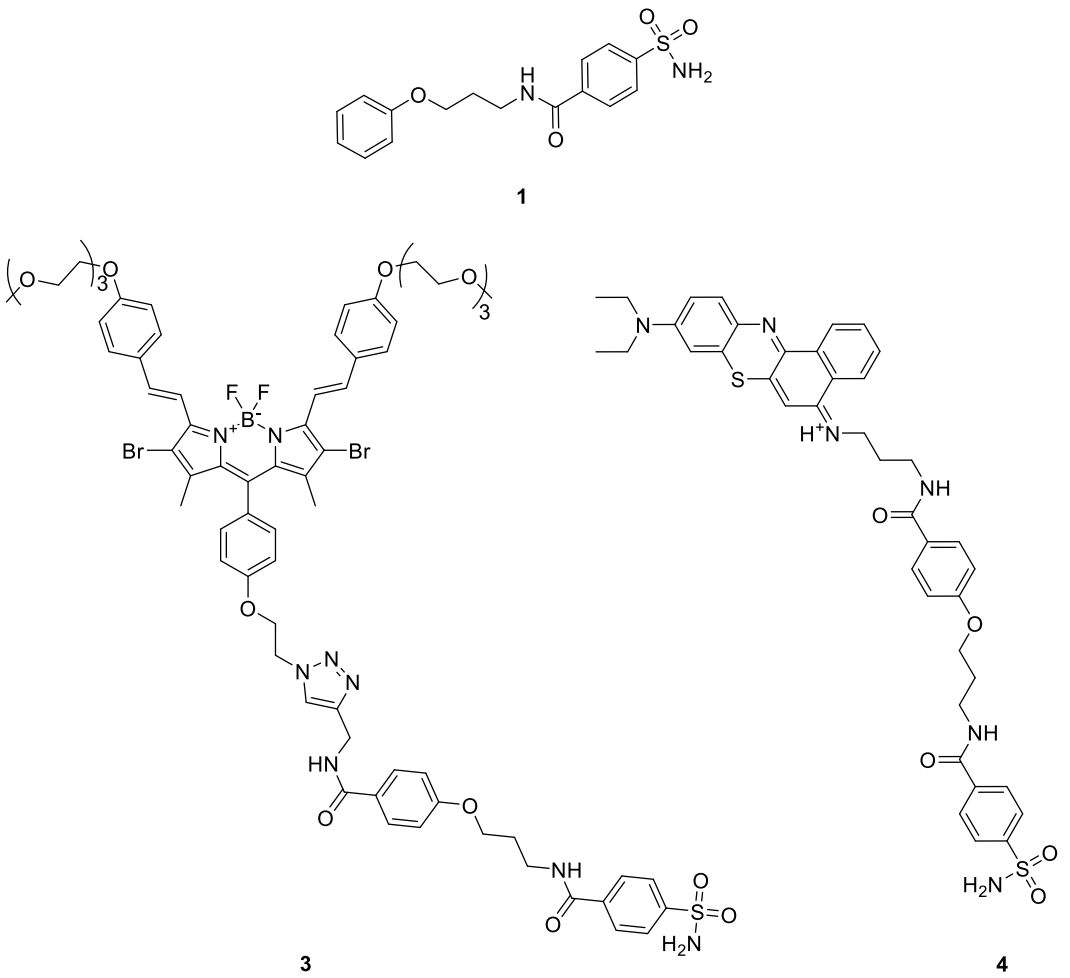

*Figure 12: Structure of inhibitor **2** and target compounds **3** and **4**.*

2. Results and discussions

In order to ensure an optimal interaction between the ligand and the active site of CA IX, we considered necessary to distance the PS group from the sulfonamide unit to prevent a detrimental steric hindrance. In the available crystal structure of the complex between CA II and inhibitor **1**, analog of **2**, the phenol unit of the ligand is inside the funnel of the active site, but in proximity of its entrance[55].

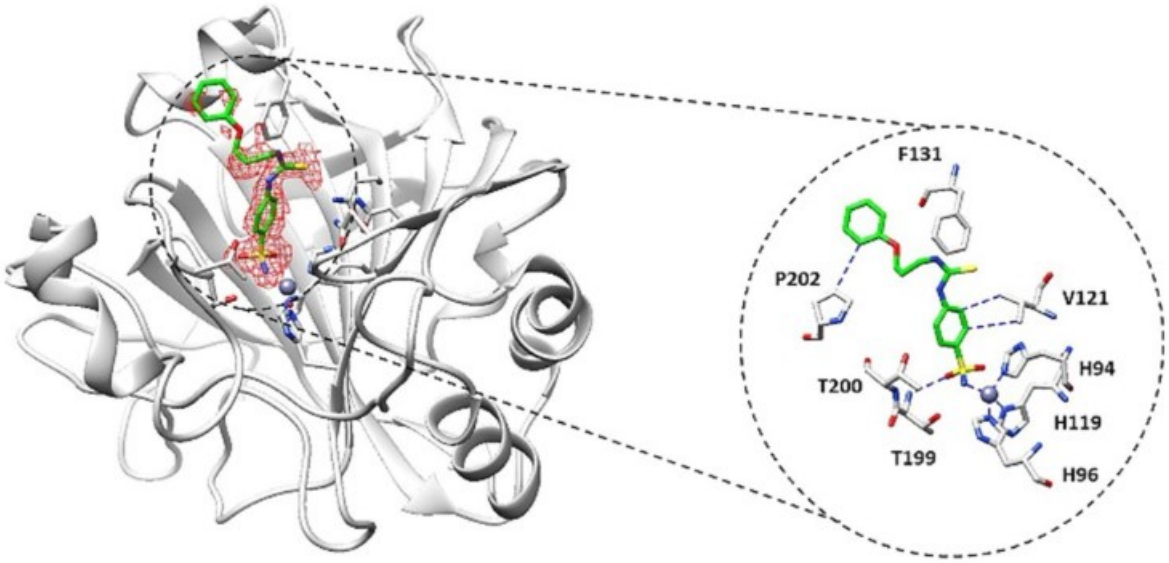

Figure 13: X-ray structure oh hCAII-1 complex. Image taken by reference.

We then considered that it was not necessary a particularly long distance to allow the PS to be in close proximity to the CA IX and, consequently, to the cell for an effective activity in PDT and, at the same time, to avoid an unfavourable hindrance that would impair the proper binding of the ligand to the active site of the enzyme.

2.1. Synthesis of the ligand for hCAIX

For the proper binding to hCA IX, several functional groups could be taken into account, such as sulfonamides, phenols, and coumarins. Considering our research group's previous findings on hCA binding, we opted to utilize a sulfonamide as the binding group for this project, specifically the ligand **2**, which was modified to facilitate subsequent conjugation with the photosensitizer. In designing the ligand, we also took into account a method to connect it to the photosensitizer under mild conditions. Subsequently, we undertook the synthesis of **7** following the procedure outlined in scheme 1.

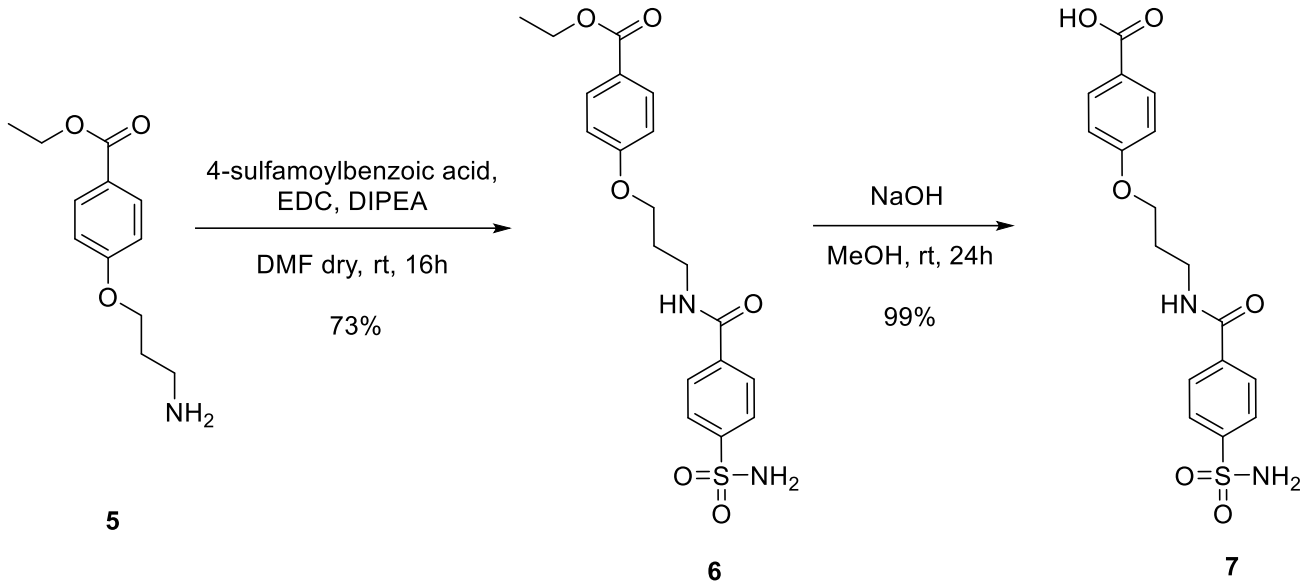

*Scheme 1: Synthetic route for the synthesis of ligand **7***

Compound **5**, prepared by reduction of azido derivatives obtained following the procedure reported in literature[56]**,** was coupled together with the commercially available 4-sulfamoylbenzoic acid to obtain compound **6**. We used EDC as a coupling reagent since its primary byproduct 1-ethyl-3-(3-dimethylaminopropyl)urea is water soluble and can thus easily be removed during the work-up of the reaction. The subsequent step in the synthesis for compound **7** was the hydrolysis of the methyl ester of derivative **6**. The correct identity of the product was confirmed by ^{1}H-NMR (Figure 14) where the presence of the signal for the sulfonamide at 7.47 ppm and the presence of carboxylic acid at 12.59 are diagnostic for compound **7**.

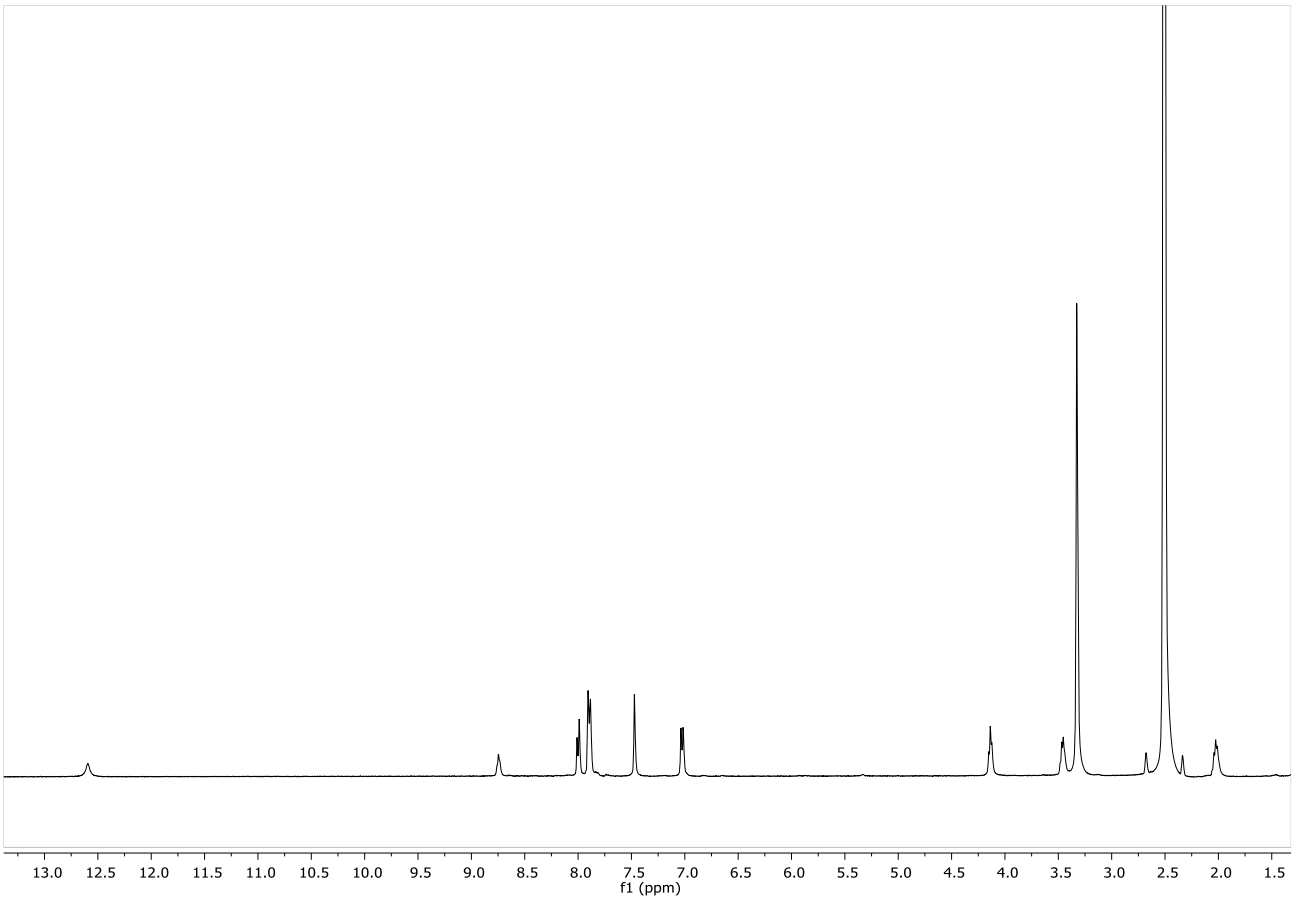

*Figure 14:^{1}H-NMR spectrum (400 MHz, 298 K) of compound **7** in DMSO-d_6*

2.2 Synthesis of the BODIPY photosensitizer

For the BODIPY-based PS we selected a derivative already published and used for analog purposes that seemed to satisfy our needs[25]. Starting from the well-known BODIPY **8**, compound **9** was obtained by substituting bromine with an azido group using sodium azide. The procedure reported in literature for this reaction provides the use of high temperature (100 °C) for 24 hours but in this condition, we observed the degradation of starting material. Compound **9** was on the contrary obtained at room temperature using a very concentrated solution of sodium azide in DMF. This transformation is crucial for the subsequent attachment of the BODIPY to the ligand through a click reaction. Then, NBS was used to attach two bromo atoms on the BODIPY core of compound **9**, resulting in the formation of compound **10**. Finally, the PS **11** was obtained exploiting the Knoevenagel reaction[57] using 4-(2-(2-(2-methoxyethoxy)ethoxy)ethoxy)benzaldehyde. Despite of the procedure reported in literature, the compound was obtained in sealed tube by replacing acetic acid with p-toluenesulfonic acid. The two short PEG chains were included to increase the solubility in aqueous environment.

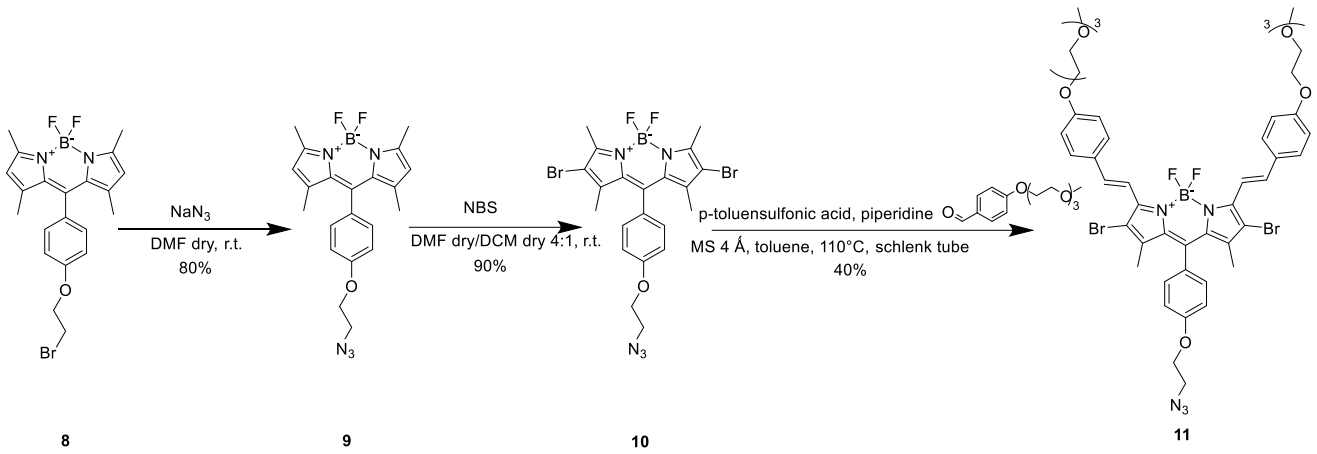

Scheme 2: Synthetic route for the synthetize of the BODIPY PS.

The ^{1}H-NMR spectra (Figure 15) demonstrated the disappearance of the peak related to the methyl groups of BODIPY core and the appearance of two peaks, at δ=8.13 and 7.64 ppm with a J value of 16.6 Hz, corresponding to the protons of the two double bonds.

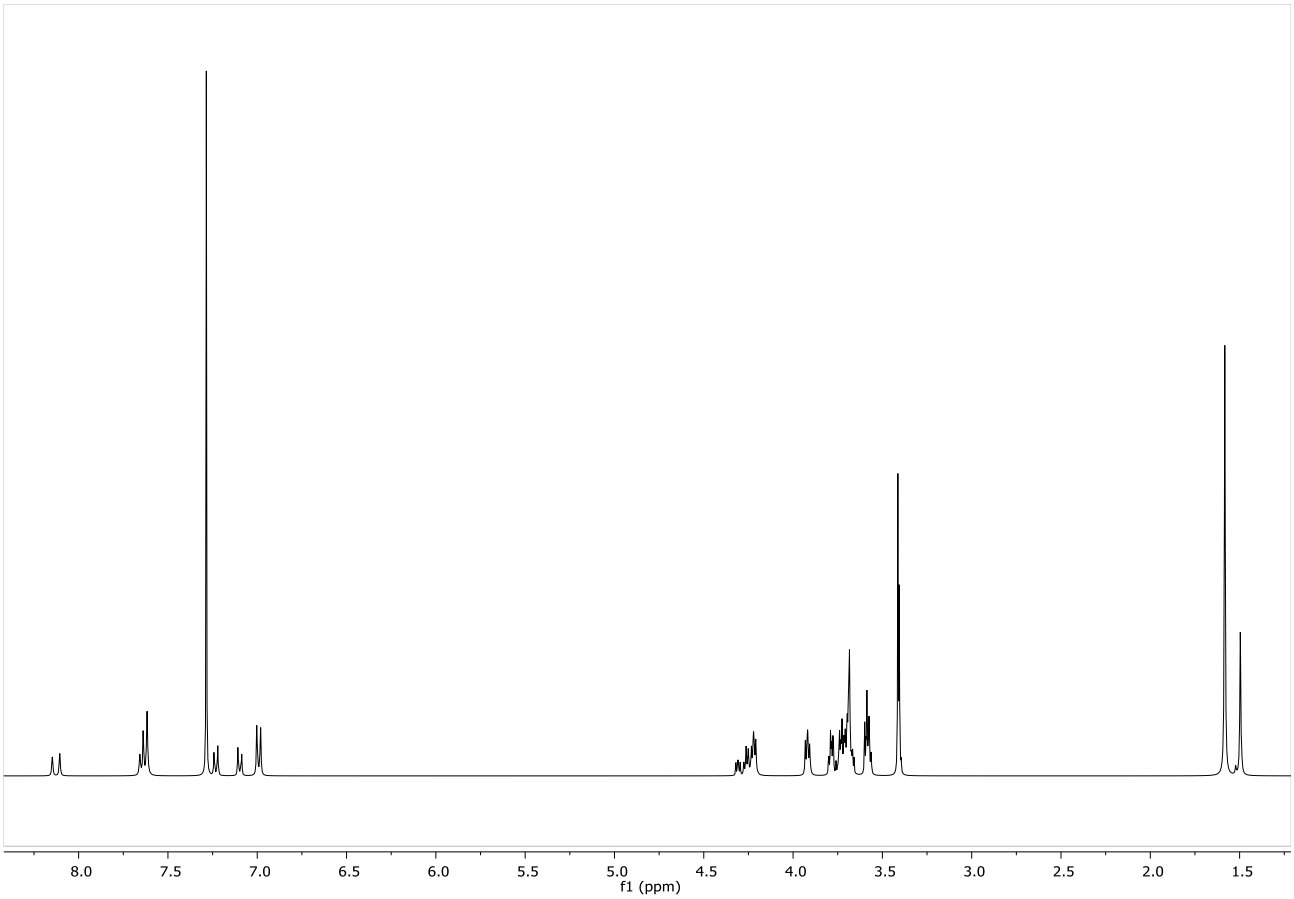

*Figure 15: ^{1}H-NMR spectrum (400 MHz, 298 K) of compound **11** in $CDCl_3$.*

2.3 Synthesis of phenothiazine photosensitizer

ENBS is a PS reported in an article by Peng and colleagues[26]. Its principal feature is the production of ROS as reported in the introduction.

Starting from the results reported in literature, we synthetized a similar photosensitizer using a different linker. For the synthesis, two essential reagents are required: the Bunte's salt, an organic thiosulfonic acid, and naphtylamine. The aromatic amine should possess an unoccupied para position on the ring, allowing for the cyclization reaction that leads to the formation of the PS.

The synthesis of Bunte's salt **14** was carried out starting from p-fluoro-nitrobenzene, following the reported procedure[58]. The fluoro group was substituted with diethylamine through an S_NAr reaction. Subsequently, the nitro group was reduced to amine by using H_2 in the presence of Pd/C as catalyst. To attach the thiosulfonic group, compound **13** was dissolved in an aqueous mixture of $Al_2(SO_4)_3$, $ZnCl_2$, $Na_2S_2O_3$, and $K_2Cr_2O_7$. This reaction yielded compound **14,** the desired Bunte's salt.

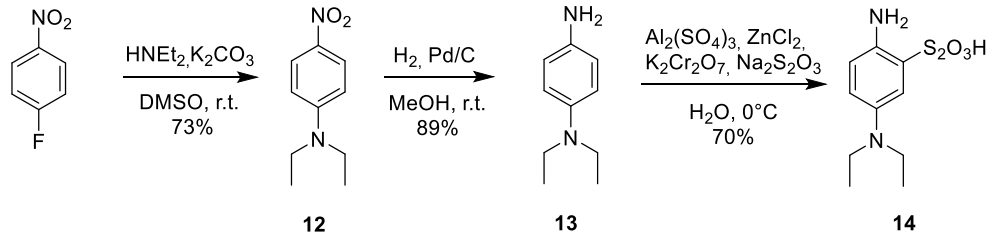

Scheme 3: Bunte's salt synthetic strategy

In order to assess whether the cyclization reaction would yield the desired PS, we initiated the process with bromonaphthalene. This compound was coupled with 1,3-diaminopropane through an Ulmann-like coupling reaction. For this reaction, we dissolved the two reagents with proline, potassium carbonate, and copper iodide. The potassium carbonate is needed to deprotonate the proline which can then chelate the Cu^+ forming the pre-catalyst. The diamine then binds the copper atom followed by an oxidative addition of the bromobenzene. Lastly a reductive elimination takes place reforming the initial pre-catalyst and giving our desired product **15**. The cyclization reaction between compound **14** and **15** was carried out using potassium dichromate.

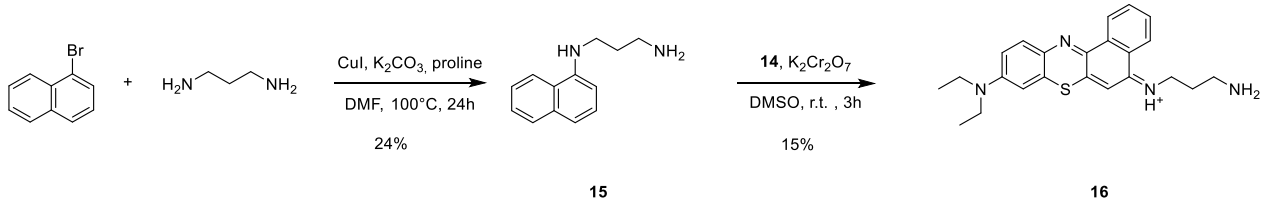

Scheme 4:Synthetic strategy for ENBS

The absence in the ^{1}H-NMR spectrum of one aromatic signal for naphthalene motif and another one in ortho to the S group confirm the presence of compound **16** to the ^{1}H-NMR.

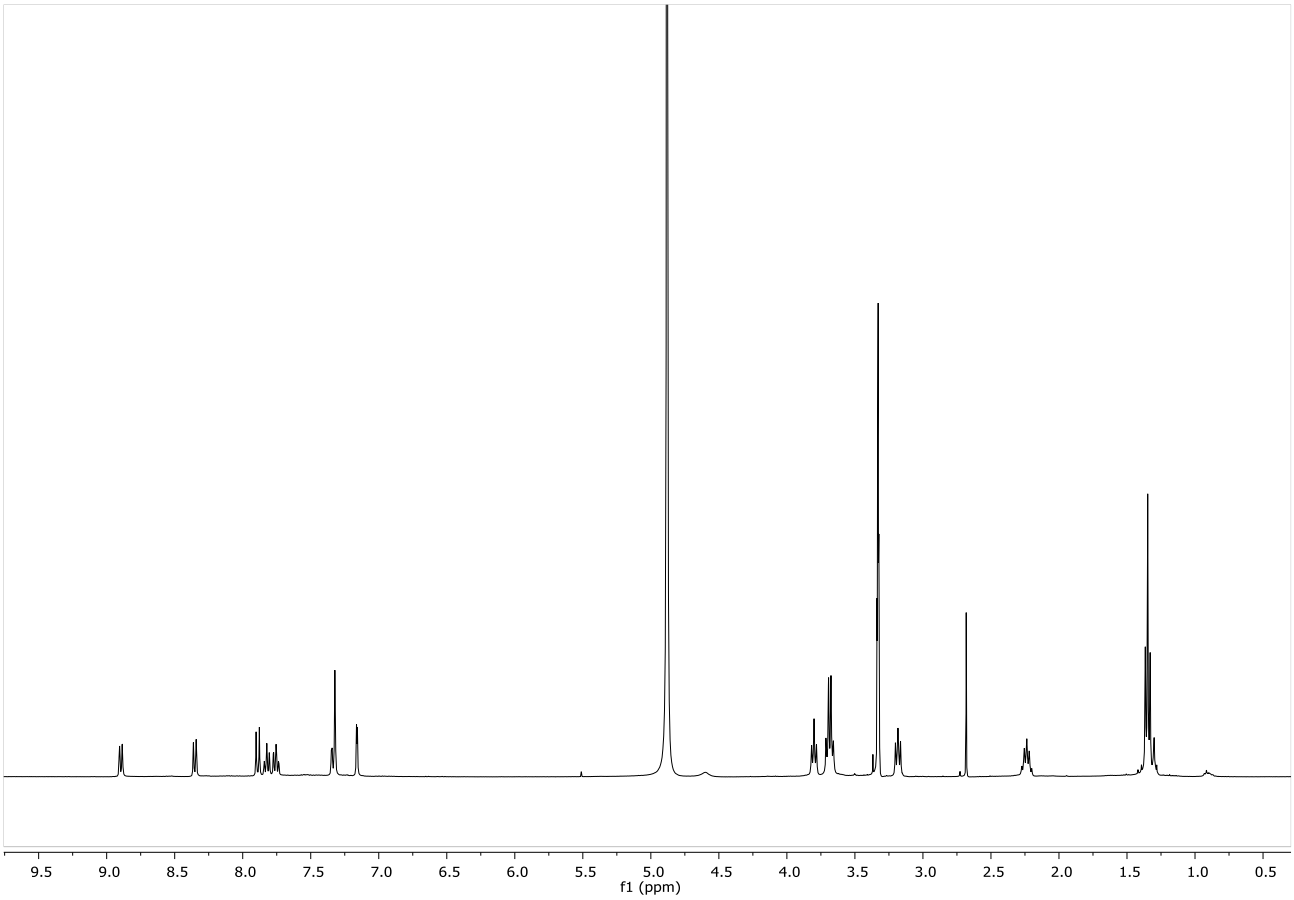

*Figure 16: ^{1}H-NMR spectrum (400 MHz, 298 K) of compound **16** in MeOD.*

2.4 Synthesis of the inhibitor-PS conjugates

Once the two photosensitizer **11** and **16** have been prepared, we could perform the synthesis of the two designed inhibitor-PS conjugates.. For the final step, compound **7** needed to be modified to introduce a terminal alkyne group in order to exploit a click reaction with azide moiety on BODIPI-based photosensitizer **11**[59]. This was accomplished by coupling compound **7** with propargylamine using HBTU as a coupling agent, resulting in the formation of compound **17**. Compound **17** was then reacted with compound **11**, sodium ascorbate and copper sulfate. The sodium ascorbate is used to reduce the copper from Cu^{2+} to Cu^{+}. Once reduced the copper can act as the catalyzer for the click reaction to selectively obtain the 1,4 product (scheme 5).

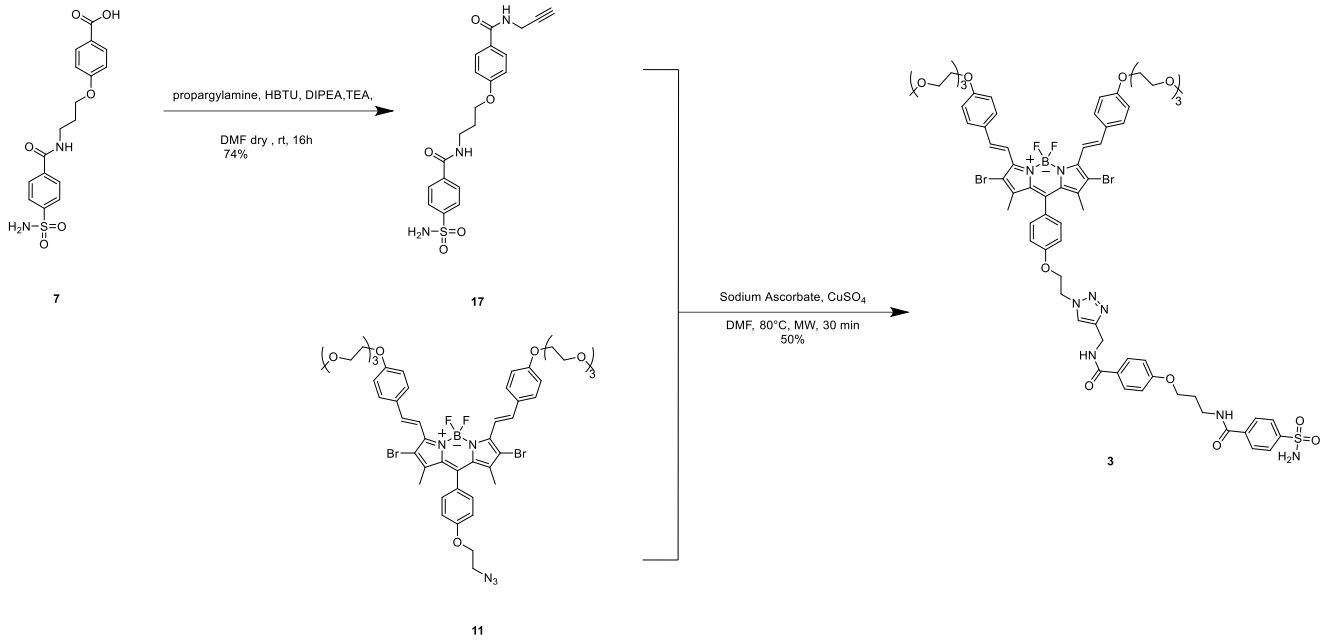

*Scheme 5: Synthesis of ligand **3***

The final compound **3** was then completely characterized by NMR spectroscopy which, by comparison with the spectra of the two precursors **17** and **11**, confirmed its identity thanks in particular to the singlet of triazole at 8.05 ppm and the absence of the alkyne signal (Figure 17).

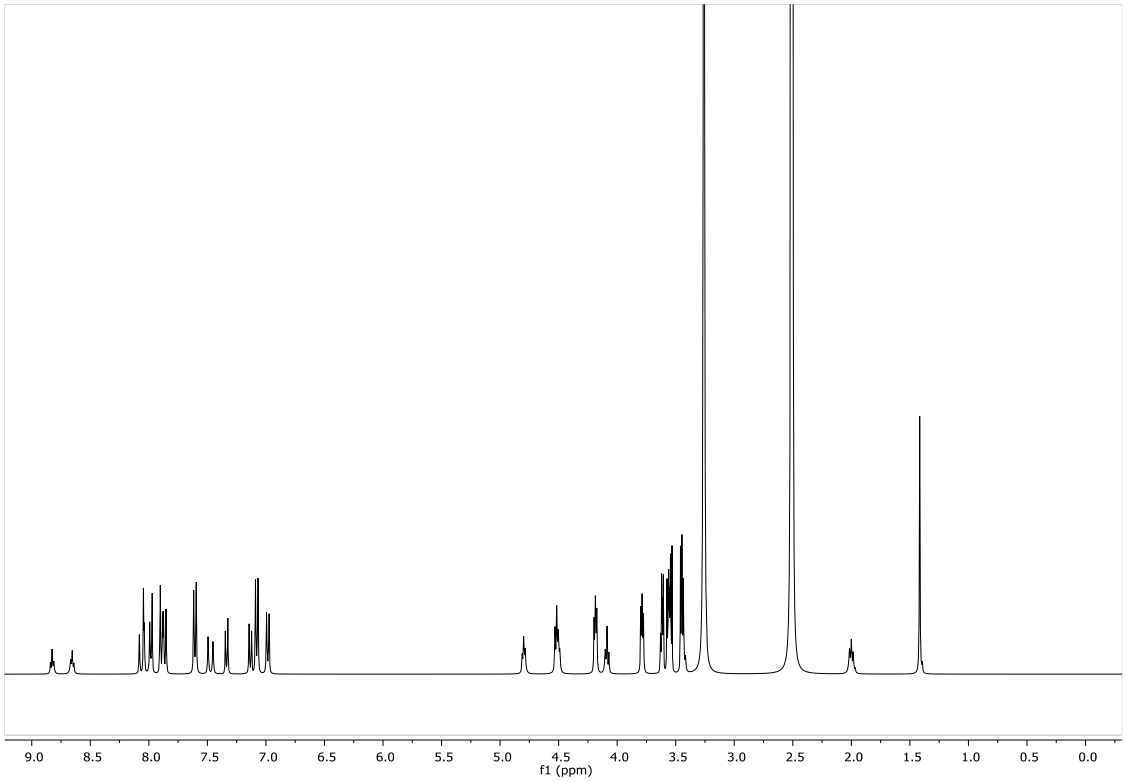

*Figure 17: ^{1}H-NMR spectrum (400 MHz, 298 K) of compound **3** in DMSO-d_6.*

The second inhibitor-PS conjugate **4** was synthesized by the amide formation between the ENBS-based PS **16** and the inhibitor **7** using EDC as a coupling agent. Compound **4** was isolated with an

unexpectedly poor yield of only 19% (scheme 6) This, at least in part, seemed to be ascribable to the difficulties met during the work-up, in particular, in the extraction process strongly affected by the deep blue color of both aqueous and organic phase, resulted, for this reason, very difficult to distinguish, and by the very poor solubility of the desired product in both if them and the possible formation of a not detected third phase, perhaps even solid.

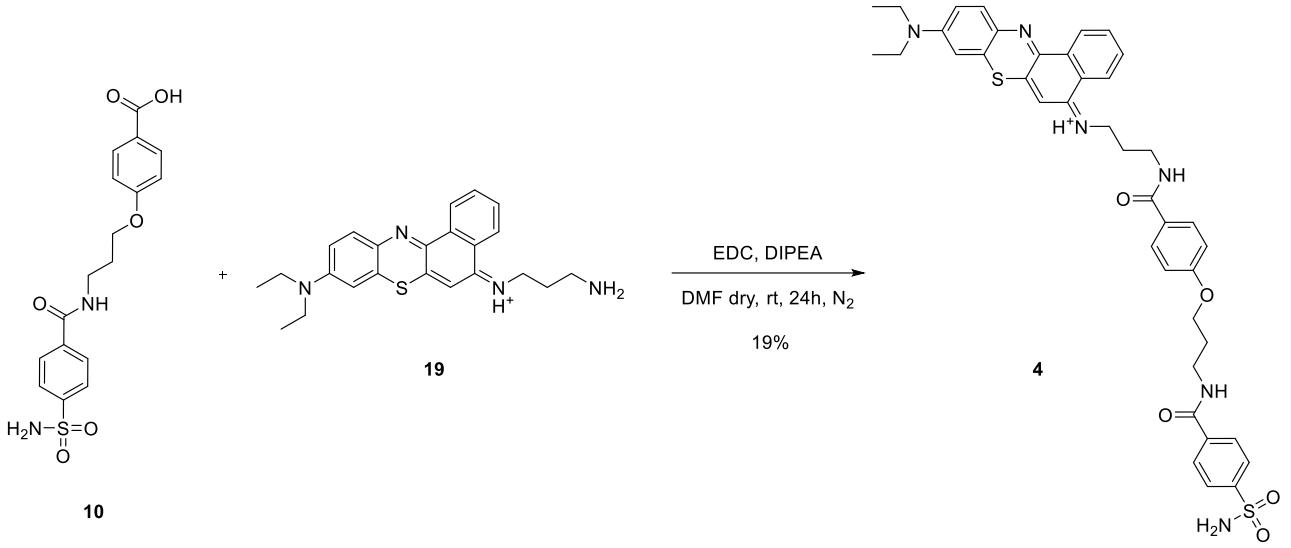

*Scheme 6: Synthesis of ligand **4***

In the ^{1}H-NMR spectrum of **4** (Figure 18), the peak at 3.63 ppm, corresponding to the CH_2 of the propyl chain directly bonded to the NH_2 in the EtNBS reagent, displayed, upon the reaction, a downfield shift with respect to the resonance at 3.18 ppm observed for **7**, indicating successful conversion of the amino group into an amide. However, the spectrum evidenced also the presence of some impurities that, also due to the very small amount of product obtained, we were not able to remove.

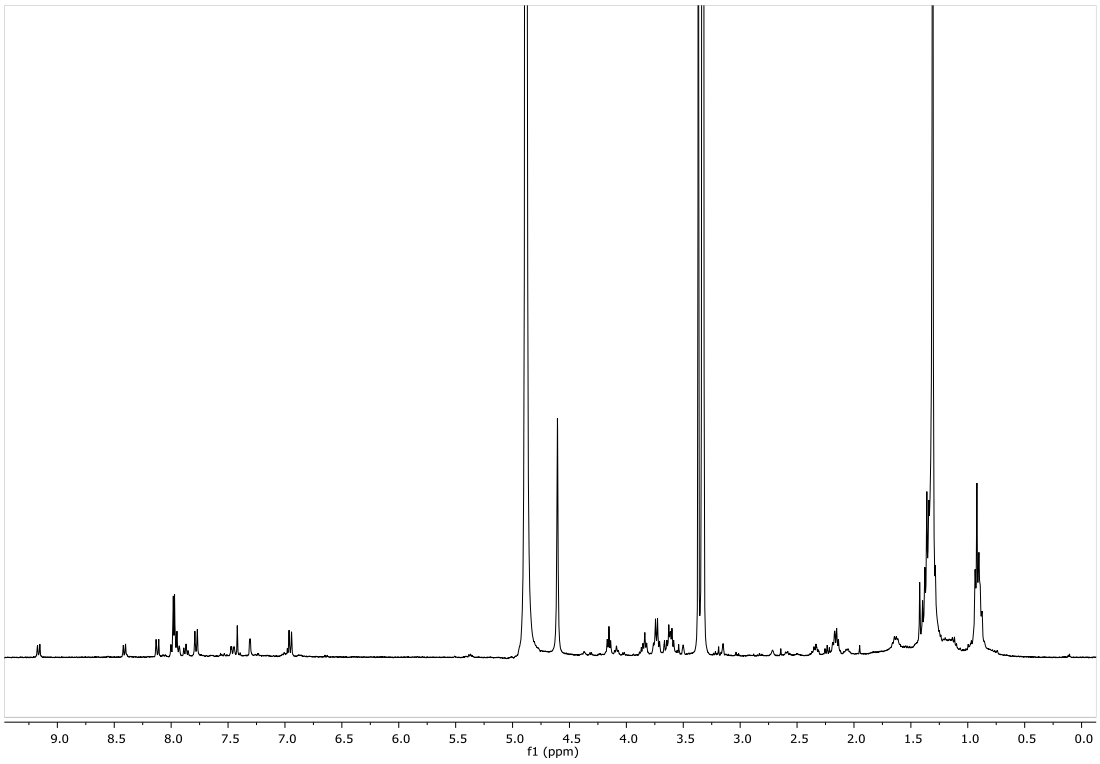

*Figure 18: ^{1}H-NMR spectrum (400 MHz, 298 K) of compound **4** in MeOD.*

2.5 Studies on ligand 3

The next step after the synthesis of the two target **3** and **4** was the study of solubility, inhibition and singlet oxygen production. We obtained enough amount of compound **3** to perform all studies while, unfortunately, we didn't have enough compound **4** to carry out the same studies.

2.5.1 Solubility study

We undertook an assessment of the solubility characteristics of compound **3** with a look, in perspective, to the possible biological tests with cells. The evaluation involved the determination of its absorbance at a concentration of 10 μM in a PBS solution with a 10% concentration of DMSO (blue line). Our observations revealed the presence of two absorption peaks at 623 and 683 nm (Figure 19). This finding suggests a potential tendency of compound **3** to form dimers, with the band at 623 nm likely corresponding to the dimeric species. Despite this, complete solubility was not achieved in this medium. To address this, we conducted further measurements in the presence of BSA (Bovine Serum Albumin), which is known for its ability to disperse partially soluble compounds in aqueous environments through interactions. Using50 μM BSA in PBS, we obtained a solution of **3** with a very low percentage of DMSO(0.5%) maintaining a concentration of 10 μM. The BSA led to an increase in absorption (grey line), which further amplified when the DMSO concentration was raised to 10% (orange line). These results support the notion that the inclusion of BSA enhances the solubility of compound **3** in the tested medium. In fact, is well-known that BSA is able to include, in its hydrophobic cavity, the organic molecules preventing their aggregation and, subsequently, enhancing

their solubility in aqueous media[60]. Notably, the spectral profile remained unchanged, suggesting that despite the presence of BSA, compound **3** may still be prone to dimerization. Alternatively, the band at 623 nm could correspond to a vibronic band.

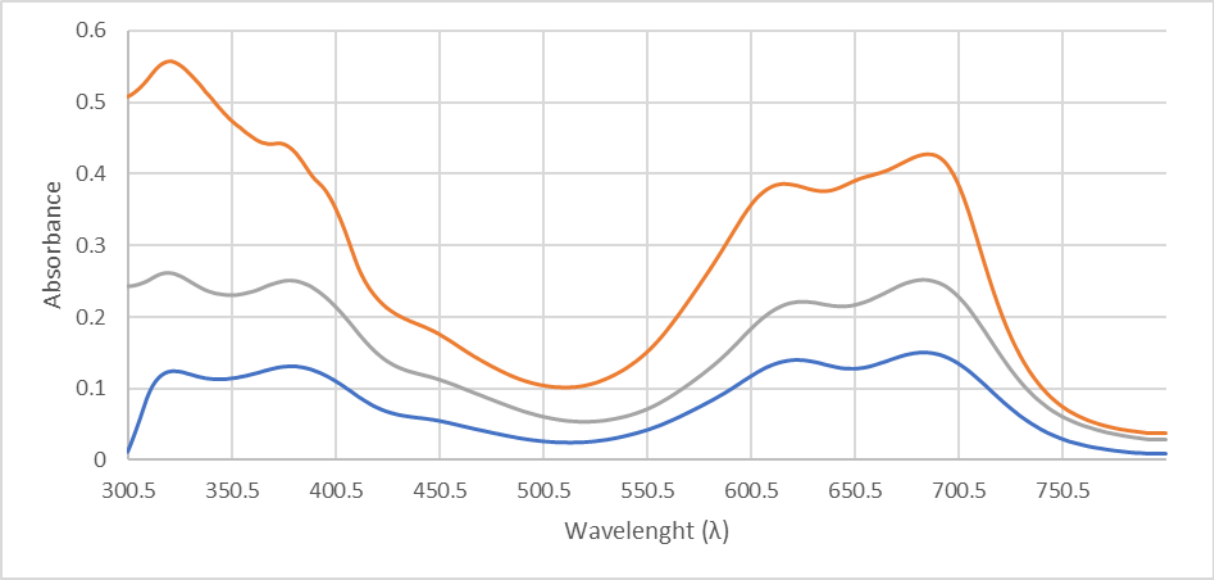

*Figure 19: Stacking of UV-vis spectra of compound **3**. Blue line: UV-vis spectrum in PBS with 10% of DMSO; grey line: Uv-vis spectrum in 50 µM BSA and 0.5% DMSO; orange line: : Uv-vis spectrum in 50 µM BSA and 10% DMSO*

Furthermore, we conducted additional experiments utilizing TWEEN 20, a polysorbate surfactant known for its ability to mitigate non-covalent interactions between hydrophobic components. In our study, TWEEN 20 was employed to disrupt any potential dimers. The absorption spectra of compound **3** (20 µM) were recorded in a PBS solution (10 mL) with 1% TWEEN 20, revealing a reduction in the observed band at 623 nm, which we attributed to the disruption of dimers (Figure 20).

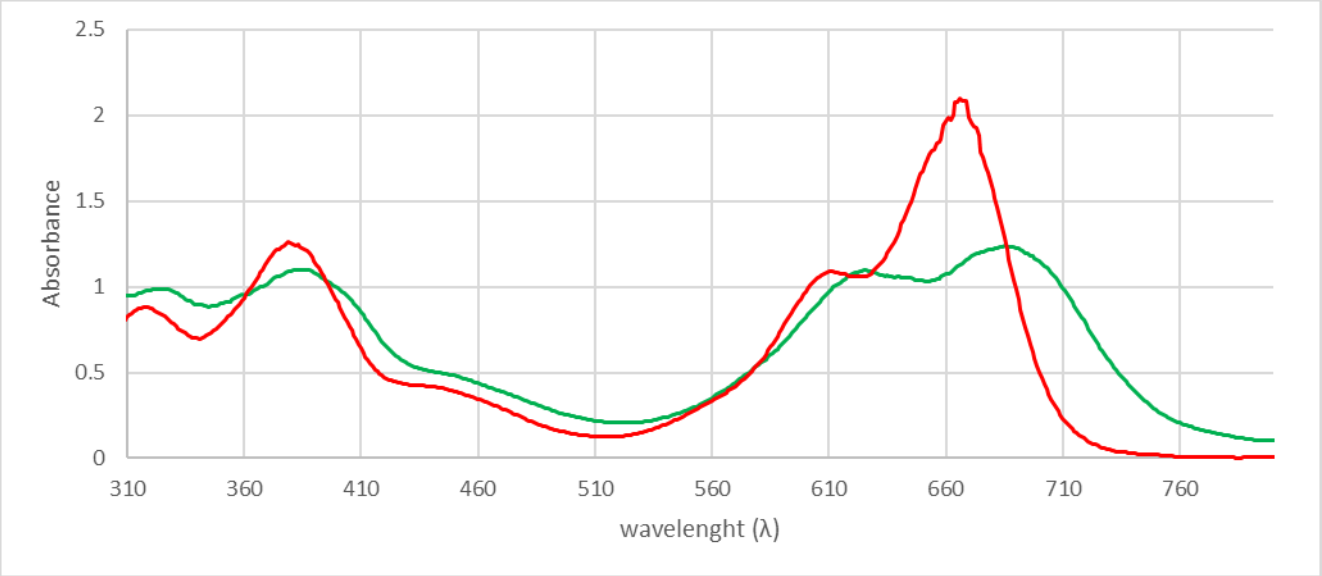

Figure 20: Absorption spectra of compound 15 (20 µM) in PBS and DMSO 10% + BSA 50 µM (green line) and in PBS and DMSO 10% + TWEEN 20 1% (red line).

2.5.2 Inhibition study

Subsequently, the behavior of compound **3** was examined in relation to its interactions with carbonic anhydrases. Through a collaboration with the research team led by Professor C. T. Supuran at the University of Florence, the compound's inhibitory activity against specific human CAs (hCAs) was investigated. The assessment of enzyme inhibition was conducted by evaluating the CA-catalyzed hydration of CO_2 using UV-vis-assisted stopped-flow technique[55]. To serve as a benchmark, Acetazolamide (AAZ), a well-established drug for the treatment of glaucoma associated with CAs dysregulation, was utilized. The K_i values for ligand **3** and AAZ were determined for three distinct hCAs, namely hCA I, II, and IX, as presented in Table 1.

Compound	*K_i [µM]*		
	hCA I	*hCA II*	*hCA IX*
2[55]	0.008 ± 0.001	0.004 ± 0.001	0.022 ± 0.001
3	4.073 ± 0.003	0.055 ± 0.003	0.092 ± 0.005
AAZ	0.25 ± 0.01	0.012 ± 0.001	0.025 ± 0.001

*Table 6: Inhibition constants of Compound **21** utilizing Acetazolamide (AAZ) as a reference*

Based on the obtained outcomes, it can be observed that compound **3** demonstrates more potent inhibition of hCA II and IX in comparison to hCA I, for which, rather surprisingly, is much less active than the corresponding compound **2**. In the case of our main interest, although the K_i for **3** against hCA IX is marginally higher, it remains comparable to those of **2** and AAZ. This indicates that the

addition of this photosensitizer to the ligand does not introduce substantial steric hindrance capable of significantly diminishing the inhibitory attributes of the sulfonamide unit.

2.5.3 Singlet Oxygen Quantum Yield

An initial examination was conducted to assess the capacity of compound **3** to generate singlet oxygen, with the experiment taking place in DMSO. For this assessment, 1,3-diphenylisobenzofuran (DPBF) was employed as a $^1O_2$ trap, while Methylene Blue (MB) served as the necessary reference compound (R) (ϕ_Δ=0.52)[25]. Compound **3**, when dissolved in DMSO, was added to a DPBF solution (60 µM) in DMSO until its absorption band intensity reached 0.1 (final concentration of **3** was 2 µM). To stimulate compound **3**, the solution was exposed to irradiation at 660 nm for a duration of 15 minutes. Throughout this period, an absorption spectrum was recorded every 1.5 minutes (refer to Figure 21). Notably, a substantial reduction in the DPBF absorption band at 408 nm was observed during the course of the experiment. The relative singlet oxygen quantum yield of compound **3** was determined to be 0.33, calculated using the provided equation:

$$\phi_\Delta(PS) = \phi_\Delta(R)\frac{m_{PS}}{m_R}\frac{F_R}{F_{PS}}\frac{PF_R}{PF_{PS}}$$

where ϕ_Δ (R) denotes the singlet oxygen quantum yield of the reference compound, 'm' represents the slope of a plot illustrating the change in DPBF absorption at 408 nm in the presence of PS (m_{PS}) or R (m_R) during the period of irradiation, 'F' stands for the absorption correction factor ($F = 1\text{-}10^{-OD}$, where OD refers to the Optical Density at the irradiation wavelength), and 'PF' indicates the absorbed photonic flux (µEinstein dm^{-3} s^{-1}). It is important to note that 'F' and 'PF' are dependent on the wavelength. Thus, when irradiated at the same wavelength, both the **3** and R (MB) share the same 'F' and 'PF' values.

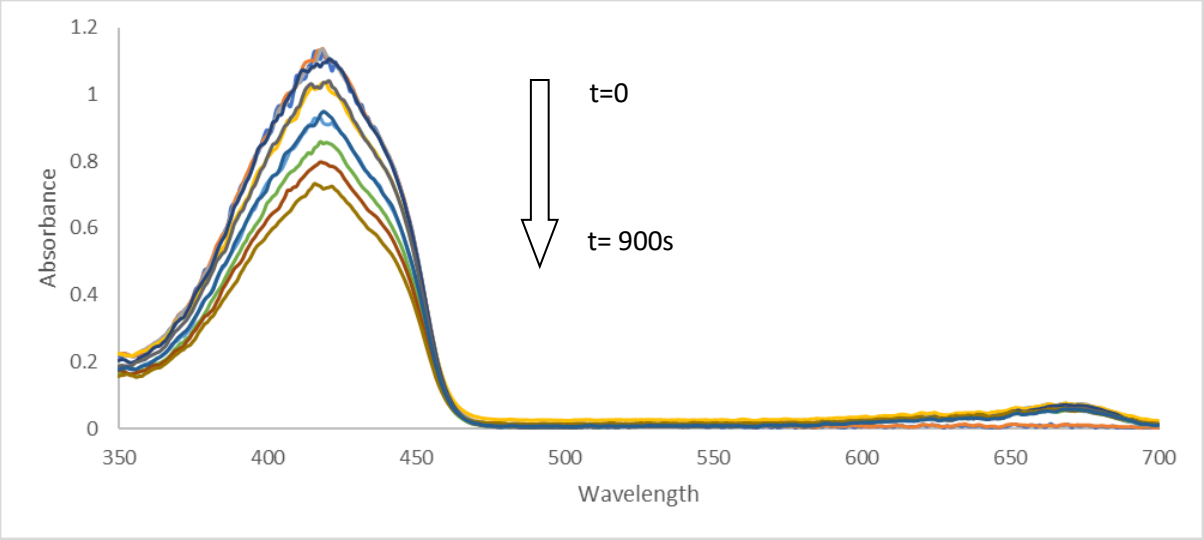

*Figure 21: Time dependent absorption spectra changes of DPBF in the presence compound **21** in DMSO*

The resulting absorption maxima of DPBF at 408 nm were then plotted against time (see Figure 22), illustrating a reduction in the DPBF absorption over time, directly corresponding to the quantity of singlet oxygen produced.

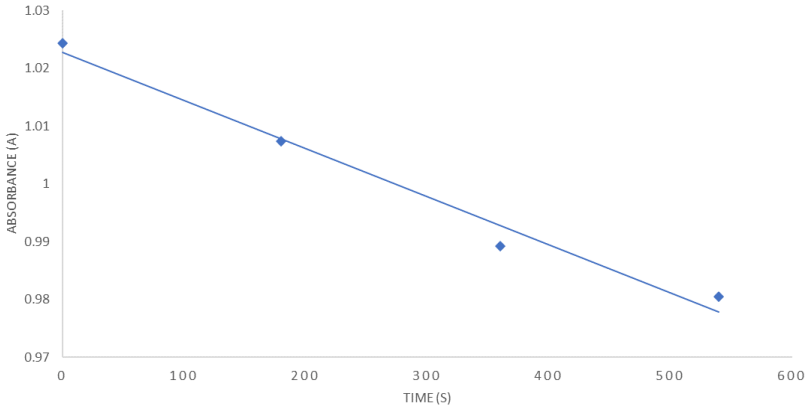

*Figure 22: Decrease of DPBF maximum absorption in presence of **3** due to the production of singlet oxygen.*

3. Conclusion

This chapter was focused on the synthesis of two conjugates combining a photosensitizer and a ligand, designed to selectively bind to CA IX, impede its catalytic activity, and induce apoptosis in tumor cells through the generation of singlet oxygen and/or reactive oxygen species (ROS).

The synthesis process involved the creation of ligand **7**, incorporating a sulfonamide component, based on a reference molecule previously identified for its promising inhibitory properties against CA IX, as affirmed by our research team. As for the photosensitizer segment, a BODIPY unit **11** was prepared, featuring two short PEG chains to enhance its solubility in aqueous environments, along with a suitably functionalized spacer for the conjugation with ligand **7**.

Additionally, a secondary photosensitizer **16**, constructed on the phenothiazine structure, was successfully developed, incorporating an amino terminal unit to facilitate its coupling with the inhibitor units. The synthesis of compound **3**, resulting from the click of ligand **17** and photosensitizer **11**, was followed by comprehensive investigations concerning its binding and inhibitory characteristics, singlet oxygen production, and water solubility. Notably, compound **3** exhibited a K_i value of 0.0925 µM towards hCA IX and demonstrated a singlet oxygen quantum yield of 0.33 in DMSO. Unfortunately, we didn't have enough time to perform the same studies for ligand **4** and to expand the studies of compound **3**. In future, the idea is to study the target compounds **3** and **4** to evaluate their *in vivo* ability of inhibition exploiting cancer cells in hypoxic conditions that, therefore, overexpresses the hCAIX.

4. Experimental part

General information

Materials and methods: All solvents were dried using standard procedures. All other reagents were of reagent-grade quality, obtained from commercial suppliers and were used without further purification. "Brine" refers to a saturated aqueous solution of NaCl. Unless otherwise specified, solutions of common inorganic salts used in workups are aqueous solutions. Reactions were monitored by TLC using 0.25 mm Merck silica gel plates (60 F_{254}). As stains $KMnO_4$ and H_2SO_4 were used for oxidizable compounds, Ninhydrin for ammines-containing compounds and 2,4-Dinitrophenylhydrazine for carbonylic compounds. NMR spectra were recorded at 400 MHz for ^1H and 100 MHz for the ^{13}C, on a Bruker Avance 400 spectrometers. Chemical shifts (δ) are expressed in ppm using the residual solvent signal as an internal reference (7.26 ppm for $CHCl_3$, 4.80 ppm for Water, 4.78 and 3.31 ppm for CH_3OH, and 2.5 ppm for DMSO). Coupling constants (J values) are given in hertz (Hz) and multiplicities are reported using the following abbreviation (s = singlet, d = doublet, t = triplet, q = quartet, m = multiplet, br. s = broad signal). ESI-MS spectra were recorded on an Waters' SQ detector spectrometer.

Synthesis of ethyl 4-(3-(4-sulfamoylbenzamido)propoxy)benzoate (6)

Under N_2 atmosphere, 4-sulfamoylbenzoic acid (200 mg, 0.994 mmol) was dissolved in dry DMF (5 mL). Then EDC (210 mg, 1.09 mmol) and DIPEA (0,4 mL, 2.98 mmol) were added to the solution. Compound **5** (244 mg, 0.994 mmol) in DMF (5 mL) was then added to the reaction mixture. The reaction was stirred at room temperature for 16 hours, and monitored via TLC (DCM:MeOH 8:2, stain: ninhydrin). It was diluted with AcOEt (50 mL), washed with brine (3 x 50 mL), dried with Na_2SO_4, filtered, and concentrated under reduced pressure. The resulting crude was dissolved in a minimum amount of DMF. Water was then added to precipitate the desired product as a white solid. Yield=69% (134 mg)

^1H-NMR (400 MHz, DMSO-d_6): $\boldsymbol{\delta}$(ppm) = 8.69 (t, J = 5.6 Hz, 1H, NH), 7.99 (d, J = 8.6 Hz, 2H, H_c), 7.97 – 7.85 (m, 4H, H_a H_d), 7.43 (s, 2H, NH_2), 7.05 (d, J = 9.0 Hz, 2H, H_b), 4.28 (q, J = 7.1 Hz, 2H, OCH_2 *ester*), 4.15 (t, J = 6.2 Hz, 2H, OCH_2), 3.46 (q, J = 6.5 Hz, 2H, CH_2NH), 2.03 (p, J = 6.5 Hz, 2H, OCH_2CH_2), 1.31 (t, J = 7.1 Hz, 3H, CH_3).

^{13}C-NMR (100 MHz, DMSO-d_6): $\boldsymbol{\delta}$(ppm) = 165.9 ($CONH_2$), 162.9 (*C*OOMe),146.7(CSO_2NH_2), 138.0 (*C*$CONH_2$), 131.6 (C_a), 128.3(C_c), 126.1(C_d), 122.6 (*C*COOMe), 114.9 (C_b), 66.3 (OCH_2), 60.7 (OCH_2 *ester*), 36.9 (CH_2NH), 29.2 ($CH_2CH_2CH_2$), 14.7 (CH_3).

ESI-MS: m/z calc: 406.45, found: 429.32 $[M+Na]^+$

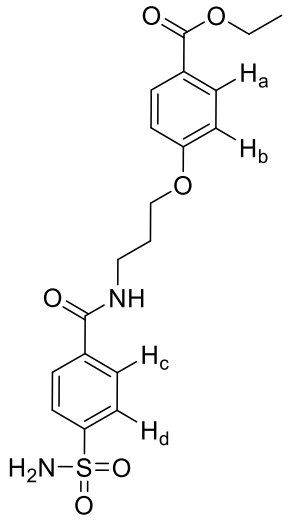

Synthesis of 4-(3-(4-sulfamoylbenzamido)propoxy)benzoic acid (7)

Methyl 4-(3-(4-sulfamoylbenzamido)propoxy)benzoate (**9**) (140 mg , 0.355 mmol) was dissolved in MeOH (15 mL). Then NaOH (40 mg, 1 mmol) was dissolved in water and added to the solution. The mixture was stirred at room temperature for 24 hours. The reaction was monitored via TLC (DCM:MeOH 8:2, stain: ninhydrin). After which, amberlite® was added to the solution until pH=7 was reached and stirred for another hour. The suspension was filtered and washed with MeOH. The solvent was removed under reduced pressure obtaining the desired product as a white solid.
Yield= quantitative (134 mg)

^{1}H-NMR (400 MHz, MeOD): ***δ***(ppm) = 7.91-8.03 (m , 6H, H_a H_c H_d), 7.00 (d, *J* = 7.0 Hz, 2H, H_b), 4.18 (t, *J* = 4.2 Hz, 2H, OCH_2), 3.63 (t, J = 6.9 , 2H, CH_2NH), 2.16 (m, 2H, $CH_2CH_2CH_2$)

^{13}C-NMR (100 MHz, DMSO-*d*$_6$): ***δ***(ppm) = 167.6(COOH), 165.8(COONH), 162.7(C-O), 146.7 (CSO_2NH_2), 137.9(*C*$CONH_2$), 131.8(C_a), 128.2(C_c), 126.1(C_d), 123.4(*C*COOMe), 114.8(C_b), 66.2(CH_2O), 36.9(CH_2NH), 29,2($CH_2CH_2CH_2$)

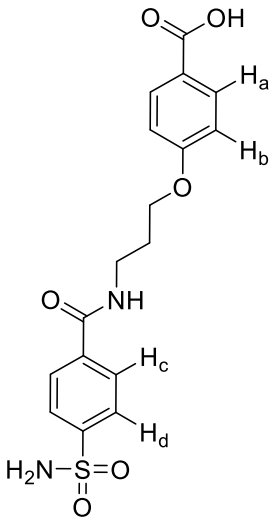

ESI-MS: m/z calc: 378.15, found: 401.48 $[M+Na]^+$, 417.23 $[M+K]^+$

Synthesis of Compound 9

Compound **8** (262.3 mg , 0.587 mmol) and NaN_3 (93.3 mg, 1.435 mmol) were dissolved in DMF (3.9 mL). The reaction mixture was stirred at room temperature for 20 hours and monitored via TLC (DCM:Hex 1:1). The mixture was diluted with water (50 mL) and extracted with chloroform (3 x 50 mL). The organic phase was washed with water and brine (3 x 50 mL), dried with Na_2SO_4, filtered, and concentrated under reduced pressure. The desired product was obtained as a dark red solid with a yield of 87%.

Yield=87% (0.208) g

^{1}H-NMR (400 MHz, $CDCl_3$): δ(ppm) = 7.22 (dt, *J* = 8.7 Hz, 2.7 Hz, 2H, H_d), 7.06 (dt, *J* = 8.7 Hz, 2.7 Hz, 2H, H_e), 6.00 (s, 2H, H_b), 4.23 (t, *J* = 4.9 Hz, 2H, OCH_2), 3.69 (t, *J* = 4.9 Hz, 2H, CH_2N_3), 2.57 (s, 6H, H_a), 1.45 (s, 6H, H_c)

The spectroscopic data found are in agreement with those reported in literature [61].

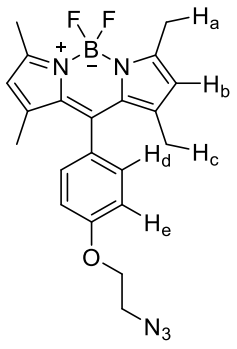

Synthesis of Compound 10

Compound **9** (104 mg , 0.508 mmol) was dissolved in a solution of DMF-DCM (4:1, 5 mL). Then a solution of NBS (90.8 mg , 1.016 mmol) in DCM (0.5 mL) was added. The reaction mixture was stirred at room temperature for one hour and monitored via TLC (DCM:Hex 1:1). The mixture was diluted with DCM (50 mL) and washed with water (1 x 50 mL) and brine (3 x 50 mL). The resulting organic phase was dried with Na_2SO_4, filtered, and concentrated under reduced pressure. The crude purified through flash chromatography (SiO_2, DCM/Hex 1:1) to obtain the pure product as a pink solid.

Yield=90 % (129 mg)

^{1}H-NMR (400 MHz, $CDCl_3$): δ(ppm) = 7.18 (dt, *J* = 8.7 Hz, 2.7 Hz, 2H, H_c), 7.08 (dt, *J* = 8.7 Hz, 2.7 Hz, 2H, H_d), 4.25 (t, *J* = 5.2 Hz, 2H, OCH_2), 3.70 (t, *J* = 5.2 Hz, 2H, CH_2N_3), 2.63 (s, 6H, H_a), 1.45 (s, 6H, H_b)

The spectroscopic data found are in agreement with those reported in literature [61].

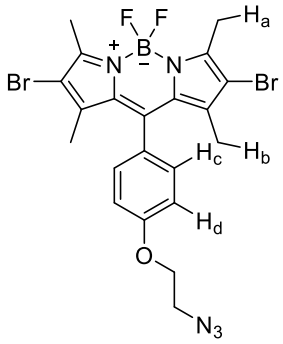

Synthesis of Compound 11

Compound **10** (58.5 mg , 0.103 mmol), 4-[2-[2-(2-methoxyethoxy)ethoxy]ethoxy]benzaldehyde (66.2 mg, 0.246 mmol), piperidine (0.34 mL, 3.09 mmol) and toluenesulfonic acid (587.8 mg, 3.09 mmol) were dissolved in toluene (6 mL) in sealed tube. The reaction was stirred at 110°C for 16 hours, and monitored via TLC (DCM:MeOH 95:5). The solvent was removed under reduced pressure. The crude was purified via flash chromatography (SiO_2, Hex:AcOEt 8:2 to 6:4) and the desired product was obtained as a blue solid.

Yield=39% (110 mg)

^{1}H-NMR (400 MHz, $CDCl_3$): ***δ***(ppm) = 8.13 (d, *J* = 16.6 Hz, 2H, H_k), 7.64 (m, 6H, H_i H_j), 7.23 (d, *J* = 8.6 Hz, 2H, H_m), 7.10 (d, *J* = 8.6 Hz, 2H, H_n), 6.99 (d, *J* = 8.9 Hz, 4H, H_h), 4.26 (t, *J* = 4.8 Hz, 2H, H_o), 4.22 (t, *J* = 4.9 Hz, 4H, H_g), 3.92 (t, *J* = 4.9 Hz, 4H, H_f), 3.76-3.89 (m, 4H, H_c), 3.70-3.75 (m, 8H, H_d H_e), 3.57-3.61 (m, 6H, H_b H_p), 3.41 (s, 6H, H_a), 1.50 (s, 6H, H_l)

The spectroscopic data found are in agreement with those reported in literature [61].

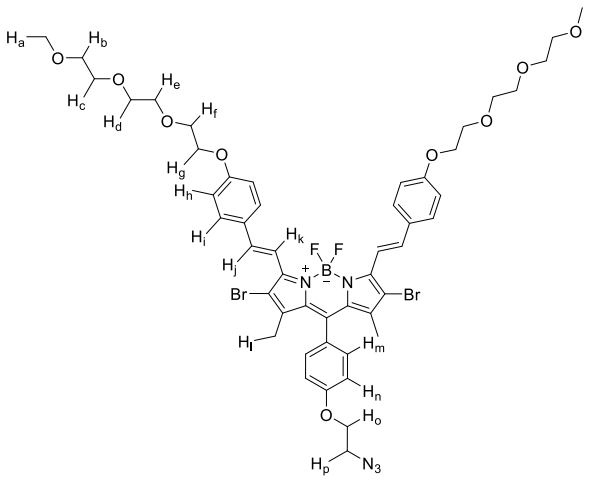

Synthesis of N-(prop-2-yn-1-yl)-4-(3-(4-sulfamoylbenzamido)propoxy)benzamide (17)

Under N_2 atmosphere, 4-(3-(4-sulfamoylbenzamido)propoxy)benzoic acid **7** (91 mg, 0.24 mmol) was dissolved in dry DMF (3 mL). Then HBTU (91 mg, 0.24 mmol) and DIPEA (0,0418 mL, 0,24 mmol) were added to the solution. The mixture was stirred for 10 minutes and a solution of propargylamine (15.4 µL, 0.24 mmol) and triethylamine (67 µL, 0.48 mmol) was added. The reaction was stirred for another 16 hours at room temperature and monitored via TLC (DCM:MeOH 9:1). The reaction mixture was concentrated under reduced pressure and precipitated in DCM (15 mL), giving the desired product as a beige solid.

Yield=74% (74 mg)

^{1}H-NMR (400 MHz, DMSO-d_6): $\boldsymbol{\delta}$(ppm) = 8.68 (m , 2H, NH), 8.00 (d, J = 8.6 Hz, 2H, H_c), 7.90 (d, J = 8.6 Hz, 2H, H_d), 7.83 (d, J = 8.6 Hz, 2H, H_a), 7.42 (s, 2H, NH_2), 7.00 (d, J = 8.9 Hz, 2H, H_b), 4.13 (t, J = 6.3 Hz, 2H, OCH_2), 4.04 (m, 2H, CH_2CCH), 3.46 (q, J = 6.7 Hz, 5.8 Hz, 2H, NHCH_2CH$_2$), 3.06 (t, J = 2.6 Hz, 1H, CH), 2.03 (m, 2H, CH$_2$CH_2CH$_2$)

^{13}C-NMR (100 MHz, DMSO-d_6): $\boldsymbol{\delta}$(ppm) = 165.60($CONH_2$), 161.35(C-O), 146.59(CSO_2NH_2), 137.71 (CCONH$_2$), 129.60(C_a), 128.26(C_c), 126.56(C_d), 126.03(CCONH$_2$), 114.48(C_b), 82.01(CCH), 73.13(CCH), 66,05(OCH_2), 36.74(NHCH$_2$CH$_2$), 29.21(CH$_2C$H$_2$CH$_2$), 28.88(CH$_2$CCH)
ESI-MS: m/z calc: 415.32, found: 416.22 $[M+H]^+$, 438.09 $[M+Na]^+$, 454.02 $[M+K]^+$

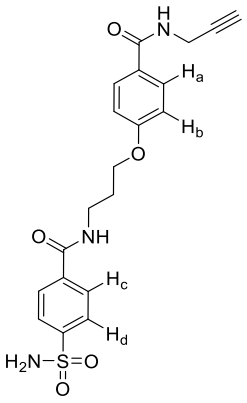

Synthesis of BODIPY-Ligand conjugate (3)

Compound **14** (28 mg, 10.026 mmol), N-(prop-2-yn-1-yl)-4-(3-(4-sulfamoylbenzamido)propoxy) benzamide (**20**) (8.71. mg, 0.021 mmol), sodium ascorbate (13 mg, 0.065 mmol), and copper sulfate pentahydrate (1.7 mg, 0.010 mmol) were dissolved in DMF (2 mL). The reaction was heated in the microwave at 80°C and 100 W for 30 minutes, then monitored via TLC (DCM:MeOH 95:5). The crude product was then purified via flash chromatography (SiO_2, Hex: Acetone 2:8). The desired product was obtained as blue solid.

Yield=40% (12.4 mg)

^{1}H-NMR (400 MHz, DMSO-d_6): $\boldsymbol{\delta}$(ppm) = 8.83 (t, J = 5.7 Hz, 1H, NH), 8.65 (t, J = 5.6 Hz, 1H, NH), 8.06 (d, J = 16.6 Hz, 2H, H_k), 8.05 (s, 1H, H_q), 7.98 (d, J = 8.5 Hz, 2H, H_x), 7.89 (d, J = 8.5 Hz, 2H, H_y), 7.86(d, J = 8.9 Hz, 2H, H_s) 7.61 (d, J = 8.9 Hz, 4H, H_i), 7.47 (d, J = 16.6 Hz, 2H, H_j), 7.34 (d, J = 8.7 Hz, 2H, H_n), 7.13 (d, J = 8.7 Hz, 2H, H_m), 7.08 (d, J = 8.8 Hz, 4H, H_h), 6.98 (d, J = 8.9 Hz, 2H, H_t), 4.80 (t, J = 5.0 Hz, 2H, H_o), 4.52 (m, 4H, H_p H_r), 4.19 (t, J = 4.7 Hz, 4H, H_g), 4.09 (t, J = 5.8 Hz, 2H, H_u), 3.79 (t, J = 4.7 Hz, 4H, H_f), 3.59-3.64 (m, 4H, H_c), 3.52-3.58 (m, 8H, H_d H_e), 3.42-3.47 (m, 6H, H_b H_w), 2.00 (m, 2H, H_v), 1.42 (s, 6 H_l)

^{13}C-NMR (100 MHz, DMSO-d_6): $\boldsymbol{\delta}$(ppm) = 166.2(*C*ONH), 165.7(*C*OC_u), 161.5(*C*C_h), 160.5(*C*C_n), 147.9(CS), 146.6(CNB), 146.0(*C*$_l$), 141.5(*C*CC_m), 139.1(*C*C_x), 138.6(C_i), 132.4(C_t), 130.3(C_x), 129.5(C_y), 129.3(C_i*C*C_j), 128.3(*C*C_s), 126.6(C_q), 126.1(C_s), 116.1(N*C*CBr), 115.9(C_j), 114.4(C_h), 113.0(C_k), 110.1(CBr), 71.8(C_b), 70.5(C_d, C_e), 70.3(C_c), 70.1(C_f), 69.3(C_g), 68.0(C_u), 66.1(C_a), 58.5(C_p), 36.9(C_r), 35.3(C_w), 29.2(C_v), 14.2(C_i).

ESI-MS: m/z calc: 1480.37 , found: 1506.09 $[M+Na]^+$

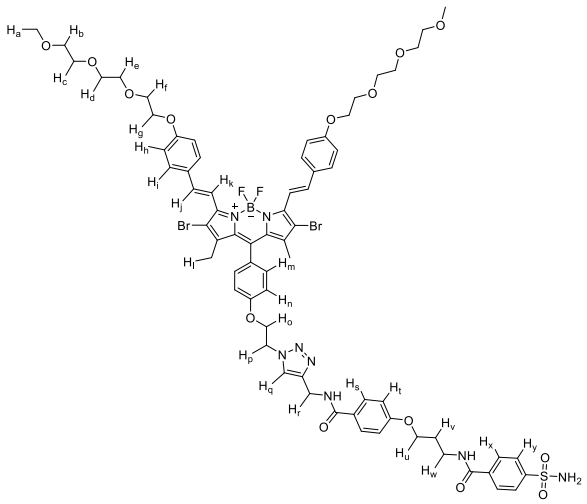

Synthesis of N,N-diethyl-4-nitroaniline (12)

Diethyl ammine (3 mL, 10.6 mmol), potassium carbonate (1.465 g, 10.6 mmol) and p-fluoro-nitrobenzene (1 g, 7.1 mmol) were dissolved in DMSO (3.4 mL). The reaction mixture was stirred at 100°C for 4 hours and monitored via TLC (Hex:AcOEt 9:1). Water (50 mL) was then added and the precipitate was filtered, obtaining the desired product as a yellow solid.

Yield= 73% (1g)

^{1}H-NMR (400 MHz, $CDCl_3$): $\boldsymbol{\delta}$(ppm) = 8.12 (d, J = 7.9 Hz, 2H, H_a), 6.60 (d, J = 7.9 Hz, 2H, H_b), 3.18 (q, J = 7.4 Hz, 4H, CH_2), 1.25 (t, J = 7.4 Hz, 6H, CH_3)

The spectroscopic data found are in agreement with those reported in literature [62].

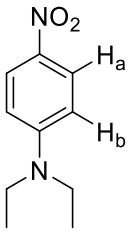

Synthesis of N^1,N^1-diethylbenzene-1,4-diamine (13)

N,N-diethyl-4-nitroaniline (**12**) (0.6 g, 3.1 mmol) was dissolved in methanol (11 mL). Then a catalytic amount of Pd/C was added. H_2 was influxed inside the flask for 5 hours at room temperature. The reaction was monitored via TLC (Hex:AcOEt 8:2). The mixture was filtered and washed with MeOH. The solution was concentrated under reduced pressure giving the desired product as a dark brown oil.
Yield= 89% (456 mg)

^{1}H-NMR (400 MHz, $CDCl_3$): δ(ppm) = 6.68 (s, 4H, ArH), 3.15-3.45 (br.s, 2H, NH_2) 3.23 (q, J = 6.9 Hz, 4H, CH_2), 1.11 (t, J = 6.9 Hz, 6H, CH_3)

The spectroscopic data found are in agreement with those reported in literature [63].

Synthesis of 1-amino-4-(diethylamino)-2-sulfosulfanylbenzene (14)

p-diethylamino aniline (**13**) (456 mg, 2.78 mmol) was dissolved in water (5 mL). Then aluminum sulfate (2 g, 3.17 mmol), sodium thiosulfate (1 g, 6.38 mmol), and zinc chloride (530 mg, 3.9 mmol) were added to the reaction mixture. After a few minutes the reaction mixture was placed in an ice bath. An aqueous solution (4 mL) of potassium dichromate (250 mg, 0.86 mmol) was added dropwise over a period of 20 minutes. The mixture was stirred for 3 hours, filtered and washed with acetone. The resulting dark green solid was refluxed in methanol for 1 hour and filtered to give the desired product as a dark grey solid.

Yield=70% (580 mg)

^{1}H-NMR (400 MHz, D_2O): δ(ppm) = 8.04 (s, 1H, H_b), 7.79 (d, J = 9.0 Hz, 1H, H_a), 7.50 (d, J = 9.0 Hz, 1H, H_c), 3.85-4.05 (br.s, 10H, CH_2CH_3)

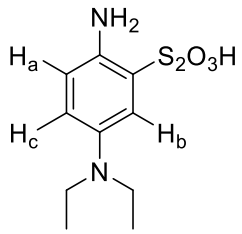

The spectroscopic data found are in agreement with those reported in literature.[64]

Synthesis of N-(1-Naphthyl)-1,3-propanediamine (15)

Under N_2 atmosphere, bromonaphtalene (1.4 mL, 10 mmol), 1,3-propandiamine (2,5 mL, 30 mmol), proline (230 mg, 2 mmol), potassium carbonate (2.76 g, 20 mmol), and copper iodide (190 mg, 1 mmol) were dissolved in dry DMF (20 mL). The reaction was stirred at 100°C for 24 hours, and monitored via TLC (Hex:AcOEt 8:2). The mixture was extracted with AcOEt (3 x 100 mL). The combined organic layers were dried over Na_2SO_4, filtered and concentrated under reduced pressure. The crude product was purified via flash chromatography (SiO_2, Hex:AcOEt 8:2, then DCM:MeOH 1:1) obtaining the desired product as a brown oil.
Yield=24% (485 mg)

^{1}H-NMR (400 MHz, $CDCl_3$): $\boldsymbol{\delta}$(ppm) = 7.87 (m, 1H, H_g), 7.80 (m, 1H, H_d), 7.45 (m, 2H, H_f H_e), 7.37 (t, J = 7.7 Hz, 1H, H_b), 7.24 (d, J = 8.1 Hz, 1H, H_a), 6.61 (d, J = 7.7 Hz, 1H, H_c), 3.41 (t, J = 6.5 Hz, 2H, C$H_2$$NH_2$), 3.00 (t, J = 6.5 Hz, 2H, CH_2NH), 3.41 (m, 2H, CH_2C$H_2$$CH_2$)

The spectroscopic data found are in agreement with those reported in literature.[64].

Synthesis of the EtNBS derivative (16)

1-amino-4-(diethylamino)-2-sulfosulfanylbenzene (**14**) (248 mg, 0.898 mmol) and N-(naphthalenyl) propane-1,3-diamine (**15**) (246 mg, 1.23 mmol) were dissolved in DMSO (6 mL), then potassium dichromate (265 mg, 0.900 mmol) was added. After the mixture was stirred at room temperature for 20 min, methanol (40 mL) and hydrochloric acid (1M, 8 mL) were added to above mixture. The reaction was stirred for another 40 min at room temperature, and monitored via TLC (DCM:MeOH 8:1). When the reaction was complete, methanol and water were removed under reduced pressure. The remaining solution was poured into a saturated solution of sodium chloride (100 mL). The suspension was then filtered and the blue solid was washed with water. The crude was purified via flash chromatography (SiO_2, DCM:MeOH 8:1). The desired product was obtained as a blue solid.

Yield= 15% (53 mg)

^{1}H-NMR (400 MHz, MeOD): $\boldsymbol{\delta}$(ppm) = 8.90 (d, J = 8.1 Hz, 1H, H_e), 8.35 (d, J = 8.1 Hz, 1H, H_h), 7.89 (d, J = 9.5 Hz, 1H, H_b), 7.82 (t, J = 7.1 Hz, 1H, H_f), 7.75 (t, J = 7.1 Hz, 1H, H_g), 7.33 (m, 2H, H_a H_d), 7.16 (d, J = 2,6 Hz, 1H, H_c), 3.80 (t, J = 7.1 Hz, 2H, C$H_2$$NH_2$), 3.68 (q, J = 7.1 Hz, 4H, C$H_2$$CH_3$), 3.18 (t, J = 7.6 Hz, 2H, NHCH_2), 2.24 (m, 2H, CH_2C$H_2$$CH_2$), 1,34 (t, J = 7.1 Hz, 6H, CH_3)

^{13}C-NMR (100 MHz, MeOD): $\boldsymbol{\delta}$(ppm) = 156.6(N*C*CC_h), 154.9(C=NH), 143.5(C_bCN), 140.8(CNEt_2), 137.2(*C*C_h), 136.9(C_f), 136.7(C_g), 135.9(C_e), 134.5(C_d*C*S), 133.1(*C*C_e), 128.6(C_c*C*S), 127.7(C_h), 126.3(C_b), 121.4(C_c), 108.6(C_a), 105.6(C_d), 49.6(*C*$H_2$$CH_3$), 44.8(*C*$H_2$NH), 41.0(*C*$H_2$$NH_2$), 30.3($CH_2$*C*$H_2$$CH_2$), 15.8($CH_3$)

Synthesis of EtNBS-Ligand (4)

Under N_2 atmosphere, compound **10** (43 mg, 0.114 mmol) was dissolved in dry DMF (5 mL). Then EDC (48 mg, 0.25 mmol) and DIPEA (0,12 mL, 0.684 mmol) were added to the solution. Compound **19** (45 mg, 0,114 mmol) in DMF (5 mL) was then added to the reaction mixture. The reaction was stirred at room temperature for 24 hours, and monitored via TLC (DCM:MeOH 8:2,). It was diluted with water (20 mL) and washed with DCM (3 x 30 mL). After the extraction a blue solid was observed

in the funnel. The solid was dissolved in methanol. The solution was concentrated under reduced pressure giving the desired product as a blue solid.

Yield=19% (19 mg)

^{1}H-NMR (400 MHz, MeOD): $\boldsymbol{\delta}$(ppm) = 9.17 (d, J = 7.8 Hz, 1H, H_j), 8.41 (d, J = 8.2 Hz, 1H, H_g), 8.12 (d, J = 9.3 Hz, 1H, H_e), 7.91-8.02 (m, 5H, H_i H_s H_t), 7.87 (t, J = 7.4 Hz, 1H, H_h), 7.78 (d, J = 9.0 Hz, 2H, H_n), 7.46 (dd, J = 9.3 Hz, J = 2.9 Hz, 1H, H_d), 7.42 (s, 1H, H_f), 7.31 (d, J = 2.9 Hz, 1H, H_c), 6.95 (d, J = 9.0 Hz, 2H, H_o), 4.15 (t, J = 6.0 Hz, 2H, H_p), 3.84 (t, J = 6.5 Hz, 2H, H_k), 3.74 (q, J = 7,3 Hz, 4H, H_b), 3.61 (m, J = 4H, H_m H_r), 2.16 (m, 4H, H_l H_q).

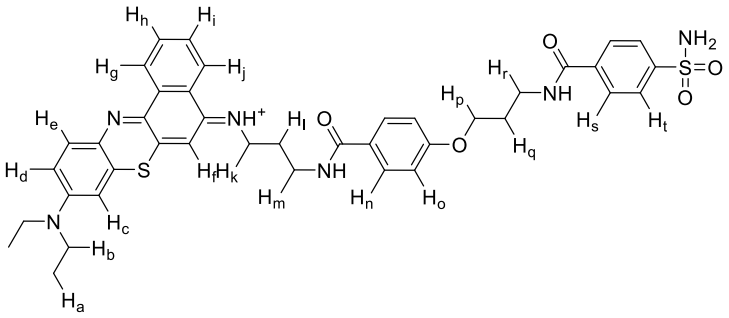

5. Bibliography

(1) Roumeliotis, S.; Roumeliotis, A.; Dounousi, E.; Eleftheriadis, T.; Liakopoulos, V. Chapter Four - Biomarkers of Vascular Calcification in Serum. In *Advances in Clinical Chemistry*; Makowski, G. S., Ed.; Elsevier, 2020; Vol. 98, pp 91–147. https://doi.org/10.1016/bs.acc.2020.02.004.

(2) Lehenkari, P.; Hentunen, T. A.; Laitala-Leinonen, T.; Tuukkanen, J.; Väänänen, H. K. Carbonic Anhydrase II Plays a Major Role in Osteoclast Differentiation and Bone Resorption by Effecting the Steady State Intracellular pH and Ca2+. *Experimental Cell Research* **1998**, *242* (1), 128–137. https://doi.org/10.1006/excr.1998.4071.

(3) Nishimori, I.; Minakuchi, T.; Onishi, S.; Vullo, D.; Cecchi, A.; Scozzafava, A.; Supuran, C. T. Carbonic Anhydrase Inhibitors: Cloning, Characterization, and Inhibition Studies of the Cytosolic Isozyme III with Sulfonamides. *Bioorganic & Medicinal Chemistry* **2007**, *15* (23), 7229–7236. https://doi.org/10.1016/j.bmc.2007.08.037.

(4) Hong, J. H.; Muhammad, E.; Zheng, C.; Hershkovitz, E.; Alkrinawi, S.; Loewenthal, N.; Parvari, R.; Muallem, S. Essential Role of Carbonic Anhydrase XII in Secretory Gland Fluid and HCO3− Secretion Revealed by Disease Causing Human Mutation. *The Journal of Physiology* **2015**, *593* (24), 5299–5312. https://doi.org/10.1113/JP271378.

(5) Benesch, R. Carbonic Anhydrase and Calcification. *Annals of the New York Academy of Sciences* **1984**, *429* (1), 457–458. https://doi.org/10.1111/j.1749-6632.1984.tb12371.x.

(6) Mboge, M. Y.; Mahon, B. P.; McKenna, R.; Frost, S. C. Carbonic Anhydrases: Role in pH Control and Cancer. *Metabolites* **2018**, *8* (1), 19. https://doi.org/10.3390/metabo8010019.

(7) Henry, R. P. Multiple Roles of Carbonic Anhydrase in Cellular Transport and Metabolism. *Annual Review of Physiology* **1996**, *58* (1), 523–538. https://doi.org/10.1146/annurev.ph.58.030196.002515.

(8) Supuran, C. T. Carbonic Anhydrases: Novel Therapeutic Applications for Inhibitors and Activators. *Nature Review Drug Discovery* **2008**, *7* (2), 168–181. https://doi.org/10.1038/nrd2467.

(9) Alterio, V.; Di Fiore, A.; D'Ambrosio, K.; Supuran, C. T.; De Simone, G. Multiple Binding Modes of Inhibitors to Carbonic Anhydrases: How to Design Specific Drugs Targeting 15 Different Isoforms? *Chemical Review* **2012**, *112* (8), 4421–4468. https://doi.org/10.1021/cr200176r.

(10) *Carbonic Anhydrase: Its Inhibitors and Activators*; Conway, C. T. S., Andrea Scozzafava, Janet, Ed.; CRC Press: Boca Raton, 2004. https://doi.org/10.4324/9780203475300.

(11) Supuran, C. T.; Scozzafava, A.; Casini, A. Carbonic Anhydrase Inhibitors. *Medicinal Research Reviews* **2003**, *23* (2), 146–189. https://doi.org/10.1002/med.10025.

(12) Kivelä, J.; Parkkila, S.; Parkkila, A.-K.; Leinonen, J.; Rajaniemi, H. Salivary Carbonic Anhydrase Isoenzyme VI. *The Journal of Physiology* **1999**, *520* (2), 315–320. https://doi.org/10.1111/j.1469-7793.1999.t01-1-00315.x.

(13) Ekinci, D.; Karagoz, L.; Ekinci, D.; Senturk, M.; Supuran, C. T. Carbonic Anhydrase Inhibitors: In Vitro Inhibition of α Isoforms (hCA I, hCA II, bCA III, hCA IV) by Flavonoids. *Journal of Enzyme Inhibition and Medicinal Chemistry* **2013**, *28* (2), 283–288. https://doi.org/10.3109/14756366.2011.643303.

(14) Y. Mboge, M.; McKenna, R.; C. Frost, S. Advances in Anti-Cancer Drug Development Targeting Carbonic Anhydrase IX and XII. In *Topics in Anti-Cancer Research*; Atta-ur-Rahman, Zaman, K., Eds.; BENTHAM SCIENCE PUBLISHERS, 2016; pp 3–42. https://doi.org/10.2174/9781681083339116050004.

(15) Kalinin, S.; Malkova, A.; Sharonova, T.; Sharoyko, V.; Bunev, A.; Supuran, C. T.; Krasavin, M. Carbonic Anhydrase IX Inhibitors as Candidates for Combination Therapy of Solid Tumors. *International Journal of Molecular Science* **2021**, *22* (24), 13405. https://doi.org/10.3390/ijms222413405.

(16) Alterio, V.; Hilvo, M.; Fiore, A. D.; Supuran, C. T.; Pan, P.; Parkkila, S.; Scaloni, A.; Pastorek, J.; Pastorekova, S.; Pedone, C.; Scozzafava, A.; Monti, S. M.; Simone, G. D. Crystal Structure of the Catalytic Domain of the Tumor-Associated Human Carbonic Anhydrase IX *Proceedings of the National Academy of Sciences* **2009***, 106* (38) 16233. https://doi.org/10.1073/pnas.0908301106

(17) Vaupel, P.; Mayer, A. Hypoxia in Cancer: Significance and Impact on Clinical Outcome. *Cancer Metastasis Review* **2007**, *26* (2), 225–239. https://doi.org/10.1007/s10555-007-9055-1.

(18) Maxwell, P. H.; Wiesener, M. S.; Chang, G.-W.; Clifford, S. C.; Vaux, E. C.; Cockman, M. E.; Wykoff, C. C.; Pugh, C. W.; Maher, E. R.; Ratcliffe, P. J. The Tumour Suppressor Protein VHL Targets Hypoxia-Inducible Factors for Oxygen-Dependent Proteolysis. *Nature* **1999**, *399* (6733), 271–275. https://doi.org/10.1038/20459.

(19) Jaakkola, P.; Mole, D. R.; Tian, Y.-M.; Wilson, M. I.; Gielbert, J.; Gaskell, S. J.; Kriegsheim, A. von; Hebestreit, H. F.; Mukherji, M.; Schofield, C. J.; Maxwell, P. H.; Pugh, ‡ Christopher W.; Ratcliffe, ‡ Peter J. Targeting of HIF-α to the von Hippel-Lindau Ubiquitylation Complex by O2-

Regulated Prolyl Hydroxylation. *Science* **2001**, *292* (5516), 468–472. https://doi.org/10.1126/science.1059796.

(20) Weidemann, A.; Johnson, R. S. Biology of HIF-1α. *Cell Death and Differation* **2008**, *15* (4), 621–627. https://doi.org/10.1038/cdd.2008.12.

(21) Sebti, S. M.; Hamilton, A. D. Design of Growth Factor Antagonists with Antiangiogenic and Antitumor Properties. *Oncogene* **2000**, *19* (56), 6566–6573. https://doi.org/10.1038/sj.onc.1204121.

(22) Pastorekova, S.; Gillies, R. J. The Role of Carbonic Anhydrase IX in Cancer Development: Links to Hypoxia, Acidosis, and Beyond. *Cancer Metastasis Review* **2019**, *38* (1–2), 65–77. https://doi.org/10.1007/s10555-019-09799-0.

(23) Li, J.; Shi, K.; Sabet, Z. F.; Fu, W.; Zhou, H.; Xu, S.; Liu, T.; You, M.; Cao, M.; Xu, M.; Cui, X.; Hu, B.; Liu, Y.; Chen, C. New Power of Self-Assembling Carbonic Anhydrase Inhibitor: Short Peptide–Constructed Nanofibers Inspire Hypoxic Cancer Therapy. *Science Advances* **2019**, *5* (9), eaax0937. https://doi.org/10.1126/sciadv.aax0937.

(24) Jiang, Y.; Li, J.; Zeng, Z.; Xie, C.; Lyu, Y.; Pu, K. Organic Photodynamic Nanoinhibitor for Synergistic Cancer Therapy. *Angewandte Chemie International Edition* **2019**, *58* (24), 8161–8165. https://doi.org/10.1002/anie.201903968.

(25) Jung, H. S.; Han, J.; Shi, H.; Koo, S.; Singh, H.; Kim, H.-J.; Sessler, J. L.; Lee, J. Y.; Kim, J.-H.; Kim, J. S. Overcoming the Limits of Hypoxia in Photodynamic Therapy: A Carbonic Anhydrase IX-Targeted Approach. *Jorunal of the American Chemical Society* **2017**, *139* (22), 7595–7602. https://doi.org/10.1021/jacs.7b02396.

(26) Su, X.; Wang, W.-J.; Cao, Q.; Zhang, H.; Liu, B.; Ling, Y.; Zhou, X.; Mao, Z.-W. A Carbonic Anhydrase IX (CAIX)-Anchored Rhenium(I) Photosensitizer Evokes Pyroptosis for Enhanced Anti-Tumor Immunity. *Angewandte Chemie International Edition* **2022**, *61* (8), e202115800. https://doi.org/10.1002/anie.202115800.

(27) Correia, J. H.; Rodrigues, J. A.; Pimenta, S.; Dong, T.; Yang, Z. Photodynamic Therapy Review: Principles, Photosensitizers, Applications, and Future Directions. *Pharmaceutics* **2021**, *13* (9), 1332. https://doi.org/10.3390/pharmaceutics13091332.

(28) Rocha, L. G. B. Development of a Novel Photosensitizer for Photodynamic Therapy of Cancer.

(29) Celli, J. P.; Spring, B. Q.; Rizvi, I.; Evans, C. L.; Samkoe, K. S.; Verma, S.; Pogue, B. W.; Hasan, T. Imaging and Photodynamic Therapy: Mechanisms, Monitoring, and Optimization. *Chemical Review* **2010**, *110* (5), 2795–2838. https://doi.org/10.1021/cr900300p.

(30) Foote, C. S. DEFINITION OF TYPE I and TYPE II PHOTOSENSITIZED OXIDATION. *Photochem & Photobiology* **1991**, *54* (5), 659–659. https://doi.org/10.1111/j.1751-1097.1991.tb02071.x.

(31) Yano, S.; Hirohara, S.; Obata, M.; Hagiya, Y.; Ogura, S.; Ikeda, A.; Kataoka, H.; Tanaka, M.; Joh, T. Current States and Future Views in Photodynamic Therapy. *Journal of Photochemistry and Photobiology C: Photochemistry Reviews* **2011**, *12* (1), 46–67. https://doi.org/10.1016/j.jphotochemrev.2011.06.001.

(32) Agostinis, P.; Berg, K.; Cengel, K. A.; Foster, T. H.; Girotti, A. W.; Gollnick, S. O.; Hahn, S. M.; Hamblin, M. R.; Juzeniene, A.; Kessel, D.; Korbelik, M.; Moan, J.; Mroz, P.; Nowis, D.; Piette, J.; Wilson, B. C.; Golab, J. Photodynamic Therapy of Cancer: An Update. *CA: A Cancer Journal for Clinicians* **2011**, *61* (4), 250–281. https://doi.org/10.3322/caac.20114.

(33) Simpson, C. R.; Kohl, M.; Essenpreis, M.; Cope, M. Near-Infrared Optical Properties of Ex Vivo Human Skin and Subcutaneous Tissues Measured Using the Monte Carlo Inversion Technique. *Physics in Medicine and Biology* **1998**, *43* (9), 2465. https://doi.org/10.1088/0031-9155/43/9/003.

(34) Gao, J.; Chen, Z.; Li, X.; Yang, M.; Lv, J.; Li, H.; Yuan, Z. Chemiluminescence in Combination with Organic Photosensitizers: Beyond the Light Penetration Depth Limit of Photodynamic Therapy. *International Journal of Molecular Sciences* **2022**, *23* (20), 12556. https://doi.org/10.3390/ijms232012556.

(35) Mallidi, S.; Anbil, S.; Bulin, A.-L.; Obaid, G.; Ichikawa, M.; Hasan, T. Beyond the Barriers of Light Penetration: Strategies, Perspectives and Possibilities for Photodynamic Therapy. *Theranostics* **2016**, *6* (13), 2458–2487. https://doi.org/10.7150/thno.16183.

(36) Fan, W.; Huang, P.; Chen, X. Overcoming the Achilles' Heel of Photodynamic Therapy. *Chemical Society Review* **2016**, *45* (23), 6488–6519. https://doi.org/10.1039/C6CS00616G.

(37) Korman, A. J.; Garrett-Thomson, S. C.; Lonberg, N. The Foundations of Immune Checkpoint Blockade and the Ipilimumab Approval Decennial. *Nature Review Drug Discovery* **2022**, *21* (7), 509–528. https://doi.org/10.1038/s41573-021-00345-8.

(38) Allison, R. R.; Moghissi, K. Photodynamic Therapy (PDT): PDT Mechanisms. *Clinical Endoscopy* **2013**, *46* (1), 24–29. https://doi.org/10.5946/ce.2013.46.1.24.

(39) Ketelut-Carneiro, N.; Fitzgerald, K. A. Apoptosis, Pyroptosis, and Necroptosis—Oh My! The Many Ways a Cell Can Die. *Journal of Molecular Biology* **2022**, *434* (4), 167378. https://doi.org/10.1016/j.jmb.2021.167378.

(40) Wang, Y.; Gao, W.; Shi, X.; Ding, J.; Liu, W.; He, H.; Wang, K.; Shao, F. Chemotherapy Drugs Induce Pyroptosis through Caspase-3 Cleavage of a Gasdermin. *Nature* **2017**, *547* (7661), 99–103. https://doi.org/10.1038/nature22393.

(41) Ding, J.; Wang, K.; Liu, W.; She, Y.; Sun, Q.; Shi, J.; Sun, H.; Wang, D.-C.; Shao, F. Pore-Forming Activity and Structural Autoinhibition of the Gasdermin Family. *Nature* **2016**, *535* (7610), 111–116. https://doi.org/10.1038/nature18590.

(42) Shi, J.; Zhao, Y.; Wang, K.; Shi, X.; Wang, Y.; Huang, H.; Zhuang, Y.; Cai, T.; Wang, F.; Shao, F. Cleavage of GSDMD by Inflammatory Caspases Determines Pyroptotic Cell Death. *Nature* **2015**, *526* (7575), 660–665. https://doi.org/10.1038/nature15514.

(43) Wang, Q.; Wang, Y.; Ding, J.; Wang, C.; Zhou, X.; Gao, W.; Huang, H.; Shao, F.; Liu, Z. A Bioorthogonal System Reveals Antitumour Immune Function of Pyroptosis. *Nature* **2020**, *579* (7799), 421–426. https://doi.org/10.1038/s41586-020-2079-1.

(44) Bai, R.; Lang, Y.; Shao, J.; Deng, Y.; Refuhati, R.; Cui, L. The Role of NLRP3 Inflammasome in Cerebrovascular Diseases Pathology and Possible Therapeutic Targets. *ASN Neuro* **2021**, *13*, 175909142110181. https://doi.org/10.1177/17590914211018100.

(45) Zhao, X.; Liu, J.; Fan, J.; Chao, H.; Peng, X. Recent Progress in Photosensitizers for Overcoming the Challenges of Photodynamic Therapy: From Molecular Design to Application. *Chemical Society Review* **2021**, *50* (6), 4185–4219. https://doi.org/10.1039/D0CS00173B.

(46) Kamkaew, A.; Lim, S. H.; Lee, H. B.; Kiew, L. V.; Chung, L. Y.; Burgess, K. BODIPY Dyes in Photodynamic Therapy. *Chemical Society Review* **2013**, *42* (1), 77–88. https://doi.org/10.1039/C2CS35216H.

(47) Sun, W.; Zhao, X.; Fan, J.; Du, J.; Peng, X. Boron Dipyrromethene Nano-Photosensitizers for Anticancer Phototherapies. *Small* **2019**, *15* (32), 1804927. https://doi.org/10.1002/smll.201804927.

(48) Zhao, J.; Xu, K.; Yang, W.; Wang, Z.; Zhong, F. The Triplet Excited State of Bodipy: Formation, Modulation and Application. *Chemical Society Review* **2015**, *44* (24), 8904–8939. https://doi.org/10.1039/C5CS00364D.

(49) Li, M.; Xia, J.; Tian, R.; Wang, J.; Fan, J.; Du, J.; Long, S.; Song, X.; Foley, J. W.; Peng, X. Near-Infrared Light-Initiated Molecular Superoxide Radical Generator: Rejuvenating Photodynamic Therapy against Hypoxic Tumors. *Journal of the American Chemical Society* **2018**, *140* (44), 14851–14859. https://doi.org/10.1021/jacs.8b08658.

(50) Li, M.; Xia, J.; Tian, R.; Wang, J.; Fan, J.; Du, J.; Long, S.; Song, X.; Foley, J. W.; Peng, X. Near-Infrared Light-Initiated Molecular Superoxide Radical Generator: Rejuvenating Photodynamic Therapy against Hypoxic Tumors. *Journal of the American Chemical Society* **2018**, *140* (44), 14851–14859. https://doi.org/10.1021/jacs.8b08658.

(51) De Simone, G.; Supuran, C. T. Carbonic Anhydrase IX: Biochemical and Crystallographic Characterization of a Novel Antitumor Target. *Biochimica et Biophysica Acta (BBA) - Proteins and Proteomics* **2010**, *1804* (2), 404–409. https://doi.org/10.1016/j.bbapap.2009.07.027.

(52) Innocenti, A.; Vullo, D.; Scozzafava, A.; Supuran, C. T. Carbonic Anhydrase Inhibitors: Interactions of Phenols with the 12 Catalytically Active Mammalian Isoforms (CA I–XIV). *Bioorganic & Medicinal Chemistry Letters* **2008**, *18* (5), 1583–1587. https://doi.org/10.1016/j.bmcl.2008.01.077.

(53) Maresca, A.; Temperini, C.; Vu, H.; Pham, N. B.; Poulsen, S.-A.; Scozzafava, A.; Quinn, R. J.; Supuran, C. T. Non-Zinc Mediated Inhibition of Carbonic Anhydrases: Coumarins Are a New Class of Suicide Inhibitors. *Journal of the American Chemical Society* **2009**, *131* (8), 3057–3062. https://doi.org/10.1021/ja809683v.

(54) Dubois, L.; Lieuwes, N. G.; Maresca, A.; Thiry, A.; Supuran, C. T.; Scozzafava, A.; Wouters, B. G.; Lambin, P. Imaging of CA IX with Fluorescent Labelled Sulfonamides Distinguishes Hypoxic and (Re)-Oxygenated Cells in a Xenograft Tumour Model. *Radiotherapy and Oncology* **2009**, *92* (3), 423–428. https://doi.org/10.1016/j.radonc.2009.06.019.

(55) Sbravati, D.; Bonardi, A.; Bua, S.; Angeli, A.; Ferraroni, M.; Nocentini, A.; Casnati, A.; Gratteri, P.; Sansone, F.; Supuran, C. T. Calixarenes Incorporating Sulfonamide Moieties: Versatile Ligands for Carbonic Anhydrases Inhibition. *Chemistry A European Journal* **2022**, *28* (6), e202103527. https://doi.org/10.1002/chem.202103527.

(56) Hernández-Vázquez, E.; Chávez-Riveros, A.; Romo-Pérez, A.; Ramírez-Apán, M. T.; Chávez-Blanco, A. D.; Morales-Bárcenas, R.; Dueñas-González, A.; Miranda, L. D. Cytotoxic Activity and Structure–Activity Relationship of Triazole-Containing Bis(Aryl Ether) Macrocycles. *ChemMedChem* **2018**, *13* (12), 1193–1209. https://doi.org/10.1002/cmdc.201800075.

(57) Zhu, S.; Zhang, J.; Vegesna, G.; Tiwari, A.; Luo, F.-T.; Zeller, M.; Luck, R.; Li, H.; Green, S.; Liu, H. Controlled Knoevenagel Reactions of Methyl Groups of 1,3,5,7-Tetramethyl BODIPY Dyes for Unique BODIPY Dyes. *RSC Advances* **2012**, *2* (2), 404–407. https://doi.org/10.1039/C1RA00678A.

(58) Verma, S.; Sallum, U. W.; Athar, H.; Rosenblum, L.; Foley, J. W.; Hasan, T. Antimicrobial Photodynamic Efficacy of Side-Chain Functionalized Benzo *[a]* Phenothiazinium Dyes. *Photochemistry and Photobiology* **2009**, *85* (1), 111–118. https://doi.org/10.1111/j.1751-1097.2008.00403.x.

(59) Kolb, H. C.; Sharpless, K. B. The Growing Impact of Click Chemistry on Drug Discovery. *Drug Discovery Today* **2003**, *8* (24), 1128–1137. https://doi.org/10.1016/S1359-6446(03)02933-7.

(60) Pezzuoli, D.; Cozzolino, M.; Montali, C.; Brancaleon, L.; Bianchini, P.; Zantedeschi, M.; Bonardi, S.; Viappiani, C.; Abbruzzetti, S. Serum Albumins Are Efficient Delivery Systems for the Photosensitizer Hypericin in Photosensitization-Based Treatments against Staphylococcus Aureus. *Food Control* **2018**, *94*, 254–262. https://doi.org/10.1016/j.foodcont.2018.07.027.

(61) Jung, H. S.; Han, J.; Shi, H.; Koo, S.; Singh, H.; Kim, H.-J.; Sessler, J. L.; Lee, J. Y.; Kim, J.-H.; Kim, J. S. Overcoming the Limits of Hypoxia in Photodynamic Therapy: A Carbonic Anhydrase IX-Targeted Approach. *Journal of the American Chemical Society* **2017**, *139* (22), 7595–7602. https://doi.org/10.1021/jacs.7b02396.

(62) Zhang, Y.; Yang, X.; Yao, Q.; Ma, D. CuI/DMPAO-Catalyzed *N* -Arylation of Acyclic Secondary Amines. *Organic Letters* **2012**, *14* (12), 3056–3059. https://doi.org/10.1021/ol301135c.

(63) Mikhailine, A. A.; Grasa Mannino, G. A.; Colacot, T. J. Catalyst-Directed Chemoselective Double Amination of Bromo-Chloro(Hetero)Arenes: A Synthetic Route toward Advanced Amino-Aniline Intermediates. *Organic Letters* **2018**, *20* (8), 2301–2305. https://doi.org/10.1021/acs.orglett.8b00646.

(64) Frade, V. H. J.; Sousa, M. J.; Moura, J. C. V. P.; Gonçalves, M. S. T. Synthesis, Characterisation and Antimicrobial Activity of New Benzo[a]Phenoxazine Based Fluorophores. *Tetrahedron Letters* **2007**, *48* (47), 8347–8352. https://doi.org/10.1016/j.tetlet.2007.09.108.

Chapter 5: Carbohydrate-based derivatives as immunostimulants against encapsulated bacteria

1. Introduction

Starting from the starch, passing to the cellulose, and ending with the recognition role, carbohydrates are fundamental for life on Earth. For these and many other reasons, carbohydrates are the most abundant biomolecules in the world. A highly regulated multistep process, cellular glycosylation is found in all life forms, though it varies significantly across different taxa[1]. In mammalian cells, glycans can be bonded to proteins and lipids on the cell surface, as well as in the cytoplasm or even the nucleus. In contrast to viruses, which typically exploit the glycosylation machinery of host cells, bacterial species, fungi, and parasites carry their own set of glycosylation enzymes to decorate their surface with glycans. Bacteria, for example, possess a dense glycan coat exposed to their outer surface or as a polysaccharide capsule, and some species even contain properly glycosylated glycoproteins. Each of these glycoforms can engage with the immune system, triggering the generation of antibodies specific to carbohydrates. As a result, they present appealing prospects for the development of vaccines.

1.1 Carbohydrates as immunogenic elements in vaccines

Vaccines are one of the most important tools against pathogens and cancer. The birth of the vaccine is due to Edward Jenner, in 1796, who exploited cowpox to immunize the human body against smallpox. The use of cowpox gives the origin of the name vaccine, which is derived from cow, in Latin *vacca*[2]. Conventional vaccines typically involve using inactivated or weakened forms of pathogens achieved through the reduction of pathogen virulence using physical or chemical means[3]. Advances in science and technology, particularly in immunology and molecular biology, have led to an increased focus on developing subunit vaccines. These vaccines rely on short, specific fragments of pathogens to address the limitations associated with traditional vaccines, such as concerns about low biosafety (risk of reversion to virulence), inefficient pathogen cultivation, and the potential for allergies and autoimmune reactions[4]. Additionally, epitope-based vaccines play a crucial role in current vaccine research, offering several advantages over traditional vaccines. These advantages include heightened specificity, improved safety, simplified production, and storage, as well as enhanced stability. Consequently, epitope-based vaccines have garnered growing interest within the field of vaccine research[5]. Avery and Heidelberger initially proposed the idea of carbohydrate-based antibacterial vaccines in the 1920s[6]. Their groundbreaking work revealed the immunogenic nature of capsular polysaccharides (CPSs) from the Gram-positive bacterium *Streptococcus pneumoniae* and more in general, the CPS of every bacterium. Nevertheless, polysaccharide vaccines, when used independently, demonstrate effectiveness only in adult populations and temporally limited[7]. To overcome this limitation, carbohydrate-based conjugate (glycoconjugate) vaccines have been developed. The fundamental concept involves the covalent linking of a highly immunogenic carrier

molecule, such as a protein, to carbohydrate antigens[8]. To understand this concept, we must understand how the human immune response works.

1.2 Immune response in the human body

The human immune system operates as a complex network of biomolecules and cells responsible for defending the body against both internal and external threats, encompassing bacterial and viral infections, as well as cancer. It comprises two main types of immune responses: innate immunity and adaptive immunity (Figure 1). Innate immunity is triggered by recognizing pathogen-associated molecular patterns (PAMPs), such as glycolipids or nucleic acids, through pattern recognition receptors (PRRs) on the surfaces of macrophages, neutrophils, and dendritic cells[9]. While innate immunity is characterized by a rapid onset, the response lacks specificity and repeated exposure to the same PAMPs results in a consistent immune reaction[10]. In contrast, adaptive immunity targets specific antigens or small-molecule haptens based on the recognition of chemical epitopes and functionalities. Antibodies play a crucial role in the adaptive immune response by precisely identifying surface-exposed chemical epitopes on foreign antigens with high specificity and affinity. The humoral component of the adaptive immune system generates diverse antibody repertoires by maturing and hypermutating B cell receptors after exposure to foreign pathogenic epitopes, facilitated by appropriate costimulatory signals initiated during the innate response[11].

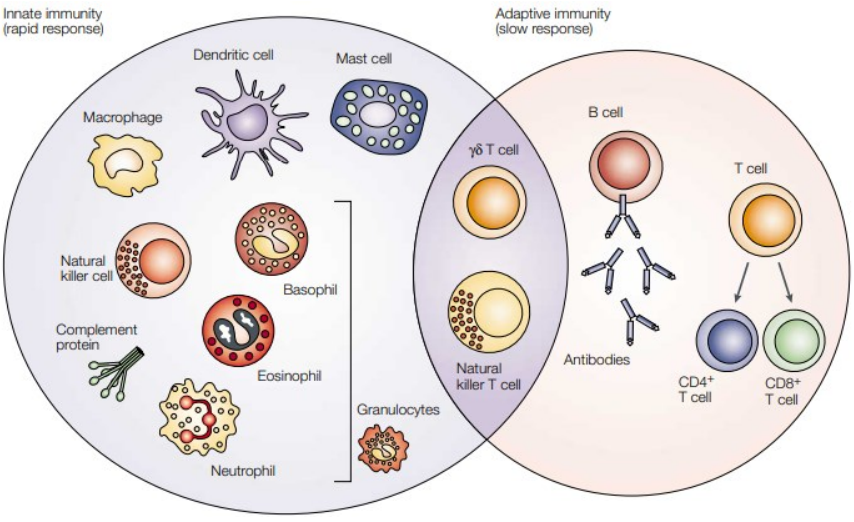

Figure 1: Innate and adaptive immunities. Image taken from reference [12].

Regarding vaccine development, PRR agonists plays a pivotal role as immunogenic carrier molecule[13]. Achieving optimal antigen-specific and memory immune responses constitutes the primary goal of vaccination. While T cells and B cells, key players in the adaptive immune system, carry out these responses, their initiation and quality are predetermined at the innate level. Both macrophages and B cells can function in the antigen-presenting role. However, dendritic cells (DCs)

excel as superior professional antigen-presenting cells (APCs). This superiority is attributed to the unique ability of DCs to sample and present antigens, along with their efficient detection of pathogens through the expression of the previously mentioned PRRs[14].

1.3 Antibodies switching and immunogenic memory[15]

When DCs sample the pathogens, in a few days they are transported to lymph nodes and spleen. Here, thanks to the presence of T cell-dependent antigen, starts the formation of the germinal centers (GCs). At this point, the production of specific antibodies starts through follicular dendritic cells (FDCs), T follicular helper (T_{FH}), and B cells that express antibodies as receptors (BCRs). The germinal center is divided into two regions: light and dark zone (Figure 2).

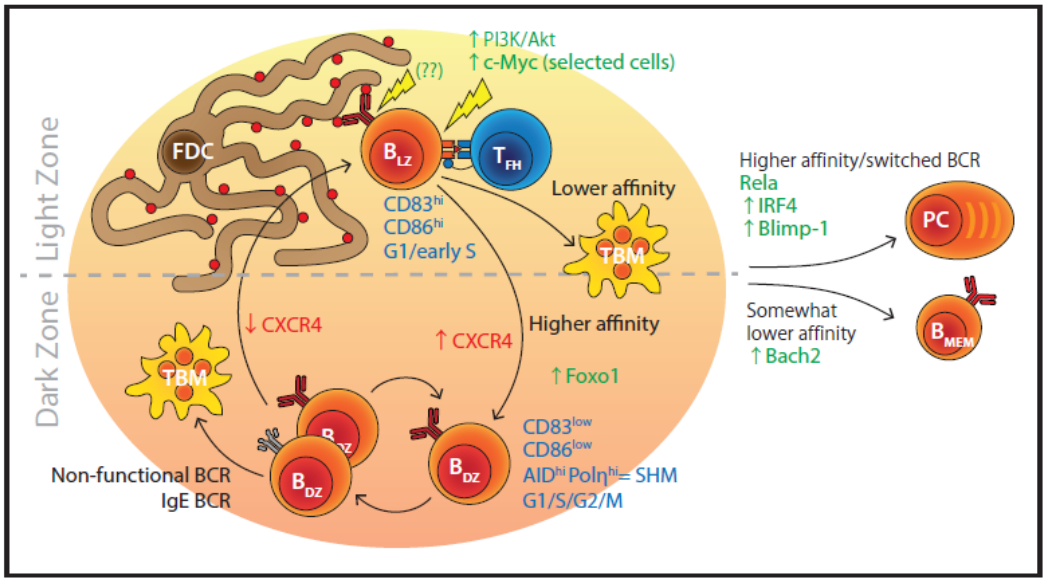

Figure 2: Overview of the GC Reaction. Reprinted from Immunity, 45, Mesin, L.; Ersching, J.; Victora, G. D., Germinal Center B Cell Dynamics, 471, © (2016), with permission from Elsevier.[16].

The light zone is rich in FDC and BCR, the dark zone in T_{FH}. FDC presents the antigen of pathogens, and BCR binds it through the antibody exposed on its surface. The BCR takes up the antigen, processes it, and exposes it on its surface using the major histocompatibility complex II (MHC II)[17]. This complex can interact with T_{FH}, allowing BCR to do not undergo apoptosis. The lack of this interaction does not allow the switching from IgM to IgG, responsible for immunogenic memory. Therefore, the T_{FH} leads the BCR to enter in the dark zone and to be subjected to random mutations of the Ig gene. After the mutation, BCRs move through the light zone and interact again with the antigens exposed by FDC. The BCR with a major affinity presents more antigens to T_{FH} and has more possibilities to reenter the dark zone and start again the process of affinity maturation. Gradually, the BCRs with the highest affinity exit from GC becoming plasma cells and memory B cells.

1.4 Glycoconjugate vaccine

Glycoconjugate vaccines typically consist of three essential components: a carbohydrate antigen, a carrier molecule, and a linker[18]. In the development process of these vaccines, the initial step is to identify the target antigen, conserved, and exposed on the cell surface to facilitate immune recognition. Following this, the appropriate carrier molecule is selected to serve as an immunostimulator, enhancing the immunogenicity of the system that, otherwise, if simply based on carbohydrate antigen would be weak. The final step involves identifying a linker for coupling the carbohydrate antigen and the carrier molecule, guided by conjugation chemistry and related reaction conditions. Licensed in Cuba in 2004, Quimi-Hib[19] (Figure 3) is a glycoconjugate vaccine representing a milestone as the first licensed vaccine of its kind based on a synthetic carbohydrate antigen. Comprising a synthetic antigen with an average of seven repeating units of ribosyl rybitol phosphate, this vaccine is conjugated to a thiolated TT (tetanus toxoid) carrier protein through a 3-(maleimido)-propylamide linker. The synthesis of the poly(ribosyl ribitolphosphate), a crucial component of Quimi-Hib, involved a large-scale production achieved through a one-step polycondensation reaction.

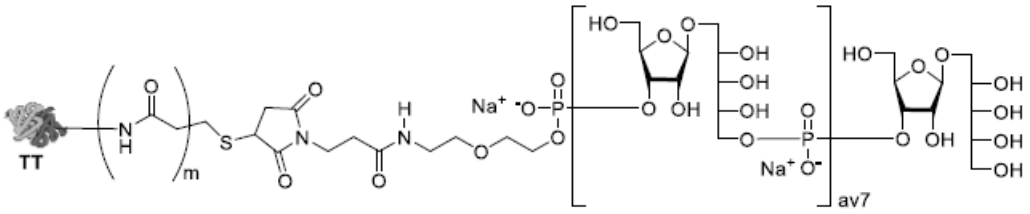

Figure 3: Chemical structure of Quimi-Hib. Image taken by reference [20].

We can categorize glycoconjugate vaccines into three distinct types based on the properties of carbohydrate antigens, carrier molecules, and preparation methods[18].

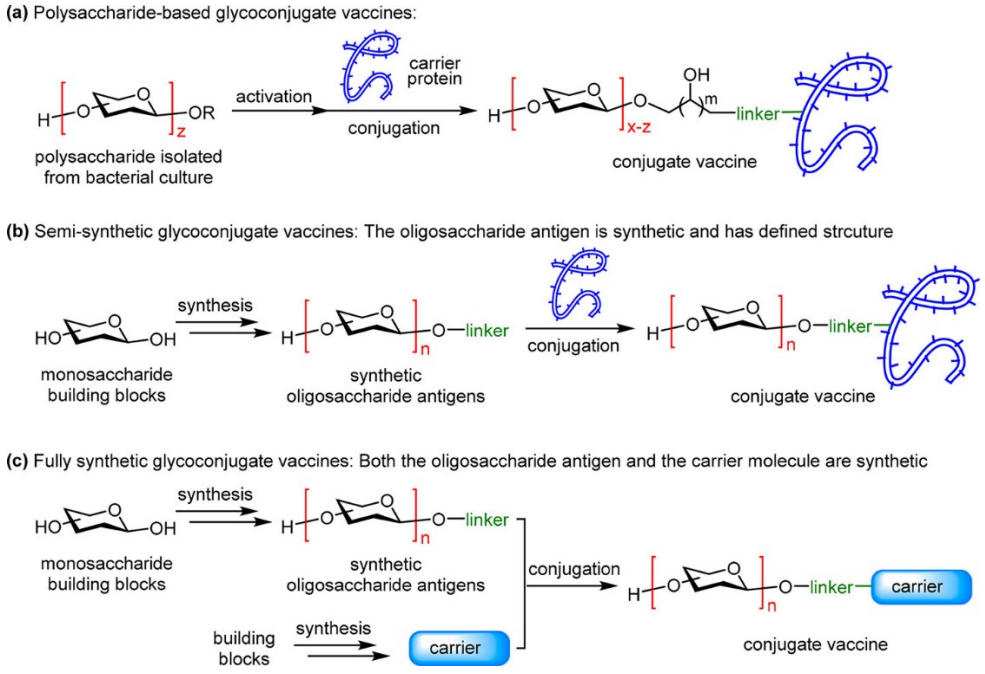

Figure 4: Three major classes of glycoconjugate vaccines. Image taken by reference[18].

One type of glycoconjugate vaccine involves polysaccharides derived from natural sources, such as bacterial cultures, directly conjugated with carrier proteins[21]. Another type, known as semi-synthetic conjugate vaccines (Figure 4b), comprises synthetic oligosaccharide antigens linked to carrier proteins, where the structure of carbohydrate antigens and their linkage to carrier proteins are well-defined, although the protein's conjugation sites are usually undefined (an example is Quimi-Hib). The third type of glycoconjugate vaccines (Figure 4c) features synthetic carbohydrate antigens conjugated with synthetic carrier molecules like lipids, glycolipids, glycopeptides, and synthetic oligosaccharides, as well as other synthetic materials, and are referred to as fully synthetic glycoconjugate vaccines. An example is the monophosphorylated derivative of *Neisseria meningitidis* lipid A (MPLA) as a completely synthetic immunostimulant (Figure 5). Differing from conventional protein conjugate vaccines, this investigation utilized the bacterial antigen α-(2→9)-polysialic acid, focusing specifically on the CPS of serotype C of *Neisseria meningitidis*, as a model to assess the immunogenicity of MPLA conjugates[22].

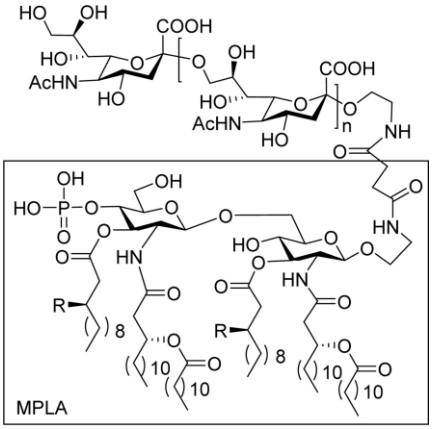

Figure 5: synthetic glycoconjugates containing the repeating unit of CPS of serotype C of Neisseria meningitidis. Image taken by reference[22].

1.5 Carbohydrates in Gram-positive and Gram-negative bacteria

The ubiquity of bacteria, their synergy with the environment, and with many living things are a consequence of their essentiality for life on Earth. We can identify two main classes of bacteria: Gram-positive and Gram-negative bacteria (Figure 6).

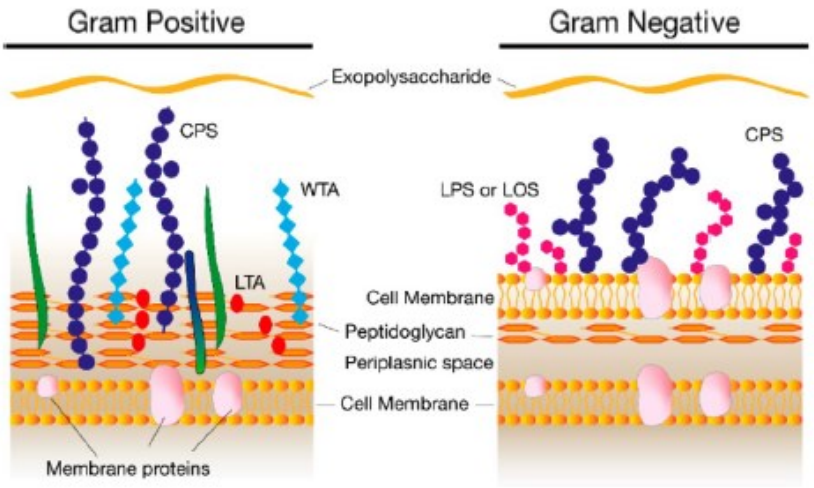

Figure 6: Gram-positive and Gram-negative bacteria. Image taken by reference[23].

The bacterial cell wall is encased in a dense layer comprising polysaccharides and glycoproteins, recognized as the glycocalyx. This configuration enables bacteria to not only thrive in their surroundings but also facilitates the exchange of nutrients from the external environment and the elimination of internal waste products. Typically, the outermost surface of both Gram-positive and Gram-negative bacteria displays capsular polysaccharides (CPS)[24] which can exhibit varying structures even within the same bacterial species, allowing for their utilization in serotyping. In the case of Gram-negative bacteria, there is an outer membrane (OM) housing lipopolysaccharide (LPS), CPS, and proteins (Figure 6). A thin peptidoglycan layer is positioned between the OM and the inner

cytoplasmic cell membrane. Conversely, Gram-positive bacteria lack an outer membrane and are enveloped by a considerably thicker layer of peptidoglycans compared to their Gram-negative counterparts. Carbohydrates perform several important roles in bacteria's life, from protection against ionic and mechanical stress to the communication and recognition role[1]. Capsular polysaccharide has critical roles in interaction with the human body: bacterial adhesion, host cell infection, and protection against the immune defense[25]. Due to the efficient way they infect the human body, in third and sixth position of the list of the causes of mortality, there are two diseases caused by bacteria: lower respiratory (i.e., *Streptococcus pneumoniae*) infections and diarrhea[26].

1.6 Streptococcus pneumoniae and serotype 19F

S. pneumoniae, identified as a Gram-positive organism, significantly contributes to a spectrum of illnesses, encompassing pneumonia, otitis media, meningitis, and septicemia[27]. The virulence of pneumococci is ascribed to various elements, including the variable capsular polysaccharide (CPS), pneumolysin toxin, and surface lectins. Bentley and colleagues meticulously deciphered the DNA sequence of capsular biosynthesis genes for all 90 serotypes of *S. pneumoniae*, revealing a distinctive CPS composition for each serotype[28]. In children, a handful of types, such as 6A, 14, 19F, and 23F, are responsible for a significant portion of pneumococcal diseases, constituting almost 60% of all infections. Conversely, in adults, serotypes 3, 19F, and 6A only accounted for 31% of isolations[29]. Among these serotypes, 19F is particularly virulent causing numerous upper respiratory and meningitis infections, especially in children and immunodeficient individuals. It is characterized by a trisaccharide repetitive unit illustrated in Figure 7, comprising *N*-acetylmannosamine unit linked by a β 1-4 linkage to glucose, connected with α 1-2 linkage to rhamnose. The repetitive trisaccharide units are linked together through a phosphate group connecting the anomeric position of the α-rhamnose with position 4 of ManNAc.

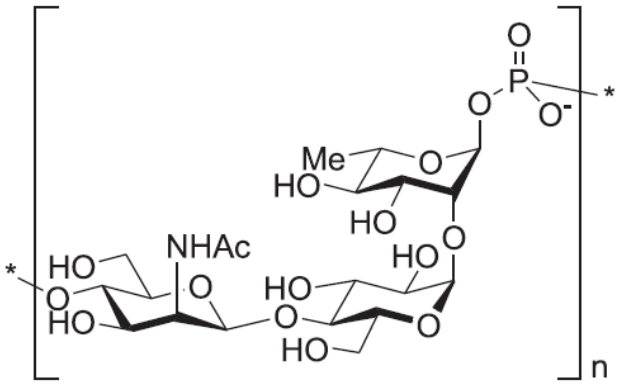

Figure 7: Molecular structure of 19-SP CPS repeating unit

The first-generation carbohydrate-based vaccine against *S. pneumoniae*, PPV23 (Pneumovax®, Merck), covers the 23 most prevalent serotypes and is available in the United States and Europe, though conflicting efficacy data have been reported[30]. To enhance immunogenicity, licensed glycoconjugate vaccines like PCV7 (Prevnar®), PCV13 (Prevnar 13™), and PCV10 (GlaxoSmithKline's Synflorix™) have been developed and commercialized. Despite the incorporation of *S. pneumoniae* CPS-based glycoconjugate vaccines into routine immunization programs and the broader coverage of strains, concerns persist regarding diseases caused by serotypes not addressed by the existing vaccines in the long term[31]. Moreover, Seeberger et al. successfully synthesized the hexasaccharide repeating unit of *S. pneumoniae* serotype 12F, a serotype not included in marketed formulations[32].

1.7 *Campylobacter Jejuni* and serotypes HS 23/36

Diarrheal diseases pose a significant public health challenge, ranking second among the leading causes of death in children under five years and sixth in the global burden of disability-adjusted life-years (DALY)[33]. Six pathogens account for 78% of all attributable diarrhea, with Campylobacter spp. being one of them[34]. Campylobacter spp. are estimated to cause approximately 400 million cases of campylobacteriosis each year[35], and 90% of these cases are attributed to the enteric Gram-negative bacterium (GNB) *Campylobacter Jejuni*. While campylobacteriosis is generally considered self-limiting, it has been linked to various post-infection chronic sequelae, including Guillain−Barré autoimmune syndrome (GBS), with an estimated prevalence of 1/1000 cases of *C. jejuni* infection[36]. Indeed, *C. jejuni* lipooligosaccharides (LOSs), a truncated form of lipopolysaccharides (LPSs), contain α-*N*-acetyl-D-neuraminic acid (α-Neu5Ac) moieties that mimic gangliosides[37]. Gangliosides are glycosphingolipids abundant in the human peripheral nervous system. Notably, this molecular mimicry is not limited to specific *C. jejuni* strains. An effective strategy currently advocated for minimizing *C. jejuni* infections involves the development of vaccines designed for human use. However, a significant challenge in this endeavor is the production of lipooligosaccharides (LOSs) that mimic human gangliosides by this enteric Gram-negative bacterium (GNB). This obstacle poses a substantial barrier to the development of immunoprophylactic tools due to the potential risk of triggering Guillain–Barré syndrome (GBS). Consequently, live attenuated and killed whole-cell vaccines are discouraged, with subunit vaccines emerging as a safer alternative. A significant structural modification is the incorporation of O-methyl phosphoramidate (MeOPN) moieties at diverse positions in these polysaccharides, with up to 70% prevalence in *C. jejuni* isolates. Remarkably, this feature has never been detected in any other living organisms until now. Among the most diffuse serotypes of *C. Jejuni*, HS 23/36 is the only one of which we know the stereochemistry of the phosphoramidate making it the most reproducible repeating unit of CPS[38]. It is characterized

by a trisaccharide repetitive unit illustrated in Figure 8, comprising N-acetylglucosamine units linked by a β 1-3 linkage to galactose with a phosporoamidate in position 2,4 or 6, connected with α 1-2 linkage to altroheptose. One unit is connected to another unit between the reducing end of altroheptose to position 3 of N-acetylglucosamine.

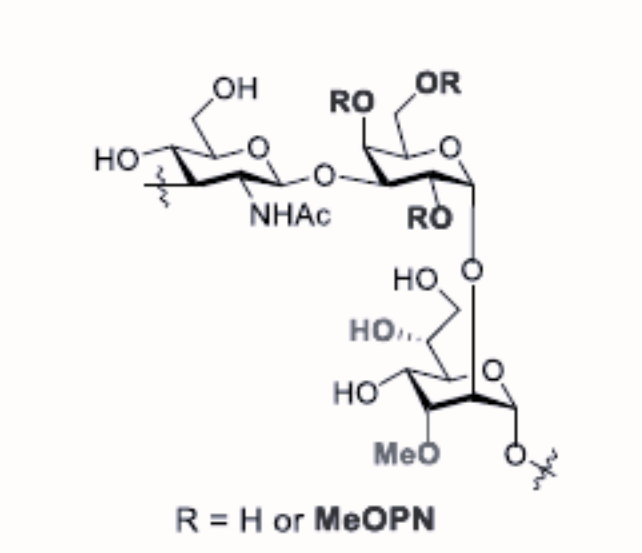

Figure 8: molecular structure of C. Jejuni HS 23/36 CPS repeating unit. Image adapted by reference[39].

Guerry and colleagues demonstrated the feasibility of CPS-based vaccines against *C. jejuni* in 2009 by creating a glycoconjugate, $CPS_{81\text{-}176}$-CRM_{197}, administered subcutaneously to mice[40]. This conjugate not only provided significant protection upon intranasal challenge with homologous *C. jejuni* strains but also ensured complete protection against diarrheal disease in the New World monkey *Aotus nancymaae* model following orogastric challenge with C. jejuni strain 81-176 (serotype HS23/36). The dose-dependent production of CPS-specific IgG further underscored its efficacy. Despite its promising outcomes in a non-human primate model, a phase 1 clinical trial in 2014 (ClinicalTrials.gov NCT02067676) yielded limited immune responses in most subjects. This was attributed to the absence of MeOPN moieties on isolated CPS[41].

1.8 Calix[n]arenes as immunostimulant

The previous paragraph reported several times on the use of CPS as antigen for the production of antibodies against bacteria. Anti-carbohydrate antibodies often display affinities that are several factors lower compared to their protein- and peptide-specific counterparts. The distinctive limitation observed in the affinity of anti-carbohydrate antibodies finds partial compensation through their multivalent nature. These antibodies adopt a clustered configuration, confronting numerous densely displayed antigen molecules simultaneously, thereby amplifying the impact of the immune response. This phenomenon deals with the so-called glycoside cluster effect[42], actually identified in the recognition process occurring between carbohydrate binding proteins and their saccharide substrates.

As described in the introduction of the thesis, the calixarene scaffold results in a good platform for the presentation of multiple units of saccharides. Based on the efficiency of the calixarenes as scaffolds to exploit the glycoside cluster effect, Geraci *et al.*[43] designed, synthesized, and studied a calix[4]arene-based immunostimulant. In this work, calix[4]arene was functionalized at the upper rim with four units of Tn antigen (red) and at the lower rim with an immunoadjuvant moiety (green), tripalmitoyl-S-glycerylcysteinyl-serine (P_3CS) (Figure 9).

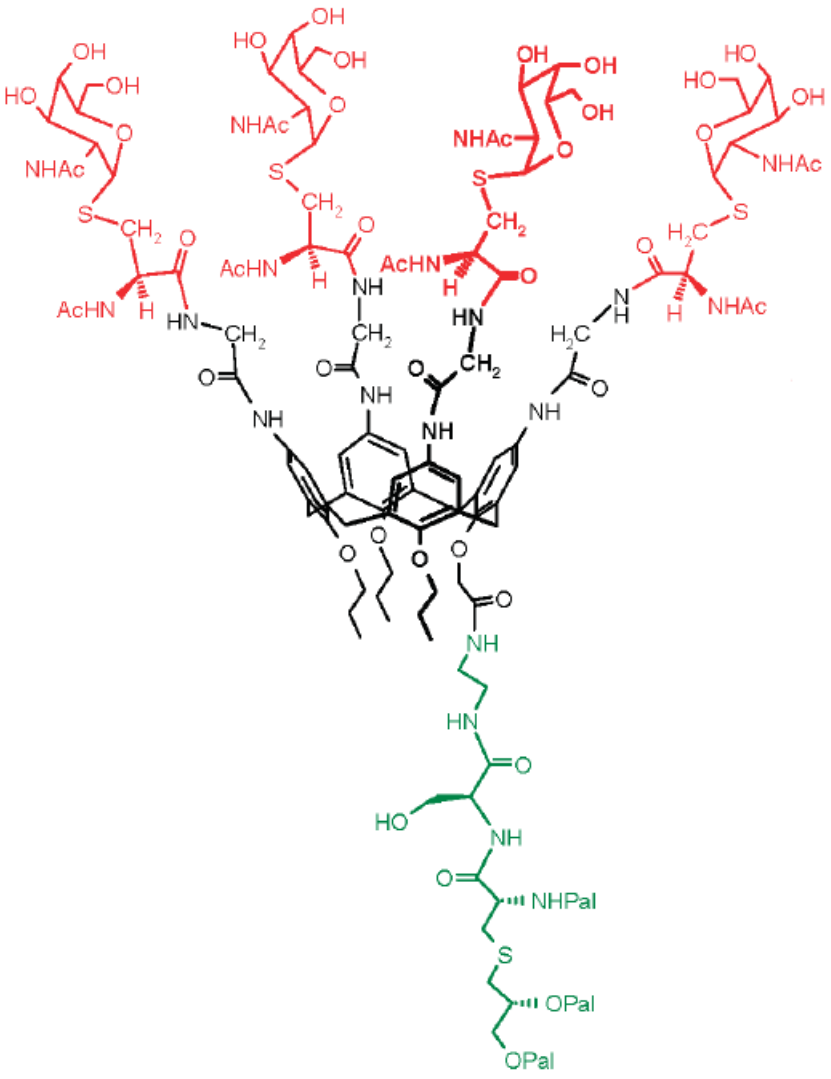

Figure 9: Structure of calixarene-based vaccine proposed by Geraci. Image taken by reference[43].

Specific tumor-associated carbohydrate antigens (TAs) such as Tn, cryptic in normal epithelial cells, are overexpressed on the surface of tumor cells as portion of a great family of glycoproteins, the mucines. TAs are autoantigens showing a weak immunogenicity and the presence of adjuvant plays an important role in immunostimulation. The efficiency of calixarene was evaluated by the ELISA assay with sera of the groups of immunized mice. The value of IgG in the mice immunized with the

calixarene vaccine candidate was 2-fold higher compared to that observed upon treatement with the monovalent analog using the same equivalents of saccharide (0.120 μM/mouse for monovalent and 0.030 μM/mouse for tetravalent), showing the presence of the glycoside cluster effect.

The study of the calixarene as a scaffold to exploit the cluster effect, exploring different geometries, was performed by my research group, in collaboration with Federica Compostella's research group at the University of Milan[44]. In that work, different geometries of calix[4]arene (1,3-alternate, mobile, cone geometries) and calix[6]arene functionalized at the upper rim with N-acetyl-β-D-mannosamine residues were investigated (Figure 10). As mentioned before, this sugar is one of the three saccharides of the repeating unit of the *Streptococcus Pneumoniae* serotype 19F (SP 19F) CPS (Figure 7). Among the three monosaccharides, β-ManNAc is supposed to be the immunodominant element.

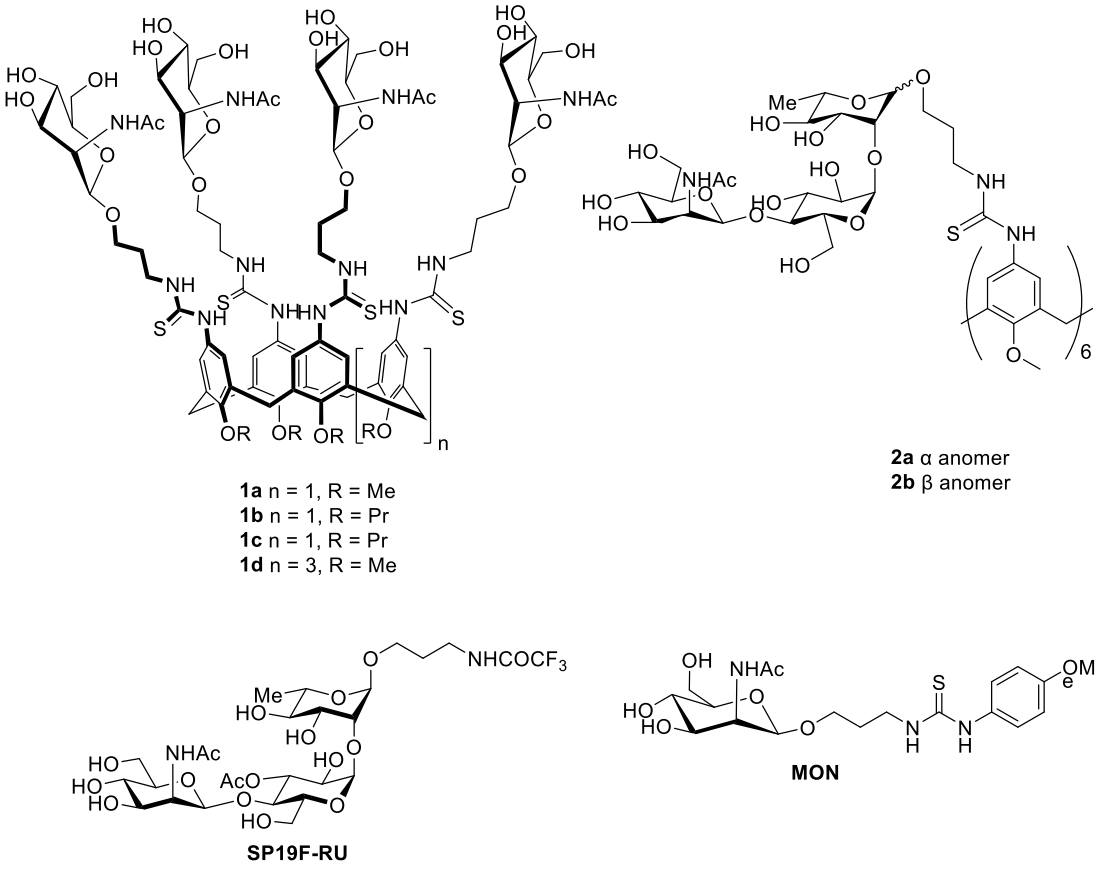

Figure 10: Molecular structures of calixarenes synthesized by our research group

Through competitive ELISA assays, the ability of those multivalent systems to inhibit the binding of anti-19F antibodies to SP 19F native polysaccharide linked to the plate surface was studied. All the calixarenes showed a better inhibition ability compared to the monovalent analog **MON** (Table 1). In particular, the blocked geometries **1b** and **1c** displayed a low efficacy compared to the mobile isomer **1a** which evidently can adapt itself for better interaction with the antibodies as it allows the epitope

units to better adapt to the binding sites. Compound **1d** resulted in a better scaffold compared to **1a** for the presence of two more units of saccharide.

Compound	IC_{50} (mg/mL)	Max inhibition (%)
19F	1.8×10^{-4}	100 ± 2
1a		34 ± 7
1b		10 ± 2
1c	1.2×10^{-1}	21 ± 3
1d	9.5×10^{-2}	48 ± 8
MON		16 ± 7
SP19F-RU	2.1×10^{-2}	52 ± 4
2a	1.9×10^{-3}	78 ± 8
2b	8.6×10^{-4}	75 ± 7

Table 1: Results of the competitive ELISA assay

Calix[6]arenes **2a** and **2b** functionalized with the α and β anomer, respectively, of the trisaccharide showed an inhibition ability 1.5-fold higher compared to the SP 19F repeating unit **SP19F-RU** and close to the 80% of inhibition with respect the natural CPS despite the rather limited number of repeating trisaccharide units exposed (4 or six). In general, it had been concluded that the conformationally mobile derivatives, in particular the calix[6]arene-based ones, were promising compounds because they seem to well reproduce the CPS folding and exposure to the specific antibodies. Therefore, they deserved further studies as potential immunostimulant compounds.

The interesting ability of calixarene-based derivatives to act as immunostimulants was recently reaffirmed by da Silva Neto *et al.*[45] who synthesized two calixarenes as anti-cocaine vaccines. In this work, calix[4]- and calix[8]arene were functionalized at the lower rim with n-butyl groups to conserve the cone geometry and at the upper rim with cocaine units linked through hexanoic acid as spacer. The goal of this work was to modulate the biodistribution of cocaine with antibodies avoiding the overcome of blood-brain barrier (BBB). The test was performed by injection of calixarene in mice showing a high production of IgG against cocaine. The immunized mice were subjected to brain scintigraphy, after the administration of cocaine analog ^{99m}Tc-TRODAT-1, to evaluate the biodistribution showing a low level of this analog in the brain.

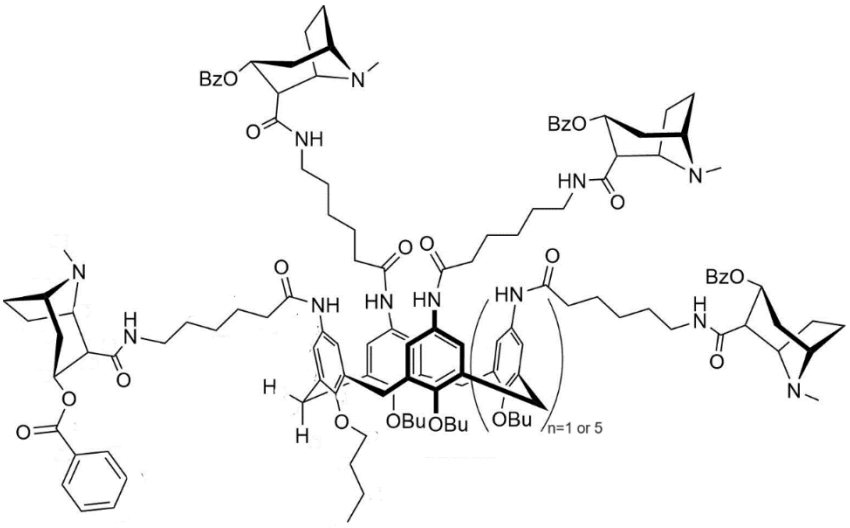

Figure 11: The two anti-cocaine vaccines proposed by da Silva Neto. Image adapted by reference[45].

Based on the results reported in the literature and the work of our research group, we designed two compounds, calix[4]- and calix[6]arene functionalized with the same trisaccharide of the repeating unit of the SP 19F CPS, prepared by Federica Compostella's research group.

During my period abroad, at the Institut Pasteur by the Laurence Mulard's research group, I took part to the synthesis and scale up of a trisaccharide for the development of a vaccine against *C. jejuni* HS 23/36. In perspective this could be linked to a calixarene scaffold.

2. Results and discussions

2.1 Calix[n]arene as immunostimulant of antibodies against SP 19F

As described in the introduction of this chapter, my research group explored the calixarene as a scaffold to exploit the glycoside effect for interaction with antibodies against SP 19F[44]. This work led to the conclusion that conformationally free calixarenes are the best scaffold for this goal. We started from this evidence to design, in collaboration with Federica Compostella (University of Milan), two glycocalixarenes (**3** and **4**, Figure 12) with the aim of verifying their ability of stimulating the production of antibodies against SP 19F. At the same time, two galactosylated analogues (**5** and **6**) were prepared to use as negative control.

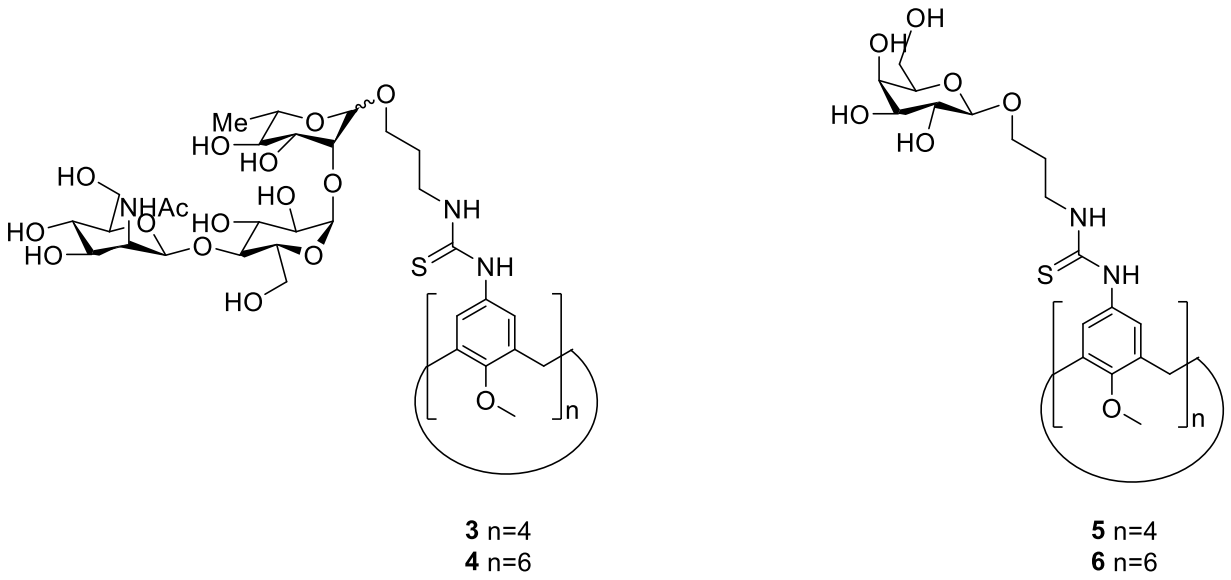

Figure 12: Molecular structure of target compounds.

The two target compounds **3** and **4** were designed with methoxy groups at the lower rim of calixarene scaffolds and with the trisaccharide as immunogenic elements exploiting the aminopropyl linker.

To establish the immunogenicity of trisaccharide and to exclude a possible effect by the simple calixarene scaffolds, the two negative controls **5** and **6** were designed based on the same calixarene scaffolds as **4** and **5** but bearing a non-related sugar (galactose) with the same aminopropyl linker.

2.1.1 Synthesis of potential immunostimulants 3 and 4

The conjugation between calixarene scaffolds and sugar moieties was performed exploiting the click reaction between the aminopropyl linker on trisaccharide **7** and the isothiocyanate units on calixarene scaffolds **8** and **9**. The trisaccharide was prepared by Federica Compostella's research group following the procedure reported in literature[46] and exploiting the same modification performed in the previous work[44]. Using the procedure reported in literature[44], the calix[4]arene **8** and the calix[6]arene **9** were synthetized and exploited to obtain the glycocalixarenes **3** and **4** (Scheme 1).

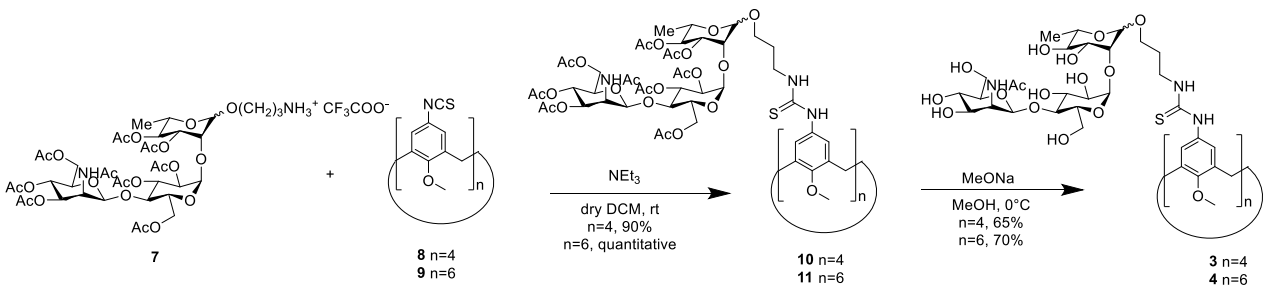

*Scheme 1: Synthetic route of immunostimulant targets **3** and **4**.*

The trisaccharide unit **7** was used as a mixture of anomers because, in the previous work, the data collected by ELISA tests suggested no preferential affinity between anti-SP 19F antibodies and a

specific anomer. The synthesis of the two glycocalixarenes was performed with the same method but, for glycocalix[4]arene **8** was necessary a higher amount of trisaccharide per unit of isothiocyanate (1.5) compared to the synthesis of glycocalix[6]arene **9** (1.25 eq). This could be explained by the lower reactivity for the complete functionalization of scaffold **8** due to major steric hindrance compared to the calix[6]arene **9**. In fact, the structure of the calix[6]arene **9** is more flexible compared to the calix[4]arene **8**. This phenomenon is observable also through the ^{1}H NMR comparison between calixarenes **8** and **9**. For simplicity, analysing the aromatic peaks, the calixarene **8** has four peaks due to the interconversion between the cone conformer and the partial cone conformer (in ratio 4:1, respectively), in deuterated chloroform at 25°C. On the other hand, at the same temperature and the same solvent, the higher flexibility of the calix[6]arene **9** leads to obtain sharp singlets for the aromatic hydrogen to the ^{1}H NMR analysis (Figure 13).

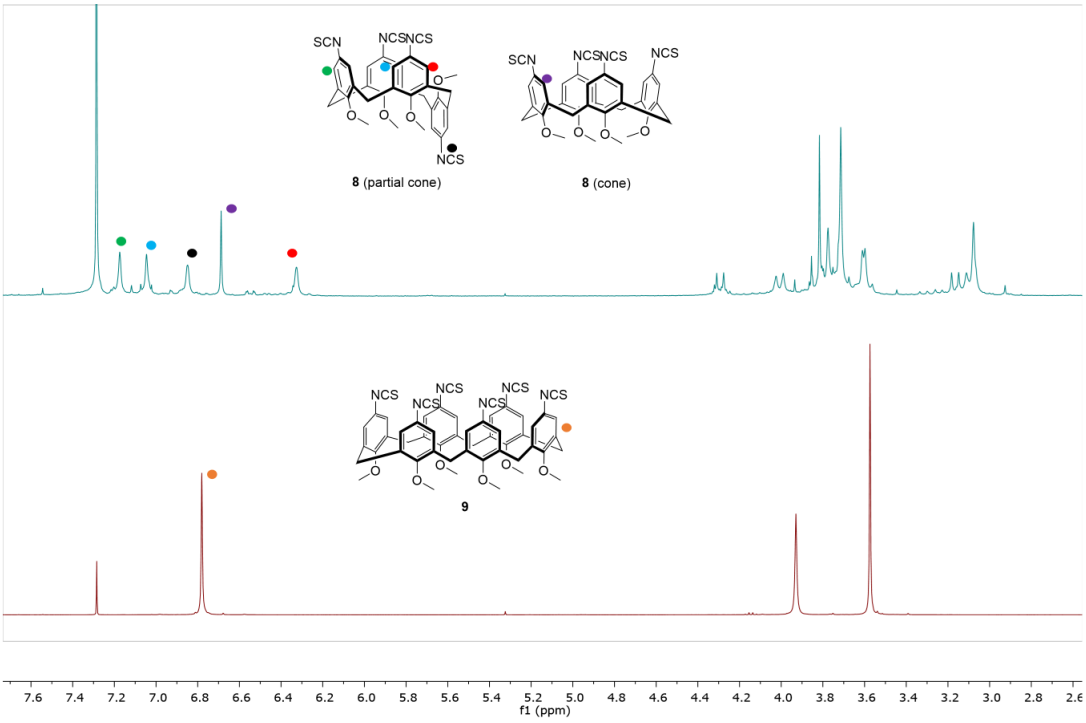

*Figure 13: ^{1}H NMR spectra of calixarene scaffolds **8** and **9** in $CDCl_3$ (400 MHz, 298K)*

For both compounds, the ^{1}H-NMR spectra and mass analysis confirmed the successful outcome of the coupling reactions. In the Figure 14, it is reported the spectrum of the new synthetized glycocalix[4]arene **10**. The broad signals for the aromatic protons indicate a slow interconversion between the partial cone and the cone conformers generating a beginning of coalescence.

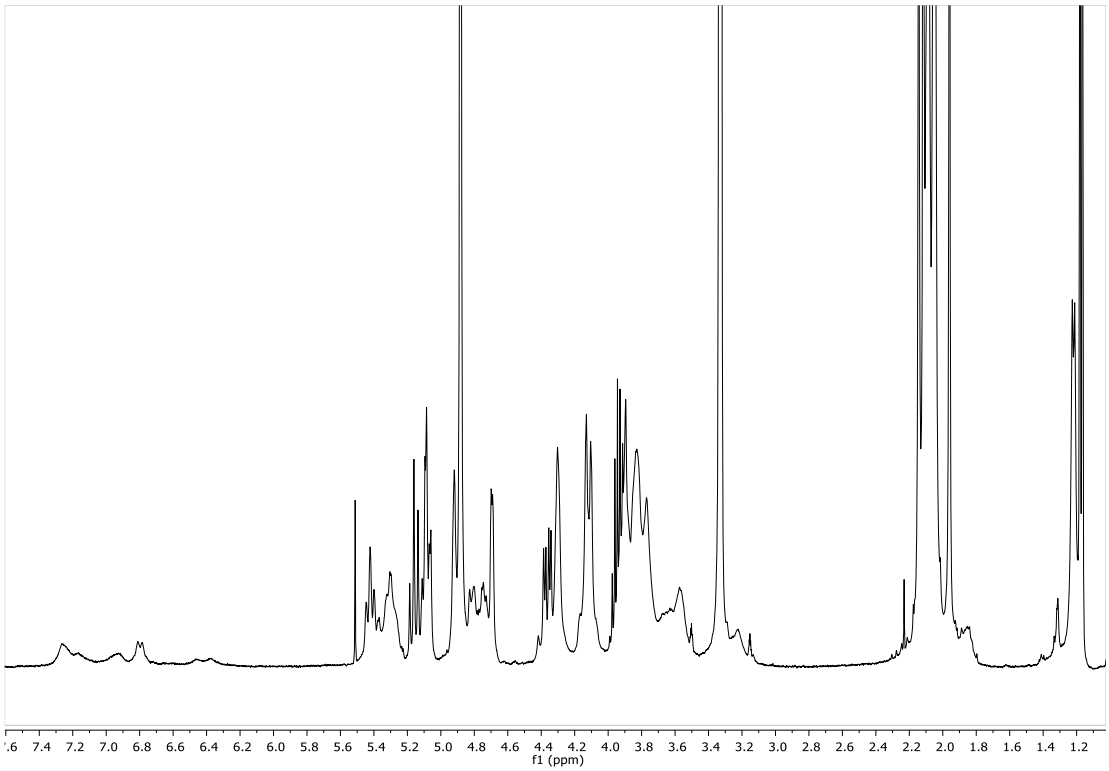

*Figure 14: ^{1}H NMR spectra of glycocalixarene **10** in MeOD (400 MHz, 298 °K)*

Through the Zemplen deacetylation[47], we obtained the two target compounds **3** and **4**. These reaction were carried out at 0 °C to avoid possible epimerization on thioureidomannosides, as reported in literature[48]. Compound **3** was fully characterized by NMR and HRMS; the spectroscopic data recorded for compound **4** are in agreement with those reported in literature[44]. Moreover, the ^{1}H-NMR comparison of the two target compounds demonstrates the higher flexibility of the larger glycocalixarene **4** (Figure 15). In fact, the presence of several broad signals for the aromatic peaks in spectrum of the compound **3** means that the conformational freedom is lower compared to compound **4** the aromatic protons of which result in a single broad signal.

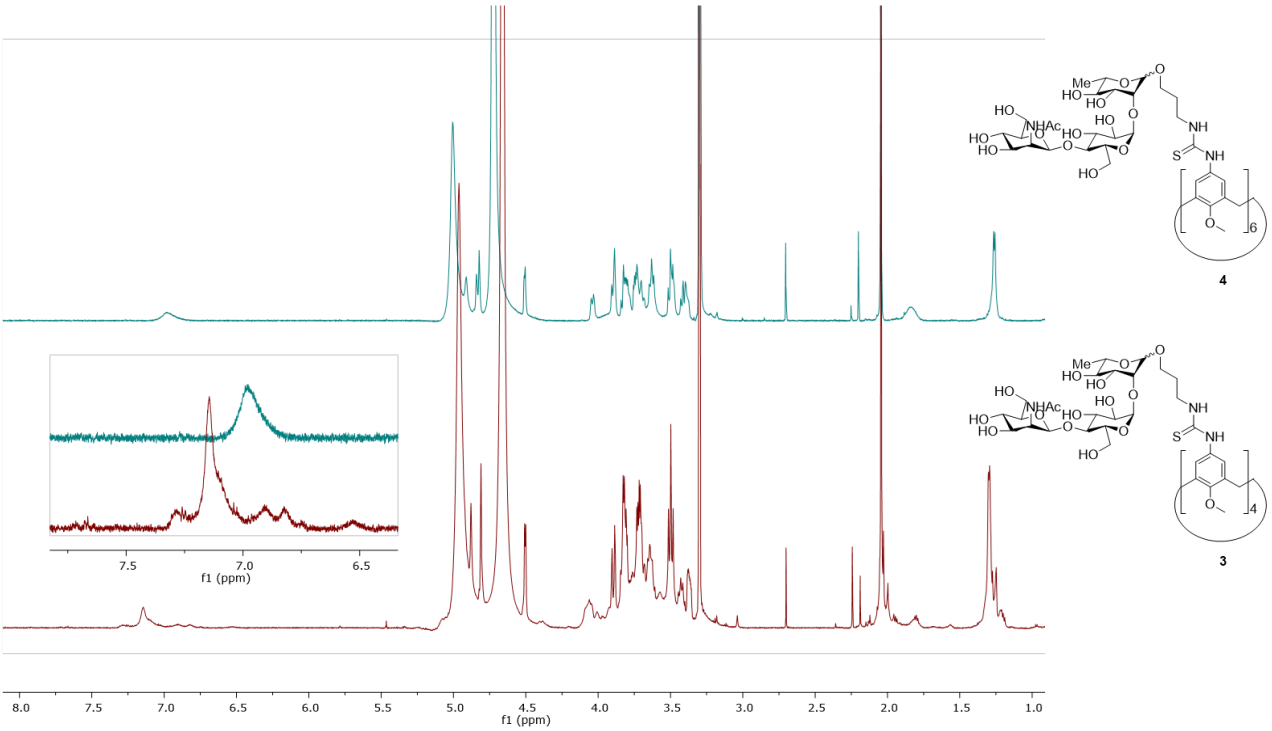

*Figure 15: ^{1}H NMR spectra of calixarenes **3** and **4** in mixture D_2O/MeOD (600 MHz, 298K); in the inset, the signals relative to the aromatic protons.*

2.1.2 Synthesis of galactocalixarenes as negative control

To synthetize the two negative controls, we started by the functionalization of galactose with aminopropyl linker protected with Boc group (Scheme 2).

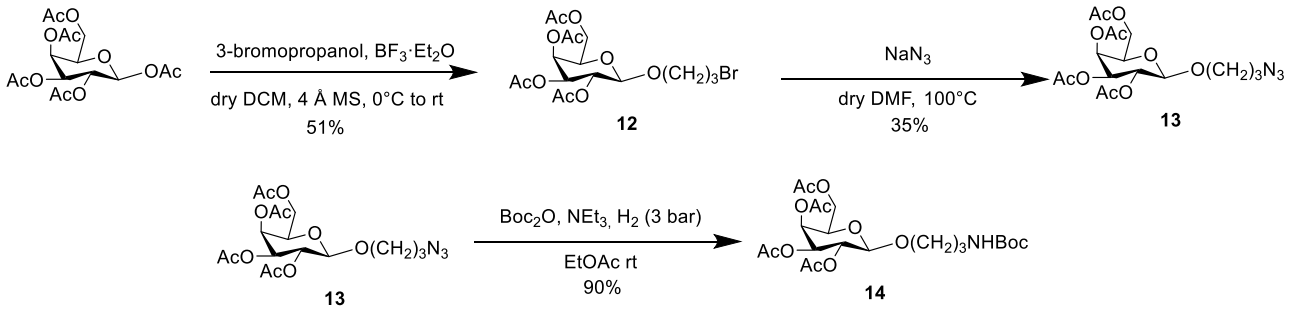

Scheme 2: The functionalization with linker.

Starting from β-D-galactose pentaacetate, a glycosylation reaction with 3-bromopropanol and BF_3•Et_2O as promoter was carried out. The product was purified and used directly to obtain the azido derivative **13** by displacement of bromine, as reported by Joosten *et al*[49]. Then, the azido group was reduced and protected in the same step to obtain the Boc protected amine **7**, as reported by Szekely *et al*[50]. The necessity to protect amine is due to the degradation of product during the reaction probably caused by the side reaction between amine and ester groups on sugar. The ^{1}H-NMR spectrum of compound **14** confirms the presence of the product by diagnostic signal associated to Boc group and to the signal of the hydrogen of urethane group (Figure 16).

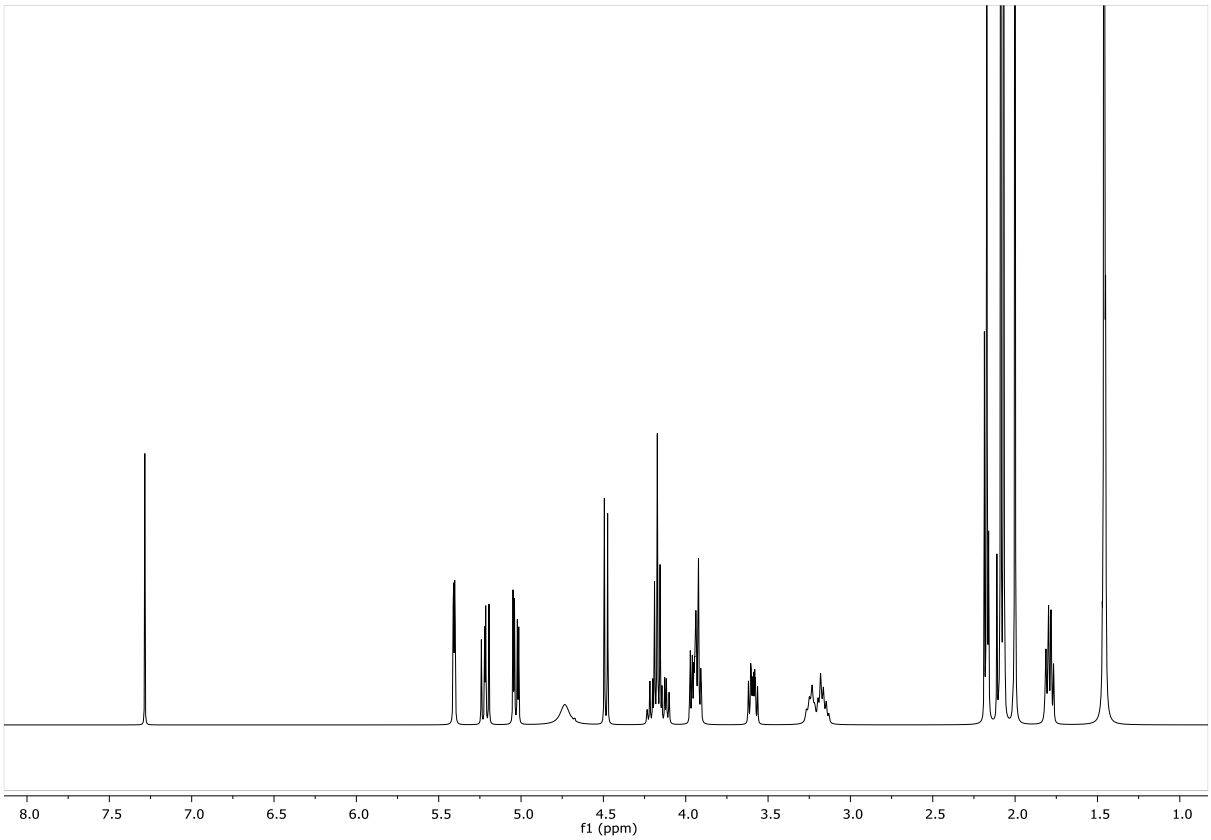

*Figure 16: ^{1}H NMR spectrum of compound **14** in $CDCl_3$ (400 MHz, 298K).*

To obtain the glycocalixarenes **5** and **6**, the first step is the deprotection of compound **14** from Boc group, performed without solvent and using HCl in gas phase (Scheme 3), as reported by Verscheuren *et al*[51].

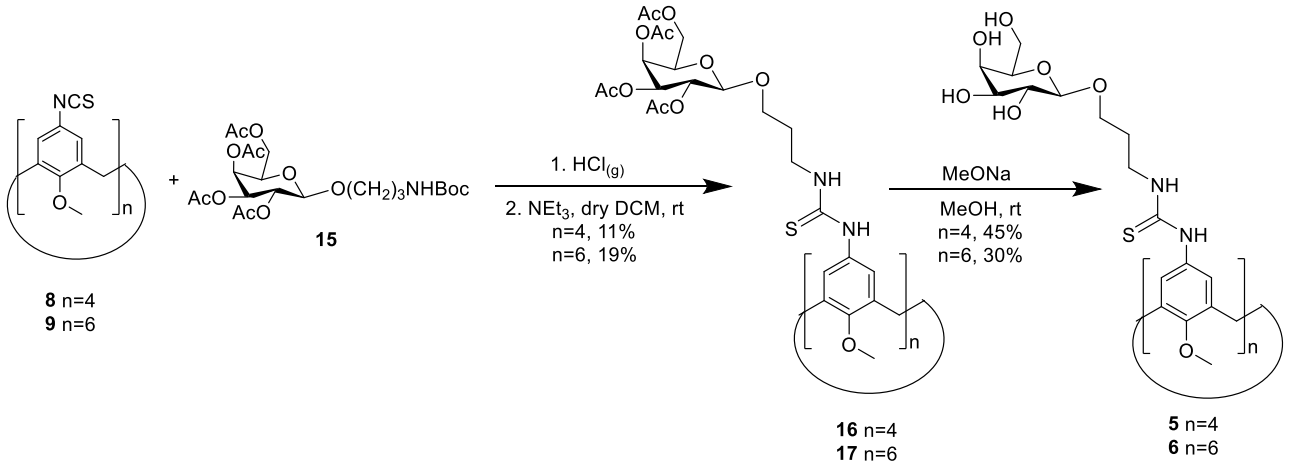

Scheme 3: Synthesis of negative controls.

This unusual method to deprotect the Boc group was exploited to compensate the unsuccessful trial performed to obtain the compound **16** and **17**. The deprotection using trifluoroacetic acid was performed several times but we never isolated the conjugated products. The conjugation reaction, performed through the method reported in the scheme, allowed us to obtain compound **16** and **17** with

low yields. The product **16** and **17** were characterized by NMR and ESI-MS. During the characterization by NMR, for compound **16** we could observe significant changes in the spectra depending on the solvent and temperature (Figure 17).

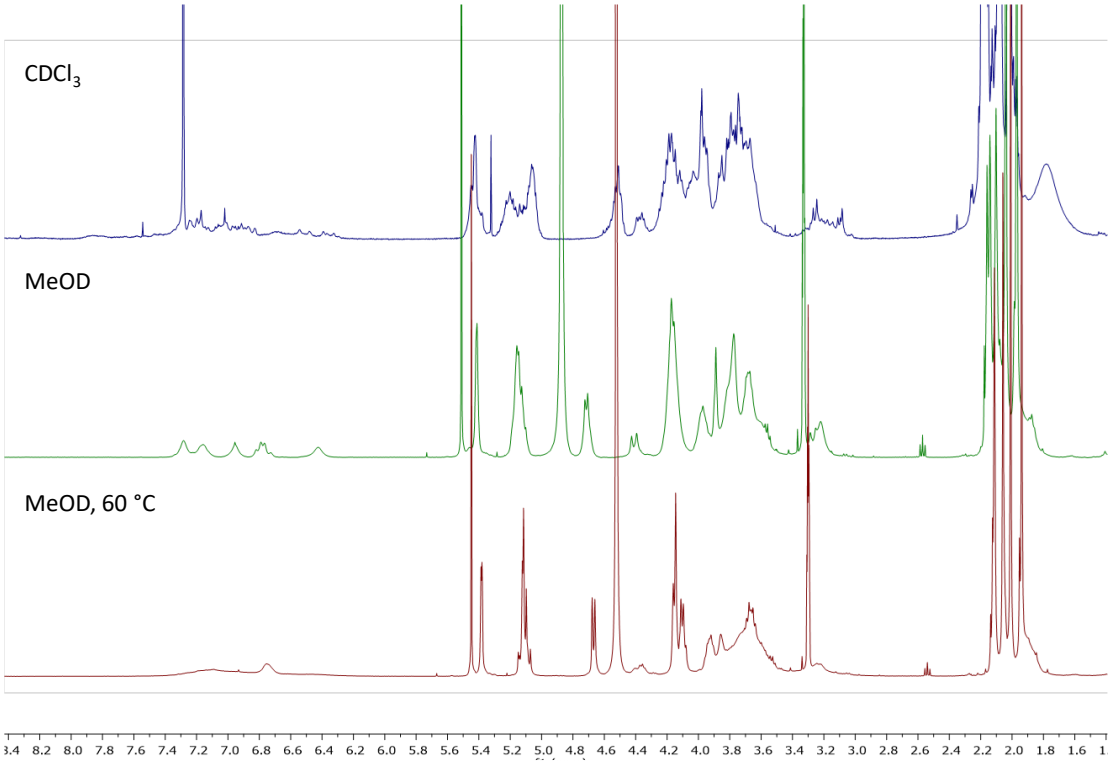

Figure 17: ^{1}H NMR spectra of compound 16. Top: in $CDCl_3$ (298 K, 400 MHz); in the middle: MeOD (298 K, 400 MHz); bottom: MeOD (333 K, 400 MHz)

The presence of several aromatic signals in chloroform suggests that the presence of hydrogen bonds (for example between thiourea and acetyl groups) interferes with the mobility of calixarene **16**. This assumption was validated by using methanol as solvent. In fact, this solvent can break the hydrogen bonds increasing the flexibility of glycocalixarene **16** as conformed by the presence of aromatic signals, like the pattern recorded in methanol for compound **10**. The mobility of calixarene scaffold was further increased by temperature, recording the ^{1}H NMR spectrum at 60 °C. In this condition, the signal associated to the sugar moiety became sharper and the aromatic signals resulted closer to coalescence. The behaviour of this compound makes impossible the ^{13}C-NMR analysis.

Also, glycocalixarene **17** was analysed by ^{1}H-NMR in chloroform and in methanol showing a different behaviour compared to **16** (Figure 18). In fact, in $CDCl_3$ there are one broad signal for the aromatic protons indicating a faster conversion among conformers while in methanol the same signal becomes sharper confirming an increasing mobility due to the absence of intermolecular hydrogen bonds. For this compound, ^{13}C-NMR characterization was possible.

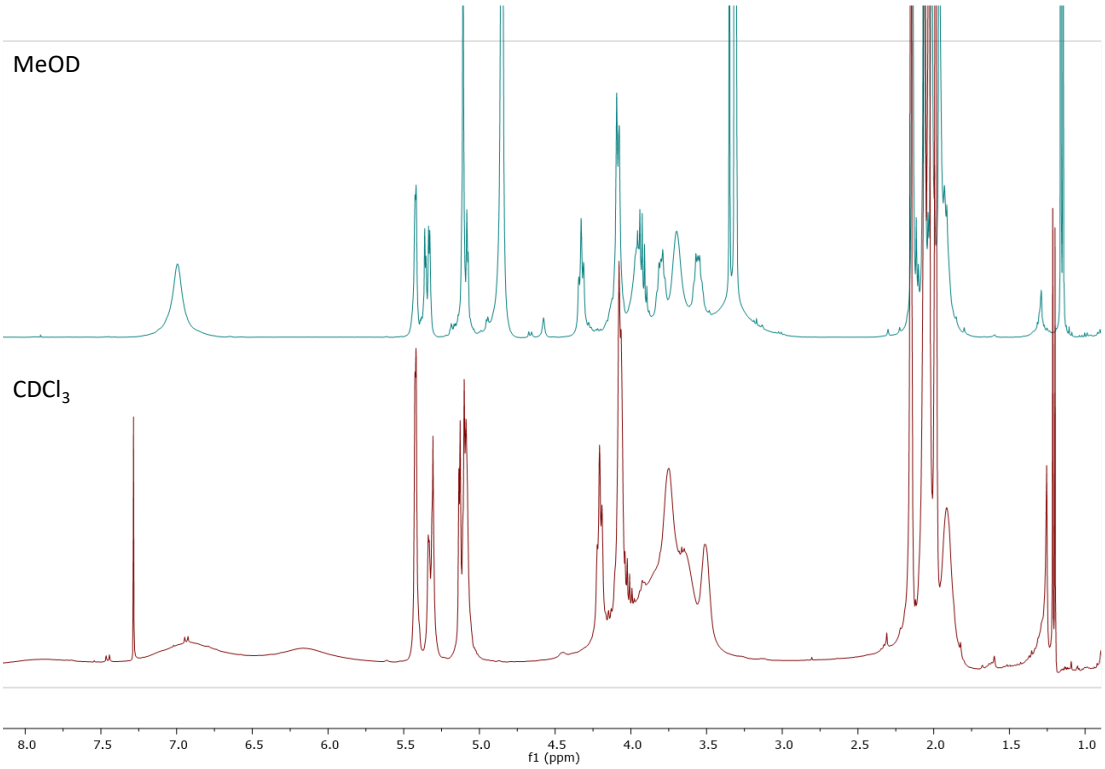

*Figure 18: ^{1}H NMR spectra of compound **17**. Top: MeOD (298 K, 400 MHz); bottom: in $CDCl_3$ (298 K, 400 MHz)*

Finally, the reactions of deacetylation were performed obtaining the two negative controls **5** and **6**. The low solubility of compound **5** allowed the NMR characterization only at 80 °C in deuterated DMSO (Figure 19) while compound **6** was characterized in the same solvent but at 25 °C (Figure 20). The outcome of both reactions was confirmed by the presence of the signals for the OH groups, the upfield shift of the galactose signals and the absence of acetyl group signals.

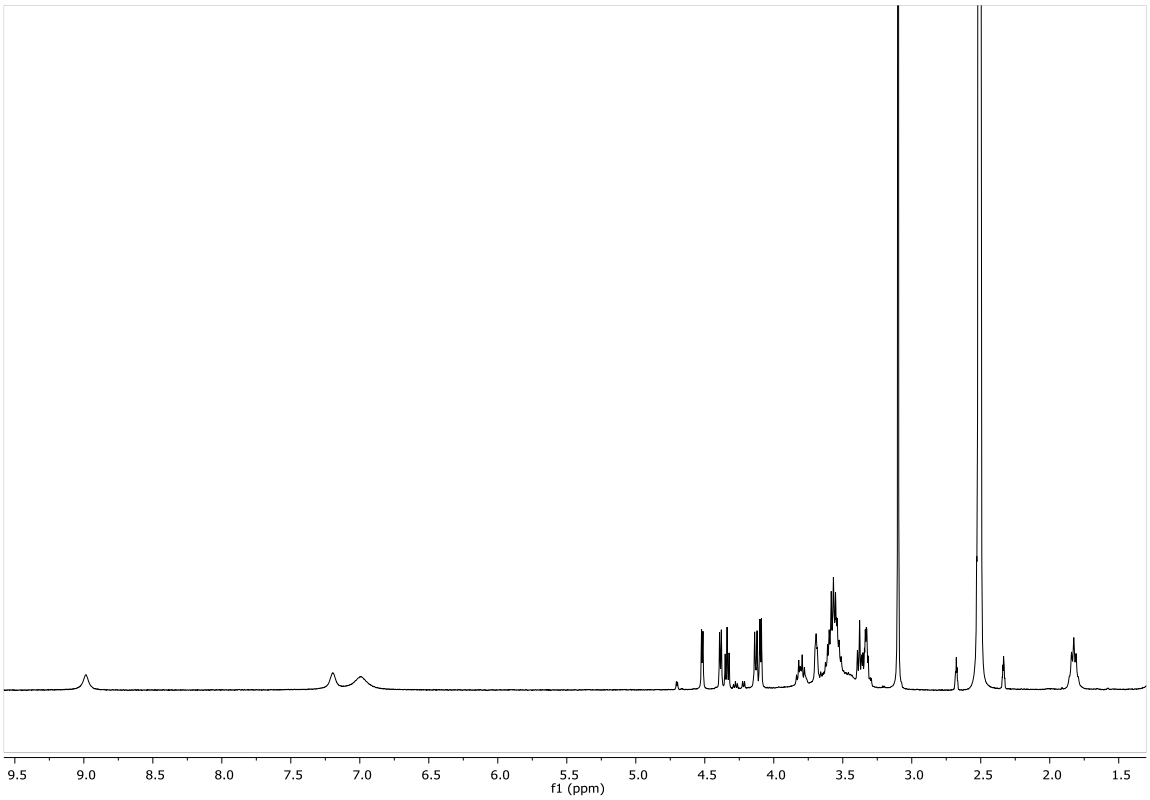

*Figure 19: ^{1}H NMR spectra of compound **5** in DMSO-d_6 (400 MHz, 353 K)*

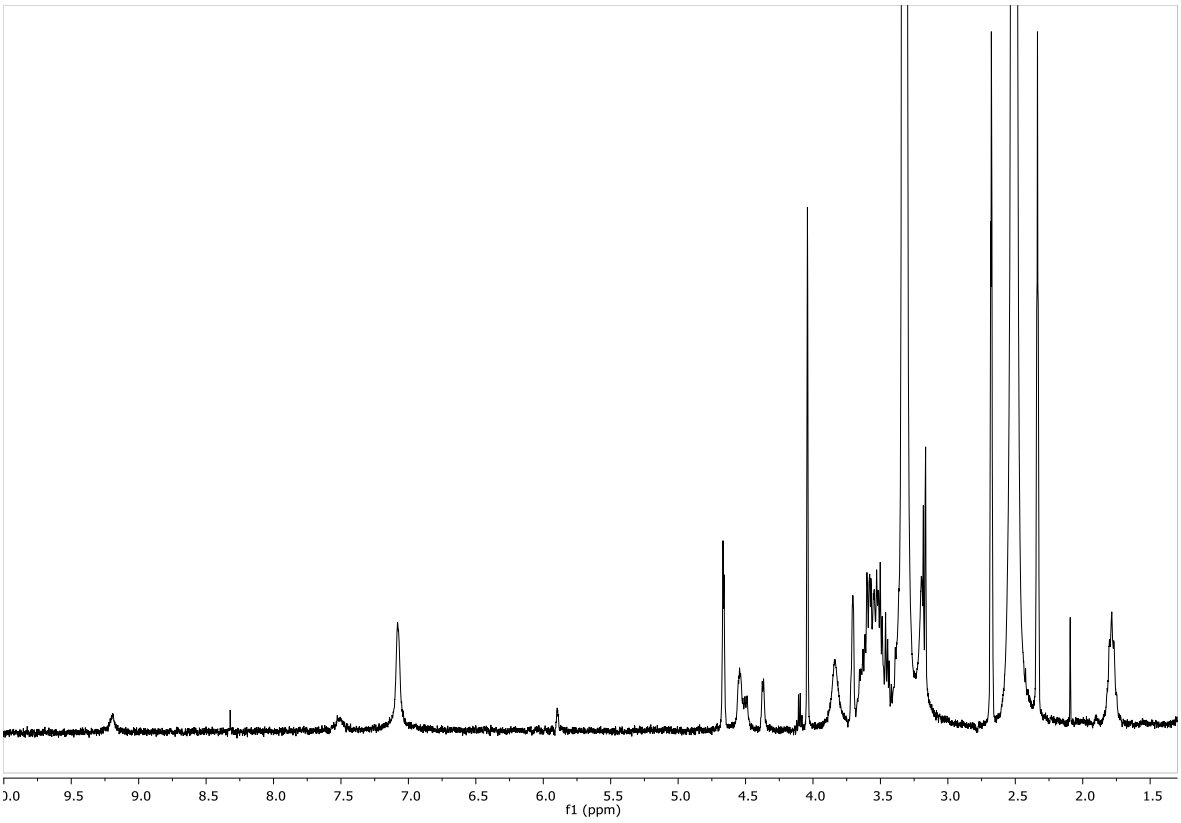

*Figure 20: ^{1}H NMR spectra of compound **6** in DMSO-d_6 (400 MHz, 298 K)*

2.1.3 Immunization studies

Once obtained the desired compounds, the studies to evaluate the immunostimulant ability of glycocalixarene **3** and **4** were performed by Prof. Sho Yamasaki and Sheige Ishizuka at the University of Osaka, in Japan, using a mice model. The experiments were carried out using five members groups of female BALB/cAJcl mice. Each group was treated by injections of 200 μL of of a phosphate buffer solution containing one of the glycocalixarene **3**-**6** at 2.5 or 3.75 μM concentration (Table 2) and 12 μL of Alhydrogel as adjuvant. A boost, constituted by the same dose and composition as the first injection, was administered after 24 weeks. The injection with calixarene **3** at 3.75 μM in mice group 4 was performed to have the same concentration of trisaccharide as for compound **4** in mice group 3. This comparison should have given an idea about the role of the specific exposition provided by the two different scaffolds, being the amount of epitope in the body the same for both experiments.

Mice group	Compounds	[Compound] (μM)	[Saccharide] (μM)
Control	NO ANTIGEN		
2	**3**	2.5	10
3	**4**	2.5	15
4	**3**	3.75	15
5	**5**	2.5	10
6	**6**	2.5	15
7	**PPS19F**	2 μg as positive control	

Table 2: Set of immunization experiments.

The levels of sera anti-SP19F IgG and IgM were monitored once a week by ELISA tests. The data were collected for 9 weeks plotting the reciprocal of EC_{50} recorded by ELISA (Figure 21).

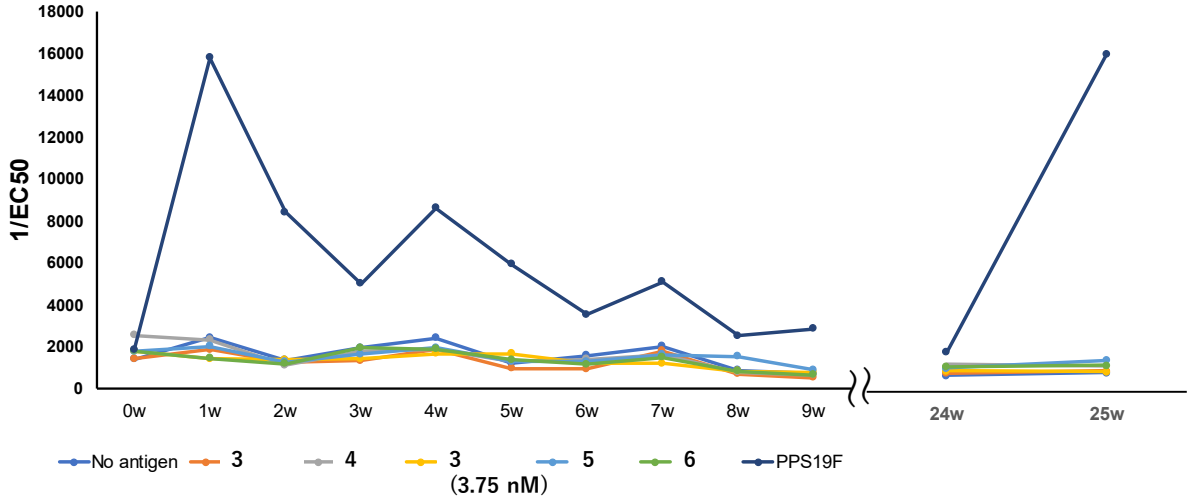

Figure 21: the graphical results of the immunization tests.

Unfortunately, both compounds **3** and **4** did not elicit production of anti-SP19F antibodies. The polysaccharide of SP 19F (PPS19F), despite its poor immunogenicity, showed a more efficient ability to induce the production of antibodies These results are probably due to the lack of an immunogenic element in the structure of the two compounds. Therefore, in order to validate this hypothesis and to obtain a potential glycoconjugate vaccine, a calixarene linked at the upper rim with trisaccharide and at the lower rim with an immunostimulating element, will be synthetized in the future.

2.2 Synthesis of trisaccharide as immunogenic elements against *Campylobacter Jejuni* HS 23/36

During a period of six months in Laurence Mulard's lab at the Institut Pasteur, in Paris, I focussed my activity on the synthesis of the trisaccharide repeating unit of *C. Jejuni* HS23/36 CPS (Figure 8) to exploit it for the development of a vaccine. Indeed, this group works on the development of synthetic glycovaccines based on the use of oligosaccharide as immunogenic element against the target bacterium, as reported for *Shigella Flexneri* serotype 2a[52–54].

Starting from the composition of the CPS (Figure 8) and their previous experience in oligomerization[55], Laurence Mulard's research group preferred to design the synthesis of the orthogonally protected trisaccharide **18** that in perspective should undergo oligomerization through glycosylation to afford longer oligosaccharides (Figure 22) or, in alternative, be linked, through a proper spacer, in multiple copies to a core that could be constituted by a calix[n]arene.

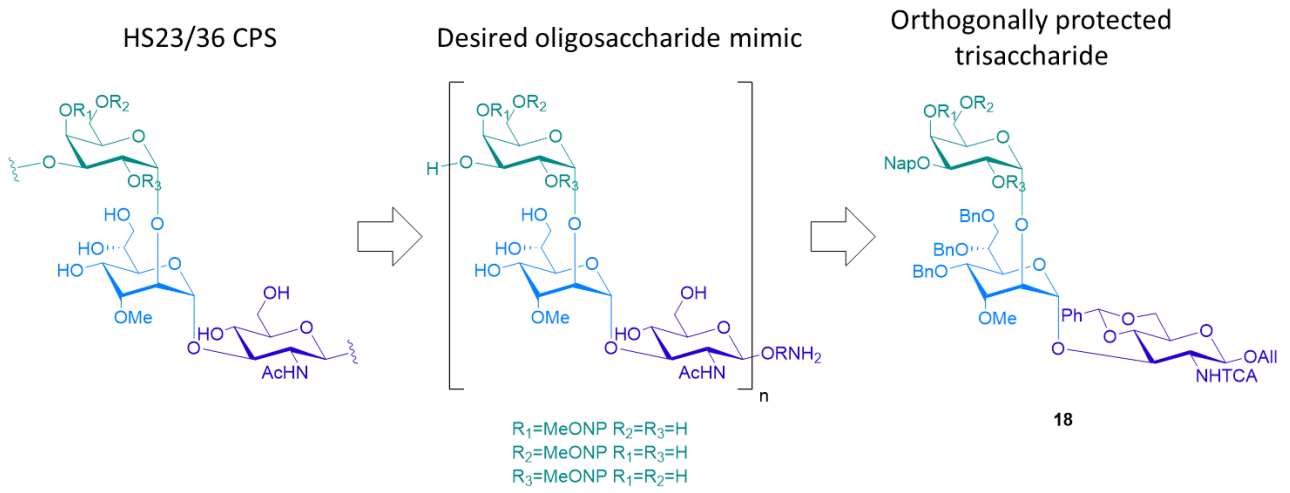

Figure 22: Retrosynthetic scheme from HS 23/36 CPS to trisaccharide.

2.2.1 From trisaccharide to monosaccharides

The trisaccharide repeating unit is composed by galactose, altroheptose and glucosamine units (Figure 7). For its synthesis the three monosaccharides **19**, **20** and **21** had been identified by Mulard as suitable building blocks (Figure 23).

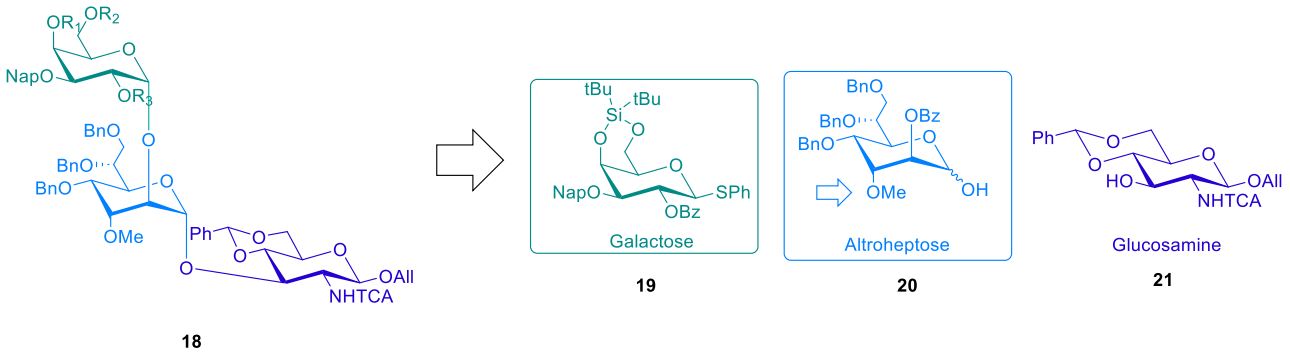

Figure 23: Retrosynthetic scheme from trisaccharide to monosaccharides

When I started my activity in this project, glucosamine **21** was already present in lab, previously prepared as reported by Hu *et al*[56], and the synthetic procedure for the preparation of galactoside **19** was already available in literature[57]. In contrast, the synthesis of altroheptose **20** represented a hard challenge. In fact, in the literature, all attempts to synthesize the trisaccharide target reports the simpler 6-deoxy analog[38,58,59]. For its preparation there are two key steps: the homologation to pass from hexose to heptose and the isomerization of 2 and 3 positions to obtain the altrose configuration. Glucose was selected as starting material due to the knowledge in Mulard's group on homologation[60] (Scheme 4).

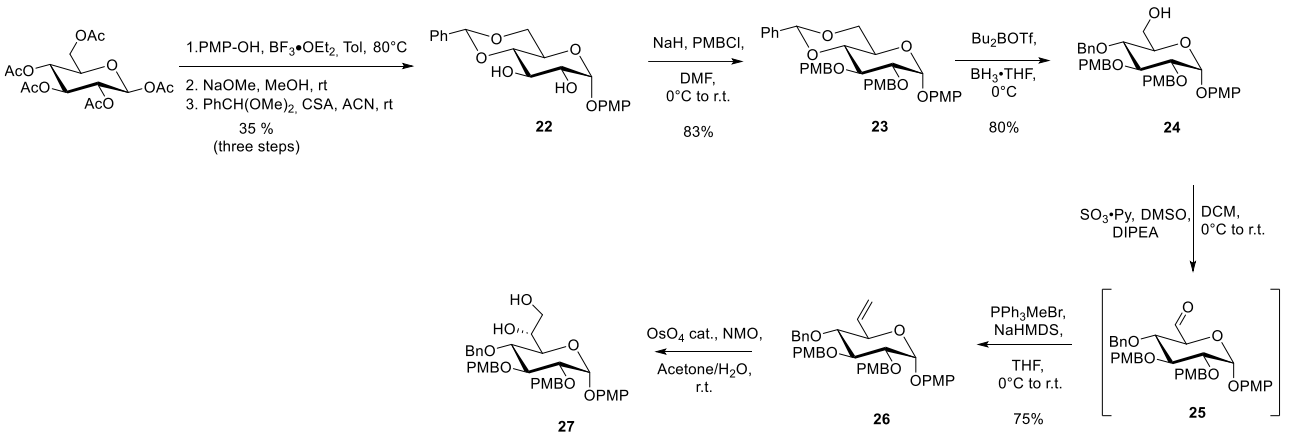

Scheme 4: The homologation part of altroheptose unit synthetic strategy.

Starting from D-glucose pentaacetate, p-methoxyphenol (PMP-OH) was introduced at the anomeric position by glycosylation using BF_3•Et_2O as promoter. The reaction was conducted at 80 °C to favour the formation of the thermodynamic α anomer[61]. In this condition, the α/β ratio was around 8:2 but degradation also occurred leading to a low yield. Initially, the α/β anomers were separated by several purification procedures through flash column chromatography using large amount of eluent. Considering the large scale of this step (50 g), we tried to find an alternative method to obtain pure α anomer. Deacetylation and subsequent benzylidene introduction using benzaldehyde dimethyl acetal and 10-camphorsulfonic acid as acidic catalyst had been initially performed on pure α anomer. During this protection reaction, it was observed a large amount of precipitate due to the insolubility of benzylidene product. Starting from this observation, we thus performed the same reaction on α/β mixture to verify the possibility of exploiting the higher insolubility of one anomer compared to the other one. We indeed observed the selective precipitation of α anomer **22** as confirmed by the ^{1}H-NMR analysis (Figure 24) that is in agreement with the data reported in literature[62].

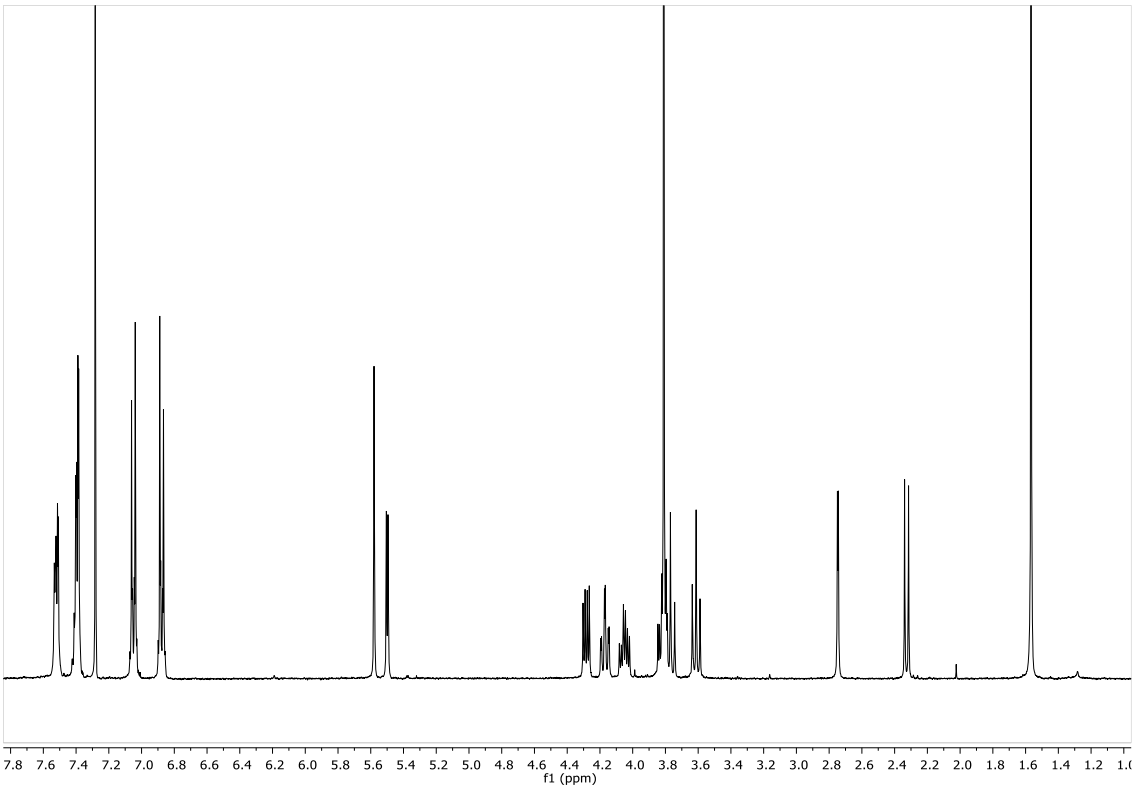

*Figure 24: ^{1}H-NMR of **22** in $CDCl_3$ (298 K, 400 MHz)*

Then, through the protection of second and third positions with p-methoxybenzyl group, we obtained compound **23**. The selective opening of benzylidene was performed to obtain the primary alcohol exploiting the reduction with BH_3•THF. This reaction was carried out using Bu_2BOTf as Lewis acid to promote the deprotection of position 6 thanks to the selective interaction between the Lewis acid and oxygen in 6 due to the steric hindrance of the Bu_2BOTf[63]. The identity of compound **24** was confirmed by ^{1}H-NMR analysis thanks to the disappearance of the benzylidene signal and the downshift of the protons in position 6 (Figure 25).

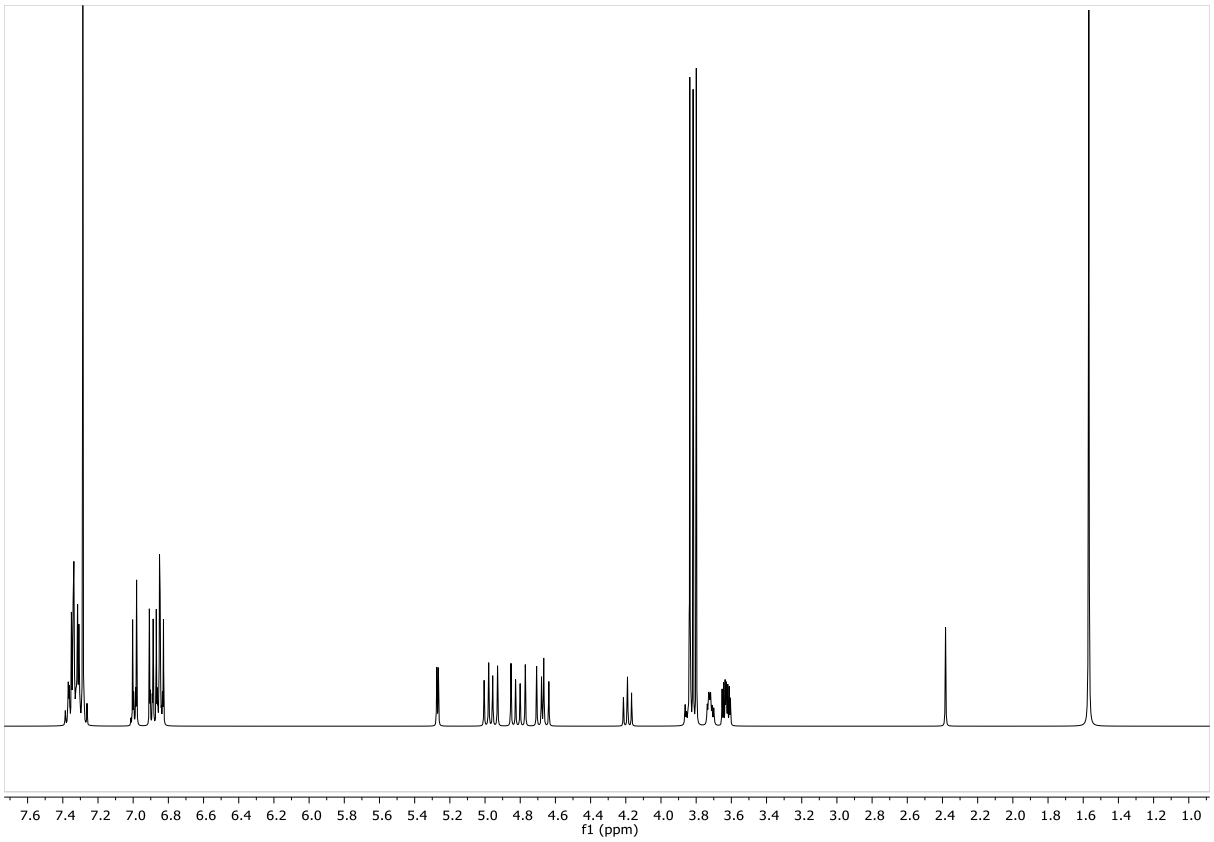

*Figure 25: ^{1}H-NMR of **24** in $CDCl_3$ (298 K, 400 MHz)*

With the free primary alcohol available, we performed the oxidation and Wittig reaction to convert hexose in heptose. The aldehyde was obtained through Parikh-Doering oxidation and directly used for the Wittig reaction. This reaction was carried out using methyl triphenyl phosphonium bromide as ylide precursor and NaHMDS as base. The compound **26** was completely characterized by NMR and HRMS to confirm the successful outcome of the reaction, particularly thanks to the presence of the characteristic signal of the alkene at ^{1}H-NMR (Figure 26).

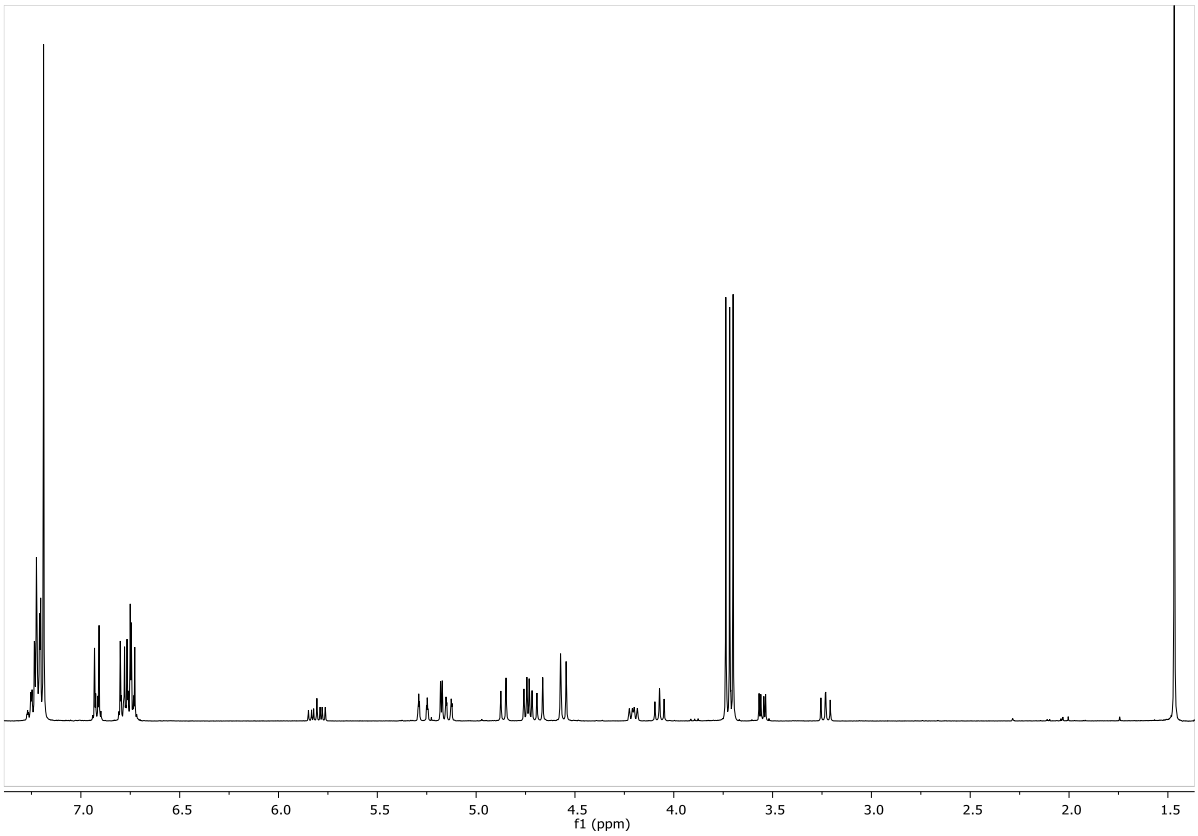

*Figure 26: ^{1}H-NMR of **26** in $CDCl_3$ (298 K, 400 MHz)*

The diol formation was performed using a catalyst amount of osmium tetroxide and a mixture of acetone and water (9:1) and *N*-methylmorpholine *N*-oxide to regenerate the osmium tetroxide in order to use the minimum amount of osmium limiting the use of this very toxic reagent. The osmylation reaction is possible on both α and β faces generating two possible diastereoisomers, respectively R and S. The purification with flash column chromatography was enough to obtain both isomers pure. From the structure of CPS, we know the absolute configuration of altroheptose that is R for the carbon in 6. Preliminary studies showed which isomer was of R configuration using NOE analysis and we continued the synthesis with this one. The presence of pure R isomer **27** was confirmed by ^{1}H-NMR analysis (Figure 27).

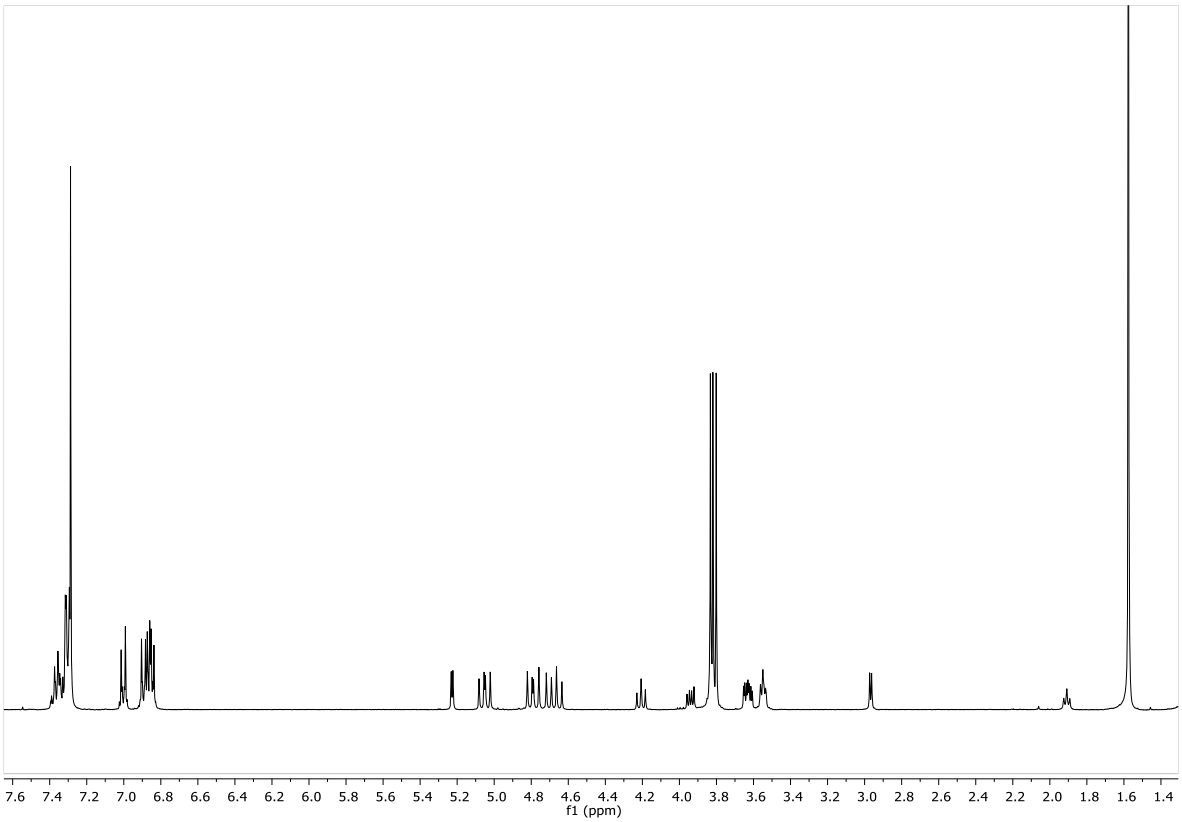

*Figure 27: ^{1}H-NMR of **27** in $CDCl_3$ (298 K, 400 MHz)*

Once obtained the heptose, we proceeded with the second phase of the preparation finalized to the isomerization at positions 2 and 3 (Scheme 5).

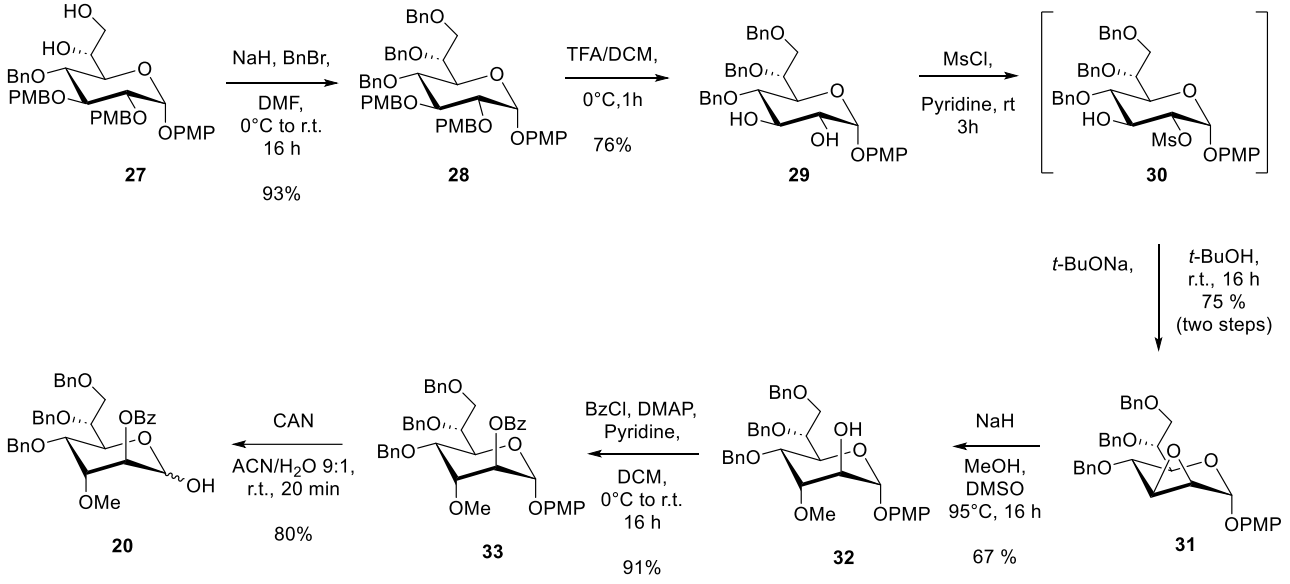

Scheme 5: The isomerization part of altroheptose unit synthetic strategy

The two hydroxyl groups of **27** were protected with benzyl groups to obtain **28**. Then, exploiting a selective deprotection with trifluoroacetic acid, we performed the p-methoxyphenyl removal leading to compound **29**. The isomerization of the position 2 and 3 was performed by epoxide opening

strategy. To obtain the correct isomerization of the two positions, we need to selectively form the epoxide on β-face (β-epoxide). Therefore, the selective functionalization OH in second position of α-sugar plays a crucial role. Indeed, using the similar approach reported by Pasetto and Franck[64], this reaction was performed using methanesulfonyl chloride in pyridine obtaining the selective conversion of hydroxyl group in second position in a good leaving group and the compound **30** was used directly to perform the epoxide formation in t-BuOH as solvent and sodium t-butoxide as base to deprotonate hydroxyl group in 3 obtaining the epoxide **31**. The successful outcome of this reaction was confirmed by ^{1}H-NMR analysis thanks to the presence of epoxide signal at low ppm (Figure 28).

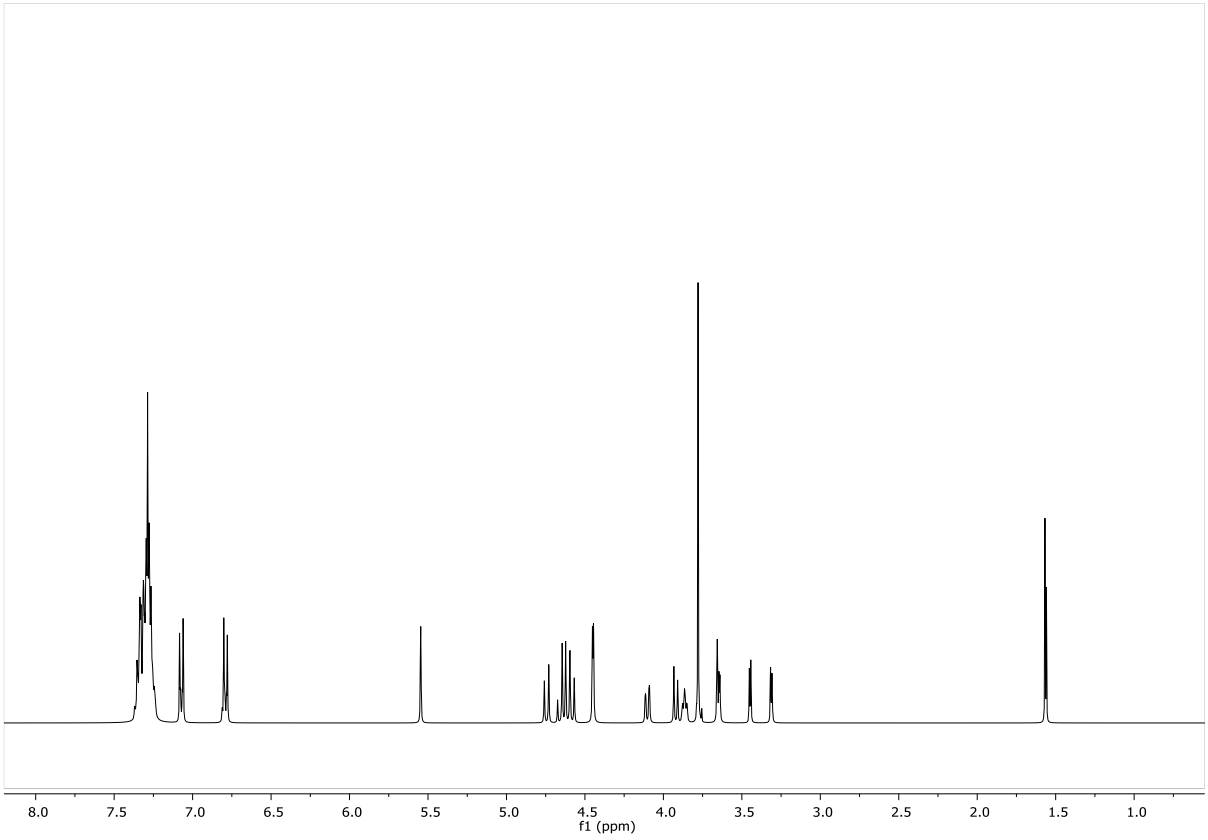

*Figure 28: ^{1}H-NMR of **31** in $CDCl_3$ (298 K, 400 MHz).*

The epoxide opening is the second key step of the whole synthetic route that allows the isomerization of positions 2 and 3 to pass from glucose to altrose configuration. In this step, using sodium methoxide as nucleophile, it was performed the methoxy introduction in position 3. This reaction was studied and performed several times (Table 3) to increase the yield and to reduce the formation of by product **32b** (Scheme 6). Each attempt was carried out using 150 mg of epoxide **31**.

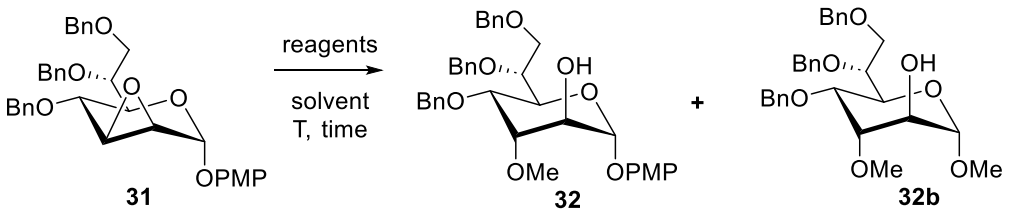

Scheme 6: Opening epoxide studies.

Experiment	T (°C)	Solvent	Time	Reagent	Results
1	95	DMSO	16 h	MeONa (24% in MeOH), $Mg(MeO)_2$ (5-10% in MeOH) (both 15 equivalents)	No conversion
2	95	DMF	4 h	Methanol/NaH (15 equivalents)	28%**32**+37% **32b**
3	95	DMSO	48 h	NaOMe powder (5 equivalents)	No conversion
4	rt	DCM	16 h	NaOMe, 5-crown-15 (5 equivalents)	No conversion
5	95	DMSO	16 h	NaOMe (24% in MeOH) (15 equivalents)	**32b** (55%)
6	-10	MeOH/DCM	16 h	TMSOTf	No conversion
7	reflux	ACN/MeOH	16 h	NH_4Cl	No conversion
8	95	DMSO	16 h	Methanol/NaH (15 equivalents)	67% **32**
9	reflux	Toluene/DCM	16 h	NaOMe in MeOH (24% in MeOH)	40% **32**
10	reflux	Toluene/THF	16 h	MeOH/NaH	No conversion

Table 7: Opening epoxide studies.

Following a procedure reported in literature[64], the first experiment was performed using sodium methoxide and magnesium methoxide in DMSO at 95 °C, but we isolated only starting material. Nishiyama *et al.*[65] studied the epoxide opening on α- and β-oxarine synthetizing altrose from glucose. We tried the same procedure to obtain compound **32** and we could indeed isolate it but also obtaining, for the first time, the by-product **32b**. The hypothesis that we formulated to explain the formation of

by-product **32b** is the possible formation of epoxide between positions 1 and 2 and a consequent reaction with sodium methoxide that leads to **32b**. Therefore, the reaction was carried out using less equivalent of sodium methoxide (used in powder to have a better control of the equivalents used) but in this case we did not observe any conversion of the starting material. Evaluating the problem of poor reactivity, we tried to use 15-crown-5 exploiting the complexation of sodium to enhance the reactivity of methoxide. Also in this case, we isolated only the starting epoxide **31**. Another attempt to obtain **32** was performed using a large excess of sodium methoxide in DMSO at 95 °C but, in this case, we obtained only by-product **32b**. In parallel, we tried the epoxide opening in acidic condition using a Lewis acid and a Brønsted acid to evaluate the effect of the two different approaches. In both cases, we did not observe any conversion. Trying to combine the approach reported in literature and our data, we used the same reagent and temperature of the second experiments but DMSO as solvent. This condition led to obtain product **32**. To increase the yield, two attempts using toluene as solvent were carried out obtaining, in the experiment 9, the compound **32**. The idea behind the use of toluene as solvent is due to the hypothesized presence of π-π interactions between the aromatic rings of the benzyl groups that generate steric hindrance influencing the reactivity of the epoxide **31**. This hypothesis was not further explored due to the lack of time. So, the reaction was performed using 1 gram of epoxide and the product **32** obtained was characterized by ^{1}H-NMR analysis which the presence of the methoxy group that confirm the presence of opening epoxide. The configuration was evaluated by NOESY analysis and the interaction between proton in position 3 with protons in 1 and 4 confirmed the altrose configuration.

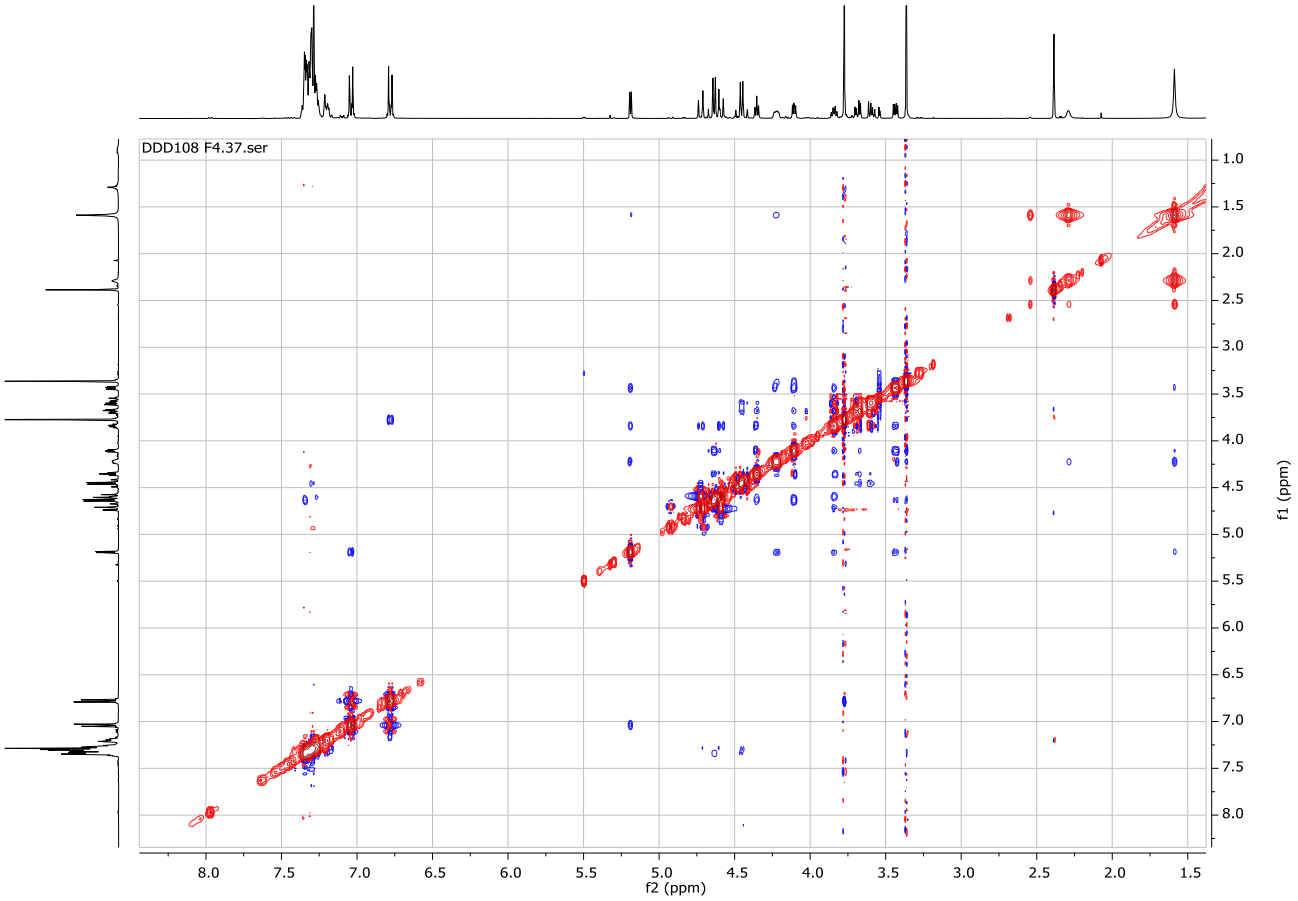

*Figure 29: NOESY analysis of compound **32**.*

Then, the OH in position 2 was protected with benzoyl group to obtain compound **33** and p-methoxyphenol group was removed by oxidation with ammonium cerium (IV) nitrate (CAN) obtaining the final compound **20** as mixture of α and β anomers. The HRMS analysis confirmed the presence of the desired product.

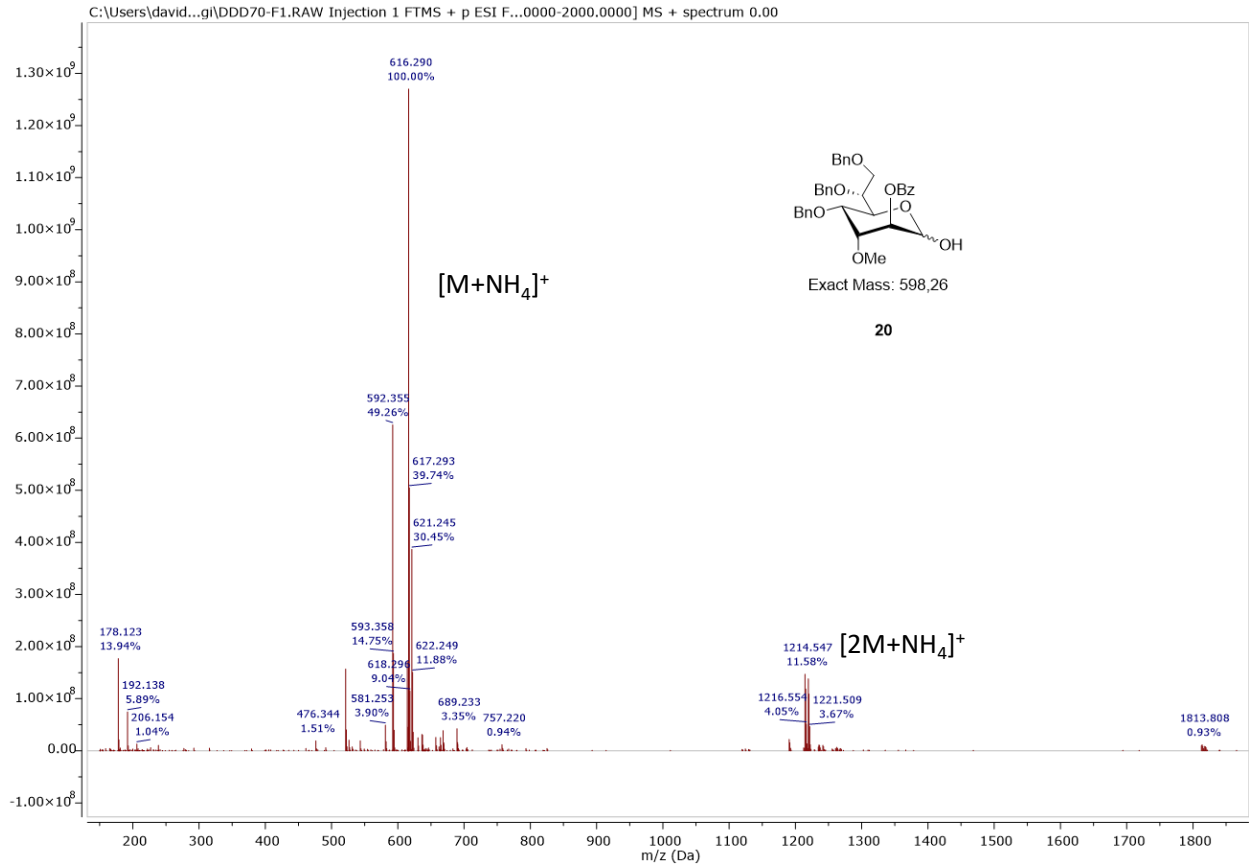

*Figure 30: HRMS spectrum of compound **20***

2.2.2 Glycosylation studies

Through the different possibilities of arrangement of trisaccharide, we had to consider which linkage through glycosylation are the easiest to make in order to have the most efficient synthesis of one trisaccharide.

As described above, from the epoxide opening reaction performed in certain conditions we obtained byproduct **32b**. To avoid of wasting the right derivative **32**, we exploited **32b** as acceptor to set up the the glycosylation reaction with galactoside **19** as donor (Scheme 7).

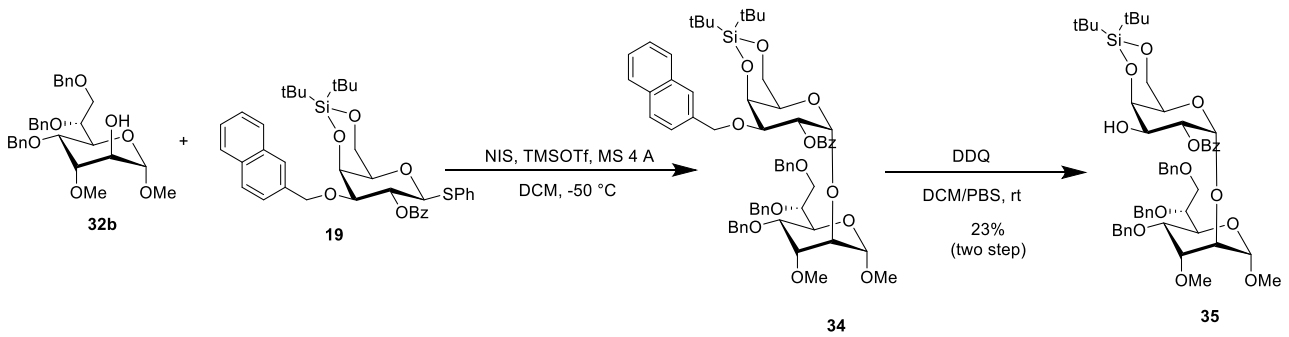

*Scheme 7: Glycosylation reaction using **32b** as acceptor and **19** as donor and subsequent deprotection.*

Starting from the conditions reported in literature[57], the reaction was performed using N-iodosuccinimide for the activation of thiol, TMSOTf as catalyst and DCM as solvent at -50 °C. In this case, the donor **19** was used in excess (1.5 equivalents) to maximize the complete reaction of acceptor **32b** but this excess caused the formation also of hemiacetal of **19** as byproduct. The presence of this byproduct made impossible the isolation of disaccharide **34**. We thus decided to perform the selective cleavage of napthylmethyl group, by oxidation with DDQ, to exploit the different polarities of the two molecules allowing us to isolate the disaccharide **35** as confirmed by ^{1}H-NMR spectrum (Figure 31).

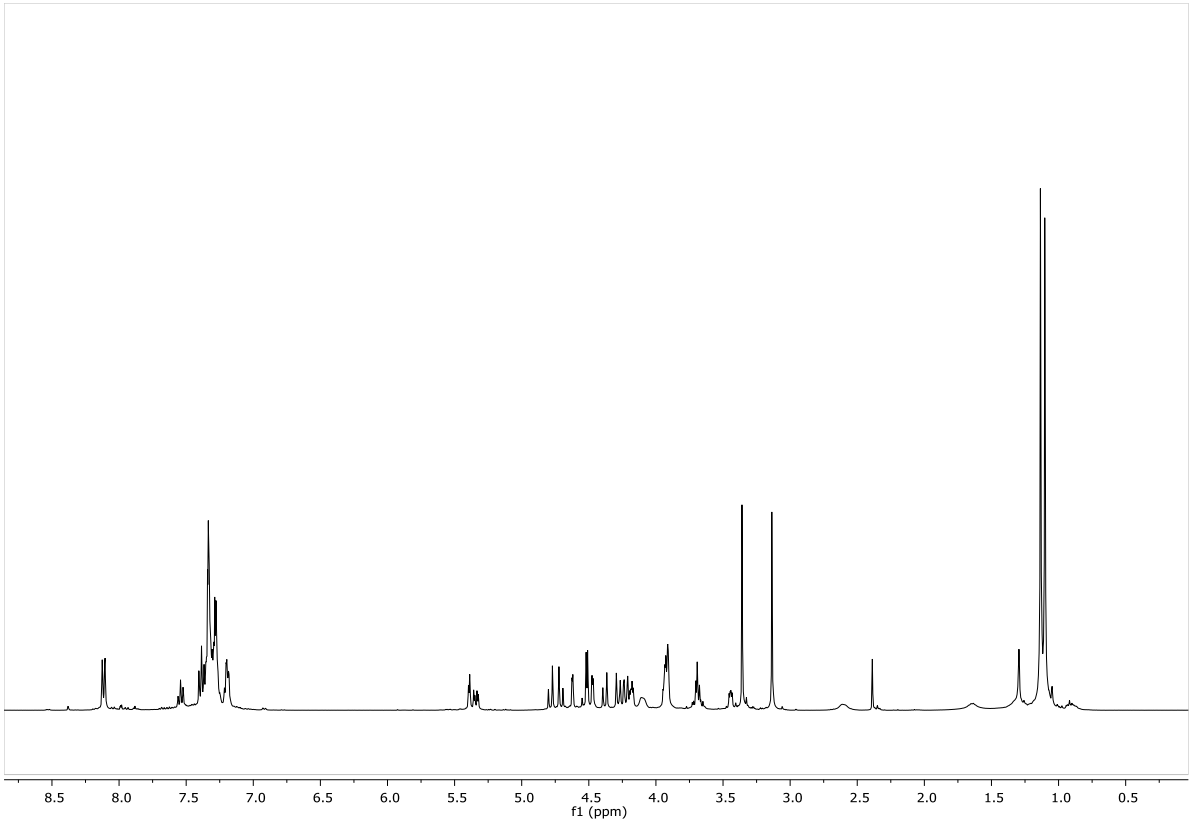

*Figure 31: ^{1}H-NMR of **35** in $CDCl_3$ (298 K, 400 MHz).*

The presence of the di-tert-butylsilylidene group on galactoside is able to direct α-selective galactosylation as reported in literature[66]. To evaluate the configuration of disaccharide **35**, NOESY and HSQC-nD studies were recorded. Especially with the latter one, the ^{1}H-^{13}C coupling constants ($^{1}J_{CH}$) were recorded and compared with those reported in literature, confirming the glycoside α-(1→2) bond (Figure 32).

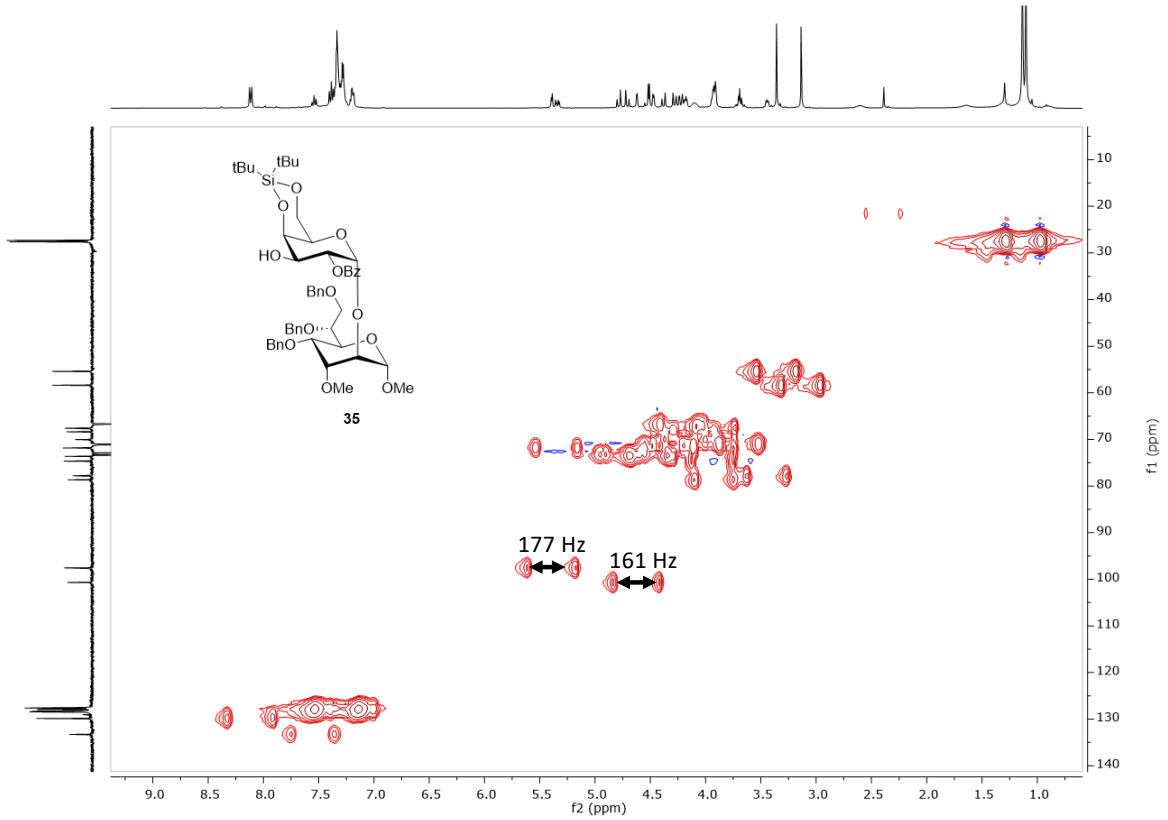

Figure 32: $^{1}J_{CH}$ of anomeric protons of galactose (177 Hz) and altroheptose (161 Hz).

Considering the impossibility to remove methyl from anomeric position of **35**, we decided to continue the synthesis of the trisaccharide using the disaccharide **35** as acceptor and modifying the glucosamine **21** in the donor. This glycosylation step allowed us to study the performance about the use of glucosamine analog as donor for the possible oligomerization. Therefore, we synthetized the donor **39** and then we performed the glycosylation to obtain trisaccharide **40** (Scheme 8).

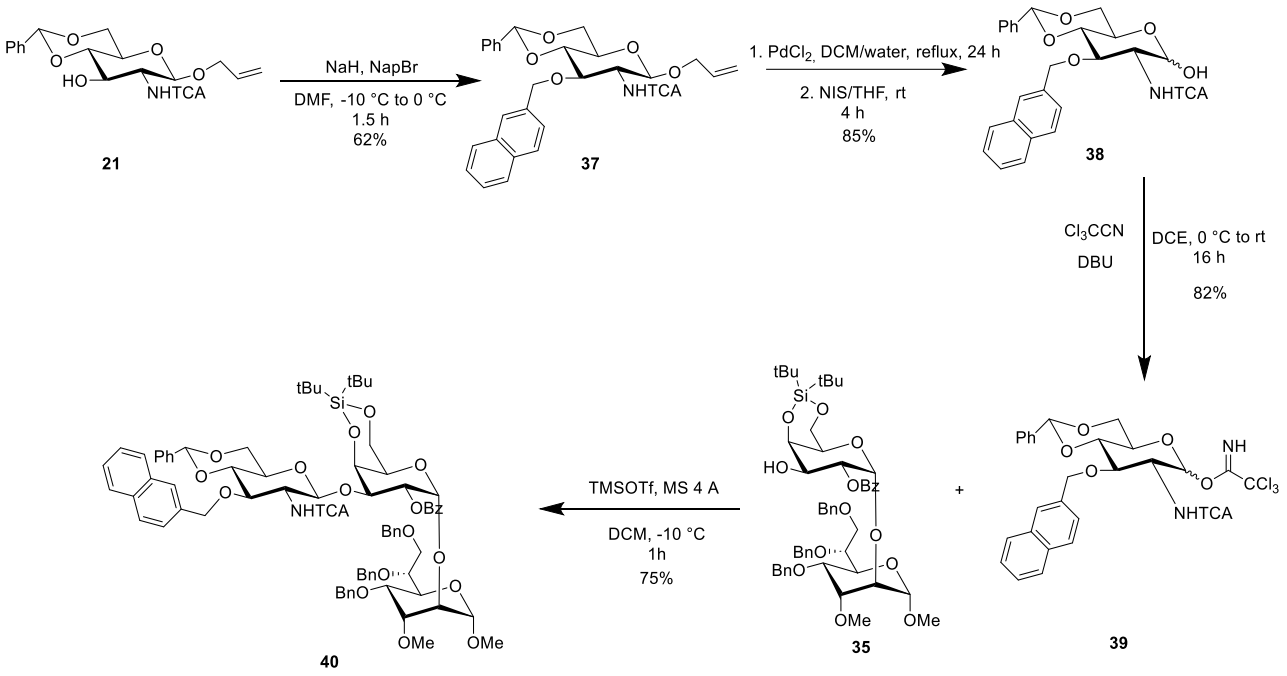

*Scheme 8: Synthesis of trisaccharide **40***

After the introduction of naphtylmethyl group in position 3 of glucosamine, the allyl group removal was performed to obtain **38** that was directly used for the activation with trichloroacetonitrile. The donor **39** was used for the glycosylation reaction with acceptor **35**, using TMSOTf as catalyst, to obtain trisaccharide **40**. Through ^{1}H-NMR analysis we identified the trisaccharide (Figure 33).

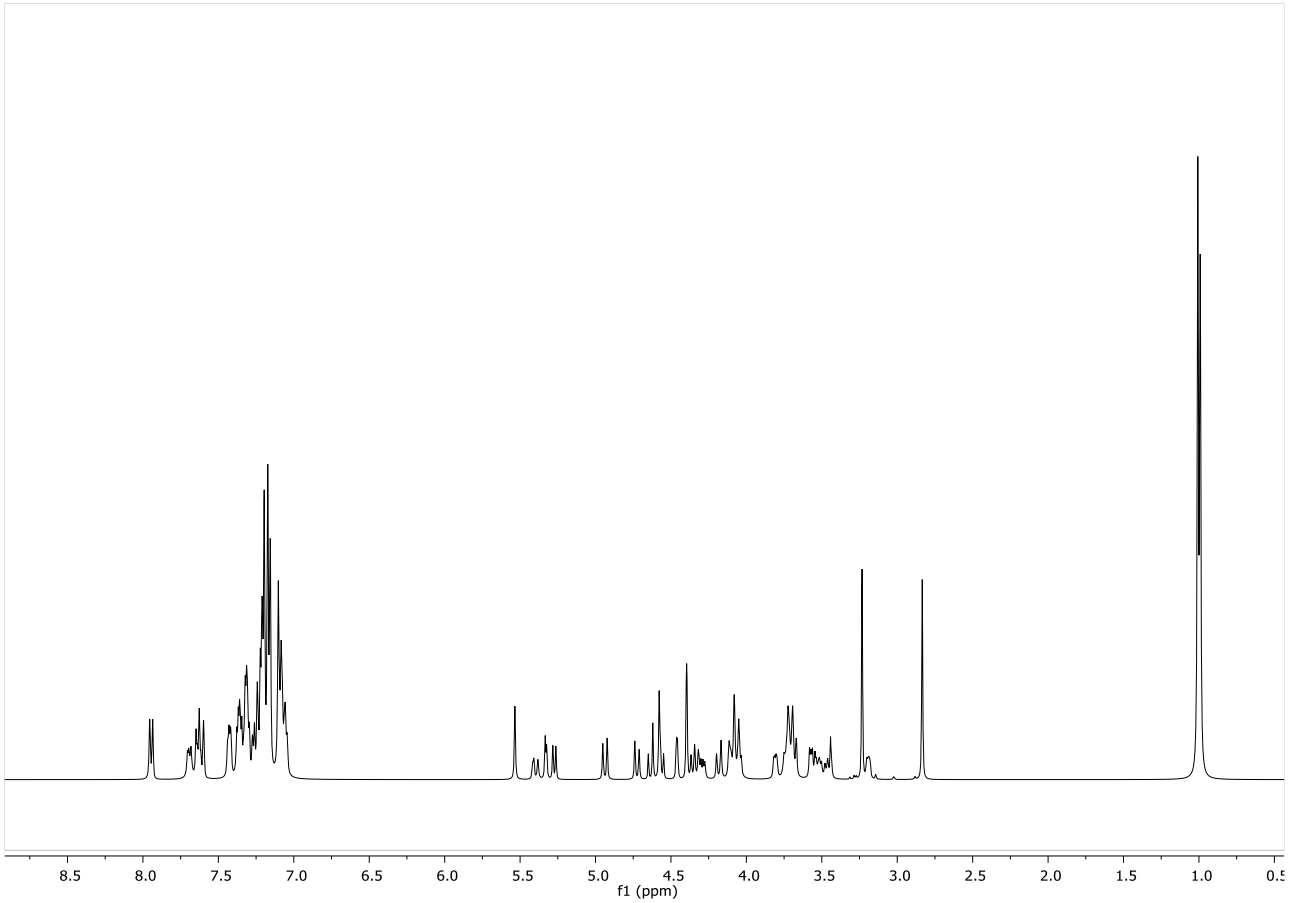

*Figure 33: ^{1}H-NMR of **40** in $CDCl_3$ (298 °K, 400 MHz).*

The presence of trichloroacetate group on amine of unit **39** allowed us to exploit neighboring group participation to obtain the selective β-(1→3) glycosidic bond. In the same way performed for the disaccharide, HSQC-nD study confirms the presence of β anomer for glucosamine (Figure 34).

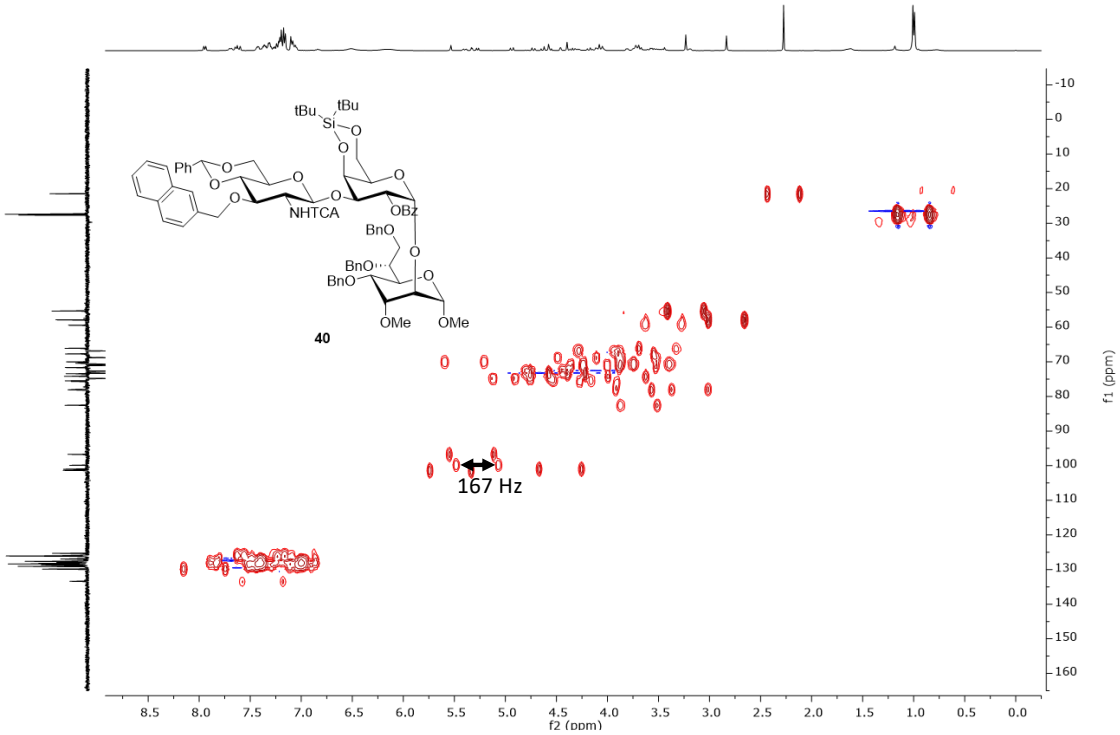

Figure 34: $^{1}J_{CH}$ of anomeric protons of glucosamine (167 Hz).

2.2.3 From monosaccharides to trisaccharide

After the glycosylation studies, we finally performed the glycosylation reactions to obtain the designed trisaccharide **18**. Starting from the activation of altroheptose **20**, we performed the glycosylation reaction using the same strategy previously exploited to obtain the trisaccharide **40** (Scheme 9).

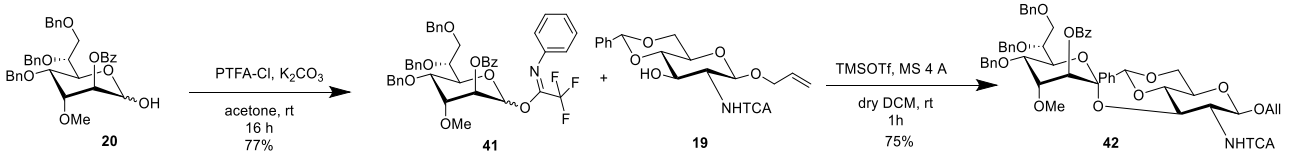

*Scheme 9: Synthesis of disaccharide **42***

The donor **41**, obtained by the reaction between 2,2,2-trifluoro-N-phenylacetimidoyl chloride (PTFA-Cl) and hemiacetal **20**, was used in the glycosylation reaction with **20** using TMSOTf as catalyst. The successful outcome of the reaction was confirmed by ^{1}H-NMR analysis (Figure 35).

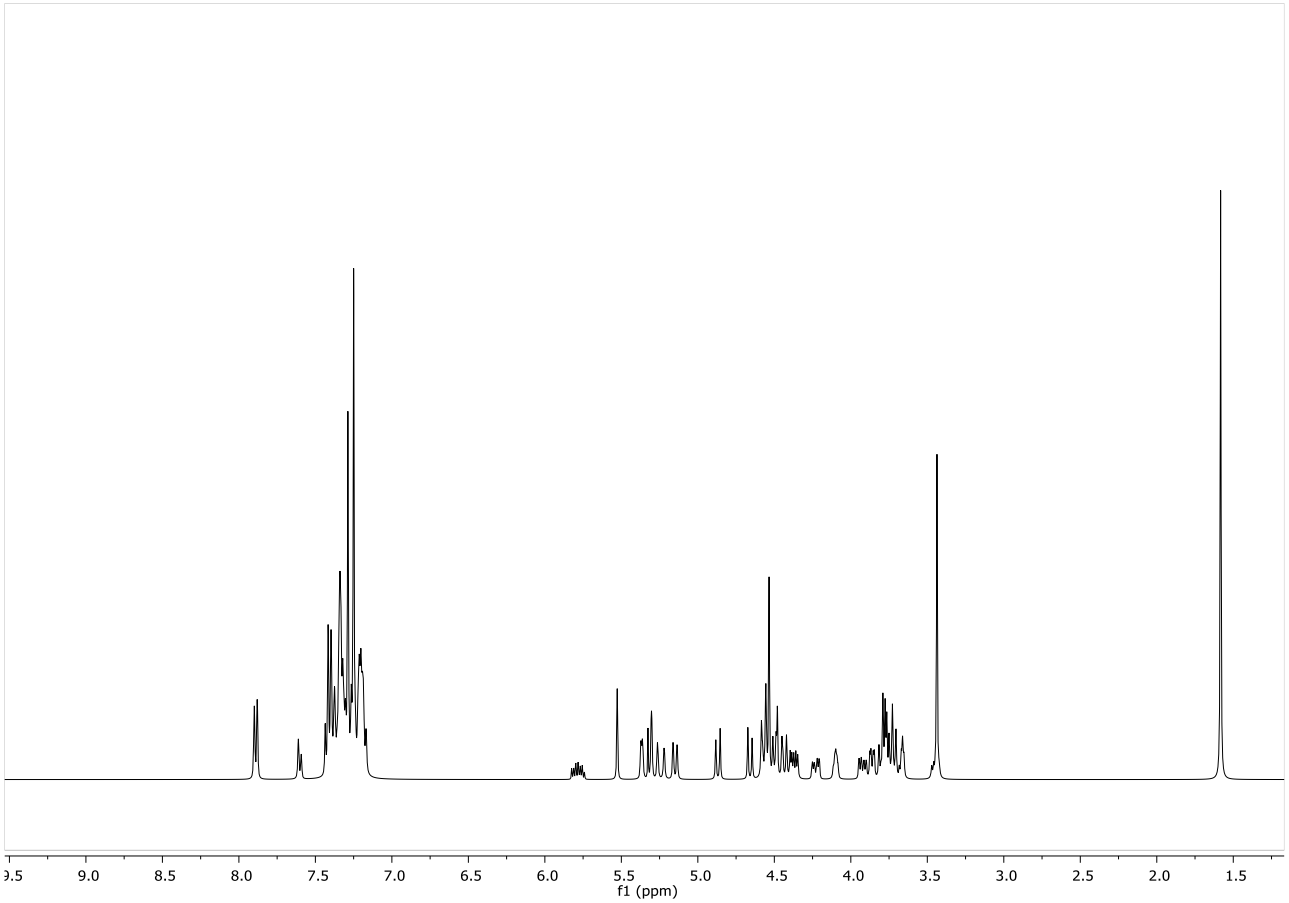

*Figure 35: ^{1}H-NMR of **42** in $CDCl_3$ (298 K, 400 MHz).*

Through the HSQC-nD experiment, in particular observing the $^{1}J_{CH}$ for anomeric carbon of altroheptose and comparing it with that relative to the same atoms in disaccharide **35**, we could conclude that the anchimeric effect, due to the presence of the participating benzoyl group, allowed us to obtain the α-selective glycosylation.

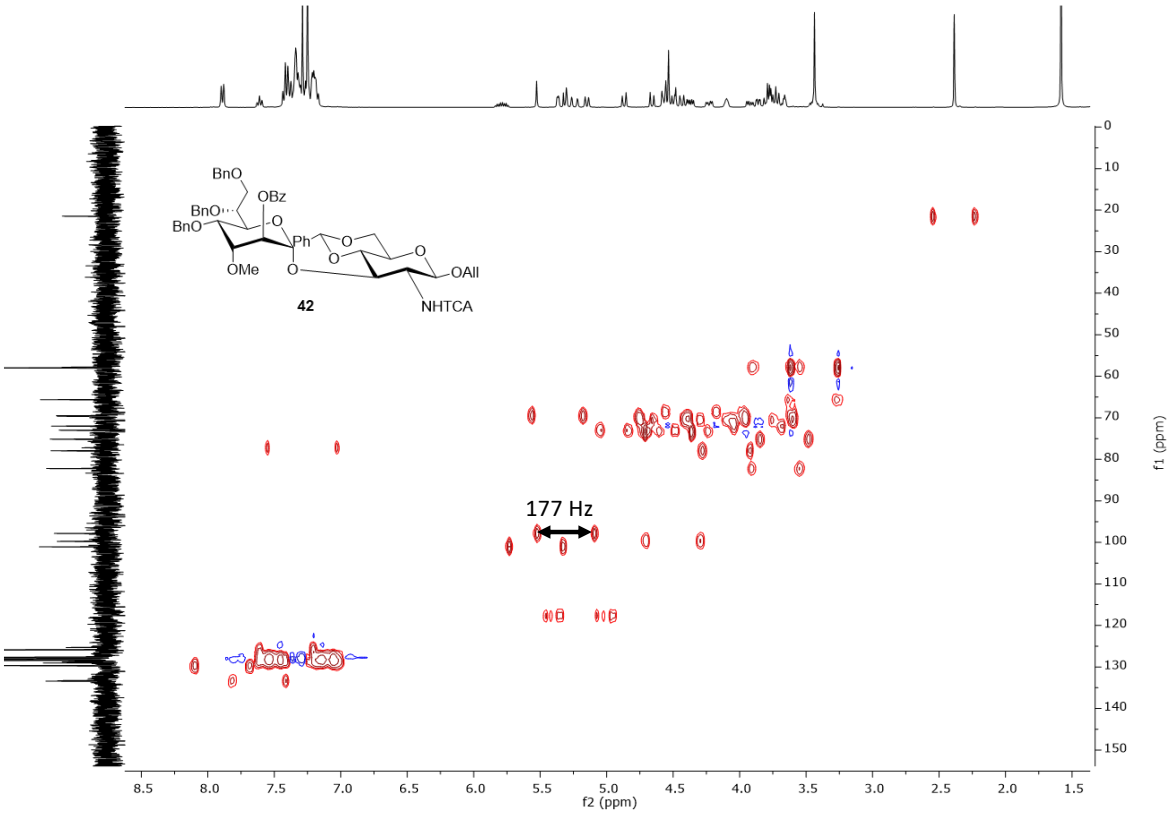

Figure 36: $^{1}J_{CH}$ of anomeric protons of glucosamine (177 Hz).

The deprotection from the benzoyl group with sodium methoxide gave us the acceptor **43** that was used to perform the final glycosylation with **19** as donor (Scheme 10).

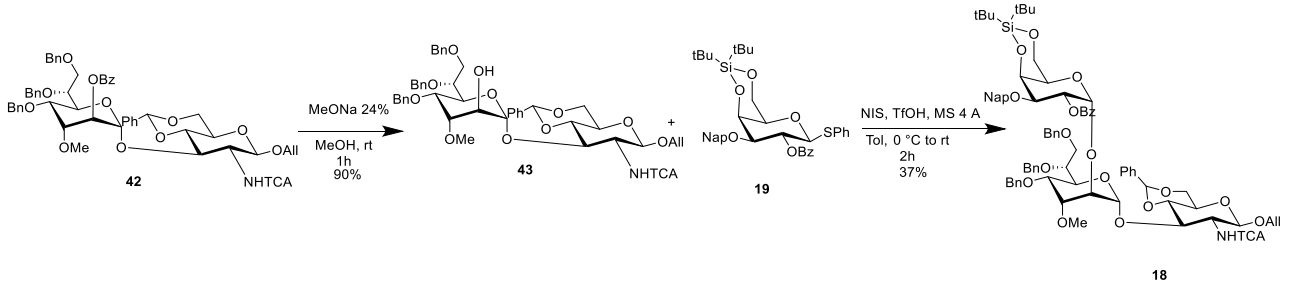

*Scheme 10:Synthesis of trisaccharide **18***

Considering the low yield obtained in the reaction producing the disaccharide **35**, we changed the protocol carrying out this reaction at room temperature and using triflic acid as catalyst having a slight increase of the yield. The HRMS confirmed the identity of the trisaccharide **18** as adduct with ammonium providing the signal at m/z = 1493.532 corresponding to $[M+NH_4]^+$.

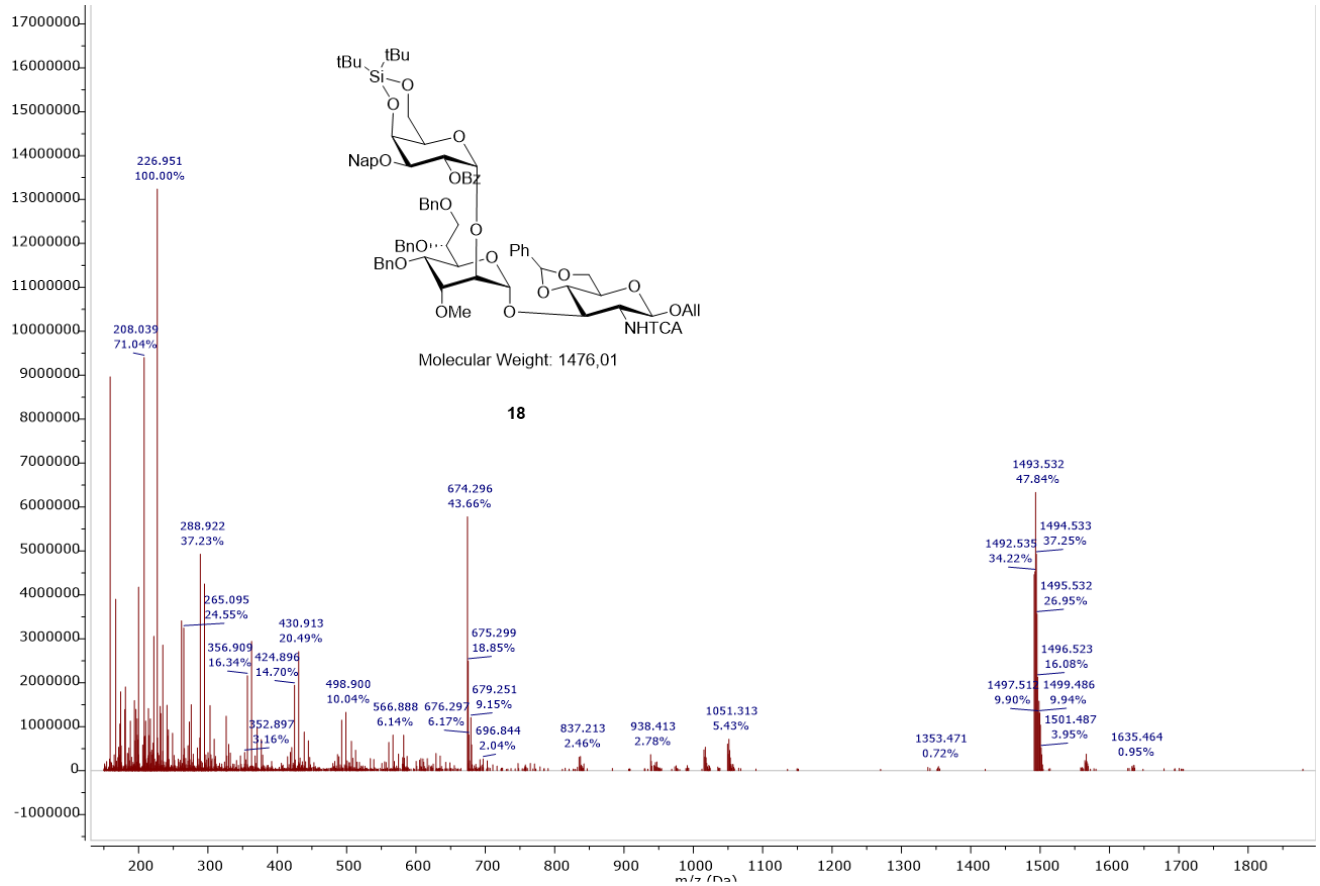

*Figure 37: HRMS spectrum of compound **18***

3. Conclusions

In this chapter, it is described the work finalised at the synthesis of saccharide species and glycosylated calixarenes for the development of immunogenic species against bacteria. In the first part, we focused on the synthesis of glycocalix[4]arene **3** and glycocalix[6]arene **4** functionalized with the same trisaccharide of the repeating unit of SP-19F CPS prepared by Federica Compostella's research group and subsequently conjugated with a linker to the macrocyclic scaffold. To perform functionalization, we exploited the click reaction between isothiocyanate on calixarenes scaffolds and amino group on linker. The same strategy was exploited to obtain the negative controls **5** and **6** by the functionalization with galactose using the same linker used for compound **3** and **4**. Then, the immunostimulation ability of these compounds was studied by mice immunization. Unfortunately, after several weeks, we did not observe any immunization against SP 19F. In future, we are planning to synthesize a more sophisticated derivative having in its structure even an adjuvant species such as an immunogenic peptide in order to provide the polyglycosylated calixarene to show effective immunostimulation ability.

In the second part of this chapter, we dealt the synthesis of the trisaccharide constituting the repeating unit of *C. Jejuni* HS 23/36 CPS. This work was realized in the Laurence Mulard's lab, with her

research group, at Institut Pasteur, in Paris. The synthesis of this trisaccharide **18** was divided in three parts: the synthesis of one of the three monosaccharide, the glycosylation studies and the trisaccharide formation. Most of the time was spent in the synthesis of altroheptose unit **20** that required several attempts for the optimization of the key step of the synthesis. At the end, the trisaccharide was obtained and in the future can be used both for the preparation of oligomers composed of several trisaccharide units and for the functionalization of calixarene scaffolds to obtain immunostimulant species against *C. Jejuni* HS 23/36 with the final aim of setting up a new example of saccharide-based synthetic vaccine. We designed a calix[6]arene-based immunostimulant of antibodies against *C. Jejuni* HS23/36 (Figure 38).

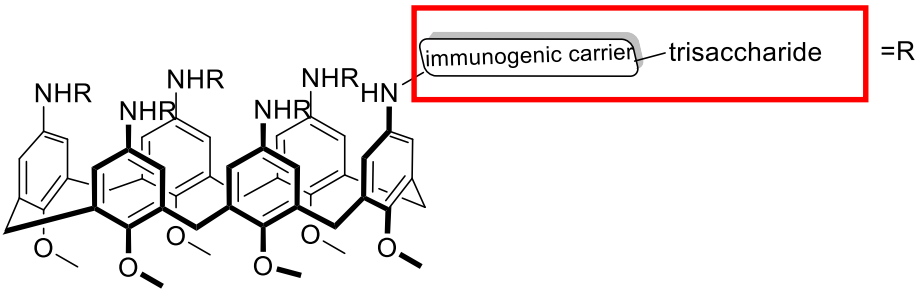

Figure 38: hypothetical structure of potential calix[6] arene-based immunostimulant.

The absence of immunogenicity observed for compounds **3** and **4** led us to develop the glycocalixarene reported in the Figure 38 with immunogenic carrier elements for each trisaccharide to maximize the immune response.

4. Experimental section

4.1 Synthesis of potential calixarene-based immunostimulants for antibodies anti-SP19F

General information

Commercially available reagents and solvents were used without carrying out any prior purification or treatment except as indicated. All moisture- and air-sensitive reactions were conducted under a nitrogen atmosphere. Dry solvents were prepared according to standard procedures and stored in the presence of molecular sieves. Monitoring of synthetic processes was performed by direct-phase thin-layer chromatography (TLC) using 60 F254 silica gel plates. Reverse phase TLC were performed using silica gel 60 RP-18F-254 on aluminium sheets. Merck silica gel 60 was used for flash chromatography (40–63 μm) and for preparative TLC plates (10–12 μm). Sigma Aldrich C18 reverse

phase silica gel was used for flash chromatography. For the detection of reagents and products with amine groups, the TLCs were sprayed with a 5% solution of ninhydrin in ethanol; for those with phenolic groups, a solution of $FeCl_3$ in water was used; for the detection of hydroxyl groups, a solution of 10% H_2SO_4 in ethanol; and for easily oxidized compounds, a 0.05% solution of $KMnO_4$ in water was used. Flash chromatography columns on silica gel 60 (230-400 mesh), under nitrogen pressure, and commercial preparative TLC 20×20 cm, silica gel F_{254}, 0.5 mm were used for product purification. Product characterization was performed by ^1H and ^{13}C NMR spectroscopy and mass spectrometry using the ESI technique. NMR spectra were recorded with Bruker AVANCE 400 spectrometer (^1H at 400 MHz, ^{13}C at 100 MHz); chemical shift values are reported in ppm using the resonance frequency of the partially deuterated solvent as a reference. Mass spectra were recorded with a single quadrupole SQ detector spectrometer, Waters. High-resolution mass spectra (HRMS) were obtained in the positive ion mode using a Q-TOF mass spectrometer equipped with an electrospray ion source.

5,11,17,23,-Tetrakis-N-[3-(2-acetamido-3,4,6-tri-O-acetyl-2-deoxy-β-D-mannopyranosyl-(1→4)-2,3,6-tri-O-acetyl-α-D-glucopyranosyl-(1→2)-3,4-di-O-acetyl-L-rhamnopyranosyloxy)-propylthioureido]-25,26,27,28-tetramethoxycalix[4]arene (10)

In a two-neck round-bottom flask, trisaccharide **7** (24.6 mg, 0.024 mmol) and **8** (2.8 mg, 0.004 mmol) were dissolved in dry DCM (3 mL). Then, NEt_3 (28 µL, 0.197 mmol) was added under Ar atmosphere. The mixture was stirred for 48 hours at room temperature. The reaction was monitored by TLC (DCM/MeOH 98:2, visualized by H_2SO_4). Then, the reaction was quenched by the removal of the solvent at reduced pressure. The desired product was obtained after column chromatography (DCM/MeOH 98:2) as a white solid.

Yield=90% (16.2 mg)

^1H NMR (400 MHz, MeOD) δ (ppm): 7.11 (br, 8H, ArH), 5.39 (br t, 4H, H-1′), 5.27 (br t, 4H, H-3′) 5.15–5.02 (m, 8H, H-4″,H-4), 4.79 (s, 4H, H-3), 4.74 (br, 4H, H-1″), 4.69 (br, 4H, H-2′), 4.62 (br,4H, H-2″), 4.50 (br, 4H, H-1), 4.39 (dd, 6H, H-6a″) 4.28 (br, 6H, H-6a′), 4.13 (br, 18H, H-2, H-5′, H-6b′), 4.05 (d, J=12.0 Hz, 6H, H-6b″), 3.86 (br, 12H, CH_2NHCS), 3.75 (br, 6H, H-4′), 3.66 (br, 6H, H-5″), 3.45 (br, 18H, H5, OCH_2) 2.16 (s, 18H, CH_3CO), 2.12 (s, 36H, CH_3CO), 2.11 (s, 18H, CH_3CO), 2.061 (s, 18H, CH_3CO), 2.056 (s, 18H, CH_3CO), 2.05 (s, 18H, CH_3CO), 2.03 (s, 18H, CH_3CO), 2.01 (s, 18H, CH_3CO), 1.75 (br, 12H,$CH_2CH_2CH_2CH_2$), 1.23 (d, J=5.8 Hz, 18H, H-6).

ESI-MS: m/z calc 4397.46 found: 1468.49 $[M+3H]^{3+}$, 1475.81 $[M+2H+Na]^{3+}$

5,11,17,23,29,35-Hexakis-N-[3-(2-acetamido-3,4,6-tri-O-acetyl-2-deoxy-β-D-mannopyranosyl-(1→4)-2,3,6-tri-O-acetyl-α-D-glucopyranosyl-(1→2)-3,4-di-O-acetyl-L-rhamnopyranosyloxy)-propylthioureido]-37,38,39,40,41,42-hexamethoxycalix[6]arene (11)

In a two-neck round-bottom flask, trisaccharide **7** (24.2 mg, 0.023 mmol) and **9** (3.25 mg, 0.003 mmol) were dissolved in dry DCM (3 mL). Then, NEt_3 (21 μL, 0.157 mmol) was added under Ar atmosphere. The mixture was stirred for 48 hours at room temperature. The reaction was monitored by TLC (DCM/MeOH 98:2, visualized by H_2SO_4). Then, the reaction was quenched by the removal of the solvent at reduced pressure. The desired product was obtained after column chromatography (DCM/MeOH 98:2) as a white solid.

Yield= quantitative (14.7 mg)

^{1}H NMR (400 MHz,$CDCl_3$) δ (ppm): 7.11 (br, 12H, ArH), 5.93 (d, *J*=7.3 Hz, 6H, NHAc), 5.60 (br, 6H, H-1′), 5.41 (t, *J*=9.1 Hz, 6H, H-3′) 5.17–5.02 (m, 12H, H-4″,H-4), 4.96 (dd, $J_{3,2}$=3.0, $J_{3,4}$=10.1 Hz, 6H, H-3), 4.93 (dd, $J_{3'',2''}$=5.8, $J_{3'',4''}$=9.9 Hz, 6H, H-3″) 4.74 (br, 6H, H-1″), 4.69 (br, 6H, H-2′), 4.62 (br, 6H, H-2″), 4.50 (br, 6H, H-1), 4.39 (dd, 6H, H-6a″) 4.28 (br, 6H, H-6a′), 4.13 (br, 18H, H-2, H-5′, H-6b′), 4.05 (d, *J*=12.0 Hz, 6H, H-6b″), 3.86 (br, 12H, CH_2N), 3.75 (br, 6H, H-4′), 3.66 (br, 6H, H-5″), 3.45 (br, 18H, H-5, OCH_2) 2.16 (s, 18H, CH_3CO), 2.12 (s, 36H, CH_3CO), 2.11 (s, 18H, CH_3CO), 2.061 (s, 18H, CH_3CO), 2.056 (s, 18H, CH_3CO), 2.05 (s, 18H, CH_3CO), 2.03 (s, 18H, CH_3CO), 2.01 (s, 18H, CH_3CO), 1.75 (br, 12H, $CH_2C\mathit{H}_2CH_2$), 1.23 (d, *J*=5.8 Hz, 18H, H-6).

The spectroscopic data found are in agreement with those reported in the literature[44].

5,11,17,23-tetraakis-N-[3-(2-acetamido-2-deoxy-β-Dmannopyranosyl-(1→4)-α-D-glucopyranosyl-(1→2)-L-rhamnopyranosyloxy)-propyl-thioureido]-25,26,27,28-tetramethoxycalix[4]arene (3)

To a solution of the peracetylated compound **10** in MeOH at 0 °C, freshly prepared MeONa was added until to pH 9. The progress of the reaction was followed by ESI-MS and TLC (AcOEt/iPrOH/H_2O 6:3:1, visualized by H_2SO_4). The solution was stirred for 3 h, after which Amberlite IR-120 (H^+) was added and the mixture was stirred at rt till neutral pH. The resin was filtered off and the solvent was removed under reduced pressure. The pure product was obtained after purification by C18 reverse phase column chromatography (H_2O and then MeOH) as a white solid.

Yield= 65% (8.173 mg)

^{1}H NMR (400 MHz, MeOD/D_2O 9/1) δ (ppm): 7.36-6.53 (m, 8H, ArH), 4.99 (br s, 4H, H-1′), 4.88 (br, 4H, H-1″), 4.81 (br, 4H, H-1), 4.51 (br s, 4H, H-2″), 4.08–3.33 (ovelapped, 96H, H-3″, H-4″, H-5″, H-6a,b″, H-2′, H-3′, H-4′, H-5′, H-6a,b′, H-2, H-3, H-4, H-5, OCH_2, CH_2N, OCH_3, $ArCH_2Ar$), 2.04 (s, 20H, $CH_2CH_2CH_2$), $NHCOCH_3$) 1.29 (br, 12H, H-6).

^{13}C NMR (101 MHz, MeOD/D_2O 9/1) δ (ppm): 174.4, 99.4, 98.1, 97.8, 78.7, 76.9, 72.5, 72.4, 71.6, 70.5, 70.1, 68.9, 66.7, 65.2, 60.4, 59.9, 53.5, 42.0, 28.8, 21.8, 16.7.

HRMS (ESI-TOF) m/z: calc 3053.128, found: 1272.33 $(M+2Na)^{2+}$

5,11,17,23,29,35-Hexakis-N-[3-(2-acetamido-2-deoxy-β-Dmannopyranosyl-(1→4)-α-D-glucopyranosyl-(1→2)-L-rhamnopyranosyloxy)-propyl-thioureido]-37,38,39,40,41,42-hexamethoxycalix[6]arene (4)

To a solution of the peracetylated compound **11** in MeOH at 0 °C, freshly prepared MeONa was added until to pH 9. The progress of the reaction was followed by ESI-MS and TLC (AcOEt/iPrOH/H_2O 6:3:1). The solution was stirred for 3 h, after which Amberlite IR-120 (H^+) was added and the mixture was stirred at rt till neutral pH. The resin was filtered off and the solvent was removed under reduced pressure. The pure product was obtained after purification by C18 reverse phase column chromatography (H_2O and then MeOH) as a white solid.

Yield=70% (9.182 mg)

^{1}H NMR (400 MHz, MeOD/D_2O 75/25) δ (ppm): 7.04 (br, 12H, ArH), 5.11 (br, 6H, H1′), 4.83 (s, 6H, H1″), 4.67 (br, 6H, H1), 4.63 (br, OH), 4.53 (br, 6H, H2″), 4.24–3.27 (overlapped, 144H, H-3″, H-4″, H-5″, H-6a,b″, H-2′, H-3′, H-4′, H-5′, H-6a,b′, H-2, H-3, H-4, H-5, OCH_2, CH_2N, OCH_3, $ArCH_2Ar$), 2.07 (s, 18H, $NHCOCH_3$),1.90 (br, 12H, $CH_2CH_2CH_2$), 1.34 (br, 18H, H-6).

The spectroscopic data found are in agreement with those reported in the literature[44].

3-Azidopropyl 2,3,4,6-Tetra-O-acetyl-β-D-galactopyranoside (13)

A solution of 1,2,3,4,6-penta-O-acetyl-β-D-galactopyranoside (5.000 g, 11.78 mmol) and 3-bromopropanol (1.600 mL, 17.67 mmol) in dry DCM (50 mL), containing molecular sieve 4 Å (0.750 g) was chilled to 0 °C. Subsequently, $BF_3 \cdot Et_2O$ (7.500 mL, 24.33 mmol) was added over 2 minutes. The resulting mixture was kept stirring for 16 hours and monitored by TLC (Tol/EtOAc 8:1, visualized by H_2SO_4). Then was neutralized with NEt_3, and subjected to sequential washes with $NaHCO_3$ saturated solution, water, and aqueous saturated NaCl. After drying with Na_2SO_4, filtration,

and concentration, the residue was purified by flash column chromatography (Tol/EtOAc 8:1), yielding compound **12** (2.831 g, 51%) as a slightly yellow syrup. Compound **12** (2.831 g, 5.981 mmol) was dissolved in dry DMF (20 ml), and NaN_3 (1.950 g, 29.90 mmol) was added. The resulting mixture was kept stirring at 100 °C for 16 hours and monitored by TLC (Tol/EtOAc 8:1, visualized by H_2SO_4). Then was filtered, and co-concentrated with toluene. The residue was dissolved in DCM (20 mL), washed with brine (20 mL), dried by Na_2SO_4, filtered, and concentrated, obtaining product **6** as a slightly yellow syrup.

Yield=35% (0.920 g)

^{1}H NMR (400 MHz, $CDCl_3$) δ(ppm): 5.41 (dd, *J* = 3.4, 1.1 Hz, 1H, H-4), 5.22 (dd, *J* = 10.5, 7.9 Hz, 1H, H-4), 5.04 (dd, *J* = 10.5, 3.4 Hz, 1H, H-3), 4.49 (d, *J* = 7.9 Hz, 1H, H-1), 4.25 – 4.10 (m, 2H, H-6AA+H-6b), 4.03 – 3.90 (m, 2H, H-5 and OCH*H*$CH_2CH_2N_3$), 3.68 – 3.58 (m, 1H, OCH*H*$CH_2CH_2N_3$), 3.39 (t, *J* = 6.1, 2.2 Hz, 2H, C*H*$_2N_3$), 2.21 – 1.97 (m, 12H, CH_3CO), 1.97 – 1.78 (m, 2H, OCH_2*CH*$_2CH_2N_3$).

The spectroscopic data found are in agreement with those reported in the literature[49].

3-(N-tert-butyloxycarbonyl)aminopropyl-2,3,4,6-tri-O-acetyl-β-D-galactopyranoside (14)

In a Parr flask, azide derivate **13** (0.200 g, 0.461 mmol) was dissolved in AcOEt (10 mL). Then, Et_3N (0.130 mL, 0.94 mmol), di-*tert*-butyl dicarbonate (0.153 g, 0.700 mmol), and a catalytic amount of 10% Pd/C were added. The solution was kept stirring at room temperature, under 3 bar of hydrogen, and monitored using TLC (DCM/MeOH 98:2, visualized by ninhydrin). After 2 hours, the solution was filtered through celite. The solvent was evaporated, and the crude was purified by column chromatography (DCM/MeOH 98:2) to give the product as a colorless oil.

Yield= 82% (0.190 g)

^{1}H NMR (400 MHz, $CDCl_3$)= δ 5.41 (2d, *J* = 3.4, 1H, H-4), 5.26 – 5.16 (m, 1H, H-2), 5.03 (2d, 3.4 Hz, 1H, H-3), 4.73 (brs, 1H, N*H*Boc), 4.48 (d, *J* = 7.9 Hz, 1H, H-1), 4.27 – 4.08 (m, 2H, H-6), 4.00 – 3.88 (m, 2H, H-5, OCH_2), 3.59 (m,1H, OCH_2), 3.20 (m, 2H, C*H*$_2$NHBoc), 2.22 – 1.95 (m, 12H, CH_3-CO), 1.85 – 1.72 (m, 2H, CH_2C*H*$_2CH_2$), 1.46 (s, 9H, tBu).

^{13}C NMR (101 MHz, $CDCl_3$) δ(ppm)= 170.41 (CH_3-*C*O), 170.26 (CH_3-*C*O),), 170.17 (CH_3-*C*O),), 169.51 (CH_3-*C*O),), 156.01 (*C*OBoc), 101.29 (C-1), 79.3 (*C*$(CH_3)_3$) 70.91 (C-3) 70.73 (C-5), 68.80 (C-2), 67.80 (OCH_2), 67.06 (C-4), 61.31 (C-6), 37.83 (*C*H_2NHBoc), 29.73 (CH_2*C*H_2CH_2), 28.43 (C(*C*$H_3)_3$) 20.59 (CO*C*H_3).

ESI-MS: m/z calc 505.52 found: 505.47 $[M+H]^+$, 406.40 $[M\text{-}Boc+H]^+$

General procedure for the conjugation with galactose unit (compound 16 and 17)

In a flask containing the compound **14** (1.25 equivalents for each isothiocyanate group) was fluxed HCl generated by the addition of sulfuric acid to sodium chloride. The reaction was kept stirring at room temperature and was monitored using TLC (eluent: DCM/MeOH 8:2, visualized with ninhydrin). After 2 hours, the reaction was complete, and the product was obtained **15** as a brown solid. The crude was then transferred in a two-necked flask using dry DCM (10 mL), under Argon flow. Then, **8** or **9** (1 equivalent) was added. To the flask, Et_3N (50 equivalents) was added. The reaction was kept stirring at room temperature and was monitored using TLC (eluent: DCM/MeOH 20:1, visualized with sulfuric acid). After 48 hours, the reaction was complete, and the solvent was evaporated under reduced pressure. The product was isolated through chromatographic separation (DCM/iPrOH 98:2 to 97:3) as a white solid.

5,11,17,23-tetrakis(3-(2,3,4,6-tri-O-acetyl-β-D-galactopyranosyloxy)-propylthioureido]-25,26,27,28-tetramethoxycalix[4]arene (16)

Yield=11% (34.34 mg)

^{1}H NMR (400 MHz, MeOD, 60 °C) δ (ppm): 7-25-6.38 (m, 8H, ArH), 5.38 (dd, *J* = 3.0, 1.1 Hz, 4H, H-4), 5.19 – 5.05 (m, 8H, H-2+H-3), 4.67 (d, *J* = 7.0 Hz, 4H, H-1), 4.43 –3.45 (m, 48H, H-6a+H-6b+H-5+OCH_3+ArCH_2Ar+CH_2N+OCH_2), 2.24 – 1.73 (m, 56H, CH_3CO+$OCH_2CH_2CH_2$). ESI-MS: m/z calc 2329.75 found: 1164.60 $[M]^{2+}$, 1176.28 $[M+Na+H]^{2+}$

5,11,17,23,29,35-hexakis(3-(2,3,4,6-tri-O-acetyl-β-D-galactopyranosyloxy)-propylthioureido]- 37,38,39,40,41,42-hexamethoxycalix[6]arene (17)

Yield=19% (43.12 mg)

^{1}H NMR (400 MHz, CD_3OD) δ (ppm): 7.01 (br s, 12H, ArH), 5.49 – 5.42 (m, 6H, H-4), 5.36 (dd, *J* = 10.0, 3.5 Hz, 6H, H-3), 5.12 (d, *J* = 9.8 Hz, 12H, H-2+H-1), 4.35 (t, J = 6.6 Hz, 6H, H-5), 4.15 – 4.06 (m, 12H, H6a-H6b), 4.04 – 3.90 (m, 12H, ArCH_2Ar), 3.82 (m, 6H, NC*H*H), 3.72 (br s, 30H, OCH_3+OCH_2), 3.57 (br s, 6H, NC*H*H), 2.24 – 1.87 (m, 84H, CH_3CO+$OCH_2CH_2CH_2$).

^{13}C NMR (101 MHz, CD_3OD) δ (ppm): 180.6 (NHCS), 170.9 (C=O), 170.7 (C=O), 170.6 (C=O), 170.2 (C=O), 154.1 (Ar), 134.9 (Ar), 133.4 (Ar), 125.4 (Ar), 96.3 (C-1), 68.3 (C-4), 68.0 (C-2), 67.8

(C-3), 66.3 (C-5), 66.0 (NCH_2), 61.7 (C-6), 60.1 (OCH_3), 41.6 (OCH_2), 30.0 (Ar*C*H_2Ar), 28.8 ($OCH_2CH_2CH_2$), 19.5 (*C*H_3CO), 19.3 (*C*H_3CO), 19.2 (*C*H_3CO).

ESI-MS: m/z calc 3495.75 found: 1749.56 $[M+2H]^{2+}$, 1759.07 $[M+H+Na]^{2+}$, 1770.51 $[M+2Na]^{2+}$, 1778.36 $[M+Na+K]^{2+}$

General procedure for deacetylation of galactose derivatives (compound 5 and 6)

After the isolation of the compound, peracetylated glycocalixarenes were dissolved in MeOH, and freshly prepared CH_3ONa (solution) was added until pH 8-9. The mixture was stirred at rt for 1.5 h. The progress of the reaction was followed by ESI-MS and TLC (AcOEt/iPrOH/H_2O 6:3:1, visualized by H_2SO_4). After the complete deacetylation, the Amberlite resin IR-120 (H^+) was added for quenching and stirred for another 30 minutes till neutral pH. After the resin removal by filtration on the paper filter, the solvent was evaporated under vacuum to give the final product.

5,11,17,23-tetrakis[(aminopropyl-β-D-galactopiranosyl)thioureido]-25,26,27,28-tetramethoxycalix[4]arene (5)

Yield=4.7 % (10.9 mg)

^{1}H NMR (400 MHz, DMSO-d_6) δ (ppm): 8.99 (br s, 4H, NH), 7.20 (br s, 4H, NH), 6.99 (br s, 8H, ArH), 4.52 (d, *J* = 4.0 Hz, 4H, OH), 4.42 – 4.31 (m, 8H, OH), 4.13 (d, *J* = 6.9 Hz, 4H, H-1), 4.09 (d, *J* = 4.5 Hz, 4H, OH), 3.85 – 3.28 (m, 86H, H-2,H-3,H-4,H-5, H-6, H-6', OC*H*$_3$, OC*H*$_2$, C*H*$_2$NH, ArCH_2Ar) 1.83 (p, *J* = 6.7 Hz, 8H, $OCH_2CH_2CH_2$).

ESI-MS: m/z calc 1657.89 found: 848.48 $[M+H+K]^{2+}$, 1658.96 $[M+H]^+$, 1697.12 $[M+K]^+$

5,11,17,23,29,35-hexakis[(aminopropyl-β-D-galactopiranosyl)thioureido]-37,38,39,40,41,42-hexamethoxycalix[6]arene (6)

Yield= 5.7 % (8.68 mg)

^{1}H NMR (400 MHz, DMSO-d_6) δ (ppm): 9.66 (br s, 6H, NH), 7.95 (br s, 6H, NH), 7.11 (s, 12H, ArH), 4.66 (br s, 30H, OH+H-1), 3.97 – 3.02 (m, 90H, H-2,H-3,H-4,H-5, H-6, H-6', OC*H*$_3$, OC*H*$_2$, C*H*$_2$NH, ArCH_2Ar), 1.78 (p, *J* = 7.3 Hz, 12H).

^{13}C NMR (101 MHz, DMSO) δ (ppm): 181.0, 152.9, 135.1, 134.2, 124.3, 99.4, 71.7, 70.1, 69.3, 69.0, 65.6, 61.1, 60.5, 41.7, 29.1.

ESI-MS: m/z calc 2498.76 found: 1249.56 $[M+2H]^{2+}$, 1272.33 $[M+2Na]^{2+}$

4.2 Synthesis of trisaccharide CPS repeating unit of *C. Jejuni* HS 23/36

General information

Anhydrous (Anhyd.) solvents and solvents for purification including dichloromethane (DCM), 1,2-dichloroethane (DCE), tetrahydrofuran (THF), N,N-dimethylformamide (DMF), methanol (MeOH), acetonitrile (ACN), pyridine (Py), and toluene (Tol) were delivered from commercial suppliers and used as received. Reactions requiring anhyd. conditions were run under an argon (Ar) atmosphere. Freshly activated 4 Å MS were prepared before use by heating with a hot air gun (20–30 min) under high vacuum. Analytical TLC was performed using silica gel 60 F254, 0.25 mm pre-coated TLC aluminium foil plates. Compounds were visualized using UV (λ = 254 nm) and orcinol (1 mg/m) in 10% aqueous (aq.) H2SO4 with charring. Automated flash column chromatography was carried out using prepacked columns of silica gel (40 μm particle size). Manual flash column chromatography was carried out using silica gel (40–63 μm particle size). NMR spectra were recorded at 303 K on a Bruker Avance spectrometer equipped with a BBO probe at 400 MHz (1 H) and 101 MHz (13C). Spectra were recorded in $CDCl_3$ or DMSO-d_6. HRMS spectra were recorded in the positive-ion electrospray ionization (ESI+) mode on a Q exactive mass spectrometer (Thermo Fisher Scientific) equipped with a H-ESI II Probe source. Solutions were prepared using 1:1 MeCN/H2O containing 0.1% formic acid. In the case of sensitive compounds, solutions were prepared using 1:1 MeOH/H2O to which was added 10 mM ammonium acetate.

p-methoxyphenyl 4,6-O-benzylidene-α-D-glucopyranoside (22)

A solution of β-D-glucopyranose peracetylate (50.00 g, 128.1 mmol) and 4-methoxyphenol (23.85 g, 192.14 mmol) in dry toluene (384 mL) was cooled at 0 °C and then was added BF_3•Et_2O (23.88 mL, 192.14 mmol). The solution was kept stirring at 80 °C. The reaction was monitored through TLC (Tol/EtOAc 8:2, visualized with H_2SO_4). After 90 minutes, the solution was diluted with toluene (100 mL) and let cooling at room temperature and then poured into ice. Then, to the mixture, was added saturated sodium carbonate solution (500 ml). The organic phase was separated and washed with a saturated sodium carbonate solution (2x500 mL), water (1x500 mL), and brine (1x500 mL). The organic phase was collected and dried with Na_2SO_4, and the solvent was evaporated under reduced pressure. The crude was purified via flash column chromatography (Tol/EtOAc 8:2). The mixture of anomer obtained was dissolved in MeOH (171.6 mL) and a solution of 24% sodium methoxide in methanol was added (6.50 mL) and solution was kept stirring for 16 hours. The reaction was monitored by TLC (Tol/EtOAc 7:3, visualized with H_2SO_4). At the end of the reaction, the Amberlite IR-120 (H^+) was added and the mixture was stirred at rt till neutral pH. The resin was filtered off and

the solvent was removed under reduced pressure. The crude was dissolved in dry ACN (228.9 mL) and camphorsulfonic acid (0.226 g, 1.14 mmol). Then, benzaldehyde dimethyl acetal was added (18.89 mL, 125.9 mmol) and the solution was kept stirring for 16 hours. The reaction was monitored by TLC (Tol/EtOAc 8:2, visualized with H_2SO_4). At the end of the reaction, the mixture was filtered, and the product was obtained as a white powder.

Yield=20% (9.59 g)

^{1}H NMR (400 MHz,$CDCl_3$) δ (ppm): 7.55 – 7.48 (m, 2H, ArH of benzylidene), 7.44 – 7.36 (m, 3H, ArH of benzylidiene), 7.08 – 7.02 (m, 2H, ArH of 4-methoxyphenol group), 6.91 – 6.84 (m, 2H, ArH of 4-methoxyphenol group), 5.58 (s, 1H, CH of benzylidene), 5.50 (d, *J* = 4.0 Hz, 1H, H-1), 4.28 (dd, J = 10.3, 4.9 Hz, 1H, H-6a), 4.17 (td, *J* = 9.3, 2.2 Hz, 1H, H-3), 4.05 (td, *J* = 9.9, 4.9 Hz, 1H, H-5), 3.86 – 3.73 (m, 5H, H-6b, H-2, OCH_3), 3.61 (t, *J* = 9.4 Hz, 1H, H-4), 2.75 (d, *J* = 2.2 Hz, 1H, OH-3), 2.33 (d, *J* = 9.7 Hz, 1H, OH-2).

The spectroscopic data found are in agreement with those reported in the literature[62].

p-methoxyphenyl-2,3-di-O-p-methoxybenzyl-4,6-di-O-benzylidene-α-D-glucopyranoside (23)

A solution of compound **22** (14.50 g, 38.73 mmol) in dry DMF (193.6 mL) was cooled at 0 °C. Then, was added 60% sodium hydride in oil (3.255 g, 135.5 mmol) and the solution was kept stirring at rt for 15 minutes. Finally, the p-methoxybenzyl chloride (21.76 mL, 154.9 mmol) was added and the solution was kept stirring for 16 hours. The reaction was monitored by TLC (Tol/EtOAc 8:2, visualized with H_2SO_4). After the disappearance of starting material, methanol (10 mL) was added to the solution. The solution was diluted with EtOAc (300 mL) and washed with a saturated ammonium chloride solution (400 mL), water (400 mL) and brine (400 mL). The organic phase was collected and dried with Na_2SO_4, and the solvent was evaporated under reduced pressure. The crude was purified by crystallization in hot cyclohexane (100 mL). The product was obtained as a white powder.

Yield=98% (23.30 g)

^{1}H NMR (400 MHz, $CDCl_3$) δ (ppm): 7.57 – 7.49 (m, 2H, ArH of benzylidene), 7.43 – 7.27 (m, 7H, ArH of benzylidiene+ ArH of p-methoxybenzyl group), 7.08 – 6.98 (m, 2H, ArH of 4-methoxyphenol group), 6.94 – 6.81 (m, 6H, ArH of 4-methoxyphenol group+ ArH of p-methoxybenzyl group), 5.59 (s, 1H, CH of benzylidene), 5.29 (d, *J* = 3.7 Hz, 1H, H-1), 4.92 – 4.69 (m, 4H, CH_2 of p-methoxybenzyl group), 4.33 – 4.18 (m, 2H, H-6a+H-5), 4.05 (td, *J* = 10.0, 4.9 Hz, 1H, H-3), 3.88 – 3.79 (m, 9H, 3 OCH_3), 3.78 – 3.66 (m, 3H, H-4+H-6b+H-2).

^{13}C NMR (101 MHz, $CDCl_3$) δ (ppm): 159.5 (*C*-OCH_3), 159.3 (*C*-OCH_3), 155.3 (*C*-OCH_3), 150.8 (Ar), 137.5 (Ar), 131.1 (Ar), 130.3 (Ar), 129.7 (Ar), 129.0 (Ar), 128.3 (Ar), 126.2 (Ar), 118.5 (Ar), 114.7 (Ar), 114.0 (Ar), 113.8 (Ar), 101.4 (CH benzylidene) , 97.7 (C-1), 82.1 (C-4) , 78.9 (C-2), 78.3 (C-5), 75.1 (CH_2 of p-methoxybenzyl group), 73.4 (CH_2 of p-methoxybenzyl group), 69.0 (C-6), 63.2 (C-3) , 55.7 (OCH_3), 55.3 (OCH_3).

HRMS (ESI-TOF) m/z: calc 614.25, found: 632.28 $[M+NH_4]^+$

p-methoxyphenyl-2,3-di-O-p-methoxybenzyl-4-O-benzyl-α-D-glucopyranoside (24)

A solution of **23** (23.05 g, 37.42 mmol) in BH_3•THF (175.9 mL) was cooled at 0 °C. Then, was added 1 M di-butyl-boryltriflate in DCM (37.42 mL, 37.42 mmol). The solution was kept stirring at 0 °C for 20 minutes. The reaction was monitored by TLC (Tol/EtOAc 8:2, visualized with H_2SO_4). At the end of the reaction, NEt_3 (500 µL) was added, followed by MeOH (10 mL). The solution was diluted with DCM (200 mL) and washed with saturated sodium carbonate solution (300 mL), water (300 mL), brine (300 mL). The organic phase was collected and dried with Na_2SO_4 and the solvent was co-evaporated under reduced pressure with methanol (2x100 mL). The crude was purified by flash column chromatography (Tol/EtOAc 9:1) and the product was obtained as a yellow oil.

Yield= 58% (13.48 g)

^{1}H NMR (400 MHz, $CDCl_3$) δ (ppm): 7.36 – 7.30 (m, 9H, ArH of benzyl and p-methoxynezyl groups), 6.99 (m, 2H, ArH of 4-methoxyphenol group), 6.92 – 6.82 (m, 6H, ArH of 4-methoxyphenol group and p-methoxybenzyl groups), 5.27 (d, *J* = 3.5 Hz, H-1), 4.97 (dd, *J* = 19.8, 10.8 Hz, 2H, CH_2), 4.87 – 4.75 (m, 2H, CH_2), 4.67 (dd, *J* = 16.4, 11.4 Hz, 2H, CH_2), 4.19 (t, *J* = 9.2 Hz, 1H, H-3), 3.88 – 3.78 (m, 10H, 3OCH_3+H-5), 3.76 – 3.68 (m, 2H, H-6a+H-6b), 3.65-3.60 (m, 2H, H-4+H-2).

^{13}C NMR (101 MHz, $CDCl_3$) δ (ppm): 159.3 (*C*-OCH_3), 155.1 (*C*-OCH_3), 150.7 (*C*-OCH_3), 138.2 (Ar), 131.0 (Ar), 130.2 (Ar), 129.6 (Ar), 129.6 (Ar), 128.5 (Ar), 128.2 (Ar), 128.0 (Ar), 127.9 (Ar), 118.3 (Ar), 114.6 (Ar), 113.9 (Ar), 113.9 (Ar), 96.6 (C-1), 81.6 (H-5), 79.7 (C-2), 77.2 (C-4), 75.5 (CH_2) , 75.1 (CH_2), 73.0 (CH_2), 71.5 (C-5), 61.7 (C-6), 55.6 (OCH_3), 55.3 (OCH_3).

HRMS (ESI-TOF) m/z: calc 616.25, found: 634.28 $[M+NH_4]^+$

p-methoxyphenyl-6-methylene-2,3-di-O-p-methoxybenzyl-4-O-benzyl-α-D-glucopyranoside (26)

To a solution of **24** (13.48 g, 21.86 mmol) in dry DCM (153.0 mL) were added DIPEA (11.42 mL, 65.67 mmol) and dry DMSO (7.76 mL, 109.29 mmol). The solution was cooled at 0 °C and was added sulfur trioxide pyridine complex (10.43 g, 65.57 mmol). The solution was kept stirring at rt for 3 hours and monitored by TLC (Tol/EtOAc 8:2, visualized with H_2SO_4). After the complete conversion, the solution was diluted with DCM (100 mL) and was washed with saturated ammonium chloride solution (200 mL), water (200 mL) and brine (200 mL). The organic phase was collected and dried with Na_2SO_4, and the solvent was evaporated obtaining the product **25** as an orange oil. In parallel, methyl triphenylphosphonium bromide (25.77 g, 72.13 mmol) was suspended in dry THF (120.2 mL) and was cooled at 0 °C. Then, 1 M NaHMDS in THF (61.20 mL, 61.20 mmol) was added. This solution was kept stirring at rt for 3 hours and then was cooled at 0 °C, before the addition of the compound **25** dissolved in dry THF (10 mL). The solution was kept stirring at rt for 16 hours and was monitored by TLC (Tol/EtOAc 9:1, visualized with H_2SO_4). At the end of the reaction, the solution was diluted with EtOAc (200 mL) and washed with saturated ammonium chloride solution (300 mL) and brine (300 mL). The organic phase was collected and dried with Na_2SO_4 and the solvent was evaporated. The crude was purified by flash column chromatography (Tol/EtOAc 95:5) to obtain the product as a colorless oil.

Yield= 71% (9.532 g)

^{1}H NMR (400 MHz, $CDCl_3$) δ (ppm): 7.35 – 7.27 (m, 9H, ArH of benzyl and p-methoxybenzyl groups), 7.03 – 6.97 (m, 2H, ArH of 4-methoxyphenol group), 6.91 – 6.78 (m, 6H, ArH of 4-methoxyphenol group and p-methoxybenzyl groups), 5.88 (ddd, *J* = 17.0, 10.5, 6.2 Hz, 1H, *H*C=CH_2), 5.34 (dt, *J* = 17.2, 1.5 Hz, 1H, HC=C*H*H), 5.25 (d, *J* = 3.6 Hz, 1H, H-1), 5.21 (ddd, *J* = 10.5, 1.7, 1.1 Hz, 1H, HC=C*H*H), 4.93 (d, *J* = 10.4 Hz, 1H, CH_2), 4.81 (dd, *J* = 10.6, 5.9 Hz, 2H, CH_2), 4.75 (d, *J* = 11.7 Hz, 1H, CH_2), 4.63 (d, *J* = 11.2 Hz, 2H, CH_2), 4.28 (dd, *J* = 9.9, 6.3 Hz, 1H, H-5), 4.14 (t, *J* = 9.2 Hz, 1H, H-3), 3.83 – 3.74 (m, 9H, 3OCH_3), 3.62 (dd, *J* = 9.6, 3.6 Hz, 1H, H-2), 3.30 (dd, *J* = 9.9, 8.9 Hz, 1H, H-4).

^{13}C NMR (101 MHz, $CDCl_3$) δ (ppm): 159.3 (*C*-OCH_3), 155.1 (*C*-OCH_3), 150.7 (*C*-OCH_3), 135.0 (H*C*=CH_2) (Ar), 131.0 (Ar), 129.6 (Ar), 129.6 (Ar), 129.3 (Ar), 128.4 (Ar), 127.9 (Ar), 127.7 (Ar), 118.41 (Ar), 118.12 (HC=*C*H_2) , 114.5 (Ar), 113.9 (Ar), 113.8 (Ar), 96.6 (C-1), 82.2 (C-3), 81.3 (C-4), 79.6 (C-2) , 75.5 (CH_2), 75.2 (CH_2), 72.9 (C-5) 55.6 (OCH_3), 55.3 (OCH_3).

HRMS (ESI-TOF) m/z: calc 612.27, found: 630.30 $[M+NH_4]^+$

p-methoxyphenyl-2,3-di-O-p-methoxybenzyl-4-O-benzyl-D-glycero-α-D-gluco-heptopyranoside (27)

To a solution of **26** (8.940 g, 14.59 mmol) in 9:1 Acetone/H_2O (218.9 mL) was added *N*-methylmorpholine *N*-oxide (3.419 g, 29.18 mmol). Then, 4% osmium tetraoxide in water (4.621 mL, 0.732 mmol) was added and the solution was kept stirring at rt for 5 hours. The reaction was monitored by TLC (Tol/EtOAc 9:1, visualized with H_2SO_4). At the disappearance of starting material, a saturated sodium thiosulfate solution (300 ml) was added. The product was extracted with DCM (2x200 mL). The organic layers were collected and washed with brine (300 mL), dried and the solvent evaporated. The product was obtained by flash column chromatography (DCM/cyclohexane/acetone 7:1:2) as colorless needle-like crystals.

Yield=64% (6.03 g)

^{1}H NMR (400 MHz, $CDCl_3$) δ (ppm): 7.41 – 7.29 (m, 9H, ArH of benzyl and p-methoxynezyl groups), 7.10 – 6.95 (m, 2H, ArH of 4-methoxyphenol group), 6.93 – 6.79 (m, 6H, ArH of 4-methoxyphenol and p-methoxybenzyl groups), 5.23 (d, *J* = 3.6 Hz, 1H, H-1), 5.05 (dd, *J* = 13.5, 10.7 Hz, 2H, CH_2), 4.84 – 4.75 (m, 2H, CH_2), 4.68 (dd, *J* = 22.2, 11.3 Hz, 2H, CH_2), 4.21 (t, *J* = 9.2 Hz, 1H, H-3), 3.94 (dd, *J* = 9.9, 5.2 Hz, 1H, H-6), 3.87 – 3.77 (m, 9H, 3OCH_3), 3.63 (m, 2H, H-2+H-5), 3.55 (dd, *J* = 6.5, 4.1 Hz, 2H, H-7), 2.97 (d, *J* = 4.2 Hz, 1H, OH-6), 1.91 (t, *J* = 6.5 Hz, 1H, OH-7).

^{13}C NMR (101 MHz, $CDCl_3$) δ (ppm): 159.3 (*C*-OCH_3), 155.1 (*C*-OCH_3), 150.7 (*C*-OCH_3), 138.6 (Ar), 133.0 (Ar), 129.7 (Ar), 128.6 (Ar), 128.1 (Ar), 118.5 (Ar), 114.6 (Ar), 114.0 (Ar), 113.9 (Ar), 96.4 (C-1), 81.8 (C-3), 79.7 (C-2), 77.2 (C-5), 75.4 (CH_2), 74.9 (CH_2), 73.0 (CH_2), 72.7 (C-4), 70.9 (C-6), 63.1 (C-7), 55.6 (OCH_3), 55.3 (OCH_3), 55.3 (OCH_3).

HRMS (ESI-TOF) m/z: calc 646.28, found: 648.33 $[M]^+$

p-methoxyphenyl-2,3-di-O-p-methoxybenzyl-4,6,7-tri-O-benzyl-D-glycero-α-D-gluco-heptopyranoside (28)

A solution of compound **27** (5.400 g, 8.351 mmol) in dry DMF (83.52 mL) was cooled at 0° C. Then, was added 60% sodium hydride in oil (1.200 g, 18.37 mmol) and the solution was kept stirring at rt for 15 minutes. Finally, the benzyl bromide (2.182 mL, 18.37 mmol) was added, and the solution was kept stirring for 16 hours. The reaction was monitored by TLC (Tol/EtOAc 8:2, visualized with H_2SO_4). After the disappearance of starting material, methanol (10 mL) was added to the solution. The solution was diluted with EtOAc (300 mL) and washed with a saturated ammonium chloride solution (400 mL), water (400 mL) and brine (400 mL). The organic phase was collected and dried with Na_2SO_4, and the solvent was evaporated under reduced pressure. The product was obtained by flash column chromatography (Tol/EtOAc 9:1) as a colorless oil.

Yield=90% (6.21 g)

^{1}H NMR (400 MHz, $CDCl_3$) δ (ppm): 7.39 – 7.17 (m, 19H, ArH of benzyl and p-methoxynezyl groups), 7.12 – 7.03 (m, 2H, ArH of 4-methoxyphenol group), 6.91 – 6.84 (m, 4H, ArH of p-methoxynezyl groups), 6.82 – 6.74 (m, 2H, ArH of 4-methoxyphenol group), 5.26 (d, J = 3.5 Hz, 1H, H-1), 4.95 (dd, J = 28.4, 10.6 Hz, 2H, CH_2), 4.83 – 4.73 (m, 2H, CH_2), 4.68 – 4.57 (m, 4H, $2CH_2$), 4.52 – 4.39 (m, 2H, CH_2), 4.22 – 4.13 (m, 2H, H3+H5), 3.97 (ddd, J = 6.4, 4.8, 1.3 Hz, 1H, H-4), 3.85 – 3.77 (m, 9H, $3OCH_3$), 3.77 – 3.57 (m, 4H, H-6+H-7a+H-7b+H-2).

^{13}C NMR (101 MHz, $CDCl_3$) δ (ppm): 159.4 (*C*-OCH_3), 159.2 (*C*-OCH_3), 155.2 (*C*-OCH_3), 151.0 (Ar), 138.6 (Ar), 138.4 (Ar), 131.0 (Ar), 130.3 (Ar), 129.7 (Ar), 129.5 (Ar), 129.0 (Ar), 128.4 (Ar), 128.3 (Ar), 128.2 (Ar), 128.1 (Ar), 127.7 (Ar), 127.6 (Ar), 127.6 (Ar), 127.5 (Ar), 127.3 (Ar), 118.9 (Ar), 114.5 (Ar), 113.9 (Ar), 113.9 (Ar), 96.7 (C-1), 82.2 (C-3), 79.9 (C-2), 78.2 (C-4), 78.0 (CH_2), 75.5 (CH_2), 74.7 (CH_2), 73.2 (CH_2), 72.8 (CH_2) , 72.5 (C-6),71.2 (C-5), 70.6 (C-7), 55.6 (OCH_3), 55.3 (OCH_3), 55.3 (OCH_3).

HRMS (ESI-TOF) m/z: calc 826.98, found: 644.93 $[M+NH_4]^+$

p-methoxyphenyl-4,6,7-tri-O-benzyl-D-glycero-α-D-gluco-heptopyranoside (29)

To a solution of **28** (6.90 g, 8.35 mmol) in dry DCM (75.20 mL) was cooled at 0 °C and was added trifluoroacetic acid (8.35 mL, 109.1 mmol). The solution was kept stirring at 0 °C and monitored by TLC (Tol/EtOAc 8:2, visualized with H_2SO_4). After 1 hour, was added MeOH (10 mL) and the solution was diluted with DCM (75 mL). Then, the solution was washed with saturated sodium carbonate solution (150 mL) and brine (150 mL). The organic phase was collected and dried with Na_2SO_4, and the solvent was evaporated under reduced pressure. The crude was purified by flash column chromatography (Tol/EtOAc 8:2) to obtain the product as a white solid.

Yield=70% (3.43 g)

^{1}H NMR (400 MHz, $CDCl_3$) δ (ppm): 7.42-7.20 (m, 15H, ArH of benzyl groups), 7.12 – 7.03 (m, 2H, ArH of 4-methoxyphenol group), 6.83 – 6.70 (m, 2H, ArH of 4-methoxyphenol group), 5.37 (d, *J* = 3.8 Hz, 1H, H-1), 4.87 (d, *J* = 11.2 Hz, 2H, CH_2), 4.72 (d, *J* = 11.2 Hz, 2H, CH_2), 4.69 – 4.59 (m, 2H, CH_2), 4.50 (dd, *J* = 11.9, 9.1 Hz, 2H, CH_2), 4.20 (d, *J* = 10.2 Hz, 1H, H-4), 4.09-4.00 (m, 2H, H-3+H-6), 3.89 – 3.57 (m, 7H, H-2+H-5+H-7a+H-7b+ OCH_3), 2.54 (s, 1H, OH-3), 2.18 (d, *J* = 9.8 Hz, 1H, OH-2).

^{13}C NMR (101 MHz, $CDCl_3$) δ (ppm): 155.5 (*C*-OCH_3), 150.4 (Ar), 138.5 (Ar), 138.4 (Ar), 138.2 (Ar), 128.5 (Ar), 128.4 (Ar), 128.2 (Ar), 128.0 (Ar), 127.8 (Ar), 127.7 (Ar), 127.7 (Ar), 127.6 (Ar),

127.4 (Ar), 119.0 (Ar), 114.7 (Ar), 98.3 (C-1), 77.9+77.8 (C-6,C-5), 75.8 (C-3), 74.5 (CH_2), 73.3 (CH_2), 72.6 (CH_2), 72.6 (C-2), 71.4 (C-4), 70.2 (C-7), 55.6 (OCH_3).

HRMS (ESI-TOF) m/z: calc 586.29, found: 604.29 $[M+NH_4]^+$

p-methoxyphenyl-2,3-anhydro-4,6,7-tri-O-benzyl-D-glycero-α-D-gluco-heptopyranoside (31)

To a solution of **29** (0.538 g, 0.953 mmol) in pyridine (8.2 mL) was added methansulfonyl chloride (0.087 mL, 1.14 mmol). The solution was kept stirring at rt for 4 hours. The reaction was monitored by TLC (Tol/EtOAc 8:2, visualized with H_2SO_4). At the end of the reaction, the solvent was evaporated, and the crude was dissolved in EtOAc (50 mL) and washed with saturated ammonium chloride solution (50 mL) and brine (50 mL). The organic phase was collected and dried with Na_2SO_4, and the solvent was evaporated under reduced pressure. The crude with compound **30** was dissolved in t-BuOH (11.4 mL) and then, was added sodium tert-butoxide (0.165 g, 1.713 mmol). The reaction was kept stirring at rt for 16 hours and monitored by TLC (Tol/EtOAc 8:2, visualized with H_2SO_4). At the disappearance of starting material, the solution was diluted with EtOAc (40 mL) and washed with saturated ammonium chloride solution (50 mL) and brine (50 mL). The organic phase was collected and dried with Na_2SO_4, and the solvent was evaporated under reduced pressure to obtain the product as an orange oil.

Yield=54% (0.291 g)

^{1}H NMR (400 MHz, $CDCl_3$) δ (ppm): 7.40 – 7.19 (m, 15H, ArH of benzyl groups), 7.12 – 7.00 (m, 2H, ArH of 4-methoxyphenol group), 6.84 – 6.73 (m, 2H, ArH of 4-methoxyphenol group), 5.55 (s, 1H, H-1), 4.74 (d, *J* = 11.3 Hz, 1H, CH_2), 4.70 – 4.54 (m, 3H, CH_2), 4.49 – 4.41 (m, 2H, CH_2), 4.10 (dd, *J* = 9.7, 1.8 Hz, 1H, H-5), 3.92 (d, *J* = 9.6 Hz, 1H, H-4), 3.87 (ddd, *J* = 6.9, 5.0, 1.8 Hz, 1H, H-6), 3.78 (s, 3H, OCH_3), 3.70 – 3.62 (m, 2H, H-7a+H-7b), 3.45 (d, *J* = 3.7 Hz, 1H, H-3), 3.31 (d, *J* = 3.6 Hz, 1H, H-2).

^{13}C NMR (101 MHz, $CDCl_3$) δ (ppm): 152.1 (*C*-OCH_3), 150.8 (Ar), 150.8 (Ar), 138.6 (Ar), 138.4 (Ar), 137.4 (Ar), 128.5 (Ar), 128.3 (Ar), 128.1 (Ar), 128.0 (Ar), 127.8 (Ar), 127.6 (Ar), 127.45 (Ar), 127.3 (Ar), 118.6 (Ar), 114.6 (Ar), 94.8 (C-1), 78.0 (C-6), 73.2 (CH_2) , 72.4 (CH_2), 72.0 (CH_2), 70.4 (C-7), 69.0 (C-4), 68.5 (C-5), 55.6 (OCH_3), 53.6 (C-3), 49.5 (C-2).

HRMS (ESI-TOF) m/z: calc 568.61, found: 686.28 $[M+NH_4]^+$

p-methoxyphenyl-4,6,7-tri-O-benzyl-3-O-methyl-D-glycero-α-D-altro-heptopyranoside (32)

To a solution of **31** (1.000 g, 1.76 mmol) in dry DMSO (3.500 mL) and MeOH dry (7.030 mL) was carefully added 60% sodium hydride in oil (1.125 g, 28.14 mmol). The solution was kept stirring at 95 °C for 16 hours. The reaction was monitored by TLC (Tol/EtOAc 8:2, visualized with H_2SO_4). At the end of the reaction, the solution was left cooling at rt and then, diluted with EtOAc (50 mL). The solution was washed with saturated ammonium chloride solution (50 mL) and brine (50 mL) and the organic phase was collected and dried with Na_2SO_4 and the solvent was evaporated under reduced pressure. The crude was purified by flash column chromatography (Tol/EtOAc 8:2) to obtain the product as a colorless oil.

Yield= 64% (0.638 g)

^{1}H NMR (400 MHz, $CDCl_3$) δ (ppm): 7.41 – 7.15 (m, 15H, ArH of benzyl groups), 7.09 – 6.99 (m, 2H, ArH of 4-methoxyphenol group), 6.84 – 6.73 (m, 2H, ArH of 4-methoxyphenol group), 5.19 (d, *J* = 4.1 Hz, 1H, H-1), 4.77 – 4.53 (m, 4H, $2CH_2$), 4.53 – 4.40 (m, 2H, CH_2), 4.35 (t, *J* = 5.0 Hz, 1H, H-5), 4.22 (dd, J = 8.2, 4.2 Hz, 1H, H-2), 4.11 (dd, *J* = 5.2, 3.5 Hz, 1H, H-4), 3.84 (dt, *J* = 5.8, 4.3 Hz, 1H, H-6), 3.77 (s, 3H, $ArOCH_3$), 3.68 (dd, *J* = 10.4, 4.0 Hz, 1H, H-7a), 3.65 – 3.51 (m, 1H, H-7b), 3.44 (dd, *J* = 7.8, 3.6 Hz, 1H, H-3), 3.36 (s, 3H, OCH_3), 2.31 (d, J = 19.1 Hz, 1H, OH-3).

^{13}C NMR (101 MHz, $CDCl_3$) δ (ppm): 155.2 (*C*-OCH_3), 150.9 (Ar), 138.3 (Ar), 138.3 (Ar), 138.2 (Ar), 129.0 (Ar), 128.4 (Ar), 128.3 (Ar), 128.3 (Ar), 128.2 (Ar), 128.0 (Ar), 127.6 (Ar), 127.6 (Ar), 125.3 (Ar), 119.1 (Ar), 114.4 (Ar), 101.3 (C-1), 79.5 (C-3), 77.7 (C-6), 73.4 (CH_2), 72.9 (C-5), 72.5 (CH_2), 71.8 (CH_2), 71.1 (C-4), 70.3 (C-7), 69.7 (C-2), 57.8 (3-OCH_3), 55.6($ArOCH_3$).

HRMS (ESI-TOF) m/z: calc 600.71, found: 618.30 $[M+NH_4]^+$

p-methoxyphenyl-2-O-benzoyl-4,6,7-tri-O-benzyl-3-O-methyl-D-glycero-α-D-altro-heptopyranoside (33)

To a solution of X (0.290 g, 0.48 mmol) in dry DCM (4.800 mL) were added NEt_3 (0.262 mL, 1.932 mmol) and 4-dimethyl-aminopyridine (0.006 g, 0.0482 mmol). The solution was cooled at 0 °C and then, was added benzoyl chloride (0.17 mL, 1.452 mmol). The reaction was monitored by TLC (Tol/EtOAc 8:2, visualized with H_2SO_4). The solution was kept stirring for 16 hours and then, the solution was diluted with DCM (50 mL). The solution was washed with saturated ammonium chloride solution (50 mL) and brine (50 mL). the organic phase was collected and dried with Na_2SO_4 and the

solvent was evaporated under reduced pressure. The crude was purified by flash column chromatography (Tol/EtOAc 8:2) to obtain the product as a colorless oil.

Yield= 90% (0.306 g)

^{1}H NMR (400 MHz, $CDCl_3$) δ (ppm): 8.02 – 7.93 (m, 2H, ArH of benzoyl group), 7.69 – 7.60 (m, 1H, ArH of benzoyl group), 7.51 – 7.40 (m, 2H, ArH of benzoyl group), 7.36 – 7.17 (m, 15 H, ArH of benzyl groups), 7.09 – 7.00 (m, 2H, ArH of 4-methoxyphenyl group), 6.82 – 6.72 (m, 2H, ArH of 4-methoxyphenyl group), 5.53 (dd, *J* = 3.8, 1.4 Hz, 1H, H-2), 5.32 (s, 1H, H-1), 4.75 (s, 2H, CH_2), 4.66 – 4.49 (m, 5H, 2 CH_2+H-5), 4.13 – 4.04 (m, 2H, H-4+H-6), 3.84 – 3.72 (m, 5H, H-7a+H-7b+ArOCH_3), 3.67 (t, *J* = 3.4 Hz, 1H, H-3), 3.60 (s, 3H, OCH_3).

^{13}C NMR (101 MHz, $CDCl_3$) δ (ppm): 177.6 (C=O), 150.8 (C-OCH_3), 139.0 (Ar), 138.5 (Ar), 133.5 (Ar), 133.0 (Ar), 129.8 (Ar), 129.5 (Ar), 128.5 (Ar), 128.4 (Ar), 128.3 (Ar), 128.23 (Ar), 128.1 (Ar), 127.8 (Ar), 127.7 (Ar), 127.6 (Ar), 127.5 (Ar), 127.3 (Ar), 118.9 (Ar), 114.5 (Ar), 97.6 (C-1), 79.5 (C-6), 75.6 (C-3), 73.3 (CH_2), 73.1 (CH_2), 71.6 (C-4), 71.4 (CH_2+C-7), 69.0 (C-2), 68.8 (C-5), 58.4 (OCH_3), 55.6 (ArOCH_3).

HRMS (ESI-TOF) m/z: calc 704.82, found: 722.30 $[M+NH_4]^+$

2-O-benzoyl-4,6,7-tri-O-benzyl-3-O-methyl-D-glycero-α/β-D-altro-heptopyranoside (20)

To a solution of X (0.478 g, 0.74 mmol) in ACN/H_2O 9:1 (38.48 mL) was added ammonium cerium (IV) nitrate (1.952 g, 3.70 mmol). The solution was kept stirring for 20 minutes and monitored through TLC (Tol/EtOAc 8:2, visualized H_2SO_4). After 20 minutes, DCM was added to the solution and washed with water, dried with Na_2SO_4, and the solvent was evaporated under reduced pressure. The crude was purified by flash column chromatography (Tol/EtOAc 8:2) to obtain product as a white solid.

Yield=80% (0.344 g, 81% α and 19% β)

α anomer:

^{1}H NMR of α (400 MHz, $CDCl_3$) δ (ppm): 8.04 – 7.74 (m, 2H, ArH of benzoyl group), 7.60 – 7.45 (m, 1H, ArH of benzoyl group), 7.36 – 6.99 (m, 15H, ArH of benzyl and benzoyl groups), 5.11 (dd, J = 4.1, 1.4 Hz, 1H, C-2), 5.02 (d, J = 10.7 Hz, 1H, H-1), 4.92 (d, *J* = 11.2 Hz, 1H, OH), 4.84 – 4.66 (m, 2H, CH_2), 4.51 – 4.40 (m, 4H, 2 CH_2), 4.24 (dd, *J* = 9.5, 1.4 Hz, 1H, H-5), 4.08 – 3.95 (m, 3H,

H-4+H-6), 3.75 – 3.63 (m, 2H, H-7a+H-7b), 3.60 (ddd, *J* = 4.2, 2.9, 1.3 Hz, 1H, H-3), 3.48 (s, 3H, OCH_3).

^{13}C NMR (101 MHz, $CDCl_3$) δ (ppm): 165.08 (C=O), 139.1 (Ar), 138.5 (Ar), 137.4 (Ar), 133.5 (Ar), 129.8 (Ar), 129.3 (Ar), 128.6 (Ar), 128.4 (Ar), 128.4 (Ar), 128.3 (Ar), 128.2 (Ar), 128.0 (Ar), 127.7 (Ar), 127.6 (Ar), 127.5 (Ar), 127.3 (Ar), 92.8 (C-1), 80.0 (C-6), 76.9 (C-3), 73.5 (CH_2), 73.2 (CH_2), 72.0 (CH_2), 71.7 (C-5), 71.6 (C-7), 69.0 (C-2), 60.2 (OCH_3).

β anomer:

^{1}H NMR (400 MHz, $CDCl_3$) δ (ppm): 8.04 – 7.74 (m, 2H, ArH of benzoyl group), 7.60 – 7.45 (m, 1H, ArH of benzoyl group), 7.36 – 6.99 (m, 15H, ArH of benzyl and benzoyl groups), 5.16 (m, 2H, H-1+H-2), 4.84 – 4.66 (m, 2H, CH_2), 4.51 – 4.40 (m, 4H, 2 CH_2), 4.08 – 3.95 (m, 2H, H-5+H-6), 3.88 (dd, *J* = 9.0, 3.1 Hz, 1H, H-4), 3.75 – 3.63 (m, 2H, H-7a+H-7b), 3.55 – 3.51 (m, H-3), 3.40 (s, 3H, OCH_3).

^{13}C NMR (101 MHz, $CDCl_3$) δ (ppm): 165.7 (C=O), 138.9 (Ar), 138.4 (Ar), 137.5 (Ar), 133.5 (Ar), 129.5 (Ar), 129.3 (Ar), 129.1 (Ar), 128.4 (Ar), 128.4 (Ar), 128.3 (Ar), 128.0 (Ar), 127.9 (Ar), 127.7 (Ar), 127.6 (Ar), 127.6 (Ar), 127.4 (Ar), 91.6 (C-1), 79.4 (C-6), 75.5 (C-3), 74.3 (C-5), 73.3 (CH_2), 73.2 (CH_2), 72.1 (C-4), 72.0 (C-7), 71.2 (CH_2), 70.4 (C-2), 59.3 (OCH_3).

HRMS (ESI-TOF) m/z: calc 598.69, found: 616.29 $[M+NH_4]^+$

Methyl(2-O-benzoyl-4,6-O-di-tert-butylsilylene-α-D-galactopyranosyl)-(1→2)-4,6,7-tri-O-benzyl-3-O-methyl-D-glycero-α-D-altro-heptopyranoside (35)

To a solution of acceptor **32b** (0.120 g, 0.241 mmol) and donor **19** (0.201 g, 0.314 mmol) in dry DCM (1.7 mL) was added 4 Å MS (0.100 g). The solution was kept stirring for 1 hour at rt, then was cooled at -40 °C. NIS (0.066 g, 0.291 mmol) and triflic acid (3.614 µL, 0.040 mmol) were added. The reaction was monitored through TLC (Tol/EtOAc 9:1, visualized H_2SO_4) and kept stirring for 2 hours at -50 °C. At the end of the reaction, NEt_3 was added (1 mL), and the solution was filtered and diluted with DCM (5 mL). The solution was washed with a saturated sodium thiosulfate solution (10 mL), and brine (10 mL), the organic phase was dried with Na_2SO_4, and the solvent was evaporated under reduced pressure. The crude was purified by flash column chromatography (Tol/EtOAc 9:1) to obtain most of the product in a mixture with hydrolyzed galactose. The crude with **34** was dissolved in 19:1 DCM/PBS (1.500 mL) and DDQ (0.022 mL, 0.17 mmol) was added. The solution was kept stirring at rt and monitored through TLC (Tol/EtOAc 85:15, visualized H_2SO_4). After 24 hours, the solvent was evaporated, and the crude dissolved in EtOAc (50 mL). The organic phase was washed with

water (50 mL) and brine (50 mL), dried with Na_2SO_4, and the solvent was evaporated under reduced pressure. The crude was purified by flash column chromatography (Tol/EtOAc 9:1)

Yield=23% (0.050 mg)

^{1}H NMR (400 MHz, $CDCl_3$) δ (ppm): 8.11 (dt, J = 8.3, 1.3 Hz, 2H, ArH of benzoyl group), 7.63 – 7.47 (m, 1H, ArH of benzoyl group), 7.43 – 7.16 (m, 17H, ArH of benzoyl and benzyl groups), 5.39 (d, J = 3.8 Hz, 1H, H-1'), 5.34 (ddd, J = 10.1, 3.8, 1.3 Hz, 1H, H-2'), 4.81 – 4.67 (m, 2H, OCH2Ph), 4.62 (d, J = 2.7 Hz, 1H, H-1), 4.49 (dd, J = 17.2, 3.9 Hz, 3H, OCH_2Ph+H-4'), 4.38 (d, J = 11.7 Hz, 1H, H-6a'), 4.32 – 4.21 (m, 2H, H-6b'), 4.19 (m, 1H, H-4), 4.10 (br s, 1H, H-3'), 3.97 – 3.86 (m, 4H, H-2+H-5+H-6+H-5'), 3.76 – 3.62 (m, 2H, H-7ab), 3.44 (dd, J = 5.9, 3.4 Hz, 1H, H-3), 3.36 (s, 3H, OCH_3 in 1), 3.14 (s, 3H, OCH_3 in 1), 2.60 (s, 1H, OH), 1.24 – 1.04 (m, 18H, tBu).

^{13}C NMR (101 MHz, $CDCl_3$) δ (ppm) 166.5, 138.8, 138.3, 138.1, 133.3, 129.9, 129.0, 128.4, 128.4, 128.3, 128.2, 128.2, 127.8, 127.6, 127.6, 127.6, 127.5, 127.5, 100.7, 97.5, 78.7, 77.8, 74.7, 73.6, 73.4, 72.9, 71.8, 71.8, 71.1, 71.0, 70.0, 68.4, 67.6, 66.7, 58.4, 55.4, 27.6, 27.3.
HRMS (ESI-TOF) m/z: calc 914.43, found: 932.46 $[M+NH_4]^+$

Allyl-4,6-O-benzylidiene-3-O-naphtyl-2-deoxy-2-trichloroacetamido-β-D-glucopyranoside (37)

A solution of **21** (1.236 g, 2.73 mmol) in DMF (27.30 mL) was cooled at -10 °C.60% sodium hydride in oil (0.218 g, 5.46 mmol) and 2-(Bromomethyl)naphthalene (1.401 g, 8.19 mmol) were added. The solution was kept stirring at -10 °C and was monitored through TLC (Tol/EtOAc 8:2, visualized H_2SO_4). After 1.5 hours, MeOH (5 mL) was added and the solution was diluted with EtOAc (100 mL), washed with a saturated solution of ammonium chloride (100 mL) and brine (100 mL). The organic phase was collected and dried with Na_2SO_4, and the solvent was evaporated under reduced pressure. The crude was purified by flash column chromatography (Tol/EtOAc 9:1) to obtain the product as a white solid.

Yield=62% (1.023 g)

^{1}H NMR (400 MHz, $CDCl_3$) δ (ppm): 7.88 – 7.71 (m, 5H, ArH), 7.60 – 7.39 (m, 7H, ArH), 6.90 (d, *J* = 7.6 Hz, 1H, NH), 5.88 (dddd, *J* = 16.8, 10.3, 6.3, 5.3 Hz, 1H, C*H*=CH_2), 5.64 (s, 1H, CH of benzylidene), 5.31 (dq, *J* = 17.2, 1.6 Hz, 1H, Allyl CH_2), 5.22 (dq, *J* = 10.4, 1.4 Hz, 1H, Allyl CH_2), 5.07 (d, *J* = 11.5 Hz, 1H, OCH_2Nap), 5.03 (d, *J* = 8.3 Hz, 1H, H-1), 4.90 (d, *J* = 11.5 Hz, 1H, OCH_2Nap), 4.45 – 4.33 (m, 3H, H-3+H-6a+CH=C*H*H), 4.12 (ddt, *J* = 12.7,0 6.3, 1.3 Hz, 1H,

CH=C*H*H), 3.86 (t, *J* = 10.3 Hz, 1H,H-6b), 3.80 (t, *J* = 9.2 Hz, 1H, H-4), 3.62 – 3.54 (m, 2H, H-2+H-5).

^{13}C NMR (101 MHz, $CDCl_3$) δ(ppm): 161.9 (C=O), 137.2 (Ar), 135.2 (Ar), 133.3 (*C*H=CH_2), 133.2 (Ar), 133.1 (Ar), 129.1 (Ar), 128.3 (Ar), 128.3 (Ar), 128.0 (Ar), 127.7 (Ar), 127.2 (Ar), 126.2 (Ar), 126.1 (Ar), 126.0 (Ar), 118.3 (Allyl CH_2), 101.4 (CHPh), 98.9 (C-1), 92.5 (CCl_3), 82.7 (C-4), 75.8 (C-3), 74.8 (CH_2Naph), 70.7 (CH=*C*H_2), 68.7 (C-6), 66.1 (C-2), 59.0 (C-5).

HRMS (ESI-TOF) m/z: calc 591.102, found: 609.132 $[M+NH_4]^+$

Methyl-(4,6-O-benzylidiene-3-O-naphtyl-2-deoxy-2-trichloroacetamido-β-D-glucopyranoside)-(1→3)-(2-O-benzoyl-3-O-(2-napthylmethyl)-4,6-O-di-tert-butylsilylene-α-D-galactopyranosyl)-(1→2)-4,6,7-tri-O-benzyl-3-O-methyl-D-glycero-α-D-altro-heptopyranoside (40)

To a solution of **37** (0.500 mg, 0.851 mmol) in 75:25 DCM/H_2O (18.00 mL) was added $PdCl_2$ (0.020 g, 0.071 mmol), and the solution was kept stirring at reflux for 24 hours. The reaction was monitored through TLC (Tol/EtOAc 85:15, visualized with H_2SO_4). After 1 day, the reaction was cooled at rt and NIS (0.381 g, 1.692 mmol) in THF (5.000 mL). The reaction was monitored through TLC (Tol/EtOAc 85:15, visualized with H_2SO_4) and after 2 hours a saturated solution of sodium thiosulfate (50 mL) was added. The solution was filtered on celite and celite pad was washed with DCM (50 mL). The organic layer was separated and washed with saturated sodium thiosulfate solution (50 mL), saturated sodium bicarbonate solution (50 mL) and brine (50 mL). The organic phase was collected and dried with Na_2SO_4, and the solvent was evaporated under reduced pressure. The crude was purified by flash column chromatography (DCM/MeOH 98:2) to obtain the product as a brown solid with a yield of 90% (0.420 g). The hemiacetal **38** (0.200 g, 0.34 mmol) was dissolved in dry DCE (3.400 mL) and cooled at 0° C. DBU (0.015 g, 0.090 mmol) and trichloroacetonitrile (0.2827 mL, 1.690 mmol) were added. The reaction was kept stirring at rt and monitored through TLC (Tol/EtOAc+1% NEt_3 9:1, visualized with H_2SO_4). After 16 hours, the solvent was evaporated, and the crude was purified by flash column chromatography (Tol/EtOAc+1% NEt_3 9:1) to obtain the donor with a yield of 77% (0.193 g). The donor **39** (0.107 g, 0.18 mmol) and the acceptor **35** (0.050 g, 0.100 mmol) were dissolved in dry DCM (2.000 mL) and 4 Å MS (0.100 g) were added. The solution was kept stirring for 1 hour and then was cooled at -10 °C and TMSOTf (2.353 μL) was added. The solution was kept stirring at -10 °C for 1 hour. The reaction was monitored through TLC (Tol/EtOAc 8:2, visualized H_2SO_4). At the disappearance of the donor, NEt_3 was added (1 mL), the

solution was filtered, and the solvent was evaporated under reduced pressure. The crude was purified by flash column chromatography (Tol/EtOAc 9:1) as a colorless oil.

Yield=72% (0.071 g)

^{1}H NMR (400 MHz, $CDCl_3$) δ (ppm): 7.95 (d, *J* = 7.7 Hz, 2H, ArH of benzoyl), 7.74 – 7.56 (m, 5H, ArH on benzoyl and benzylidene), 7.47 – 7.00 (m, 27H), 6.89 – 6.79 (m, 1H, NH), 5.53 (s, 1H, CHPh), 5.40 (dd, *J* = 10.5, 3.7 Hz, 1H, H-2'), 5.33 (d, *J* = 3.9 Hz, 1H, H-1'), 5.27 (d, *J* = 8.0 Hz, 1H, H-1''), 4.94 (d, *J* = 11.5 Hz, 1H, H-6a'), 4.73 (d, *J* = 11.3 Hz, 1H, H-6b'), 4.68 – 4.52 (m, 3H, H-4'+OCH_2), 4.50 – 3.99 (m, 13H, H-5'+H-3'+H-3''+H-5''+4OCH_2+H-1), 3.80-3.40 (m, 10H, H-4+H-5+H-6+H-7ab+H-6ab''+H-2''+H-4''+H-2), 3.23 (s, 3H, OCH_3 in 3), 3.19 (dd, *J* = 6.3, 3.3 Hz, 1H, H-3), 2.83 (s, 3H, OCH_3 in 1), 1.00 (d, *J* = 6.4 Hz, 18H, tBu).

^{13}C NMR (101 MHz, $CDCl_3$) δ (ppm): 165.9, 163.6, 161.9, 138.6, 138.2, 138.1, 137.9, 137.2, 135.3, 133.4, 133.2, 133.0, 129.9, 129.8, 129.2, 129.1, 128.6, 128.4, 128.4, 128.3, 128.2, 128.2, 128.2, 127.9, 127.7, 127.7, 127.7, 127.6, 127.6, 127.5, 127.0, 126.1, 126.1, 126.0, 125.3, 101.4, 101.0, 99.9, 96.7, 92.2, 91.9, 82.6, 78.1, 78.0, 75.7, 75.5, 74.8, 74.2, 73.4, 73.4, 72.7, 71.7, 71.1, 70.7, 70.4, 70.0, 68.8, 67.7, 66.9, 66.1, 59.4, 57.9, 55.4.

HRMS (ESI-TOF) m/z: calc 1449.48, found: 1467.51 $[M+NH_4]^+$

^{1}H NMR (400 MHz, $CDCl_3$) δ (ppm): 7.93 – 7.81 (m, 4H, ArH), 7.64 – 7.55 (m, 3H, ArH), 7.55 – 7.45 (m, 2H, ArH), 7.37 – 7.26 (m, 3H, ArH), 5.00 (d, *J* = 11.8 Hz, 1H, OCH*H*Naph), 4.85 (d, *J* = 11.9 Hz, 1H, OCH*H*Naph), 4.65 – 4.55 (m, 2H, H-1+H-4), 4.32 – 4.21 (m, 2H, H-6), 4.09 (t, *J* = 9.4 Hz, 1H, H-2), 3.45 (dd, *J* = 9.0, 3.1 Hz, 1H, H-3), 3.38 (p, *J* = 1.3 Hz, 1H, H-5), 1.11 (d, *J* = 4.8 Hz, 18H, tBu).

^{13}C NMR (101 MHz, $CDCl_3$) δ (ppm): 132.6 (Ar), 129.0 (Ar), 128.9 (Ar), 128.4 (Ar), 128.2 (Ar), 127.9(Ar), 127.7 (Ar), 127.7 (Ar), 126.7 (Ar), 126.2 (Ar), 126.0 (Ar), 125.8 (Ar), 125.3 (Ar), 89.3 (C-1), 81.8 (C-3), 75.3 (C-5), 70.6 (C-6), 69.5 (C-4), 68.6 (C-2), 67.4 (CH_2Nap), 27.7 (tBu), 27.6 (tBu).

HRMS (ESI-TOF) m/z: calc 552.80, found: 570.14 $[M+NH_4]^+$

Allyl(2-O-benzoyl-4,6,7-tri-O-benzyl-3-O-methyl-D-glycero-α-D-altro-heptopyranosyl)-(1→3)-4,6-O-benzylidiene-2-deoxy-2-trichloroacetamido-β-D-glucopyranoside (42)

To a solution of **20** (0.100 g, 0.173 mmol) in dry acetone (1.721 mL) were added K_2CO_3 (0.052 g, 0.33 mmol) and 2,2,2-trifluoro-N-phenylacetimidoyl chloride (0.067 mL, 0.25 mmol). The reaction was monitored through TLC (Tol/EtOAc 8:2, visualized H_2SO_4). The suspension was kept stirring for 16 hours and then filtered on celite and the solvent evaporated under reduced pressure. The crude was purified by flash column chromatography (Tol/EtOAc 9:1) to obtain the product as a white powder with a yield of 77% (0.100 g). The activated hemiacetal **41** was dissolved in dry DCM (2.6 mL). Acceptor Y (0.088 g, 0.19 mmol) and 4 Å MS (0.100 g) were added. The solution was kept stirring for 1 hour and then was cooled at 0 °C and TMSOTf (2.353 µL) was added. The solution was kept stirring at 0 °C for 1 hour. The reaction was monitored through TLC (Tol/EtOAc 8:2, visualized H_2SO_4). At the disappearance of the donor, NEt_3 was added (1 mL), the solution was filtered and the solvent was evaporated under reduced pressure. The crude was purified by flash column chromatography (Tol/EtOAc 9:1) as a colorless oil.

Yield= 75% (0.101 g)

^{1}H NMR (400 MHz, $CDCl_3$) δ (ppm): 7.93 – 7.85 (m, 2H, ArH of benzoyl group), 7.67 – 7.56 (m, 1H, ArH of benzoyl group), 7.47 – 7.13 (m, 27H, ArH of benzylidene, benzoyl and benzyl groups), 5.79 (ddt, *J* = 17.3, 10.5, 5.6 Hz, 1H, C*H*=CH_2), 5.53 (s, 1H, C*H* of benzylidene), 5.37 (dd, *J* = 4.3, 1.9 Hz, 1H, H-2), 5.30 (d, *J* = 1.9 Hz, 1H, H-1), 5.24 (dq, J = 17.2, 1.6 Hz, 1H, allyl CH_2), 5.15 (dq, *J* = 10.4, 1.4 Hz, 1H, allyl CH_2), 4.87 (d, *J* = 11.3 Hz, 1H, OCH_2Ph), 4.66 (d, J = 11.3 Hz, 1H, OCH_2Ph), 4.60 – 4.34 (m, 9H, H-5+H-1'+H-6a'+H-6b'+H-3'+2 OCH_2Ph), 4.23 (ddt, *J* = 12.8, 5.3, 1.5 Hz, 1H, CH=C*H*H), 4.10 (dt, J = 6.3, 3.6 Hz, 1H, H-6), 3.92 (ddt, *J* = 12.7, 5.9, 1.4 Hz, 1H, CH=CH*H*), 3.86 (dd, *J* = 8.7, 3.0 Hz, 1H, H-4), 3.84 – 3.69 (m, 3H, H-4' +H-7ab), 3.66 (t, *J* = 3.7 Hz, 1H, H-3), 3.44 (s, 4H, H-2'+OCH_3).

^{13}C NMR (101 MHz, $CDCl_3$) δ (ppm): 165.0, 161.9, 138.7, 138.2, 137.9, 137.0, 133.4, 133.3, 129.8, 129.7, 129.6, 129.0, 128.8, 128.4, 128.4, 128.4, 128.3, 128.2, 128.1, 128.1, 128.0, 127.7, 127.6, 125.9, 125.3, 117.6, 101.1, 99.8, 97.8, 93.9, 82.2, 77.9, 77.2, 75.1, 73.4, 73.0, 72.9, 72.0, 70.7, 69.5, 68.7, 65.6, 58.0.

HRMS (ESI-TOF) m/z: calc 1033.39, found: 1051.70 $[M+NH_4]^+$

Allyl(4,6,7-tri-O-benzyl-3-O-methyl-D-glycero-α-D-altro-heptopyranosyl)-(1→3)-4,6-O-benzylidiene-2-deoxy-2-trichloroacetamido-β-D-glucopyranoside (43)

To a solution of 42 (0.140 g, 0.14 mmol) in MeOH (2.000 mL) was added 24% sodium methoxide in methanol (0.092 mL, 0.41 mmol). The reaction was monitored through TLC (Tol/EtOAc 8:2, visualized H_2SO_4). The solution was kept stirring for 45 minutes and then Amberlite IR-120 (H^+) was added. The solution was kept stirring until pH=7 and filtrate. The solution was evaporated under reduced pressure and the crude was purified by flash column chromatography (Tol/EtOAc 8:2) to obtain the product as a white solid.

Yield=93% (0.118 g)

^{1}H NMR (400 MHz, $CDCl_3$) δ (ppm): 7.51 – 7.12 (m, 20H, ArH of benzyl and benzylidene groups), 5.85 (dddd, *J* = 17.2, 10.4, 6.1, 5.2 Hz, 1H, C*H*=CH_2), 5.58 (s, 1H, C*H* of benzylidene), 5.29 (dq, *J* = 17.2, 1.6 Hz, 1H, allyl CH_2), 5.19 (dq, *J* = 10.4, 1.4 Hz, 1H, allyl CH_2), 4.87 (d, *J* = 5.6 Hz, 1H, H-1), 4.79 (d, *J* = 8.3 Hz, 1H, H-1'), 4.69 (d, *J* = 11.6 Hz, 1H, OCH_2Ph), 4.55 (s, 4H, 2 OCH_2Ph), 4.51 – 4.26 (m, 5H, OCH_2Ph+H-3'+H-6ab'+H-5), 4.05 (ddt, *J* = 12.8, 6.2, 1.4 Hz, 1H, CH=C*H*H), 3.98 – 3.87 (m, 2H, H-2+H-4), 3.87 – 3.55 (m, 6H, CH=C*H*H+H-2'+H-5'+H-6+H-7ab), 3.42 (td, *J* = 9.9, 5.1 Hz, 1H, H-4'), 3.31 (dd, *J* = 8.3, 3.3 Hz, 1H, H-3), 3.21 (s, 3H, OCH_3), 2.19 (d, *J* = 2.9 Hz, 1H, OH).

^{13}C NMR (101 MHz, $CDCl_3$) δ (ppm): 138.2, 138.1, 137.8, 137.1, 133.4, 129.0, 128.5, 128.5, 128.3, 128.3, 128.0, 127.8, 127.7, 127.6, 126.0, 118.0, 101.3, 100.9, 99.5, 81.6, 79.0, 77.2, 76.4, 73.5, 73.2, 72.4, 71.4, 71.0, 70.7, 69.9, 69.8, 68.7, 66.0, 58.0, 57.3.

HRMS (ESI-TOF) m/z: calc 929.28, found: 946.65 $[M+NH_4]^+$

Allyl(2-O-benzoyl-3-O-(2-napthylmethyl)-4,6-O-di-tert-butylsilylene-α-D-galactopyranosyl)-(1→2)-(4,6,7-tri-O-benzyl-3-O-methyl-D-glycero-α-D-altro-heptopyranosyl)-(1→3)-4,6-O-benzylidiene-2-deoxy-2-trichloroacetamido-β-D-glucopyranoside (18)

To a solution of **43** (0.118 g, 0.131 mmol) and donor **19** (0.109 g, 0.172 mmol) in dry DCM (4.2 mL) was added 4 Å MS (0.100 g). The solution was kept stirring for 1 hour at rt, then was cooled at 0 °C. NIS (0.066 g, 0.291 mmol) and triflic acid (3.614 µL, 0.040 mmol) were added. The reaction was monitored through TLC (Tol/EtOAc 8:2, visualized H_2SO_4) and kept stirring for 2 hours at rt. At the end of the reaction, NEt_3 was added (1 mL), and the solution was filtered and diluted with DCM (5 mL). The solution was washed with a saturated sodium thiosulfate solution (10 mL), and brine (10 mL), the organic phase was dried with Na_2SO_4, and the solvent was evaporated under reduced

pressure. The crude was purified by flash column chromatography (Tol/EtOAc 9:1) to obtain the product as a yellow oil.

Yield=17% (0.033 mg)

^{1}H NMR (400 MHz, $CDCl_3$) δ (ppm): 8.32 – 6.76 (m, 35H, ArH of naphtyl, benzyl, benzoyl and benzylidene groups), 5.78 (ddt, *J* = 17.3, 10.8, 5.5 Hz, 1H, C*H*=CH_2), 5.51 – 5.42 (m, 2H, H-1, H-2''), 5.40 (s, 1H, CHPh), 5.24 (dq, *J* = 17.2, 1.6 Hz, 1H, allyl CH_2), 5.18 – 5.11 (m, 2H, allyl CH_2+H-1'), 4.89 – 4.62 (m, 3H, OCH_2Ph+H-6a''), 4.54-4.27 (m, 8H, H-6b''+H-3'+H-6ab'+H-5+H-1''+H-6+H-3'', H-5''), 4.22 (ddt, J = 12.7, 5.3, 1.5 Hz, 1H, CH=C*H*H), 4.14 (d, *J* = 11.7 Hz, 1H, OCH_2), 3.98 (dd, *J* = 5.0, 2.7 Hz, 1H, H-4), 3.96 – 3.55 (m, 12H, CH=C*H*H+H-2+H-7ab+ OCH_2Ph, H-2'+H-5'), 3.50 (m, 1H, H-4'), 3.39 (m, 2H, H-3, H-4''), 3.07 (s, 3H, OCH_3), 1.21 – 1.01 (m, 18H, tBu).

^{13}C NMR (101 MHz, $CDCl_3$) δ (ppm): 165.9, 161.9, 138.6, 138.2, 137.1, 136.1, 133.3, 133.3, 133.0, 130.1, 129.8, 129.0, 128.5, 128.4, 128.4, 128.2, 128.1, 128.1, 127.8, 127.7, 127.5, 127.3, 126.1, 126.0, 125.9, 125.5, 125.3, 117.6, 101.2, 100.2, 99.0, 96.3, 82.5, 75.4, 73.3, 72.6, 72.4, 72.0, 71.0, 70.8, 70.6, 70.4, 70.2, 70.1, 68.8, 67.7, 66.5, 57.7, 53.4, 27.7, 27.3, 23.4, 21.5, 20.7.

HRMS (ESI-TOF) m/z: calc 1476.01, found: 1494.53 $[M+NH_4]^+$

5. Bibliography

(1) Varki, A. Biological Roles of Glycans. *Glycobiology* **2017**, *27* (1), 3–49. https://doi.org/10.1093/glycob/cww086.

(2) Hilleman, M. R. Vaccines in Historic Evolution and Perspective: A Narrative of Vaccine Discoveries. *Vaccine* **2000**, *18* (15), 1436–1447. https://doi.org/10.1016/S0264-410X(99)00434-X.

(3) Karch, C. P.; Burkhard, P. Vaccine Technologies: From Whole Organisms to Rationally Designed Protein Assemblies. *Biochemical Pharmacology* **2016**, *120*, 1–14. https://doi.org/10.1016/j.bcp.2016.05.001.

(4) Skwarczynski, M.; Toth, I. Recent Advances in Peptide-Based Subunit Nanovaccines. *Nanomed.* **2014**, *9* (17), 2657–2669. https://doi.org/10.2217/nnm.14.187.

(5) Hajighahramani, N.; Nezafat, N.; Eslami, M.; Negahdaripour, M.; Rahmatabadi, S. S.; Ghasemi, Y. Immunoinformatics Analysis and in Silico Designing of a Novel Multi-Epitope Peptide Vaccine against Staphylococcus Aureus. *Infections, Genetics and Evolution* **2017**, *48*, 83–94. https://doi.org/10.1016/j.meegid.2016.12.010.

(6) Heidelberger, M.; Avery, O. T. THE SOLUBLE SPECIFIC SUBSTANCE OF PNEUMOCOCCUS. *Journal of the Experimental Medicine* **1923**, *38* (1), 73–79. https://doi.org/10.1084/jem.38.1.73.

(7) Avci, F. Y.; Kasper, D. L. How Bacterial Carbohydrates Influence the Adaptive Immune System. *Annual Review of Immunology* **2010**, *28* (1), 107–130. https://doi.org/10.1146/annurev-immunol-030409-101159.

(8) Adamo, R.; Nilo, A.; Castagner, B.; Boutureira, O.; Berti, F.; Bernardes, G. J. L. Synthetically Defined Glycoprotein Vaccines: Current Status and Future Directions. *Chemical Science* **2013**, *4* (8), 2995–3008. https://doi.org/10.1039/C3SC50862E.

(9) Brubaker, S. W.; Bonham, K. S.; Zanoni, I.; Kagan, J. C. Innate Immune Pattern Recognition: A Cell Biological Perspective. *Annual Review of Immunology* **2015**, *33*, 257–290. https://doi.org/10.1146/annurev-immunol-032414-112240.

(10) Varki, A. Since There Are PAMPs and DAMPs, There Must Be SAMPs? Glycan "Self-Associated Molecular Patterns" Dampen Innate Immunity, but Pathogens Can Mimic Them. *Glycobiology* **2011**, *21* (9), 1121–1124. https://doi.org/10.1093/glycob/cwr087.

(11) Iwasaki, A.; Medzhitov, R. Regulation of Adaptive Immunity by the Innate Immune System. *Science* **2010**, *327* (5963), 291–295. https://doi.org/10.1126/science.1183021.

(12) Dranoff, G. Cytokines in Cancer Pathogenesis and Cancer Therapy. *Nature Review Cancer* **2004**, *4* (1), 11–22. https://doi.org/10.1038/nrc1252.

(13) Lynn, G. M.; Sedlik, C.; Baharom, F.; Zhu, Y.; Ramirez-Valdez, R. A.; Coble, V. L.; Tobin, K.; Nichols, S. R.; Itzkowitz, Y.; Zaidi, N.; Gammon, J. M.; Blobel, N. J.; Denizeau, J.; de la Rochere, P.; Francica, B. J.; Decker, B.; Maciejewski, M.; Cheung, J.; Yamane, H.; Smelkinson, M. G.; Francica, J. R.; Laga, R.; Bernstock, J. D.; Seymour, L. W.; Drake, C. G.; Jewell, C. M.; Lantz, O.; Piaggio, E.; Ishizuka, A. S.; Seder, R. A. Peptide–TLR-7/8a Conjugate Vaccines Chemically Programmed for Nanoparticle Self-Assembly Enhance CD8 T-Cell Immunity to Tumor Antigens. *Nature Biotechnology* **2020**, *38* (3), 320–332. https://doi.org/10.1038/s41587-019-0390-x.

(14) Qian, C.; Cao, X. Dendritic Cells in the Regulation of Immunity and Inflammation. *Seminars in Immunology* **2018**, *35*, 3–11. https://doi.org/10.1016/j.smim.2017.12.002.

(15) Rappuoli, R. Glycoconjugate Vaccines: Principles and Mechanisms. *Science Translation Medicine* **2018**, *10* (456), eaat4615. https://doi.org/10.1126/scitranslmed.aat4615.

(16) Mesin, L.; Ersching, J.; Victora, G. D. Germinal Center B Cell Dynamics. *Immunity* **2016**, *45* (3), 471–482. https://doi.org/10.1016/j.immuni.2016.09.001.

(17) Avci, F. Y.; Li, X.; Tsuji, M.; Kasper, D. L. A Mechanism for Glycoconjugate Vaccine Activation of the Adaptive Immune System and Its Implications for Vaccine Design. *Nature Medicine* **2011**, *17* (12), 1602–1609. https://doi.org/10.1038/nm.2535.

(18) Rohokale, R.; Guo, Z. Development in the Concept of Bacterial Polysaccharide Repeating Unit-Based Antibacterial Conjugate Vaccines. *ACS Infectious Disease* **2023**, *9* (2), 178–212. https://doi.org/10.1021/acsinfecdis.2c00559.

(19) Verez-Bencomo, V.; Fernández-Santana, V.; Hardy, E.; Toledo, M. E.; Rodríguez, M. C.; Heynngnezz, L.; Rodriguez, A.; Baly, A.; Herrera, L.; Izquierdo, M.; Villar, A.; Valdés, Y.; Cosme, K.; Deler, M. L.; Montane, M.; Garcia, E.; Ramos, A.; Aguilar, A.; Medina, E.; Toraño, G.; Sosa, I.; Hernandez, I.; Martínez, R.; Muzachio, A.; Carmenates, A.; Costa, L.; Cardoso, F.; Campa, C.; Diaz, M.; Roy, R. A Synthetic Conjugate Polysaccharide Vaccine Against Haemophilus Influenzae Type b. *Science* **2004**, *305* (5683), 522–525. https://doi.org/10.1126/science.1095209.

(20) Colombo, C.; Pitirollo, O.; Lay, L. Recent Advances in the Synthesis of Glycoconjugates for Vaccine Development. *Molecules* **2018**, *23* (7), 1712. https://doi.org/10.3390/molecules23071712.

(21) Jones, C. Vaccines Based on the Cell Surface Carbohydrates of Pathogenic Bacteria. *Anais da Academia Brasileira de Ciências* **2005**, *77* (2), 293–324. https://doi.org/10.1590/s0001-37652005000200009.

(22) Liao, G.; Zhou, Z.; Suryawanshi, S.; Mondal, M. A.; Guo, Z. Fully Synthetic Self-Adjuvanting α-2,9-Oligosialic Acid Based Conjugate Vaccines against Group C Meningitis. *ACS Central Science* **2016**, *2* (4), 210–218. https://doi.org/10.1021/acscentsci.5b00364.

(23) Del Bino, L.; Østerlid, K. E.; Wu, D.-Y.; Nonne, F.; Romano, M. R.; Codée, J.; Adamo, R. Synthetic Glycans to Improve Current Glycoconjugate Vaccines and Fight Antimicrobial Resistance. *Chemical Review* **2022**, *122* (20), 15672–15716. https://doi.org/10.1021/acs.chemrev.2c00021.

(24) Hendrickx, A. P. A.; Budzik, J. M.; Oh, S.-Y.; Schneewind, O. Architects at the Bacterial Surface — Sortases and the Assembly of Pili with Isopeptide Bonds. *Nature Review Microbiology* **2011**, *9* (3), 166–176. https://doi.org/10.1038/nrmicro2520.

(25) Taylor, C. M.; Roberts, I. S. Capsular Polysaccharides and Their Role in Virulence. *Contribution to Microbiology* **2005**, *12*, 55–66. https://doi.org/10.1159/000081689.

(26) Doron, S.; Gorbach, S. L. Bacterial Infections: Overview. In *International Encyclopedia of Public Health*; Heggenhougen, H. K. (Kris), Ed.; Academic Press: Oxford, 2008; pp 273–282. https://doi.org/10.1016/B978-012373960-5.00596-7.

(27) Geno, K. A.; Gilbert, G. L.; Song, J. Y.; Skovsted, I. C.; Klugman, K. P.; Jones, C.; Konradsen, H. B.; Nahm, M. H. Pneumococcal Capsules and Their Types: Past, Present, and Future. *Clinical Microbiology Review* **2015**, *28* (3), 871–899. https://doi.org/10.1128/CMR.00024-15.

(28) Miyaji, E. N.; Oliveira, M. L. S.; Carvalho, E.; Ho, P. L. Serotype-Independent Pneumococcal Vaccines. *Cellular and Molecular Life Science CMLS* **2013**, *70* (18), 3303–3326. https://doi.org/10.1007/s00018-012-1234-8.

(29) Gray, B. M.; Converse, G. M.; Dillon, H. C. Serotypes of Streptococcus Pneumoniae Causing Disease. *Journal of Infectious Disease* **1979**, *140* (6), 979–983. https://doi.org/10.1093/infdis/140.6.979.

(30) Trotter, C. L.; Waight, P.; Andrews, N. J.; Slack, M.; Efstratiou, A.; George, R.; Miller, E. Epidemiology of Invasive Pneumococcal Disease in the Pre-Conjugate Vaccine Era: England and Wales, 1996-2006. *Journal of Infection* **2010**, *60* (3), 200–208. https://doi.org/10.1016/j.jinf.2009.12.008.

(31) Pelton, S. I.; Loughlin, A. M.; Marchant, C. D. Seven Valent Pneumococcal Conjugate Vaccine Immunization in Two Boston Communities: Changes in Serotypes and Antimicrobial Susceptibility among Streptococcus Pneumoniae Isolates. *Pediatric Infectious Disease Journal* **2004**, *23* (11), 1015–1022. https://doi.org/10.1097/01.inf.0000143645.58215.f0.

(32) Seeberger, P. H.; Pereira, C. L.; Govindan, S. Total Synthesis of a Streptococcus Pneumoniae Serotype 12F CPS Repeating Unit Hexasaccharide. *Beilstein Journal of Organic Chemistry* **2017**, *13*, 164–173. https://doi.org/10.3762/bjoc.13.19.

(33) GBD 2013 Mortality and Causes of Death Collaborators. Global, Regional, and National Age-Sex Specific All-Cause and Cause-Specific Mortality for 240 Causes of Death, 1990-2013: A Systematic Analysis for the Global Burden of Disease Study 2013. *Lancet London England.* **2015**, *385* (9963), 117–171. https://doi.org/10.1016/S0140-6736(14)61682-2.

(34) Platts-Mills, J. A.; Liu, J.; Rogawski, E. T.; Kabir, F.; Lertsethtakarn, P.; Siguas, M.; Khan, S. S.; Praharaj, I.; Murei, A.; Nshama, R.; Mujaga, B.; Havt, A.; Maciel, I. A.; McMurry, T. L.; Operario, D. J.; Taniuchi, M.; Gratz, J.; Stroup, S. E.; Roberts, J. H.; Kalam, A.; Aziz, F.; Qureshi, S.; Islam, M. O.; Sakpaisal, P.; Silapong, S.; Yori, P. P.; Rajendiran, R.; Benny, B.; McGrath, M.; McCormick, B. J. J.; Seidman, J. C.; Lang, D.; Gottlieb, M.; Guerrant, R. L.; Lima, A. A. M.; Leite, J. P.; Samie, A.; Bessong, P. O.; Page, N.; Bodhidatta, L.; Mason, C.; Shrestha, S.; Kiwelu, I.; Mduma, E. R.; Iqbal, N. T.; Bhutta, Z. A.; Ahmed, T.; Haque, R.; Kang, G.; Kosek, M. N.; Houpt, E. R.; Acosta, A. M.; Burga, R. R. de; Chavez, C. B.; Flores, J. T.; Olotegui, M. P.; Pinedo, S. R.; Trigoso, D. R.; Vasquez, A. O.; Ahmed, I.; Alam, D.; Ali, A.; Rasheed, M.; Soofi, S.; Turab, A.; Yousafzai, A.; Zaidi, A. K.; Shrestha, B.; Rayamajhi, B. B.;

Strand, T.; Ammu, G.; Babji, S.; Bose, A.; George, A. T.; Hariraju, D.; Jennifer, M. S.; John, S.; Kaki, S.; Karunakaran, P.; Koshy, B.; Lazarus, R. P.; Muliyil, J.; Ragasudha, P.; Raghava, M. V.; Raju, S.; Ramachandran, A.; Ramadas, R.; Ramanujam, K.; Rose, A.; Roshan, R.; Sharma, S. L.; Sundaram, S.; Thomas, R. J.; Pan, W. K.; Ambikapathi, R.; Carreon, J. D.; Doan, V.; Hoest, C.; Knobler, S.; Miller, M. A.; Psaki, S.; Rasmussen, Z.; Richard, S. A.; Tountas, K. H.; Svensen, E.; Amour, C.; Bayyo, E.; Mvungi, R.; Pascal, J.; Yarrot, L.; Barrett, L.; Dillingham, R.; Petri, W. A.; Scharf, R.; Ahmed, A. S.; Alam, M. A.; Haque, U.; Hossain, M. I.; Islam, M.; Mahfuz, M.; Mondal, D.; Nahar, B.; Tofail, F.; Chandyo, R. K.; Shrestha, P. S.; Shrestha, R.; Ulak, M.; Bauck, A.; Black, R.; Caulfield, L.; Checkley, W.; Lee, G.; Schulze, K.; Scott, S.; Murray-Kolb, L. E.; Ross, A. C.; Schaefer, B.; Simons, S.; Pendergast, L.; Abreu, C. B.; Costa, H.; Moura, A. D.; Filho, J. Q.; Leite, Á. M.; Lima, N. L.; Lima, I. F.; Maciel, B. L.; Medeiros, P. H.; Moraes, M.; Mota, F. S.; Oriá, R. B.; Quetz, J.; Soares, A. M.; Mota, R. M.; Patil, C. L.; Mahopo, C.; Maphula, A.; Nyathi, E. Use of Quantitative Molecular Diagnostic Methods to Assess the Aetiology, Burden, and Clinical Characteristics of Diarrhoea in Children in Low-Resource Settings: A Reanalysis of the MAL-ED Cohort Study. *Lancet Global Health* **2018**, *6* (12), e1309–e1318. https://doi.org/10.1016/S2214-109X(18)30349-8.

(35) Hoffmann, S.; Batz, M. B.; Morris, J. G. Annual Cost of Illness and Quality-Adjusted Life Year Losses in the United States Due to 14 Foodborne Pathogens††The Views Expressed Herein Are Those of the Authors and Do Not Necessarily Reflect the Views of the Economic Research Service or the U.S. Department of Agriculture. *Journal of Food Protection* **2012**, *75* (7), 1292–1302. https://doi.org/10.4315/0362-028X.JFP-11-417.

(36) Kuwabara, S.; Yuki, N. Axonal Guillain-Barré Syndrome: Concepts and Controversies. *Lancet Neurology* **2013**, *12* (12), 1180–1188. https://doi.org/10.1016/S1474-4422(13)70215-1.

(37) Perera, V. N.; Nachamkin, I.; Ung, H.; Patterson, J. H.; McConville, M. J.; Coloe, P. J.; Fry, B. N. Molecular Mimicry in Campylobacter Jejuni: Role of the Lipo-Oligosaccharide Core Oligosaccharide in Inducing Anti-Ganglioside Antibodies. *FEMS Immunology and Medical Microbiology* **2007**, *50* (1), 27–36. https://doi.org/10.1111/j.1574-695X.2007.00225.x.

(38) Thota, V. N.; Ferguson, M. J.; Sweeney, R. P.; Lowary, T. L. Synthesis of the Campylobacter Jejuni 81-176 Strain Capsular Polysaccharide Repeating Unit Reveals the Absolute Configuration of Its O-Methyl Phosphoramidate Motif. *Angewandte Chemie International Edition* **2018**, *130* (47), 15818–15822. https://doi.org/10.1002/ange.201810222.

(39) Cloutier, M.; Gauthier, C. Progress toward the Development of Glycan-Based Vaccines against Campylobacteriosis. *ACS Infectious Disease* **2021**, *7* (5), 969–986. https://doi.org/10.1021/acsinfecdis.0c00332.

(40) Monteiro, M. A.; Baqar, S.; Hall, E. R.; Chen, Y.-H.; Porter, C. K.; Bentzel, D. E.; Applebee, L.; Guerry, P. Capsule Polysaccharide Conjugate Vaccine against Diarrheal Disease Caused by Campylobacter Jejuni. *Infection and Immunity* **2009**, *77* (3), 1128–1136. https://doi.org/10.1128/IAI.01056-08.

(41) Jagusztyn-Krynicka, E. K.; Łaniewski, P.; Wyszyńska, A. Update on Campylobacter Jejuni Vaccine Development for Preventing Human Campylobacteriosis. *Expert Review Vaccines* **2009**, *8* (5), 625–645. https://doi.org/10.1586/erv.09.21.

(42) Lundquist, J. J.; Toone, E. J. The Cluster Glycoside Effect. *Chemical Review* **2002**, *102* (2), 555–578. https://doi.org/10.1021/cr000418f.

(43) Geraci, C.; Consoli, G. M. L.; Galante, E.; Bousquet, E.; Pappalardo, M.; Spadaro, A. Calix[4]Arene Decorated with Four Tn Antigen Glycomimetic Units and P3CS Immunoadjuvant: Synthesis, Characterization, and Anticancer Immunological Evaluation. *Bioconjugate Chemistry* **2008**, *19* (3), 751–758. https://doi.org/10.1021/bc700411w.

(44) Giuliani, M.; Faroldi, F.; Morelli, L.; Torre, E.; Lombardi, G.; Fallarini, S.; Sansone, F.; Compostella, F. Exploring Calixarene-Based Clusters for Efficient Functional Presentation of Streptococcus Pneumoniae Saccharides. *Bioorganic Chemistry* **2019**, *93*, 103305. https://doi.org/10.1016/j.bioorg.2019.103305.

(45) da Silva Neto, L.; da Silva Maia, A. F.; Godin, A. M.; de Almeida Augusto, P. S.; Pereira, R. L. G.; Caligiorne, S. M.; Alves, R. B.; Fernandes, S. O. A.; Cardoso, V. N.; Goulart, G. A. C.; Martins, F. T.; das Neves, M. de C. L.; Garcia, F. D.; de Fátima, Â. Calix[n]Arene-Based Immunogens: A New Non-Proteic Strategy for Anti-Cocaine Vaccine. *Journal of Advanced Research* **2022**, *38*, 285–298. https://doi.org/10.1016/j.jare.2021.09.003.

(46) Legnani, L.; Ronchi, S.; Fallarini, S.; Lombardi, G.; Campo, F.; Panza, L.; Lay, L.; Poletti, L.; Toma, L.; Ronchetti, F.; Compostella, F. Synthesis, Molecular Dynamics Simulations, and Biology of a Carba-Analogue of the Trisaccharide Repeating Unit of Streptococcus pneumoniae19F Capsular Polysaccharide. *Organic and Biomolecular Chemistry* **2009**, *7* (21), 4428–4436. https://doi.org/10.1039/B911323A.

(47) Zemplén Deacetylation. In *Comprehensive Organic Name Reactions and Reagents*; John Wiley & Sons, Ltd, 2010; pp 3123–3128. https://doi.org/10.1002/9780470638859.conrr691.

(48) Benito, J. M.; Mellet, C. O.; Sadalapure, K.; Lindhorst, T. K.; Defaye, J.; García Fernández, J. M. Synthesis and Anomeric Stability of (1→6)-Thiourea-Linked Pseudooligosaccharides. *Carbohydrates Research* **1999**, *320* (1), 37–48. https://doi.org/10.1016/S0008-6215(99)00141-X.

(49) Joosten, J. A. F.; Loimaranta, V.; Appeldoorn, C. C. M.; Haataja, S.; El Maate, F. A.; Liskamp, R. M. J.; Finne, J.; Pieters, R. J. Inhibition of Streptococcus Suis Adhesion by Dendritic Galabiose Compounds at Low Nanomolar Concentration. *Journal of Medicinal Chemistry* **2004**, *47* (26), 6499–6508. https://doi.org/10.1021/jm049476+.

(50) Szekely, T.; Roy, O.; Dériaud, E.; Job, A.; Lo-Man, R.; Leclerc, C.; Taillefumier, C. Design, Synthesis, and Immunological Evaluation of a Multicomponent Construct Based on a Glycotripeptoid Core Comprising B and T Cell Epitopes and a Toll-like Receptor 7 Agonist That Elicits Potent Immune Responses. *Journal of Medicinal Chemistry* **2018**, *61* (21), 9568–9582. https://doi.org/10.1021/acs.jmedchem.8b00960.

(51) Verschueren, R. H.; Gilles, P.; Mileghem, S. V.; Borggraeve, W. M. D. Solvent-Free N-Boc Deprotection by Ex Situ Generation of Hydrogen Chloride Gas. *Organic and Biomolecular Chemistry* **2021**, *19* (26), 5782–5787. https://doi.org/10.1039/D1OB00728A.

(52) van der Put, R. M. F.; Smitsman, C.; de Haan, A.; Hamzink, M.; Timmermans, H.; Uittenbogaard, J.; Westdijk, J.; Stork, M.; Ophorst, O.; Thouron, F.; Guerreiro, C.; Sansonetti, P. J.; Phalipon, A.; Mulard, L. A. The First-in-Human Synthetic Glycan-Based Conjugate Vaccine Candidate against Shigella. *ACS Central Science.* **2022**, *8* (4), 449–460. https://doi.org/10.1021/acscentsci.1c01479.

(53) Bélot, F.; Guerreiro, C.; Baleux, F.; Mulard, L. A. Synthesis of Two Linear PADRE Conjugates Bearing a Deca- or Pentadecasaccharide B Epitope as Potential Synthetic Vaccines against Shigella Flexneri Serotype 2a Infection. *Chemistry –An European Journal* **2005**, *11* (5), 1625–1635. https://doi.org/10.1002/chem.200400903.

(54) Meron-Sudai, S.; Asato, V.; Adler, A.; Bialik, A.; Goren, S.; Ariel-Cohen, O.; Reizis, A.; Mulard, L. A.; Phalipon, A.; Cohen, D. A Shigella Flexneri 2a Synthetic Glycan-Based Vaccine Induces a Long-Lasting Immune Response in Adults. *Npj Vaccines* **2023**, *8* (1), 1–10. https://doi.org/10.1038/s41541-023-00624-y.

(55) van der Put, R. M. F.; Kim, T. H.; Guerreiro, C.; Thouron, F.; Hoogerhout, P.; Sansonetti, P. J.; Westdijk, J.; Stork, M.; Phalipon, A.; Mulard, L. A. A Synthetic Carbohydrate Conjugate Vaccine Candidate against Shigellosis: Improved Bioconjugation and Impact of Alum on Immunogenicity. *Bioconjugate Chemistry* **2016**, *27* (4), 883–892. https://doi.org/10.1021/acs.bioconjchem.5b00617.

(56) Hu, Z.; Bongat White, A. F.; Mulard, L. A. Efficient Iterative Synthesis of O-Acetylated Tri- to Pentadecasaccharides Related to the Lipopolysaccharide of Shigella Flexneri Type 3 a through Di- and Trisaccharide Glycosyl Donors. *Chemistry – An Asian Journal* **2017**, *12* (4), 419–439. https://doi.org/10.1002/asia.201600819.

(57) Hada, N.; Umeda, Y.; Kumada, H.; Shimazaki, Y.; Yamano, K.; Schweizer, F.; Oshima, N.; Takeda, T.; Kiuchi, F. Synthesis of the Non-Reducing End Oligosaccharides of Glycosphingolipids from *Ascaris Suum*. *Chemical and Pharmaceutical Bulletin (Tokyo)* **2019**, *67* (2), 143–154. https://doi.org/10.1248/cpb.c18-00768.

(58) Yun, M.; Nam Shin, J. E. Synthesis of the 2′-Azidoethyl Trisaccharide, 6d-altroHepp-GlcNAc-Gal Hapten, an O-Antigenic Repeating Unit of Campylobacter Jejuni Serotypes O:23 and O:36. *Bulletin of Korean Chemical Society* **2008**, *29* (7), 1315–1319. https://doi.org/10.5012/bkcs.2008.29.7.1315.

(59) Yun, M.; Yoon, S.; Shin, Y.; Keun, H. C.; Nam Shin, J. E. Synthesis of 2′-Azidoethyl Trisaccharide, α-D-Gal-(1→2)- 6d-α-D-Altro-Hepp-(1→3)-β-D-GlcNAc, an O-Antigenic Repeating Unit of C. Jejuni O:23 and O:36. *Archives of Pharmacal Research* **2004**, *27* (2), 143–150. https://doi.org/10.1007/BF02980097.

(60) Dhara, D.; Mulard, L. A.; Hollenstein, M. Expedient Synthesis of L-Heptose Derived Septacidin Building Blocks from l-Glucose. *Carbohydrates Research* **2023**, *534*, 108985. https://doi.org/10.1016/j.carres.2023.108985.

(61) Sokolov, V. M.; Zakharov, V. I.; Studentsov, E. P. Stereoselectivity of Reactions at the Glycoside Center of Carbohydrates: VII. Synthesis of Aryl α- and -β-D-Glucopyranosides by Helferich, Catalyzed by Boron Trifluoride Etherate. *Russian Journal of General Chemistry* **2002**, *72* (5), 806–811. https://doi.org/10.1023/A:1019532924135.

(62) Zhang, L.; Xu, P.; Liu, B.; Yu, B. Chemical Synthesis of Fucosylated Chondroitin Sulfate Oligosaccharides. *Journal of Organic Chemistry* **2020**, *85* (24), 15908–15919. https://doi.org/10.1021/acs.joc.0c01009.

(63) Ohlin, M.; Johnsson, R.; Ellervik, U. Regioselective Reductive Openings of 4,6-Benzylidene Acetals: Synthetic and Mechanistic Aspects. *Carbohydrates Research* **2011**, *346* (12), 1358–1370. https://doi.org/10.1016/j.carres.2011.03.032.

(64) Pasetto, P.; Franck, R. W. Synthesis of Both Possible Isomers of the Northwest Quadrant of Altromycin B. *Journal of Organic Chemistry* **2003**, *68* (21), 8042–8060. https://doi.org/10.1021/jo034607k.

(65) Nishiyama, K.; Nakayama, T.; Natsugari, H.; Takahashi, H. Synthesis of Ether-Linked Sugar by Nucleophilic Opening of Carbohydrate Oxiranes. *Synthesis* **2008**, *2008* (23), 3761–3768. https://doi.org/10.1055/s-0028-1083221.

(66) Imamura, A.; Ando, H.; Korogi, S.; Tanabe, G.; Muraoka, O.; Ishida, H.; Kiso, M. Di-Tert-Butylsilylene (DTBS) Group-Directed α-Selective Galactosylation Unaffected by C-2

Participating Functionalities. *Tetrahedron Letters* **2003**, *44* (35), 6725–6728. https://doi.org/10.1016/S0040-4039(03)01647-2.